OCRWM	Scientific Analysis Cover Sheet	1. QA: QA Page 1 of 443

2. Scientific Analyses Title	
Saturated Zone In-Situ Testing	
3. DI (Including Revision Number)	
ANL-NBS-HS-000039, REV 00	
4. Total Attachments	5. Attachment Numbers - Number of pages in each
Not Applicable	Not Applicable

	Printed Name	Signature	Date
6. Originator	P.W. Reimus, M.J. Umari	Paul W. Reimus Amjad M.J. Umari	12/23/03 12/23/03
7. Checker	J. Turin, E. Kalinina		12-23-03
8. QER	K. Gilkerson		12-23-03
9. Responsible Manager/Lead	S.P. Kuzio		12/23/03
10. Responsible Manager	P.R. Dixon		12/23/03

11. Remarks

This scientific analysis report represents a joint effort by the Los Alamos National Laboratory, the U.S. Geological Survey, and the Sandia National Laboratories. In addition to the organizations mentioned above, the field-testing efforts described in this report were supported by Yucca Mountain Project M&O contractors (TRW and BSC), the Nye County Nuclear Waste Repository Project Office, and the U. S. Department of Energy.

Revision History

12. Revision/ICN No.	13. Description of Revision/Change
REV 00	Initial issue.

INTENTIONALLY LEFT BLANK

CONTENTS

CONTENTS (Continued)

Page

CONTENTS (Continued)

Page

CONTENTS (Continued)

CONTENTS (Continued)

Page

INTENTIONALLY LEFT BLANK

FIGURES

Page

FIGURES (Continued)

Page

FIGURES (Continued)

Page

FIGURES (Continued)

Page

FIGURES (Continued)

Page

FIGURES (Continued)

Page

FIGURES (Continued)

Page

FIGURES (Continued)

Page

FIGURES (Continued)

Page

FIGURES (Continued)

Page

TABLES

TABLES (Continued)

TABLES (Continued)

Page

INTENTIONALLY LEFT BLANK

ACRONYMS

1-D	one-dimensional
2-D	two-dimensional
2,6 DFBA	2,6 difluorobenzoic acid or 2,6 difluorobenzoate
3-D	three-dimensional
ACC	accession number
AP	administrative procedure
ATC	Alluvial Testing Complex
BET	Brunauer-Emmet-Teller
BSC	Bechtel/SAIC Company
BTC	breakthrough curve
CDF	cumulative distribution function
CEC	cation exchange capacity
CML	carboxylate-modified latex
CRW	constant-rate withdrawal
CRWMS M&O	Civilian Radioactive Waste Management System Management and Operating Contractor
DFBA	difluorobenzoic acid or difluorobenzoate
DIRS	Document Input Reference System
DOE	U.S. Department of Energy
DTN	data tracking number
EDTA	ethylenediamine tetraacetic acid
EWDP	Early Warning Drilling Program
FBA	fluorinated benzoic acid or fluorinated benzoate
HPLC	high-pressure liquid chromatography
ICP-AES	inductively-coupled-plasma, atomic-emission spectroscopy
KTI	key technical issue
LA	License Application
LANL	Los Alamos National Laboratory
LBNL	Lawrence Berkeley National Laboratory
MTC	mass transfer coefficient (for matrix diffusion)
N/A	not applicable
NC-EWDP	Nye County Early Warning Drilling Program
NRC	U.S. Nuclear Regulatory Commission
NTS	Nevada Test Site
NWRPO	[Nye County] Nuclear Waste Repository Project Office

ACRONYMS (Continued)

OCRWM	Office of Civilian Radioactive Waste Management
PA	performance assessment
PC	personal computer
PDF	probability distribution function
PFBA	pentafluorobenzoic acid or pentafluorobenzoate
PTFE	polytetrafluoroethylene
Pyridone	3-carbamoyl-2-pyridone
Q	qualified
QA	quality assurance
QAP	Quality Assurance Program
RMSE	root-mean-square error
SR	site recommendation
STN	software tracking number
SZ	saturated zone
TBD	to be determined
TeFBA	2,3,4,5 tetrafluorobenzoic acid
TFBA	2,4,5 trifluorobenzoic acid
TSPA	Total Systems Performance Assessment
TSPA-SR	Total Systems Performance Assessment – Site Recommendation
TSPA-LA	Total Systems Performance Assessment – License Application
TWP	Technical Work Plan
USGS	U.S. Geological Survey
UV	ultraviolet
XRD	X-ray diffraction
YMP	Yucca Mountain Project

ABBREVIATIONS

bgs	below ground surface
cm	centimeter
eq	equivalent
ft	feet
g	gram
gal	gallon
gpm	gallons per minute
hr	hour
in	inch
kg	kilogram

ABBREVIATIONS (Continued)

L	liter
m	meter
M	moles per liter
meq	milliequivalent
min	minute
mL	milliliter
mm	millimeter
sec	second
yr	year

There are many wells cited in this scientific analysis report. Table 1 lists the full name of the well and its abbreviation. In general, a well is introduced in the document by its full name but referred to in the remainder of the document by its abbreviation.

Table 1. Wells Discussed in this Scientific Analysis Report and their Abbreviations

Name	Abbreviation
NC-EWDP-4PA, NC-EWDP-4PB	N/A*
NC-EWDP-15P	N/A
NC-EWDP-19D/D1 (19D drilled, then re-drilled as 19D1 with 19D filled with grout below 700 ft where vertical deviation occurred)	19D1
NC-EWDP-19IM1, NC-EWDP-19IM2	19IM1, 19IM2
NC-EWDP-19P	19P
UE-25 b#1	b#1
UE-25 c#1	c#1
UE-25 c#2	c#2
UE-25 c#3	c#3
UE-25 ONC-1	ONC-1
UE-25 p#1	p#1
UE-25 J-13	J-13
UE-25 WT#3	WT#3
UE-25 WT#13	WT#13
UE-25 WT#14	WT#14
UE-25 WT#17	WT#17
USW H-4	H-4
USW WT#1	WT#1
Washburn-1X	N/A

NOTE: *N/A in this table means that an abbreviation is not applicable to a given well in this report.

INTENTIONALLY LEFT BLANK

1. PURPOSE

The purpose of this scientific analysis is to document the results and interpretations of field experiments that have been conducted to test and validate conceptual flow and radionuclide transport models in the saturated zone (SZ) near Yucca Mountain. The test interpretations provide estimates of flow and transport parameters that are used in the development of parameter distributions for Total System Performance Assessment (TSPA) calculations. These parameter distributions are documented in the revisions to the SZ flow model report (BSC 2003 [162649]), the SZ transport model report (BSC 2003 [162419]), the SZ colloid transport report (BSC 2003 [162729]), and the SZ transport model abstraction report (BSC 2003 [164870]). Specifically, this scientific analysis report provides the following information that contributes to the assessment of the capability of the SZ to serve as a barrier for waste isolation for the Yucca Mountain repository system:

- The bases for selection of conceptual flow and transport models in the saturated volcanics and the saturated alluvium located near Yucca Mountain.

- Results and interpretations of hydraulic and tracer tests conducted in saturated fractured volcanics at the C-wells complex near Yucca Mountain. The test interpretations include estimates of hydraulic conductivities, anisotropy in hydraulic conductivity, storativities, total porosities, effective porosities, longitudinal dispersivities, matrix diffusion mass transfer coefficients, matrix diffusion coefficients, fracture apertures, and colloid transport parameters.

- Results and interpretations of hydraulic and tracer tests conducted in saturated alluvium at the Alluvium Testing Complex (ATC), which is located at the southwestern corner of the Nevada Test Site (NTS). The test interpretations include estimates of hydraulic conductivities, storativities, total porosities, effective porosities, longitudinal dispersivities, matrix diffusion mass transfer coefficients, and colloid transport parameters.

- Comparisons of sorption parameter estimates for a reactive solute tracer (lithium ion) derived from both the C-wells field tracer tests and laboratory tests using C-wells core samples.

- Sorption parameter estimates for lithium ion derived from laboratory tests using alluvium samples from NC-EWDP-19D1 (one of the wells at the ATC) so that a comparison of laboratory- and field-derived sorption parameters can be made in saturated alluvium if cross-hole tracer tests are conducted at the ATC.

The comparisons between laboratory- and field-derived sorption parameter estimates for lithium ion are used to assess whether sorption parameters determined in the laboratory can be used reliably to predict field-scale transport. Favorable comparisons of lithium-ion sorption will lend credibility to the Yucca Mountain Project's (YMP) use of laboratory-derived radionuclide sorption parameters when modeling field-scale radionuclide transport. The use of laboratory data for radionuclides is necessary because radionuclides cannot be tested in the field.

Saturated-zone geochemistry measurements, including Eh and pH, and water-level measurements are not addressed in this scientific analysis because they can be used directly as inputs (without intermediate analyses) in downstream analysis and model reports. Geochemistry measurements are used extensively in the scientific analysis report *Geochemical and Isotopic Constraints on Groundwater Flow Directions and Magnitudes, Mixing, and Recharge at Yucca Mountain,* ANL-NBS-HS-000021, (BSC 2003 [162657], Section 6) to delineate flow pathways; Eh and pH measurements are factored into the development of radionuclide K_d distributions in Attachment I of the model report *Site-Scale Saturated Zone Transport,* MDL-NBS-HS-000010, (BSC 2003 [162419]) and in the model report *Radionuclide Transport Models Under Ambient Conditions,* MDL-NBS-HS-000008, (BSC 2003 [163228]); and water-level measurements are used as calibration targets in the model report *Site-Scale Saturated Zone Flow Model,* MDL-NBS-HS-000011, (BSC 2003 [162649]).

The work activities in this scientific analysis are governed by the work direction and planning document *Technical Work Plan for: Saturated Zone Flow and Transport Modeling and Testing,* TWP-NBS-MD-000002 (BSC 2003 [166034], Section 2.6), Work Package ASZM04. The purpose and scope of these activities are to (1) document the basis for conceptual flow and transport models in the SZ, (2) abstract transport parameters derived from SZ field testing for use in TSPA analyses, and (3) assess whether sorption parameters determined in the laboratory can be used reliably to predict field-scale transport.

The field and laboratory testing of the saturated fractured volcanics (e.g., C-wells and associated laboratory tests) were completed prior to preparation of the TWP, so none of the investigations in the fractured volcanics described in this scientific analysis are mentioned in the TWP. Conversely, the TWP mentions some testing activities that are not reported in this analysis report because they were deferred. These deferred activities include cross-hole tracer testing at the ATC involving sorbing tracers and stable-isotope-tagged natural colloids, which is more fully described in BSC (2002 [158198]).

The data and analyses documented in this report will be used as scientific supporting information in other Project reports that are currently under revision, including:

- The SZ flow model report (BSC 2003 [162649])
- The SZ transport model report (BSC 2003 [162419])
- The SZ colloid transport scientific analysis report (BSC 2003 [162729])
- The SZ transport model abstraction report (BSC 2003 [164870]).

A potential limitation of this scientific analysis is that the bases for the conceptual models and the estimates of flow and transport parameters are derived from tests conducted at only one location in the saturated fractured volcanics (C-wells complex) and one location in the saturated alluvium (ATC). The flow and transport characteristics at these locations may not necessarily be representative of the characteristics at other locations along the flow pathway(s) from the repository to the accessible environment. However, to compensate for this potential limitation, several other sources of information are used to develop broader uncertainty distributions for flow and transport parameters in the TSPA analyses than SZ in-situ testing data would indicate.

The development and bases of these distributions are documented in the SZ transport model abstractions report (BSC 2003 [164870]), where it is shown that the overall parameter distributions used in the TSPA analyses include considerations of literature data, expert elicitation input, and peer review input. The only uncertainty distribution presented in this analysis report is one for the north-south/east-west anisotropy ratio of horizontal hydraulic conductivity in the fractured volcanics (Section 6.2.6).

This scientific analysis report does not provide the technical basis for inclusion of any of the SZ features, events, and processes (FEPs). However, SZ FEPs that are included in the Total Systems Performance Assessment for the License Application (TSPA-LA) and supported by the results of this report are listed in Table 6.1-3. The rationale for excluding a FEP from the TSPA-LA model will be given in the report *Features, Events, and Processes in SZ Flow and Transport* REV 02 (BSC 2003 [163128]).

(NOTE: In this report, a unique six-digit numerical identifier (the Document Input Reference System [DIRS] number) is placed in the text following the reference callout (e.g., BSC 2003 [166034]). The purpose of the DIRS numbers is to assist the reader in locating a specific reference in the DIRS database.)

INTENTIONALLY LEFT BLANK

2. QUALITY ASSURANCE

Development of this scientific analysis report and the supporting analyses has been determined to be subject to the Office of Civilian Waste Management (OCRWM) quality assurance (QA) program (BSC 2003 [166034], Section 8), Work Package ASZM04. Approved QA procedures identified in the technical work plan (BSC 2003 [166034], Section 4) have been used to conduct and document the activities described in this scientific analysis report. The technical work plan also identifies the methods used to control the electronic management of data (BSC 2003 [166034], Section 8), and these methods were implemented in the documentation of the activities described in the TWP.

This analysis reports on the saturated zone, which is a natural barrier classified in the *Q-List* (BSC 2003 [165179]) as SC (Safety Category) because it is important to waste isolation, as defined in AP-2.22Q, *Classification Analyses and Maintenance of the Q-List*. The results of this report are important to the demonstration of compliance with the post-closure performance objectives prescribed in 10 CFR 63.113 [156605]. The report contributes to the analysis and modeling data used to support performance assessment; the conclusions do not directly impact engineered features important to safety, as defined in AP-2.22Q.

INTENTIONALLY LEFT BLANK

3. SOFTWARE

3.1 SOFTWARE TRACKED BY CONFIGURATION MANAGEMENT

The computer codes used directly in this scientific analysis are summarized in Table 3-1. The qualification status of the software is indicated in the electronic DIRS database and in the Software Configuration Management System Baseline Report. All software was obtained from Software Configuration Management (SCM) and is appropriate for the application. Qualified codes were used only within the range of validation as required by AP-SI.1Q, *Software Management.*

Table 3-1. Software Used in Support of This Scientific Analysis

Software Name and Version (V)	Software Tracking Number (STN)/DIRS Number	Description	Computer and Platform Identification
2WELLS_2D V 1.0	10665-1.0-00 [159067]	This software is used in the analysis of longitudinal dispersivity in the Prow Pass Tuff C-wells field tracer test. It is used to obtain predicted tracer responses in homogeneous, isotropic, confined (2-D) aquifers under partial recirculation conditions. It has been used both to correct dispersion-coefficient estimates for dispersion caused by a dipole-flow pattern and for pre-test predictions of ATC cross-hole tracer tests.	LANL, PC, Windows 2000/NT
2WELLS_3D V 1.0	10667-1.0-00 [159036]	This software is used to obtain predicted tracer responses in homogeneous, isotropic, confined three-dimensional (3-D) aquifers under partial recirculation conditions. It has been used both to correct dispersion-coefficient estimates for dispersion caused by a dipole-flow pattern and for pre-test predictions of ATC cross-hole tracer tests.	LANL, PC, Windows 2000/NT
DIFFCELL V 2.0	10557-2.0-00 [159063]	This software is used in the analysis of laboratory diffusion cell experiments. It provides a numerical solution to an equation describing one-dimensional (1-D) diffusive transport through a rock wafer with time-dependent concentration boundary conditions.	LANL, PC, Windows 2000/NT
EQUIL_FIT V 1.0	10668-1.0-00 [159064]	This software is used to obtain cation- exchange coefficients, given experimental data on cation sorption (both for sorbing and displaced cations) and given independent cation-exchange-capacity measurements.	LANL, PC, Windows 2000/NT
Filter.vi V 1.0	10970-1.0-00 [162668]	This software uses the standard Butterworth filter with standard coefficients. It is for filtering higher-frequency diurnal pressure changes due to barometric pressure changes and tidal effects.	USGS, PC, Windows 2000/NT, 4.0/98

Table 3-1 (Continued). Software Used in Support of This Scientific Analysis

Software Name and Version (V)	Software Tracking Number (STN)/DIRS Number	Description	Computer and Platform Identification
Injection_ Pump-back.vi V 1.0	10675-1.0-00 [162749]	This software is used for tracer test analysis for single-well testing. Analysis considers tracer injection, drift, and pumpback.	USGS, PC, Windows 2000/NT
rcv2amos.exe and MOENCH.vi, Function(1), V 1.0	10583-1.0-00 [162750]	The software routine rcv2amos.exe is used to analyze cross-hole tracer tests. In conjunction with the use of rcv2amos.exe, the routine MOENCH.vi was developed to serve as a user interface and to display the results.	USGS, PC, Windows 2000/NT, 4.0/98
MOENCH.vi Function(2) V 1.0	10582-1.0-00 [162752]	This software is used for the analysis of cross-hole tracer tests.	USGS, PC, Windows 2000/NT, 4.0/98
MULTRAN V 1.0	10666-1.0-00 [159068]	This is a two-dimensional (2-D) numerical model that uses an implicit-in-time, alternating-direction, finite-difference method to solve the equations describing multicomponent transport of sorbing and nonsorbing solutes in a dual-porosity medium. This software is used for analysis of laboratory crushed-rock and alluvium column experiments. It is also used for the analysis of the first peak in the Bullfrog Tuff C-wells field tracer test and for prediction and analysis of ATC tracer experiments.	LANL, PC, Windows 2000/NT
Neuman.vi V 1.0	10972-1.0-00 [162754]	This software displays the standard and accepted type curve for unconfined aquifers and allows the fitting of the input data curves over the type curve. The .vi extension displays the appropriate resulting hydrologic parameters associated with the data curve matching (transmissivity and storativity).	USGS, PC, Windows 2000/NT, 4.0/98
PEST V 5.5	10289-5.5-00 [161564]	This software assists in data interpretation, model calibration, and predictive analysis. PEST adjusts model parameters and/or excitations until the fit between model output and field or laboratory observations is optimized in the weighted least-squares sense.	USGS, PC, Windows 2000
RECIRC.vi V 1.0	10673-1.0-00 [164432]	This program is used for recirculating and partial-recirculation cross-hole tracer test analysis.	USGS, PC, Windows 98/NT 4.0/2000
RELAP V. 2.0	10551-2.0-00 [159065]	This software models tracer transport by convoluting a Laplace-domain transfer function for transport through dual-porosity media with transfer functions that describe tracer injection, mixing in the injection and production wellbores (or flow manifolds in laboratory experiments), and recirculation of the product fluid (in field experiments only). It also performs curve fits to field or laboratory tracer test data to obtain the best-fitting transport parameter values.	LANL, PC, Windows 2000/NT

Table 3-1 (Continued). Software Used in Support of This Scientific Analysis

Software Name and Version (V)	Software Tracking Number (STN)/DIRS Number	Description	Computer and Platform Identification
RETRAN V 2.0	10552-2.0-00 [159066]	This software models reactive transport in dual-porosity media with a general, nonlinear sorption isotherm and with time-varying flow rates.	LANL, PC, Windows 2000/NT
Streltsova-Adams.vi V 1.0	10971-1.0-00 [162756]	This software displays the standard and accepted Streltsova-Adams type curve for fractured aquifers and allows the fitting of the input data curves over this type curve. The .vi extension displays the appropriate resulting hydrologic parameters associated with the data curve matching (transmissivity and storativity).	USGS, PC, Windows 2000/NT, 4.0/98
Theis.vi V 1.0	10974-1.0-00 [162758]	This software displays the standard and accepted Theis type curve and allows the fitting of the input data curves over this type curve. The .vi extension displays the appropriate resulting hydrologic parameters associated with the data curve matching (transmissivity and storativity).	USGS, PC, Windows 2000/NT, 4.0/98

3.2 EXEMPT SOFTWARE

Commercial, off-the-shelf software used in support of this scientific analysis report is listed in Table 3-2. This software is exempt from the requirements of AP-SI.1Q, *Software Management.*

Table 3-2. Exempt Software Used in Support of This Scientific Analysis

Software Name and Version (V)	Description	Computer and Platform Identification
Microsoft Excel, 97 SR-1	The commercial software, Microsoft Excel, 97 SR-1, was used for statistical analysis of data and plotting graphs. Only built-in standard functions in this software were used. No software routines or macros were used with the software to prepare this report. The output was visually checked for correctness, and the results of all calculations were hand-checked.	PC, Windows 2000/NT

Calculations and spreadsheets used in this analysis can be found in the Technical Data Management System (TDMS) within data packages that have been assigned DTN numbers. Alternatively, some calculations and spreadsheets can be found in scientific notebooks. Calculations and spreadsheets are not included as attachments to this report because of their voluminous nature.

INTENTIONALLY LEFT BLANK

4. INPUTS

4.1 DATA AND PARAMETERS

The data used in interpretation of the hydraulic tests discussed in Section 6.2 have been submitted as data packages (Table 4-1) to the TDMS. Data packages submitted to the U.S. Department of Energy (DOE) are available for inspection at the DOE, Office of Repository Development, Records Processing Center in Las Vegas, Nevada. The data and other technical information providing input for the development of parameters documented in this scientific analysis are identified in Table 4-1. The listed data and the technical information are appropriate sources for the analyses documented in this report. A brief description of the data, the data tracking number (DTN) used as input, or the source of the data are listed in Table 4-1. The table is divided according to the sections in this analysis in which the data are used. The qualification status of data input is indicated in the TDMS and in the DIRS database.

This document may be affected by technical product input information that requires confirmation. Any changes to the document that may occur as a result of completing the confirmation activities will be reflected in subsequent interim change notices or revisions.

Table 4-1. Input Data

Data Description	Data Tracking Number (DTN) or Source
Section 6.1	
Results of hydraulic tests in Miocene tuffaceous rocks at the C-hole complex, 1995 to 1997, Yucca Mountain, Nevada.	GS030508312314.003 [164425]
Revised bedrock geologic map of the Yucca Mountain area.	GS980608314221.002 [107024]
Well completion information for NC-EWDP-19D1.	MO0112DQRWLNYE.018 [157187]
Well completion information for NC-EWDP-19P.	MO0112DQRWLNYE.014 [157184]
Stratigraphic and lithologic information for NC-EWDP-19D1.	GS011008314211.001 [158690]
Well completion information for NC-EWDP-19IM1.	MO0306NYE05259.165 [165876]
Well completion information for NC-EWDP-19IM2.	MO0306NYE05260.166 [165877]
Hydraulic information from the C-hole complex and the Yucca Mountain area.	GS930908312313.008 [166332]
Section 6.2	
Results of hydraulic tests in Miocene tuffaceous rocks at the C-hole complex, 1995 to 1997, Yucca Mountain, Nevada.	GS030508312314.003 [164425]
Water-level altitude data from four wells in the continuous network, May through December 1996.	GS970308312314.002 [161273]
Pump test data collected at the C-wells complex 5/7/96 – 12/31/96.	GS981008312314.003 [144464]

Table 4-1 (Continued). Input Data

Data Description	Data Tracking Number (DTN) or Source
Section 6.2 (Continued)	
Transducer, barometric pressure, and discharge data collected from 4/18/98 in support of the ongoing hydraulic tracer tests being conducted at the UE-25 C-wells complex, Nevada.	GS990408312315.002 [140115]
UE-25 ONC-1 transducer pressures, April, 1995 to December, 1997.	MO0212SPANYESJ.149 [161274]
Section 6.3	
Results of hydraulic tests in Miocene tuffaceous rocks at the C-hole complex, 1995 to 1997, Yucca Mountain, Nevada.	GS030508312314.003 [164425]
Concentrations of 2,6 –DFBA and pyridone from tracer test conducted at the C-wells complex, 1/8/97 – 7/11/97.	GS010508312315.001 [155860]
Data obtained from the analysis of the iodide tracer test water samples collected during the 2/13/96 convergent tracer test conducted at the C-wells complex.	GS960808312315.001 [159235]
Tracer recovery data from testing in the Prow Pass interval.	GS990208312315.001 [159238]
Transducer, barometric pressure, and discharge data collected from 4/18/98 in support of the ongoing hydraulic tracer tests being conducted at the UE-25 C-wells complex, Nevada.	GS990408312315.002 [140115]
Prow Pass reactive-tracer-test field data.	LAPR831231AQ99.001 [140134]
Bullfrog reactive tracer test data.	LA0007PR831231.001 [156043]
Injection and production flow rates for Prow Pass test.	GS010799992315.001 [157067]
Mineral abundance data of C-well tuffs from UE-25 c#1 and c#2.	MO0012MINLCHOL.000 [153370]
Sorbing element concentration data of J-13 and C-3 well water from UE-25 c#1 and c#2.	MO0012SORBCHOL.000 [153375]
PFBA and bromide tracer diffusion in tuff from UE-25 c#1.	MO0012DIFFCHOL.000 [159243]
Porosity data for UE-25 c#1, c#2, and c#3.	MO0012POROCHOL.000 [153376]
Permeability data for UE-25 c#1, c#2, and c#3.	MO0012PERMCHOL.000 [153368]
Bromide and PFBA sorption data onto C-wells tuffs.	LA0302PR831231.001 [162605]
Mineralogy data for Central Bullfrog Tuff from UE-25 c#2, 2406 ft (non-Q).	LA9909PR831231.004 [129623]
Bromide and lithium tracer movement in crushed tuff columns for UE-25 c#2 tuff.	LA0301PR831231.001 [162603]
Cation exchange capacity data for lithium displacing other cations from C-wells tuffs.	MO0012CATECHOL.000 [153371]

Table 4-1 (Continued). Input Data

Data Description	Data Tracking Number (DTN) or Source
Section 6.3 (Continued)	
Cation exchange capacity data for cesium displacing other cations from C-wells tuffs.	LA0302PR831341.001 [162604]
Iodide concentrations in C-wells fractured core experiments.	LA0212PR831231.001 [162607]
Lithium, bromide, and PFBA concentrations in C-wells fractured core experiments.	LA0212PR831231.003 [162609]
Sodium and calcium concentrations in fractured core experiments in all C-wells cores except for core UE-25 c#2, 1745 ft.	LA0212PR831231.002 [162608]
Sodium and calcium concentrations in fractured core experiments in core UE-25 c#2, 1745 ft.	LA0212PR831231.005 [166215]
2,3,4,5 TeFBA Response in Prow Pass from UE-25 c#1 to UE-25 c#2, 1998	MO0308SPATRCRC.000 [164821]
Pump test data collected at the C-wells complex 1/8/97 - 3/31/97.	GS981008312314.002 [147068]
Pumping test data collected at the C-wells complex, 5/7/96 - 12/31/96.	GS981008312314.003 [144464]
Results of flow surveys.	GS930908312313.008 [166332]
Additional technical information for tracer tests.	Reimus (2000 [165125]), Reimus (2000 [162855]), Reimus (2000 [162852]), Reimus (2003 [165129], including Attachment A)
Section 6.4	
NC-EWDP-19D, ATC single-hole hydraulic testing associated with the July 7, 2000 to April 26, 2001 tracer study.	GS020708312316.001 [162678]
Flow rates, pressures, and temperatures for hydraulic and tracer testing at the NC-EWDP-19D, NC-EWDP-19IM1, and NC-EWDP-19IM2 Alluvial Testing Complex from December 18, 2001 to March 22, 2002.	GS020908312316.002 [162679]
Background pressures and temperatures during barometric monitoring at the NC-EWDP-19D, NC-EWDP-19IM1, and NC-EWDP-19IM2 Alluvial Testing Complex from May 1, 2002 through July 3, 2002.	GS020908312316.003 [162680]
Grain size analysis of alluvium samples from wells 19D and 19P of the Alluvial Test Complex.	LA0201JS831421.001 [162613]
Section 6.5	
Grain size distribution data for alluvium from NC-EWDP-19P and -19D.	LA0201JS831421.001 [162613]
2,6 DFBA and I concentrations in single-well tracer test with 2-day rest period in NC-EWDP-19D1.	UN0102SPA008KS.003 [162614]

Table 4-1 (Continued). Input Data

Data Description	Data Tracking Number (DTN) or Source
Section 6.5 (Continued)	
Concentration data set for tracers (2,6-difluorobenzoic acid and iodide) used for the 48 hour shut-in test at the Alluvial Tracer Complex in Nye County, Nevada in samples collected during the period 02/27/01 through 04/25/01.	UN0109SPA008KS.005 [162681]
2,4 DFBA and Cl concentrations in single-well tracer test with 0.5-hr rest period in NC-EWDP-19D1.	UN0109SPA008IF.006 [162442]
PFBA concentrations in single-well tracer test with 30-day rest period in NC-EWDP-19D1.	UN0109SPA008KS.007 [162615]
Bromide concentrations in single-well tracer test with 30-day rest period in NC-EWDP-19D1.	UN0109SPA008KS.008 [162616]
2,4 DFBA concentrations in single-well tracer test in interval #4 of NC-EWDP-19D1.	MO0205UCC008IF.001 [162617]
Microsphere concentrations in single-well tracer tests in NC-EWDP-19D1.	LA0207PR831352.001 [162431]
Mineralogy data for alluvium from NC-EWDP-19P and -19D.	LA0201JS831321.001 [162623]
BET surface areas for alluvium from NC-EWDP-19P and -19D.	LA0201JS831421.002 [162625]
Cation exchange capacity data for alluvium from NC-EWDP-19P and -19D.	LA0201JS831341.001 [162627]
Cation concentrations from lithium batch sorption experiments using alluvium from different intervals in NC-EWDP-19P and -19D.	LA0302JS831341.001 [162628]
Groundwater chemistry data from NC-EWDP-19D1.	LA0303PR831232.001 [162781]
Constituent concentrations from column experiments with highest injection concentrations of LiBr using alluvium from NC-EWDP-19D.	LA0201JS831361.001 [162629]
Constituent concentrations from column experiments with intermediate injection concentrations of LiBr using alluvium from NC-EWDP-19D.	LA0201JS831361.007 [162630]
Constituent concentrations from column experiments with lowest injection concentrations of LiBr using alluvium from NC-EWDP-19D.	LA0201JS831361.005 [166205]
NC-EWDP-19D, ATC single-hole hydraulic testing associated with the July 7, 2000 to April 26, 2001 tracer study.	GS020708312316.001 [162678]
Geophysical log data from borehole NC-EWDP-19D.	MO0105GPLOG19D.000 [163480]
Drawdown data for NC-EWDP boreholes.	GS020908312316.002 [162679]

4.2 CRITERIA

The general requirements to be satisfied by the TSPA are stated in 10 CFR 63.114 [156605]. Technical requirements to be satisfied by the TSPA are identified in the *Yucca Mountain Project Requirements Document* (Canori and Leitner 2003 [161770]). The acceptance criteria that will be used by the Nuclear Regulatory Commission (NRC) to determine whether the technical requirements have been met are identified in the Yucca Mountain Review Plan (YMRP) (NRC 2003 [163274]). The pertinent requirements and criteria for this report are summarized in Table 4-2.

Table 4-2. Project Requirements and YMRP Acceptance Criteria Applicable to This Scientific Analysis Report

Requirement Number[a]	Requirement Title[a]	10 CFR 63 Link	YMRP Acceptance Criteria[b]
PRD-002/T-014	Performance Objectives for the Geologic Repository After Permanent Closure	10 CFR 63.113 (a)	2.2.1.1.3, criteria 2 and 3
PRD -002/T-015	Requirements for Performance Assessment	10 CFR 63.114 (a)-(c) and (e)-(g)	2.2.1.3.8.3, criteria 1 to 4 2.2.1.3.9.3, criteria 1 to 5
PRD -002/T-016	Requirements for Multiple Barriers	10 CFR 63.115 (a)-(c)	2.2.1.1.3, criteria 2 and 3

NOTE: [a] from Canori and Leitner (2003 [161770])
[b] from NRC (2003 [163274]).

The acceptance criteria identified in Sections 2.2.1.1.3, 2.2.1.3.8.3, and 2.2.1.3.9.3 of the YMRP (NRC 2003 [163274] are given below, followed by a short description of how this scientific analysis helps to address the criteria or why this scientific analysis does not address the criteria. In cases where subsidiary criteria are listed in the YMRP for a given criterion, only the subsidiary criteria addressed by this scientific analysis are listed below.

Section 2.2.1.1.3 *Acceptance Criteria* [for 2.2.1.1 *System Description and Demonstration of Multiple Barriers*], which are based on meeting the requirements at 10 CFR 63.113 [156605](a) and 63.115(a)–(c):

- Acceptance Criterion 1, Identification of Barriers is Adequate:

  "Barriers relied on to achieve compliance with 10 CFR 63.113(b), as demonstrated in the total system performance assessment, are adequately identified, and are clearly linked to their capability. The barriers identified include at least one from the engineered system and one from the natural system."

  This criterion is not directly addressed in this scientific analysis. The purpose of this scientific analysis is to document the results and interpretations of field experiments that have been conducted in the saturated zone (SZ) natural barrier. Other documents serve to identify barriers in the engineered and natural systems.

- Acceptance Criterion 2, Description of Barrier Capability to Isolate Waste is Acceptable:

  "The capability of the identified barriers to prevent or substantially reduce the rate of movement of water or radionuclides from the Yucca Mountain repository to the accessible environment, or prevent the release or substantially reduce the release rate of radionuclides from the waste is adequately identified and described."

  Section 6 of this scientific analysis describes the saturated zone barrier capability to isolate waste in that it documents the results and interpretations of in-situ testing of this barrier. Specifically, the in-situ field tests were designed to (1) discriminate between alternative conceptual models of flow and transport in the saturated zone barrier, (2) obtain estimates of flow and transport parameters to support the development of parameter distributions used in downstream SZ flow and transport models, and (3) identify uncertainties associated with both conceptual models and parameter estimates.

  - Section 6.2 addresses these topics for water flow in the saturated volcanics.
  - Section 6.3 addresses these topics for solute and colloid transport in the saturated volcanics. This section also addresses the ability to predict field-scale sorption behavior in the saturated volcanics using laboratory estimates of sorption parameters.
  - Section 6.4 addresses the above topics for water flow in the saturated alluvium.
  - Section 6.5 addresses the above topics for nonsorbing solute transport and colloid transport in the saturated alluvium.

- Acceptance Criterion 3, Technical Basis for Barrier Capability Is Adequately Presented:

  "The technical bases are consistent with the technical basis for the performance assessment. The technical basis for assertions of barrier capability is commensurate with the importance of each barrier's capability and the associated uncertainties."

  Section 6 of this scientific analysis is dedicated to presenting a key part of the technical basis for the saturated-zone barrier in the natural system. Specifically, it presents the technical basis related to in-situ testing of the saturated zone barrier.

Section 2.2.1.3.8.3 *Acceptance Criteria* [for 2.2.1.3.8 *Flow Paths in the Saturated Zone*], which are based on meeting the requirements of 10 CFR 63.114(a)–(c) and (e)–(g), relating to flow paths in the saturated zone model abstraction:

- Acceptance Criterion 1, System Description and Model Integration are Adequate:

  Of the ten subsidiary criteria listed under this primary criterion in the YMRP, this scientific analysis directly addresses only the following one.

  "The description of the aspects of hydrology, geology, geochemistry, design features, physical phenomena, and couplings, that may affect flow paths in the saturated zone, is

adequate. Conditions and assumptions in the abstraction of flow paths in the saturated zone are readily identified, and consistent with the body of data presented in the description."

Specifically, Sections 6.2 and 6.4 of this scientific analysis describe aspects of the hydrology and geology that may affect flow paths in the saturated volcanics and saturated alluvium, respectively. Other processes or features that may affect flow paths and all other subsidiary criteria are addressed primarily in other documents.

- Acceptance Criterion 2, Data are Sufficient for Model Justification:

  This scientific analysis, by itself, does not completely address this criterion. However, Sections 6.2 and 6.4 help in addressing all four of the subsidiary criteria listed under this criterion in the YMRP (for saturated volcanics and saturated alluvium, respectively).

  1) "Geological, hydrological, and geochemical values used in the license application to evaluate flow paths in the saturated zone are adequately justified. Adequate descriptions of how the data were used, interpreted, and appropriately synthesized into the parameters are provided."

     – The justification of hydrological values used in the license application is provided, in part, in Sections 6.2 and 6.4 of this scientific analysis.

  2) "Sufficient data have been collected on the natural system to establish initial and boundary conditions for the abstraction of flow paths in the saturated zone."

     – The hydrological data collected on the natural system are described in Sections 6.2 and 6.4 of this scientific analysis, although this report does not address sufficiency of the data for abstraction of flow paths.

  3) "Data on the geology, hydrology, and geochemistry of the saturated zone used in the total system performance assessment abstraction are based on appropriate techniques. These techniques may include laboratory experiments, site-specific field measurements, natural analog research, and process-level modeling studies. As appropriate, sensitivity or uncertainty analyses, used to support the U.S. Department of Energy total system performance assessment abstraction, are adequate to determine the possible need for additional data."

     – Sections 6.2 and 6.4 of this scientific analysis describe the techniques used to obtain in-situ hydrological data in the saturated volcanics and alluvium, respectively. Uncertainties in the data are also discussed in these sections.

  4) "Sufficient information is provided to substantiate that the proposed mathematical groundwater modeling approach and proposed model(s) are calibrated and applicable to site conditions."

- Sections 6.2 and 6.4 of this scientific analysis provide some of the information needed to substantiate that the groundwater modeling approach is calibrated and applicable to site conditions.

- Acceptance Criterion 3, Data Uncertainty is Characterized and Propagated Through the Model Abstraction:

  1) "Models use parameter values, assumed ranges, probability distributions, and/or bounding assumptions that are technically defensible, and reasonably account for uncertainties and variabilities, and do not result in an under-representation of the risk estimate."

     - Sections 6.2 and 6.4 of this scientific analysis provide some of the technical basis for the parameter values, assumed ranges, probability distributions and bounding assumptions used in flow models. They also provide some of the technical basis for uncertainties and variabilities in hydrologic parameters.

  2) Uncertainty is adequately represented in parameter development for conceptual models, process-level models, and alternative conceptual models considered in developing the abstraction of flow paths in the saturated zone. This may be done either through sensitivity analyses or use of conservative limits. For example, sensitivity analyses and/or similar analyses are sufficient to identify saturated zone flow parameters that are expected to significantly affect the abstraction model outcome."

     - Sections 6.2 and 6.4 of this scientific analysis provide some of the technical basis for uncertainties in hydrologic parameters used in flow models.

- Acceptance Criterion 4, Model Uncertainty is Characterized and Propagated Through the Model Abstraction:

  This scientific analysis, by itself, does not completely address this criterion. However, Sections 6.2 and 6.4 help in addressing all four of the subsidiary criteria listed under this criterion in the YMRP (for saturated volcanics and saturated alluvium, respectively).

  1) "Alternative modeling approaches of features, events, and processes are considered and are consistent with available data and current scientific understanding, and the results and limitations are appropriately considered in the abstraction."

     - Alternative conceptual models of flow in the saturated volcanics and alluvium are considered in Sections 6.2 and 6.4, respectively, of this scientific analysis when hydrological data are interpreted.

  2) "Conceptual model uncertainties are adequately defined and documented, and effects on conclusions regarding performance are properly assessed. For example, uncertainty in data interpretations is considered by analyzing reasonable conceptual flow models that are supported by site data, or by demonstrating through sensitivity studies that the uncertainties have little impact on repository performance."

- Alternative conceptual models of flow in the saturated volcanics and alluvium are considered in Sections 6.2 and 6.4, respectively, of this scientific analysis when hydrological data are interpreted.

3) "Consideration of conceptual model uncertainty is consistent with available site characterization data, laboratory experiments, field measurements, natural analog information and process-level modeling studies; and the treatment of conceptual model uncertainty does not result in an under-representation of the risk estimate."

- Sections 6.2 and 6.4 of this scientific analysis describe the hydrological site characterization data and field measurements that should be considered for assessing conceptual model uncertainty in the saturated volcanics and saturated alluvium, respectively.

4) "Appropriate alternative modeling approaches are consistent with available data and current scientific knowledge, and appropriately consider their results and limitations, using tests and analyses that are sensitive to the processes modeled."

- Alternative conceptual models of flow in the saturated volcanics and alluvium are considered in Sections 6.2 and 6.4, respectively, of this scientific analysis when hydrological data are interpreted.

- Acceptance Criterion 5, Model Abstraction Output is Supported by Objective Comparisons:

  This criterion is not directly addressed in this scientific analysis. Other documents serve to address this criterion.

Section 2.2.1.3.9.3 *Acceptance Criteria* [for 2.2.1.3.9 *Radionuclide Transport in the Saturated Zone*], which are based on meeting the requirements of 10 CFR 63.114(a)–(c) and (e)–(g), relating to the radionuclide transport in the saturated zone model abstraction:

- Acceptance Criterion 1, System Description and Model Integration are Adequate:

  This scientific analysis, by itself, does not completely address this criterion. However, Sections 6.3 and 6.5 help in addressing the following three subsidiary criteria listed under this criterion in the YMRP (for saturated volcanics and saturated alluvium, respectively).

1) "The description of the aspects of hydrology, geology, geochemistry, design features, physical phenomena, and couplings, that may affect radionuclide transport in the saturated zone, is adequate. For example, the description includes changes in transport properties in the saturated zone, from water-rock interaction. Conditions and assumptions in the abstraction of radionuclide transport in the saturated zone are readily identified, and consistent with the body of data presented in the description."

- Sections 6.3 and 6.5 of this scientific analysis describe some of the aspects of the hydrology, geochemistry, physical phenomena, and couplings that may affect radionuclide transport in the saturated volcanics and alluvium, respectively.

2) "The abstraction of radionuclide transport in the saturated zone uses assumptions, technical bases, data, and models that are appropriate and consistent with other related U.S. Department of Energy abstractions. For example, assumptions used for radionuclide transport in the saturated zone are consistent with the total system performance assessment abstractions of radionuclide release rates and solubility limits, and flow paths in the saturated zone (Sections 2.2.1.3.4 and 2.2.1.3.8 of the Yucca Mountain Review Plan, respectively). The descriptions and technical bases provide transparent and traceable support for the abstraction of radionuclide transport in the saturated zone."

   - Sections 6.3 and 6.5 of this scientific analysis help address the appropriateness f assumptions, technical bases, data, and models used in the abstractions of radionuclide transport in the saturated volcanics and alluvium, respectively.

3) "Sufficient data and technical bases for the inclusion of features, events, and processes related to radionuclide transport in the saturated zone in the total system performance assessment abstraction are provided."

   - Sections 6.3 and 6.5 of this scientific analysis provide much of the data and technical bases for inclusion of features, events, and processes related to radionuclide transport in the saturated volcanics and alluvium, respectively.

- Acceptance Criterion 2, Data are Sufficient for Model Justification:

  This scientific analysis, by itself, does not completely address this criterion. However, Sections 6.3 and 6.5 help in addressing all three of the subsidiary criteria listed under this criterion in the YMRP (for saturated volcanics and saturated alluvium, respectively).

  1) "Geological, hydrological, and geochemical values used in the license application are adequately justified (e.g., flow path lengths, sorption coefficients, retardation factors, colloid concentrations, etc.). Adequate descriptions of how the data were used, interpreted, and appropriately synthesized into the parameters are provided."

     - The justification of sorption coefficients and retardation factors are provided, in part, in Sections 6.3 and 6.5 of this scientific analysis (for the saturated volcanics and saturated alluvium, respectively).

  2) "Sufficient data have been collected on the natural system to establish initial and boundary conditions for the total system performance assessment abstraction of radionuclide transport in the saturated zone."

     - Some of the data used to establish boundary conditions are described in Sections 6.3 and 6.5 of this scientific analysis (for the saturated volcanics and saturated alluvium, respectively).

  3) "Data on the geology, hydrology, and geochemistry of the saturated zone, including the influence of structural features, fracture distributions, fracture properties, and stratigraphy, used in the total system performance assessment abstraction are based

on appropriate techniques. These techniques may include laboratory experiments, site-specific field measurements, natural analog research, and process-level modeling studies. As appropriate, sensitivity or uncertainty analyses, used to support the U.S. Department of Energy total system performance assessment abstraction, are adequate to determine the possible need for additional data."

- Techniques for obtaining data to support conceptual transport models, including flow porosity and matrix diffusion are described in detail in Sections 6.3 and 6.5 of this scientific analysis (for the saturated volcanics and saturated alluvium, respectively).

- Acceptance Criterion 3, Data Uncertainty is Characterized and Propagated Through the Model Abstraction:

  This scientific analysis, by itself, does not completely address this criterion. However, Sections 6.3 and 6.5 help in addressing the following four subsidiary criteria listed under this criterion in the YMRP (for saturated volcanics and saturated alluvium, respectively).

  1) "Models use parameter values, assumed ranges, probability distributions, and bounding assumptions that are technically defensible, reasonably account for uncertainties and variabilities, and do not result in an under-representation of the risk estimate."

     - Sections 6.3 and 6.5 of this scientific analysis provide some of the technical basis for the parameter values, assumed ranges, probability distributions and bounding assumptions used in radionuclide transport models. They also provide some of the technical basis for uncertainties and variabilities in transport parameters.

  2) "For those radionuclides where the total system performance assessment abstraction indicates that transport in fractures and matrix in the saturated zone is important to waste isolation: (i) estimated flow and transport parameters are appropriate and valid, based on techniques that may include laboratory experiments, field measurements, natural analog research, and process-level modeling studies conducted under conditions relevant to the saturated zone at Yucca Mountain; and (ii) models are demonstrated to adequately predict field transport test results. For example, if a sorption coefficient approach is used, the assumptions implicit in that approach are validated."

     - Sections 6.3 and 6.5 of this scientific analysis address the appropriateness and validity of transport parameter estimates, including the sorption coefficient approach, in the saturated volcanics and saturated alluvium, respectively. These sections also describe assessments of alternative conceptual transport models for their adequacy to predict field transport test results.

  3) "Parameter values for processes, such as matrix diffusion, dispersion, and ground-water mixing, are based on reasonable assumptions about climate, aquifer properties, and ground-water volumetric fluxes (Section 2.2.1.3.8 of the Yucca Mountain Review Plan)."

- Sections 6.3 and 6.5 of this scientific analysis address assumptions about aquifer properties as they relate to matrix diffusion, dispersion, and other transport processes (for the saturated volcanics and saturated alluvium, respectively).

4) "Uncertainty is adequately represented in parameter development for conceptual models, process-level models, and alternative conceptual models considered in developing the abstraction of radionuclide transport in the saturated zone. This may be done either through sensitivity analyses or use of conservative limits."

- Sections 6.3 and 6.5 of this scientific analysis provide some of the technical basis for uncertainties in parameters used in radionuclide transport models in the saturated zone.

- Acceptance Criterion 4, Model Uncertainty is Characterized and Propagated Through the Model Abstraction:

This scientific analysis, by itself, does not completely address this criterion. However, Sections 6.3 and 6.5 help in addressing all four of the subsidiary criteria listed under this criterion in the YMRP (for saturated volcanics and saturated alluvium, respectively):

1) "Alternative modeling approaches of features, events, and processes are considered and are consistent with available data and current scientific understanding, and the results and limitations are appropriately considered in the abstraction."

- Alternative conceptual models of transport in the saturated volcanics and alluvium are considered in Sections 6.3 and 6.5, respectively, of this scientific analysis when tracer test data are interpreted.

2) "Conceptual model uncertainties are adequately defined and documented, and effects on conclusions regarding performance are properly assessed."

- Uncertainties associated with alternative conceptual models of transport in the saturated volcanics and alluvium are considered in Sections 6.3 and 6.5, respectively, of this scientific analysis.

3) "Consideration of conceptual model uncertainty is consistent with available site-characterization data, laboratory experiments, field measurements, natural analog information and process-level modeling studies; and the treatment of conceptual model uncertainty does not result in an under-representation of the risk estimate."

- Sections 6.3 and 6.5 of this scientific analysis describe the site-characterization data and field measurements (field tracer test data and supporting laboratory data) that should be considered for assessing conceptual model uncertainty in the saturated volcanics and saturated alluvium, respectively.

4) "Appropriate alternative modeling approaches are consistent with available data and current scientific knowledge, and appropriately consider their results and limitations using tests and analyses that are sensitive to the processes modeled. For example, for

radionuclide transport through fractures, the U.S. Department of Energy adequately considers alternative modeling approaches to develop its understanding of fracture distributions and ranges of fracture flow and transport properties in the saturated zone."

- Alternative conceptual models of transport in the saturated volcanics and alluvium are considered in Sections 6.3 and 6.5, respectively, of this scientific analysis when tracer test data are interpreted.

- Acceptance Criterion 5, Model Abstraction Output is Supported by Objective Comparisons:

  This scientific analysis, by itself, does not completely address this criterion. However, Sections 6.3 and 6.5 help in addressing the following three subsidiary criteria listed under this criterion in the YMRP (for saturated volcanics and saturated alluvium, respectively).

  1) The models implemented in this total system performance assessment abstraction provide results consistent with output from detailed process-level models and/or empirical observations (laboratory and field testings and/or natural analogs).

     - Sections 6.3 and 6.5 describe both laboratory and field observations that can be used for consistency checks of abstraction models (for the saturated volcanics and saturated alluvium, respectively).

  2) Outputs of radionuclide transport in the saturated zone abstractions reasonably produce or bound the results of corresponding process-level models, empirical observations, or both. The U.S. Department of Energy-abstracted models for radionuclide transport in the saturated zone are based on the same hydrological, geological, and geochemical assumptions and approximations shown to be appropriate for closely analogous natural systems or laboratory experimental systems.

     - Sections 6.3 and 6.5 provide both laboratory and field observations that can be used for comparisons with the outputs of abstraction models (for the saturated volcanics and saturated alluvium, respectively).

  3) Sensitivity analyses or bounding analyses are provided, to support the total system performance assessment abstraction of radionuclide transport in the saturated zone, that cover ranges consistent with site data, field or laboratory experiments and tests, and natural analog research.

     - Sections 6.3 and 6.5 provide both laboratory and field data that can be used for these sensitivity or bounding analyses (for the saturated volcanics and saturated alluvium, respectively).

4.3 CODES AND STANDARDS

No industrial or technical codes or standards other than those discussed in Section 4.2 apply directly to the activities described in this report.

INTENTIONALLY LEFT BLANK

5. ASSUMPTIONS

A list of the assumptions used in this scientific analysis is provided in Table 5-1. Subsections where assumptions are used are identified. The rationale for each assumption is also provided.

Table 5-1. Assumptions

Number	Assumption	Rationale	Location in Report
1	Flow to a pumping well is derived from an aquifer of infinite extent.	Analyses of aquifer properties are based on this assumption but the faults functioning as boundaries do not support this. Boundary effects were minimized but could not be eliminated.	Section 6.2.3
2	Flow to a pumping well from an aquifer is radial (for hydraulic test interpretations)	Vertical flow could be ignored in hydraulic tests of multiple intervals because the analytical results were similar to the hydraulic test of one interval where flow was radial.	Section 6.2.3
3	Flow to a pumping well is from an infinite, homogeneous, isotropic, confined aquifer for all hydraulic tests analyzed using the Theis (1935 [150327]) method.	Simplification of structural and lithologic complexities is necessary to analysis by the Theis method. The consistency of multiple analyses of varying test parameters indicates either that errors are consistent or that calculated values approximate actual values of hydraulic properties.	Section 6.2.3
4	Input parameters measured in a borehole were the same throughout the thickness of that hydrogeologic interval.	Simplification of structural and lithologic complexities is necessary to analysis by the Theis method. The consistency of multiple analyses of varying test parameters indicates either that errors are consistent or that calculated values approximate actual values of hydraulic properties.	Section 6.2.3
5	For water to reach the pumping well from the intervals that did not have open sliding sleeves, a downward component of flow must have occurred.	The downward flow was assumed by the investigators to be much less than radial flow to the pumping well in order to analyze the drawdown from the non-open intervals by the methods outlined in Section.	Section 6.2.3.1.1
6	Matrix permeability is negligible compared to fracture permeability in interpretations of tracer responses in fractured volcanic tuffs.	Matrix permeabilities of intact tuff matrices range from 2 to 6 orders of magnitude lower than bulk permeabilities measured in field hydraulic tests.	Sections 6.3.1, 6.3.4, and 6.3.9.2

Table 5-1 (Continued). Assumptions

Number	Assumption	Rationale	Location in Report
7	Matrix diffusion of carboxylate-modified latex microspheres is negligible in field tracer tests in fractured volcanic rocks.	The microspheres are large, which will tend to physically exclude them from small pores, and they have diffusion coefficients 2 to 3 orders of magnitude lower than solutes.	Section 6.3.4
8	Solute transport in fractured volcanic rocks can be effectively modeled using the 1-D advection-dispersion equation in fractures with 1-D diffusive transport into the matrix (perpendicular to the fractures). Furthermore, fractures can be assumed to be parallel-plate channels that are either equally spaced or embedded in a matrix of infinite extent.	These assumptions capture the general behavior observed in all the laboratory and field experiments in fractured volcanic rocks. Nonidealities such as rough-walled fractures and multiple flow pathways in fractures are accommodated through an adjustable longitudinal dispersivity.	Sections 6.3.4 and 6.3.9.2
9	Solute concentration gradients across fracture apertures were negligible in field and laboratory tracer experiments in fractured volcanic rocks.	Given the time scales of the experiments in fractured rocks (lab and field) and the small distances associated with fracture apertures, diffusion should have effectively eliminated any concentration gradients across apertures.	Sections 6.3.1, 6.3.4, and 6.3.9.2
10	Solute and microsphere tracers that are injected simultaneously in field tracer tests experience the same mean residence time, dispersivity, and mass fraction of tracer participating in the test.	The simultaneous injection ensures that the tracers should follow the same flow pathways between the injection and production wells. Thus, the tracers should experience the same mean residence time, dispersivity, and mass fraction participating in the tracer test.	Section 6.3.4
11	The two tracer peaks in the Bullfrog Tuff multiple-tracer field test represent two different sets of flow pathways between the injection and production well.	Only one tracer peak was observed in an earlier test in the same test configuration when a smaller volume of tracer solution was injected. The greater injection volume in the multiple tracer test likely resulted in a fraction of the tracer mass entering pathways that were not accessed in the first tracer test.	Section 6.3.4
12	The tracers following the flow pathways resulting in the first tracer peak in the Bullfrog Tuff began entering these pathways 4 hours after the injection began in the injection well.	Flow surveys indicated that the largest zone of outflow in the injection well was near the top of the injection interval. If the tracer solution "sank" in the borehole due to its greater density than the ambient ground water, then this flow zone would have been accessed about 3-4 hours after the start of injection (when the injection interval became "filled" with tracer solution).	Section 6.3.4

Table 5-1 (Continued). Assumptions

Number	Assumption	Rationale	Location in Report
13	The matrix diffusion coefficient of lithium ion is two-thirds that of bromide.	The free ion diffusion coefficient of Li^+ at infinite dilution should be about 0.5 times that of Br^- (Newman 1973 [148719], p. 230, Table 75-1), but a factor of 0.67 was used because Li^+ and Br^- should tend to diffuse together to maintain local charge balance.	Sections 6.3.4 and 6.3.9.2
14	Lithium ion experienced equilibrium sorption conditions (i.e., fast sorption kinetics) in all field tracer tests.	The residence times in the field tests were all quite long relative to times required for Li^+ sorption equilibration in laboratory experiments.	Sections 6.3.4
15	The microspheres experienced linear filtration and detachment processes in all field tracer tests (i.e., these processes could be modeled assuming linear first-order rate constants).	This is a common assumption throughout the literature, and it is the easiest to parameterize and implement in process models and TSPA calculations.	Section 6.3.4
16	All the microspheres following a given flow pathway in the Bullfrog Tuff field test had the same filtration rate constant, but these microspheres could be split into fractions that had different detachment rate constants (a discrete distribution of detachment rate constants) to fit the microsphere responses.	This assumption was necessary to obtain a good fit to the microsphere responses in the Bullfrog Tuff test (a single detachment rate constant offered a poor fit).	Section 6.3.4
17	The production and recirculation rates in the Bullfrog Tuff field reactive tracer test remained constant throughout the test for the purposes of interpreting the tracer tests.	Recirculation was actually stopped after 40 days, but by this time, both tracer peaks had long past and the tracer responses were well into their tails. It was assumed that recirculation continued because the RELAP V 2.0 (STN: 10551-2.0-00 [159065]) code cannot simulate transients. Separate simulations using MULTRAN V 1.0 (STN: 10666-1.0-00 [159068]) indicated that there was negligible effect of the ceasing of recirculation on the tracer responses.	Section 6.3.4
18	The test intervals in the C-wells field tracer tests were reasonably confined so that flow in the intervals should have varied somewhere between radial and linear (constant velocity) for the purposes of interpreting tracer tests.	Hydraulic responses indicated a reasonable degree of confinement of intervals.	Section 6.3.4
19	The microspheres in the Bullfrog Tuff field tracer test did not experience a 4-hr delay in entering the flow pathways that resulted in the first tracer peaks in this test.	The microsphere injection did not begin until 3.5 hours after the solutes, which was about the time the solutes were assumed to start entering the flow pathways resulting in the first peaks.	Section 6.3.4

Table 5-1 (Continued). Assumptions

Number	Assumption	Rationale	Location in Report
20	75% of the flow in the Bullfrog Tuff field reactive tracer test occurred through pathways that resulted in the first tracer peak, and 25% occurred through pathways that resulted in the second tracer peak.	This assumption is consistent with flow surveys in the injection and production wells, if it is assumed that the first tracer peak was the result of flow pathways in the upper part of the test interval.	Section 6.3.4
21	Bromide and PFBA effectively bound the sizes of radionuclide solute species expected in the SZ beneath Yucca Mountain.	Bromide is a simple halide, while PFBA is a large aromatic organic molecule. The latter should be similar in size or larger than radionuclide complexes with carbonate or other potential inorganic complexants. This assumption does not apply to colloidal radionuclides (including complexes to large natural organic matter).	Section 6.3.4
22	A confined, homogeneous, isotropic flow system was assumed for the purposes of estimating flow porosity in the field tracer tests.	This assumption is made because it is the simplest possible assumption that is still consistent with the data. Assuming anything else would involve making implications about the system that, while reasonable, cannot be supported by direct evidence.	Sections 6.3.4, 6.5.2, and 6.5.3
23	The interval thicknesses in field tracer tests are equal to the distances between the packers that isolate test zones.	This assumption is made because it is the simplest possible assumption that is consistent with the data. Assuming anything else would involve making implications about the system that cannot be supported by direct evidence.	Sections 6.3.1, 6.3.4, and 6.5.3
24	Injection and production intervals behave as well-mixed regions during field tracer tests.	Although this assumption may not be strictly correct, it simulates an exponential release of tracer from the injection and production intervals that is thought to be representative of field behavior in the boreholes.	Sections 6.3.1, 6.3.4, 6.5.2, and 6.5.3
25	The variance in tracer responses due to recirculation and the variance due to true hydrodynamic dispersion are additive (i.e., these two processes are independent).	Either process can occur without the other, and there is no fundamental reason why recirculation and true hydrodynamic dispersion should be dependent on one another.	Section 6.3.4
26	Tracer movement through diffusion cell wafers follows the 1-D diffusion equation.	The diffusion cell experiments are designed for 1-D diffusion measurements, and advection was eliminated or minimized by ensuring the same pressure/head on both sides of diffusion cell wafers.	Section 6.3.8
27	The density of crushed tuff and alluvium grains is 2.65 g/cm^3.	2.65 g/cm^3 is the density of most silicate phases, which dominate the mineralogy of the tuffs and alluvium.	Sections 6.3.4, 6.3.9, 6.5.3, and 6.5.5

Table 5-1 (Continued). Assumptions

Number	Assumption	Rationale	Location in Report
28	The Peclet number and matrix diffusion parameters for iodide in transport experiments conducted at different flow rates in fractured cores were the same at each flow rate. Also, the mean residence times in these tests were inversely proportional to the flow rate.	These assumptions are consistent with no geometrical changes occurring in the fractured cores. Geometrical changes were avoided or minimized to the extent possible.	Section 6.3.9
29	Ion exchange was fast enough in the fractured core experiments to satisfy the local equilibrium approximation (assumed in the MULTRAN V 1.0 (STN: 10666-1.0-00 [159068]) model).	The experimental results of Section 6.3.10.1 suggest that this is a reasonable assumption.	Section 6.3.9
30	Lithium cation exchange capacities in the fractured cores and packed porous-media columns were the same as those measured in batch experiments on the same tuff or alluvium samples.	There was no basis for choosing any other cation exchange capacities other than what was measured on the same materials.	Sections 6.3.9 and 6.5.5
31	Lithium sorption occurred in both fractures and matrix in the second peak of the Bullfrog Tuff field reactive tracer test and in the second test in the Lower Bullfrog Tuff fractured core.	Better fits to the lithium responses in these tests were obtained when making this assumption than when assuming sorption only in the matrix.	Sections 6.3.4 and 6.3.9
32	Transport through saturated alluvium may either follow single-porosity or dual-porosity behavior, with the latter involving either diffusion into low-permeability layers or diffusion into grains (or both).	These are the most plausible possibilities for transport in saturated alluvium.	Sections 6.5.1, 6.5.2, and 6.5.3
33	For diffusion into low-permeability layers in saturated alluvium, the layers are assumed to be of uniform thickness and uniform spacing.	These assumptions are made for convenience to simplify modeling. It is believed that they should effectively capture the behavior of layered systems.	Sections 6.5.1, 6.5.2, and 6.5.3.
34	Radial flow occurs in single-well tracer tests in saturated alluvium (for the purposes of modeling single-well tests with MULTRAN V 1.0 (STN: 10666-1.0-00 [159068])).	This assumption is made for convenience to simplify modeling.	Section 6.5.2.
35	Alluvium grains are spherical for the purposes of modeling diffusion into and out of grains in the MULTRAN V 1.0 (STN: 10666-1.0-00 [159068]) model.	This assumption is made for convenience in modeling diffusion into grains. A distribution of grain sizes can be specified to effectively simulate odd-shaped grains.	Section 6.5.2

Table 5-1 (Continued). Assumptions

Number	Assumption	Rationale	Location in Report
36	The flow system parameters of Tables 6.5-1 and 6.5-4 are valid for use in predictive simulations of single-well and cross-hole tracer tests, respectively, in saturated alluvium using MULTRAN V 1.0 (STN: 10666-1.0-00 [159068]).	The parameters were chosen for convenience, although they were believed to be representative (see text in Section 6.5.2).	Sections 6.5.2 and 6.5.3
37	"Correction factors" to adjust first, peak, and mean arrival times for 2-D (confined) flow to 3-D (unconfined) flow are the same regardless of the value of longitudinal dispersivity.	This assumption is made for convenience, but it seems very reasonable if dispersion is only longitudinal (parallel to flow streamlines). Also, the assumption seemed to hold in 2WELLS_2D V 1.0 (10665-1.0-00 [159067]) and 2WELLS_3D V 1.0 (10667-1.0-00 [159036]) simulations.	Section 6.5.3
38	"Correction factors" to adjust for the effects of recirculation are the same for first and peak arrival times.	This assumption is made for convenience, but it appeared to be approximately correct in 2WELLS_2D V 1.0 (10665-1.0-00 [159067]) and 2WELLS_3D V 1.0 (10667-1.0-00 [159036]) simulations.	Section 6.5.3
39	"Correction factors" for various adjustments in tracer arrival times (to account for effects of recirculation, confined vs. unconfined flow, dispersion) are linearly independent and commutative.	This assumption is made for convenience, but it seems reasonable given that there is no reason to expect the different processes to be interdependent.	Section 6.5.3
40	"Drift" with the ambient ground-water flow caused the differences in the tracer responses in the three single-well tracer tests with different "rest periods" conducted at NC-EWDP-19D1.	The responses of tracers with different diffusion coefficients used in each test were identical, which rules out the possibility that the different responses were caused by diffusion into stagnant water in the system. This leaves "drift" as the only plausible explanation for the different tracer responses as a function of rest period.	Section 6.5.4
41	The tracer mass corresponding to the peak in the three single-well tracer tests at NC-EWDP-19D1 moved directly upgradient during injection and then drifted back toward the well during the rest period.	This assumption is consistent with the fact that the single-well test with the longest rest period had the shortest peak arrival time. Also, the assumption of moving directly upgradient results in the lowest possible estimate of ambient groundwater velocity.	Section 6.5.4
42	Differences in mean- and late- arrival times of tracers in the three single-well tracer tests at NC-EWDP-19D1 were due to tracer mass that had moved directly downgradient during the tracer injections.	The mean- and late-arrival times are both much more strongly influenced by late arriving tracer mass, which logically should have moved downgradient during injection (and taken longer to recover than mass that moved upgradient). Also, the assumption of moving directly downgradient results in the largest possible estimate of ambient ground water velocity.	Section 6.5.4

Table 5-1 (Continued). Assumptions

Number	Assumption	Rationale	Location in Report
43	Radial flow in a confined aquifer occurred in the three single-well tracer tests at NC-EWDP-19D1 (for the purposes of estimating ambient ground water velocity).	This assumption was made for convenience in estimating ambient ground water velocity. Although it may not be strictly correct, it is qualitatively consistent with flow spreading out from the injection well during injection and converging to the well during production.	Section 6.5.4
44	Ambient flow in the saturated alluvium at NC-EWDP-19D1 was unidirectional in the three single-well tracer tests.	Flow should have been effectively unidirectional (with minor variations as a result of heterogeneities) at the scale of the tests.	Section 6.5.4
45	The tracer mass associated with the peak and mean arrival times in the single-well tracer tests at NC-EWDP-19D1 corresponded to the midpoints of the tracer solution injection volume.	The midpoint of the tracer injection volume should be the most likely volume associated with the peak and mean tracer concentrations.	Section 6.5.4
46	The tracer mass associated with high fractional recoveries in the single well tracer tests at NC-EWDP-19D1 was at the leading edge of the tracer injection volume (i.e., among the first tracer mass injected).	This assumption is consistent with the tracer mass being the latest recovered mass in the single-well tracer tests.	Section 6.5.4
47	Dispersion (longitudinal and transverse) during the rest periods of the single-well tracer tests at NC-EWDP-19D1 had approximately the same effect on tracer arrival times in each test.	This assumption is made for convenience. It seems to be reasonable, although it was not verified.	Section 6.5.4
48	The microsphere response in the single-well test at NC-EWDP-19D1 was entirely due to detachment of microspheres after 90 hours of pumping.	By this time, 72% of the solutes had been recovered, but only 26% of the microspheres, so it seemed reasonable to assume that the microspheres that were being recovered were detaching from alluvium surfaces.	Section 6.5.4.6
49	The microspheres remaining on the alluvium surfaces after 90 hours of pumping in the single-well tracer test at NC-EWDP-19D1 were equal to the total number of spheres injected times the fraction of spheres not recovered (1 - f_{sphere}) minus the fraction of solutes not recovered (1 - f_{solute}) at any given point in time.	Subtracting (1 - f_{solute}) from (1 - f_{sphere}) is a correction that accounts for the fraction of spheres that would not have been recovered at a given time even if they did not interact with alluvium surfaces.	Section 6.5.4.6

INTENTIONALLY LEFT BLANK

6. ANALYSIS

6.1 INTRODUCTION

The saturated zone (SZ) near Yucca Mountain, along potential flow paths from the repository to the accessible environment, can be divided into two regimes: (1) fractured tuffs that underlie the repository and that extend for several kilometers to the south of Yucca Mountain (in the general direction of flow), and (2) valley-fill or alluvium deposits that the water table transitions into several kilometers before the current ~18-kilometer (km) performance compliance boundary (10 CFR 63 [156605], Subpart 63.302). Radionuclides released from the repository would first have to travel through the saturated fractured tuffs and then through the saturated alluvium to reach the compliance boundary. To support the characterization of the saturated fractured tuffs, several hydraulic and tracer tests were conducted at a three-well complex (UE-25 c#1, UE-25 c#2, and UE-25 c#3, hereafter referred to as c#1, c#2, and c#3, respectively, in this report) known as the C-wells. This complex is located approximately 2 km southeast of the repository footprint. Hydraulic tests conducted at the C-wells are discussed in Section 6.2 of this report, and tracer tests at the C-wells are discussed in Section 6.3. To support the characterization of the saturated alluvium, both hydraulic and tracer testing were conducted at the Alluvial Testing Complex (ATC), well NC-EWDP-19D1 (hereafter referred to as 19D1 in this report), which is located just outside the southwest corner of the Nevada Test Site (NTS), essentially right at the compliance boundary. Hydraulic tests conducted at the ATC are discussed in Section 6.4 of this report, and tracer tests at the ATC are discussed in Section 6.5. In addition to presenting the results and interpretations of field tracer testing conducted at the C-wells and the ATC, this report also presents the results and interpretations of laboratory transport tests conducted to help support the interpretation of field tracer tests (Sections 6.3 and 6.5). Transport properties of the alluvium are discussed in Section 6.5.

6.1.1 Hydrogeologic Settings

6.1.1.1 C-Wells

Figure 6.1-1 shows the location and surface layout of the C-wells. The wells were drilled on a two-tiered drill pad in a channel of an ephemeral stream that cuts through Bow Ridge, a spur of Yucca Mountain. The lower tier of the pad, in which borehole c#1 was drilled, is at an altitude of 1,130.5 m above mean sea level. The upper tier, in which boreholes c#2 and c#3 were drilled, is at an altitude of 1,132.3 m. The C-wells are 30.4 to 76.6 m apart at the land surface, but they deviate substantially at depth (Geldon 1993 [101045], p. 6, Figure 2; p. 8, Figure 4) (see Figure 6.1-1 and Table 6.1-1 below).

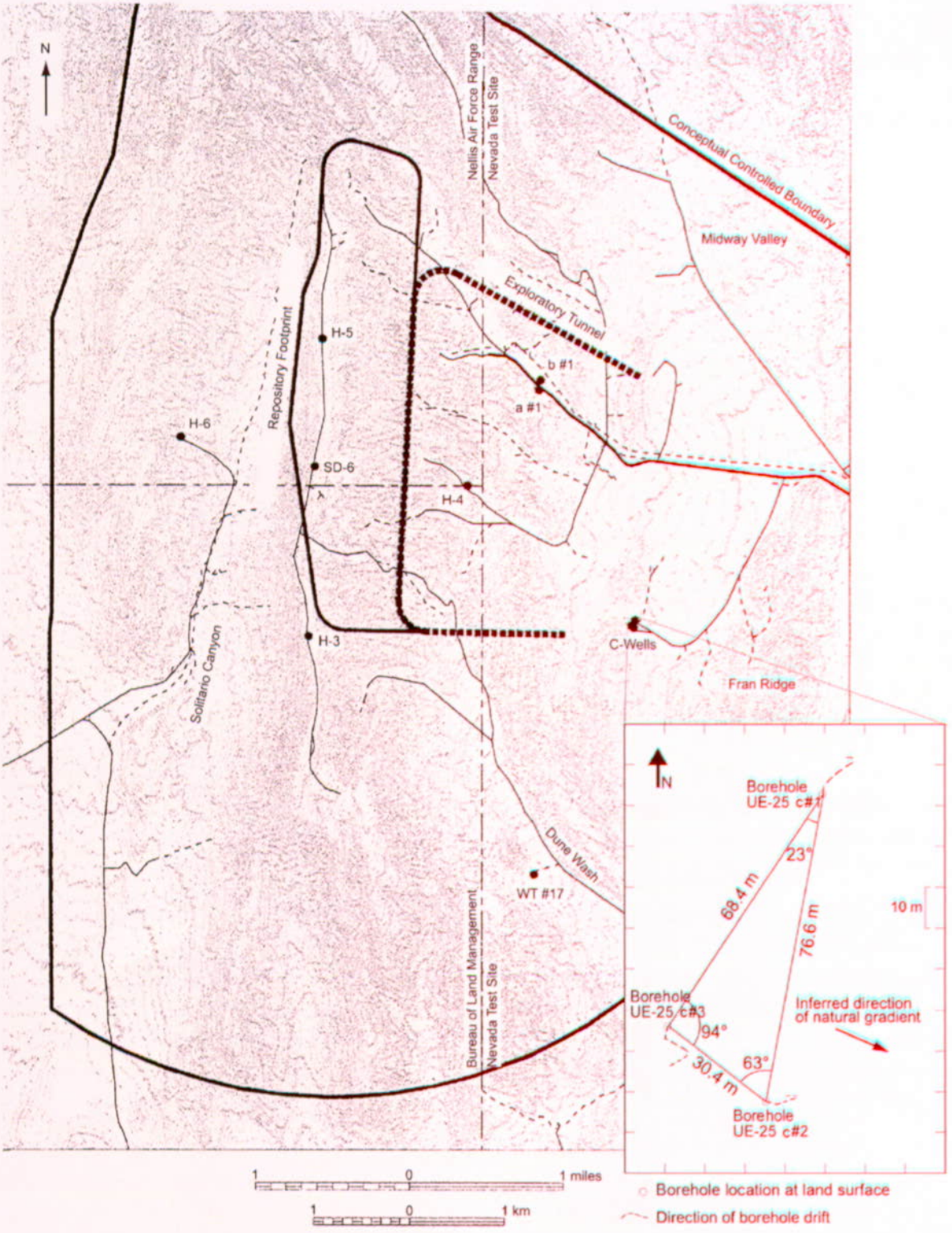

Source: Based on Geldon (1998 et al. [129721], p 3, Figure 1).

Figure 6.1-1. Location and Surface Layout of the C-wells Complex

Table 6.1-1. Approximate Interborehole Distances at the Midpoints of Hydrogeologic Intervals as Monitored During Hydraulic Tests at the C-wells Complex, August 1995 to April 1996

	Borehole Data			Interborehole Distances	
	c#1	c#2	c#3	c#1 – c#3	c#2 – c#3
Calico Hills					
Top depth (m)	418	416	417	78.6	29.0
Bottom depth (m)	547	531	540		
Midpoint depth (m)	483	474	478		
North coordinate (m)	230,771	230,691	230,703		
East coordinate (m)	173,646	173,633	173,607		
Distance north/south from c#3 (m)	68.3	12.2	—		
Distance east/west from c#3 (m)	39.3	26.2	—		
Prow Pass					
Top depth (m)	549	533	542	81.1	28.6
Bottom depth (m)	605	606	610		
Midpoint depth (m)	577	569	576		
North coordinate (m)	230,772	230,691	230,702		
East coordinate (m)	173,648	173,634	173,607		
Distance north/south from c#3 (m)	70.4	11.0	—		
Distance east/west from c#3 (m)	40.2	26.5	—		
Upper Bullfrog					
Top depth (m)	607	607	612	83.2	28.6
Bottom depth (m)	698	696	695		
Midpoint depth (m)	653	652	653		
North coordinate (m)	230,773	230,691	230,701		
East coordinate (m)	173,648	173,634	173,607		
Distance north/south from c#3 (m)	72.2	9.75	—		
Distance east/west from c#3 (m)	41.4	26.8	—		
Lower Bullfrog					
Top depth (m)	700	698	697	85.6	29.3
Bottom depth (m)	797	792	813		
Midpoint depth (m)	749	745	755		
North coordinate (m)	230,774	230,692	230,700		
East coordinate (m)	173,649	173,633	173,606		
Distance north/south from c#3 (m)	73.8	8.84	—		
Distance east/west from c#3 (m)	43.3	27.7	—		

Table 6.1-1 (Continued). Approximate Interborehole Distances at the Midpoints of Hydrogeologic Intervals as Monitored During Hydraulic Tests at the C-wells Complex, August 1995 to April 1996

	Borehole Data			Interborehole Distances	
	c#1	c#2	c#3	c#1 – c#3	c#2 – c#3
Upper Tram					
Top depth (m)	799	794	814	86.9	29.6
Bottom depth (m)	870	870	878		
Midpoint depth (m)	834	832	846		
North coordinate (m)	230,774	230,691	230,700		
East coordinate (m)	173,648	173,632	173,604		
Distance north/south from c#3 (m)	74.7	8.53	—		
Distance east/west from c#3 (m)	44.2	28.3	—		
Lower Tram					
Top depth (m)	872	871	879	87.2	29.9
Bottom depth (m)	898	903	900		
Midpoint depth (m)	885	887	890		
North coordinate (m)	230,774	230,691	230,700		
East coordinate (m)	173,648	173,632	173,603		
Distance north/south from c#3 (m)	74.7	8.23	—		
Distance east/west from c#3 (m)	44.8	28.6	—		

DTN: GS030508312314.003 ([164425], p. 6, Table 1).

NOTE: North and south are referenced to Nevada State Zone 2 coordinates. Depths in c#3 and interborehole distances changed slightly in April 1996 when instrumentation in c#3 was reconfigured.

The C-wells were completed to a depth of 914 m below land surface in Miocene tuffaceous rocks, mainly of the Paintbrush Group, the Calico Hills Formation, and the Crater Flat Group (Table 6.1-2), which are overlain by 0 to 24 m of Quaternary alluvium. The geology below the water table at the C-wells is depicted in Figure 6.1-2, along with fracture densities and estimated average matrix porosities in each unit. The tuffaceous rocks are estimated to be 1,040 to 1,590 m thick in the vicinity of the C-wells complex, where they consist of nonwelded to densely welded ash-flow tuff with intervals of ash-fall tuff and volcaniclastic rocks (Geldon 1993 [101045]; Geldon et al. 1998 [129721]). The tuffaceous rocks have pervasive tectonic and cooling fractures that strike predominantly north-northeast to north-northwest and dip westward at angles of 50° to 87° (Geldon 1996 [100396], pp. 7 to 9). Several thousand meters of Paleozoic limestone and dolomite likely underlie the tuffaceous rocks about 460 m below the bottom of the C-wells or ~1370 m below land surface (based on extrapolations from relations in borehole UE-25 p#1, presented by Carr et al. 1986 [102046]. Hereafter, in this report, UE-25 p#1 is referred to as p#1; see Table 1 for a list of abbreviations.).

Table 6.1-2. Stratigraphy of Miocene Tuffaceous Rocks in the C-wells Area

Geologic Unit	Depth Below Land Surface (m)				
	USW H-4	c#1	c#2	c#3	UE-25 p#1
Timber Mountain Group					
Rainier Mesa Tuff	not present	not present	not present	not present	39–55
Paintbrush Group					
Tiva Canyon Tuff	0–65	0–96	21–88	24–88	55–81
Topopah Spring Tuff	65–400	96–406	88–401	88–396	81–381
Calico Hills Formation	400–496	406–516	401–510	396–496	381–436
Crater Flat Group					
Prow Pass Tuff	496–693	516–656	510–652	496–644	436–558
Bullfrog Tuff	693–812	656–828	652–829	644–814	558–691
Tram Tuff	812–1,164	828–914+	829–914+	814–914+	691–873
Lithic Ridge Tuff	1,164–1,219+	not reached	not reached	not reached	873–1,068

DTN: GS030508312314.003 ([164425] p. 7, Table 2).

In the vicinity of the C-wells complex, northerly and northwesterly trending, high-angle faults, such as the Paintbrush Canyon, Midway Valley, and Bow Ridge faults, have brecciated, offset, and tilted the tuffaceous rocks (Day et al. 1998 [101557]; Dickerson and Drake 1998 [102781]). Figure 6.1-3 shows major faults and structural features in the vicinity of Yucca Mountain. The dip of the tuffaceous rocks increases from 5° to 10° eastward at the crest of Yucca Mountain to about 20° eastward at the C-wells complex (Frizzell and Shulters 1990 [105454], Map I-2046). At the C-wells complex, the north-striking Midway Valley fault or Paintbrush Canyon fault dropped Miocene tuffaceous rocks down to the west. Those rocks later were dropped to the northeast by a northwest-striking fault that cuts through Bow Ridge (Figure 6.1-3).

Hydrogeologic data and numerical modeling indicate that groundwater recharge in the Yucca Mountain area discharges mostly to Carson Slough, Ash Meadows, Alkali Flat, the lower Amargosa River Valley, and Death Valley (D'Agnese et al. 1997 [100131]). Locally, groundwater flows mainly through Tertiary volcanic rocks and Quaternary and Tertiary alluvium and lacustrine deposits. Controlled largely by faults and related fractures, groundwater flows from basin to basin, mainly through deeper Paleozoic carbonate rocks (Faunt 1997 [100146]). Cohen et al. (1996 [156651]) demonstrated by two-dimensional (2-D) numerical modeling that water in Miocene rocks at the C-wells complex could be derived from the Paleozoic carbonate rocks by upward flow along the Paintbrush Canyon, Midway Valley, or Bow Ridge faults. Geldon et al. (1998 [129721], pp. 23 to 25, Figure 2; p. 31) concluded that a northwest-trending zone of discontinuous faults between Bow Ridge and Antler Wash also transmits groundwater.

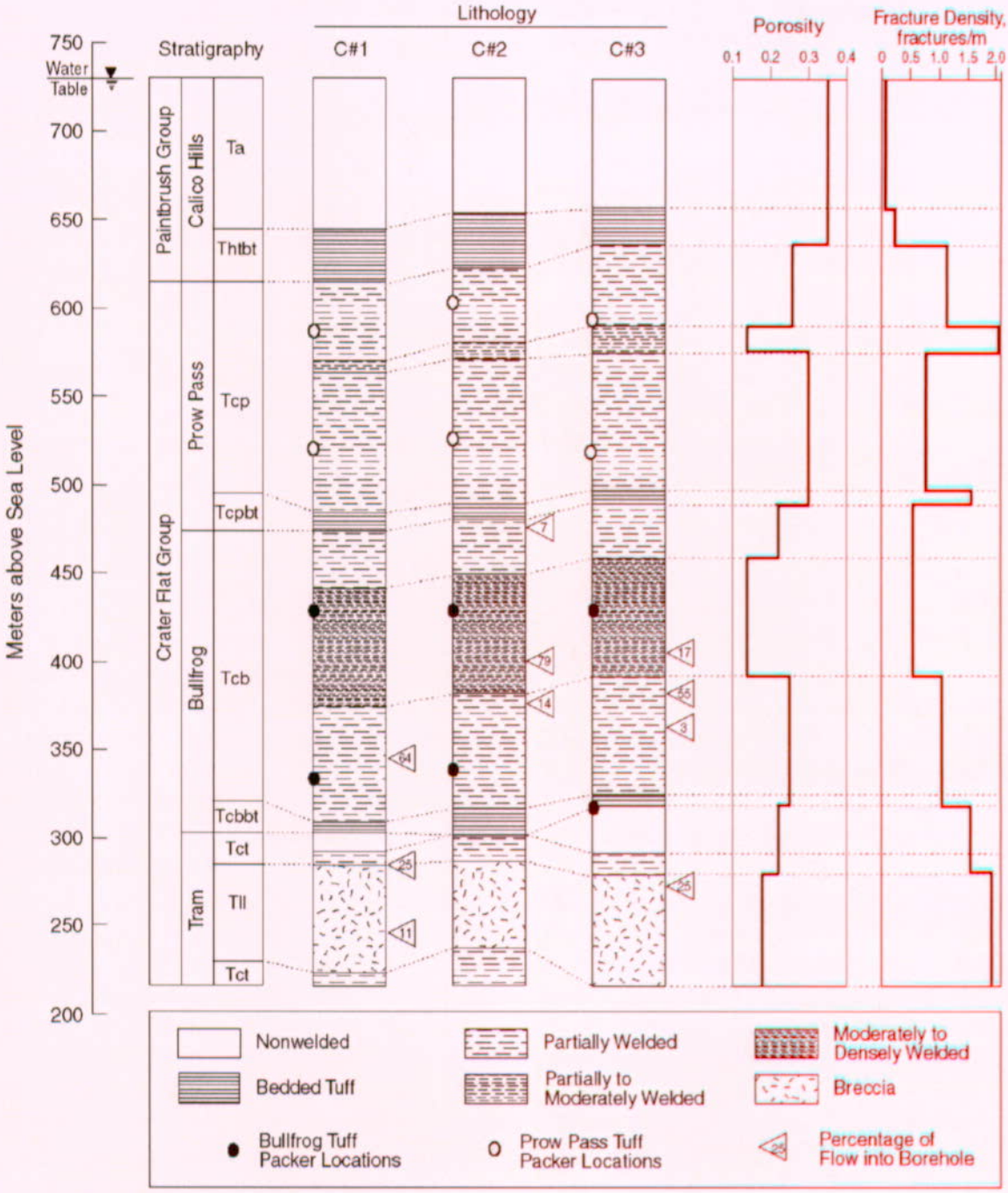

Source: Information derived from Geldon (1993 [101045], pp. 35 to 37, 68 to 70). Packer locations from DTN: GS030508312314.003 [164425]; flow survey information from DTN: GS930908312313.008 ([166332], MOL.19951115.0127 through MOL.19951115.0131).

NOTE: Packer locations indicate intervals in which tracer tests described in this report were conducted (note that the tracer tests were conducted between UE-25 c#2 and c#3). Fracture densities shown are from borehole UE-25 c#1.

Figure 6.1-2. Stratigraphy, Lithology, Matrix Porosity, Fracture Density, and Inflow From Open-Hole Flow Surveys at the C-wells

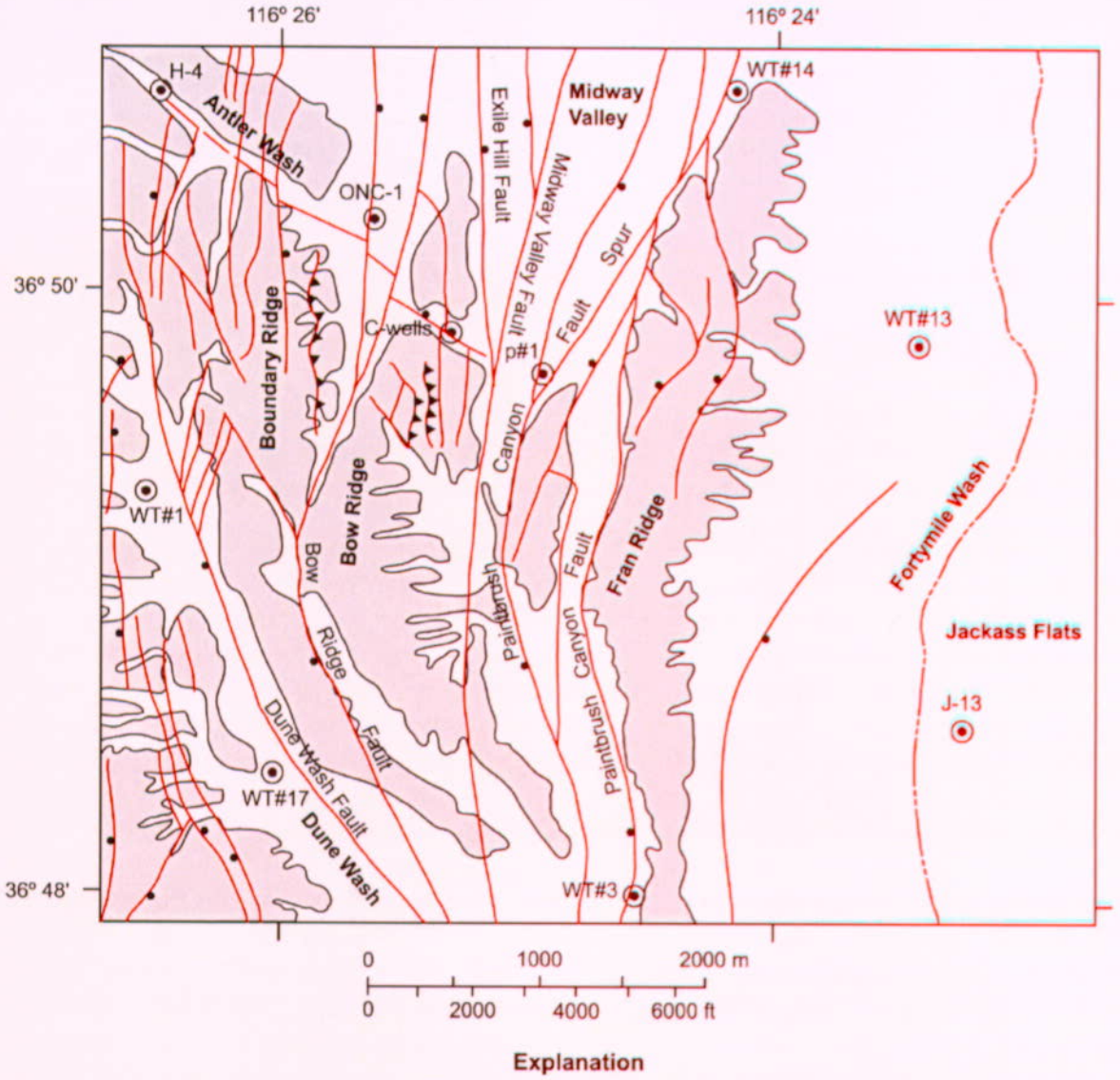

Explanation

- Alluvium
- Miocene Tuffaceous Rocks
- Borehole
- Geologic Contact
- Fault Trace: the fault may be partly or entirely concealed by alluvium. Where inferred, the trace is dashed. Ball symbols indicate the downthrown side of a normal fault; teeth indicate the upthrown side of a reverse fault.

Borehole Abbreviations

WT#1	USW WT#1
WT#3	UE-25 WT#3
WT#13	UE-25 WT#13
WT#14	UE-25 WT#14
WT#17	UE-25 WT#17
ONC-1	UE-25 ONC-1
H-4	USW H-4
J-13	UE-25 J-13
p#1	UE-25 p#1
C-wells	UE-25 c#1, c#2, and c#3

DTN: GS980608314221.002 [107024].

NOTE: The geology is based on Day et al. (1998 [100027]).

Figure 6.1-3. Generalized Geologic Map Showing the Location of the C-wells Complex and Nearby Boreholes

The water table in the Miocene tuffaceous rocks at Yucca Mountain in the vicinity of the C-wells complex ranges from about 335 to 520 m below land surface (O'Brien et al. 1995 [101279], p. 3, Table 1; pp. 35 to 69) and in the C-wells from 400 to 402 m. These depths all correspond to a water-table elevation of approximately 730 m above mean sea level in the vicinity of the C-wells. Water in the tuffaceous rocks generally flows southeasterly (Ervin et al. 1994 [100633]; Tucci and Burkhardt 1995 [101060]), but flow patterns are disrupted by faults acting as conduits or barriers to flow. Water-level data are sparse in the vicinity of the C-wells complex, but the Paintbrush Canyon, Bow Ridge, and other faults apparently created a groundwater divide centered on Bow Ridge and Boundary Ridge that directs flow southward to Dune Wash, northward to Midway Valley, and eastward to Fortymile Wash (Figure 6.1-4). Flow from the west into the area of the C-wells is inhibited by the north-striking Solitario Canyon fault (shown in Figure 6.1-3; Tucci and Burkhardt 1995 [101060]). For the purpose of Figure 6.1-4, the Solitario Canyon fault is assumed to be a constant-head boundary, whereas discharge areas north, east, and south of the C-wells complex are assumed to be head-dependent flux boundaries.

The Miocene tuffs near the C-wells complex behave as a single fissure-block aquifer, in which the volume and direction of groundwater flow are controlled mainly by proximity to faults, fracture zones, and partings (Geldon et al. 1998 [129721], p. 4). In a fissure-block aquifer, the permeability of the matrix is essentially negligible compared to the permeability of the fractures; and, hence, the aquifer behaves as a "dual-porosity" system in which the matrix acts as a reservoir for stagnant groundwater and flow occurs almost exclusively in fractures. Fractures in transmissive intervals have no preferred orientation, and fracture density appears unrelated to the extent of welding and permeability. Matrix permeability of the Calico Hills Formation and the Crater Flat Group within 5 km of the C-wells complex reaches 20 mDarcy. On the basis of barometric efficiency and specific storage, the average effective porosity of the Calico Hills Formation near the water table in the C-wells was determined to be 36 percent (Geldon et al. 1997 [156827], p. 11). The Crater Flat Group is much less porous than the Calico Hills Formation. The average porosity of those geologic units in the C-wells is 21 percent (computed from porosity values reported by Geldon 1993 [101045], pp. 60 to 62). Despite the influence of fractures, rock within about 3 km of the C-wells complex responds to hydraulic tests in a manner that is consistent with the response of a porous medium. In this analysis report, such a rock mass is referred to as an "equivalent porous medium," where the word "equivalent" indicates that the medium is not a true porous medium, but that, at the scale of observation, volume-averaged properties normally assigned to porous media can describe the hydraulic behavior of the rock mass.

Borehole flow surveys in combination with geophysical logs and aquifer tests show that flow within the tuffs at the C-wells complex comes primarily from discrete intervals (Figure 6.1-2). The total thickness of transmissive intervals identified in individual boreholes ranges from 165 to 274 m (Geldon 1996 [100396], pp. 13 to 20). Hydraulic tests conducted in 1984 indicated that those intervals have layered heterogeneity (Geldon 1996 [100396], pp. 9 to 69). Figure 6.1-5 is a depiction of the hydrogeologic intervals identified in the C-wells during hydraulic and tracer testing from 1995 to 1997 (Geldon 1996 [100396], pp. 9 to 69).

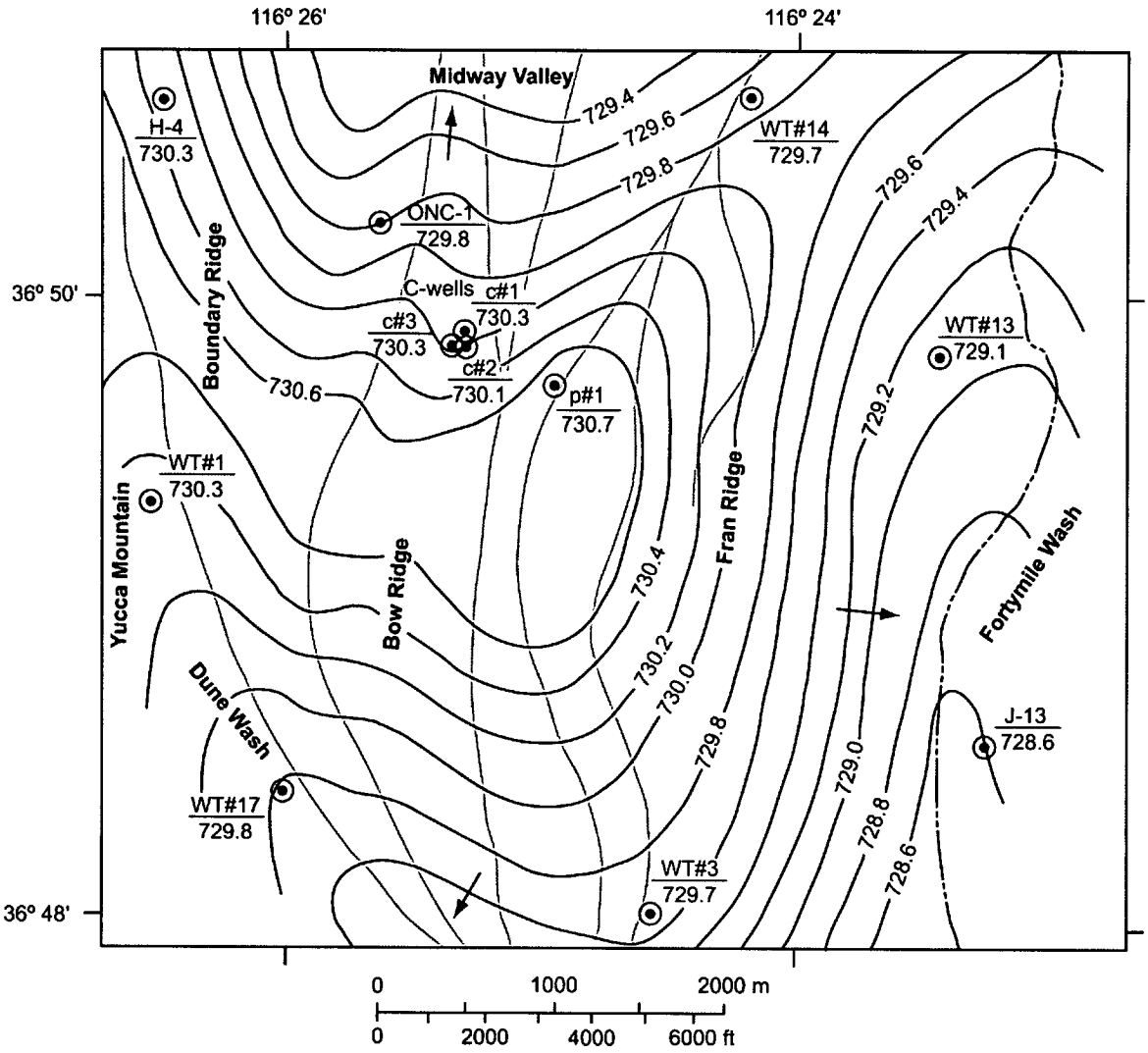

Explanation

H-4 / 730.3 — **Borehole.** The circle indicates the position of the borehole; the numbers show the borehole number (above the line) and the water level altitude, in meters above NGVD of 1929 (below the line). Complete borehole designations are listed in Figure 3.

730.0 — **Potentiometric Surface.** The contours give the altitude above NGVD of 1929 at which water would have stood in tightly cased wells completed in the Miocene tuffaceous rocks in May 1995. The water-level altitude in UE-25 p#1 is estimated from the measured hydraulic head of Paleozoic carbonate rocks and the vertical head gradient between the Paleozoic carbonate rocks and Miocine tuffaceous rocks in the borehole. The arrows on the contour lines indicate the inferred direction of natural gradient. The countour interval is 0.2 m.

Fault Trace.

Source: Geldon et al. (2002, [161163], p. 8, Figure 3); Nye County Nuclear Waste Repository Project Office (1995 [156859], ONC-1 Drilling log).

Figure 6.1-4. Potentiometric Surface of the Miocene Tuffaceous Rocks in the Vicinity of the C-wells Complex, May 1995

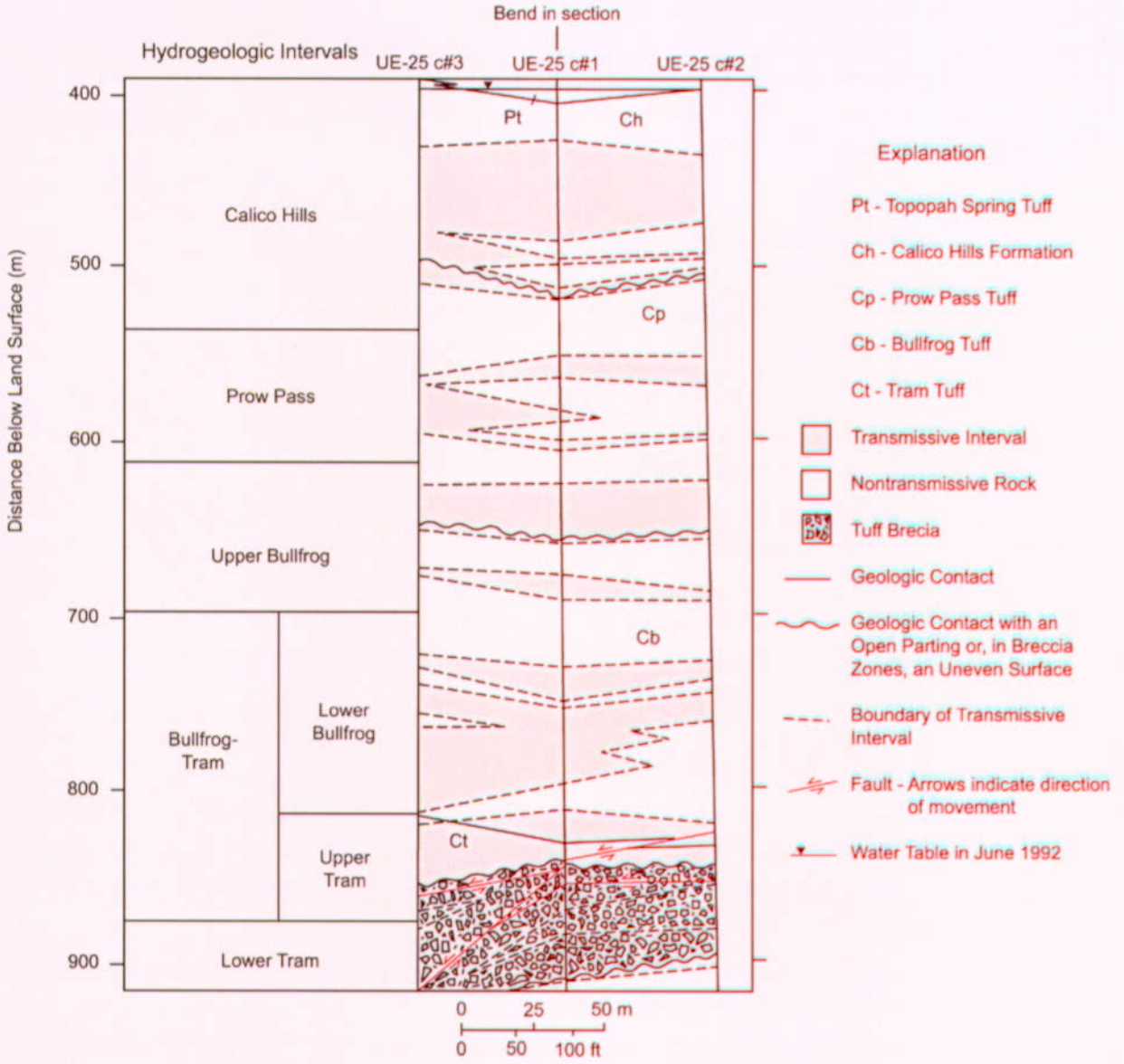

DTN: GS030508312314.003 ([164425], p. 9, Figure 4).

Figure 6.1-5. Hydrogeologic Intervals in the C-wells Identified During Hydraulic and Tracer Testing from 1995 to 1997

6.1.1.2 Alluvial Testing Complex

The SZ flow system to the south of Yucca Mountain transitions from a fractured tuff aquifer to a valley-fill (alluvium) aquifer before reaching the ~18-km performance compliance boundary at the southern boundary of the NTS. Characterization of the valley-fill system was conducted just outside the southwest corner of the NTS at the ATC, which is the site of the Nye County Early Warning Drilling Program (NC-EWDP) wells NC-EWDP-19D1, -19P, -19IM1, and -19IM2 (these wells will be referred to as 19D1, 19P, 19IM1, and 19IM2 in this report; see Table 1). The location of the ATC is shown in Figure 6.1-6 (labeled as "NC-EWDP-19D"). The surface layout of the wells at the ATC is shown in Figure 6.1-7.

Well 19D1 was drilled using a mud/rotary technique in March and April 2000 to a total depth of 441.4 m below land surface, with the water table being encountered at ~108.5 m below land surface. The "D1" designation is used because the well was re-drilled after a significant vertical deviation occurred during the original drilling of the "D" well. The "D" well was filled with a bentonite grout below ~213 m (~700 ft), where the deviation occurred, and the well was then re-drilled to total depth. Well 19D1 was completed using 18-cm (7.0-in) outer dimension and 15.8-cm (6.24-in) inner dimension steel pipe to allow pumps, packers, pressure transducers, and tracer injection equipment to be lowered into the hole. This completion also allows for installation of the Westbay monitoring/sampling system that Nye County uses for long-term monitoring.

A piezometer well, 19P, was drilled just prior to drilling 19D1 at a location that ultimately ended up being ~25 m northeast of 19D1 at land surface. 19P was drilled using an air/hammer technique in March 2000 to a total depth of 142 m below land surface, with the water table being encountered at 111 m (366 ft) below land surface. This well was completed with a 7.3-cm (2-7/8-in) outer diameter pipe casing and was screened from 109 to 139.5 m (358 to 458 ft) below land surface. The screened interval was developed by air injection. The well was intended to serve as a piezometer/monitoring well during pumping of 19D/D1.

Wells 19IM1 and 19IM2 were drilled and completed in August and September, respectively, of 2001. 19IM1 was completed to a depth of 308.6 m (1,012.5 ft) below land surface, and 19IM2 was competed to 294.3 m (965.6 ft) below land surface. Figure 6.1-8 shows the completions of 19D1, 19P, 19IM1, and 19IM2 along with the site lithology as determined from on-site geological logging during drilling.

As Figure 6.1-8 shows, 19D1 was screened over seven different depth intervals, with the bottom three intervals completed below the valley-fill deposits. A volcanic tuff was encountered at about 248 m (815 ft) below land surface, and a claystone/siltstone was encountered at ~375 m (~1230 ft) below land surface. Although these intervals are potentially significant, they were not the primary focus of the ATC investigations. Thus, 19IM1 and 19IM2 were drilled and completed only to the depth of the highest screened interval in the volcanic tuff in 19D1. It was desirable to have one interval completed below the valley-fill deposits in each well so that hydraulic communication between the valley fill and the underlying tuff could be investigated. The wells were developed by air injection just below each of the screened intervals and also by pumping for 48 hours (hr) under open-hole conditions. In the case of 19D1, the well was pumped in an open-hole configuration (no packers or plugs) at ~610 liters per minute (L/min) (~160 gallons per minute) (gpm) with a total drawdown of 4.6 to 6.1 m (15 to 20 ft). The

hydrogeologic setting in the vicinity of the ATC, and especially to the north of the ATC along Fortymile Wash, is in the process of being established. Understanding of the hydrogeologic setting near the 18-km compliance boundary is a major goal of the NC-EWDP.

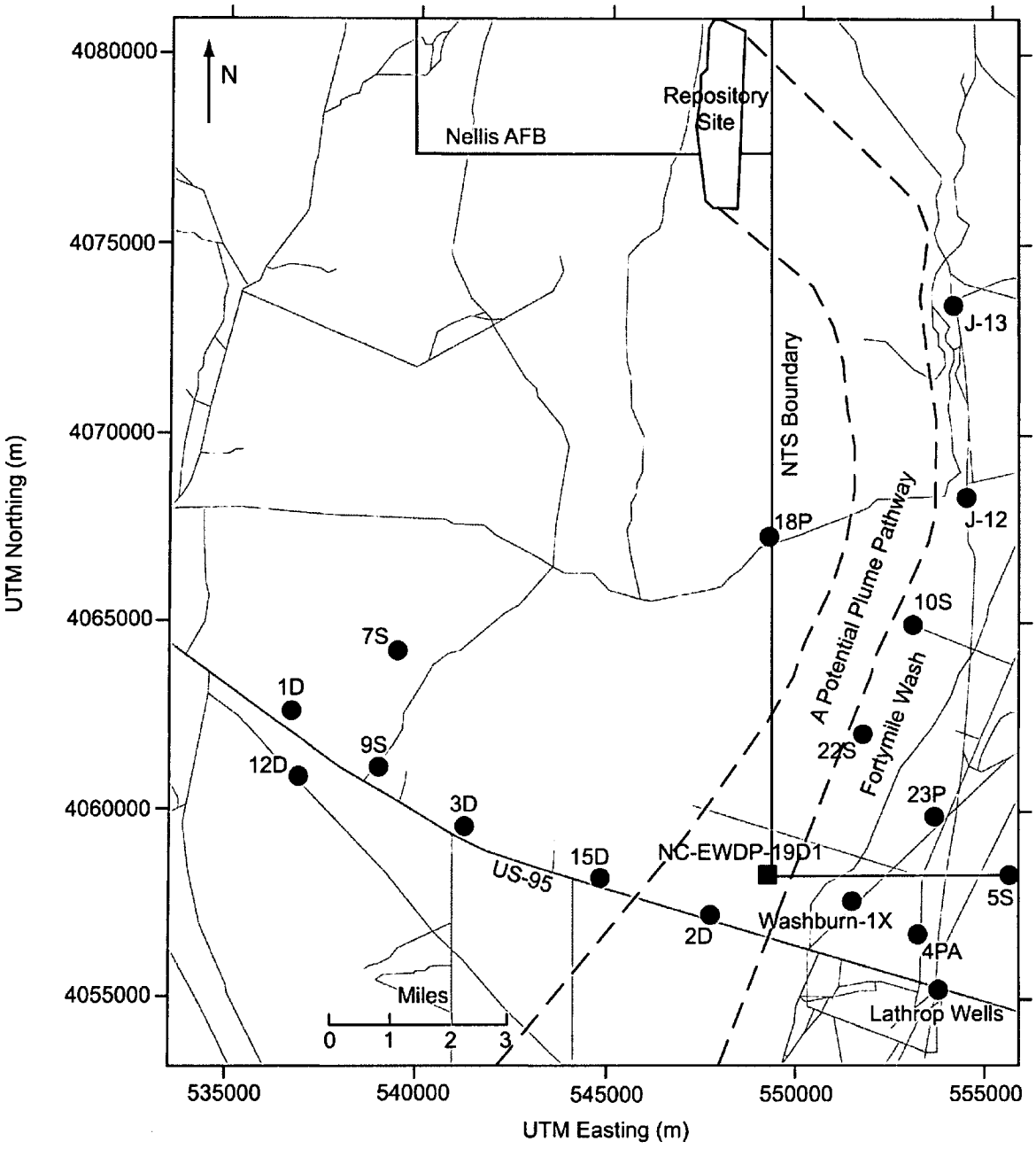

Figure is for illustration purposes only. DTN: MO0107COV01057.000 [157194] is used as reference only.

NOTE: The black circles indicate locations of other wells.

Figure 6.1-6. Map Showing Location of Alluvium Testing Complex (Well NC-EWDP-19D1 - black square) in Relation to the Repository Footprint and the Nevada Test Site

ATC SITE LAYOUT

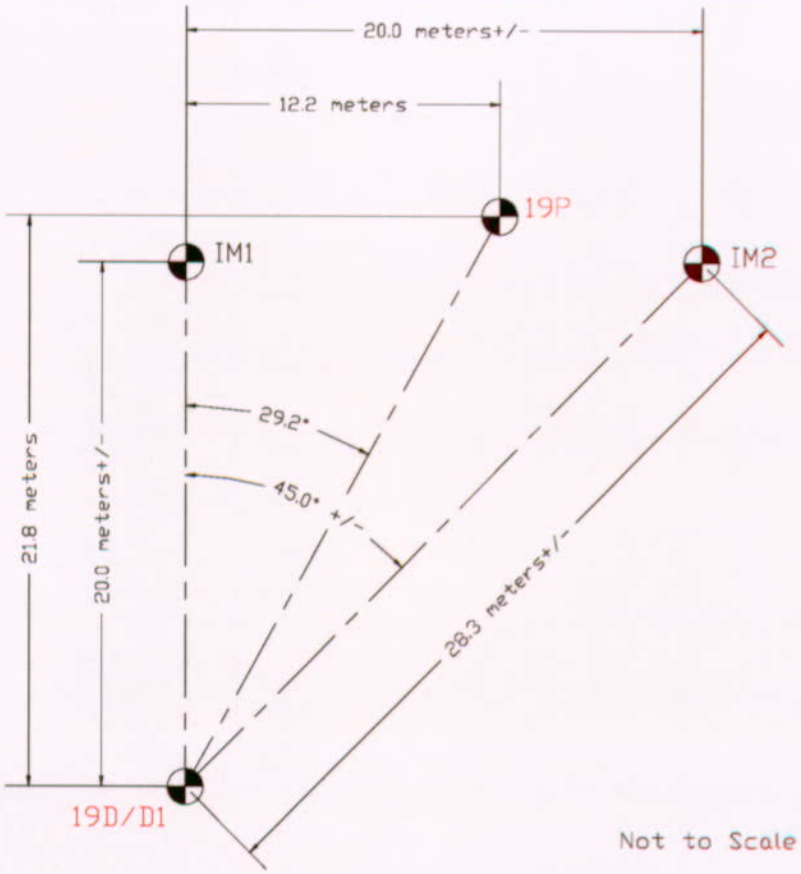

For illustration purposes only. Source: BSC (2002 [158198], p. 34, Figure 2).

NOTE: Full well names are preceded by "NC-EWDP-."

Figure 6.1-7. Surface Layout of the Alluvium Testing Complex

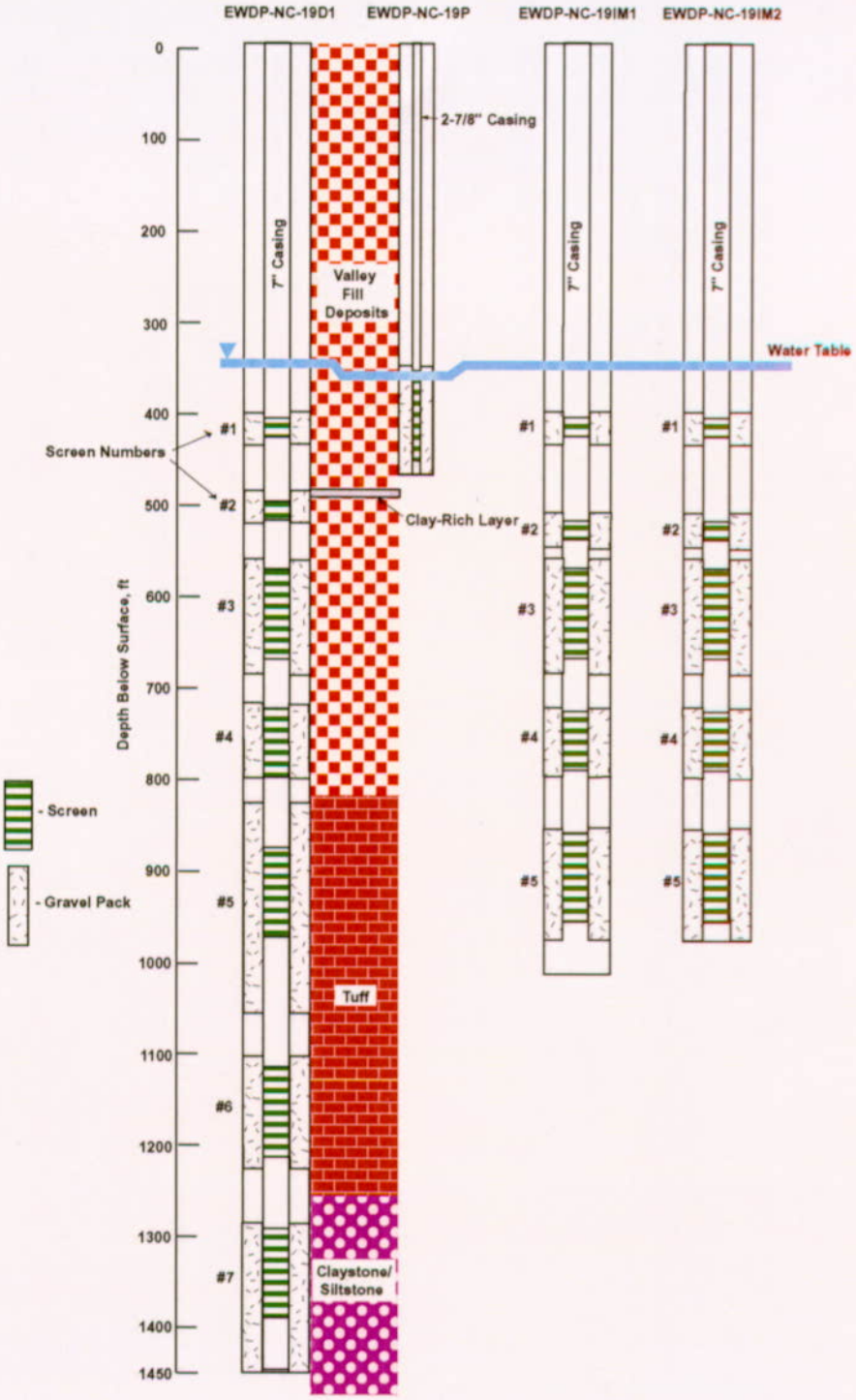

DTNs: MO0112DQRWLNYE.018 [157187] (19D1 completion); MO0112DQRWLNYE.014 [157184] (19P completion); GS011008314211.001 [158690] (19D1 lithologic log); MO0306NYE05259.165 [165876] (19IM1 well completion), MO0306NYE05260.166 [165877] (19IM2 well completion).

NOTE: The water table is higher in NC-EWDP-19D1 than in -19P because hydraulic head increases with depth. The white spaces between gravel packs below the water table are "grout and bentonite seals." The Nye County Nuclear Waste Repository Project Office reports all depths in feet.

Figure 6.1-8. Schematic Diagram of NC-EWDP-19D1, -19P, -19IM1, and -19IM2 Completions

6.1.2 Sequence of Hydraulic and Tracer Tests

Figure 6.1-9 is a graphical timeline showing the sequence of hydraulic and tracer tests conducted at the C-wells since May 1995. Each of the tests is described in detail in Sections 6.2 and 6.3. In this report, the C-wells tracer tests are split into two general categories: (1) tests involving only nonsorbing solute tracers and (2) tests involving combinations of nonsorbing and reactive solute tracers and colloid tracers (polystyrene microspheres). The former tests were conducted and interpreted primarily by the U.S. Geological Survey (USGS), and the latter were conducted and interpreted primarily by the Los Alamos National Laboratory (LANL). LANL also conducted two nonsorbing solute-only tracer tests to prepare for a multiple tracer test in the Lower Bullfrog Tuff, but these tests were not quantitatively interpreted because they were conducted primarily to determine which well, c#1 or c#2, would serve as a better injection well for multiple tracer testing when pumping c#3.

The distinction between the nonsorbing (USGS) and the multiple tracer tests (LANL) is important because the two organizations, while working closely together, took different approaches to interpreting the tracer tests. These different approaches result in different transport parameter estimates derived from the tracer responses (see Section 6.3.5 for a discussion of these differences and how they affect uncertainty). Both approaches are presented so that readers can gain an appreciation for the uncertainties in parameter estimation associated with the different methods and assumptions and can also make informed decisions about which approach they may want to give more weight when determining parameter distributions for performance assessments.

Single-well hydraulic and tracer tests were conducted in 19D1 in 2000 and 2001 (prior to the drilling of 19IM1 and 19IM2), and cross-hole hydraulic testing was conducted in the ATC wells in late 2001 and early 2002 (using 19D1 as the production well and 19IM1 and 19IM2 as observation wells). These tests are described in Sections 6.4 and 6.5 of this scientific analysis report.

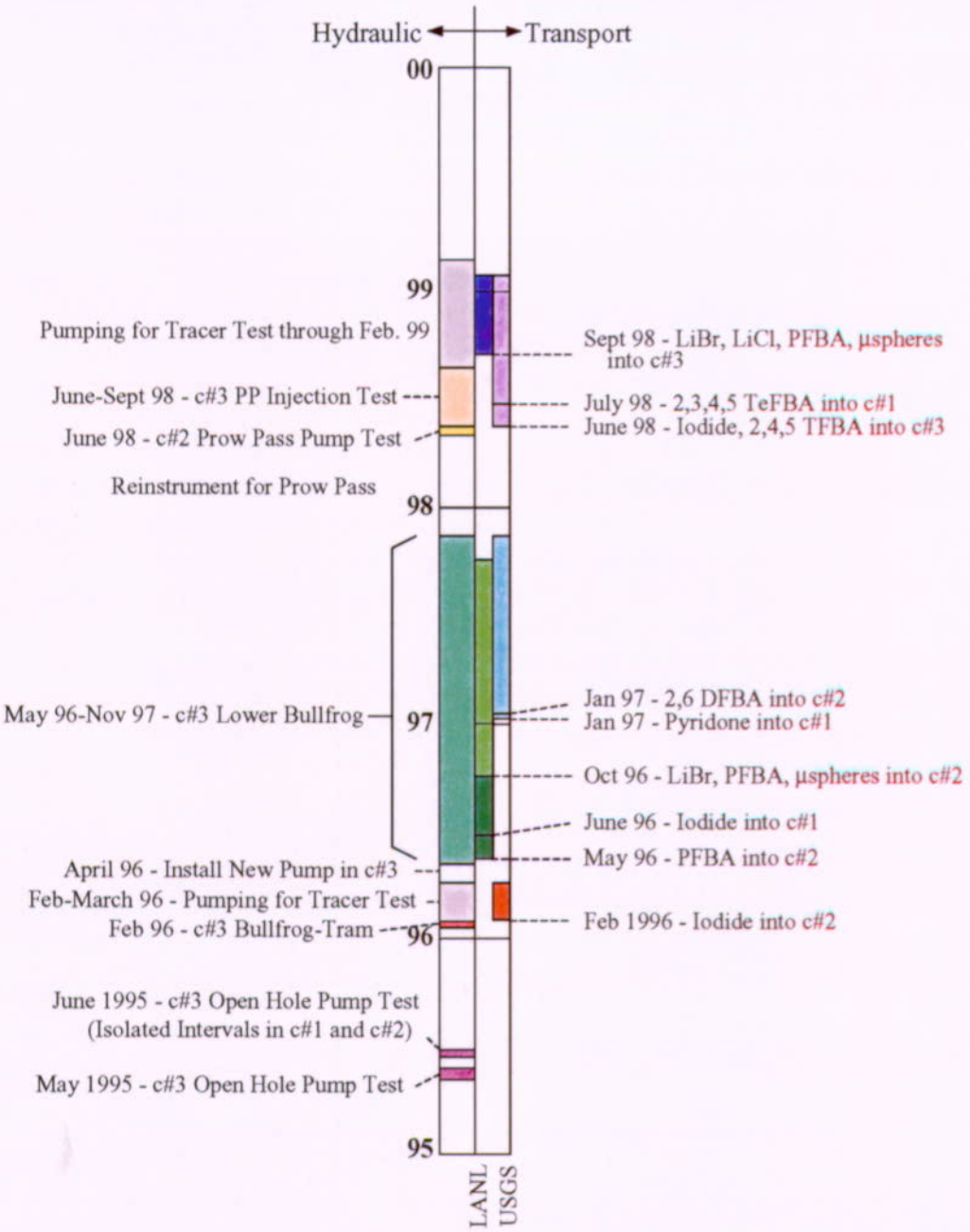

For illustration purposes only.

NOTE: The tests listed in the figure are discussed at length in Sections 6.2 and 6.3 and referenced in those sections.

Figure 6.1-9. Timeline for C-wells Hydraulic and Tracer Tests

6.1.3 Features, Events, and Processes Supported by This Scientific Analysis

The development of a comprehensive list of features, events, and processes (FEPs) potentially relevant to post-closure performance of the Yucca Mountain repository is an ongoing, iterative process based on site-specific information, design, and regulations. The approach for developing an initial list of FEPs in support of the TSPA-SR (CRWMS M&O 2000 [153246]) was documented in Freeze et al. (2001 [154365]). To support the TSPA-LA, the FEPs list was re-evaluated in accordance with *The Enhanced Plan for Features, Events, and Processes (FEPs) at Yucca Mountain* (BSC 2002 [158966], Section 3.2) and the KTI letter report *Response to Additional Information Needs on TSPAI 2.05 and TSPAI 2.06*, REG-WIS-PA-000003, (Freeze 2003 [165394]). The resulting list of FEPs to be evaluated for the TSPA-LA is documented in DTN: MO0307SEPFEPS4.000 [164527]).

This scientific analysis report does not provide the technical basis for inclusion of any of the FEPs; however, Table 6.1-3 lists the saturated-zone-related FEPs included in the TSPA-LA that are supported by the results of the analyses described in this document, and Table 6.1.3 serves as a cross-reference to FEPs-relevant sections of this report. Also, Table 6.1-3 lists the reports in which the TSPA dispositions for the included saturated-zone FEPs are located. The rationale for excluding a saturated-zone-related FEP from the TSPA-LA model will be documented in the revision (REV 02) of *Features, Events, and Processes in SZ Flow and Transport* (BSC 2003 [163128]), which may cite information from this scientific analysis report.

Table 6.1-3. Saturated Zone Included FEPs Supported by the Results in This Scientific Analysis Report

FEP Number and Name	FEP Description	Relevant Section of this Report	Report in Which TSPA Disposition is Located
1.2.02.01.0A Fractures	Groundwater flow in the Yucca Mountain region and transport of any released radionuclides may take place along fractures. The rate of flow and the extent of transport in fractures are influenced by characteristics such as orientation, aperture, asperity, fracture length, connectivity, and the nature of any linings or in-fills.	Flow in fractures is addressed throughout Section 6.2. Transport in fractures is addressed throughout Section 6.3.	*SZ Flow and Transport Model Abstraction*, MDL-NBS-HS-000021 (BSC 2003 [164870]).
1.2.02.02.0A Faults	Numerous faults of various sizes have been noted in the Yucca Mountain region and, specifically, in the repository area. Faults may represent an alteration of the rock permeability and continuity of the rock mass, alteration or short-circuiting of the flow paths and flow distributions close to the repository, and unexpected pathways through the repository.	The influence of faults on flow in the saturated volcanics is addressed in Section 6.1.1.1 and in several places in Section 6.2.	*SZ Flow and Transport Model Abstraction*, MDL-NBS-HS-000021 (BSC 2003 [164870]).

Table 6.1-3 (Continued). Saturated Zone Included FEPs Supported by the Results in This Scientific Analysis Report

FEP Number and Name	FEP Description	Relevant Section of this Report	Report in Which TSPA Disposition is Located
2.2.03.02.0A Rock Properties of Host Rock and Other Units	Physical properties such as porosity and permeability of the relevant rock units, soils, and alluvium are necessary for the performance assessment. Possible heterogeneities in these properties should be considered. Questions concerning events and processes that may cause these physical properties to change over time are considered in other FEPs.	Rock properties as they relate to flow and transport are addressed throughout Sections 6.1 through 6.5.	*SZ Flow and Transport Model Abstraction*, MDL-NBS-HS-000021 (BSC 2003 [164870]).
2.2.07.13.0A Water-Conducting Features in the SZ	Geologic features in the saturated zone may affect groundwater flow by providing preferred pathways for flow.	Geologic features affecting flow in the volcanics are addressed in Section 6.1.1.1 and throughout Section 6.2. Geologic features affecting flow in the alluvium are addressed in Section 6.4.	*SZ Flow and Transport Model Abstraction*, MDL-NBS-HS-000021 (BSC 2003 [164870]).
2.2.07.15.0A Advection and Dispersion in the SZ	Advection and dispersion processes affect contaminant transport in the SZ.	Advection and dispersion effects on transport are discussed in many places in Sections 6.3 (volcanics) and 6.5 (alluvium).	*Site-Scale Saturated Zone Transport*, MDL-NBS-HS-000010 (BSC 2003 [162419]).
2.2.07.17.0A Diffusion in the SZ	Molecular diffusion processes may affect radionuclide transport in the SZ.	Molecular diffusion processes in the volcanics are addressed in several places in Section 6.3. In Section 6.5, molecular diffusion is discussed for the alluvium, but it was concluded that it did not have a major effect on transport in ATC single-well tracer tests.	*Site-Scale Saturated Zone Transport*, MDL-NBS-HS-000010 (BSC 2003 [162419]).
2.2.08.08.0A Matrix Diffusion in the SZ	Matrix diffusion is the process by which radionuclides and other species transported in the SZ by advective flow in fractures or other pathways move into the matrix of the porous rock by diffusion. Matrix diffusion can be a very efficient retarding mechanism, especially for strongly sorbed radionuclides, due to the increase in rock surface accessible to sorption.	The effects of matrix diffusion on transport in the volcanics are discussed in Sections 6.3.4.2 and 6.3.4.3. Observations and parameterizations of matrix diffusion in the volcanics are addressed in several places in Section 6.3. Matrix diffusion in the alluvium is discussed in Section 6.5, but it was concluded that matrix diffusion did not have a significant effect on transport in ATC single-well tracer tests.	*Site-Scale Saturated Zone Transport*, MDL-NBS-HS-000010 (BSC 2003 [162419]).

Table 6.1-3 (Continued). Saturated Zone Included FEPs Supported by the Results in This Scientific Analysis Report

FEP Number and Name	FEP Description	Relevant Section of this Report	Report in Which TSPA Disposition is Located
2.2.08.10.0A Colloidal Transport in the SZ	Radionuclides may be transported in groundwater in the SZ as colloidal species. Types of colloids include true colloids, pseudo colloids, and microbial colloids.	Colloid transport in the volcanics is addressed in Section 6.3.4. Colloid detachment rates in the alluvium are addressed in Section 6.5.4.6. Colloid-facilitated transport of radionuclides is not directly addressed in this report.	*SZ Flow and Transport Model Abstraction*, MDL-NBS-HS-000021 (BSC 2003 [164870]).
2.2.12.00.0B Undetected Features in the SZ	This FEP is related to undetected features in the SZ portion of the geosphere that can affect long-term performance of the disposal system. Undetected but important features may be present, and may have significant impacts. These features include unknown active fracture zones, inhomogeneities, faults and features connecting different zones of rock, and different geometries for fracture zones.	The potential influence of undetected features (primarily faults) on flow in the volcanics is discussed throughout Section 6.2. The potential influence of layered heterogeneity on flow in the alluvium is discussed in Section 6.4.	*SZ Flow and Transport Model Abstraction*, MDL-NBS-HS-000021 (BSC 2003 [164870]).

6.2 HYDROLOGIC PROPERTIES OF FRACTURED TUFFS (C-WELLS COMPLEX)

The hydrologic properties of the fractured tuffs at Yucca Mountain were obtained as part of on-going investigations of the hydrologic and geologic suitability of Yucca Mountain as a high-level nuclear waste repository by the USGS in cooperation with the DOE. Five cross-hole hydraulic tests, some in conjunction with tracer tests, were conducted by the USGS at the C-wells complex in May and June 1995, February 1996, from May 1996 to November 1997, and between April and June 1998. The first test, conducted in May 1995, is documented in Geldon et al. (1998 [129721]). The second through fourth tests (June 1995, February 1996, and May 1996 to November 1997) are documented in Geldon et al. (2002 [161163]) and reproduced in this report. The fifth test, conducted between April and June 1998, is only described in this report.

This section of the report has three parts: (1) it describes the hydraulic tests conducted, the changes in water levels in monitoring wells as a result of pumping, and analyses performed on the test data; (2) it extrapolates test results to interpret groundwater flow paths in Miocene tuffaceous rocks beyond the immediate vicinity of the C-wells complex; and (3) it evaluates the uncertainties associated with the test data, analyses, and values of hydraulic properties determined from test analyses.

The analyses performed on the test data to obtain transmissivity, hydraulic conductivity, and storativity are various analytical (as opposed to numerical) solutions of the groundwater flow equation, which assumes a radial flow regime to the pumping well, constant aquifer thickness, and a homogeneous and isotropic medium. In order to calculate anisotropy in the horizontal hydraulic conductivity, analytic solutions of the groundwater flow equation for homogeneous, anisotropic media were employed.

Use of analytic solutions that assume uniform aquifer parameters is commensurate with the spatial distribution of the available geohydrologic and geophysical data. These analytic solutions represent the first-order answer to what the hydraulic parameters at the saturated fractured volcanics are in a manner that does not inflate the knowledge base obtained from actual field data. These methods assume that the tested volume of rock has one average transmissivity and storativity value between the pumping well and the observation well. Only one number is obtained from the analysis, and one is restricted to a set of simplifying assumptions, but the knowledge base is not inflated. Alternately, the rock mass can be divided into discrete blocks with various parameter values assumed for the different blocks by using a numerical model. Non-conformance of field conditions to the simplifying assumptions required by analytic solutions is dealt with by defining a three-dimensional (3-D) flow system with sophisticated boundary conditions. However, the flexibility of being able to attribute various parameter values spatially and obviate the restrictions of the simplifying assumptions of analytic solutions is gained at the expense of a high risk of inflating the existing knowledge base. The "model" assumes its own life and can produce just as non-unique a set of parameters as can inexperienced application of analytic solutions. Analytic solutions were selected for this study to obtain a basic overall picture of the hydraulic parameter distribution in the saturated fractured volcanics at the Yucca Mountain site with as little inflation of the knowledge base derived from actual field data as possible.

At the C-wells complex, several analytic solutions to the groundwater flow equation were used. Following are the dominant modes of analysis used for each geohydrologic interval or aquifer. Details of these solutions and exceptions to the dominant modes presented here are found in Section 6.2.4. To analyze responses in the Calico Hills aquifer, which is at the water table, the Neuman (1975 [150321]) unconfined-aquifer solution was used to analyze successfully five out of six responses in this aquifer among the various tests. To analyze the Prow Pass aquifer and the Upper Bullfrog and Lower Bullfrog aquifers, which are confined below the largely unconfined Calico Hills aquifer, either confined single-porosity (Theis 1935 [150327]) or confined dual-porosity (Streltsova-Adams 1978 [150754]) solutions were mostly used, depending on whether the test duration was long enough for the fractured-rock aquifers to exhibit their dual-porosity character. To analyze the Upper Tram aquifer, which is intersected by the known faults present at the bottom of the C-wells that provide a source of recharge or "leakage," the leaky-confined Hantush (1956 [165169]) solution was used successfully for all tests.

6.2.1 Earlier Studies

Before the in-situ testing of the fractured tuffs at Yucca Mountain began in May 1995 (Geldon et al. 1998 [129721]), studies were conducted to determine hydrogeologic intervals of the rocks, flow patterns, geologic influences, geologic properties of the rocks, and the hydraulic results of an open-hole test in one of the C-wells. Most of these studies have been published and are referred to in this section. Hydrogeologic intervals discussed in this report were identified by Geldon (1996 [100396], pp. 9 to 69) on the basis of borehole geophysical logs, borehole flow surveys, cross-hole seismic tomography, and aquifer tests. Geophysical logs run in the C-wells include caliper, borehole-deviation, temperature, resistivity, gamma-gamma, acoustic, epithermal neutron, acoustic televiewer, and television logs (Geldon 1993 [101045], pp. 14 to 18). Flow surveys run in the C-wells include tracejector, heat-pulse flowmeter, spinner, and oxygen-activation surveys (Geldon 1993 [101045], pp. 14 to 18; Geldon 1996 [100396], pp. 12 to 69). Tracejector surveys using radioactive iodide were run in the C-wells during hydraulic tests conducted in 1983 and 1984. Heat-pulse flowmeter surveys were run in 1991 without the boreholes being pumped. Spinner and oxygen-activation surveys were run in borehole c#3 during the hydraulic test in June 1995 (described in Section 6.2.3.1). In 1993, a seismic tomogram was conducted between boreholes c#2 and c#3 by Lawrence Berkeley National Laboratory (LBNL) for the USGS and reported to the USGS by written communication from E. Majer, LBNL (Geldon et al. 2002 [161163], p. 2). That tomogram showed many of the hydrogeologic details evident from borehole lithologic and geophysical logs and flow surveys.

Hydraulic properties of the intervals in the C-wells and the manner in which they transmit water were determined provisionally by Geldon (1996 [100396], pp. 12 to 69) from geophysical logs, laboratory analyses, and aquifer tests. A matrix-porosity profile for the C-wells was developed from a gamma-gamma log and nine values of core porosity obtained from c#1 in 1983 (Geldon 1993 [101045], p. 62, Table 13). Geldon (1996 [100396], pp. 9 to 69) developed a matrix-permeability profile for the C-wells from permeameter tests on 89 core samples obtained from the C-wells and four nearby boreholes between 1980 and 1984. Geldon (1996 [100396], pp. 9 to 69) developed a hydraulic-conductivity profile for the C-wells by analyzing falling-head and pressure-injection tests done in c#1 in 1983. Transmissivity, hydraulic conductivity, and storativity of discrete intervals within the Calico Hills Formation and the Crater Flat Group were determined (Geldon 1996 [100396], pp. 9 to 69) from analyses of a constant-flux injection test in

c#2 and three hydraulic tests in c#2 and c#3 performed in 1984. Simultaneous monitoring of water-level and atmospheric-pressure fluctuations in 1993 established the barometric efficiency of the C-wells (Geldon et al. 1997 [156827], p. 11). The open-hole hydraulic test determined the transmissivity, hydraulic conductivity, and storativity of the composite saturated thickness of Miocene tuffaceous rocks at the C-wells complex; lateral variations in hydraulic properties within a 3.2-km radius of the C-wells complex; and possible hydraulic connection between the tuffaceous rocks and the underlying regional aquifer composed of Paleozoic carbonate rocks (Geldon et al. 1998 [129721], pp. 30, 31).

A hydraulic test conducted at the C-wells complex from May 22 to June 12, 1995 (data reside in DTN: GS960108312313.001 [164801]), indicated that the composite section of tuffaceous rocks in the vicinity of the C-wells has a transmissivity of 2,300 m^2/d (square meters per day) and a storativity of 0.003 (Geldon et al. 1998 [129721], p. 41). That test also indicated transmissivity values of 1,600 to 3,200 m^2/d and storativity values of 0.001 to 0.003 for the rocks in individual boreholes (c#1, c#2, ONC-1, and USW H-4). Hydraulic tests conducted in 1984 indicated that those intervals have layered heterogeneity (Geldon 1996 [100396], pp. 9 to 69).

6.2.2 Instrumentation Used in C-Wells Hydraulic Testing

Principal components of the equipment installed at the C-wells complex to conduct hydraulic tests from 1995 to 1997 are available commercially, but much of this hardware and software has not been used extensively because of its relatively recent development. Consequently, all of the equipment received extensive performance evaluation during prototype hydraulic tests conducted jointly with LBNL from 1992 to 1994 at a research site near Raymond, California. Modifications to system components and their assembly were made to address problems encountered during prototype testing and after the equipment was installed and initially used at the C-wells complex (Umari et al. 1994 [164543], pp. 2413 to 2422). With few exceptions (discussed below), most system components performed to specifications, despite being operated almost continuously for more than two years.

6.2.2.1 Packers

Dual-mandrel packers, manufactured by TAM International, Inc., were installed in c#1 and c#2 throughout the tests and in c#3 after August 1995. The packers are about 1.83 m long and have a deflated diameter of about 21.6 centimeters (cm) (see Geldon et al. 2002 [161163], Figure 5). Suspended on 7.30-cm-diameter tubing, each packer contains 12 pass-through tubes to allow packer-inflation lines and electrical cable to be installed in the borehole. The packers are inflated individually by injection of argon gas through 0.64-cm, stainless-steel tubing. Inflation pressures, which are about 1,034 kPa above hydrostatic pressure, range from about 2,758 to 5,861 kPa at the depths at which packers were set in the C-wells from 1995 to 1997. Packer depths from 1995 to 1997, as measured from the land surface, are listed in Table 6.2-1.

Table 6.2-1. Location of Packers Emplaced in the C-wells Complex for Hydraulic Tests, 1995 to 1997

Packer Number	Packer Depth (m below land surface)			
	UE-25 c#1	UE-25 c#2	UE-25 c#3	
			8/95–4/96	4/96–11/97
1	547.4–549.3	531.3–533.1	540.4–542.2	None
2	605.3–607.2	605.6–607.5	609.9–611.7	None
3	698.3–700.1	696.5–698.3	695.0–696.8	694.6–696.5
4	797.1–798.9	791.9–793.7	812.6–814.4	812.9–814.7
5	869.9–871.7	869.6–871.4	877.5–879.4	878.1–880.0

Output DTN: GS031008312314.004 (from Input DTN: GS030508312314.003 [164425], p. 12, Table 3).

NOTE: There were no packers in UE-25 c#3 before August 1995.

6.2.2.2 Transducers

Continuous records of pressures and temperatures in packed-off intervals during hydraulic tests were obtained using absolute pressure transducers (manufactured by Paroscientific, Inc), which record water pressure plus atmospheric pressure. The transducers used in the C-wells were strapped into brackets welded onto the 7.30-cm-diameter tubing on which the packers were suspended. Field determinations indicated a precision of 0.30 cm under pumping conditions and 0.061 cm under non-pumping conditions.

Although transducers were installed in all hydrogeologic intervals, several of the transducers failed after installation. Transducers that were operative during some or all of the hydraulic tests conducted from 1995 to 1997 and the locations of those transducers, as determined by subtracting recorded pressure heads from static water-level altitudes, are listed in Table 6.2-2. Listed transducer altitudes have an accuracy of ±0.3 m.

6.2.2.3 Barometers

A nonsubmersible, temperature-compensated pressure transducer, manufactured by Paroscientific, Inc., was used as a barometer during the 1995 to 1997 hydraulic tests. The barometer operated in a temperature-controlled office trailer at the C-wells complex. The factory-calibrated accuracy of this barometer is ±0.005 percent of its full operating range (103 kPa). The barometer was checked periodically against another barometer of the same type in the same office trailer.

6.2.2.4 Pumps

A 37-stage, 25.2- liters per second (L/s) capacity, Centrilift submersible pump was used during the hydraulic test in June 1995. The pump was suspended in borehole c#3 on 13.9-cm-diameter tubing. The pump intake depth was 450.1 m (48.0 m below the water-level altitude prior to pumping). The pump was powered by a 250-KW generator, and its frequency was regulated by a variable-speed controller. Water discharged by the pump was transported by a 15-cm-diameter pipeline to a leachfield in Fortymile Wash, about 8 km from the C-wells complex.

Table 6.2-2. Operative Transducers in the C-wells, 1995 to 1997

Borehole	Interval	Transducer		
		Number	Depth (m)	Altitude (m)
UE-25 c#1	Prow Pass	2	552.09	578.51
	Upper Bullfrog	3	610.03	520.57
	Lower Bullfrog[(a)]	4	703.04	427.56
UE-25 c#2	Calico Hills	1	519.83	612.36
	Prow Pass	2	536.28	595.91
	Upper Bullfrog	3	610.70	521.49
	Lower Bullfrog[(a)]	4	701.58	430.61
UE-25 c#3	Calico Hills[(b)]	1	533.81	598.62
	Upper Bullfrog	3	614.49	517.93
	Lower Bullfrog[(c)]	4	708.93	423.49
	Upper Tram[(d)]	5	817.68	314.75

Output DTN: GS031008312314.004 (from Input DTN: GS030508312314.003 [164425], Table 4).

NOTE: (a) Monitored Lower Bullfrog and Upper Tram together, February to March 1996.

(b) Listed transducer locations are for August 1995 to March 1996. Prior to August 1995, a single transducer was installed in the Calico Hills interval at a depth of 441.12 m (altitude = 691.30 m) to monitor the composite geologic section in c#3. After April 1996, a new transducer was installed at a depth of 691.31 m (altitude = 441.11 m) to monitor the Calico Hills, Prow Pass, and Upper Bullfrog intervals combined.

(c) Operative after April 1996.

(d) Monitored Lower Bullfrog and Upper Tram together in February and March 1996; replaced in April 1996 by a transducer at a depth of 819.32 m (altitude = 313.11 m).

The original pump was replaced in August 1995 by a 43-stage, 12.6 L/s-capacity, Centrilift submersible pump. That pump, enclosed in a protective shroud, was offset from the main part of the 7.30-cm-diameter tubing on which the packers were suspended by a 22.9-m-long "Y-block" assembly (see Geldon et al. 2002 [161163], Figure 6 for detailed drawing). The Y-block assembly was designed to allow wireline tool access past the pump for opening and closing sliding sleeves (screens installed to allow water movement to or from test intervals) and for placing a plug in the tubing to prevent recirculation of water through the pump shroud.

Although the Y-block assembly facilitated operations, its placement in the instrument string created problems that eventually caused pump performance to degrade beyond an acceptable level during hydraulic and tracer tests conducted in February and March 1996. Because the combined diameter of the Y-block assembly and main section of the instrument tubing (24.7 cm) was about the same as the borehole diameter below a depth of 463.4 m, the pump intake had to be set about 247 m above the top of the slotted section of pipe open in the test interval. Frictional head losses produced by water flowing through small openings (slots) in the intake tubing and through the tubing from the test interval to the pump intake caused the pump to operate at the limit of its designed performance range. Consequently, discharge decreased from 8.77 L/s when pumping started on February 8, 1996, to 6.18 L/s when pumping was terminated on March 29, 1996.

In April 1996, the pump-performance problem was addressed by (1) discarding the Y-block; (2) suspending a 72-stage, 12.6 L/s-capacity Centrilift pump enclosed in a narrower shroud directly on the 7.30-cm-diameter tubing; (3) lowering the pump to within about 47 m of the interval to be tested; and (4) adding 6.1 m of slotted pipe in the test interval. From May 1996 to March 1997, the reconfigured pump assembly performed without major problems and sustained a relatively constant discharge of 9.34 to 9.84 L/s. Problems with one of the generators providing power to the pump caused the pump to operate erratically between March 26 and May 8, 1997, but the pump performed adequately again after the generator problem was resolved.

6.2.2.5 Flowmeters

A McCrometer turbine-type flowmeter was used during the hydraulic test in June 1995. Subsequently, the primary device used for monitoring discharge was a differential switched capacitor, vortex flowmeter, manufactured by Endress and Hauser, measuring vortex frequency past a bluff body, with signal output converted to voltage output across a temperature-controlled resistor.

The flowmeter signal was recorded at user-specified intervals by monitoring software installed on a personal computer (PC) in the office trailer at the C-wells complex (see Section 6.2.2.6). The software program used a regression equation developed on the basis of the flowmeter calibration to convert the voltage signal from the flowmeter to a discharge rate.

6.2.2.6 Data Acquisition and Instrument Control

Data acquisition from and control of the transducers, barometer, flowmeter, and an automatic water sampler used for tracer tests was accomplished with a commercially available, graphic-language software program called LabView (Johnson 1994 [156837]). Installed on the PC in the office trailer, LabView made the PC monitor screen look and act like an instrument panel.

Two separate programs were written for data acquisition and instrument control. One program communicated with the transducers, barometer, and flowmeter; the other program communicated with the automated water sampler during tracer tests. The two programs ran simultaneously.

6.2.3 Results and Interpretations of Hydraulic Tests

The results and interpretations of the hydraulic tests discussed below include the conceptual models considered and tested.

6.2.3.1 Hydraulic Tests Conducted between June 1995 and November 1997

Three hydraulic tests were conducted at the C-wells complex from June 1995 to November 1997 (see timeline in Figure 6.1-9). During June 12 to June 22, 1995, well c#3 was pumped, without packers installed, and drawdown and recovery were measured in six hydrogeologic intervals (Figure 6.2-5) that were separated by packers in wells c#1 and c#2 (see Table 6.2-1). From February 8 to February 13, 1996, c#3 was pumped, with packers inflated to isolate the Bullfrog-Tram interval, to establish a steady-state hydraulic gradient for a tracer test in the Bullfrog-Tram interval that continued until March 29, 1996. Drawdown was analyzed in the Bullfrog-Tram

interval and in all other packed-off intervals of c#1 and c#2 that responded to pumping during the hydraulic test.

In the third hydraulic test, with packers inflated to isolate the Lower Bullfrog Tuff interval, c#3 was pumped for 553 days, from May 8, 1996 to November 12, 1997, before and during a series of tracer tests in the Lower Bullfrog interval. Drawdown was analyzed in this interval and in all other intervals of c#1 and c#2 that responded to pumping before mechanical problems developed on March 26, 1997. Drawdown was analyzed in UE-25 ONC-1 (ONC-1), USW H-4 (H-4), UE-25 WT#14 (WT#14), and UE-25 WT#3 (WT#3) for periods from 7 to 18 months to evaluate heterogeneity and scale effects in the Miocene tuffaceous rocks. Water levels in UE-25 p#1 (p#1), completed in Paleozoic carbonate rocks, were measured to detect a hydraulic connection between the Miocene tuffaceous rocks and the Paleozoic carbonate rocks in the vicinity of the C-wells.

6.2.3.1.1 Analytical Methods

Although rock at the C-wells complex is fractured pervasively, hydrogeologic intervals respond to pumping as an equivalent porous medium (Geldon 1996 [100396], pp. 12 to 69; Geldon et al. 1998 [129721], pp. 29 to 31). Because the water table occurs at or near the top of the Calico Hills interval in the vicinity of the C-wells complex, that interval typically responds to pumping as an anisotropic, unconfined aquifer. With pervasive fracturing that apparently extends to the water table (Geldon et al. 2002 [161163], p. 15]), the Prow Pass and Upper Bullfrog intervals respond to pumping as either an unconfined, fissure-block, or confined aquifer. Isolated by intervals of nonfractured rock, the Lower Bullfrog interval typically responds to pumping as a confined aquifer. Recharged by flow from fractures related to faults (identified on lithologic logs prepared by Richard W. Spengler and included in a report by Geldon (1993 [101045], pp. 35 to 37, Table 4), the Upper Tram interval typically responds to pumping as a leaky, confined aquifer without confining bed storage.

Analytical methods used for hydraulic tests discussed in this section are those of Theis (1935 [150327]) and Cooper and Jacob (1946 [150245]), for infinite, homogeneous, isotropic, confined aquifers; Neuman (1975 [150321]), for infinite, homogeneous, anisotropic, unconfined aquifers; and Streltsova-Adams (1978 [150754]), for fissure-block aquifers. Geldon (1996 [100396], pp. 21 to 69) discusses assumptions, equations, and application of these analytical methods in hydraulic tests at the C-wells complex. Analysis of drawdown in this study was restricted to observation wells because drawdown in pumping wells at the C-wells complex typically is too large and rapid to be explained solely by hydraulic properties of the pumped interval (Geldon 1996 [100396], pp. 21 to 69). This observation can be illustrated by looking at the drawdown in c#3 at 464,000 minutes (322.22 days) after pumping began on May 8, 1996. That drawdown was 599 cm. With hydraulic properties computed for the Lower Bullfrog interval in c#1 and c#2 inserted into an approximation of the Theis (1935 [150327]) equation as given by Equation 19 of Lohman (1972 [150250]), the drawdown in c#3 attributable to aquifer characteristics should have been no more than 69 to 72 cm after 322.22 days of pumping, or 12 percent of the actual recorded drawdown. Most of the drawdown in c#3 probably can be attributed to frictional head loss. Therefore, calculation of hydraulic properties from that drawdown is not reliable.

All of the analytical methods used in this study, except for the Neuman (1975 [150321]) method, assume radial flow to the pumping well, and, therefore, ignore vertical flow (application of the Neuman fully-penetrating-well solution, as was done in this report, to cases where pumping was in one interval and the analyzed drawdown response was in another, also ignores vertical flow). However, in hydraulic tests of the Bullfrog-Tram interval (February 1996) and the Lower Bullfrog interval (May 1996 to March 1997), drawdown was observed in the Calico Hills, Prow Pass, and Upper Bullfrog intervals, even though the sliding sleeves allowing direct communication between those intervals and the flow intake piping were not open. For water to reach the pumping well from the intervals that did not have open sliding sleeves, a downward component of flow must have occurred. The downward flow was assumed by the investigators to be much less than radial flow to the pumping well in order to analyze the drawdown from the non-open intervals by the methods outlined in this section. Hydraulic properties calculated under this assumption have a high level of confidence because they generally are consistent with quantitative results of the hydraulic test conducted in June 1995, which was designed such that flow from hydrogeologic intervals in c#1 and c#2 to c#3 would be largely radial.

6.2.3.1.2 Earth Tides and Barometric Effects

Previous monitoring of water levels in observation wells before, during, and after hydraulic tests conducted in the C-wells indicated that all of those boreholes respond to Earth tides and atmospheric pressure changes. With frequencies of 0.9 to 2.0 cycles per day (Galloway and Rojstaczer 1988 [156826], p. 107, Table 2), Earth tides caused water levels in the C-wells to fluctuate as much as 12 cm during a 10-day hydraulic test conducted at the C-wells complex from May to June 1995 (Geldon et al. 1998 [129721], Figure 21). Consequently, in the hydraulic testing described here, Earth-tide effects were removed from water levels, and cycles of the same frequency as Earth tides were removed from simultaneously recorded atmospheric pressures before computing the barometric efficiency of most borehole intervals. Earth-tide effects also were removed from the records of observation wells in which drawdown caused by pumping was expected to be obscured by Earth tides (boreholes H-4, WT#14, WT#3, and p#1). The boreholes requiring an Earth-tide correction to water-level records were completed in Miocene tuffaceous rocks more than 1,500 m from c#3 or were completed in a different aquifer than that of the C-wells complex (i.e., in the Paleozoic carbonate rocks). Earth-tide effects were removed from records of water levels, and cycles of the same frequency as Earth tides were removed from simultaneously recorded atmospheric pressure by applying a low-pass filter with a cutoff frequency of 0.8 cycles/day to those records. As shown in Figure 6.2-1, this filtering removes semi-diurnal changes in water levels while preserving longer-term trends.

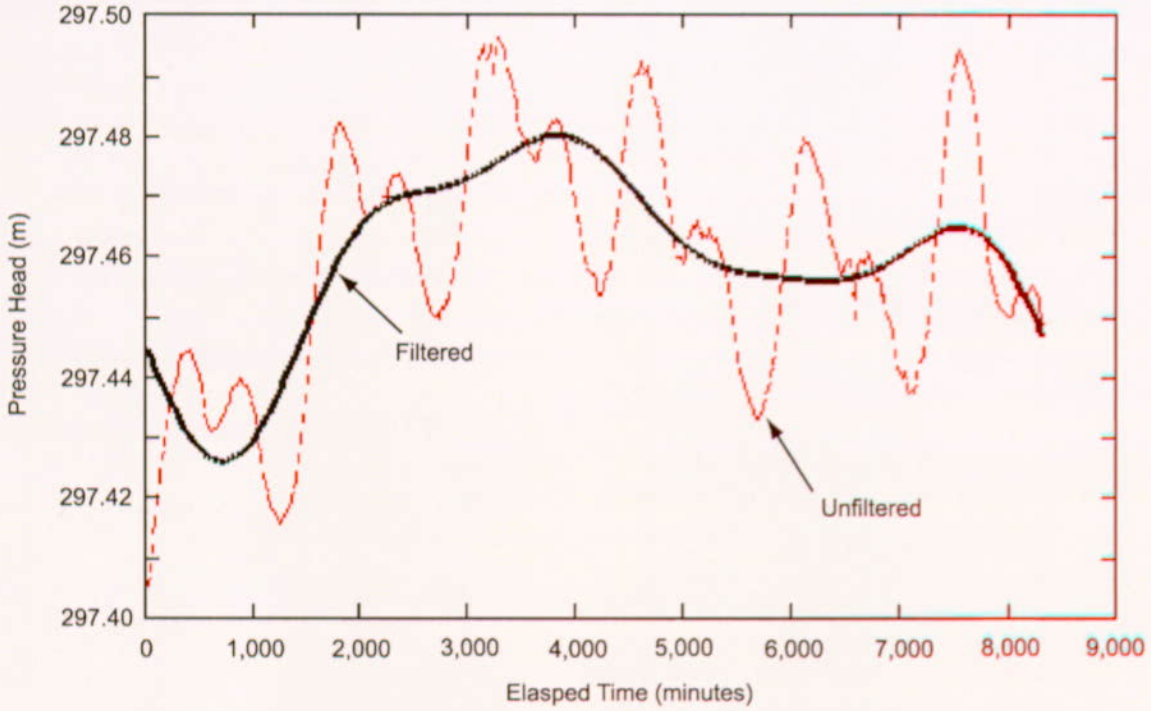

Output DTN: GS031008312314.004 (from Input DTN: GS030508312314.003 [164425], p. 16, Figure 7).

Figure 6.2-1. Result of Filtering Out Earth Tides on UE-25 c#2 Lower Bullfrog Interval Pressure Heads, June 23–29, 1995

Changes in atmospheric pressure in the vicinity of the C-wells complex typically produce synchronous (but opposite) changes in water levels in boreholes (Figure 6.2-2). The slope of a line fit to a plot of water-level change as a function of atmospheric-pressure change is called the barometric efficiency. Determination of the barometric efficiency of the Lower Bullfrog interval in c#2 is shown in Figure 6.2-3. Barometric efficiency values of borehole intervals for which drawdown was computed during this study ranged from 0.75 to 0.99 (Table 6.2-3). To compute barometrically corrected drawdown, barometric effects were removed from borehole records by subtracting the product of atmospheric-pressure change and barometric efficiency from the change in water level.

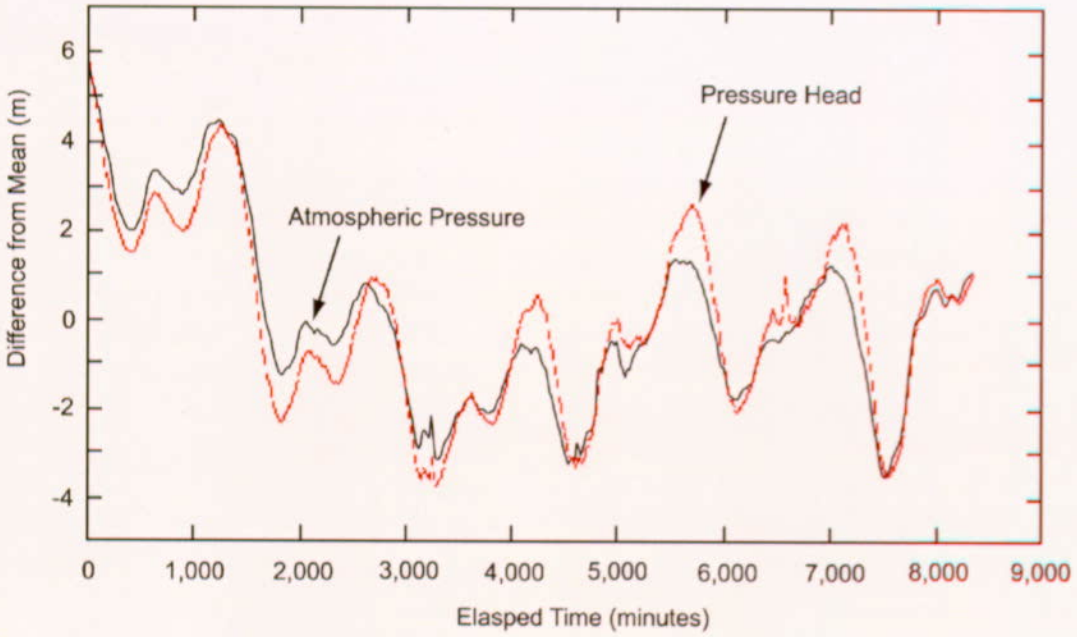

Output DTN: GS031008312314.004 (from Input DTN: GS030508312314.003 [164425], Figure 8).

Figure 6.2-2. Difference of the Atmospheric Pressure from Its Mean Plotted Against the Opposite of the Difference of Concurrent Pressure Head from Its Mean

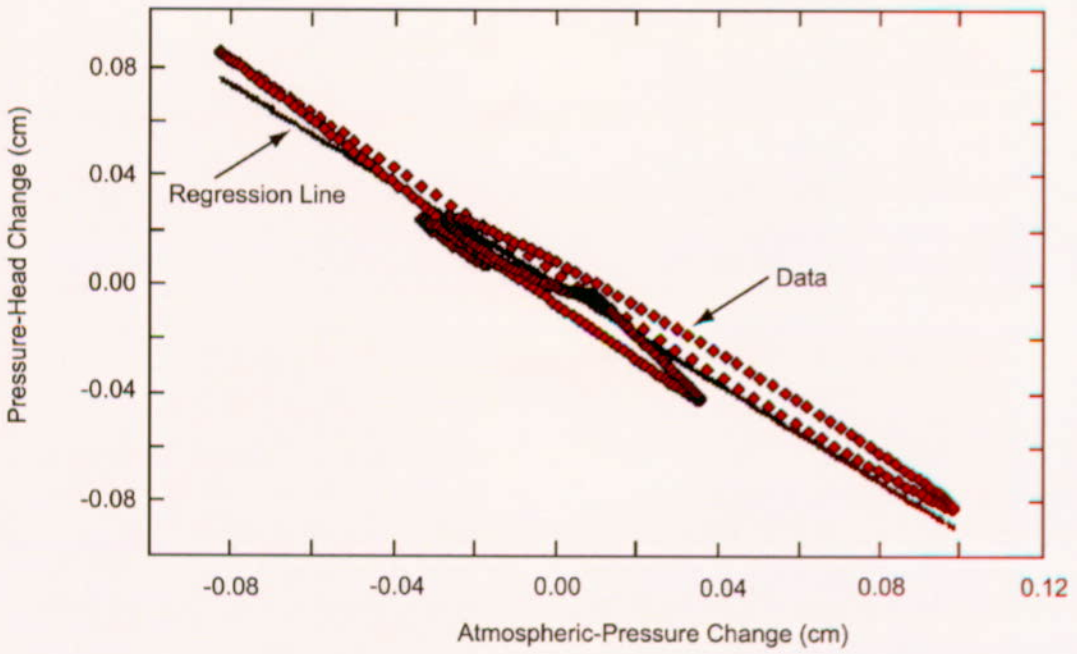

Output DTN: GS031008312314.004 (from Input DTN: GS030508312314.003 [164425], Figure 9).

Figure 6.2-3. Filtered Pressure-head Change in UE-25 c#2 Lower Bullfrog Interval as a Function of Filtered Atmospheric-Pressure Change at the C-wells Complex, June 23–29, 1995

Table 6.2-3. Barometric Efficiency Values Determined for Borehole Intervals Monitored at the C-wells Complex, Through May 13, 1996

Borehole	Interval	Barometer Location	Period of Record	Barometric Efficiency	Regression Coefficient
UE-25 c#1	Prow Pass	C-wells	June 23–29, 1995	0.96	0.98
	Upper Bullfrog	C-wells	June 24–29, 1995	0.99	0.97
	Lower Bullfrog[a]	C-wells	June 23–29, 1995	0.97	0.98
	Bullfrog-Tram	C-wells	June 23–29, 1995	0.97	0.98
UE-25 c#2	Calico Hills	C-wells	June 23–29, 1995	0.93	0.94
	Prow Pass	C-wells	June 23–29, 1995	0.93	0.97
	Upper Bullfrog	C-wells	June 23–29, 1995	0.93	0.97
	Lower Bullfrog[a]	C-wells	June 23–29, 1995	0.91	0.96
	Bullfrog-Tram	C-wells	June 23–29, 1995	0.91	0.96
UE-25 c#3	Calico Hills[b]	C-wells	February 7–8, 1996	0.83	0.89
	Lower Bullfrog	C-wells	May 9–13, 1996	0.87	0.92
	Bullfrog-Tram	C-wells	Not applicable	0.94[c]	Not applicable
UE-25 ONC-1	Prow Pass	ONC-1	July 1–Sept. 13,1995	0.99	0.90
USW H-4	Prow Pass to Lithic Ridge	ONC-1	June 8–12, 1995	0.91	0.87
UE-25 WT#14	Calico Hills	C-wells	June 4–12, 1995	0.89	0.94
UE-25 WT#3	Lower Bullfrog	C-wells	June 4–12, 1995	0.91	0.82
UE-25 p#1	Paleozoic carbonates	C-wells	Jan. 1–June 20, 1986	0.75	Not applicable

Output DTN: GS031008312314.004 (from Input DTN: GS030508312314.003 [164425], p. 18, Table 5).

NOTE: (a) Barometric efficiency of Lower Bullfrog used, also, for Bullfrog-Tram in hydraulic test February 8–13, 1996.

(b) Barometric efficiency of Calico Hills used, also, for Calico Hills-Upper Bullfrog in hydraulic test February 8–13, 1996.

(c) Barometric efficiency estimated from values for Bullfrog-Tram in c#1 and c#2.

(d) "Not applicable" means that no record was used to calculate the barometric efficiency for the Bullfrog-Tram in c#3, per se. The barometric efficiency, in this case, was "estimated" by assuming that it was the average of the barometric efficiency for the Bullfrog-Tram in c#1 and c#2.

6.2.3.1.3 Flow Distribution in the C-wells

During hydraulic tests conducted in the C-wells in February 1996 and from May 1996 to November 1997, all hydrogeologic intervals in the C-wells that were being monitored responded to pumping, regardless of the interval being pumped. Leakage around packers could have occurred, although the packers were seated in non-rugose, sparsely fractured zones, but it is extremely unlikely that all packers failed to seal properly. A more reasonable interpretation is that fractures beyond borehole walls are so interconnected that packers emplaced in the C-wells do not isolate the interval being pumped from other transmissive intervals within the volume of aquifer stressed by the pumping.

Spinner and oxygen-activation flow surveys (Figure 6.2-4) were run in c#3 during the hydraulic test in June 1995 to determine the flow distribution in the C-wells under pumping conditions.

However, those flow surveys failed to detect flow from the Prow Pass interval that was indicated by heat-pulse flowmeter surveys conducted without pumping in the C-wells in 1991 (Geldon 1996 [100396], pp. 12 to 20). Oxygen activation logs, employing high-energy "fast" neutrons, can dynamically detect water movement inside and outside of casing. The technique consists of a short neutron-activation period followed by a longer data-acquisition period; flow is detected when the measured count-rate profile does not match the expected profile for a static environment. Results of the 1991 and 1995 flow surveys were combined algebraically to estimate a flow distribution during the hydraulic test in June 1995 (Table 6.2-4). That flow distribution was adjusted for the hydraulic tests conducted in February 1996 and May 1996 to November 1997 (Table 6.2-4) by inserting discharge and drawdown values recorded at the same elapsed time in the three hydraulic tests into Equation 1c below, which is an algebraic manipulation of Equations 1a and 1b:

$$s_1 = (P_1 Q_1 / 4\pi T) W(u) \qquad \text{(Eq. 1a)}$$

$$s_2 = (P_2 Q_2 / 4\pi T) W(u) \qquad \text{(Eq. 1b)}$$

$$P_2 = Q_1 P_1 s_2 / Q_2 s_1 \qquad \text{(Eq. 1c)}$$

where

$u = r^2 S / 4Tt$ is a dimensionless parameter in which:

- r[L] = radial distance from pumping well
- S[L^0] = storativity
- T[L/T]= transmissivity of the hydrogeologic interval in question, which is the same in Equations 1a and 1b
- t[T] = elapsed time from beginning of pumping.

$W(u) = \int_u^\infty \{(e^{-u}/u)\, du\}$; $W(u)$ is the well function, which can be a confined, unconfined, or leaky well function.

- P_1[L^0] = test in June 1995.
- P_2[L^0] = the proportion of flow determined for a hydrogeologic interval during a hydraulic test in either February 1996 or May 1996 to November 1997, as appropriate.
- Q_1[L^3/T] = the average discharge during the hydraulic test in June 1995.
- Q_2[L^3/T] = the average discharge during a hydraulic test in February 1996 or May 1996 to November 1997, as appropriate.
- s_1[L] = the drawdown in a hydrogeologic interval during the hydraulic test in June 1995.
- s_2[L] = the drawdown in a hydrogeologic interval during a hydraulic test in either February 1996 or May 1996 to November 1997, as appropriate.

Equations 1a and 1b are based on the Theis equation (Theis (1935 [150327], p. 520, Equation 4) except that s is used for drawdown instead of v, and Q is used for the discharge rate instead of F.

In the three hydraulic tests discussed in this report, the Lower Bullfrog interval consistently contributed about 70 percent of the flow from observation wells to the pumping well at the C-wells complex; the Upper Tram interval consistently contributed about 20 percent of that flow; and all other intervals combined contributed about 10 percent of the total flow. To analyze the drawdown in any hydrogeologic interval, the total discharge from c#3 first was multiplied by the percentage of flow contributed by the interval being analyzed to avoid calculating erroneously large values of transmissivity and storativity (both of which are directly proportional to discharge).

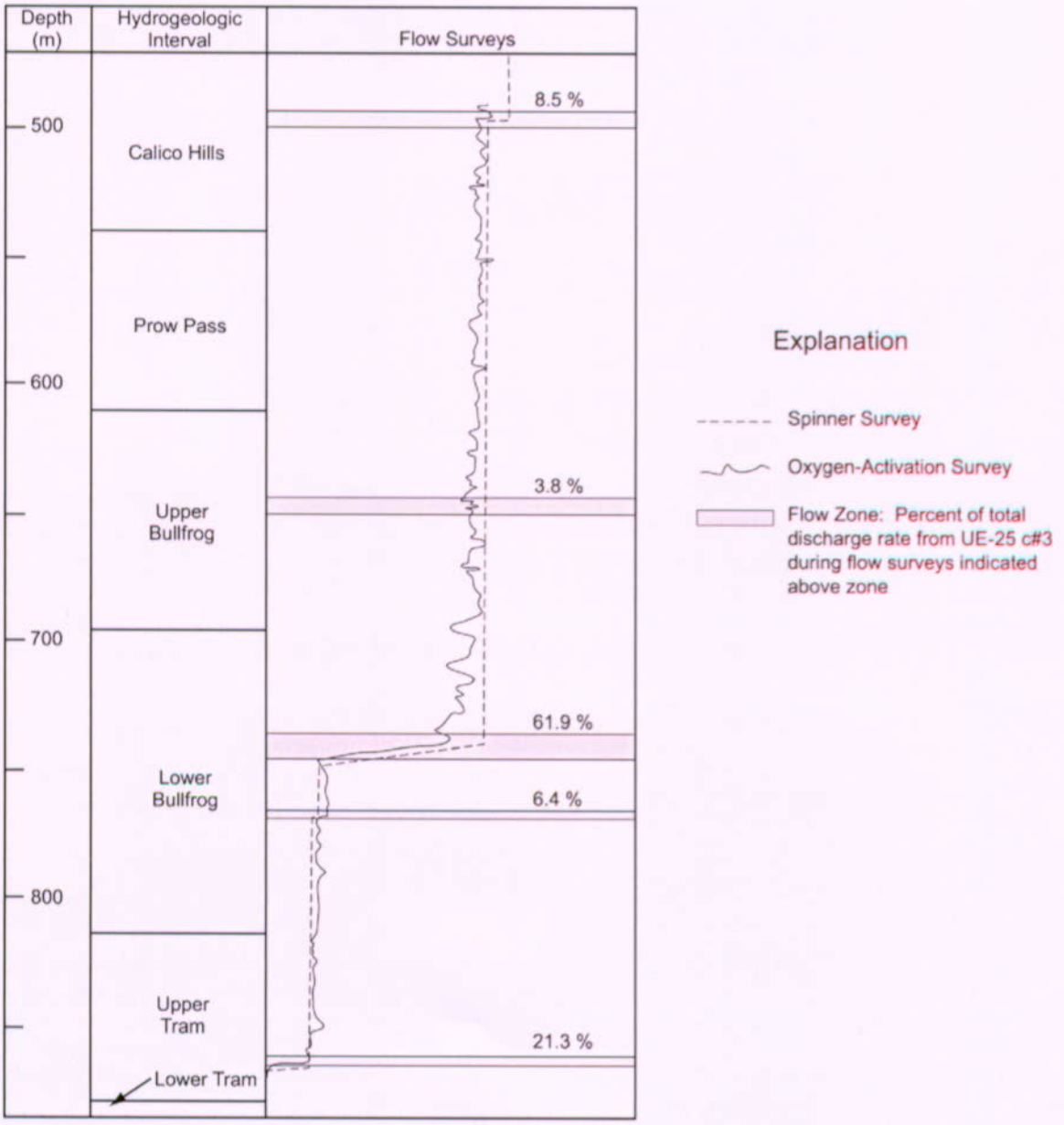

Output DTN: GS031008312314.004 (from Input DTN: GS030508312314.003 [164425], p. 19, Figure 10).

Figure 6.2-4. Flow Surveys in UE-25 c#3 During Hydraulic Testing in June 1995

Table 6.2-4. Interval Discharges 5,800 Minutes After Pumping Started in Hydraulic Tests in UE-25 c#3, June 1995 to November 1997

Hydrogeologic Unit	June 1995			February 1996			May 1996 to November 1997		
	Discharge (L/s)	Drawdown (cm)	Flow %	Discharge (L/s)	Drawdown (cm)	Flow %	Discharge (L/s)	Drawdown (cm)	Flow %
UE-25 c#1									
Calico Hills	22.5	No data	3.8	8.45	No data	0.5 (est)	9.72	No data	1.1 (est)
Prow Pass	22.5	43.0	2.9	8.45	14.0	2.5	9.72	14.9	2.3
Upper Bullfrog	22.5	52.1	3.9	8.45	21.6	4.3	9.72	19.2	3.3
Lower Bullfrog	22.5	49.7	68.3	8.45	No data	No data	9.72	21.0	66.8
Bullfrog-Tram	22.5	No data	89.4	8.45	19.5	92.7	9.72	N/A	N/A
Upper Tram	22.5	No data	21.1	8.45	No data	No data	9.72	No data	26.5
Lower Tram	22.5	No data	trace	8.45	No data	trace	9.72	No data	trace
UE-25 c#2									
Calico Hills	22.5	351.7	3.8	8.45	16.4	0.5	9.72	43.0	1.1
Prow Pass	22.5	75.6	2.9	8.45	14.6	1.5	9.72	22.2	2.0
Upper Bullfrog	22.5	62.2	3.9	8.45	25.0	4.2	9.72	26.5	3.8
Lower Bullfrog	22.5	49.4	68.3	8.45	No data	No data	9.72	21.9	70.2
Bullfrog-Tram	22.5	No data	89.4	8.45	21.0	93.8	9.72	N/A	N/A
Upper Tram	22.5	283.2	21.1	8.45	No data	No data	9.72	No data	22.9
Lower Tram	22.5	239.6	trace	8.45	No data	trace	9.72	No data	trace

Output DTN: GS031008312314.004 (from Input DTN: GS030508312314.003 [164425], p. 20, Table 6).

NOTE: The Bullfrog-Tram refers to the combined Lower Bullfrog and Upper Tram intervals tested together as one unit during the February 1996 test. Flow proportion for the Bullfrog-Tram interval shown in June 1995 is the sum of values for the Lower Bullfrog and Upper Tram intervals.

est = estimated; N/A = not applicable.

6.2.3.1.4 Monitoring Network

The monitoring network at the C-wells complex was selected after borehole c#3 was chosen as the pumping well for all hydraulic tests conducted from 1995 to 1997 on the basis of its successful performance during two hydraulic tests conducted in 1984 (Geldon 1996 [100396], pp. 48 to 68). Boreholes c#1 and c#2 were used as observation wells for the hydraulic tests conducted in June 1995 and February 1996. Boreholes ONC-1, H-4, WT#14, WT#3, and p#1 also were used as observation wells for the longer-term hydraulic test conducted from May 1996 to November 1997. Recording barometers were located at the C-wells complex during all hydraulic tests; a barometer located at borehole ONC-1 also was used during the third hydraulic test. (See Figure 6.1-3 for a map showing the location of the observation wells.)

Borehole c#3 is 900.4 m deep (Geldon 1993 [101045], p. 2). The borehole is cased and grouted to a depth of ~ 417 m, just below the water table (Geldon 1993 [101045], p. 7, Figure 3). During the hydraulic test in June 1995, c#3 did not contain packers and was open from the Calico Hills Formation to the Lower Tram interval. After packers were emplaced in August 1995,

manipulation of the packers, sliding sleeves, and slotted casing allowed selective hydraulic communication with only the Lower Bullfrog and Upper Tram intervals during hydraulic and tracer tests in February and March 1996 and with only the Lower Bullfrog interval from May 1996 to December 1997.

Borehole c#2 is 30.4 m from c#3 at the land surface (Geldon et al. 1998 [129721], p. 3, Figure 1) and 910.1 m deep (Geldon 1993 [101045], p. 2). It is cased and grouted to a depth of ~ 416.0 m (Geldon 1993 [101045], p. 7, Figure 3). Five dual-mandrel packers, suspended on 7.30-cm-diameter tubing, were emplaced in the borehole to isolate hydrogeologic intervals throughout the period of testing discussed in this report. Manipulation of packers and sliding sleeves allowed hydraulic communication with six separate hydrogeologic intervals (Figure 6.1-5 and Table 6.2-1) in June 1995, with the Lower Bullfrog and Upper Tram intervals in February and March 1996, and with the Lower Bullfrog interval from May 1996 to December 1997.

Borehole c#1 is 68.4 m from c#3 at the land surface (Geldon et al. 1998 [129721], p. 3, Figure 1) and is 897.6 m deep (Geldon 1993 [101045], p. 2). It is cased and grouted to a depth of ~ 417.9 m (Geldon 1993 [101045], p. 7, Figure 3). Five dual-mandrel packers, suspended on 7.30-cm-diameter tubing, were emplaced in the borehole to isolate hydrogeologic intervals throughout the period of testing discussed in this report. Manipulation of packers and sliding sleeves allowed hydraulic communication with the Calico Hills, Prow Pass, Upper Bullfrog, and Lower Bullfrog intervals in June 1995, with the Lower Bullfrog and Upper Tram intervals in February and March 1996 and with the Lower Bullfrog interval from May 1996 to December 1997.

Borehole ONC-1 is 842.8 m from borehole c#3 at the land surface and is 469.4 m deep (extending about 36.3 m below the water level in the borehole) (Nye County Nuclear Waste Repository Project Office 1995 [156859], ONC-1 Drilling log). The borehole is telescoped downward and has a diameter of about 13 cm in the saturated zone. Seven packers inflated between the bottom of the casing and a depth of 410 m separate the unsaturated and saturated zones; another packer emplaced at a depth of 452 m divides the saturated zone into two intervals. The upper of the saturated-zone intervals is open in the Calico Hills Formation and the Prow Pass Tuff; the lower of those intervals is open in the Prow Pass Tuff. Absolute transducers, installed in all packed-off intervals, transmitted total (atmospheric plus hydraulic) pressures to a data logger every 15 to 20 minutes during the tests reported here. Data from the lowermost transducer, positioned at a depth of 458 m, were converted to pressure heads for analysis.

Borehole H-4, which is 2,245 m from borehole c#3 at the land surface, is 1,219 m deep. The borehole diameter is 37.5 cm to a depth of 564 m and 22.2 cm below 564 m. Casing extends to a depth of 561 m; it is perforated below the water level, which was at an average depth of 518.3 m from 1985 to 1995. A packer emplaced at a depth of 1,181 m separates the Prow Pass, Bullfrog, and Tram Tuffs and the upper part of the Lithic Ridge Tuff from the lower part of the Lithic Ridge Tuff in the borehole. A 48-mm-diameter piezometer tube is installed in the upper part of the borehole, and a 62-mm-diameter piezometer tube is installed in the lower part of the borehole. (Graves et al. 1997 [101046], pp. 4 to 5, Table 1; p. 100). Differential transducers emplaced in the two monitored intervals transmitted hydraulic pressures to a data logger every 15 minutes during this study. Only the data from the upper interval were used.

Borehole WT#14, which is 2,249 m from borehole c#3 at the land surface, is 399 m deep. The borehole has a diameter of 22.2 cm below the water table, which was at an average depth of 346.4 m from 1985 to 1995. The borehole is cased to a depth of 37 m and is open in the Topopah Spring Tuff and Calico Hills Formation. A 62-mm-diameter piezometer tube is installed in the borehole. (Graves et al. 1997 [101046], pp. 4 to 5, Table 1; p. 84). A differential transducer emplaced in the piezometer tube transmitted hydraulic pressures to a data logger every 15 minutes during this study.

Borehole WT#3, which is 3,526 m from borehole c#3 at the land surface, is 348 m deep. The borehole has a diameter of 22.2 cm below the water table, which was at an average depth of 300.5 m from 1985 to 1995. The borehole is cased to a depth of 12 m and is open in the Bullfrog Tuff. A 62-mm-diameter piezometer tube is installed in the borehole. (Graves et al. 1997 [101046], pp. 4 to 5, Table 1; p. 76). A differential transducer emplaced in the piezometer tube transmitted hydraulic pressures to a data logger every 15 minutes during this study.

Borehole p#1, which is 630 m from borehole c#3 at the land surface, is 1,805 m deep. The borehole diameter decreases from 37.5 to 15.6 cm with depth. Casing and cement emplaced to a depth of 1,297 m isolate the Miocene tuffaceous rocks in the upper part of the borehole from Paleozoic carbonate rocks in the lower part of the borehole. The water level for the Paleozoic carbonate rocks in p#1 was monitored through a 38-mm-diameter piezometer tube. The average depth to water in the piezometer tube was 361.8 m from 1985 to 1995. (Graves et al. 1997 [101046], pp. 4 to 5, Table 1; p. 90). A differential transducer emplaced in the piezometer tube transmitted hydraulic pressures to a data logger every 60 minutes during this study.

6.2.3.1.5 Description of Tests

A hydraulic test (DTN: GS960108312313.002 [159228]) was conducted in June 1995 to determine hydraulic properties of six hydrogeologic intervals (Figure 6.2-5) at the C-wells complex (Table 6.2-1) (A detailed description of the field tests is contained in Umari 2002 [162858], Binder 3, Sections D-2 to D-6). The six intervals were isolated by packers in boreholes c#1 and c#2. Sliding sleeves open in the packed-off intervals of the observation wells allowed hydraulic communication with the pumping well c#3, which was uncased and contained no packers to isolate intervals. Because of malfunctioning transducers, analyzable data were obtained only from the Prow Pass, Upper Bullfrog, and Lower Bullfrog intervals of c#1 and from the Calico Hills, Prow Pass, Upper Bullfrog, and Lower Bullfrog intervals of c#2.

The hydraulic test began on June 12 and ended on June 16, after 4.03 days of pumping. (Note that data were collected over thousands of elapsed minutes, the measure of time used by data-acquisition software and needed for hydraulic calculations. For the summarizing discussions here, those time intervals are expressed in hours and days.) Recovery was monitored until June 29, by which date it appeared to be complete in all intervals. At an average discharge rate of 22.5 L/s, drawdown in c#3 rapidly increased to a maximum of 10.9 m (Figure 6.2-5). The pumping in c#3 produced drawdown ranging from 43.0 to 52.1 cm in intervals of c#1 (Figure 6.2-6) and from 49.4 to 352 cm in intervals of c#2 (Figure 6.2-7).

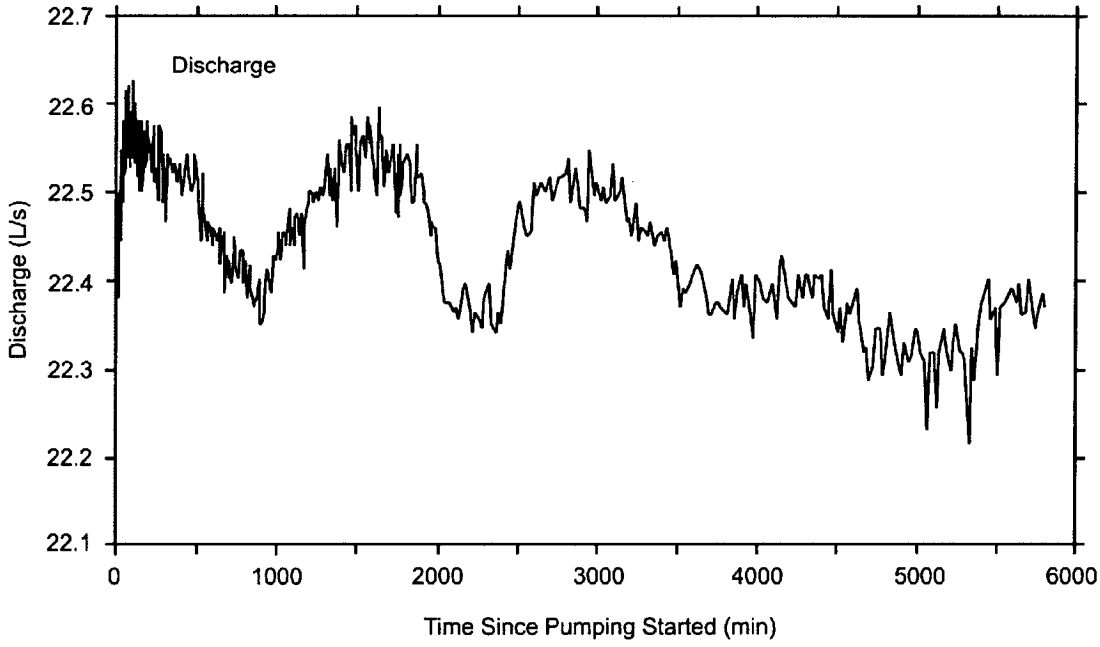

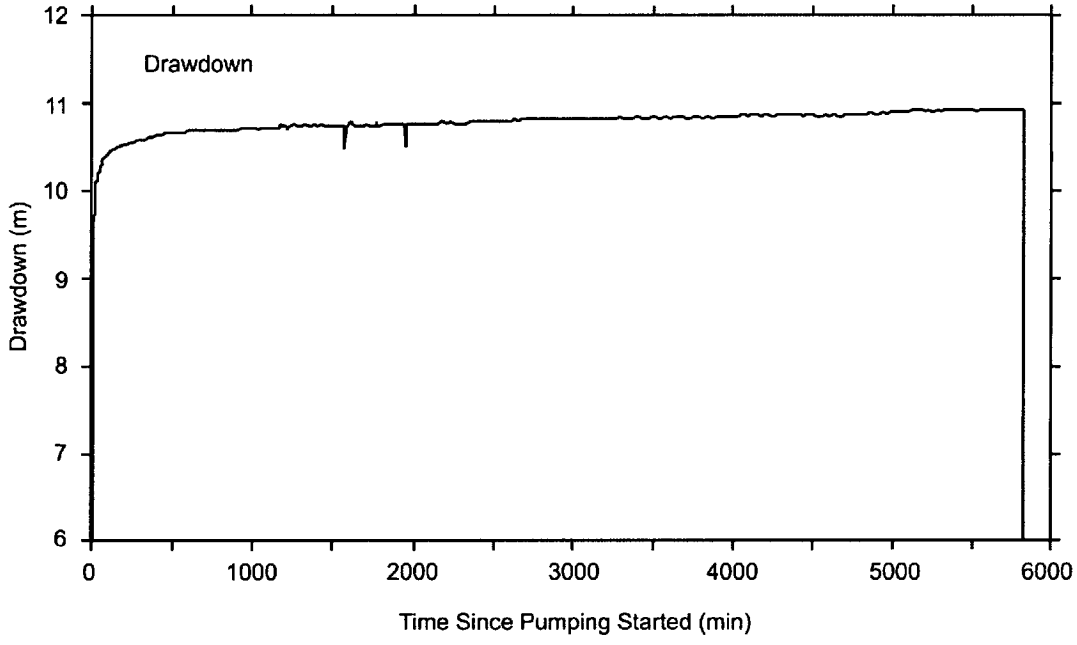

Output DTN: GS031008312314.004 (from Input DTN: GS030508312314.003 [164425], p. 22, Figure 11).

Figure 6.2-5. UE-25 c#3 Discharge and Drawdown, June 12, 1995 (~0 minutes), to June 16, 1995 (~5,800 minutes)

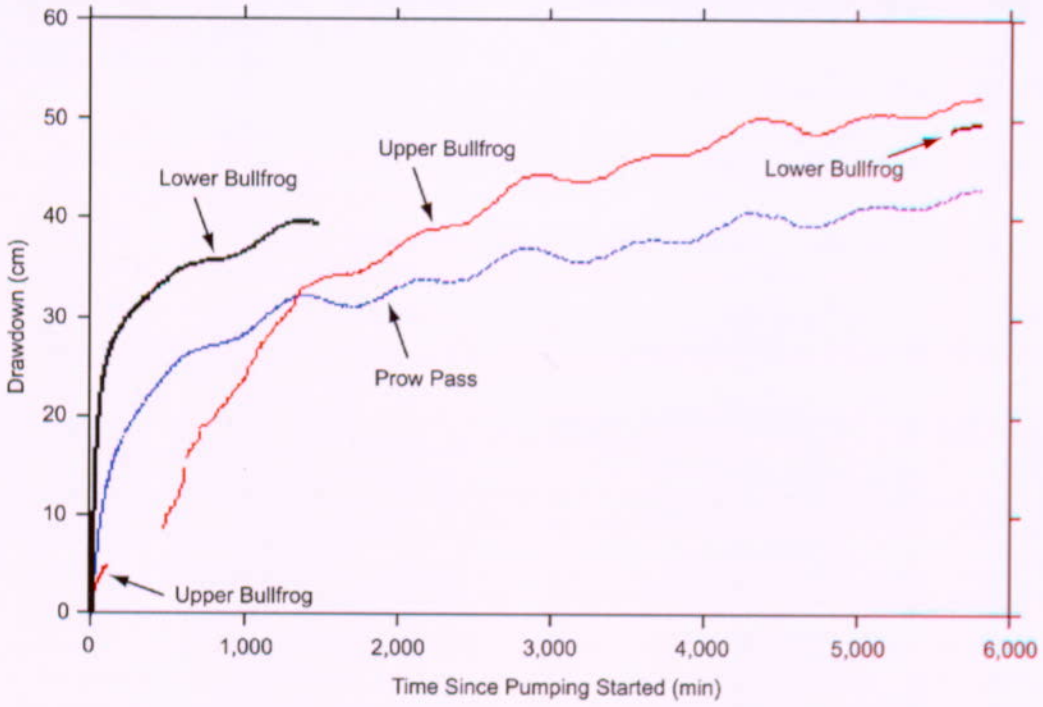

Output DTN: GS031008312314.004 (from Input DTN: GS030508312314.003 [164425], p. 23, Figure 12).

Figure 6.2-6. UE-25 c#1 Drawdown

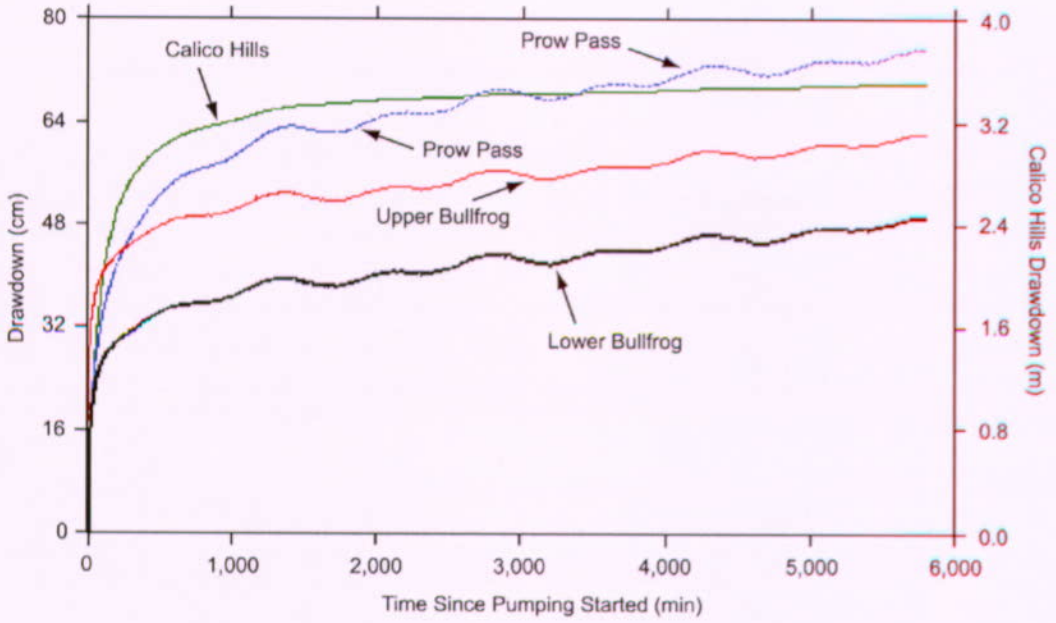

Output DTN: GS031008312314.004 (from Input DTN: GS030508312314.003 [164425], p. 23, Figure 13).

Figure 6.2-7. UE-25 c#2 Drawdown

The most permeable interval identified in the hydraulic test conducted in June 1995, the Lower Bullfrog interval, was chosen for subsequent tracer tests at the C-wells complex to increase the chance of successful transport of tracers between the injection and recovery wells. Because the transducer in the Lower Bullfrog interval of c#3 was not working, the packers between the Lower Bullfrog and Upper Tram intervals in all three of the C-wells were deflated, and the combined Lower Bullfrog and Upper Tram intervals (shown in Figure 6.1-5 as the Bullfrog-Tram interval) became the test interval for the following series of tests.

After testing pump performance in January 1996 and allowing water levels in the C-wells to recover, pumping began on February 8, 1996, to establish a steep, quasi-steady-state hydraulic gradient between c#2 (the injection well) and c#3 (the recovery well) for a conservative tracer test. Tracer injection on February 13 disturbed the hydraulic pressure in the injection interval for 12.5 hours and effectively terminated the analyzable drawdown record. The 4.85 days of drawdown recorded between the start of pumping and the injection of tracer on February 13 (when the hydraulic pressure in the injection interval was disturbed) were analyzed as an hydraulic test.

During the hydraulic test in February 1996, operation of the pump outside its optimal performance range caused discharge to decrease steadily, despite an adjustment of the pump speed on February 12, some 5,640 minutes (3.917 days) after pumping started. Prior to that adjustment, discharge decreased from 8.78 to 8.21 L/s. Adjusting the pump speed restored the discharge to 8.75 L/s, but discharge immediately began to decrease and was at 8.57 L/s when the tracer test started on February 13 (Figure 6.2-8). Although average discharge after adjusting the pump speed was 0.10 L/s larger than before that adjustment, deviation from the average discharge of 8.49 L/s was just 3 percent for the entire period of pumping.

As shown in Figure 6.2-8, the pumping produced as much as 2.86 m of drawdown in the Bullfrog-Tram interval of c#3 (96 percent of which occurred in the first 10 minutes). Adjustment of the pump speed caused a step-like increase of 0.19 m in c#3 drawdown, but it had no discernible effect on drawdown in the other C wells. Although oscillatory, drawdown in c#1 steadily increased and ranged from 14.3 to 22.1 cm in the Prow Pass, Upper Bullfrog, and Bullfrog-Tram intervals (Figure 6.2-9). Likewise oscillatory, drawdown in c#2 steadily increased and ranged from 14.9 to 25.3 cm in the Calico Hills, Prow Pass, Upper Bullfrog, and Bullfrog-Tram intervals (Figure 6.2-10). Steady increases in observation-well drawdown together with small deviations from the average discharge enabled the observation-well drawdown for the entire period before tracer injection to be analyzable.

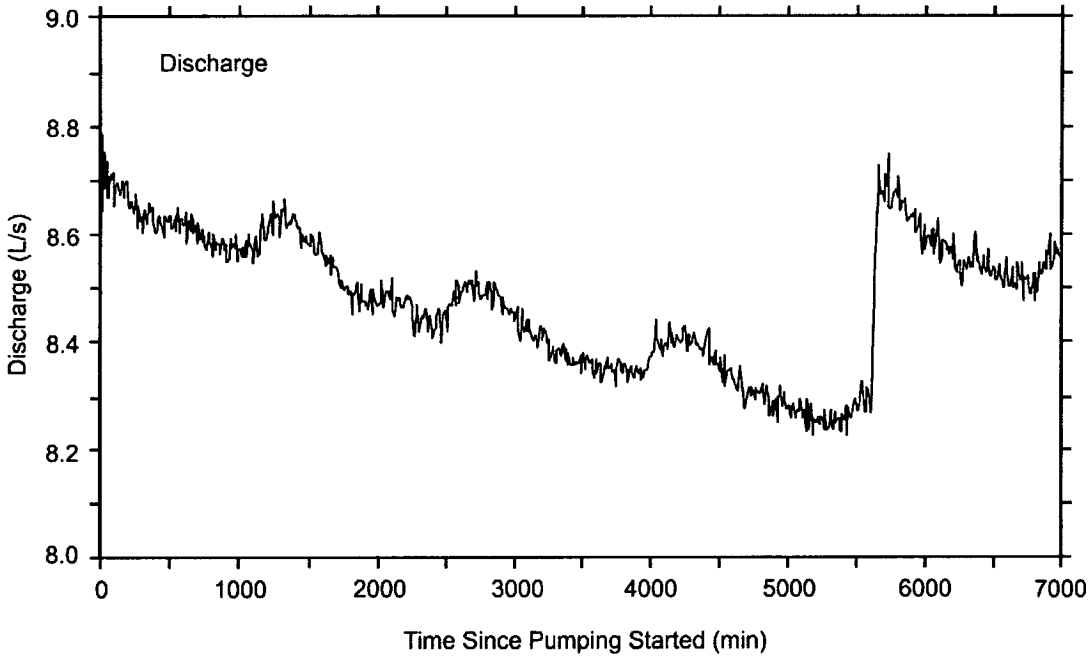

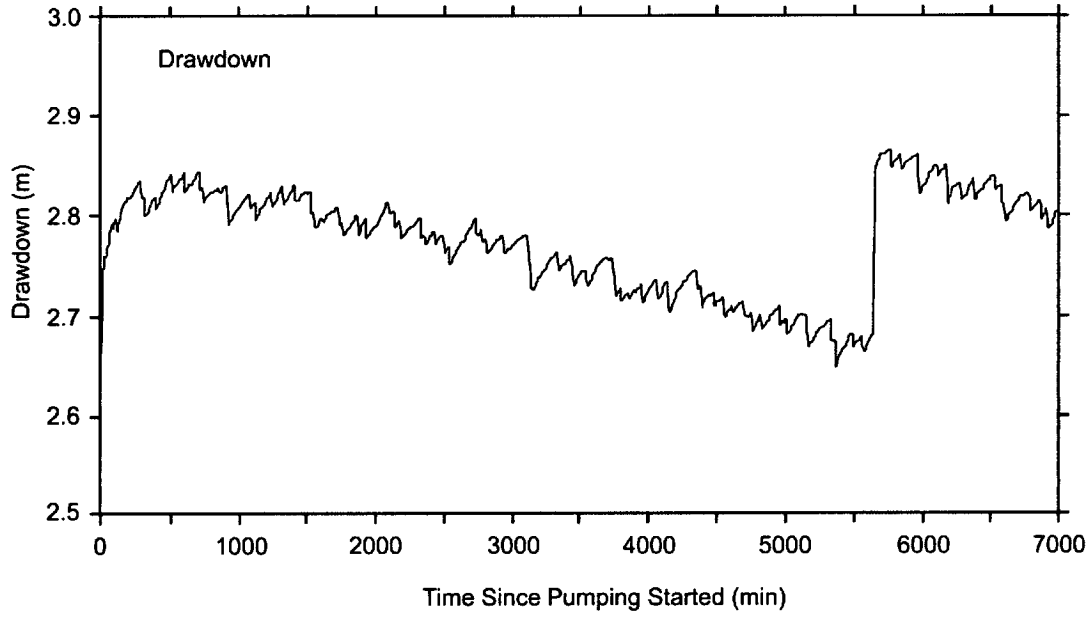

Output DTN: GS031008312314.004 (from Input DTN: GS030508312314.003 [164425], p. 24, Figure 14).

Figure 6.2-8. UE-25 c#3 Discharge and Drawdown, February 8, 1996 (~0 minutes), to February 13, 1996 (~7,000 minutes)

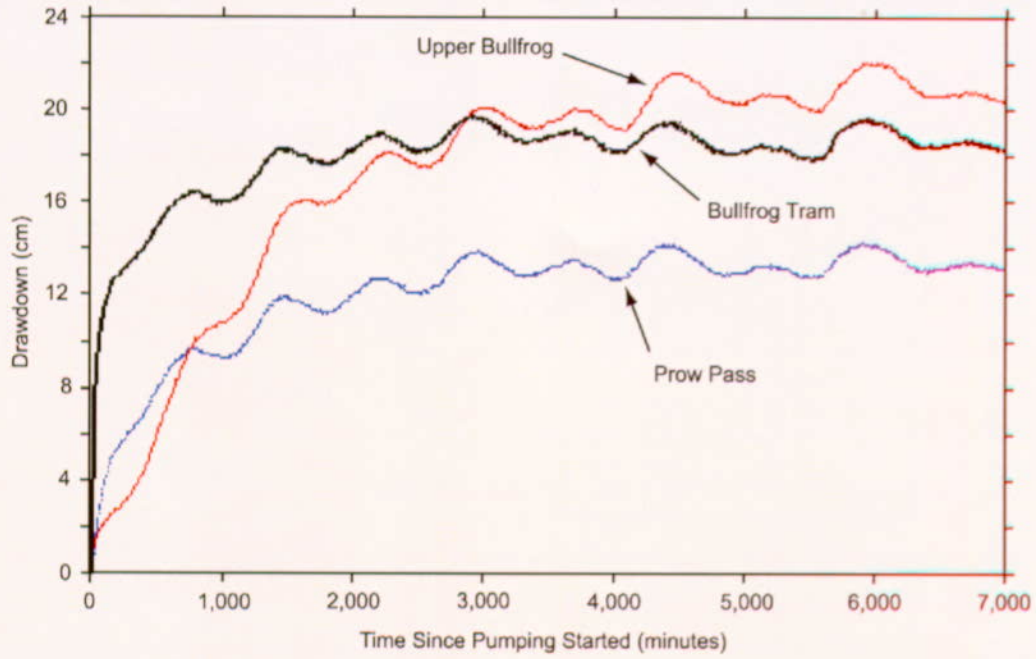

Output DTN: GS031008312314.004 (from Input DTN: GS030508312314.003 ([164425], p. 25, Figure 15).

Figure 6.2-9. UE-25 c#1 Drawdown, February 8, 1996 (~0 minutes), to February 13, 1996 (~7,000 minutes)

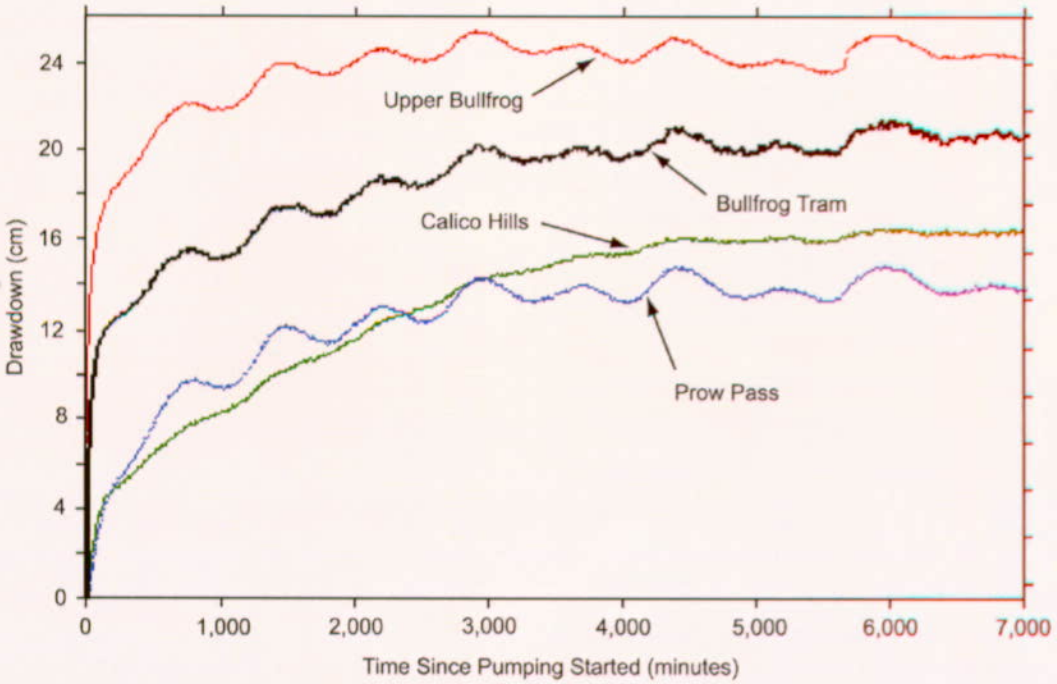

Output DTN: GS031008312314.004 (from Input DTN: GS030508312314.003 [164425], p. 25, Figure 16).

Figure 6.2-10. UE-25 c#2 Drawdown, February 8, 1996 (~0 minutes), to February 13, 1996 (~7,000 minutes)

After the tracer test in the Bullfrog-Tram interval ended in March 1996, a new transducer was installed in the Lower Bullfrog interval of c#3, and packers in the borehole were reconfigured. Subsequently, it was possible to conduct hydraulic and tracer tests in the isolated Lower Bullfrog interval. With nearly continuous pumping, a series of tracer tests was conducted in that interval by the USGS and by LANL from May 1996 to November 1997. Pumping in c#3 to establish a steep, quasi-steady-state hydraulic gradient for tracer tests in the Lower Bullfrog interval began May 8, 1996. From May 24, 1996, to March 26, 1997, the pump shut off 11 times because of problems with the generators that provided power to the site. Between March 26 and May 8, 1997, the pump operated erratically because of continued problems with one of the generators. Problems with the power supply caused the pump to shut off intermittently between May 30 and September 29, 1997, and at least once a day between October 15 and November 12, 1997. Pumping was terminated on November 12, 1997, 553.24 days after pumping started, and recovery was monitored until December 31, 1997.

Discharge between May 8, 1996, and March 26, 1997, initially oscillated between 9.6 and 9.8 L/s, eventually stabilized at about 9.4 L/s, and averaged 9.53 L/s (Figure 6.2-11). After generator problems were resolved on May 8, 1997, discharge decreased steadily from 9.3 to 8.9 L/s on November 12, 1997, and averaged 9.01 L/s. The volume of water withdrawn between May 8, 1996, and November 12, 1997, was 440.2 million L, equivalent to an average discharge of 9.21 L/s.

As in previous hydraulic tests, drawdown in the pumped well was large and reached steady-state conditions rapidly (Figure 6.2-11). Drawdown in the Lower Bullfrog interval of c#3 reached 4.8 m in 60 minutes and remained at 4.85 to 5.0 m until October 16, 1996, 161.11 days (232,000 minutes) after pumping started. After March 26, the frequent pump shutoffs kept drawdown less than 5.9 m, except during the process of restarting the pump. Pump shutoffs typically caused rapid and complete or nearly complete recovery in c#3, but those effects were reversed just as rapidly when the pump was restarted. Tracer-test operations affected drawdown in the pumped well minimally. Recovery from pumping on December 12, 1997, approximately 30 days (42,965 minutes) after pumping stopped, was 99 percent of antecedent drawdown. The prolonged period of unsteady pump discharge after March 26, 1997, effectively ended the drawdown record that could be analyzed as an hydraulic test for all observation wells except ONC-1. The analyzable drawdown record from May 8, 1996, to March 26, 1997, is 322.32 days in duration. With 11 down times ranging from 2 to 185 minutes, the pump was off for 10.82 hours (649 minutes), about 0.1 percent of the time, during that period.

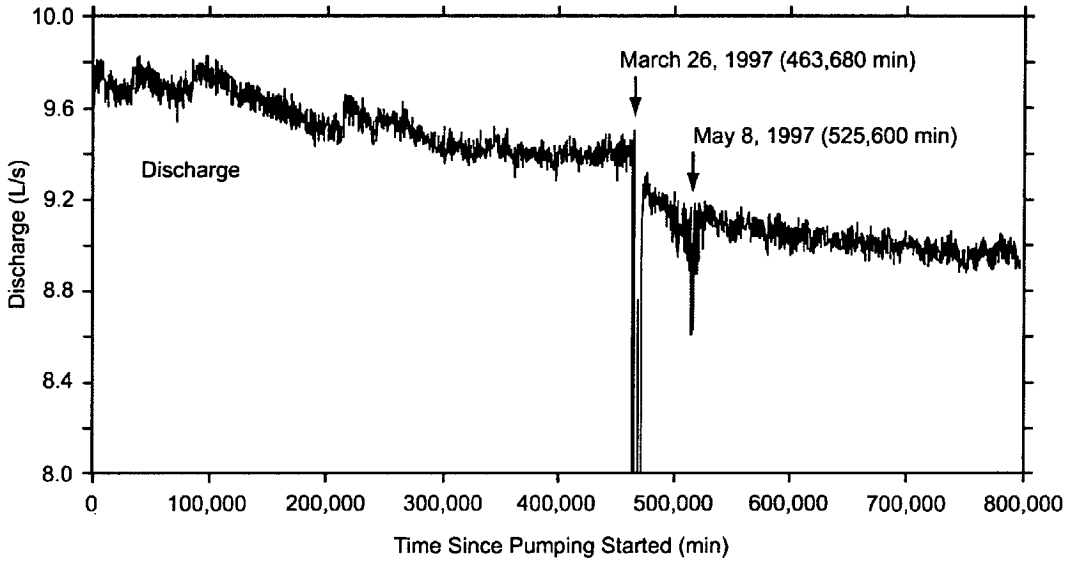

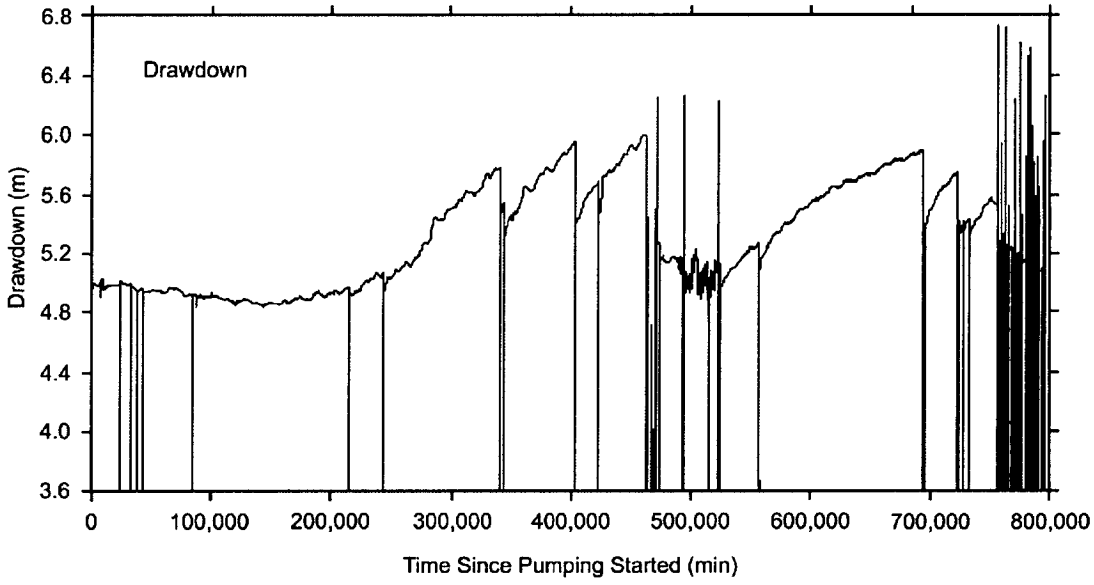

Output DTN: GS031008312314.004 (from Input DTN: GS030508312314.003 [164425], p. 26, Figure 17).

Figure 6.2-11. UE-25 c#3 Discharge and Drawdown, May 8, 1996 (~0 minutes), to November 12, 1997 (~800,000 minutes)

Drawdown in response to pumping the Lower Bullfrog interval of c#3 is known to have occurred in the Prow Pass, Upper Bullfrog, and Lower Bullfrog intervals of c#1 and in the Calico Hills, Prow Pass, Upper Bullfrog, and Lower Bullfrog intervals of c#2. Drawdown in all intervals of these boreholes generally increased steadily but was very oscillatory. Peak drawdown by March 26, 1997, ranged from about 36 to 42 cm in intervals of c#1 (Figure 6.2-12) and from about 35 to 51 cm in intervals of c#2 (Figure 6.2-13).

Disruptions of drawdown in the Lower Bullfrog and other intervals of c#1 and c#2 occurred from pump shutoffs 11 times between May 1996 and March 1997. Pump shutoffs (most of the unlabeled downward spikes in Figures 6.2-12 and 6.2-13) generally resulted in 20 to 50 percent recovery of water levels. However, these effects dissipated 50 to 500 minutes after the pump was restarted and did not affect analysis of the drawdown.

Recirculation of water during tracer tests conducted between May and November 1996 generally caused small decreases in drawdown in the Lower Bullfrog interval of c#1 or decreases followed by increases in drawdown in the Lower Bullfrog interval of c#2 at the start and end of recirculation, which generally lasted 70 to 560 minutes. However, recirculation of water in c#1 from June 17 to July 3, 1996, to facilitate transport of iodide tracer between the injection and recovery wells, caused drawdown in the Lower Bullfrog interval of c#1 to decrease in steps for 23,350 minutes (Figures 6.2-12 and 6.2-14a). Pumping water into c#1 faster than it could drain probably caused the drawdown to decrease. Periodic increases in the injection pump rate caused this decrease to occur in steps.

Tracer injection during four tests that were conducted between May 1996 and November 1997 caused increased drawdown in the Lower Bullfrog interval of c#1 or c#2 that generally lasted 180 to 750 minutes. However, following injection of 2,6 difluorobenzoic acid tracer into c#2 on January 10, 1997, drawdown in the Lower Bullfrog interval of c#2 remained high for 8,360 minutes (Figures 6.2-13 and 6.2-14b). Changes in hydraulic head associated with the dense tracer injection solution also could have produced the observed water-level changes in c#2.

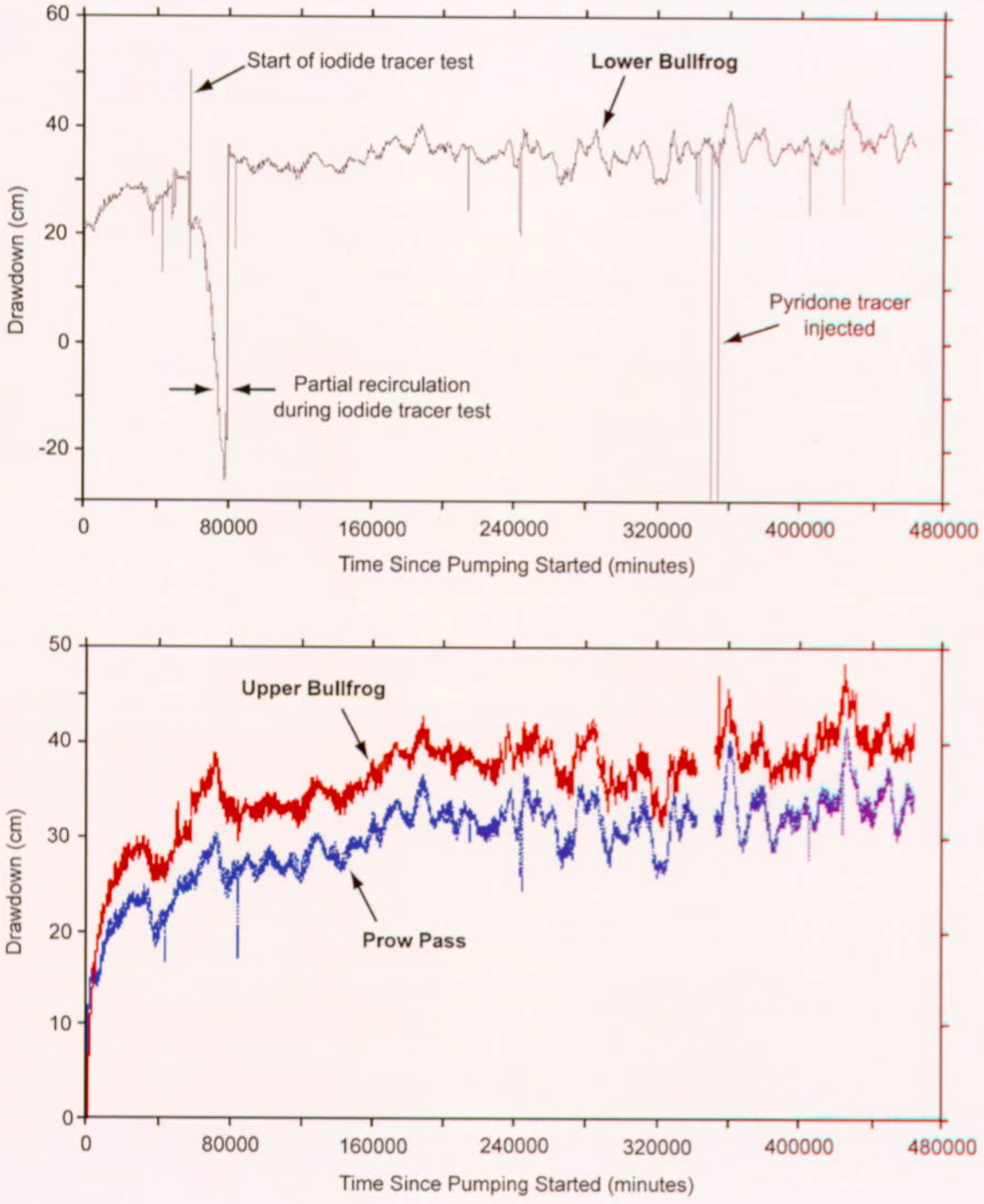

Output DTN: GS031008312314.004 (from Input DTN: GS030508312314.003 [164425], p. 27, Figure 18).

Figure 6.2-12. UE-25 c#1 Drawdown, May 8, 1996 (~0 minutes), to March 26, 1997 (~470,000 minutes)

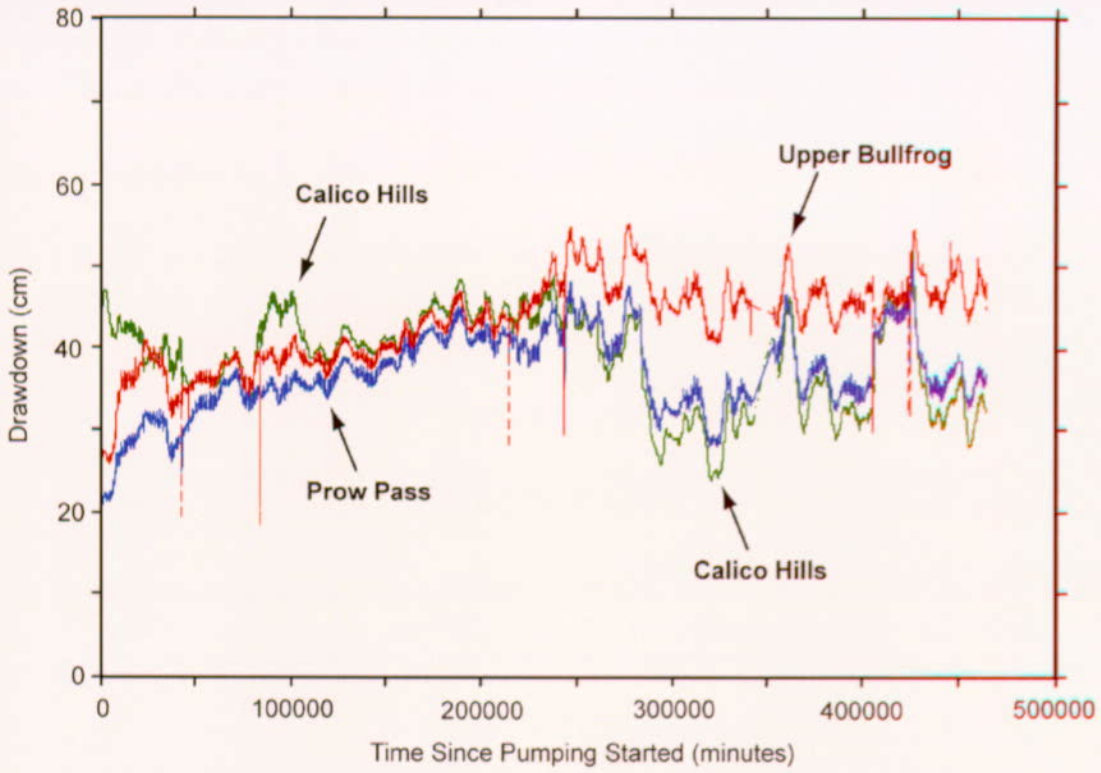

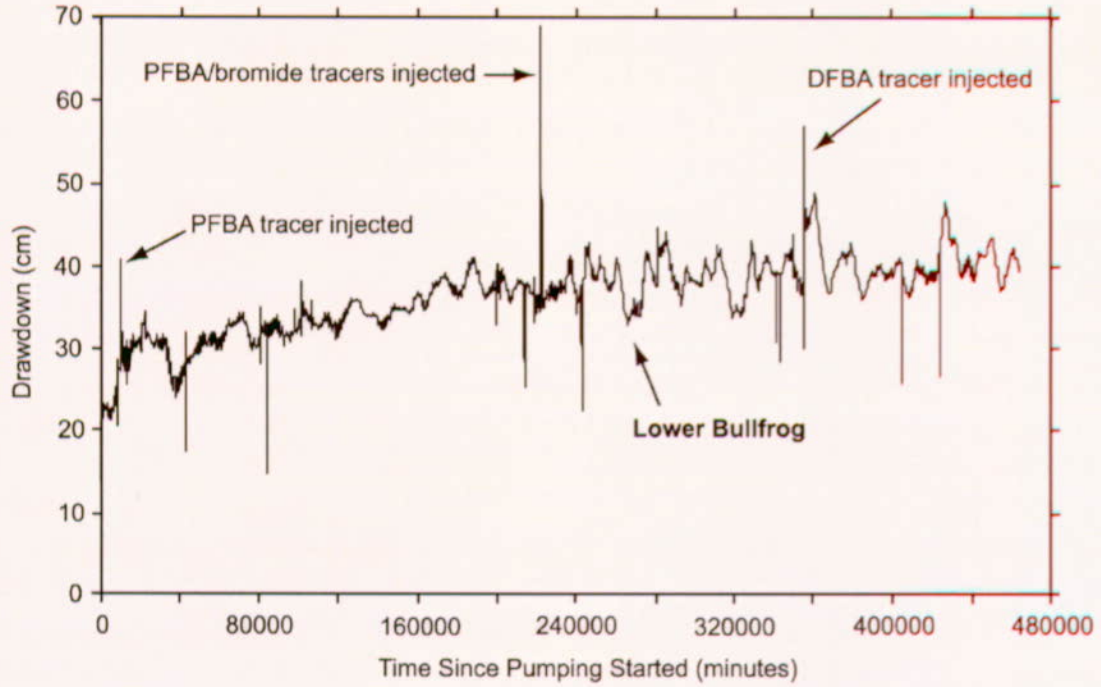

Output DTN: GS031008312314.004 (from Input DTN: GS030508312314.003 [164425], p. 28, Figure 19).

NOTE: PFBA: Pentafluorobenzoic acid; DFBA: 2,6 difluorobenzoic acid.

Figure 6.2-13. UE-25 c#2 Drawdown, May 8, 1996 (~0 minutes), to March 26, 1997 (~470,000 minutes)

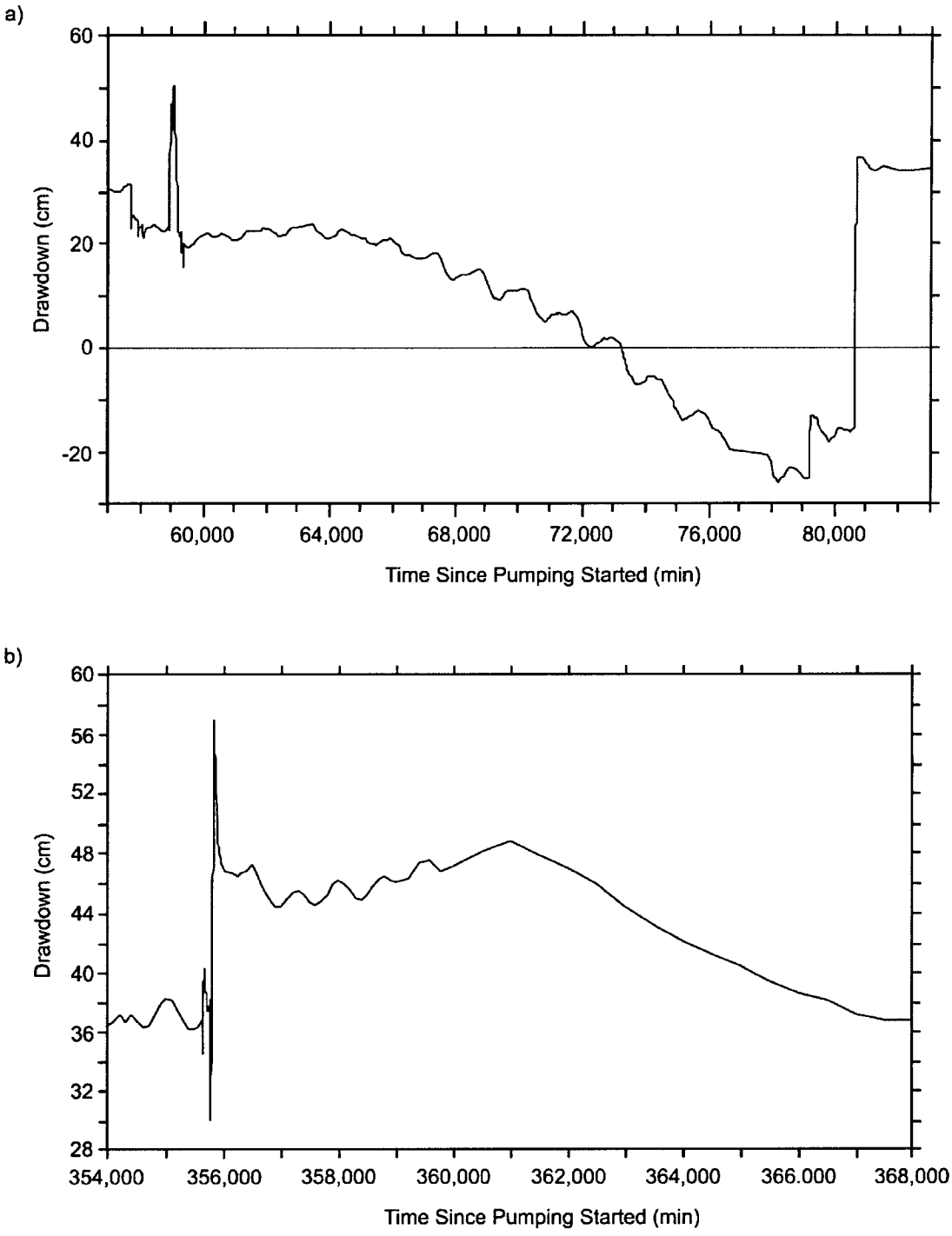

Output DTN: GS031008312314.004 (from Input DTN: GS030508312314.003 [164425], p. 29, Figure 20).

NOTE: (a) Iodide tracer test in c#1, June 17, 1996 (~57,000 minutes), to July 5, 1996 (~83,000 minutes).
(b) 2,6 DFBA tracer test in c#2, January 9, 1997 (~354,000 minutes), to January 18, 1997 (~368,000 minutes).
2,6 DFBA: 2,6 Difluorobenzoic acid.

Figure 6.2-14. Disturbance of Drawdown in Lower Bullfrog Interval of UE-25 c#1 and UE-25 c#2 by Tracer Tests in (a) 1996 and (b) 1997

Hypotheses regarding disturbances from tracer-test operations cannot be tested and, therefore, are presented only for consideration. It is important to note that (1) tracer-test operations conducted in one borehole generally did not affect drawdown in other boreholes and (2) disturbances from tracer-test operations did not affect analyses of drawdown in c#1 and c#2.

Events of unknown origin caused hydraulic heads in the Lower Bullfrog interval of c#1 and c#2 to rise 5 cm to 8 cm from June 1 to June 11, 1996 (a period of 14,800 minutes) and from November 6, 1996 to November 14, 1996 (a period of 11,900 minutes). Because six observation wells within 3.5 km of c#3 showed similar rises in hydraulic head, the events that produced these disturbances could not have been local in scale.

Shutting off the pump in c#3 on November 12, 1997, caused erratic responses in the Lower Bullfrog intervals of c#2 and c#1 that are not analyzable. Recovery in the Lower Bullfrog interval of c#1 reached a plateau from 8,000 to 38,500 minutes after pumping stopped, after which it began increasing cyclically. On December 29, 1997, 46.53 days (67,000 minutes) after pumping stopped, recovery in the Lower Bullfrog interval of c#1 was about 95 percent of the antecedent drawdown (Figure 6.2-15). The transducer in the Lower Bullfrog interval of c#2 was removed on December 9, 1997, at a time when readings from the transducer were erratic, and recovery was only about 70 percent of the antecedent drawdown.

"Recovery" (as used in the previous paragraph and in Figure 6.2-15) is a calculated value. First, the pattern of water-level decline prior to stopping the pump (antecedent water-level decline) is extrapolated beyond the time of stopping the pump. (This extrapolated antecedent water-level decline is presented as the blue antecedent drawdown curve in Figure 6.2-15.) Then, for any point in time after pump stoppage, the "recovery" is calculated as the distance from the extrapolated antecedent water level to the recovered water level. So, "recovery" is larger than the distance that the water level has rebounded relative to where it was at the point of shutting off the pump.

Pumping in the Lower Bullfrog interval of c#3 from May 1996 to March 1997 caused drawdown in all four of the observation wells beyond the C-wells complex that are completed in Miocene tuffaceous rocks. As in c#1 and c#2, drawdown in the four outlying observation wells was very oscillatory. Drawdown in these wells was not affected by pump shutoffs or tracer test operations.

Drawdown in ONC-1, the nearest observation well to the C-wells, was detected 200 minutes after pumping started and increased steadily thereafter (Figure 6.2-16). Peak drawdown by March 26, 1997, was about 28 to 30 cm. Peak drawdown when pumping ended on November 12, 1997, was about 36 to 37 cm. Recovery in ONC-1 followed a pattern similar to the Lower Bullfrog interval in c#1 (Figure 6.2-15). On December 29, 1997, 46.875 days (67,500 minutes) after pumping stopped, recovery in ONC-1 was about 76 percent of the antecedent drawdown.

Borehole WT#3, the farthest observation well from the C-wells, responded like the C-wells and ONC-1 to the pumping in c#3 that began on May 8, 1996. Drawdown in WT#3 was detected 6.34 days (9,130 minutes) after pumping started (Figure 6.2-17). Peak drawdown by March 26, 1997, was about 14 to 16 cm. Drawdown in WT#3 was more oscillatory than in the other observation wells after 166.67 days (240,000 minutes) of pumping. This behavior was possibly

because (1) WT#3 was much farther from the pumping well than the other observation wells and affected by environmental stresses that did not extend to the other wells and (2) pumping-related water-level changes in WT#3 were much smaller than in the other observation wells and, therefore, harder to separate from barometric and Earth-tide effects.

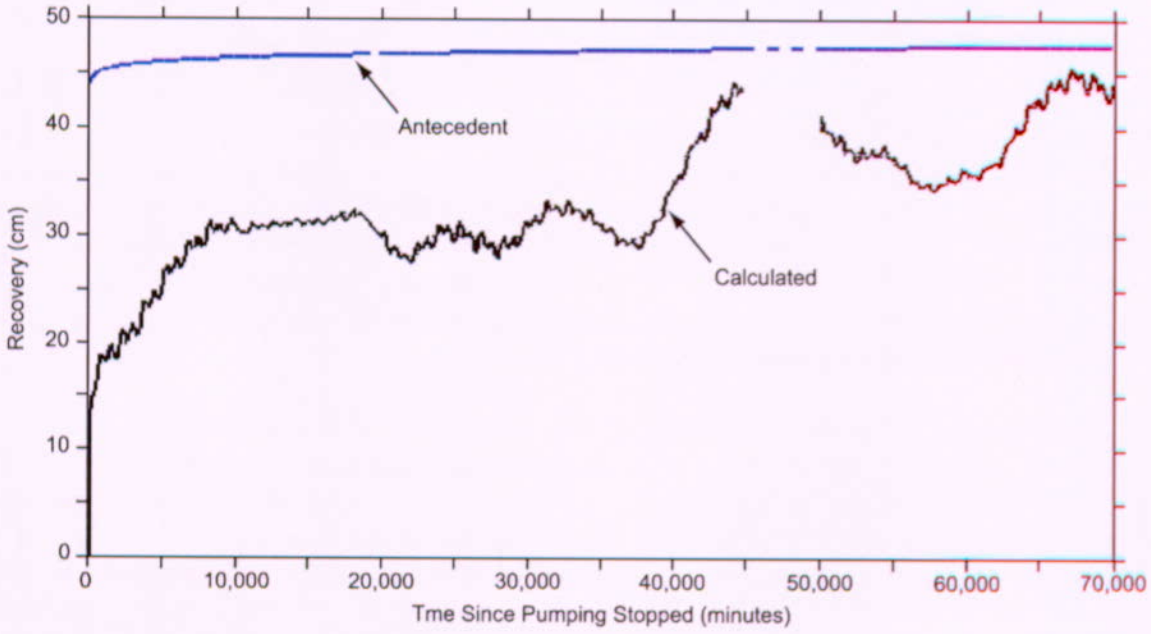

Output DTN: GS031008312314.004 (from Input DTN: GS030508312314.003 [164425], p. 30, Figure 21).

NOTE: Pump was turned off 11/12/97 at 15:59:50 PST.

Figure 6.2-15. UE-25 c#1 Lower Bullfrog Recovery, November 12, 1997 (~0 minutes), to December 31, 1997 (~70,000 minutes)

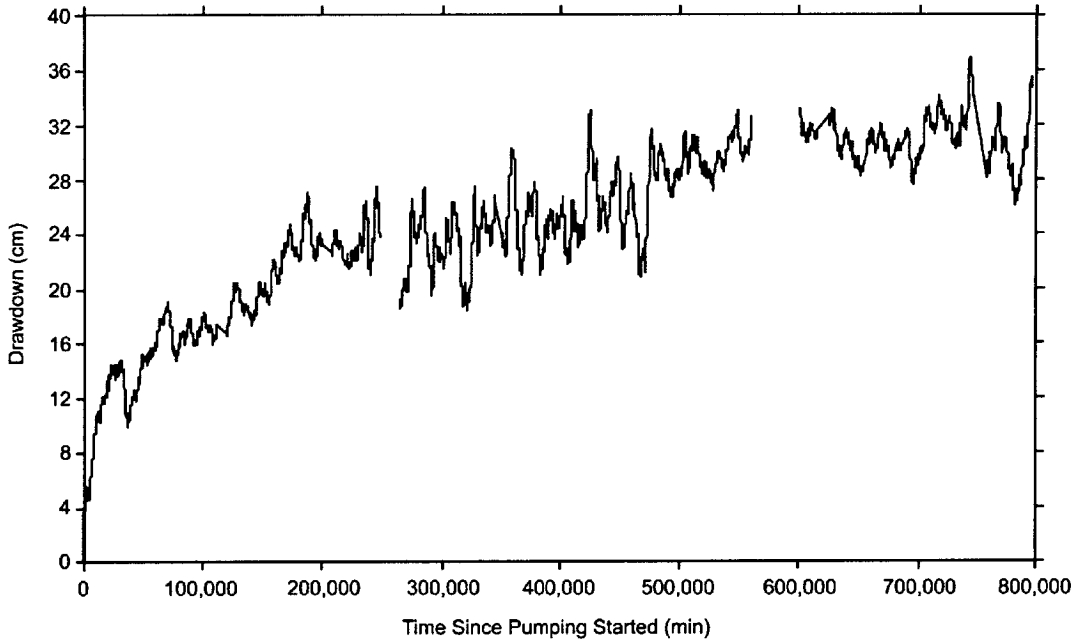

Output DTN: GS031008312314.004 (from Input DTN: GS030508312314.003 [164425], p. 31, Figure 22).

Figure 6.2-16. Drawdown in UE-25 ONC-1, May 8, 1996 (~0 minutes), to November 12, 1997 (~800,000 minutes)

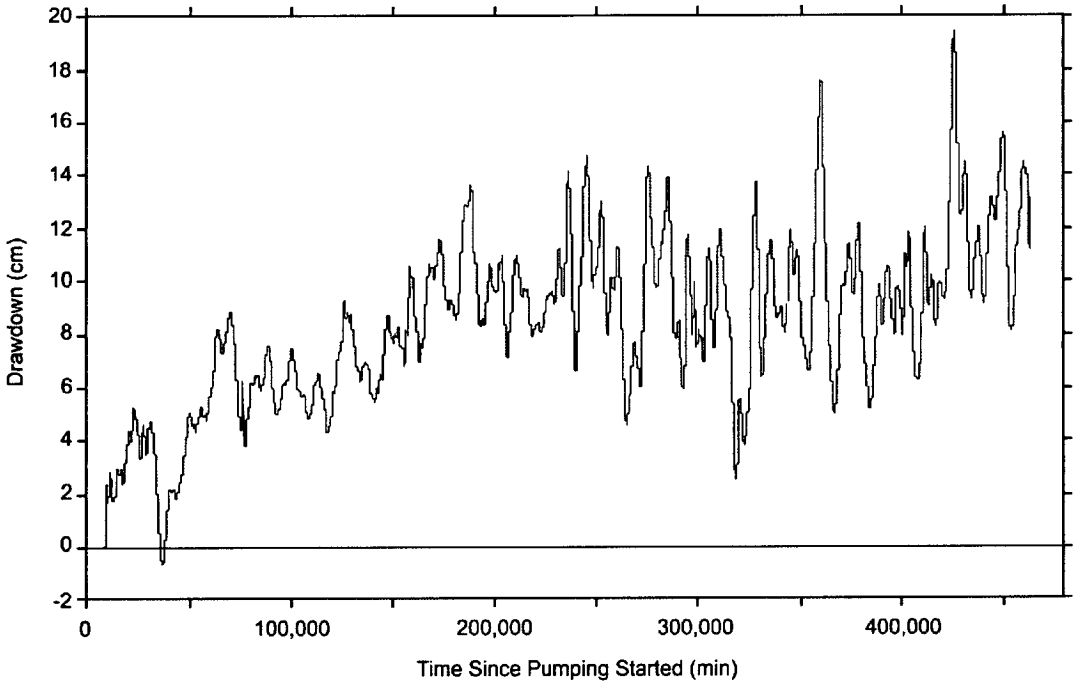

Output DTN: GS031008312314.004 (from Input DTN: GS030508312314.003 [164425], p. 31, Figure 23).

Figure 6.2-17. Drawdown in UE-25 WT#3, May 8, 1996 (~0 minutes), to March 26, 1997 (~480,000 minutes)

Unlike other observation wells monitored during the hydraulic test that began in May 1996, H-4 and WT#14 exhibited steady-state drawdown as pumping progressed (Figure 6.2-18). Drawdown in both boreholes was delayed for about 5,000 minutes after pumping started, although very small, oscillatory water-level changes, possibly caused by borehole-storage release, occurred during this time. Between 5,000 and 72,000 minutes after pumping started, drawdown increased steadily in response to pumping. Drawdown in H-4 peaked at about 22 cm; drawdown in WT#14 peaked at about 15 cm. After about 50 days (72,000 minutes) of pumping, fluxes from recharge boundaries, probably a transmissive fault, prevented further drawdown. As in a hydraulic test of the Tram interval in c#1 conducted in 1984 (Geldon 1996 [100396], pp. 67 to 68), recharge boundaries affecting H-4 and WT#14 are inferred to be faults present near the observation wells. Numerous faults are located near H-4 (Day et al. 1998 [101557]), and several segments of the Paintbrush Canyon Fault are located near WT#14 (Dickerson and Drake 1998 [102781]). Conversely, there are no known changes in stratigraphy or lithology between the C-wells and either H-4 or WT#14 that might be interpreted to create an hydraulic boundary.

6.2.3.2 Hydraulic Tests Conducted in 1998 and 1999 (Prow Pass Interval)

Pumping in c#2 to create a forced hydraulic gradient for tracer tests in the Prow Pass interval at the C-wells complex began June 2, 1998, and continued uninterrupted until September 22, 1998. (Detailed description of the field tests is contained in Umari 2002 [162858], Binder 12, Sections M-20 to M-22) The pump in c#2 shut off for 70 minutes on September 22 as one of two packers at the bottom of the Prow Pass interval (number 3) was being deflated. Injection of water into c#3 to expedite tracer transport began June 11 and continued without interruption until September 2. The injection pump was off briefly on September 2 and 3 while injection tubing was removed from c#3. Tracers were injected into c#3 on June 17 and into c#1 on July 31.

Responses of c#1, c#3, and ONC-1 to pumping June 2 to June 11, in advance of the tracer tests, were analyzed as a constant-rate withdrawal test. After water injection into c#3 began on June 11, the superimposed effects of pumping water from c#2, injecting water into c#3, injecting tracers into c#3 and c#1, operating a mixing pump in c#3 intermittently, and mechanical problems that affected pumping and injection rates made it difficult to analyze data from the C-wells quantitatively. However, ONC-1 was far enough away from the pumping and injection wells that a water-level rise in ONC-1 resulting from injecting water into c#3 clearly could be separated from relatively minor drawdown in the well caused by pumping c#2. The water-level rise in ONC-1 from June 11 to September 1 was analyzed as a constant-rate injection test.

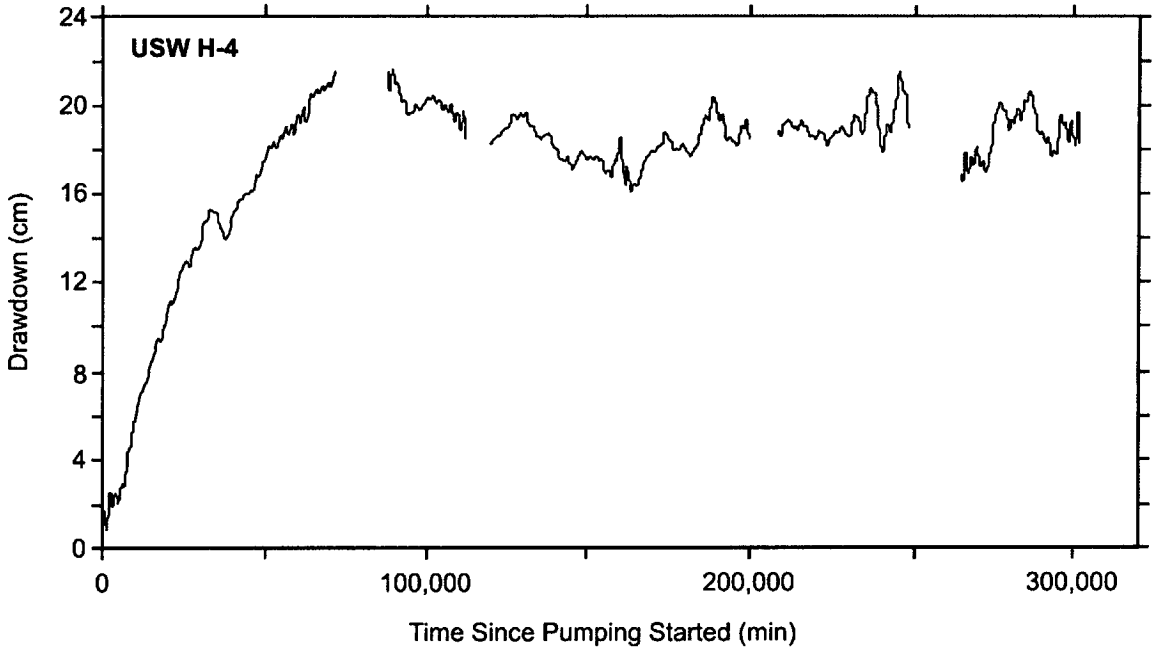

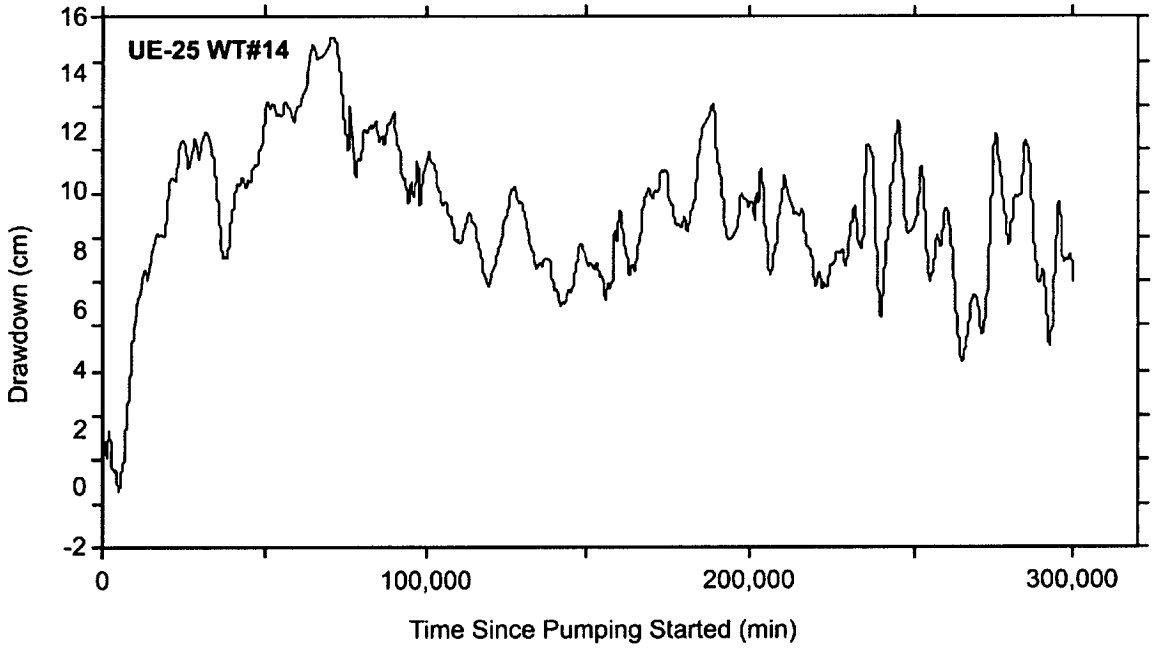

Output DTN: GS031008312314.004 (from Input DTN: GS030508312314.003 [164425], p. 32, Figure 24).

Figure 6.2-18. Drawdown in USW H-4 and UE-25 WT#14, May 8, 1996 (~0 minutes), to December 4, 1996 (~300,000 minutes)

6.2.3.2.1 Performance Tests

Hydraulic and tracer tests in the Prow Pass interval were preceded by pump-performance, step-drawdown, and 1-day hydraulic tests conducted in c#2 and c#3 from April 21 to May 29, 1998. These tests were designed primarily to determine whether c#2 could be used as a pumping well for tracer tests and what the optimum pumping rate should be. These tests also were analyzed to determine values of hydraulic properties that would be expected from a longer hydraulic test that was planned to precede tracer tests in the Prow Pass interval. Fluctuations in water and atmospheric pressures between performance tests indicated barometric efficiency values (Table 6.2-5) for the C-wells and ONC-1 that were used to analyze hydraulic tests (DTN: GS990408312315.002 [140115], DTN: MO0212SPANYESJ.149 [161274]) in the Prow Pass interval.

Table 6.2-5. Barometric Efficiency in the C-wells and UE-25 ONC-1

Interval	c#1	c#2	c#3	UE-25 ONC-1
Calico Hills	N/A	0.93	0.94	N/A
Prow Pass	0.96	0.93	1.0	0.99
Upper Bullfrog	0.99	0.93	≅1.0	N/A
Lower Bullfrog	0.97	N/A	N/A	N/A

Output DTN: GS031008312314.004, (from Input DTNs: GS990408312315.002 [140115] and MO0212SPANYESJ.149 [161274]).

NOTE: N/A: not applicable.

6.2.3.2.2 Analytical Methods

Analytical solutions were used to analyze data from hydraulic tests in the Prow Pass interval. Most of the data were analyzed using the method of Streltsova-Adams (1978 [150754]) (Strelsova-Adams.vi V 1.0, STN: 10971-1.0-00 [162756]) for a fissure-block aquifer. Analysis of data in this study was restricted to observation wells because most water-level changes in pumping wells at the C-wells complex are too large and rapid (Geldon 1996 [100396], pp. 12 to 69) to be explained solely by hydraulic properties of the pumped interval.

6.2.3.2.3 Constant-Rate Withdrawal Test

A constant-rate withdrawal (CRW) test in the Prow Pass interval started June 2, 1998. The pumping well for this test was c#2, and the observation wells for the test were c#1, c#3, and ONC-1.

Prior to starting the test, the packer in c#2 between the Prow Pass and Calico Hills intervals was deflated, and the two intervals, together, were pumped for 37 minutes at a rate of 0.57 L/s to fill tubing in the pumping well to the level of the flowmeter. After pumping stopped, the packer in c#2 between the Prow Pass and Calico Hills intervals was reinflated. With slight residual effects from the pre-test pumping (which were removed to analyze the test), pumping for the CRW test in the Prow Pass began at 16:00 hours on June 2. Discharge averaged 0.33 L/s between June 2 and 11, a period of 12,500 minutes. Pumping water into c#1 on June 5 to attempt a tracer test, injecting argon gas into c#1 on June 9 to blow sediment out of the tracer injection valve, and testing the downhole mixing pump in c#3 on June 10 briefly disturbed discharge from c#2 as well as pressures in c#1 and c#3. The CRW test was terminated on June 11, 1998, at 08:19 when operations began for a tracer test between c#3 and c#2.

The pumping in c#2 caused 135 m of drawdown in the Prow Pass interval of c#2 three minutes after pumping started. However, the water level rebounded 22 m in the next nine minutes. Subsequently, drawdown increased steadily but slowly and was about 128 m after 12,500 minutes of pumping. On the basis of values of transmissivity and storativity determined in this and previous tests in which the drawdown in the Prow Pass in observation wells was analyzed, only 1.04 percent of the 128-m drawdown in the Prow Pass of the pumped well c#2, namely 1.34 m, is estimated to have resulted from stressing the aquifer. The remainder of the drawdown is attributed to head losses in the well bore.

The pumping in c#2 caused oscillatory drawdown in the Prow Pass interval of the observation wells. After 12,500 minutes of pumping, this drawdown was 54 cm in c#3 (Figure 6.2-19), 12 cm in c#1 (Figure 6.2-20), and 0.9 cm in ONC-1. Plotted on log-log scales, drawdown in the Prow Pass interval of c#1 and c#3 indicated delayed yield that is characteristic of a fissure-block aquifer (Streltsova-Adams 1978 [150754]), Figures 6.2-21 and 6.2-22.

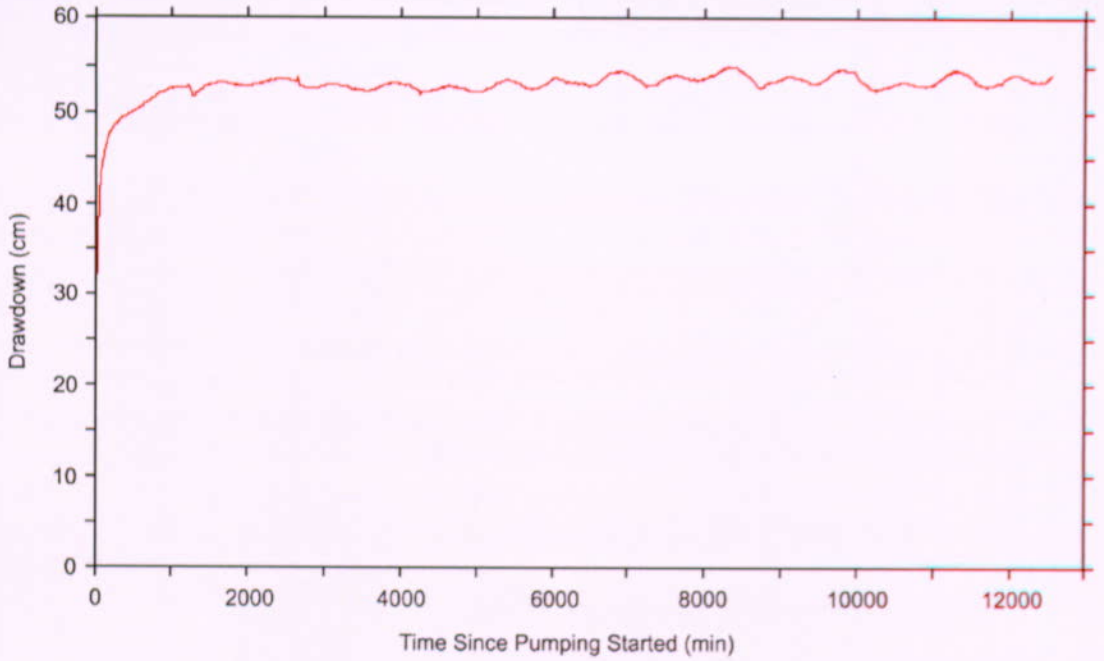

Output DTN: GS031008312314.004 (from Input DTN: GS990408312315.002 [140115]).

Figure 6.2-19. UE-25 c#3 Prow Pass Drawdown, June 2, 1998 (~0 minutes), to June 11, 1998 (~12,800 minutes)

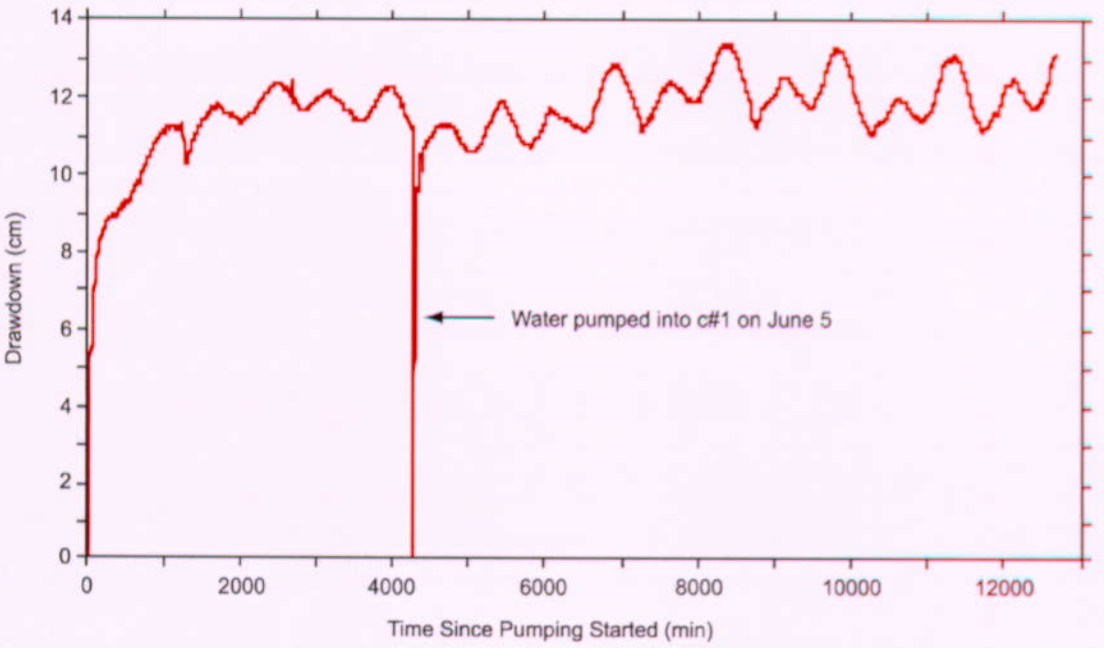

Output DTN: GS031008312314.004 (from Input DTN: GS990408312315.002 [140115]).

Figure 6.2-20. UE-25 c#1 Prow Pass Drawdown, June 2, 1998 (~0 minutes), to June 11, 1998 (~12,800 minutes)

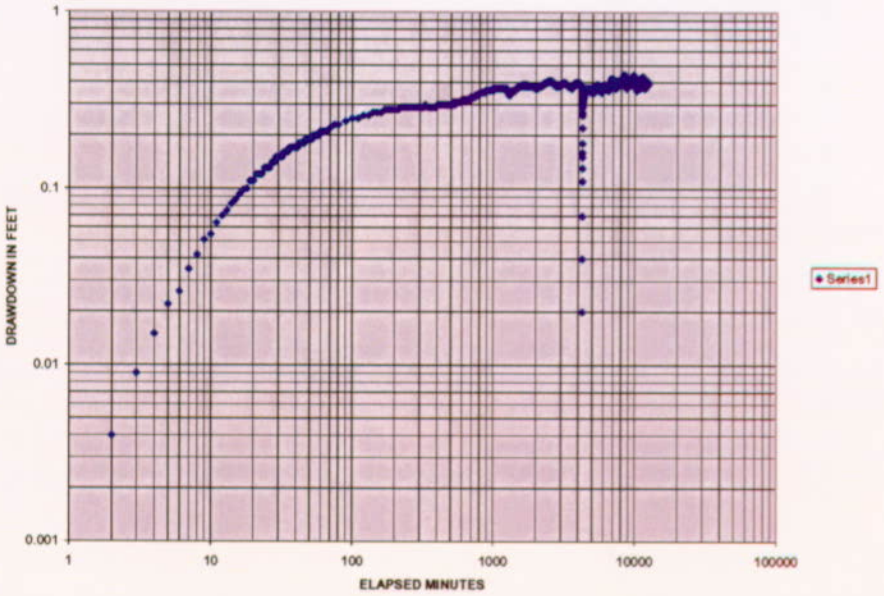

Output DTN: GS031008312314.004 (from Input DTN: GS990408312315.002 [140115]).

NOTE: English units are shown in the figure because the analysis was conducted in English units. However, parameter estimates are reported in metric units to downstream users.

Figure 6.2-21. Drawdown in the Prow Pass Interval of c#1 in Response to Pumping c#2, Starting June 2, 1998, Exhibiting Delayed Yield, Characteristic of a Fissure-block Aquifer

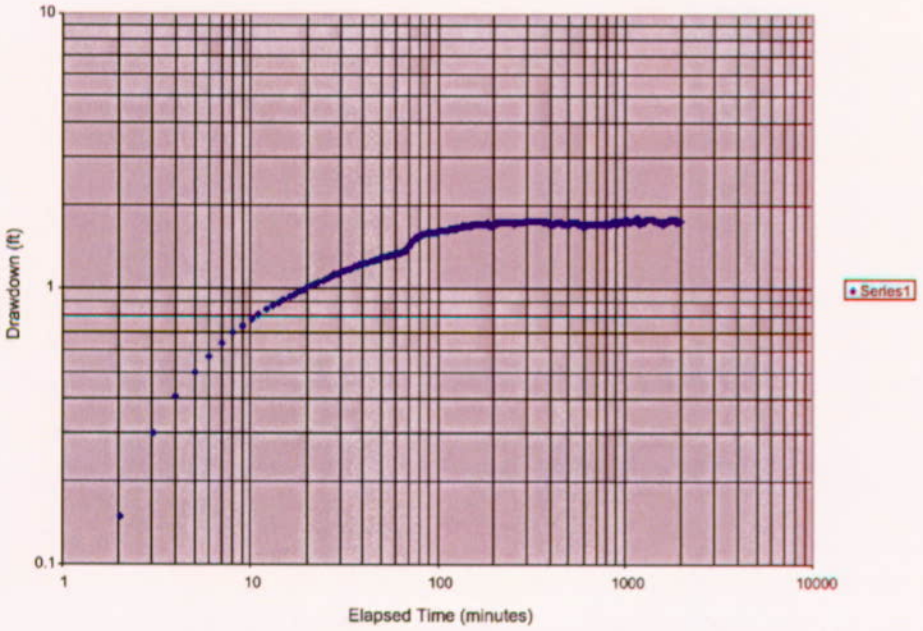

Output DTN: GS031008312314.004 (from Input DTN: GS990408312315.002 [140115]).

NOTE: English units are shown in the figure because the analysis was conducted in English units. However, parameter estimates are reported in metric units to downstream users.

Figure 6.2-22. Drawdown in the Prow Pass Interval of c#3 in Response to Pumping c#2, Starting June 2, 1998, Exhibiting Delayed Yield, Characteristic of a Fissure-block Aquifer

The pumping in c#2 indicated that the Calico Hills and Prow Pass intervals are connected by fractures beyond borehole walls because the Calico Hills responded to pumping in the Prow Pass wherever it was monitored. During the CRW test, the water level in the Calico Hills interval was drawn down as much as 19 cm in c#2 and 12 cm in c#3. In contrast, no drawdown was observed below the Prow Pass interval in c#2 and c#3 and below the Upper Bullfrog interval in c#1 during this test. The Upper Bullfrog drawdown in c#1 was 55 cm. The general lack of a response to pumping below the Prow Pass probably indicates that the highly permeable Lower Bullfrog and Upper Tram intervals in the C-wells were isolated from the Prow Pass interval during the CRW test.

The responses of the Calico Hills in the C-wells and the Upper Bullfrog in c#1 during pumping of the Prow Pass interval in c#2 made it necessary to apportion flow among the responding intervals to determine hydraulic properties. Lacking a flow survey for the test conditions, interval flow was determined by solving analytical equations simultaneously for interval discharge and transmissivity. To make the number of equations equal to the number of unknowns, it was assumed that (1) transmissivity values for the Calico Hills and Prow Pass intervals in the C-wells are constant, (2) the transmissivity of the Calico Hills is 5.6 m^2/d (on the basis of previous hydraulic tests), and (3) flow laterally and vertically within the Calico Hills interval was the same in each of the C-wells during the test. These assumptions were based on analyses and interpretations of previous hydraulic tests, borehole flow surveys, borehole geophysical logs, and other information, which are discussed in Section 6.2.4.1 and in Geldon (1996 [100396], pp. 12 to 69).

Calculations indicated that the Prow Pass interval contributed 94 percent of the total flow in c#2 and c#3 but only 24 percent of the flow in c#1. The substantially different flow from the Prow Pass in c#1 does not seem reasonable because lithologic changes that might account for variable flow do not occur in the Prow Pass interval at the C-wells complex. It is more likely that flow from the Calico Hills interval, the interconnectivity between the Calico Hills and Prow Pass, or the transmissivity of either or both the Prow Pass and Calico Hills intervals is not constant throughout the C-wells complex. Unquantifiable uncertainty results from failure to apportion flow satisfactorily.

Hydraulic properties of the Prow Pass interval determined from analyses of drawdown during the CRW test are summarized in Table 6.2-6. Input parameters (aquifer thickness, fracture half-spacing, interborehole distance, and discharge rate) needed in the analyses are also presented in Table 6.2-6.

6.2.3.2.4 Constant-Rate Injection Test

From June 11 to September 1, 1998, a period of 118,159 minutes, 676,973 L of water was pumped into c#3 to conduct tracer tests. The injection rate ranged from 0.032 to 0.16 L/s before tracers were injected into c#3 on June 17, but it subsequently was stabilized by periodic valve adjustments. From June 11 to September 1, the injection rate averaged 0.095 L/s.

As water was being injected into c#3 from June 11 to September 1, 2,311,290 L of water were withdrawn from c#2 at an average rate of 0.33 L/s. Injecting water into c#3 caused the discharge from c#2 to oscillate within a range of 0.05 L/s. The discharge from c#2 ranged from 0.30 to

0.35 L/s after water injection into c#3 started. Lowering the frequency of the pump in c#2 and increasing backpressure on it between August 3 and 31 decreased the discharge from c#2 to a range of 0.28 to 0.33 L/s after August 31.

Table 6.2-6. Hydraulic Properties of the Prow Pass Interval in the C-wells and Input Parameters Used in Obtaining Them

Borehole	c#1	c#3	ONC-1
Test dates	June 2–11, 1998	June 2–11,1998	June 11-Sep. 1, 1998
Period of record (min)	12,500	12,500	≅140,000
Analyzed data	Drawdown	Drawdown	Water-level rise
Transmissivity (m^2/d)	30	30	30
Hydraulic conductivity, fractures (m/d)	1	0.8	2
Hydraulic conductivity, matrix (m/d)	0.000003	0.0002	0.00002
Hydraulic conductivity (m/d)	No Data	No Data	No Data
Storativity, fractures	0.00004	0.00004	0.0002
Storativity, matrix	0.0003	0.0004	0.002
Storativity *	0.0004	0.0004	0.002
Distance from pumping well, c#2(m)	82.6	28.7	≅843
Transmissive thickness (m)	18.9	31.7	18.9
Fracture half-spacing (m)	0.34	2.0	0.34
Discharge (L/s)	0.078	0.309	

DTN: GS990408312315.002 [140115]. Output DTN: GS031008312314.004.

NOTE: * Combined storativity: sum of fractures and matrix storativities.

Water levels in the Prow Pass interval of c#2 oscillated as much as 10 m between readings due to injection of water into c#3. Although the water injection into c#3 caused drawdown in the Prow Pass interval of c#2 to decrease from 128 to 115 m in the first 11 days after it began, pumping in c#2 eventually predominated over the superimposed effects of the water injection. From June 22 to September 1, the range in c#2 drawdown increased from 115–125 m to 130–143 m (Figure 6.2-23).

Drawdown in the Prow Pass interval of c#3 decreased from +0.58 m to a range typically between -25 and -30 m between June 11 and September 1 (the period of continuous injection of water into c#3 [Figure 6.2-24]). This pronounced water-level rise was affected slightly by periodically adjusting the injection rate. Drawdown fluctuated markedly from +87 to -32 m while tracers were injected into c#3 on June 17 and 18.

Drawdown in the Prow Pass interval of c#1 was disturbed significantly by tracer-test operations in c#3 and c#1 from June 11 to September 1. Injection of water into c#3 decreased drawdown in c#1 from 13 to 2.8 cm between June 11 and July 27, but drawdown subsequently increased and ranged from 4.0 to 7.9 cm by September 1 (Figure 6.2-25). Injection of tracers into c#3 on June 17 increased drawdown from 8.9 cm to as much as 13 cm, whereas tracer injection in c#1 on July 31 decreased drawdown from +5.9 to -174 cm and then increased it to +10 cm. Removal of injection tubing from c#1 on June 26 to replace a cracking valve increased drawdown from 10 to

217 cm and then decreased it to -16 cm. Reinstallation of the tubing on July 13 increased drawdown from 5.5 to 10 cm and then decreased it to -1,150 cm.

Drawdown in ONC-1 decreased irregularly from +1.1 to -2.3 cm between June 11 and September 1 (Figure 6.2-26). Sharply increased drawdown about 9,000 minutes after injection of water into c#3 began may be related to tracer injection into c#3 on June 17, although the timing of this spike does not correlate precisely with the timing of tracer injection in c#3.

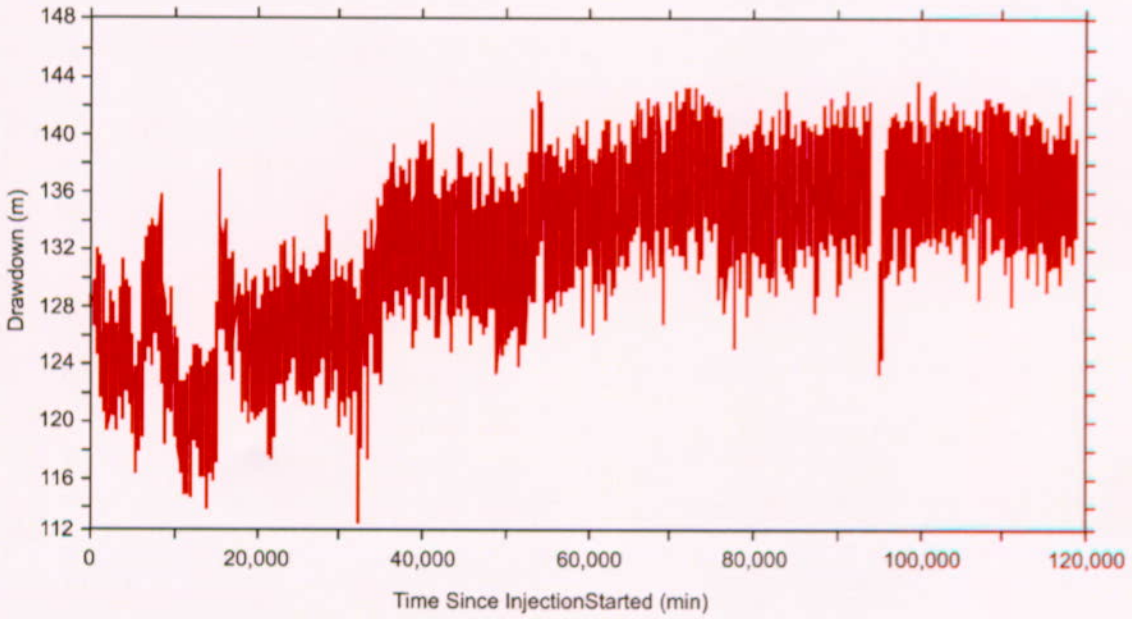

DTN: GS990408312315.002 [140115]. Output DTN: GS031008312314.004.

Figure 6.2-23. UE-25 c#2 Prow Pass Drawdown, June 11, 1998 (~0 minutes) to September 1, 1998 (~120,000 minutes)

Water-level rises in the C-wells from June 11 to September 1, 1998, were very irregular and too disturbed by tracer-test operations to be analyzed quantitatively. However, the water-level rise in ONC-1 during this period (with superimposed drawdown from pumping c#2 removed) could be matched to the type curves of Streltsova-Adams (1978 [150754]) (Streltsova-Adams.vi, V 1.0, STN: 10971-1.0-00 [162756]) for a fissure-block aquifer. This analysis (presented in Table 6.2-6) indicated a transmissivity of 30 m^2/d, a fracture hydraulic conductivity of 2 m/d, insignificant matrix hydraulic conductivity, and a storativity of 0.002 (90 percent of which is in the matrix). The Prow Pass interval in ONC-1 and the C-wells have equally low permeability, but storativity is an order of magnitude larger between ONC-1 and the C-wells than at the C-wells complex.

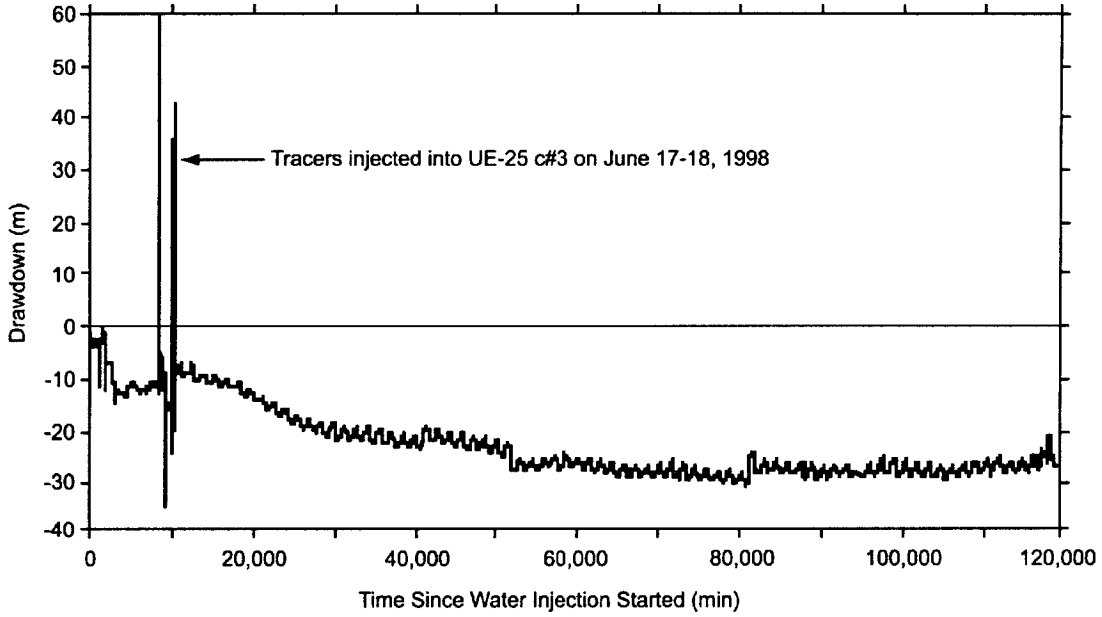

DTN: GS990408312315.002 [140115]. Output DTN: GS031008312314.004.

Figure 6.2-24. UE-25 c#3 Prow Pass Drawdown, June 11, 1998 (~0 minutes), to September 1, 1998 (~120,000 minutes)

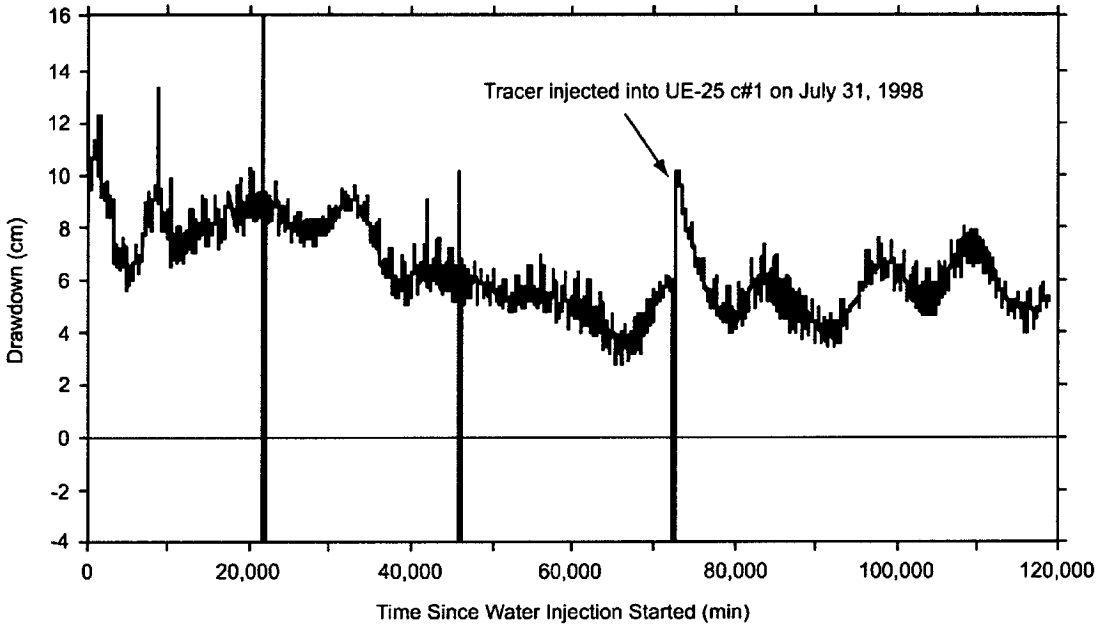

DTN: GS990408312315.002 [140115]. Output DTN: GS031008312314.004.

Figure 6.2-25. UE-25 c#1 Prow Pass Drawdown, June 11, 1998 (~0 minutes), to September 1, 1998 (~120,000 minutes)

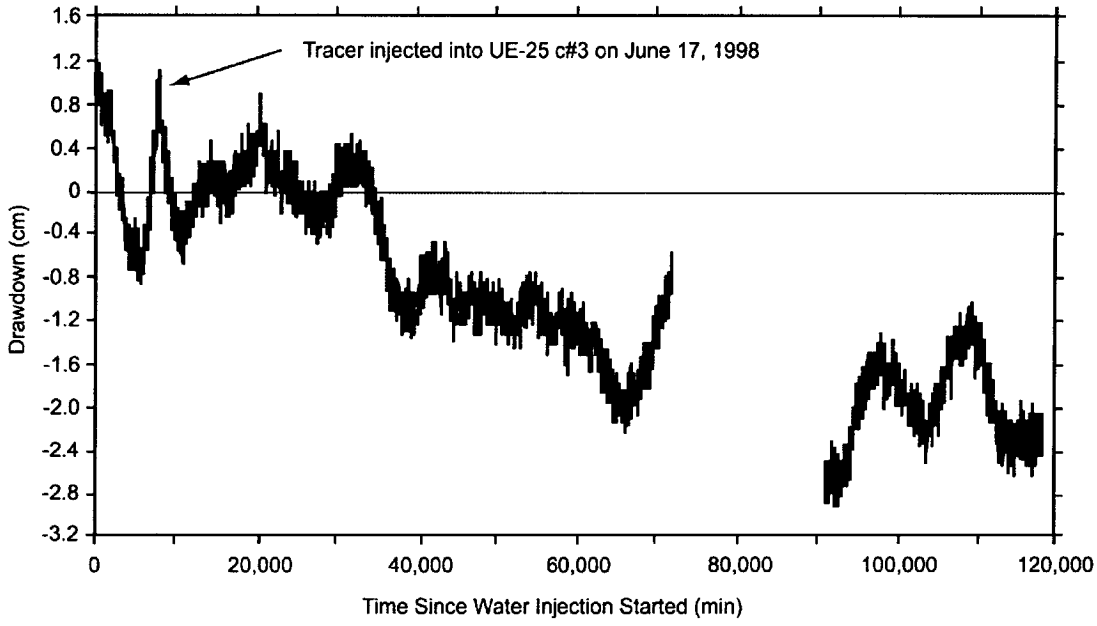

DTN: GS990408312315.002 [140115]. Output DTN: GS031008312314.004.

Figure 6.2-26. UE-25 ONC-1 Prow Pass Drawdown, June 11, 1998 (~0 minutes), to September 1, 1998 (~120,000 minutes)

6.2.4 Hydraulic Properties

Hydraulic tests conducted at the C-wells complex from 1995 to 1997 revealed much about the ability of hydrogeologic intervals in the C-wells and the Miocene tuffaceous rocks in the vicinity to store and transmit water. However, it must be emphasized that hydraulic properties computed from these tests pertain only to the structural setting in which the tests were conducted. The Lower Bullfrog interval is the most permeable interval in the C-wells because it is located in these boreholes where two intersecting faults have caused intense fracturing. The Calico Hills interval is the least permeable interval in the C-wells, probably because it is the farthest interval vertically from faults that intersect these boreholes. The combination of its large distance from faults and its low degree of welding (and, thus, high ductility) result in the Calico Hills interval being the least fractured, and, hence, least transmissive, interval at the C-wells. In a different structural setting, the Lower Bullfrog, Calico Hills, and other intervals of the Miocene tuffaceous rocks would be expected to have different hydraulic properties than indicated at the C-wells complex. For example, the Bullfrog Tuff yielded very little of the water produced from the Miocene tuffaceous rocks during a tracejector flow survey of p#1 (Craig and Robison 1984 [101040]), and the Calico Hills Formation yielded 32 percent of the water produced from the Miocene tuffaceous rocks during a tracejector flow survey of b#1 (Lahoud et al. 1984 [101049]).

Hydraulic properties for the various hydrogeologic intervals at the C-wells are discussed in the following subsections. With the exception of the Prow Pass interval, all of the hydraulic properties were derived from testing conducted prior to 1998. Properties of the Prow Pass interval were derived from testing conducted both prior to and during 1998. The 1998 testing involved pumping of only the Prow Pass interval.

In the analyses described in the following subsections, the interborehole distances were as given in Tables 6.1-1, 6.2-6, and 6.2-7; borehole diameters for all C-wells were assumed to be 27.94 cm (11 in), and aquifer thicknesses were as given under "transmissive thickness" in Tables 6.2-6 and 6.2-7.

6.2.4.1 Calico Hills Interval

The Calico Hills interval responded in most hydraulic tests, including one conducted from May to June 1984 (Geldon 1996 [100396], pp. 12 to 69), as an unconfined aquifer. In four tests conducted from 1984 to 1997, the Calico Hills interval consistently was determined to be the least permeable interval in the C-wells (Table 6.2-7). The hydraulic test in May and June 1984 indicated that the Calico Hills interval in c#1 has a transmissivity of 9 m^2/d, a horizontal hydraulic conductivity of 0.2 m/d, a vertical hydraulic conductivity of 0.3 m/d, and a specific yield of 0.003 (Geldon 1996 [100396], pp. 12 to 69). The hydraulic test in June 1995 indicated that the Calico Hills interval in c#2 has a transmissivity of 6 m^2/d, a horizontal hydraulic conductivity of 0.1 m/d, and a storativity of 0.0002. Hydraulic tests conducted in February 1996 and from May 1996 to November 1997 generally supported the previous analyses. The specific yield of 0.4 obtained for the Calico Hills in c#2 from analyzing the May 8, 1996 response is much higher than expected for fractured rock (it can go up to 30 percent for unconsolidated materials (Bouwer 1978 [162675], p. 30). A representative plot indicating a match between the data and one of the type curves of Neuman (1975 [150321]) for an unconfined, anisotropic aquifer is shown in Figure 6.2-27.

6.2.4.2 Prow Pass Interval

The Prow Pass interval generally responded to hydraulic tests conducted from June 1995 to November 1997 as a confined aquifer (Table 6.2-7). The hydraulic test in June 1995 indicated that the Prow Pass interval in c#1 had a transmissivity of 60 m^2/d, a hydraulic conductivity of 3 m/d, and a storativity of 0.0003. The same hydraulic test indicated that the Prow Pass interval in c#2 has a transmissivity of 40 m^2/d, a hydraulic conductivity of 2 m/d, and a storativity of 0.0004. Analyses of hydraulic tests conducted in February 1996 and from May 1996 to March 1997 generally produced parameter values similar to those produced by the previous analyses, even when the February 1996 response was analyzed as an unconfined-aquifer response. A representative plot indicates a match between the data and the type curve of Theis (1935 [150327]) for a confined aquifer (Figure 6.2-28).

Hydraulic testing of the Prow Pass interval conducted in 1998 by pumping c#2 indicated a fissure-block aquifer with transmissivity of 30 m^2/d in both c#1 and c#3. Fracture hydraulic conductivities derived from responses in c#1 and c#3 were 1 m/d and 0.8 m/d, respectively. Matrix hydraulic conductivities were negligible, and overall storativity was 0.0004, with most of that being attributed to the matrix. These parameter estimates are in good agreement with those derived from earlier testing in which the Prow Pass interval was not pumped directly (above). This result instills confidence in the ability to estimate hydraulic parameters for intervals that are not pumped directly but that respond to pumping other intervals. Even though comparable parameter values were obtained in c#1 by analyzing some of the test responses in the Prow Pass as either unconfined or fissure-block aquifer responses, the later interpretation is more logical because the Prow Pass interval is not at the water table.

Table 6.2-7. Results of Hydraulic Tests in Borehole UE-25 c#3, June 1995 to November 1997

Starting Date	06/12/95	02/08/96	02/08/96 c#1	05/08/96	05/08/96	06/12/95	02/08/96 c#2	05/08/96	05/08/96
Calico Hills									
Analyzed data	None	None	N/A	None	N/A	Drawdown	Drawdown	Drawdown	N/A
Period of record (min)	N/A	N/A	N/A	N/A	N/A	5,800	7,000	464,100	N/A
Aquifer type	Unconfined	Unconfined	N/A	Unconfined	N/A	Unconfined	Confined	Unconfined	N/A
Transmissive thickness (m)	60.4	60.4	N/A	60.4	N/A	45.4	45.4	45.4	N/A
Distance from pumping well (m)	78.3	78.3	N/A	78.3	N/A	29.0	29.0	29.0	N/A
Average discharge (L/s)	0.85	0.042	N/A	0.10	N/A	0.85	0.042	0.10	N/A
Transmissivity (m^2/day)	9(est)	9(est)	N/A	9(est)	N/A	6	10	4	N/A
Horizontal hydraulic conductivity (m/day)	0.2(est)	0.2(est)	N/A	0.2(est)	N/A	0.1	0.2	0.08	N/A
Vertical hydraulic conductivity (m/day)	0.3(est)	0.3(est)	N/A	0.3(est)	N/A	ND	ND	0.01	N/A
Storativity (dimensionless)	ND	ND	N/A	ND	N/A	0.0002	0.0006	0.0003	N/A
Specific yield (dimensionless)	0.003(est)	0.003(est)	N/A	0.003(est)	N/A	ND	ND	0.4	N/A
Prow Pass									
Analyzed data	Drawdown	Drawdown	Drawdown	Drawdown	N/A	Drawdown	Drawdown	Drawdown	N/A
Period of record (min)	5,800	7,000	7,000	464,100	N/A	5,800	7,000	464,100	N/A
Aquifer type	Confined	Unconfined	Confined	Confined	N/A	Confined	Confined	Confined	N/A
Transmissive thickness (m)	18.9	18.9	18.9	18.9	N/A	23.8	23.8	23.8	N/A
Distance from pumping well (m)	81.1	81.1	81.1	81.1	N/A	28.6	28.6	28.6	N/A
Average discharge (L/s)	0.65	0.21	0.21	0.22	N/A	0.65	0.13	0.19	N/A
Transmissivity (m^2/day)	60	50	60	50	N/A	40	30	30	N/A
Horizontal hydraulic conductivity (m/day)	3	3	3	3	N/A	2	1	1	N/A
Vertical hydraulic conductivity (m/day)	ND	0.0001	ND	ND	N/A	ND	ND	ND	N/A
Storativity (dimensionless)	0.0003	0.0003	0.0004	0.0002	N/A	0.0004	0.003	0.0008	N/A
Specific yield (dimensionless)	ND	ND	ND	ND	N/A	ND	ND	ND	N/A

NOTE: *First number is for fractures; second is for matrix. ND: no data; N/A: not applicable; est: estimated to be the same as values obtained from an hydraulic test in May 1984.

Table 6.2-7 (Continued). Results of Hydraulic Tests in Borehole UE-25 c#3, June 1995 to November 1997

Starting Date	06/12/95	02/08/96	02/08/96 c#1	05/08/96	05/08/96	06/12/95	02/08/96 c#2	05/08/96	05/08/96
Upper Bullfrog									
Analyzed data	Recovery	Drawdown	N/A	Drawdown	N/A	Drawdown	Drawdown	Drawdown	N/A
Period of record (min)	5,700	7,000	N/A	464,100	N/A	5,800	7,000	464,100	N/A
Aquifer type	Confined	Unconfined	N/A	Fissure-block	N/A	Confined	Confined	Confined	N/A
Transmissive thickness (m)	46.0	46.0	N/A	46.0	N/A	24.1	24.1	24.1	N/A
Distance from pumping well (m)	83.2	83.2	N/A	82.3	N/A	28.6	28.6	28.6	N/A
Average discharge (L/s)	0.88	0.37	N/A	0.32	N/A	0.88	0.36	0.36	N/A
Transmissivity (m^2/day)	90	40	N/A	50	N/A	100	100	80	N/A
Horizontal hydraulic conductivity (m/day)	2	0.8	N/A	1/0.00002*	N/A	4	4	3	N/A
Vertical hydraulic conductivity (m/day)	ND	0.5	N/A	ND	N/A	ND	ND	ND	N/A
Storativity (dimensionless)	0.00006	0.0009	N/A	0.0001/0.0009*	N/A	0.00003	0.00002	0.00002	N/A
Specific yield (dimensionless)	ND	0.002	N/A	ND	N/A	ND	ND	ND	N/A
Bullfrog-Tram									
Analyzed data	N/A	Drawdown	N/A	N/A	N/A	N/A	Drawdown	N/A	N/A
Period of record (min)	N/A	7,000	N/A	N/A	N/A	N/A	7,000	N/A	N/A
Aquifer type	N/A	Confined	N/A	N/A	N/A	N/A	Confined	N/A	N/A
Transmissive thickness (m)	N/A	112	N/A	N/A	N/A	N/A	51.2	N/A	N/A
Distance from pumping well (m)	N/A	86.3	N/A	N/A	N/A	N/A	29	N/A	N/A
Average discharge (L/s)	N/A	7.84	N/A	N/A	N/A	N/A	7.93	N/A	N/A
Transmissivity (m^2/day)	N/A	2,500	N/A	N/A	N/A	N/A	2,500	N/A	N/A
Horizontal hydraulic conductivity (m/day)	N/A	20	N/A	N/A	N/A	N/A	50	N/A	N/A
Vertical hydraulic conductivity (m/day)	N/A	ND	N/A	N/A	N/A	N/A	ND	N/A	N/A
Storativity (dimensionless)	N/A	0.0003	N/A	N/A	N/A	N/A	0.002	N/A	N/A
Specific yield (dimensionless)	N/A	ND	N/A	N/A	N/A	N/A	ND	N/A	N/A

NOTE: *First number is for fractures; second is for matrix. ND: no data; N/A: not applicable; est: estimated to be the same as values obtained from a hydraulic test in May 1984.

Table 6.2-7 (Continued). Results of Hydraulic Tests in Borehole UE-25 c#3, June 1995 to November 1997

Starting date	06/12/95	02/08/96	02/08/96 c#1	05/08/96	05/08/96	06/12/95	02/08/96 c#2	05/08/96	05/08/96
Lower Bullfrog									
Analyzed data	Recovery	None	N/A	Drawdown	Drawdown	Drawdown	None	Drawdown	Drawdown
Period of record (min)	6,300	N/A	N/A	464,100	464,100	5,800	N/A	464,100	464,100
Aquifer type	Confined	Confined	N/A	Confined	Fissure-block	Confined	Confined	Confined	Fissure-block
Transmissive thickness (m)	62.8	62.8	N/A	62.8	62.8	29.9	29.9	29.9	29.9
Distance from pumping well (m)	85.6	85.6	N/A	85.6	85.6	29.3	29.3	29.3	29.3
Average discharge (L/s)	15.3	ND	N/A	6.37	6.37	15.3	ND	6.69	6.69
Transmissivity (m^2/day)	1,800	ND	N/A	1,600	1,300	1,900	ND	1,600	1,300
Horizontal hydraulic conductivity (m/day)	30	ND	N/A	30	20/0.0004*	60	ND	50	40/0.001*
Vertical hydraulic conductivity (m/day)	ND	ND	N/A	ND	ND	ND	ND	ND	ND
Storativity (dimensionless)	0.0004	ND	N/A	0.0002	0.0002/0.002*	0.003	ND	0.001	0.002/0.02*
Specific yield (dimensionless)	ND	ND	N/A	ND	ND	ND	ND	ND	ND
Upper Tram									
Analyzed data	None	None	N/A	None	N/A	None	None	None	N/A
Period of record (min)	N/A	N/A	N/A	N/A	N/A	N/A	N/A	N/A	N/A
Aquifer type	Leaky	Leaky	N/A	Leaky	N/A	Leaky	Leaky	Leaky	N/A
Transmissive thickness (m)	49.7	49.7	N/A	49.7	N/A	21.3	21.3	21.3	N/A
Distance from pumping well (m)	86.9	86.9	N/A	86.9	N/A	29.6	29.6	29.6	N/A
Average discharge (L/s)	4.74	ND	N/A	2.52	N/A	4.74	ND	2.18	N/A
Transmissivity (m^2/day)	ND	ND	N/A	800	N/A	ND	ND	900	N/A
Horizontal hydraulic conductivity (m/day)	ND	ND	N/A	20	N/A	ND	ND	40	N/A
Vertical hydraulic conductivity (m/day)	ND	ND	N/A	ND	N/A	ND	ND	ND	N/A
Storativity (dimensionless)	ND	ND	N/A	0.0001	N/A	ND	ND	0.001	N/A
Specific yield (dimensionless)	ND	ND	N/A	ND	N/A	ND	ND	ND	N/A

Output DTN: GS031008312314.004 (from Input DTN: GS030508312314.003 [164425], pp. 34 to 35, Table 8).

NOTE: *First number is for fractures; second is for matrix. ND: no data; N/A: not applicable; est: estimated to be the same as values obtained from a hydraulic test in May 1984.

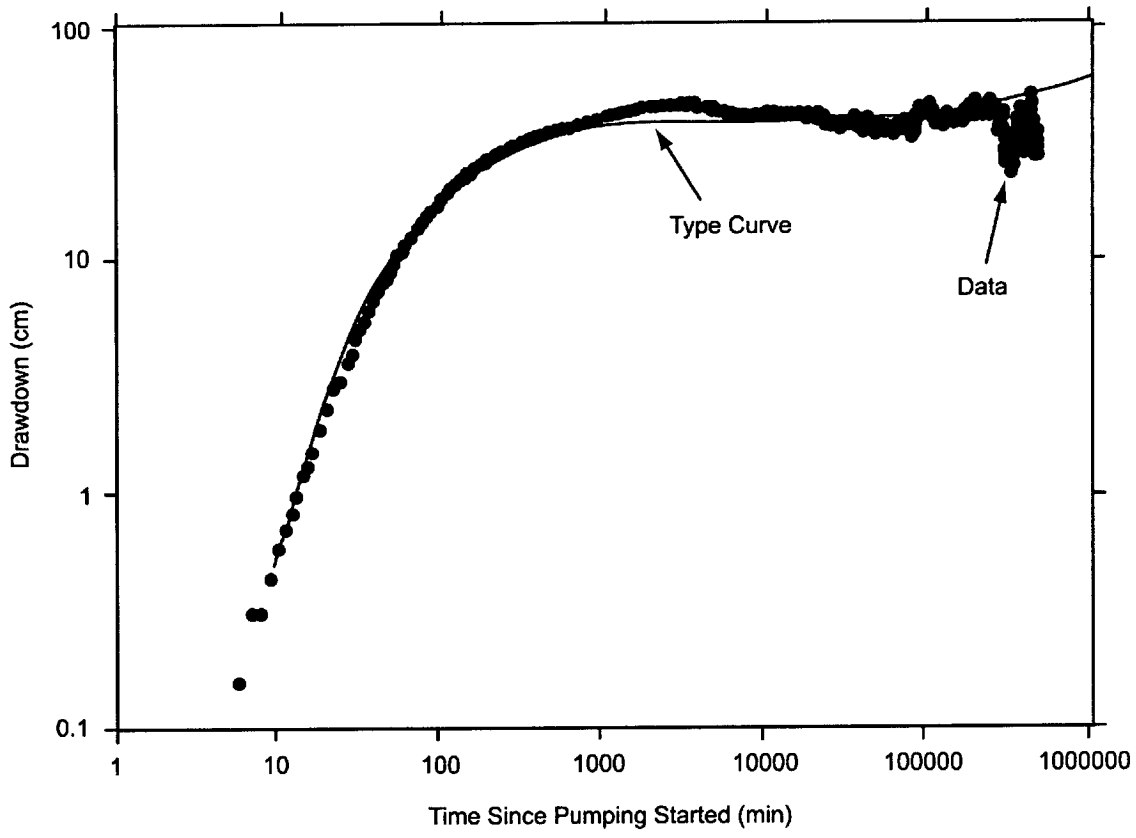

Output DTN: GS031008312314.004 (from Input DTN: GS030508312314.003 [164425], p. 36, Figure 25).

Figure 6.2-27. Analysis of Drawdown in the Calico Hills Interval of UE-25 c#2, May 8, 1996 (~0 minutes), to March 26, 1997 (~470,000 minutes), by the Method of Neuman

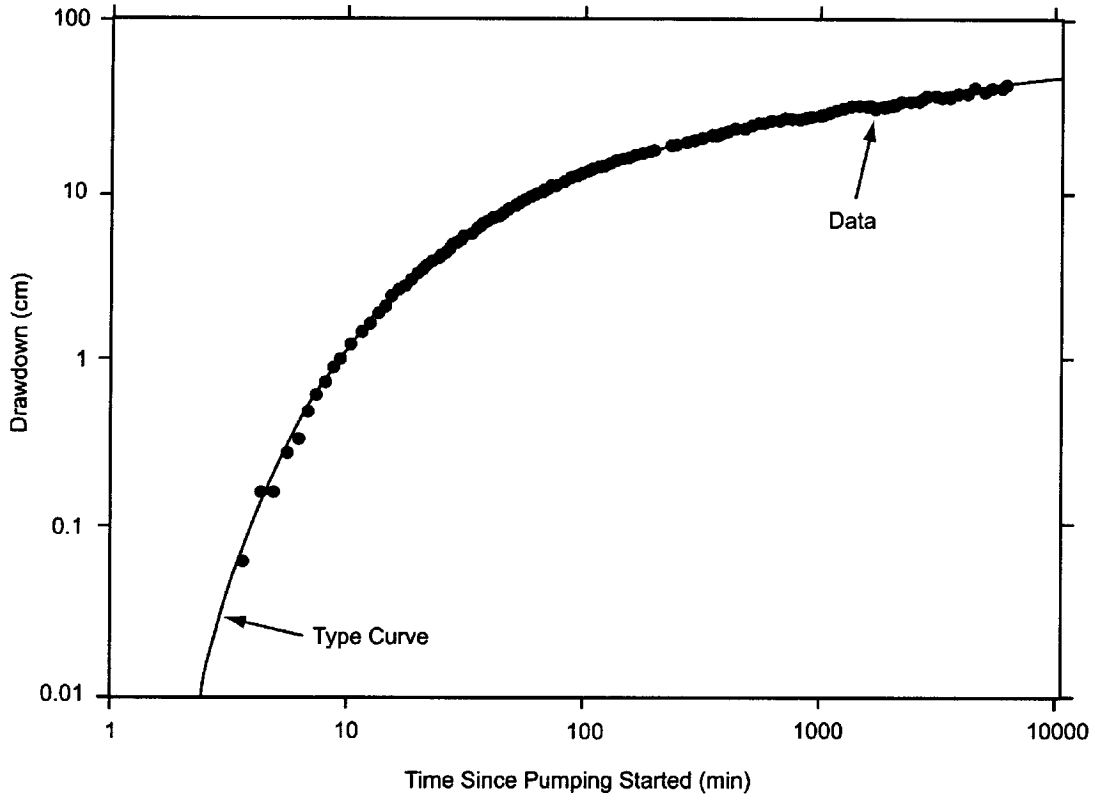

Output DTN: GS031008312314.004 (from Input DTN: GS030508312314.003 [164425], p. 37, Figure 26).

Figure 6.2-28. Analysis of Drawdown in the Prow Pass Interval of UE-25 c#1, June 12–16, 1995, by the Method of Theis

6.2.4.3 Upper Bullfrog Interval

The Upper Bullfrog interval in c#2 responded to all hydraulic tests as a confined aquifer (Table 6.2-7). Those tests consistently indicated a transmissivity of 80 to 100 m^2/d, a hydraulic conductivity of 3 to 4 m/d, and a storativity of 0.00002 to 0.00003. A representative plot indicates a match between the data and the type curve of Theis (1935 [150327]) for a confined aquifer (Figure 6.2-29).

The hydraulic test in June 1995 produced results for the Upper Bullfrog interval in c#1 that were consistent with results for that interval in c#2 (Table 6.2-7). During longer tests conducted in February 1996 and May 1996, sufficient time elapsed to reveal the effects of fractures on flow between the Upper Bullfrog interval in c#1 and open intervals in the pumping well. Analyses of drawdown (complicated by downward flow through fractures) indicated smaller values of transmissivity and hydraulic conductivity and larger values of storativity than analyses of drawdown in which the effects of fractures were not evident (Table 6.2-7). Hydraulic properties determined from hydraulic tests conducted in 1996 and 1997 using unconfined and fissure-block interpretations are less reliable than properties determined from the hydraulic test in June 1995 because of the sliding sleeve placement in the observation and pumping wells in the later tests.

Unconfined and fissure-block responses are similar; however, a fissure-block interpretation is more logical for the Upper Bullfrog aquifer than an unconfined interpretation because this aquifer is not at the water table. Also, the specific yield calculated from the unconfined solution, 0.002, seems unrealistically low.

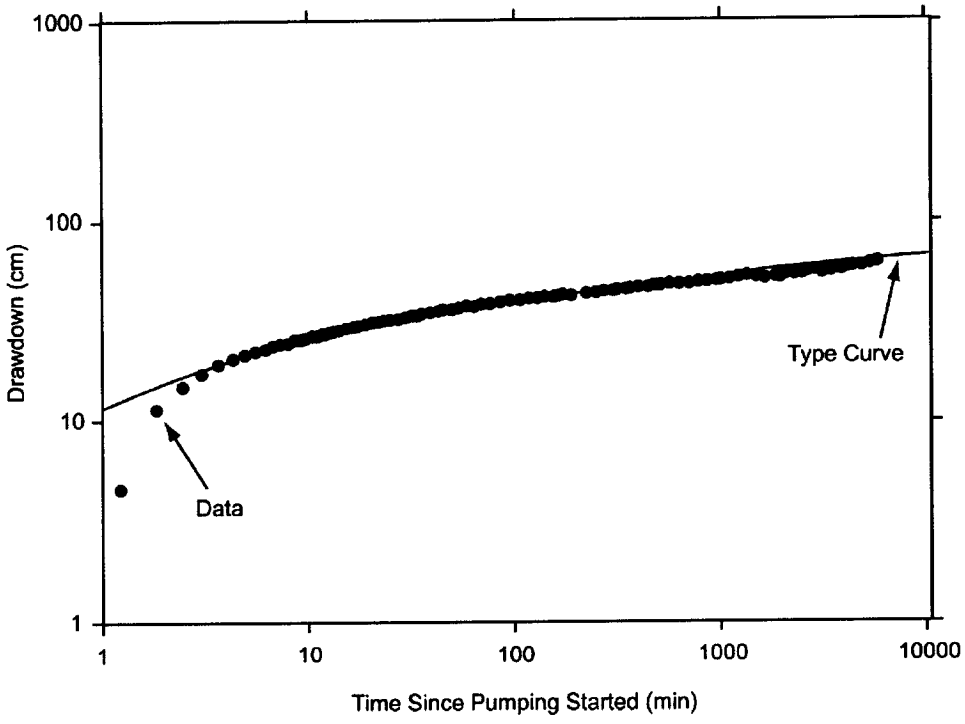

Output DTN: GS031008312314.004 (from Input DTN: GS030508312314.003 [164425], p. 38, Figure 27).

Figure 6.2-29. Analysis of Drawdown in UE-25 c#2 Upper Bullfrog Interval, June 12–16, 1995, by the Method of Theis

6.2.4.4 Lower Bullfrog Interval

Undisturbed drawdown in the Lower Bullfrog interval of c#1 and c#2 during the hydraulic test conducted from May 1996 to November 1997 can be interpreted in several ways that were not evident from previous hydraulic tests of much shorter duration. Although previous tests indicated a confined-aquifer response, the test beginning in May 1996 progressed long enough to develop a double-humped drawdown curve characteristic of a fissure-block aquifer. From 158,000 minutes (110 days) after pumping started in May 1996 to the end of the analyzed record (464,100 minutes [312 days] after pumping started), drawdown in c#1 and c#2 was greater than anticipated on the basis of extrapolating the earlier drawdown for long periods (using the equation of Theis (1935 [150327]), to extrapolate drawdown). The oscillatory pattern of drawdown in the C-wells after 158,000 minutes (110 days) of pumping can be interpreted to indicate that the spreading cone of depression encompassed volumes of the Lower Bullfrog interval that alternately were less transmissive or as transmissive as the Lower Bullfrog in the C-wells.

Values of transmissivity computed for the Lower Bullfrog interval are significantly different depending on whether the interval is considered a confined aquifer or a fissure-block aquifer (Table 6.2-7). In c#1 and c#2, transmissivity is 1,600 m^2/d if the Lower Bullfrog is analyzed as a confined aquifer (Figure 6.2-30) and 1,300 m^2/d if analyzed as a fissure-block aquifer (Figure 6.2-31). Although the two analytical solutions produced equally plausible results, the fissure-block aquifer solution is consistent with a tracer test conducted from February to March 1996 that indicated dual porosity in the Bullfrog-Tram interval (Fahy 1997 [137456], third {unnumbered} page). Also, the longer pumping required for the fissure-block aquifer response to develop and the lower transmissivity value determined from that response can be interpreted to confirm that less-transmissive rocks were reached as the cone of depression spread to increasingly distant areas during the hydraulic test that began in May 1996.

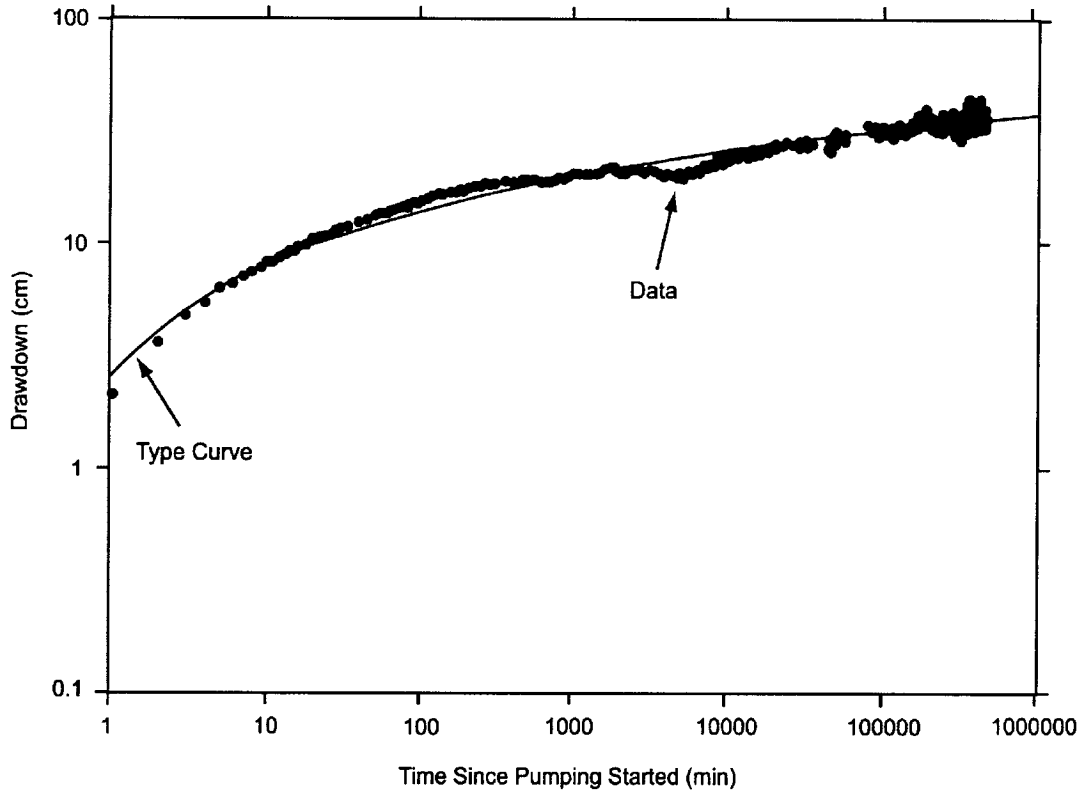

Output DTN: GS031008312314.004 (from Input DTN: GS030508312314.003 [164425], p. 39, Figure 28).

Figure 6.2-30. Analysis of Drawdown in UE-25 c#1 Lower Bullfrog Interval, May 8, 1996, to March 26, 1997, by the Method of Theis

Values of hydraulic conductivity and storativity are considerably larger in the rock mass between c#2 and c#3 than in the rock mass between c#1 and c#3. When analyzed as a confined aquifer, the hydraulic conductivity of the Lower Bullfrog interval is 50 m/d in c#2 and 30 m/d in c#1, and its storativity is 0.001 in c#2 and 0.0002 in c#1. (These hydraulic conductivities and storativities

of the interval in both boreholes are about the same as those of the fractures in the interval in both boreholes obtained when the Lower Bullfrog is analyzed as a fissure-block aquifer; see Table 6.2-7.)

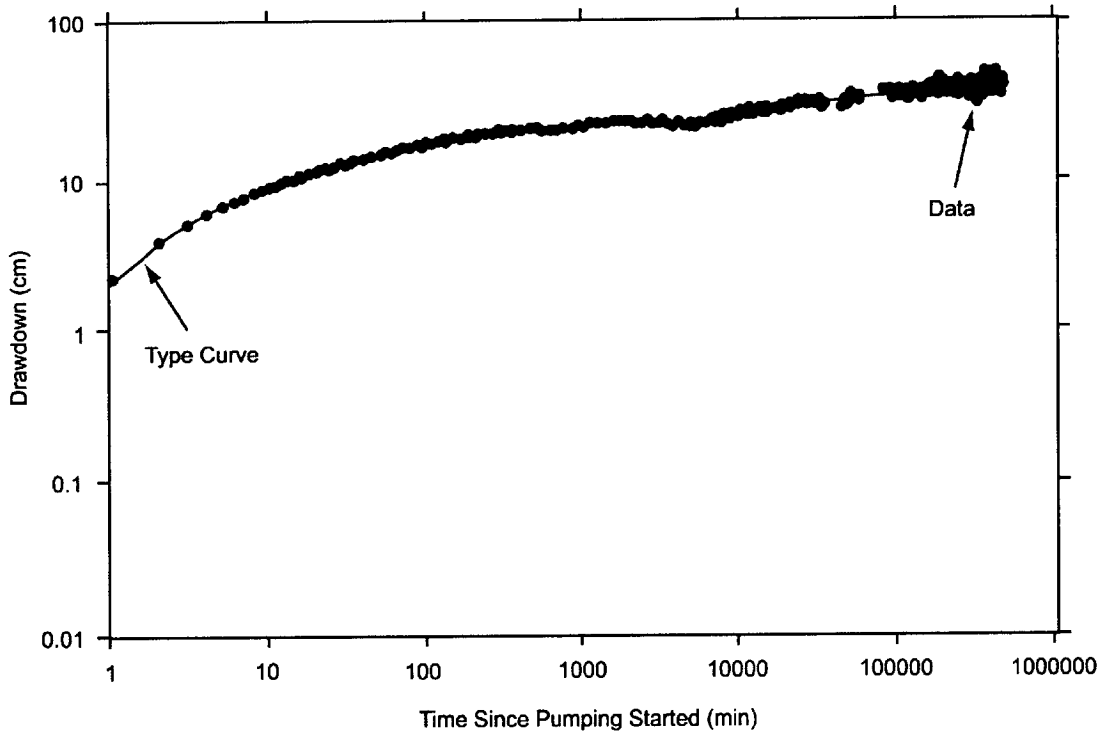

Output DTN: GS031008312314.004 (from Input DTN: GS030508312314.003 [164425], p. 39, Figure 29).

NOTE: For the analysis curve, the parameter $\tau/B = 0.05$.

Figure 6.2-31. Analysis of Drawdown in UE-25 c#1 Lower Bullfrog Interval, May 8, 1996, to March 26, 1997, by the Method of Streltsova-Adams

6.2.4.5 Upper Tram Interval

The Upper Tram interval was known from earlier hydraulic tests (conducted in 1984) to respond to pumping as a leaky aquifer without confining bed storage because of recharge from faults that intersect the C-wells in that interval (Geldon 1996 [100396], pp. 12 to 69). Although hydraulic properties of the Upper Tram ($_{UT}$) interval could not be determined directly from hydraulic tests conducted during this study (because of transducer malfunction), they could be estimated by subtracting values of hydraulic properties determined for the Lower Bullfrog ($_{LB}$) interval from those determined for the Bullfrog-Tram ($_{BT}$) interval. This is deemed acceptable based on the assumption that flow during the Bullfrog-Tram test and the Lower Bullfrog test was radial in an equivalent porous medium that is homogeneous and isotropic, composed of interconnected fractures. The following equations were used (Geldon 1996 [100396], pp. 21 to 69):

$$T_{UT} = T_{BT} - T_{LB} \quad \text{(Eq. 2)}$$

$$S_{UT} = S_{BT} - S_{LB} \quad \text{(Eq. 3)}$$

$$K_{UT} = (K_{BT} \times b_{BT} - K_{LB} \times b_{LB})/b_{UT} \quad \text{(Eq. 4)}$$

where

T = transmissivity (L^2/T)
S = storativity (dimensionless)
K = hydraulic conductivity (L/T)
b = thickness (L).

Only hydraulic properties of the Lower Bullfrog interval determined by the Theis (1935 [150327]) solution were used in these calculations because hydraulic properties of the Bullfrog-Tram interval (which includes the Lower Bullfrog) were determined by this method. These calculations indicated a transmissivity of 800 m^2/day, a hydraulic conductivity of 20 m/day, and a storativity of 0.0001 for the Upper Tram interval in c#1 and a transmissivity of 900 m^2/day, a hydraulic conductivity of 40 m/day, and a storativity of 0.001 for the Upper Tram interval in c#2 (Table 6.2-7).

6.2.4.6 Miocene Tuffaceous Rocks: Hydraulic Properties and Large-Scale Horizontal Anisotropy

Indicative of hydraulic connection through a highly developed fracture network, diverse intervals of the Miocene tuffaceous rocks in six observation wells responded to the pumping in c#3 from May 1995 to November 1997 (Table 6.2-8). The C-wells, ONC-1, and H-4 appear to be connected hydraulically through a northwest-trending zone of discontinuous faults that extends from Bow Ridge to Antler Wash (Geldon et al. 1998 [129721], pp. 23 to 25, Figure 2; p. 31). The Paintbrush Canyon and related faults that intersect WT#14 and the C-wells probably enhance hydraulic communication between those boreholes. Hydraulic communication between the C-wells and WT#3 probably is enabled both stratigraphically and structurally because those boreholes were open during hydraulic tests in the same geologic unit (the Bullfrog Tuff) and are cut by the same faults (the Paintbrush Canyon and related faults).

Analyses of the drawdown in individual observation wells (Figures 6.2-32 to 6.2-35) provide hydraulic properties of the rock mass at the scale of the distance between those boreholes and c#3 (Table 6.2-8). Analyses of drawdown in multiple observation wells, either as a function of time (normalized by dividing by the square of the distance between the observation and pumping wells) or as a function of distance at a specified time, allow computation of hydraulic properties of the tuffaceous rock mass in which all of the included observation wells are located.

Table 6.2-8. Hydraulic Properties Computed from Observation Well Responses to Pumping in UE-25 c#3, May 1995 to November 1997

Borehole	c#2	c#2	c#1	c#1
Starting date of hydraulic test	05/22/95	05/08/96	05/22/95	05/08/96
Period of record (min)	14,400	464,100	11,400	464,100
Analyzed data	Drawdown	Drawdown	Recovery	Drawdown
Geologic units in monitored interval	Calico Hills to Tram	Calico Hills to Tram	Calico Hills to Tram	Calico Hills to Tram
Aquifer type	Unconfined	Variable	Unconfined	Variable
Transmissive thickness (m)**	165	144	252	238
Distance from pumping well (m)	29.0	29.0	82.6	82.9
Average discharge (L/s)	17.9	9.53	17.9	9.53
Transmissivity (m^2/day)	2,100	2,400–2,600	1,800	2,200–2,600
Horizontal hydraulic conductivity (m/day)	13	16–18	7	9–11
Vertical hydraulic conductivity (m/day)	1.7	Not estimated	0.3	Not estimated
Storativity (dimensionless)	0.003	0.003–0.004	0.001	0.002
Specific yield (dimensionless)	0.2	Not estimated	0.01	Not estimated

Borehole	UE-25 ONC-1	USW H-4	UE-25 WT#14	UE-25 WT#3
Starting date of hydraulic test	05/08/96	05/08/96	05/08/96	05/08/96
Period of record (min)	796,663	72,000	72,000	463,500
Analyzed data	Drawdown	Drawdown	Drawdown	Drawdown
Geologic units in monitored interval	Prow Pass	Prow Pass to Lithic Ridge	Topopah Spring and Calico Hills	Bullfrog
Aquifer type	Fissure-block	Confined	Confined	Confined
Transmissive thickness (m)	193 (est)	276	Not estimated	47.5 (estimated)
Distance from pumping well (m)	843	2,245	2,249	3,526
Average discharge (L/s)	9.21	9.72	9.72	9.59
Transmissivity (m^2/day)	1,000	700	1,300	2,600
Horizontal hydraulic conductivity (m/day)	5/.002*	2	Not estimated	56
Storativity (dimensionless)	0.001/0.01*	0.002	0.002	0.002

Output DTN: GS031008312314.004 (from Input DTN: GS030508312314.003 [164425], p. 41, Table 9).

NOTE: *The first number is for fractures; the second is for matrix (values of transmissivity and hydraulic conductivity listed for UE-25 ONC-1 and USW H-4 differ from those obtained from a hydraulic test conducted from May 22 to June 1, 1995, but the values determined from the longer test beginning in May 1996 are considered more reliable).

**The sum of transmissive thicknesses of component geologic units is shown in Table 6.2-7 for the corresponding test.

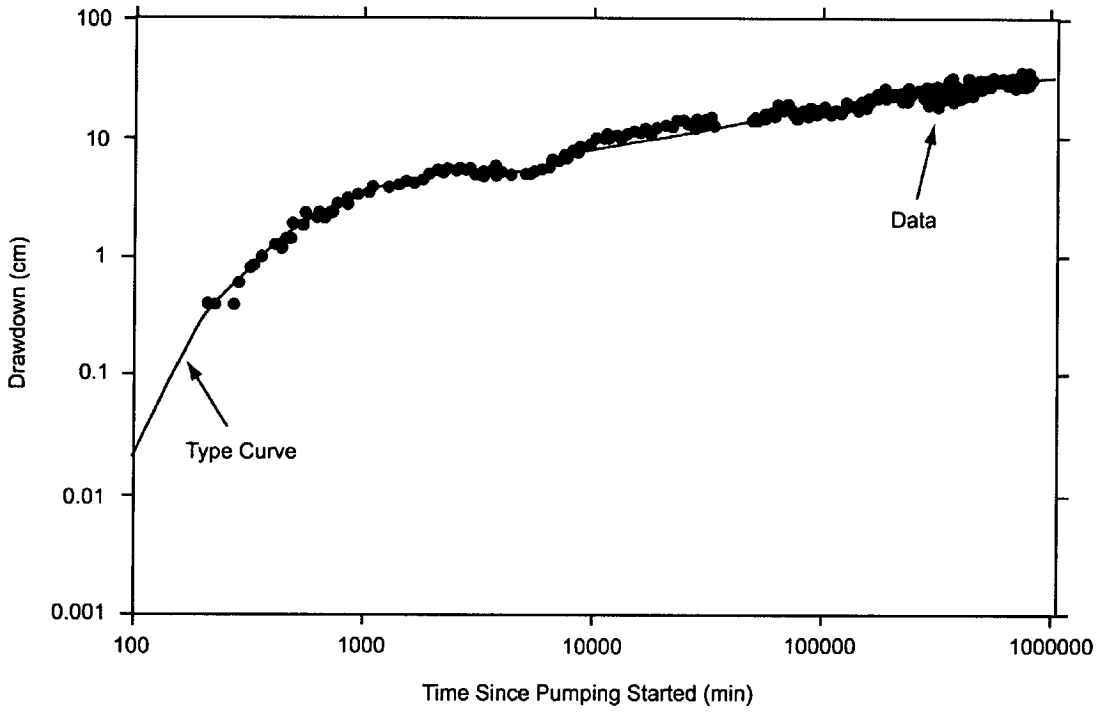

Output DTN: GS031008312314.004 (from Input DTN: GS030508312314.003 [164425], p. 42, Figure 30).

NOTE: For the analysis curve, the parameter $\tau/B = 0.05$.

Figure 6.2-32. Analysis of Drawdown in UE-25 ONC-1, May 8, 1996, to November 12, 1997, by the Method of Streltsova-Adams

Observation wells showed clear responses to the pumping, allowing computation of hydraulic parameters. Despite being 843 m from c#3, ONC-1 responded to pumping after only 200 minutes because it is in the same structural block as the C-wells (between the Bow Ridge and Paintbrush Canyon faults) and is connected by fractures related to northwest-striking faults. That fracture connection is reflected in a characteristic fissure-block aquifer response. From 200 to 2,000 minutes (up to 1.4 days), flow from fractures caused drawdown to increase as a function of log time. From 2,000 to 6,000 minutes (1.4 days to 4 days), drawdown remained relatively constant as flow occurred from the rock matrix into fractures. After 6,000 minutes (4 days), drawdown increased again as a function of log time as flow from both the fractures and matrix occurred. Drawdown conformed to the type curve of Streltsova-Adams (1978 [150754]; see Figure 6.2-32). Transmissivity computed from the type-curve match equals 1,000 m^2/d. If the transmissive thickness between the C-wells complex and ONC-1 is assumed to vary linearly between known thicknesses in c#2 and H-4, then it can be estimated to be about 193 m in ONC-1. Dividing transmissivity by the estimated transmissive thickness indicates a fracture hydraulic conductivity of 5 m/d. In comparison, the hydraulic conductivity of the matrix (Table 6.2-8) is insignificant. Computed storativity for the fractures in ONC-1 is 0.001, which is a tenth of the computed storativity of the matrix.

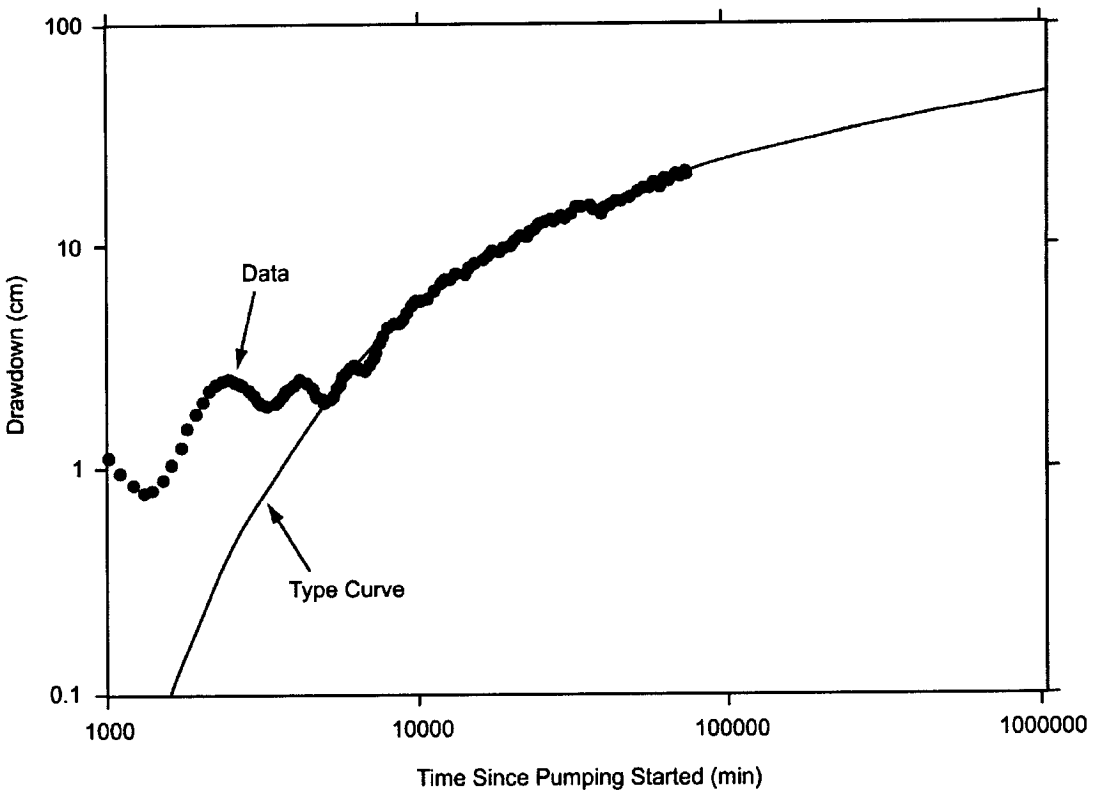

Output DTN: GS031008312314.004 (from Input DTN: GS030508312314.003 [164425], p. 42, Figure 31).

Figure 6.2-33. Analysis of Drawdown in USW H-4, May 8, 1996, to June 27, 1996, by the Method of Theis

Because of its location 2,245 m from c#3, borehole H-4 took 5,000 minutes (3.5 days) to respond to pumping. Even though an extensive effort had been made to remove the effects of Earth tides and barometric changes on water-level fluctuations, the process is approximate and residual effects are still visible in the H-4 water-level record up to 5,000 minutes. After 5,000 minutes, the effect of pumping c#3 at H-4 became discernible above the residual water-level fluctuations, and the drawdown became analyzable (Figure 6.2-33). From 5,000 to 72,000 minutes (3.5 to 50 days) after pumping started, drawdown in H-4 conformed to the type curve of Theis (1935 [150327]) for a confined aquifer (Figure 6.2-33). After 72,000 minutes (50 days), drawdown became relatively constant, probably in response to flux from a nearby fault boundary. The pre-boundary drawdown indicated transmissivity of 700 m^2/d and storativity of 0.002 (Table 6.2-8). Dividing transmissivity by the transmissive thickness obtained from a flow survey (Whitfield et al. 1984 [101366]) indicated an hydraulic conductivity of 2 m/d. The location of the recharge boundary could not be ascertained because only H-4 was affected by that boundary, and the analytical solution to determine the location of a boundary (Lohman 1972, pp. 57 to 61 [150250]) requires that at least two wells be affected by the same boundary.

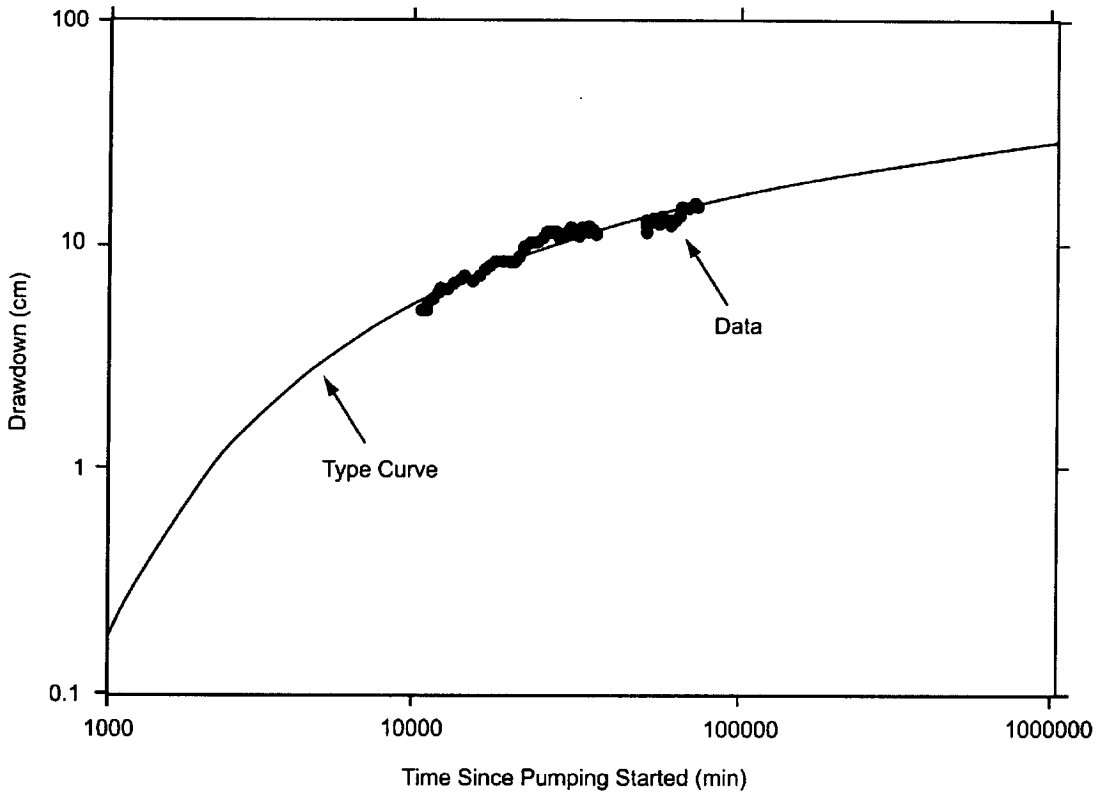

Output DTN: GS031008312314.004 (from Input DTN: GS030508312314.003 ([164425], p. 43, Figure 32).

Figure 6.2-34. Analysis of Drawdown in UE-25 WT#14, May 8, 1996, to June 27, 1996, by the Method of Theis

Located a nearly identical distance (2,249 m) from c#3, borehole WT#14 took slightly longer (5,250 minutes or 3.7 days) to respond to pumping. From 3.7 days to just over 6 days (5,250 to 9,000 minutes), a transition from borehole-storage release to release of water from the aquifer occurred. From 6 to 50 days (9,000 to 72,000 minutes) after pumping started, drawdown in WT#14 conformed to the type curve of Theis (1935 [150327]) for a confined aquifer (Figure 6.2-34). After that time, drawdown became strongly oscillatory, but those broad oscillations in the data deviated about a relatively constant value. Both the period of transition from borehole-storage release (5,250 to 9,000 minutes) and the strongly oscillatory drawdown period (after 72,000 minutes) are not shown in Figure 6.2-34, which is intended to show only the portion of the record that conforms to the confined Theis (1935 [150327]) solution. The late-time data are interpreted to represent less-than-ideal response to a recharge boundary. The pre-boundary drawdown indicates transmissivity of 1,300 m^2/d and storativity of 0.002 (Table 6.2-8). Hydraulic conductivity and the location of the boundary could not be determined because of insufficient data.

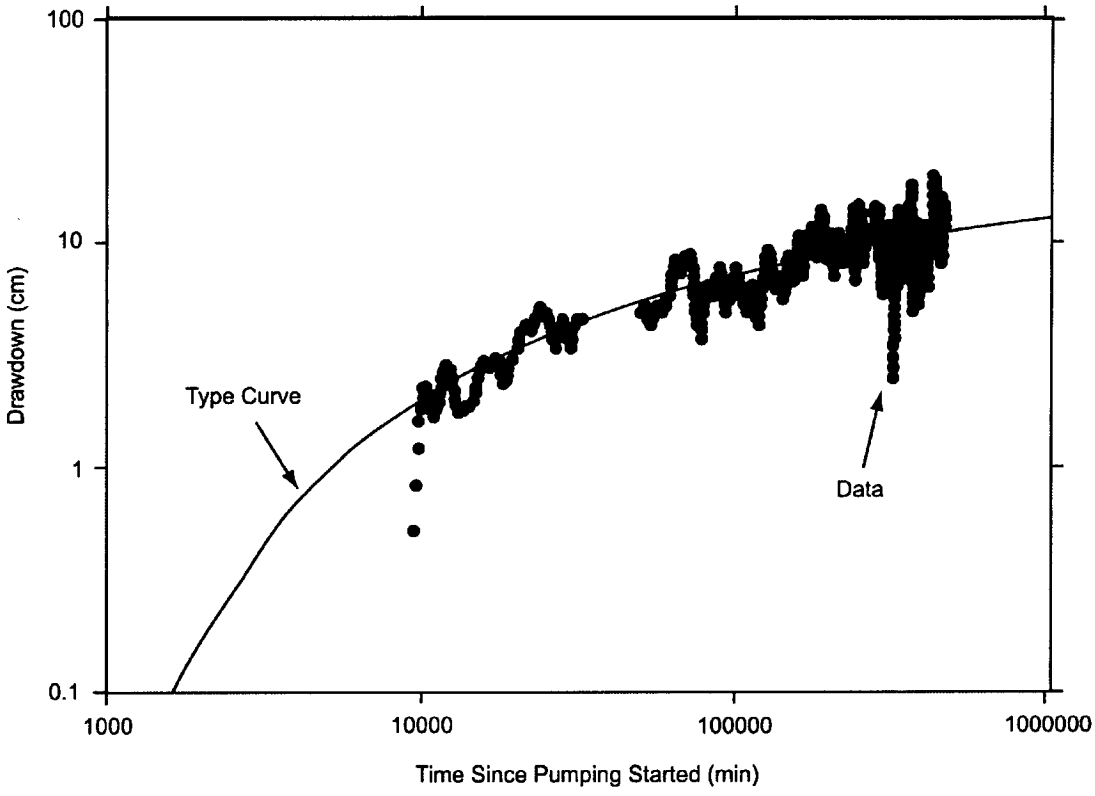

Output DTN: GS031008312314.004 (from Input DTN: GS030508312314.003 [164425], p. 43, Figure 33).

Figure 6.2-35. Analysis of Drawdown in UE-25 WT#3, May 8, 1996, to March 26, 1997, by the Method of Theis

Borehole WT#3 is located 3,526 m from c#3 and took more than 6 days (9,130 minutes) to respond to pumping. Thereafter, drawdown in WT#3 was oscillatory, but the data could be fit to the type curve of Theis (1935 [150327]) for a confined aquifer (Figure 6.2-35). The oscillations, which are substantially larger than those occurring at the other distant observation wells are likely caused by a combination of factors: (1) a possible low-quality transducer signal, (2) excessive distance from the pumping well (at 3,526 km, WT#3 is the farthest of the distant observation wells form the C-hole complex), and (3) residual Earth-tide and barometric-pressure effects remaining, even after substantial, but approximate, efforts to remove them. The solution indicated a transmissivity of 2,600 m^2/d and a storativity of 0.002 (Table 6.2-8). Dividing transmissivity by the length of the open interval in WT#3 (47.5 m) indicated a hydraulic conductivity of 56 m/d. Actual hydraulic conductivity probably is smaller than the calculated value because the thickness of transmissive rock between the C-wells complex and WT#3 probably exceeds the length of the open interval.

The transmissivity of the Miocene tuffaceous rocks appears to decrease northwestward in the area containing the observation wells used in the hydraulic test that began in May 1996. Depending on the analytical solutions used, transmissivity could be interpreted to decrease from 2,600 m^2/d in the vicinity of WT#3 to about 2,000 m^2/d in the vicinity of the C-wells. The

transmissivity of the Miocene tuffs is 1,300 m^2/d in the vicinity of WT#14, 1,000 m^2/d in the vicinity of ONC-1, and 700 m^2/d in the vicinity of H-4.

The distribution of hydraulic conductivity in the tuffs in the vicinity of the C-wells complex appears to be structurally controlled. Hydraulic conductivity in c#2 decreases sharply from a range of 20 to 60 m/d in the Upper Tram and Lower Bullfrog intervals to a range of 0.08 to 0.2 m/d in the Calico Hills interval as the vertical distance from faults that intersect the boreholes increases (Table 6.2-7). Average hydraulic conductivity of the Miocene tuffaceous rocks in c#2 is twice that of c#1 (Table 6.2-8), possibly because c#2 is located nearer to the subsurface intersection of the north-striking Paintbrush Canyon or Midway Valley faults and a northwest-striking fault (shown in Figure 6.2-36) that underlies the gap through the northern part of Bow Ridge. If spatial relations between faults and hydraulic conductivity at the C-wells complex are combined with values of hydraulic conductivity determined from analyses of drawdown in ONC-1, WT#3, and H-4 (Table 6.2-8), then a possible distribution of hydraulic conductivity for the Miocene tuffaceous rocks in the vicinity of the C-wells can be inferred (Figure 6.2-36). Clearly, this distribution is not unique: just one possible scenario that attempts to extrapolate areally the correlation between vertical proximity of geohydrologic units at the C-hole complex to faults and the hydraulic conductivities of these units. When that correlation is applied areally, relative to known geologic structures in the area while honoring the hydraulic conductivities obtained at the C-hole complex itself and the distant observation wells, ONC-1, H-4, WT#14, and WT#3, one obtains Figure 6.2-36.

In the 21-km^2 area encompassed by observation wells used in hydraulic tests at the C-wells complex from 1995 to 1997, the storativity of Miocene tuffaceous rocks in those observation wells uniformly is 0.001 to 0.003 (Table 6.2-8). Analysis of drawdown in observation wells not affected by boundaries as a function of the time divided by the square of the distance from the pumping well (Figure 6.2-37) indicates that the average storativity of the tuffs in the observation area is 0.002. This same analysis indicates that the average transmissivity of the Miocene tuffaceous rocks in the area is 2,200 m^2/d. Derivation of a single analytical solution for c#1, c#2, ONC-1, and WT#3 confirms that the Miocene tuffaceous rocks, at least as far north as lower Midway Valley in the structural block delineated by the Paintbrush Canyon, Bow Ridge, and Dune Wash faults, are a single aquifer in which flow is influenced by the same structural and stratigraphic factors.

Plots of drawdown in observation wells as a function of distance 30,000, 100,000, 200,000, 305,000, and 463,000 minutes (21, 69, 139, 212, and 322 days) after pumping started in May 1996 (drawdown contours at 30,000 and 463,000 minutes shown in Figure 6.2-38) confirm an ovoid pattern of drawdown aligned with faults extending from Bow Ridge to Antler Wash that was detected during the hydraulic test conducted from May 22 to June 1, 1995 (Geldon et al. 1998 [129721], pp. 23 to 25, Figure 2; p. 31). Analyzed by the method of Cooper and Jacob (1946 [150245]), plots of drawdown as a function of distance (Figure 6.2-39) indicate values of transmissivity ranging from 2,100 to 2,600 m^2/d and values of storativity ranging from 0.0005 to 0.002 (Table 6.2-9).

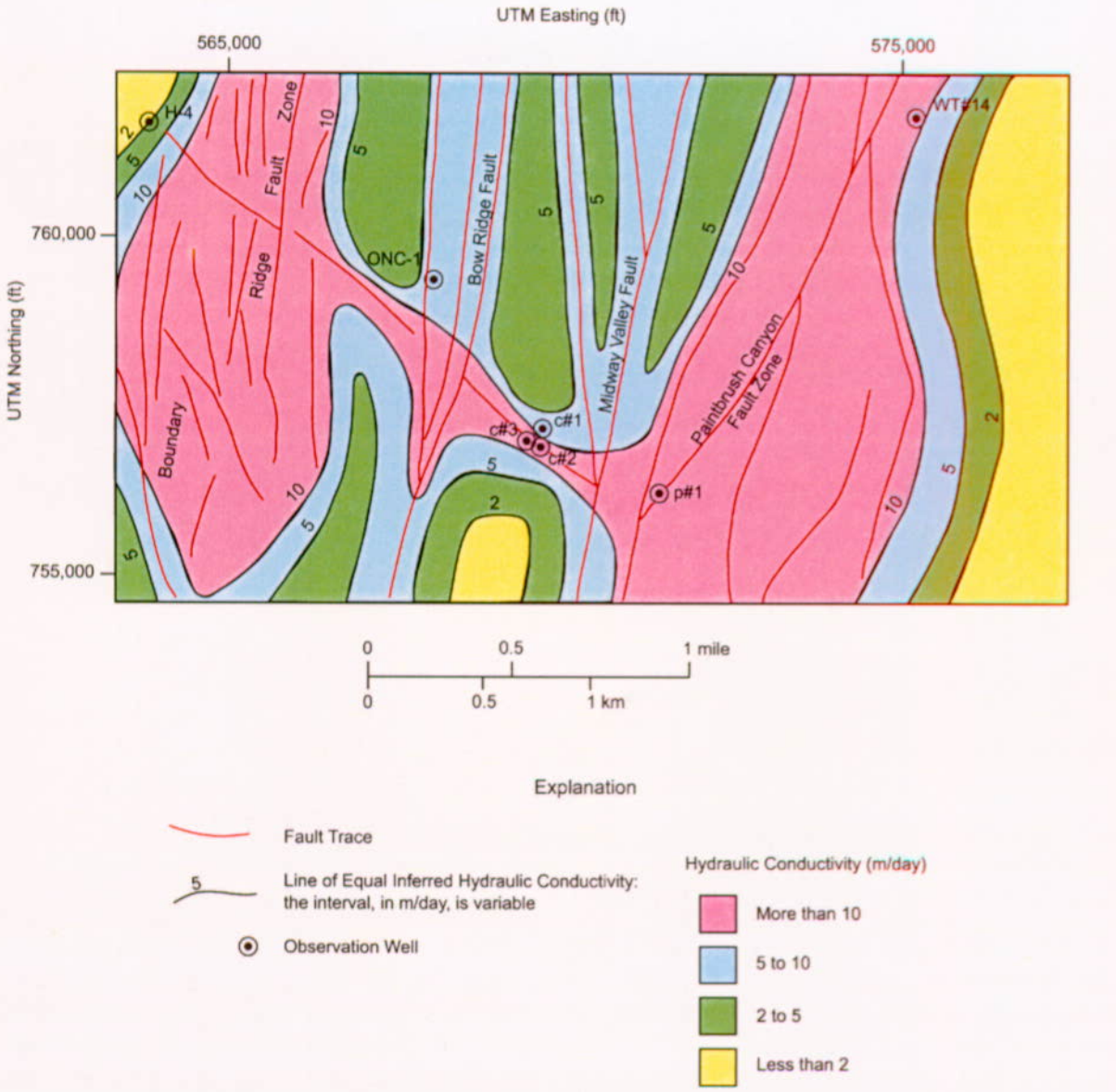

Output DTN: GS031008312314.004 (from Input DTN: GS030508312314.003 ([164425], p. 45, Figure 34).

Figure 6.2-36. Inferred Distribution of Hydraulic Conductivity of Miocene Tuffaceous Rocks in the Vicinity of the C-wells

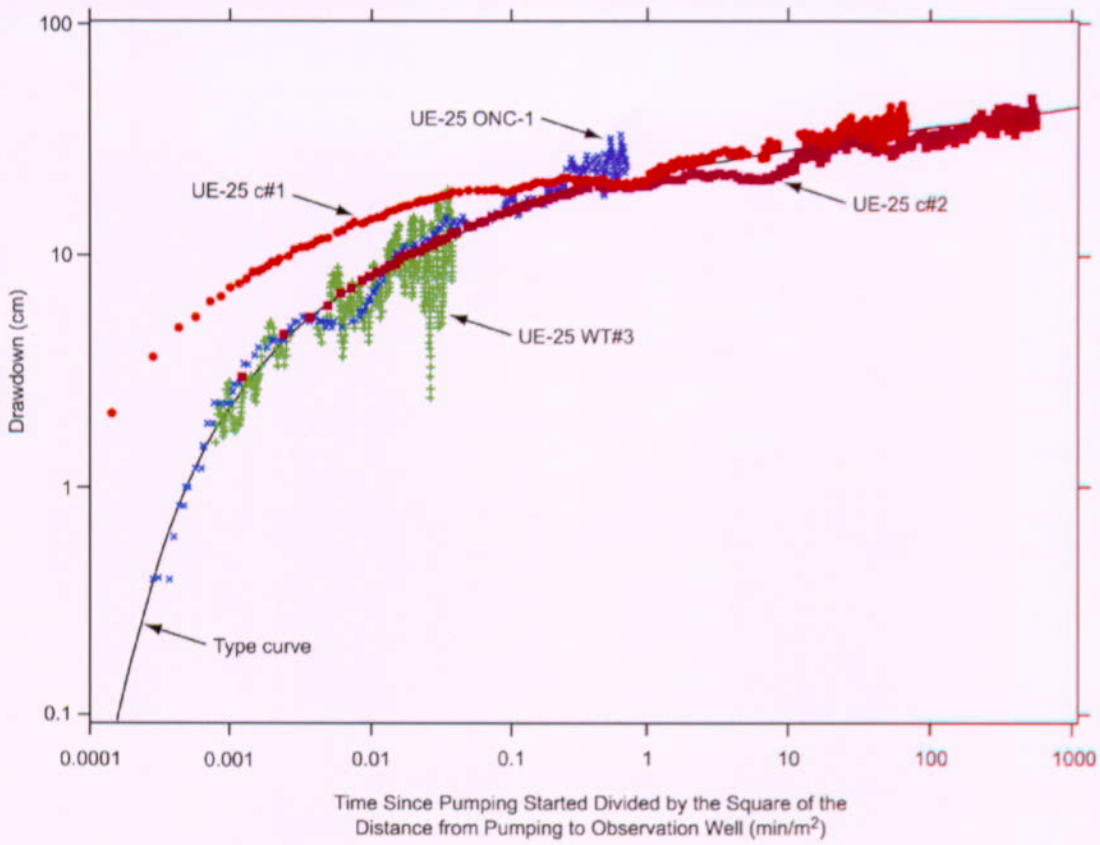

Output DTN: GS031008312314.004 (from Input DTN: GS030508312314.003 [164425], p. 46, Figure 35).

Figure 6.2-37. Analysis of Drawdown in Observation Wells as a Function of Time Divided by the Square of the Distance from the Pumping Well, UE-25 c#3

Because the higher transmissivity and lower storativity values resulting from the 30,000- and 100,000-minute analyses in Table 6.2-9 give way to more stable and consistent lower transmissivity and higher storativity values from later-time analyses, the later values appear to be more reliable. In comparison, the same type of analysis of drawdown in observation wells as a function of distance 10 days (14,000 minutes) after pumping started in May 1995 had indicated a transmissivity of 2,300 m^2/d and storativity of 0.003 (Geldon et al. 1998 [129721], p. 29). Distance-drawdown and time-drawdown analyses discussed in this section converge on similar solutions.

The ovoid pattern of drawdown aligned with faults extending from Bow Ridge to Antler Wash that was detected during the hydraulic test conducted from May 22 to June 1, 1995 (Geldon et al. 1998 [129721], pp. 23 to 25, Figure 2; p. 31) and confirmed in this study (Figure 6.2-38) indicates large-scale anisotropy caused by heterogeneity and structure. Large-scale transmissivity is higher in the direction of the long axis of the ovoid and lower in the direction perpendicular to it.

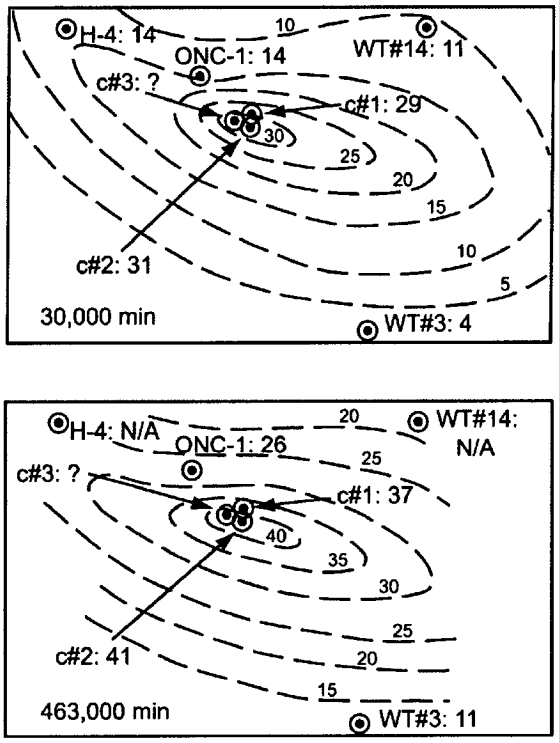

Output DTN: GS031008312314.004 (from Input DTN: GS030508312314.003 [164425], p. 46, Figure 35).

NOTE: The upper panel shows the drawdown distribution 30,000 minutes (20.8 days) after pumping started; the lower panel shows the distribution 463,000 minutes (321.5 days) after pumping started.

The reason for the question mark in the figure is that the drawdown in the aquifer at the location of the pumped well, c#3, is unknown; only the apparent drawdown in the well, which contains a lot of friction head, is known.

Figure 6.2-38. Distribution of Drawdown in Observation Wells at Two Times After Pumping Started in UE-25 c#3 on May 8, 1996

Table 6.2-9. Hydraulic Properties Determined from Drawdown in Observation Wells as a Function of Distance From the Pumping Well UE-25 c#3, May 1996 to November 1997

Time Since Pumping Started (min)	Transmissivity (m^2/day)	Storativity
30,000	2,600	0.0005
100,000	2,500	0.0009
200,000	2,100	0.002
305,000	2,300	0.001
402,000	2,200	0.001
463,000	2,200	0.001

Output DTN: GS031008312314.004 (from DTN: GS030508312314.003 [164425], p. 50, Figure 10).

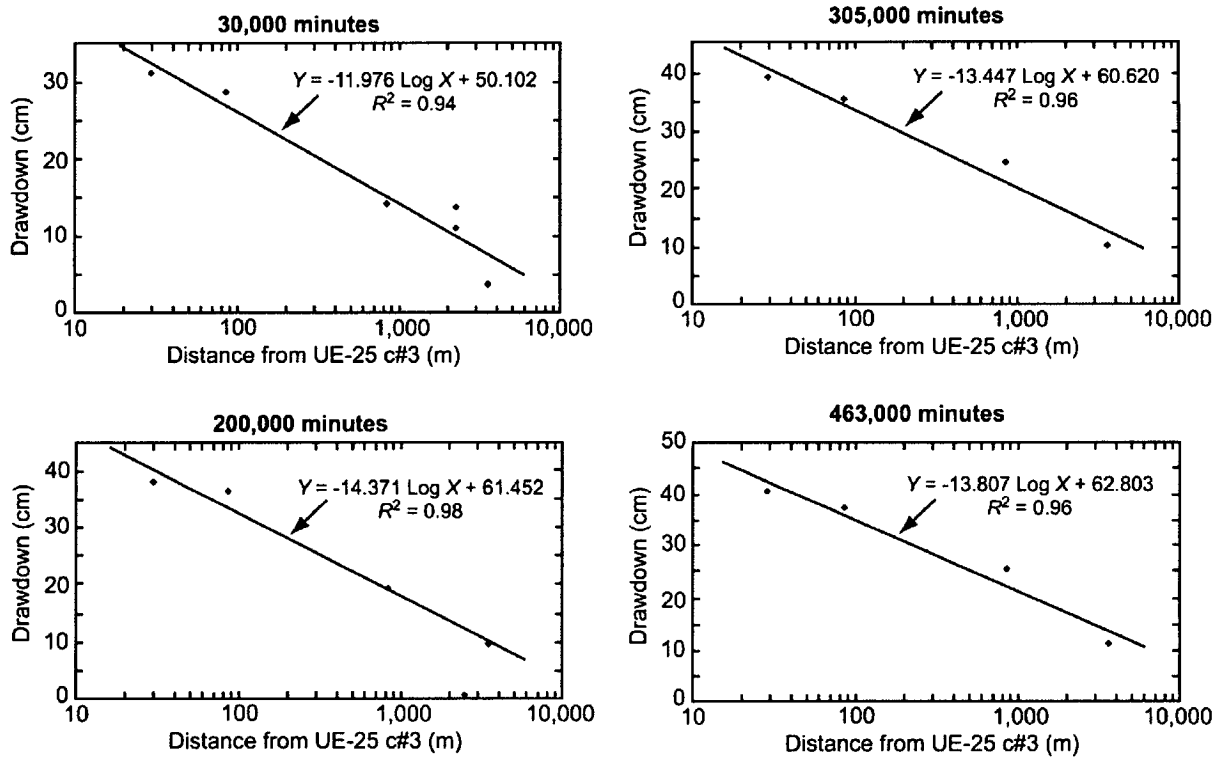

Output DTN: GS031008312314.004 (from Input DTN: GS030508312314.003 [164425], pp. 48 and 49, Figure 37).

NOTE: The panels show the drawdown analyses at 30,000 (upper left), 200,000 (lower left), 305,000 (upper right), and 463,000 (lower right) minutes after pumping started.

Figure 6.2-39. Analyses of Drawdown in Observation Wells as a Function of Distance from the Pumping Well at Various Times After Pumping Started in UE-25 c#3

6.2.4.7 Paleozoic Carbonate Rocks

Borehole p#1 was monitored during hydraulic tests in 1995 and 1996 to detect hydraulic connection between the Miocene tuffaceous rocks and Paleozoic carbonate rocks in the vicinity of the C-wells. Hydraulic connection previously had been indicated by hydraulic head measurements in p#1 and by borehole flow surveys in the C-wells. Measurements made as p#1 was being drilled in 1983 detected a 22-m difference in hydraulic heads for the Paleozoic carbonate rocks and Miocene tuffaceous rocks in p#1 (Craig and Robison 1984 [101040]), which indicated a potential for water to flow from the lower to the upper of those hydrogeologic units. Flow surveys conducted in the C-wells in 1991 detected upward flow in the lower parts of those boreholes (Geldon 1996 [100396], pp. 12 to 69) that most likely originated in the Paleozoic carbonate rocks, because the intervening tuffaceous rocks generally behave as a confining unit (Luckey et al. 1996 [100465], p. 18, Figure 7).

Although p#1 was monitored for 10 days (14,400 minutes) after pumping started in May 1995 (Geldon et al. 1998 [129721]) and for about 180 days (256,200 minutes) after pumping started in May 1996, drawdown in the Paleozoic carbonate rocks was not detected (Figure 6.2-40). This lack of drawdown could indicate that the water being pumped was drawn laterally from the Miocene tuffaceous rocks. Alternatively, the water could have been drawn upward from Paleozoic carbonate rocks without causing drawdown in the underlying aquifer if the Paleozoic rocks have a large storage capacity. Hydraulic connection between the Miocene tuffaceous rocks and Paleozoic carbonate rocks could not be confirmed or refuted by monitoring water levels in p#1 during the study reported here.

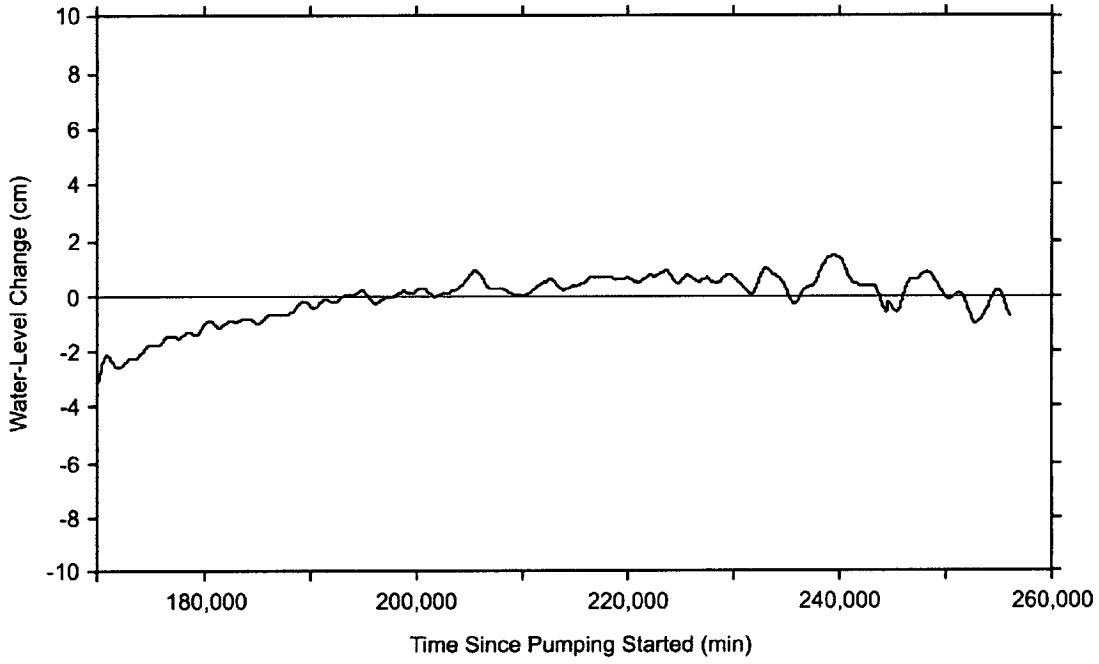

Output DTN: GS031008312314.004 (from Input DTN: GS030508312314.003 ([164425], p. 50, Figure 38).

NOTE: Water-level change is relative to the water level in p#1 prior to start of pumping in c#3 on May 8, 1996.

Figure 6.2-40. Water-level Changes in UE-25 p#1, September 3 to November 2, 1996

6.2.5 Limitations and Uncertainties

All analytical methods used in this study to determine hydraulic properties from drawdown or recovery responses assume that the aquifer is an equivalent porous medium. Although the flow system consists of a fracture network rather than a porous medium, the pressure responses conform quite well to type curves derived for either porous media or uniformly fractured media (Strelsova-Adams 1978 [150754]). Thus, the fracture network at the C-wells is apparently interconnected in such a way that the fractured tuffs respond to pumping as "an equivalent porous medium." Another fundamental assumption is that flow to the pumping well is derived from an aquifer of infinite extent. The many faults near the C-wells complex that potentially

function as either recharge or barrier boundaries make the concept of an infinite aquifer difficult to support. However, only observation wells that lay between faults bounding the structural block in which the C-wells are located were considered in the analyses, so boundary effects, while not completely eliminated, should have been minimized. Drawdown in H-4 and WT#14 obviously was affected by recharge boundaries.

All the analytical methods used in this study assume a constant thickness for the interval for which drawdown is being analyzed, whereas, in reality, the intervals have variable thicknesses. This is a necessary simplification, and extreme care was taken to define transmissive intervals in each well and a meaningful resulting assumed-interval thickness between the pumped and observation well.

In addition, all the analytical methods used in this study, except for the Neuman (1975 [150321]) method, assume radial flow to the pumping well, and, therefore, ignore vertical flow (application of the Neuman fully-penetrating-well solution, as was done in this report, to cases where pumping was in one interval and the analyzed drawdown response was in another, also ignores vertical flow). The flow from intervals other than the one being pumped that was detected during hydraulic tests in February 1996 and May 1996 to November 1997 indicates that flow during those tests actually was three-dimensional or spherical. Ignoring the vertical component of flow seems to have been justified by the generally good agreement between results of the hydraulic test in June 1995 (in which flow between observation and pumping wells was radial) and results for most intervals monitored in subsequent tests. Nevertheless, there is some inaccuracy involved in analyzing the flow from intervals that did not have open sliding sleeves above or below the pumped interval by techniques developed only for analyzing flow from the pumped interval.

The most commonly applied analytical method in this study, that of Theis (1935 [150327]), assumes flow from an infinite, homogeneous, isotropic, confined aquifer. Transected by numerous faults and variably welded, the Miocene tuffs in the vicinity of the C-wells complex are neither homogeneous nor isotropic. As a result, hydraulic gradients toward the pumping well vary directionally, a situation ignored by the mathematics of the Theis (1935 [150327]) solution. Disregarding a nonuniform hydraulic gradient seemingly would result in inaccurate computations of hydraulic properties. Consistent calculations, however, of hydraulic properties for individual intervals and the composite section of Miocene tuffaceous rocks (from test to test, from well to well, or from use of multiple observation wells in time-drawdown or distance-drawdown analyses) indicate that errors are at least being made consistently. That consistency provides confidence that calculated values approximate actual values of hydraulic properties, despite simplification of structural and lithologic complexities.

All the analytical techniques used in this study required input parameters that had to be determined or approximated for hydrogeologic intervals or boreholes in which drawdown was monitored. Included in those parameters are the distance of the interval or borehole from the pumping well, the transmissive thickness of the interval or borehole, the barometric efficiency of the interval or borehole, the proportion of flow from a given hydrogeologic interval, and the fracture spacing within a hydrogeologic interval. Errors in deriving any of those input parameters could have changed calculated hydraulic properties considerably.

Values of transmissivity and storativity determined in this study are estimated to be accurate to one significant figure, but reported values of hydraulic conductivity are more uncertain. Hydraulic conductivity can be calculated by dividing the transmissivity by either the known thickness of transmissive intervals within a test interval, the entire thickness of the test interval, or an assumed thickness of transmissive rock between the observation and pumping wells. Because the transmissive thickness was unknown, it was impossible to determine hydraulic conductivity in many analyses. Even where hydraulic conductivity could be determined, it was done with limited confidence. For example, it is impossible to know whether the hydraulic conductivity of the Lower Bullfrog interval in c#1 really is about half that in c#2 or whether these calculated hydraulic conductivity values result from dividing approximately the same transmissivity in each borehole by an assumed transmissive thickness that is twice as large in c#1 as in c#2.

6.2.6 Saturated Zone Anisotropy near the C-wells Complex

6.2.6.1 Introduction

Understanding SZ flow and transport near the high-level nuclear waste repository at Yucca Mountain is critical to a successful License Application. Because radionuclides released from the repository at Yucca Mountain must travel through the saturated fractured tuff and the saturated alluvium before reaching the compliance boundary, it is important to characterize the hydrogeologic properties of the down-gradient media. Since the completion of the site-characterization wells in 1983, several single- and cross-hole tracer and pumping tests have been conducted to gain a better understanding of the hydrogeology of the region. A number of published studies have assigned transmissivities, storativities, and anisotropy ratios to the saturated zone in this area (Farrell et al. 1999 [157319]; Ferrill et al. 1999 [118941]; Winterle and La Femina 1999 [129796]). In this scientific analysis report, reviews of the above mentioned studies are used in conjunction with independent re-analyses of the data to suggest a distribution of anisotropy ratios that are to be used in the finite-element, heat and mass transfer (FEHM) stochastic flow model of the saturated zone (Zyvoloski et al. 1997 [110491]).

6.2.6.1.1 Background

A geologic description of the C-wells complex and the surrounding area can be found in several publications (including Geldon et al. 1998 [129721], Table 1, Figure 3, Figure 5; Farrell et al. 1999 [157319]; Ferrill et al. 1999 [118941]; Winterle and La Femina 1999 [129796]). Nevertheless, one geologic characteristic bears mentioning. Based on in-situ stress-field analyses, the maximum horizontal geologic stress runs north-northeast (azimuth between 25° and 30° east of north). Therefore, any fractures oriented in this direction tend to dilate and present potential preferential flow pathways (Farrell et al. 1999 [157319], p. 4-1; Ferrill et al. 1999 [118941], p. 1). This finding supports some of the calculated principal directions of anisotropy discussed below, but not all.

Although many hydraulic tests have been conducted at the C-wells complex, only the long-term pumping test from May 8, 1996, through November 12, 1997, yielded data suitable for estimating the hydraulic properties of the medium on a broad scale beyond the immediate vicinity of the C-wells. These data may help to estimate an overall anisotropy ratio for the area.

Specifically, changes in local groundwater elevations due to pumping at the C-wells complex were monitored at several distant wells, the locations of which are shown in Figure 6.1-4 (only H-4, ONC-1, WT#3, and WT#14 exhibited sufficient drawdown for an anisotropy analysis). Well c#3 has traditionally served as the pumping well because of its record of consistent production rates.

Although several cross-hole hydraulic tests have been conducted by USGS investigators, only the long-term pumping test yielded data suitable for calculating a nonlocal anisotropy ratio. For this test, well c#3 was packed around the Lower Bullfrog interval, and water levels were monitored at H-4, ONC-1, WT#3, and WT#14. Data collected during this test were used to calculate transmissivity and storativity at each well—parameters that are necessary to estimate analytically an anisotropy ratio for the area. Although water levels were monitored at other wells, none yielded data suitable for an analytic treatment of anisotropy.

6.2.6.1.2 Technical Approaches

Water-level data for wells H-4, WT#3, and WT#14 were obtained from the DTN: GS970308312314.002 [161273]. Data from well ONC-1 were collected by Nye County under the Nye County Nuclear Waste Repository Project Office (NWRPO) QA program (QAP) (NWRPO 2003 [165947], Program Management, Quality Assurance Program). Nye County requires that the NWRPO establish and maintain a documented QAP that meets the requirements of ANSI/ASME NQA-1 and the criteria of 10 CFR 50 (2002 [165855], Appendix B). These data are available under DTN: MO0212SPANYESJ.149 [161274].

Winterle and La Femina (1999 [129796]) reduced and filtered the drawdown data for the above wells to obtain estimates of hydraulic parameters over the affected area. In the analyses presented here, the filtering of data from wells H-4, WT#3, WT#14, and ONC-1 was accomplished with Filter.vi (STN: 10970-1-00 [162668]). These filtered drawdown data are identified by Output DTNs: GS030208312314.001 and GS030208312314.002.

The first analytical anisotropy analysis in this report was calculated in Microsoft Excel™ using the standard formulation offered by Hantush (1966 [161160]); the second uses a modification of the method of Papadopulos (1967 [150265]) combined with the PEST parameter-estimation program, Version 5.5 (STN: 10289-5.5-00 [161564]). Winterle and La Femina (1999 [129796]) used AQTESOLV, Version 2.12, marketed by HydroSOLVE Inc., to analyze pump tests. Based on Geldon et al. (2002 [161163]), the authors of this report used analytical solutions of Theis (1935 [150327]) or Streltsova-Adams (1978 [150754]) for analyses of the responses at the four observation wells to pumping at c#3. These analyses were performed using Theis.vi (STN: 10974-1-00 [162758]) and Streltsova-Adams.vi (STN: 10971-1-00 [162756]), respectively.

6.2.6.2 Estimating Anisotropy

Interpretation of well test data with analytical solutions consists of inferring the hydraulic properties of the system from its measured responses based on, among other things, an assumed flow geometry (i.e., radial). The problem becomes more complicated, however, when the system geometry cannot be specified with reasonable certainty. In a layered sedimentary system lacking extreme heterogeneity, flow might reasonably be expected to be radial during an hydraulic test.

When hydraulic tests are conducted at some arbitrary point within a three-dimensional (3-D) fractured rock mass, however, the flow geometry is convoluted. Radial flow would occur only if the test were performed in a single uniform fracture of effectively infinite extent or within a network of fractures confined to a planar body in which the fractures were so densely interconnected that the network behaves like an equivalent porous medium. More likely, flow would be nonradial and variable, as fracture terminations and additional fracture intersections were reached. The nonradial nature of the cone of depression near Yucca Mountain is illustrated in Figure 6.2-38. Despite all of this, analytic solutions provide important requisite first-order answers that are commensurate with the spatial distribution of the available hydrogeologic and geophysical data, and that can only be improved by numerical modeling if that data distribution is enhanced by substantial new data-gathering efforts.

Through the fractured tuff near Yucca Mountain, there are significant heterogeneity and hydraulic properties that not only vary spatially but also differ depending upon the direction in which they are measured (both horizontally and vertically). In this analysis, transmissivity and storativity are the key parameters defining large-scale anisotropy, and their measured values reflect the heterogeneity of the media. The concept of anisotropy is typically associated with a homogeneous medium—a criterion not met here. Nevertheless, there are clearly spatial and directional variations in transmissivity, and the notion remains that, over a large enough representative elementary volume, there exists a preferential flow direction that can be termed "anisotropy."

Data from the long-term pumping test conducted from May 8, 1996, to November 12, 1997, can be used to evaluate the anisotropy of the C-wells complex and vicinity because transmissivity and storativity can be calculated at four distant wells (H-4, ONC-1, WT#3, and WT#14). The hydraulic properties measured at these wells are used to develop an estimate for the anisotropy ratio. Data from the other C-wells (c#1 and c#2) were not used in the anisotropy analysis because, according to Farrell et al. (1999 [157319], pp. 4 to 12):

- Over the small scale of observation at the C-wells, pump-test results are likely dominated by discrete fractures (i.e., inhomogeneities).
- Three-dimensional flow effects are likely.
- Recirculation from simultaneous tracer tests obscured results.

Furthermore, because anisotropy is conceptually difficult to define for heterogeneous media, it is more easily described as an average preferential flow over as large a representative elementary volume as possible. Thus, it makes little sense to attempt to define anisotropy over an heterogeneous area as small as that of the C-wells.

6.2.6.2.1 Data Filtering and Reduction

Because drawdown was measured at great distances from the pumping well (up to 3,526 m between WT#3 and c#3), natural variations in groundwater levels obscured responses due to pumping and had to be filtered out before the drawdown data could be analyzed. Drawdowns were corrected for Earth-tide effects (head fluctuations of up to 0.12 m) and atmospheric pressure change (head fluctuation of up to 0.25 m). First, the water levels were processed with a low-pass filter (Filter.vi V 1.0, STN: 10970-1-00 [162668]) to remove oscillations with a frequency greater than 0.8 cycles per day to eliminate Earth-tide effects and semi-diurnal barometric-pressure effects, leaving only the effects of long-term weather-related barometric-pressure changes. The barometric record from the C-wells complex, which was assumed to apply to all the wells, was also filtered to remove frequencies greater than 0.8 cycles per day to eliminate semi-diurnal barometric-pressure fluctuations, leaving only long-term weather-related barometric pressure changes. Using barometric efficiency values of the wells, the effects of long-term, weather-related, barometric-pressure changes were removed from the filtered water levels, leaving only the effect of c#3 pumping. The filtered and barometrically-corrected water-level data for the four observation wells can be found in Output DTNs: GS030208312314.001 and GS030208312314.002. The water-level data for H-4, WT#3, and WT#14 were obtained from DTN: GS970308312314.002 [161273], and the water levels for ONC-1 were obtained from DTN: MO0212SPANYESJ.149 [161274]. The barometric record used for the above processing was from the C-wells complex (DTN: GS981008312314.003) [144464].

Winterle and La Femina (1999 [129796], pp. 3-4 to 3-6) also applied a second stage of filtering to the long-term pumping test to remove barometric effects that reached the aquifer through the unsaturated zone by accounting for the time lag and attenuation that occurs in the unsaturated zone. Second-stage barometric pressure effects were filtered using a 2.6-day running average, multiplied by an attenuation factor of 0.6, and lagged by a period of 0.42 days.

The derivative of the filtered drawdowns with respect to the log of time was calculated for H-4, WT#3, WT#14, and ONC-1 to establish the optimum range of data to fit with the straight-line method of Cooper and Jacob (1946 [150245]). The flattest (zero-slope) portion of the resulting curve is deemed the best location for a linear fit to the drawdown data.

6.2.6.2.2 Transmissivity and Storativity Calculations

In the first analysis of this section, the Cooper-Jacob (1946 [150245]) method applied to filtered and derivative-analyzed data is used to calculate transmissivities and storativities. The key to a reasonable estimate of anisotropy is an accurate assessment of transmissivity and storativity at each monitoring well. Figure 6.2-41 is a plot of the filtered drawdowns fit with the Cooper-Jacob straight-line method to the appropriate portion of the derivative curve. Note the inconsistent slope of the fit to drawdown in well H-4 resulting in a significantly lower transmissivity at this well. Transmissivity and storativity values are presented in Table 6.2-10.

In the second analysis methodology of this report, which uses the modified Papadopulos-PEST method, the response of each of observation wells H-4, WT#14, and WT#3 is analyzed using the homogeneous, isotropic method of Theis (1935 [150327]) (Theis.vi V 1.0, STN: 10974-1-00 [162758]) for confined aquifers, and the response of observation well ONC-1 is analyzed using

the homogeneous, isotropic method of Streltsova-Adams (1978 [150754]) (Streltsova-Adams.vi, V 1.0, STN 10971-1.0-00 [162756]) for fissure-block aquifers—both type-curve-fitting techniques—to obtain transmissivity and storativity values. Three analyses were made: one with transmissivities constrained to 1,000 m^2/day, the other with the transmissivities and storativities as given in Geldon et al. (2002 [161163], p. 50; DTN: GS030508312314.003 [164425]), and the third with transmissivities and storativities obtained from analyzing the filtered and barometrically-corrected water levels processed for this report and described in the first paragraph of Section 6.2.6.2.1. The three sets of values are used to produce three sets of anisotropy magnitudes and directions as discussed below.

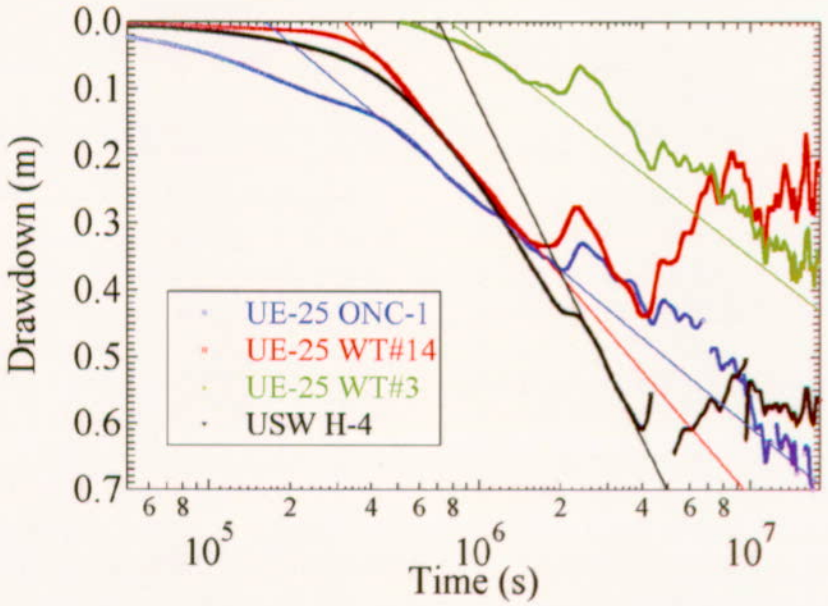

DTN: GS970308312314.002 [161273], DTN: MO0212SPANYESJ.149 [161274]. Output DTN: GS031008312314.004.

NOTE: The straight lines were fit to relatively small portions of each drawdown curve that were selected because they had the most constant derivatives (i.e., the least noisy portions of the curves). Fitting a straight line to larger portions of the curves could result in slopes and, hence, estimated transmissivities, that differ by nearly a factor of two.

Figure 6.2-41. Straight Line Fits to the Filtered and Derivative-Analyzed Data at the Four Monitoring Wells

Table 6.2-10. Transmissivities and Storativities Calculated by the Cooper-Jacob Method Using the Filtered and Derivative-Analyzed Data

Well	Cooper-Jacob* Analysis	
	T (m^2/day)	S (–)
UE-25 ONC-1	446	0.003
UE-25 WT#3	477	0.0005
UE-25 WT#14	318	0.0008
USW H-4	182	0.0007

DTN: GS970308312314.002 [161273], DTN: MO0212SPANYESJ.149 [161274]. Output DTN: GS031008312314.004.

NOTE: *The Cooper-Jacob (1946 [150245]) method was used in the analysis.

6.2.6.2.3 Previously Reported Results

Winterle and La Femina (1999 [129796], Section 4.5) processed the long-term pumping data with AQTESOLV, and their transmissivity and storativity results (obtained with the Theis 1935 [150327] method) are shown in Table 6.2-11. Considering the differences in the Cooper-Jacob (1946 [150245]) and Theis (1935 [150327]) analysis methods, as well as differences in data reduction methods, the Winterle and La Femina (1999 [129796], p. 4-25) transmissivities agree reasonably well with the results from the analyses shown in Table 6.2-10. The drawdown data from the long-term pumping test in Section 6.2.4.6 and from Winterle and La Femina (1999 [129796], p. 4-25) were also analyzed using the Theis method, and these results are reproduced in Table 6.2-11. With the exception of WT#3, the transmissivities are in good agreement with those of Winterle and La Femina (1999 [129796], p. 4-25). The difference of more than a factor of 2 in the transmissivity of WT#3 can probably be attributed to differences in data reduction methods, which lead to greater differences in parameter estimates when the overall drawdown is relatively small (as it is for WT#3).

Table 6.2-11. Transmissivities and Storativities of Distant Wells for the Long-Term Pumping Test

	Winterle and La Femina (1999)*		Based on Section 6.2.4.6	
Well	T (m^2/day)	S (–)	T (m^2/day)	S (–)
UE-25 ONC1	1,340	0.008	1,000	0.001
UE-25 WT#3	1,230	0.005	2,600	0.002
UE-25 WT#14	1,330	0.002	1,300	0.002
USW H-4	670	0.002	700	0.002

Source: *Winterle and La Femina (1999 [129796], p. 4-25).

6.2.6.2.4 ONC-1 Data

A discussion is in order regarding the quality of the Nye County water-level data collected at ONC-1. The data were collected under the NWRPO QAP. Nye County policy requires that NWRPO establish and maintain a documented QAP that meets the requirements of ANSI/ASME NQA-1 and the criteria in 10 CFR 50 (2002 [165855]). As shown in Figure 6.2-41, the filtered water levels at ONC-1 are visually consistent with the filtered QA water-level data collected at WT#3, WT#14, and H-4. In addition, the slopes of the Cooper-Jacob (1946 [150245]) fit to drawdown are comparable for ONC-1, WT#3, and WT#14. Although H-4 shows a steeper slope, this corresponds to the hypothesis that the well was drilled in a less transmissive formation. The average slope of the Cooper-Jacob lines in Figure 6.2-41 is 0.49 with a standard deviation of 0.2. At ONC-1, the slope is 0.34, which is less than one standard deviation from the mean slope of all four wells. It should also be noted that in the published literature (Farrell et al. 1999 [157319], p. 4-11; Ferrill et al. 1999 [118941], p. 6; Winterle and La Femina 1999 [129796], p. 4-25; and Geldon et al. 2002 [161163], p. 23), the transmissivity and storativity calculated near well ONC-1 using Nye County data are consistent with the transmissivities and storativities calculated at the nearby wells (WT#3, WT#14, and H-4) using YMP QA water-level data.

6.2.6.2.5 Anisotropy Ratios

Anisotropy ratio analyses performed for this report employ the analytical solution of Hantush (1966 [161160]) or a modification of the analytic solution of Papadopulos (1967 [150265]) combined with PEST (STN: 10289-5.5-00 [161564]). The analyses of Winterle and La Femina (1999 [129796], p. 4-24) and Ferrill et al. (1999 [118941], p. 6) used the Papadopulos (1967 [150265]) method. Although all techniques assume homogeneous confined aquifers with radial flow to the pumping well, some deviations from these assumptions may still yield reasonable estimates of anisotropy. In particular, these methods require as input: transmissivity, storativity, and the locations of a minimum of three monitoring wells. With this information, anisotropy ratios and principal directions may be calculated. Results from all analyses are presented in Table 6.2-12.

Using transmissivities and storativities from Table 6.2-10 with the Hantush (1966 [161160]) method yields an anisotropy ratio of 3.3 at principal direction 15° east of north. The data from H-4 were excluded from this analysis (as they were in the Winterle and La Femina (1999 [129796]) and Ferrill et al. (1999 [118941]) analyses) because including the data resulted in an undefined (negative) anisotropy ratio.

In the modified Papadopulos-PEST method, three approaches were considered. In the first approach and in order to satisfy the homogeneous, anisotropic assumption of Papadopulos (1967 [150265]), which requires that all the observation-well responses produce the same transmissivity (to honor the homogeneity assumption), Theis (1935 [150327]) (Theis.vi V 1.0, STN: 10974-1-00 [162758]) type-curve fits for H-4, WT#3, WT#14, and a Streltsova-Adams (1978 [150754]) (Streltsova-Adams.vi V 1.0, STN 10971-1.0-00 [162756]) type-curve fit for ONC-1 were constrained to produce the intermediate transmissivity value of 1,000 m^2/d (the nonconstrained values published in Geldon et al. (2002 [161163], Table 9; DTN: GS030508312314.003 [164425]) ranged from 700 m^2/d for H-4 to 2,600 m^2/d for WT#3). These constrained fits produce storativities of 0.0023, 0.0052, 0.0026, and 0.0013 for wells H-4, WT#3,

WT#14, and ONC-1, respectively. From these constrained fits, ratios of the directional transmissivity over storativity, T_d/S, were obtained after Papadopulos (1967 [150265]). The square roots of these ratios were plotted on a polar plot with the pumping well, c#3, at the center.

It is important to note that while the Theis (1935 [150327]) well function was used to develop the anisotropy ratios in this report, there is no reason why the well function cannot be replaced by another appropriate function. For example, if the medium responds as a fissure-block system, the fissure-block well function of Streltsova-Adams (1978 [150754]) may be used. Because anisotropy analyses assume that drawdown, is proportional to the well function, $W(u)$, through the relation $s = (Q/4\pi T)W(u)$, where Q is the pumping rate, substitution of other well functions should not affect the anisotropy-calculation methodology.

The modified Papadopulos-PEST method then fits an ellipse, centered at the pumping well, through the $(T_d/S)^{1/2}$ data. This fitting was done with PEST V 5.5 (STN: 10289-5.5-00 [161564]), in conjunction with a Microsoft Excel spreadsheet, which calculates the shortest distance from each of the $(T_d/S)^{1/2}$ data points to the constructed ellipse. PEST is instructed to vary the long and short axes of the ellipse and the principal direction to minimize the distances of all four $(T_d/S)^{1/2}$ data points from the ellipse. The ellipse in Figure 6.2-42 is the optimal PEST ellipse. For this fit, PEST indicates that the direction of anisotropy is 79° west of north (with a 95% confidence interval of 75° to 82°) and that the magnitude of anisotropy is 3.5:1 (with a 95% confidence interval of 2.7:1 to 4.3:1). This direction of anisotropy is consistent with the geologic evidence of the Antler Wash series of fractures and faults running northwest from the C-wells to H-4. Two types of anisotropy are present within the study area: one is the NE-SW uniformly-distributed anisotropy caused by regional stresses, and another is a NW-SE anisotropy related to the Antler Wash fault zone. The well H-4 is located along Antler Wash, northwest from the C-wells. When the well H-4 is included in the analysis, the results are greatly affected by Antler Wash and represent the NW-SE anisotropy related to this system. When the well H-4 is not included in the analysis, the results represent the NE-SW uniformly-distributed anisotropy caused by regional stresses.

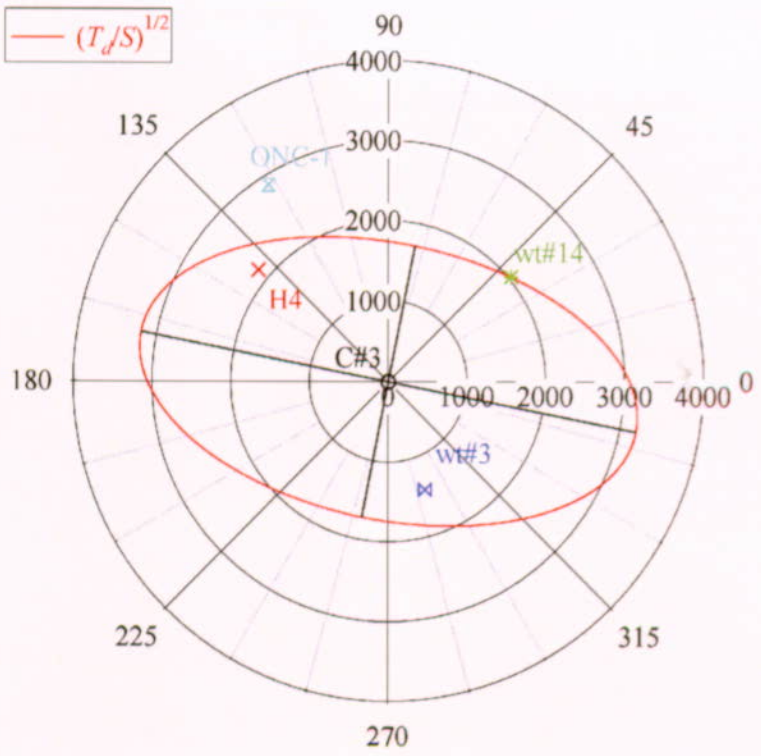

DTN: GS970308312314.002 [161273], DTN: MO0212SPANYESJ.149 [161274]. Output DTN: GS031008312314.004.

Figure 6.2-42. Optimal Papadopulos-PEST Ellipse Fit to the Square Root of the Ratio of Directional Transmissivity to Storativity for USW H-4, UE-25 WT#3, UE-25 WT#14, and UE-25 ONC-1, for the 1,000 m^2/day Transmissivity Fit for All Wells

In the second modified Papadopulos-PEST approach, an optimal PEST ellipse was obtained for the unconstrained transmissivity values from DTN: GS030508312314.003 [164425], (published in Geldon et al. 2002, [161163], p. 41, Table 9), although it violates the homogeneity requirement inherent in the Papadopulos (1967 [150265]) method. The values for T and S are 700 m^2/day and 0.002, respectively, for well H-4; 2,600 m^2/day and 0.002 for WT#3; 1,300 m^2/day and 0.002 for WT#14; and 1,000 m^2/day and 0.001 for ONC-1. From these nonconstrained fits, ratios of the directional transmissivity over storativity, T_d/S, were obtained following the Papadopulos (1967 [150265]) technique. The square roots of these ratios were plotted on a polar plot with the pumping well, c#3, at the center (Figure 6.2-43). For this fit, PEST V 5.5 (STN: 10289-5.5-00 [161564]) indicates that the direction of anisotropy is 1.1° east of north (with a 95% confidence interval of 0.5° to 1.7°) and that the magnitude of anisotropy is 5.5:1 (with a 95% confidence interval of 5.2:1 to 5.8:1).

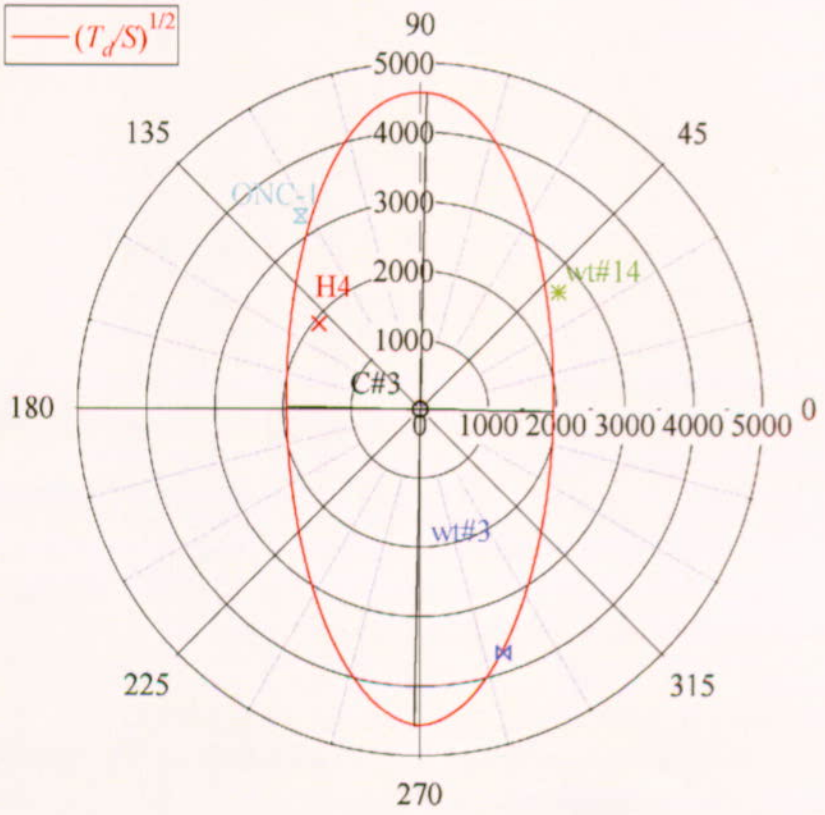

DTN: GS030508312314.003 [164425]; DTN: MO0212SPANYESJ.149 [161274]. Output DTN: GS031008312314.004.

Figure 6.2-43. Optimal Modified-Papadopulos Ellipse Fit to the Square Root of the Ratio of Directional Transmissivity to Storativity for USW H-4, UE-25 WT#3, UE-25 WT#14, and UE-25 ONC-1, Using PEST for Variable (700–2,600 m^2/day, not in order of listed wells) Transmissivities for the Four Wells

In the third modified Papadopulos-PEST approach, an optimal PEST ellipse was obtained for unconstrained transmissivity values resulting from Theis (1935 [150327]) (Theis.vi V 1.0, STN: 10974-1-00 [162758]) type-curve fits for H-4, WT#3, WT#14, and Streltsova-Adams (1978 [150754]) (Streltsova-Adams.vi V 1.0, STN: 10971-1.0-00 [162756]) type-curve fits for ONC-1, using the filtered water-level data described in the first paragraph under Section 6.2.6.2.1. The unconstrained values for T and S resulting from analyzing the filtered data are 700 m^2/day and 0.0024, respectively, for well H-4; 861 m^2/day and 0.0045 for WT#3; 743 m^2/day and 0.0029 for WT#14; and 1,230 m^2/day and 0.0012 for ONC-1. From these values, ratios of the directional transmissivity over storativity, T_d/S, were obtained after Papadopulos (1967 [150265]). The square roots of these ratios were plotted on a polar plot with the pumping well, c#3, at the center (Figure 6.2-44). For this fit, PEST V 5.5 (STN: 10289-5.5-00 [161564]) indicates that the direction of anisotropy is 34.7° west of north (with a 95% confidence interval of 31.7° to 37.7°) and that the magnitude of anisotropy is 11.3:1 (with a 95% confidence interval of 9.3:1 to 13.9:1).

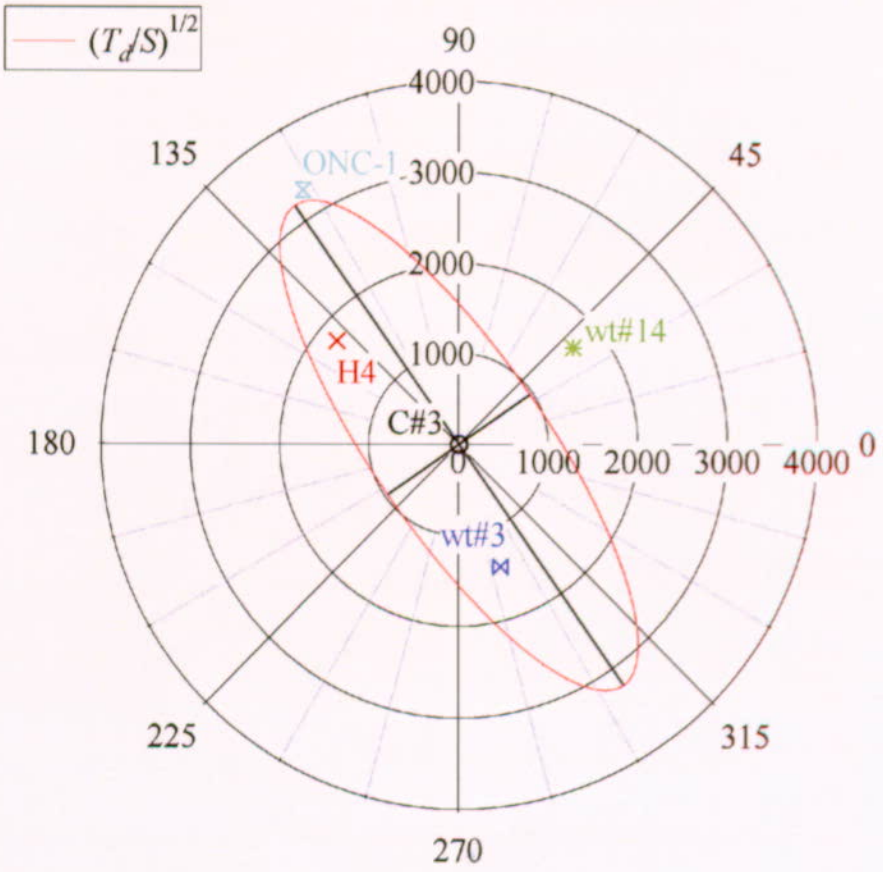

DTN: GS970308312314.002 [161273]; DTN: MO0212SPANYESJ.149 [161274]. Output DTN: GS031008312314.004.

Figure 6.2-44. Optimal Modified-Papadopulos Ellipse Fit to the Square Root of the Ratio of Directional Transmissivity to Storativity for USW H-4, UE-25 WT#3, UE-25 WT#14, and UE-25 ONC-1, using PEST, for Variable (700–1,230 m^2/day) Transmissivities Obtained from Filtered Water Levels for the Four Wells

Using the analytical solution of Papadopulos (1967 [150265]), which assumes an homogeneous, confined aquifer, Ferrill et al. (1999 [118941], p. 7) report an anisotropy ratio of 17:1 with principal direction at azimuth 30° (east of north).

The anisotropy ratio of Winterle and La Femina (1999 [129796], p. 4-23) is listed in the last row of Table 6.2-12 as 5 at 33° east of north. It should be noted that the difference in reported anisotropy between Ferrill et al. (1999 [118941], p. 7) and Winterle and La Femina (1999 [129796], p. 4-23) was solely due to a change in transmissivity for well WT#14, which decreased from 1,370 to 1,330 m^2/day due to a difference in technique for correcting barometric pressures. The sensitivity of the analytical solution is demonstrated by the 3% change in transmissivity manifesting itself as a 70% decrease in the anisotropy ratio to 5:1.

Although not listed in Table 6.2-12, the Hantush (1966 [161160]) technique was applied to the transmissivities and storativities of Section 6.2.4.6 of this report, yielding an undefined anisotropy ratio (i.e., the transmissivities do not define an ellipse). However, when the modified Papadopulos-PEST analysis methodology was applied to these transmissivities and storativities, the anisotropy ratio was estimated as 5.5, as indicated in the third row of Table 6.2-12. With the varied results, it is clear that the anisotropy ratio is highly sensitive to the locations and transmissivities of the monitoring wells. Three of the principal directions of anisotropy presented in Table 6.2-12 vary between 15° and 33°. These values agree favorably with the geologically interpreted value of between 25° and 30°, the principal directional trend of faults in the Yucca Mountain area. In the methods producing these values, H-4 was not included in the analysis, and, hence, the resulting anisotropy values appear to not be affected by the Antler Wash structure; rather, they may be showing the underlying uniformly-distributed anisotropy.

Table 6.2-12. Calculated and Reported Anisotropies and Principal Directions

Data Set Used (Method)	T_{max} (m^2/day)	T_{min} (m^2/day)	Anisotropy[b]	Azimuth[b]
Table 6.2-10 (Hantush 1966)[a]	748	229	3.3	15°E
T = 1,000 m^2/day (Papadopulos-PEST)[a]	1,863	537	3.5	79°W
T = 700 – 2,600 m^2/day (Papadopulos-PEST)[a]	3,272	599	5.5	1°E
T = 700 – 1,230 m^2/day (Papadopulos-PEST)[a]	3,047	271	11.3	35°W
Ferrill et al. (1999)[a]	5,400	315	17	30°E
Winterle and La Femina (1999)[a]	2,900	580	5	33°E

DTN: GS970308312314.002 [161273]; DTN: MO0212SPANYESJ.149 [161274]. Output DTN: GS031008312314.004.

NOTE: [a] For a description of the methods used, refer to Hantush (1966 [161160]), Papadopulos (1967 [150265]), Ferrill et al. (1999 [118941]), and Winterle and La Femina (1999 [129796]).

[b] The last two columns list reported values.

Winterle and La Femina (1999 [129796], p. 4-25) claim a low degree of confidence in their anisotropy ratio because the problem is poorly constrained (e.g., data from only the minimum number of wells necessary for a solution is used; the medium is not homogeneous; the flow is not radial; and the aquifer may not be confined). Data from well H-4 were only used in the modified Papadopulos-PEST method. When data from H-4 were not used, it was because the transmissivity for this well was consistently about half of the other wells (note that both of the analytical solutions of Hantush (1966 [161160]) and Papadopulos (1967 [150265]) require that all wells have equal or nearly equal transmissivities). The rationale for excluding H-4 from the horizontal anisotropy analysis, in some cases, was also based on the Geldon et al. (1998 [129721], p. 31) suggestion that a preferential flow path exists between well H-4 and the C-wells. However, inclusion of the H-4 data in the modified Papadopulos-PEST method and constraining the transmissivity to 1,000 m^2/day (as described above) produced a direction of anisotropy consistent with the alignment of this preferential pathway. It is also noted that after approximately 50 days of pumping, water levels in wells H-4 and WT#14 stopped responding to pumping and actually began to increase, a phenomenon attributed to a recharge or high transmissivity boundary to the east or northeast of WT#14, which could potentially be a transmissive fault. This water-level increase was never observed in well ONC-1, even after 237 days of monitoring. This result implies that not all of the assumptions used in the anisotropy analysis are justifiable. Overall, this conclusion should serve to underscore the level of uncertainty in reported anisotropy ratios.

Considering the range of values demonstrated by the various anisotropy calculations, the results in Table 6.2-12 help characterize a parameter that was not targeted explicitly for measurement when the data ultimately used to calculate it were obtained.

6.2.6.3 Interpretation and Assignment of the Anisotropy Distribution

Well-test analysis is the process of estimating hydraulic parameters of interest (in this case, transmissivity and storativity) from measured drawdown data and is known as an inverse (or parameter-estimation) problem. An inherent quality of inverse problems is that the parameters estimated via this process have some degree of uncertainty associated with their values. More importantly, when solving an inverse problem, a family of solutions should be matched to the data. Because there are typically infinitely many solutions that fit the data, reporting only a single value imparts no real information. It is much more important to examine the range of solutions and to evaluate the sensitivity of each parameter to the solution. In other words, uncertainty must be quantified. To date, there have been no attempts to assign confidence intervals to the estimated parameters. Comparing the well test results of previous researchers helps to emphasize the dependence of the estimated hydraulic parameters upon the solution technique and input data used. Analytical techniques alone cannot provide a measure of confidence in their reported solution. Therefore, it is left to scientific judgment to assign a distribution of anisotropy ratios based upon the available scientific evidence.

Practically speaking, an anisotropy ratio must be selected for each of the 200 stochastic model realizations used as input to the software code FEHM. Because the current version of FEHM (V. 2.20, STN: 10086-2.20-00 [161725]) can only implement anisotropy oriented in a north-south direction, principal directions discussed above are not applicable in the model. The net result of being unable to specify a principal direction is that uncertainty in the anisotropy ratio

can only increase. For example, the analytical result for anisotropy using the Cooper-Jacob (1946 [150245]) method is 3.3 at 15° east of north. A projection that orients the principal direction north-south (0°) results in a new anisotropy ratio of 2.5. As illustrated in Figure 6.2-45, this value was calculated by dividing the maximum y value on the anisotropy ellipse oriented 15° east of north (horizontal blue line at top) by its maximum x value (vertical green line at right). Similarly, the projected north-south anisotropy ratio for an anisotropy ratio of 5 oriented 33° east of north is 1.5. Uncertainty in the analytically calculated anisotropy ratio is propagated in the projected anisotropy ratio and magnified as a function of the uncertainty in the principal direction. In fact, this line of reasoning suggests that it is possible for the projected north-south anisotropy ratio to be significantly less than one.

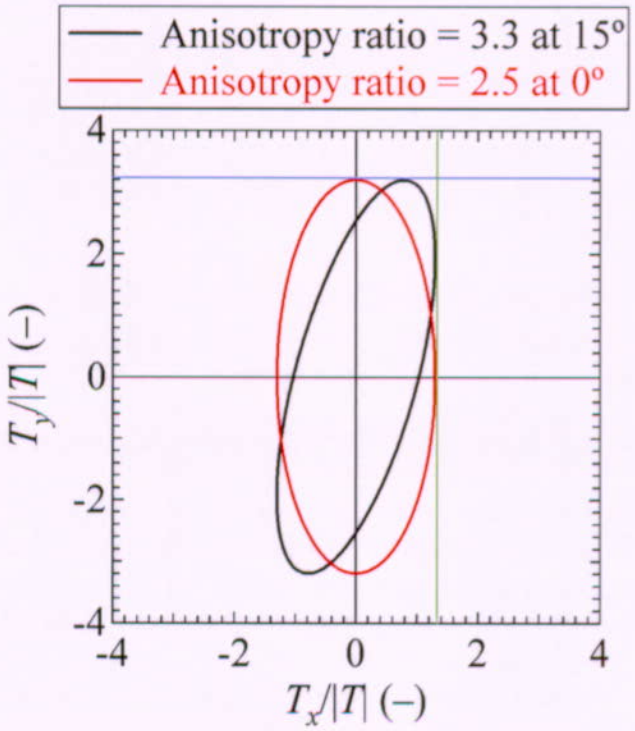

Output DTN: GS031008312314.004.

Figure 6.2-45. Anisotropy Ratio of 3.3 at 15° East of North Projected onto a North-South Anisotropy Ratio (0°) Resulting in a Projected Anisotropy Ratio of 2.5

Based on consultations with USGS staff, the YMP Parameters Team, scientific judgment, and results from the analytical anisotropy analyses, Figure 6.2-46 (a) represents the best estimate of the probability density function (PDF) for the anisotropy ratio in the saturated zone near the C-wells complex. Figure 6.2-46 (b) is the corresponding cumulative distribution function (CDF).

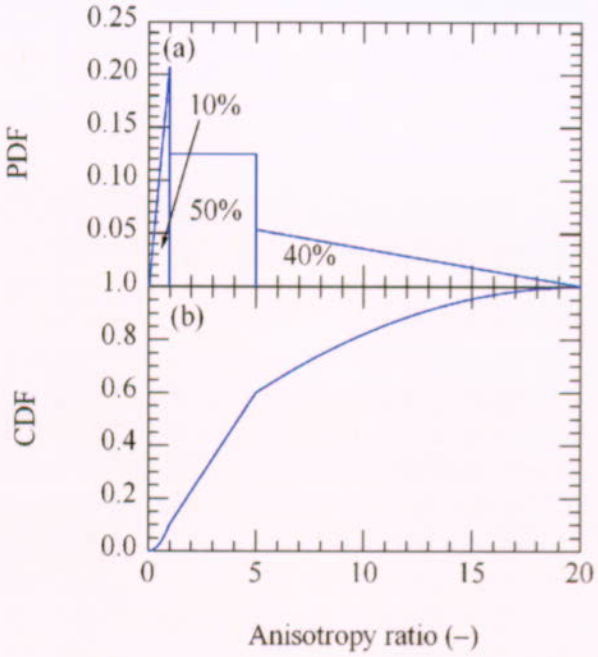

Output DTN: SN0302T0502203.001.

Figure 6.2-46. Probability Density Function (a) and Corresponding Cumulative Distribution Function (b) for the North-South/East-West Anisotropy Ratio Used in FEHM Input Files

There are several noteworthy points based on three distinct regions of the anisotropy ratio distribution (Output DTN: SN0302T0502203.001).

- *Anisotropy ratio between 5 and 20.* The maximum anisotropy ratio of 20:1 is physically based. Although features such as high transmissivity zones and fractures may yield very large anisotropy ratios locally, globally, their effects are attenuated. That is, over the area of the saturated-zone model, 45 × 30 km^2, an anisotropy ratio of 20 is the expected upper bound. Additionally, the highest calculated anisotropy ratio reported is 17:1 (Ferrill et al. 1999 [118941], p. 7). The 5.5 anisotropy ratio calculated by the second approach of the modified Papadopulos-PEST method lies in this range near its highest probability point. Therefore, between 5 and 20, a triangularly distributed anisotropy ratio is constructed that decreases to zero probability at 20. A 40% probability is assigned to this portion of the PDF.

- *Anisotropy ratio between 0.05 and 1.* Discussions among Sandia National Laboratories (SNL) and USGS staff established that, although it is likely the saturated zone is anisotropic with principal direction approximately northeast, it is possible the media could be isotropic, as well as a small probability that the principal direction could be significantly different from northeast. Correspondingly, anisotropies less than one are possible, and the minimum anisotropy ratio is set equal to the inverse of the maximum, 1:20, with a triangularly distributed 10% probability decreasing to zero at a ratio of 0.05.

The 3.5 anisotropy ratio calculated by the first approach of the modified Papadopulos-PEST method, when adjusted according to Figure 6.2-45, falls in this range.

- *Anisotropy ratio between 1 and 5.* A uniformly distributed 50% probability is assigned to the range of anisotropy ratios between 1 and 5. This interval comprises the most likely values of anisotropy ratios with no specific value more likely than another.

Figure 6.2-46 (a and b) is the best estimate for the PDF and the CDF, respectively, of north-south anisotropy ratios in the saturated zone to be modeled with FEHM.

6.2.6.4 FEHM Sensitivity Study

One last point worthy of mention is that a sensitivity analysis of FEHM V 2.20 (STN: 10086-2.20-00 [161725]) results to the anisotropy ratio demonstrated that the modeled heads are insensitive to the input anisotropy ratio. However, inferred groundwater travel times and flow pathways, which ultimately are more important for radionuclide transport predictions than heads, are more sensitive to the anisotropy ratio. Figure 6.2-47 illustrates how varying the anisotropy ratio affects the weighted root-mean-square error (RMSE) between measured and FEHM modeled heads. Note that the RMSE ranges only between 6.9 and 7.6. Although this short range demonstrates relative insensitivity of the modeled heads to the anisotropy ratio, it is encouraging to note that the minimum RMSE corresponds to an anisotropy ratio of 20.

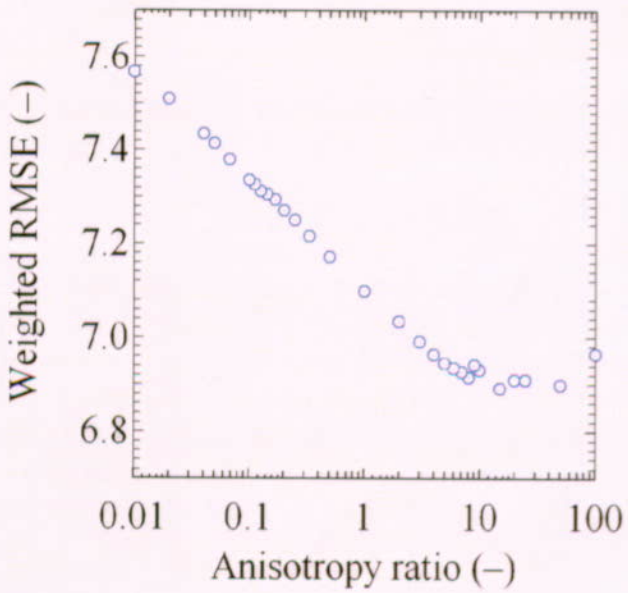

For information purposes only.

Figure 6.2-47. Weighted Root-Mean-Square Error (RMSE) Between Measured Heads and FEHM Modeled Heads Subject to a Range of Anisotropy Ratios Between 0.01 and 100

6.2.6.5 Conclusions

Although analytical and graphical techniques can produce a single, specific anisotropy ratio, this value is sensitive to both the solution technique and the analyst's interpretation of the data (e.g., what filtering parameters were used or how the slopes of drawdown were calculated). A wide distribution of anisotropy ratios is suggested to account for the significant uncertainty in this hydraulic property. Each run of FEHM V 2.20 (STN: 10086-2.20-00 [161725]) must have a single value of anisotropy assigned to the anisotropy zone of the model area, and though this is unrealistic (no single value of anisotropy truly applies to such a large heterogeneous area), drawing an anisotropy ratio from the specified distribution and running FEHM stochastically should effectively account for the uncertainty in this model parameter. Additionally, because the current version of FEHM cannot specify the principal direction of anisotropy, the range of possible north-south anisotropies is increased to consider this fact.

6.2.7 Summary of Conceptual Models And Parameters

Hydraulic tests conducted by the USGS in Miocene tuffaceous rocks at the C-wells complex, Yucca Mountain, Nevada, between May 1995 and November 1997 determined flow characteristics in six saturated-zone hydrogeologic intervals. North- and northwest-striking faults intersect boreholes of the C-wells complex, defining hydrogeologic intervals by spatially related faults and fracture zones. Flow within those intervals comes from diversely oriented fractures and from the interstices of variably welded ash-flow, ash-fall, and reworked tuff. The tuffs act as a single aquifer. About 70 percent of flow seen in hydraulic tests was contributed by the Lower Bullfrog interval, and another 20 percent came from the Upper Tram interval. Identified hydrogeologic units, and related hydraulic properties, cannot be extended far beyond the immediate vicinity of the C-wells complex due to control of those intervals by fault and fracture zones.

In several hydraulic tests from 1995 to 1997, borehole c#3 of the C-wells complex was used as the pumping well. Boreholes c#1 and c#2 (tens of meters distant) were used as observation wells. Each of the wells of the complex is about 900 m deep, and all are open below surface casings to the penetrated formations. Additional boreholes were used as observation wells in some of the hydraulic tests, including ONC-1, H-4, WT#14, WT#3, and p#1. The observation wells were completed in various intervals seen also in the holes of the C-wells complex; p#1 was completed in Paleozoic carbonate rocks. Those observation wells were sited 630 to 3,526 m from c#3, allowing some extrapolation of hydraulic characteristics from the C-wells location. The hydraulic tests were conducted to determine: (1) properties of the composite saturated-zone section in the C-wells; (2) hydraulic properties of the six intervals in those holes; and (3) heterogeneity in the tuffs, including the influence of faults. Monitoring in borehole p#1 was intended to establish whether the tuffs are connected hydraulically to the Paleozoic carbonate rocks (a regional aquifer), estimated to lie some 455 m below the C-wells.

The series of hydraulic tests began with short-term test episodes. The 10-day test of May 1995 pumped borehole c#3 at an average rate of 17.9 L/s and produced pumping-well drawdown of 7.76 m. Drawdown in observation wells ranged from 0 to 42 cm. The June 1995 test lasted four days and used packers to isolate the six saturated-zone hydrogeologic intervals of the C-wells complex. After pumping at a rate of 22.5 L/s, drawdown in the pumping well was 10.9 m, and

drawdown in monitored intervals of observation wells c#1 and c#2 ranged from 43 to 352 cm. The five-day test of February 1996 used packers to isolate and pump the Lower Bullfrog and Upper Tram intervals at a rate of 8.5 L/s. All monitored intervals responded to that pumping. Drawdown in the pumping well was 2.86 m, and drawdown in c#2 and c#1 ranged from 14 to 25 cm.

A long-term test in which the Lower Bullfrog interval was isolated was conducted over more than 550 days starting in May 1996. All monitored intervals again responded to pumping (at a rate of 9.2 L/s). Drawdown reached nearly 6 m by late March 1997 when some disruption due to pump shutoffs occurred. Drawdown in all observation wells was strongly oscillatory, with peak drawdown in the C-wells complex observation holes of 35 to 51 cm. Drawdown in distant observation wells began after hours to days of pumping and ranged from 15 to 37 cm. No drawdown had been observed in p#1 (completed in the carbonate aquifer) by December 1996.

In all of these tests, significant, rapid drawdown and recovery in the pumping well far exceeded amounts that could be predicted from hydraulic properties calculated from observation-well drawdown in the same tests. Much of that excess likely can be attributed to frictional head loss ("borehole skin") in the pumping well. Because the pumping-well drawdown largely is independent of aquifer properties, analyses of that drawdown result in misleadingly small values of transmissivity and hydraulic conductivity.

Hydrogeologic intervals in the C-wells exhibit layered heterogeneity. The Calico Hills interval is unconfined; the Prow Pass and Upper Bullfrog intervals are confined; the Lower Bullfrog interval is a fissure-block aquifer; and the Upper Tram interval received flow from cross-cutting faults in response to pumping. Transmissivity increases downhole from a range of 4 to 10 m^2/d in the Calico Hills interval to a range of 1300 to 1600 m^2/d in the Lower Bullfrog interval. This trend is reversed near the bottom of the wells: i.e., in the Upper Tram Interval, transmissivity is 800 to 900 m^2/d. Likewise, hydraulic conductivity increases downhole from about 0.2 m/d in the Calico Hills interval to a range of 20 to 50 m/d in the Lower Bullfrog and Upper Tram intervals. Storativity generally increases downhole; for example, in c#2 it increases from a range of about 0.0002 to 0.0004 in the Calico Hills and Prow Pass intervals to a range of 0.001 to 0.002 in the Lower Bullfrog and Upper Tram intervals. Order-of-magnitude differences, though, are evident between wells of the C-wells complex and nearby observation wells. These vertical distributions of hydraulic properties reflect the greater influence of faults and related fractures toward the bottom of the boreholes.

During hydraulic tests at the C-wells complex, drawdown occurred in all monitored intervals of those holes and in observation wells, regardless of the interval being pumped. That hydraulic connection across lithostratigraphic contacts likely results from interconnected faults, fractures, and intervals with large matrix permeability. The Miocene tuffaceous rocks thereby act as a single aquifer within a portion of the structural block bounded by the Paintbrush Canyon and Dune Wash faults as well as by faults cutting Boundary Ridge (extending at least as far north as lower Midway Valley). This aquifer encompasses a 21-km^2 area surrounding the C-wells complex. These hydraulic results indicate that the formal designation of multiple aquifers and confining units within the tuffaceous sequence at Yucca Mountain may not be justified.

Drawdown data from monitored wells during the long-term hydraulic test matched the type curve for a confined aquifer and indicated a transmissivity of 2,200 m^2/d and a storativity of 0.002 for the tuffs in the region around the C-wells complex. Plots of drawdown in observation wells as a function of distance during the same test showed a transmissivity of 2,100 to 2,600 m^2/d and a storativity of 0.0005 to 0.002. Analyses of drawdown in the C-wells and in outlying observation wells indicated a northwestward decrease in transmissivity from 2,600 m^2/d in WT#3 to about 2,000 m^2/d at the C-wells and, eventually, to 700 m^2/d in H-4. (Hydraulic conductivity is smallest toward the crest of Yucca Mountain and toward Jackass Flats.) Distributions of drawdown likewise were influenced strongly by northwest- and north-striking faults, as was hydraulic conductivity. Drawdown in observation well ONC-1 showed a fissure-block aquifer response during the long-term test, possibly due to a northwesterly zone of discontinuous faults that extends beneath Bow Ridge and Antler Wash. Drawdown in other observation wells reached a steady state after some 50 days of pumping, again likely in response to faults and fracture zones. Hydraulic conductivity ranges areally from less than 2 to more than 10 m/d and is largest where prominent north-striking faults are closely spaced or intersected by northwest-striking faults. Relatively large hydraulic conductivity occurs beneath Fran Ridge, Bow Ridge, and Boundary Ridge.

Uncertainties in hydraulic parameter estimates, including uncertainties associated with the data-analysis methods, are discussed in detail in Section 6.2.5. When all the contributing uncertainties are considered, storativity and transmissivity estimates are considered accurate to within one significant figure. Hydraulic conductivity estimates are considered to be somewhat less accurate because of the inherent uncertainty in the assumed transmissive thickness of a given test interval.

The responses of WT#3, WT#14, ONC-1, and in some cases H-4, to the long-term hydraulic test were analyzed for anisotropy of the hydraulic conductivity. When H-4 was not included in the analysis, the principal directions of anisotropy vary between 15°E and 33°E. These values agree favorably with the geologically interpreted value of between 25°E and 30°E, the principal directional trend of faults in the Yucca Mountain area. Because the methods producing these values do not include H-4 results, the resulting anisotropy values do not appear to be affected by the northwesterly-trending Antler Wash structure; rather, they may be showing the underlying uniformly-distributed anisotropy. When H-4 was included in the analysis of anisotropy, the influence of the northwesterly-trending Antler Wash structure is seen, and the resulting principal directions of anisotropy range from 79°W to 1°E.

Based on these analyses, a probability density function was derived for North-South/East-West anisotropy in horizontal hydraulic conductivity in the fractured volcanics (Figure 6.2-46). This probability density function reflects the uncertainty in horizontal anisotropy associated with the analysis of the long-term hydraulic test data. The probability density function assigns a probability of 0.9 to a North-South orientation of the anisotropy "ellipse," with a 0.5 probability of the anisotropy ratio ranging from 1 to 5 and a 0.4 probability of the ratio ranging from 5 to 20. Although this is a relatively wide range of possible anisotropy ratios, flow simulations indicated little sensitivity of modeled heads to the full range of ratios. However, flow rates would be expected to be more sensitive to the assumed anisotropy ratio, and the range of specific discharges used in performance assessments should reflect this uncertainty.

6.3 TRANSPORT PROPERTIES OF FRACTURED TUFFS

6.3.1 Nonsorbing Tracer Tests at the C-Wells

Nonsorbing tracer tests conducted at the C-wells complex included: (1) iodide injection into the combined Bullfrog-Tram interval; (2) injection of pentafluorobenzoic acid (PFBA) into the Lower Bullfrog interval, (3) injection of iodide into the Lower Bullfrog interval; (4) injection of 2,6 Difluorobenzoic acid (DFBA) into the Lower Bullfrog interval; (5) injection of 3-carbamoyl-2-pyridone (Pyridone) into the Lower Bullfrog interval; (6) injection of iodide and 2,4,5 trifluorobenzoic acid (TFBA) into the Prow Pass formation; and (7) injection of 2,3,4,5 tetrafluorobenzoic acid (TeFBA) into the Prow Pass formation. The sequence of testing is illustrated in Figure 6.1-9.

The purpose of testing with nonsorbing tracers was to obtain estimates of flow porosity and longitudinal dispersivity of the Bullfrog and the Prow Pass Tuffs. The approach to developing parameters was to conduct multiple tests in a cross-hole system and use different mathematical solutions to interpret the results. Consequently, uncertainties and the sensitivity of the system were better understood.

Iodide, benzoic acids (including DFBA, TFBA, TeFBA, and PFBA), and pyridone can be analyzed by high-performance liquid chromatography (HPLC) with either ultraviolet (UV) absorbance detection or fluorescence detection (pyridone). This method was selected not only because it is precise and sensitive but also because the groundwater samples can be injected directly into the instrument, allowing analyses to be conducted easily in the field for immediate test results.

All nonsorbing tracer tests were analyzed by the Moench (1989 [101146]; 1995 [148784]) single- and dual-porosity analytical solutions to the advection-dispersion equation or by superposition of these solutions. Both solutions are implemented using the MOENCH.vi Function(1) code in conjunction with the rcv2amos.exe routine (STN: 10582-1.0-00 [162750]) and the MOENCH.vi, Function(2), V 1.0 code (STN: 10583-1.0 [162752]). The first software package implements the published dimensionless solutions. The second allows for curve matching to actual, dimensional, tracer breakthrough curves. The input parameters required by the Moench single-porosity and dual-porosity solutions are:

- production rate, q_o (L/min)
- distance from the production to injection well, r_L (m)
- aquifer thickness, h (m)
- radius of production well, r_w; and injection well, r_i (m)
- thickness where mixing occurs in the production well, h_w (m)
- thickness where mixing occurs in the injection well, h_i (m)
- mass of tracer injected, M (g)

- volume of water in which the mass of tracer is dissolved prior to entering the aquifer, V (L)
- time for the tracer slug to enter the aquifer, t_{inj} (sec)
- flow porosity, ϕ_f and matrix porosity, ϕ (matrix porosity is also referred to, interchangeably, as "storage porosity" in Section 6.3)
- longitudinal dispersivity, α_L in the form of a Peclet number ($Pe = r_L/\alpha_L$) (m)
- retardation coefficients representing linear, reversible adsorption R in the fractures and R' in the matrix
- dimensionless diffusion coefficient, Gamma, which is a function of the effective coefficient of diffusion from the fractures into the matrix, D', and of h, ϕ_f, R, q_o, and the radius, b', of theoretical sphere-shaped matrix blocks of the dual-porosity aquifer
- dimensionless storage parameter, Sigma, which is a function of ϕ_f, ϕ, R, and R'
- dimensionless skin parameter, SK, which is a function of the mass transfer coefficient, k_s, representing the continuity of diffusive flux across the "skin" (such as mineral fracture-surface coatings separating fractures from matrix blocks), and of D' and b'.

In a radially-convergent flow field, the volume of interest is a cylinder centered at the production borehole and extending to the injection borehole. Moench (1989 [101146]) assumes that the injection borehole is well mixed and that the tracer is distributed over a specified fraction of the borehole interval length (i.e., the "mixing length").

Radially-convergent, flow-type curves were generated for a range of Peclet numbers. These single-porosity and dual-porosity type curves are in the form of log-log plots of dimensionless concentration, $C_D = C/C_i$, where C_i = average concentration in injection borehole after tracer injection, versus dimensionless time, $t_D = t/(\pi h \phi (r_L^2 - r_w^2)/q_o)$, where the denominator is referred to as the advective travel time, t_a. The observed field tracer breakthrough data are presented in the form of log-log plots of normalized concentration, C/C_{max} (where the concentration is normalized by the maximum observed concentration), versus time since injection. By overlaying the type curve and dimensionless breakthrough curve and matching the rising portions of the two curves, an estimate of the advective travel time, t_a, is obtained when the match point ($C_D = 1$, $t_D = 1$) is projected onto the log-time axis of the dimensionless field breakthrough curve (e.g., Figure 6.3-1, which shows this process for the tracer test described in Section 6.3.1.1.1). In addition, because dimensionless time is defined as the ratio of time since injection to the advective travel time, the value of t_a is equal to the time since injection, indicated on the time axis of the breakthrough curve, corresponding to $t_D = 1$. The Peclet number is also estimated based on the type curve match. In the dual-porosity solution, diffusion is minimal on the rising limb of the breakthrough curve, but it was calculated on the falling limb. The tail of the observed data was matched to a theoretical dual-porosity breakthrough curve with diffusion processes in which the controlling parameters include the Gamma and Sigma terms. The

physical parameters that are estimated are the matrix porosity, ϕ, and the dimensionless diffusion coefficient, Gamma.

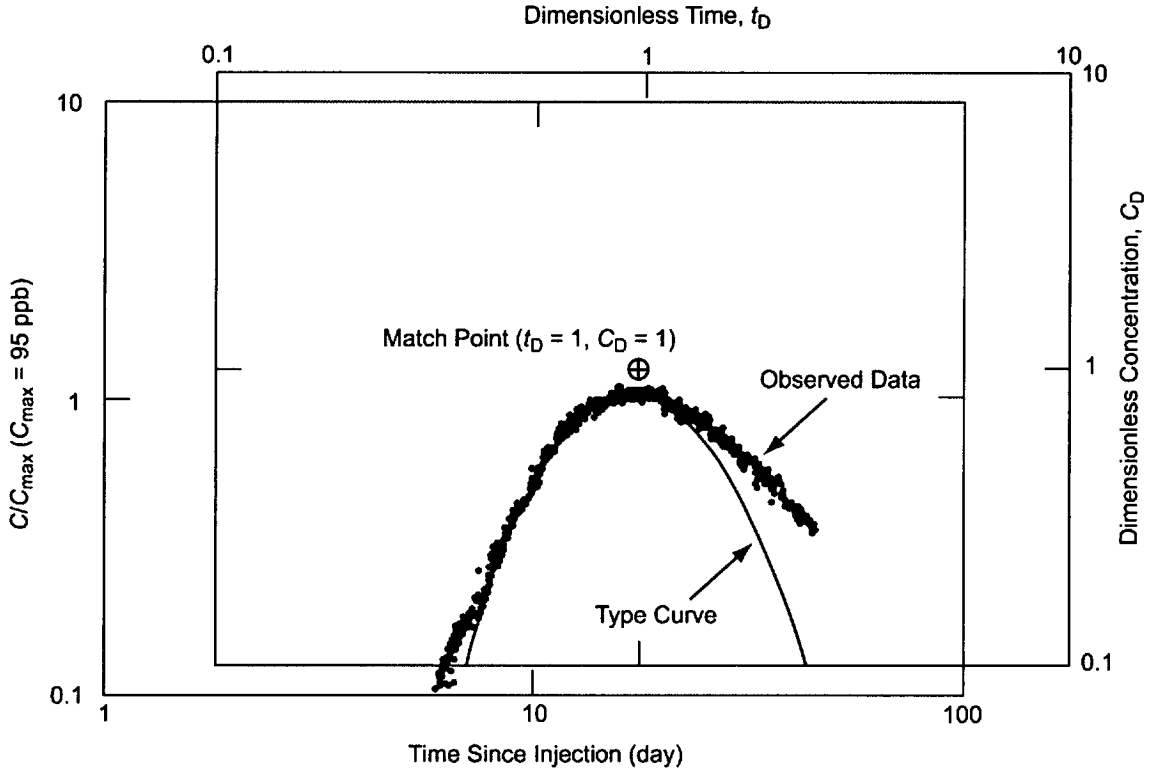

DTN: GS960808312315.001 [159235] (data); Output DTN: GS031008312315.002 (analysis).

NOTE: The Peclet number Pe = 11.

Figure 6.3-1. Type-Curve Match for Iodide Injection into UE-25 c#2

Some of the analyses of nonsorbing tracer tests in this report used the single-porosity Moench solution, some used the dual-porosity solution, and some used a combination of both, depending on the type of test. This was done to explore the effectiveness of a particular solution method in matching a particular set of data. When both the single- and dual-porosity solutions were used, the t_a and Peclet number were first obtained from the match of the single-porosity type curves to the rising limb of the data curve; then Moench's dual-porosity solution was used to obtain estimates of Gamma and Sigma by fitting to the whole data curve.

To constrain the range of parameter values (such as of flow porosity) that can result from various possible interpretations of tracer tests, the fracture characteristics of the formations in which tracer testing was conducted should be considered. Fracture orientations in the Lower Bullfrog were based on televiewer data reported in Geldon (1996 [100396], pp. 14 to 17, Table 6) and obtained in the 1980s when the boreholes were drilled. Two orientations are statistically significant. The dip and strike of the fracture planes are: 77/167 and 78/191 (first number is degrees from horizontal, and second number is degrees from due north in a clockwise direction; the two orientations are shown in Figure 6.3-2, relative to the sides of the C-wells triangle). The

fractures at the C-wells complex are moderately to steeply inclined, trend in a northerly direction, and have a probable nonuniform spacing. If transport is along fractures and faults, then the orientation data represent the possible directions of transport that may be occurring at the small scale in any interpretation.

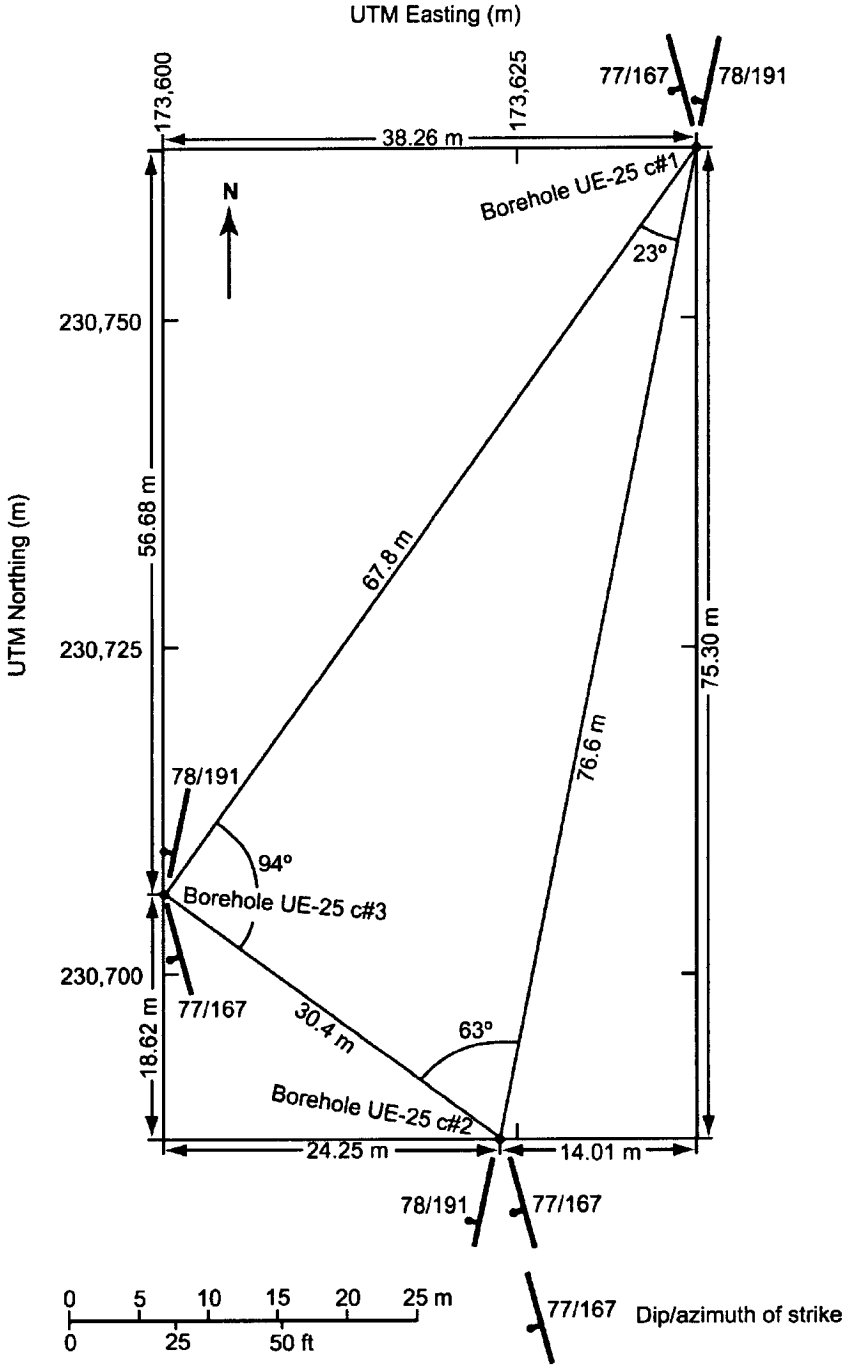

Source: Geldon (1993 [101045], p. 6 for well locations); Geldon (1996 [100396], pp. 74 to 119 for fracture information).

Figure 6.3-2. Dominant Bullfrog Tuff Fracture Sets in Each of the C-wells

6.3.1.1 Results and Interpretations of Nonsorbing Tracer Tests: Bullfrog and Tram Formations

6.3.1.1.1 Iodide Tracer Test in the Lower Bullfrog/Upper Tram Interval

Following establishment of a quasi-steady-state hydraulic gradient by pumping the recovery borehole (c#3) for about 7,000 minutes, the first convergent tracer test at the C-wells complex was initiated in the Bullfrog-Tram Tuff interval on February 13, 1996, under convergent flow field conditions (Umari 2002 [162858], Binder 4, Section F-12; Binder 5, Sections G-4 to G-12, H-1 to H-7; Binder 6, Sections H-1 to H-7, H-10 to H-11). Tracer solution was injected into the Bullfrog-Tram interval of borehole c#2 for 28 minutes at an average rate of 24.6 (liters per minute (L/m)) (6.5 gallons per minute (gpm)). This test was conducted in the most transmissive interval in the C-wells (the Bullfrog-Tram interval), over the shortest interborehole distance (from borehole c#2 to borehole c#3), and using the simplest flow field (a convergent flow field) to enhance the possibility of successful tracer recovery.

The tracer solution consisted of 5.9 kilograms (kg) of sodium iodide (of which 5 kg were iodide) dissolved in 500 liters (L) (132 gallons) of water from borehole c#3 (Umari 2002 [162858]). The tracer solution was chased with 182 L (48 gallons) of water from c#3, which was pumped into borehole c#2 to ensure evacuation of the injection string (Umari 2002 [162858]).

The chemical constituent used as a tracer was iodide with an injection concentration of 10,200 parts per million (ppm). The iodide injection from c#2 on February 13, 1996, has been discussed by Fahy (1997 [137456], second and third {unnumbered} pages). Iodide concentrations in water sampled during the tracer test were obtained by a reverse-phase, HPLC in conjunction with an ultraviolet (UV)-absorption detector (Stetzenbach and Thompson 1983 [156863], pp. 36 to 41). The field-determined detection limit for iodide was 3 µg/L. The precision of the HPLC analytical technique, as determined by comparing replicate analyses, was 2.3 percent for the field-determined concentrations and 1.61 percent for laboratory-determined concentrations.

Iodide breakthrough occurred 5.07 days after injection. The peak concentration occurred 17.75 days after injection. The test was terminated 45.1 days after injection. The iodide mass recovered was estimated as 2.347 kg, 47 percent of the injected mass (Fahy 1997 [137456], second and third {unnumbered} pages).

The tracer test was complicated by progressively decreasing discharge from the recovery well, which was caused by a mechanically failing pump. The pump discharge decreased from 510 L/m (134.7 gpm) on February 13, 1996, to 372 L/m (98.3 gpm) on March 29, 1996. For analysis of the tracer test, the median value of 444 L/m (117.3 gpm) was used as the discharge rate (The decline in discharge rate was approximately linear with time and the discharge measurements were obtained at equal time increments, so the median and mean of all measurements were essentially the same). Despite these problems, a breakthrough curve, with breakthrough and peak arrival times readily discernible, was clearly established by March 29, 1996.

Interpretation of Test

Both the single- and dual-porosity Moench (1989 [101146]; 1995 [148784]) solutions were used to interpret the iodide test in the Bullfrog-Tram interval. The rising limb was first analyzed using the single-porosity solution, as presented in Figure 6.3-1, to obtain the flow porosity and Peclet number. The dual porosity solution was then used with these parameter values to fit the whole curve and obtain the matrix porosity. Input parameters and results are the following.

- Discharge equal to the median value of 444 L/m (117.3 gpm).
- Aquifer thickness equal to the transmissive thickness of the Bullfrog-Tram interval between boreholes c#2 and c#3 (168 ft (51.2 m).
- Peclet number of 11 to 12, which corresponds to a longitudinal dispersivity of ~2.5 m.
- Advection travel time of 17.75 days (calculated from peak concentration; Figure 6.3-1).
- The flow porosity, ϕ_f, was estimated as 0.086. This porosity estimate is high if only fractures are considered as the flow pathways. Typical fracture porosities are of the order of 0.01 maximum (Freeze and Cherry 1979 [101173], p. 408).
- The complete curve match (Figure 6.3-3) results in an estimate of the matrix porosity of 0.19.

The high flow porosity values above indicate that either (1) a composite flow pathway occurred for the iodide (a combination of both fractures and matrix), or (2) flow heterogeneity resulted in much longer travel times than would be expected under ideal radial convergent flow conditions in a homogeneous, isotropic medium. In the first case, the solute is hypothesized as traveling through a connected-fracture-network segment, then through a segment of matrix until it reaches the next connected-fracture-network segment. In the second case, flow to the production well is seen as being nonuniformly distributed in the flow domain, with a relatively small amount of flow coming from the direction of the injection well. The matrix porosity estimated is reasonable, based on geophysical logging conducted at the C-wells complex (Geldon 1996 [100396], pp. 12 to 69).

The software program PEST V 5.5 (STN: 10289-5.5-00 [161564]) was used to corroborate tracer solution results and to obtain optimal parameter values based on the iodide test results. The PEST optimization started with the visual graphical match to the breakthrough curve presented in Figure 6.3-3 for which *Pe* = 11, Sigma = 2.0, and Gamma = 0.04. Three PEST runs were conducted with each of these parameters changed from the above values while the others were held constant. In the first run, PEST was given *Pe* = 11, Sigma = 1.0 (intentionally "perturbed" from its good-visual-fit value of 2.0), and Gamma = 0.04; PEST was allowed to change only Sigma. At the end of this run, PEST converged on an optimal value of Sigma = 1.7175 and an associated confidence interval for Sigma. In the second run, PEST was given the values *Pe* = 8 (intentionally perturbed from its good-visual-match value of 11), Sigma = 1.7175, and Gamma = 0.04; PEST was allowed to change only *Pe*. At the end of this run, PEST converged on an optimal value of *Pe* = 11.478 and an associated confidence interval for *Pe*. In the third run, PEST was given the values *Pe* = 11.478, Sigma = 1.7175, and Gamma = 1.0 (intentionally

perturbed from its good-visual-fit value of 0.04); PEST was allowed to change only Gamma. At the end of this run, PEST converged on an optimal value of Gamma = 0.03565 and an associated confidence interval for Gamma. The above optimal values, their associated confidence intervals, and the fit to the actual breakthrough curve that they produce are presented in Figure 6.3-4.

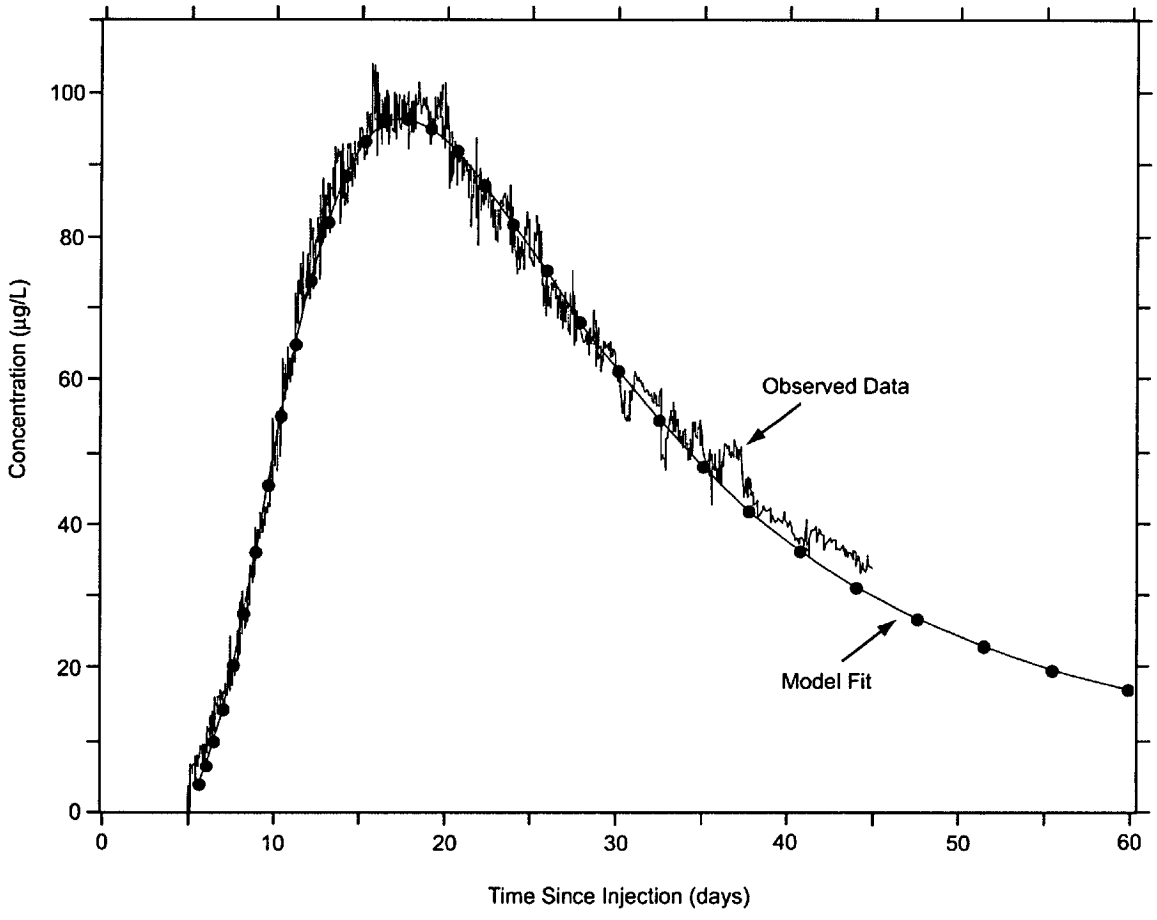

DTN: GS960808312315.001 [159235] (data); Output DTN: GS031008312315.002 (analysis).

NOTE: Estimated parameters are Peclet number Pe = 11, dispersivity α_L = 2.6 m (8.64 ft), flow porosity ϕ_f = 0.086, and matrix porosity ϕ = 0.19. The dots on the model fit curve have no significance.

Figure 6.3-3. Preliminary Moench Analytical Model for Iodide Injection in UE-25 c#2

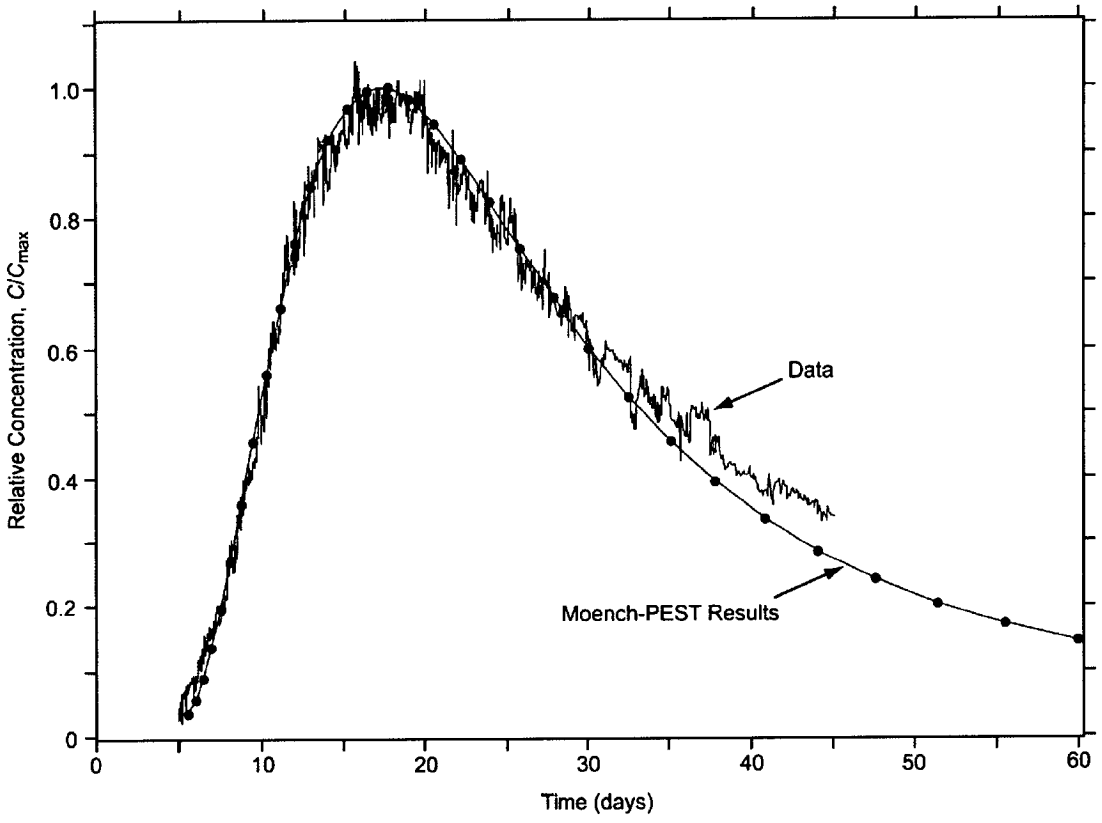

DTN: GS960808312315.001 [159235] (data); Output DTN: GS031008312315.002 (analysis).

NOTE: The breakthrough curve was matched by the PEST V 5.5 (STN: 10289-5.5-00 [161564]) program with initial estimates from a manual match. The optimal PEST results, with 95% confidence intervals in parentheses, are Pe = 11.478 (11.2276–11.7284), R = 1.0, σ = 1.71746 (1.4353–1.99962), and γ = 0.0356464 (0–0.12744), and the other estimated parameters are dispersivity α_L = 2.52 m (8.28 ft), flow porosity ϕ_f = 0.087, and matrix porosity ϕ = 0.163. The dots on the model fit curve have no significance.

Figure 6.3-4. Breakthrough Curve for February 13, 1996, Iodide Tracer Test

The visual graphical match and the optimized PEST V 5.5 (STN: 10289-5.5-00 [161564]) parameters are in good agreement. The Peclet number and dispersivity estimates vary by approximately 4 percent as can be seen by comparing the values listed in the notes under Figures 6.3-3 and 6.3-4. The flow porosity estimates vary by less than 1 percent. The visual-graphical-match matrix-porosity estimate is 0.19, and the PEST estimate is 0.163.

The difference in values is attributed to the different weights assigned to fitting/matching portions of the breakthrough curve. The rising limb is used exclusively in the visual graphical match to estimate the Peclet number and the advective travel time, and then the advective travel time is used to estimate the flow porosity. The PEST V 5.5 (STN: 10289-5.5-00 [161564]) approach uses all of the data, both rising- and falling-limb, and optimizes the fit to these data. This results in a slightly different fit than the visual graphical match. Tables 6.3-2 and 6.3-3 in Section 6.3.3 (summary section) list the parameter values obtained from all of the nonsorbing tracer testing described in Section 6.3.1.

6.3.1.1.2 Difluorobenzoic Acid Tracer Test in the Lower Bullfrog Interval

On January 10, 1997, a purely-convergent conservative tracer test was initiated from c#2 to c#3 in the Lower Bullfrog interval at an average rate of 568 L/m (Umari 2002 [162858] Binder 7, Sections J-6 to J-12, K-1 to K-9; Binder 8, Sections J-6 to J-12, K-1 to K-9; Binder 9, Sections J-6 to J-12, K-1 to K-9, K-11 to K-12, L-3). Approximately 11.35 kg of 2,6-difluorobenzoic acid (2,6 DFBA) mixed with 795 L (210 gallons) of c#3 water were injected into the Lower Bullfrog Tuff in borehole c#2, followed by 238 L (62.9 gallons) of chase water. A total of 1798 L (475 gallons) of fluid was injected, the first portion of which was the fluid in the injection string preceding the injectate solution. The average injection rate was 31.2 L/m (8.2 gpm), with a range of 28.8 to 33.0 L/m (7.6 to 8.8 gpm). The average progressive-cavity pump (injection pump) pressure, measured at the surface, was 1.541 megapascals (MPa) (223.6 psi), with a range of 1.5 to 1.6 MPa (215 to 230 psi). The chemical constituent used as a tracer in this test was 2,6 DFBA. Chemical analysis indicated that the 2,6 DFBA injectate solution had a concentration of 15,560 mg/L. The field-determined detection limit for DFBA was 40 µg/L. The precision of the HPLC analytical technique, as determined by comparing replicate analyses, was ±10 percent.

Breakthrough occurred at c#3 on January 15, 1997, 5.07 days after injection. The peak concentration occurred 13.5 days after injection. The mass recovered is estimated as 7.6 kg, which is approximately 67 percent of the injected mass (Fahy 1997 [162811]).

Interpretation of Test

Interpretation of the DFBA test using the Moench (1989 [101146]) single-porosity analytical solution for radially convergent flow produced the following results.

- Discharge rate and transmissive thickness used for the analysis were 568 L/m and 51.2 m, respectively.
- Peclet number between 12 and 15 (Figures 6.3-5, 6.3-6, and 6.3-7)
- Advection travel time between 12 and 16.5 days
- Flow porosity between 0.072 and 0.099 (Figures 6.3-6 and 6.3-7)
- Matrix porosity between 0.088 and 0.132, and a longitudinal dispersivity value between 1.94 m (6.37 feet) and 2.43 m (7.96 feet) : (Figures 6.3-6 and 6.3-7).

The range of values reflects two approaches for the complete curve match. The Peclet number of 12, flow porosity of 0.099, matrix porosity of 0.088, and a dispersivity of 2.43 m (7.96 feet) reflect matching the rising limb of the breakthrough curve and honor the initial decline closely (Figure 6.3-6). At longer times, the data and match diverge, possibly indicating secondary arrivals from longer residence time flow pathways. The alternative is to match the rising limb of the breakthrough curve and reasonably match the complete declining portion of the curve (Figure 6.3-7).

The program PEST V 5.5 (STN: 10289-5.5-00 [161564]) was applied to the DFBA test results by starting with the visual graphical match to the breakthrough curve presented in Figure 6.3-7, for which *Pe* = 15.0, Sigma = 1.7, and Gamma = 0.12.

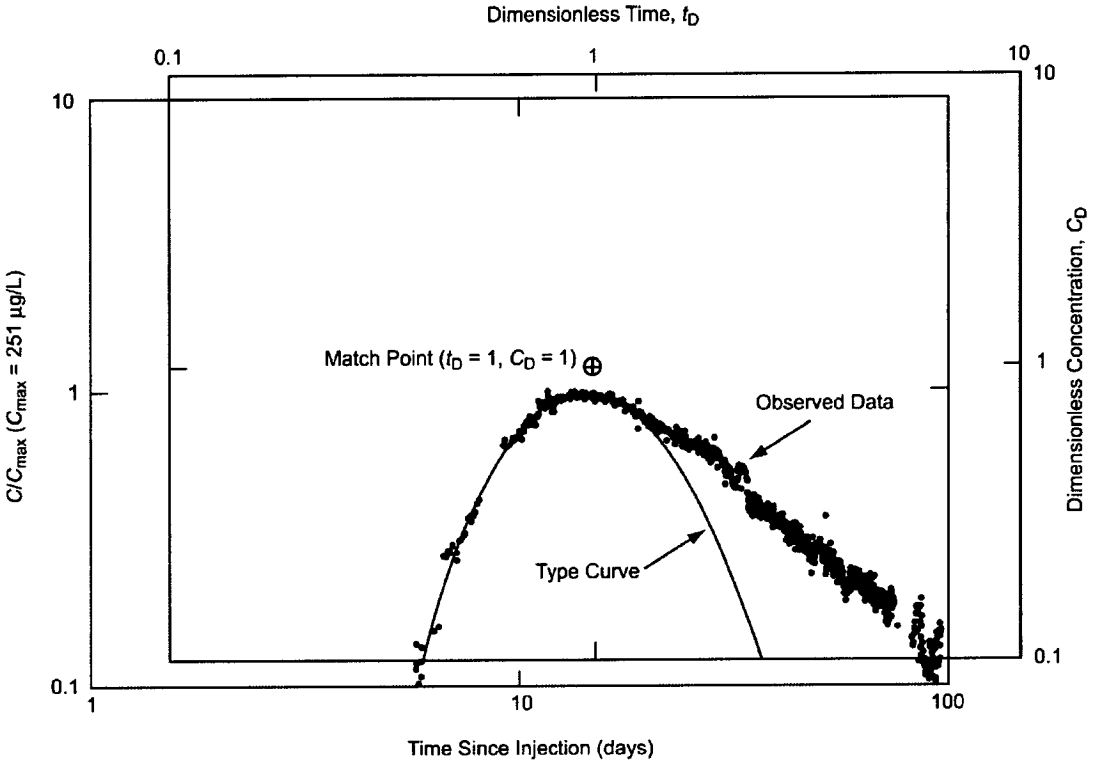

DTN: GS010508312315.001 (data) [155860]; Output DTN: GS031008312315.002 (analysis).

NOTE: The Peclet number *Pe* = 12. Only the rising limb of the observed data was fit because the falling limb could be the result of secondary arrivals.

Figure 6.3-5. Type Curve Fit for 2,6 DFBA Injection in UE-25 c#2

Three PEST V 5.5 (STN: 10289-5.5-00 [161564]) runs were conducted, each with one of these parameters changed from the above values while the other parameters were held constant. In the first run, PEST was given *Pe* = 15, Sigma = 3.0 (intentionally "perturbed" from its good-visual-fit value of 1.7), and Gamma = 0.12; PEST was allowed to change only Sigma. At the end of this run, PEST converged on an optimal value of Sigma = 1.8776 and an associated confidence interval for Sigma. In the second run, PEST was given the values *Pe* = 8 (intentionally "perturbed" from its good-visual-fit value of 15.0), Sigma = 1.8776, and Gamma = 0.12; PEST was allowed to change only *Pe*. At the end of this run, PEST converged on an optimal value of *Pe* = 15.8 and an associated confidence interval for *Pe*. In the third run, PEST was given the values *Pe* = 15.8, Sigma = 1.8776, and Gamma = 1.0 (intentionally perturbed from its good-visual-fit value of 0.12); PEST was allowed to change only Gamma. At the end of this run, PEST converged on an optimal value of Gamma = 0.11793 and an associated confidence interval

for Gamma. The above optimal values, their associated confidence intervals, and the fit to the actual breakthrough curve that they produce are presented in Figure 6.3-8.

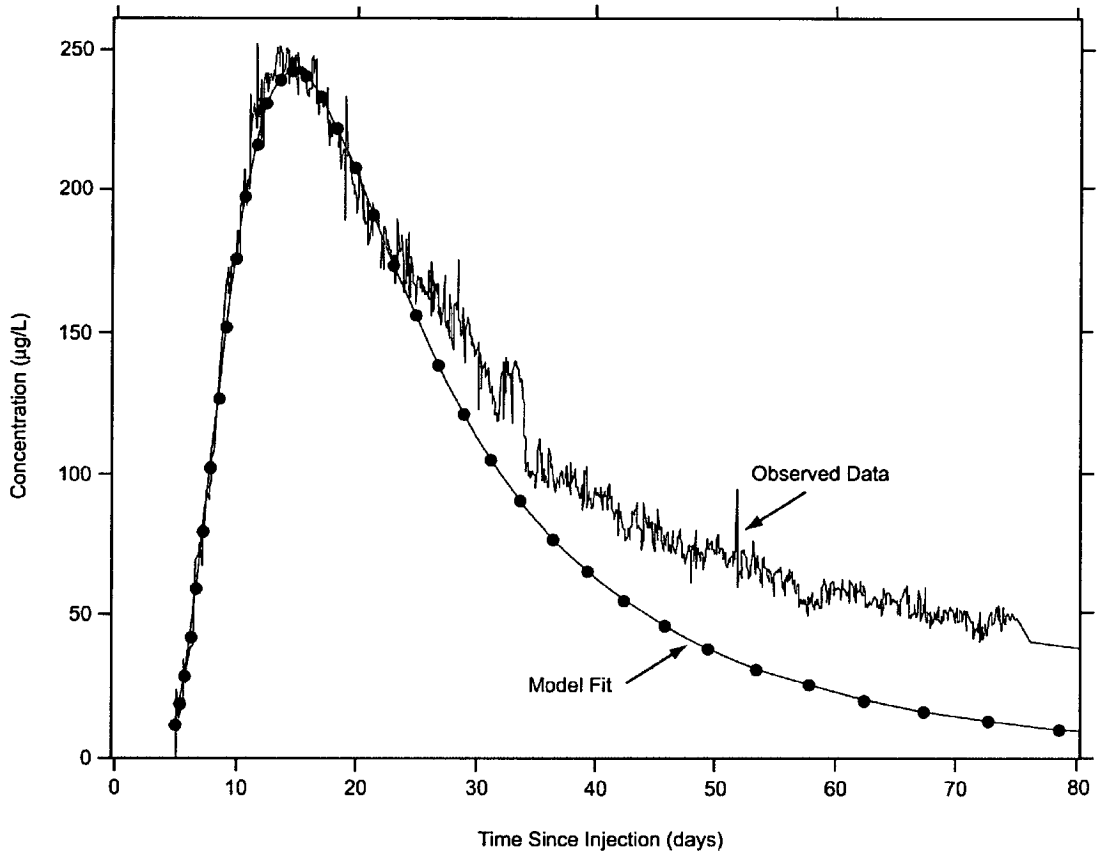

DTN: GS010508312315.001 (data) [155860]; Output DTN: GS031008312315.002 (analysis).

NOTE: The Fit 1 estimated parameters are Peclet number Pe = 12, dispersivity α_L = 2.4 m (7.96 ft), flow porosity ϕ_f = 0.099, and matrix porosity ϕ = 0.088. Only the rising limb of the observed data was fit because the falling limb could be the result of secondary arrivals. The dots on the model fit curve have no significance.

Figure 6.3-6. Fit 1 Preliminary Moench Analytical Model for 2,6 DFBA Injection in UE-25 c#2

The visual-graphical match and the optimized PEST V 5.5 (STN: 10289-5.5-00 [161564]) parameters are in good agreement. The Peclet number and dispersivity estimates vary by approximately 5 percent as can be seen by comparing the values listed in the notes under Figures 6.3-7 and 6.3-8. The flow porosity estimates are identical. The visual-graphical-match matrix porosity estimate is 0.132, and the PEST estimate is 0.146.

6.3.1.1.3 Pyridone Tracer Test in the Lower Bullfrog Interval from c#1 to c#3

On January 9, 1997, approximately 3.018 kg of 3-carbamoyl-2-pyridone (pyridone), mixed with 795 L (210 gallons) of borehole c#3 water, was injected into borehole c#1, followed by 252 L

(66.6 gallons) of chase water to test the Lower Bullfrog interval (Umari 2002 [162858], Binder 7, Sections J-6 to J-12, K-1 to K-9; Binder 8, Sections J-6 to J-12, K-1 to K-9; Binder 9, Sections J-6 to J-12, K-1 to K-9, K-11 to K-12, L-3). This injection was made while c#3 was being pumped at an average rate of 572 L/m (151.1 gpm).

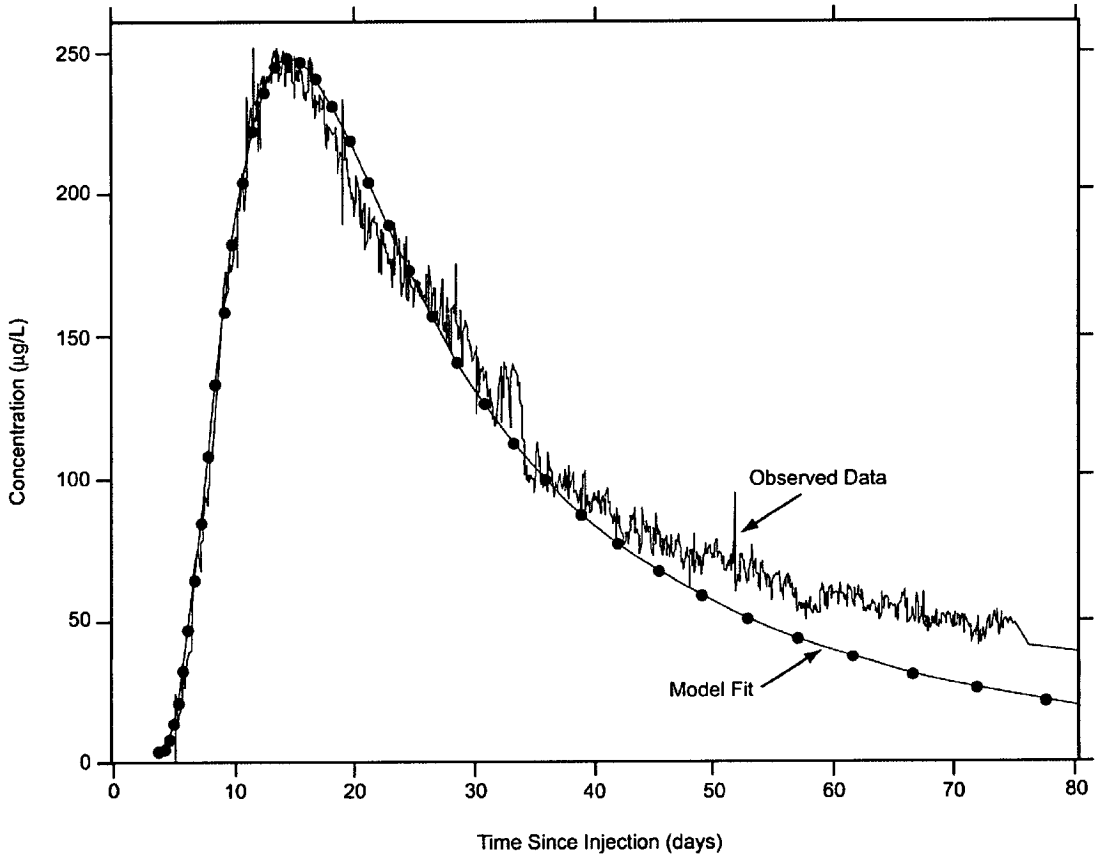

DTN: GS010508312315.001 (data) [155860]; Output DTN: GS031008312315.002 (analysis).

NOTE: The Fit 2 estimated parameters are Peclet number Pe = 15, dispersivity α_L = 1.9 m (6.37 ft), flow porosity ϕ_f = 0.072, and matrix porosity ϕ = 0.132. The dots on the model fit curve have no significance.

Figure 6.3-7. Fit 2 Preliminary Moench Analytical Model for 2,6 DFBA Injection in UE-25 c#2

A total of 2,082 L (550 gallons) of fluid were injected, the first portion of which was the fluid in the injection string preceding the injectate solution. The average injection rate was 0.38 L/s (6.1 gpm), with a range of 16.8 to 37.2 L/m (4.4 to 9.8 gpm). The average progressive-cavity pump (injection pump) pressure, measured at the surface, was 1.743 MPa (252.8 psi), with a range of 0.3 to 2 MPa (50 to 300 psi). Chemical analysis indicated that the pyridone injectate solution had an average concentration of 2,998 mg/L (or 2,998,000 µg/L). The field-determined detection limit for pyridone was 0.1 µg/L. The precision of the HPLC/fluorometry analytical technique, as determined by comparing replicate analyses, was ±10 percent.

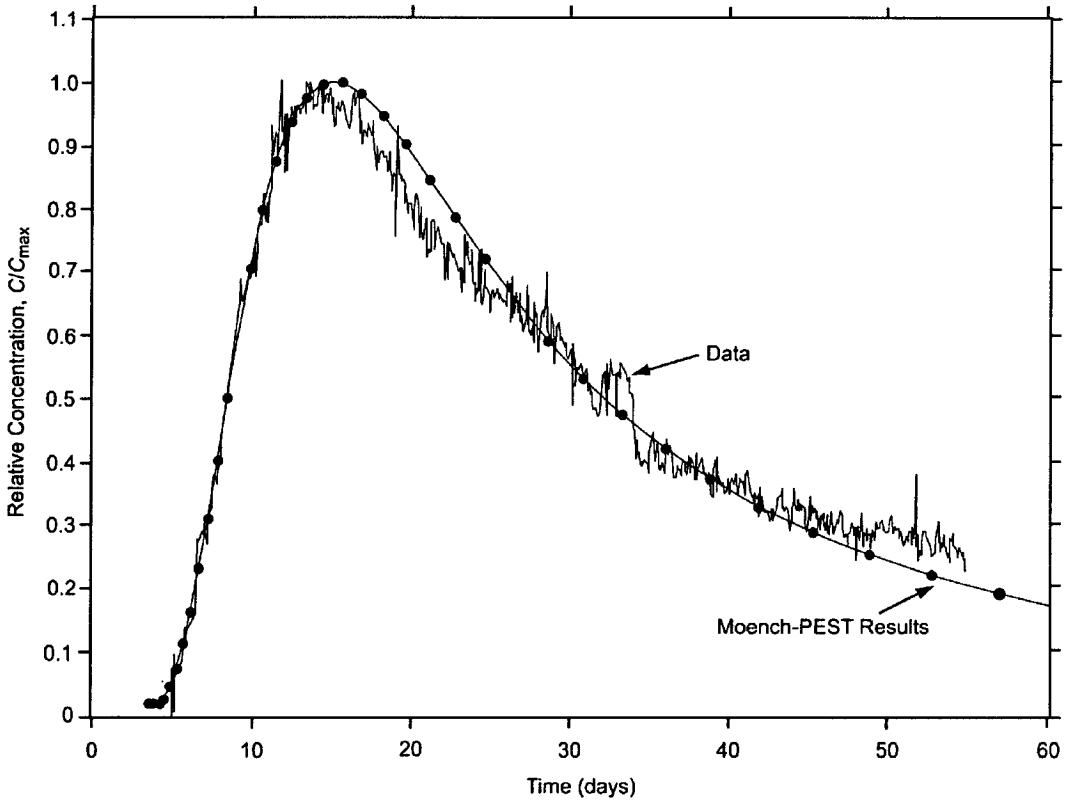

DTN: GS010508312315.001 (data) [155860]; Output DTN: GS031008312315.002 (analysis).

NOTE: The breakthrough curve was matched by the PEST V 5.5 (STN: 10289-5.5-00 [161564]) program with initial estimates from a manual match. The optimal PEST results, with 95% confidence intervals in parentheses, are Pe = 15.7954 (15.4998–16.091), R = 1.0, σ = 1.87763 (1.65457–2.10068), and γ = 0.117934 (0.01741397–0.218454), and the other estimated parameters are dispersivity α_L = 1.83 m (6.01 ft), flow porosity ϕ_f = 0.072, and matrix porosity ϕ = 0.146. The dots on the model fit curve have no significance.

Figure 6.3-8. Breakthrough Curve for January 10, 1997, DFBA Tracer Test

Breakthrough at c#3 occurred on March 27, 1997, 56.3 days after injection. The concentration of pyridone continued to increase but at a gradually-decreasing rate until the end of the test (the test was terminated before a clear peak was observed). The maximum concentration of Pyridone reached was 0.210 µg/L (parts per billion [ppb]), or 210 parts per trillion (ppt), which was determined by analyses in the laboratory where detection limits were much lower than 0.1 µg/L.

The precision of the pyridone concentration values varies. For concentrations less than 100 ppt, errors exceeded ±10%, based on replicate sample analyses. Concentrations of pyridone less than 100 ppt are shown as open-circles on Figure 6.3-9. The filled-circles indicate concentrations of pyridone greater than 100 ppt and those samples with replicate errors less than or equal to ±10%.

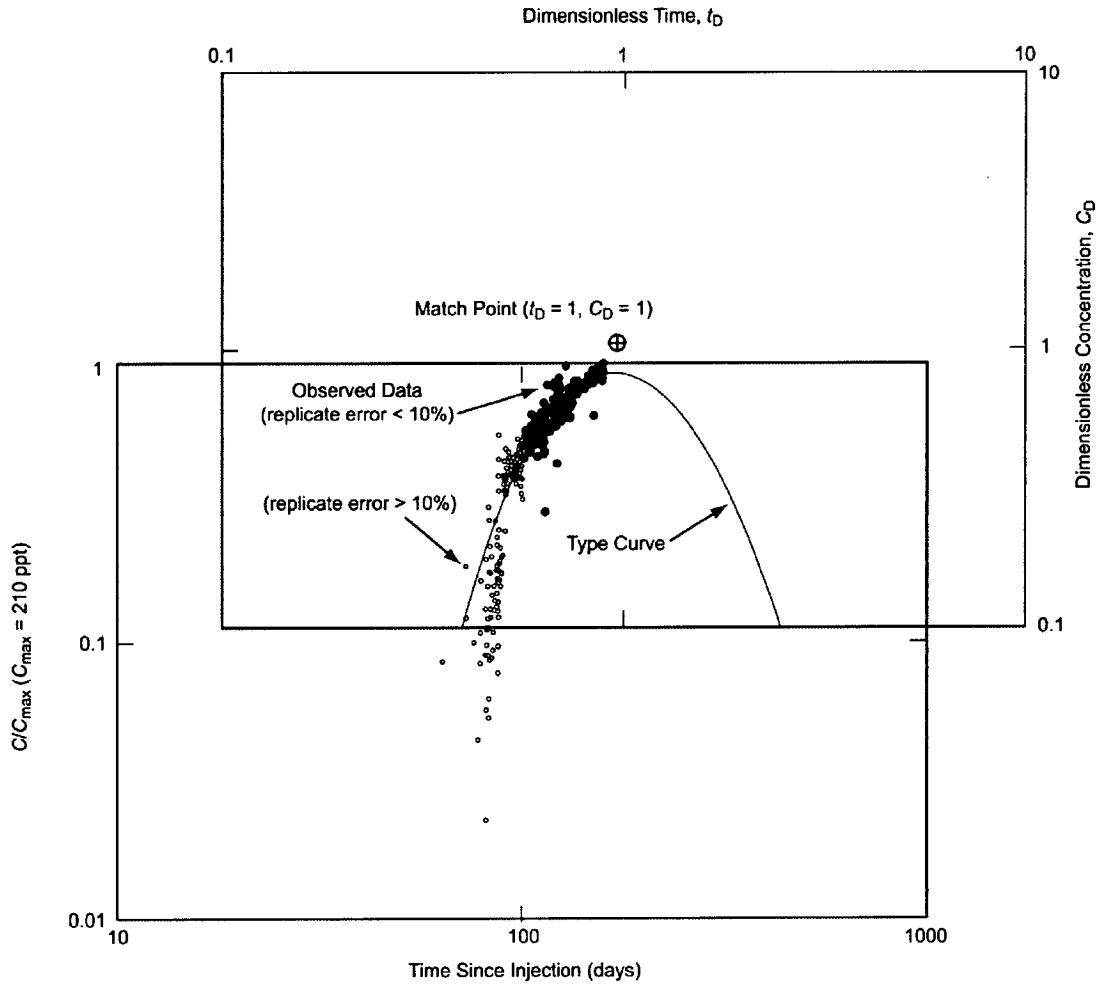

DTN: GS010508312315.001 (data) [155860]; Output DTN: GS031008312315.002 (analysis).

NOTE: The Peclet number *Pe* = 11.

Figure 6.3-9. Type Curve for Pyridone Injection in UE-25 c#1

Interpretation of Test

Because the pyridone test was terminated before a peak concentration was reached, only the rising limb part of the test was analyzed. The type curve depicted in Figure 6.3-9 fits the rising limb well. Assuming that the 0.210 µg/L concentration of pyridone is the maximum for the breakthrough curve, the dual-porosity (Moench 1995 [148784]) analytical solution with a Peclet number of 11 matches the pyridone dimensionless concentration against the dimensionless time curve (Figure 6.3-9). (The single-porosity analytical solution (Moench 1989 [101146]) would have produced a similar result if used to fit the rising limb because the matrix diffusion effects do not manifest themselves until the falling-limb phase of the test.)

6.3.1.1.4 PFBA and Iodide Tracer Tests in the Lower Bullfrog Interval

In cooperation with the USGS, LANL conducted two "pilot" tracer tests, each involving the injection of a single nonsorbing tracer in the Lower Bullfrog interval during 1996. These tests were conducted primarily to determine which well, c#1 or c#2, would serve as a better injection well for the planned multiple-tracer test. The primary motivation was the concern that the responses of both sorbing and colloid tracers might be highly attenuated or excessively delayed relative to nonsorbing tracers, which could make test durations impractically long. Thus, it was desirable to determine which potential injection well yielded the quickest and highest-concentration responses at the production well, c#3. It was not taken for granted that the best response would be from c#2, the injection well closest to c#3, because c#1 and c#3 are more closely aligned with the predominant fracture strike direction at the C-wells than c#2 and c#3.

The first pilot tracer test involved the injection of approximately 10 kg of PFBA into the lower Bullfrog interval in well c#2 on May 15, 1996. This same interval in c#3 was pumped continuously at about 575 L/min throughout the test (starting on May 8, 1996, prior to tracer injection). The PFBA was dissolved in ~1000 L of groundwater from c#3. The test was conducted under partial recirculation conditions with about 20 L/min of the water produced from c#3 (~3.5% of production rate) being continuously reinjected into c#2. The recirculation was initiated approximately 24 hr before tracer injection to establish a steady flow field, and it was continued for 23 days after injection. The tracer solution was plumbed into the recirculation loop such that there were no flow interruptions during injection. Information pertaining to the PFBA pilot test is documented in Reimus (2000 [165126]).

The second pilot test involved the injection of about 12.7 kg of iodide (~15 kg of sodium iodide dissolved in ~1000 L of groundwater from c#3) into the Lower Bullfrog interval in c#1. It was conducted in a manner very similar to the PFBA pilot test and was initiated on June 18, 1996. The recirculation rate in this test was about 15 L/min (~2.6% of production rate), and recirculation continued for ~16 days after injection. Production from c#3 was maintained at ~575 L/m throughout the test, the same as that of the PFBA pilot test. Information pertaining to the iodide pilot test is documented in Reimus (2000 [165127]).

It was clear a few days after the injection of iodide into c#1 that the PFBA response from c#2 was much more conducive to multiple-tracer testing than the iodide response from c#1. The results of the PFBA test are relevant to the interpretation of the multiple-tracer test conducted in the Lower Bullfrog interval, so they are discussed in Section 6.3.4 of this report along with the results of the multiple-tracer test. The iodide response between c#1 and c#3 is shown in Figure 6.3-10. This response is complicated by the initially high and gradually declining iodide background concentrations, which are attributed to the residual iodide in the aquifer from the February 13, 1996, injection of iodide into the Bullfrog-Tram interval in c#2. However, there is clear evidence of a peak occurring about 2 months after injection. The estimated iodide recovery from the c#1 injection by October 1, 1996, (after correcting for the declining background by assuming that it followed an exponential decay) was ~13% of the injected iodide mass (Reimus 2003 [165129], Attachment A). In contrast, the PFBA recovery from c#2 was about 72% on October 1, 1996 (Reimus 2003 [165129], Attachment A). Neither the PFBA nor the iodide pilot tracer tests were interpreted quantitatively.

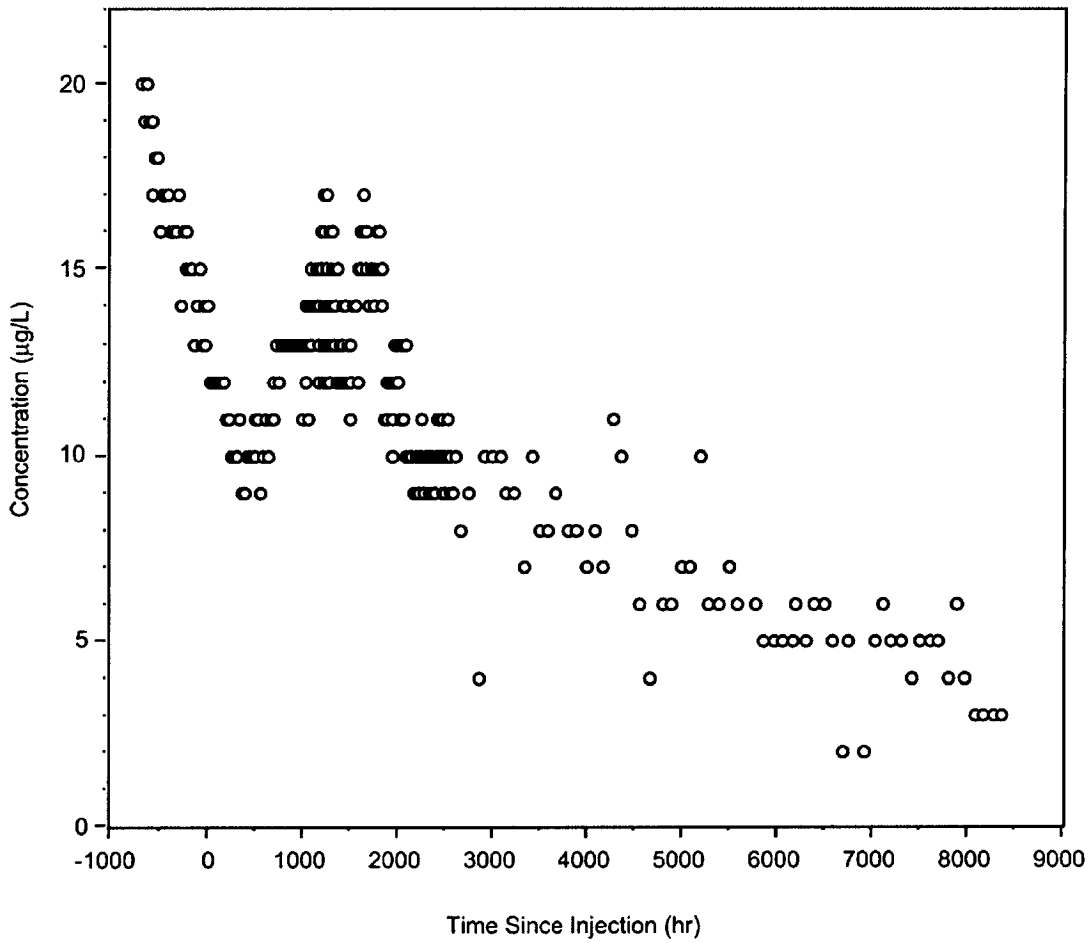

DTN: LA0007PR831231.001 [156043] (data).

NOTE: The breakthrough curve is a result of injection of ~12.7 kg of iodide into c#1 on June 18, 1996; the declining background prior to and immediately after injection is due to recovery of iodide from a February 1996 iodide injection into c#2; and the estimated recovery from c#1 accounting c#2 background was ~13% through June 1, 1997.

Figure 6.3-10. Breakthrough Curve for Iodide Injection in UE-25 c#1

6.3.1.2 Results and Interpretations of Nonsorbing Tracer Tests: Prow Pass Formation

6.3.1.2.1 2,4,5 Trifluorobenzoic Acid and Iodide Test from c#3 to c#2

On June 17, 1998, a partial-recirculation nonsorbing tracer test was initiated from c#3 to c#2 by injecting approximately 14.83 kg of 2,4,5 trifluorobenzoic acid (TFBA) and 12.26 kg of iodide (in the form of sodium iodide) into the Prow Pass interval of c#3 while c#2 was pumped at the rate of approximately 5.2 gpm (19.7 L/m). The concentration of 2,4,5 TFBA was 14,239 ppm in the injected slug and that of iodide 14,307 ppm. Of the 5.2 gpm (19.7 L/m) pumped from c#2, 1.5 gpm (5.7 L/m) was continuously reinjected into the Prow Pass interval of c#3 (Umari 2002

[162858], Binder 13, Sections M-29 to M-36; Binder 14, Sections M-29 to M-36, M-40, M-43 to M-44).

Approximately 40 hours after the injection, breakthrough of both tracers occurred in c#2. The peak for the 2,4,5 TFBA occurred 6.74 days after injection, and the peak for iodide at 7 days after injection (Figure 6.3-11).

The iodide and 2,4,5 TFBA breakthrough curves were analyzed using the single- and dual-porosity analytical solutions of the advection-dispersion equation as given in Moench (1989 [101146]; 1995 [148784]). These solutions were used, as is, for a hypothetical purely convergent flow field, and they were also lagged and superposed to obtain the solution for the actual partial-recirculation flow field (see Section 6.3.1.2.1.2). The curves were first analyzed assuming Moench's single-porosity solution for both the convergent and the partially recirculating flow-field assumptions, using the entire curves for the matches, to obtain the flow porosity and longitudinal dispersivity. In this case, the aquifer is considered to be an equivalent porous medium made up of a network of fractures, some of them continuous, and some potentially discontinuous with connecting segments of matrix (Fahy 1997 [137456], fourth and fifth {unnumbered} pages). The porosity of this network of fractures and connecting segments of matrix, through which flow of solutes occurs, is referred to herein as "flow porosity" (Fahy 1997 [137456], fourth and fifth {unnumbered} pages). The curves were then analyzed assuming a dual-porosity system, also using the entire curves for the match. In addition to the above network of fractures and connecting segments of matrix, the dual-porosity medium is conceptualized as having a storage component consisting of dead-end fractures and the part of the matrix not contributing to the flow network.

The flow porosity and longitudinal dispersivity are different for each of the solutions presented. The retardation coefficient used for all solutions was 1.0, assuming that iodide and 2,4,5 TFBA are considered nonsorbing with respect to the Prow Pass Tuff. All the solutions used the following input parameters:

- Production rate of 19.7 L/m (5.2 gpm; represents the average rate for the test).
- Aquifer thickness of 61 m (200 ft, packed-off interval, rounded to one significant figure) (Umari 2002 [162858], Binder 10, Section L-11, pp. 70 to 71, Section L-9, pp. 57 to 58).
- Distance between injection and production wells of 29 m (95.15 ft) (see Table 6.2-6).
- Radii of injection and production wells of 13.97 cm (5.5 in.) (assumed for rugose, variable-diameter open-hole portion of C-wells where all testing was conducted, based on C-wells caliper logs (Geldon 1993 [101045], p. 10).
- Borehole mixing length of 30.5 m (100.07 ft; assumed, as discussed below).
- Recirculation rate of 5.7 L/m (for the partially-recirculation solution)

6.3.1.2.1.1 Single-Porosity, Purely Convergent Interpretation

The single-porosity, purely convergent solution is obtained directly from the Moench (1989 [101146]) solution to the advection-dispersion equation. A best visually-matching single-porosity solution corresponding to flow porosity and longitudinal dispersivity values of 0.0007 and 1.45 m, respectively, is presented in Figure 6.3-12, along with the iodide and 2,4,5 TFBA breakthrough curves. All breakthrough curves, such as the ones in Figure 6.3-12, were normalized by dividing the measured concentrations by the maximum concentration, C_{max}, rather than by the concentration of the injected mass slug, C_0. Longitudinal dispersivity is a measure of the media's ability to disperse a solute along streamlines. Transverse dispersivity, which represents the media's ability to disperse a solute in a direction perpendicular to streamlines, is not obtainable from this analysis method and flow geometry. The longitudinal dispersivity of 1.45 m and the 29-m flow length correspond to a Peclet number of 20.

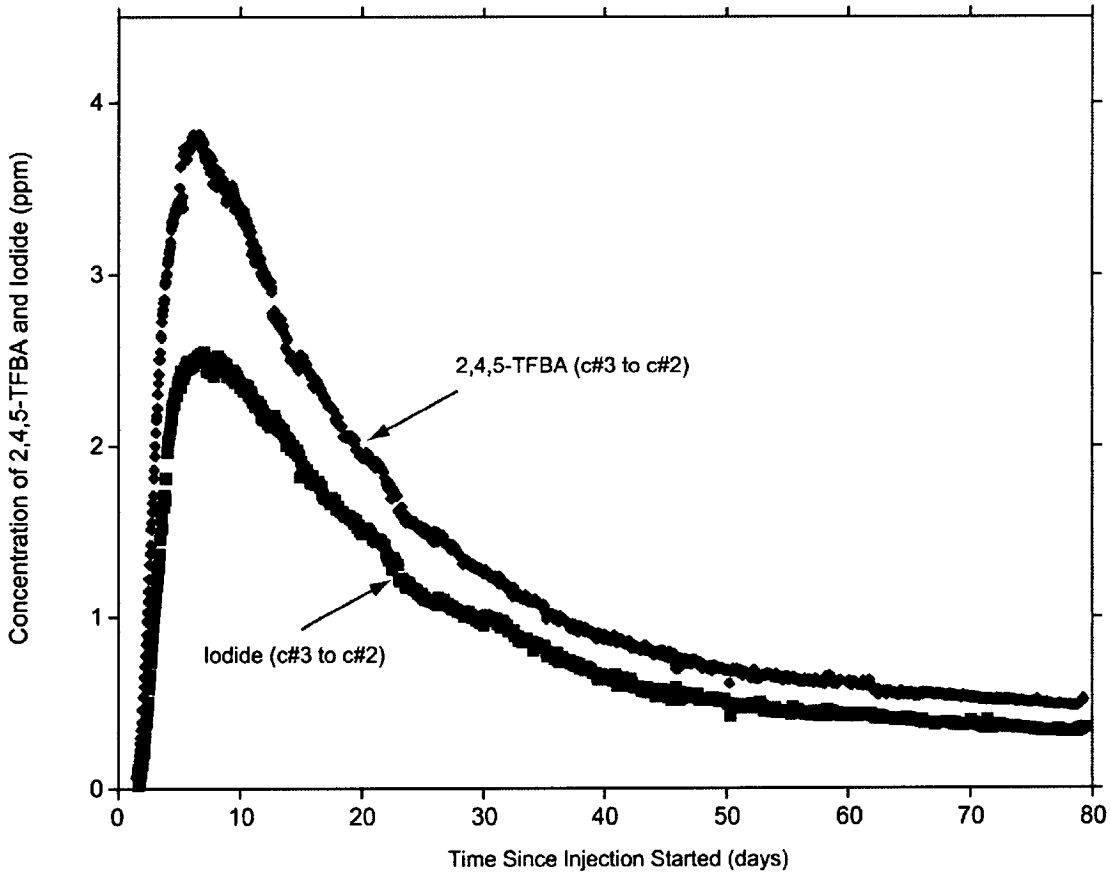

DTN: GS990208312315.001 [159238] (data).

NOTE: C#2 and C#3 refer to UE-25 c#2 and UE-25 c#3, respectively.

Figure 6.3-11. Breakthrough Curves for 2,4,5 TFBA and Iodide Tracer Test from UE-25 c#3 to UE-25 c#2

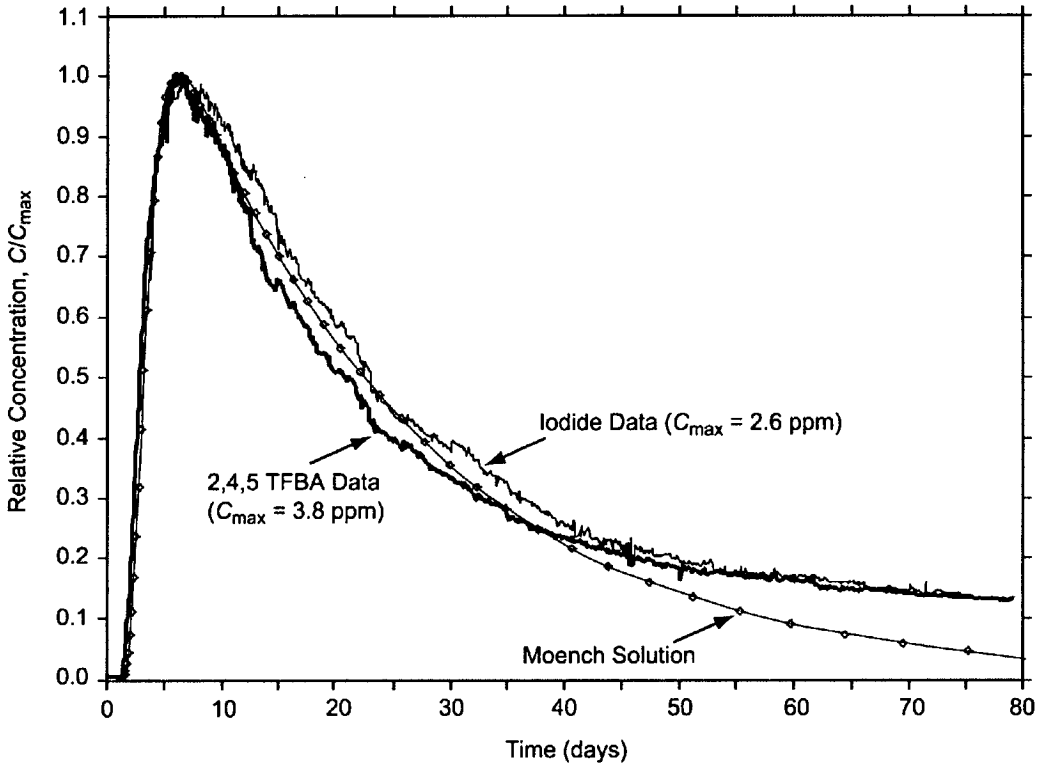

DTN: GS990208312315.001 [159238] (data); Output DTN: GS031008312315.002 (analysis).

NOTE: Flow porosity = 0.0007, storage porosity was not applicable because a single-porosity medium was assumed, and longitudinal dispersivity = 1.45 m. The dots on the model fit curve have no significance.

Figure 6.3-12. Breakthrough Curve for June 17, 1998, 2,4,5 TFBA and Iodide Tracer Test Matched by the Single-Porosity, Purely Convergent Moench Solution

The matched values of longitudinal dispersivity and flow porosity may be sensitive to the mixing lengths assumed for the injection and pumped wells. The mixing lengths represent those lengths within the boreholes through which the tracer enters or exits the aquifer. The 30.5-m mixing length assumed for all solutions is based on the thickness of the transmissive interval within the packed-off Prow Pass interval in c#3 (see Table 6.2-6) and is consistent with the hydrogeology of the interval (Geldon 1996 [100396], pp. 9 to 69).

The residence time of the tracer slug within the borehole is directly proportional to the mixing length. Data collected during the tracer injection indicate that the borehole was flushed in 8.5 hrs (the concentration in the injected interval was measured in the field and found to rise from below detection limit to 2,721 ppm and then back to below detection limit in 8.5 hrs, 8:00 A.M. to 4:30 P.M.) (Umari 2002 [162858], Binder 13, p. 91). When the mixing length is reduced to 0.3 m and only the rising limb of the actual breakthrough curve is matched to the theoretical breakthrough curve from the single-porosity solution of Moench (1989 [101146], assuming minimal diffusion during the rising limb), a longitudinal dispersivity value of 4.27 m and a flow porosity value of 0.0016 are obtained as fitting parameters. Changing the mixing length from 30.5 m to 0.3 m constitutes a two-orders-of-magnitude change in this parameter. Corresponding to this change in the assumed mixing length, the estimates of longitudinal dispersivity and flow porosity change

from 1.45 m and 0.0007 (for a 30.5-m mixing length) and to 4.3 m and 0.0016 (for a 0.3-m mixing length). This is a three-fold change of longitudinal dispersivity and a two-fold change of flow porosity, both less than one order of magnitude. The estimated parameters, therefore, are not very sensitive to the mixing length.

The above porosity value of 0.0007 is in the range of 0.00001 to 0.01 cited in the literature to represent fracture porosity (see, for example, Freeze and Cherry 1979 [101173], p. 408). This implies that the flow network for this test in the Prow Pass Tuff is composed predominantly of fractures.

6.3.1.2.1.2 Single-Porosity, Partially Recirculating Interpretation

When the purely convergent flow field of Figure 6.3-12 is replaced by a partially recirculating flow field, the resulting solution to the advection-dispersion equation changes from the curve labeled "Moench solution" in Figure 6.3-12 to the curve labeled "Modified Moench solution" shown in Figure 6.3-13. The difference between the two solutions reflects the difference in flow field representation and in the fitted values of longitudinal dispersivity and flow porosity used (or implied) for each solution. Two elements of partial recirculation are represented in the partial-recirculation solution, which is obtained using the RECIRC.vi V 1.0 code (STN: 10673-1.0-00 [164432]). Rather than straight converging rays into the production well, the partially recirculating flow field streamlines that are within the capture zone of the production well emanate from the injection well and curve towards the production well (Figure 6.3-14a). The streamlines shown in Figure 6.3-14a are lines of equal stream function values, in which the stream function of the partial-recirculation field is calculated as the sum of the stream functions of a 19.8 L/m sink (production rate) and a 5.7 L/m source (recirculation rate) in a confined aquifer of constant thickness (2-D flow). The volume of rock between pairs of these curved streamlines emanating from the injection well and curving towards the production well constitute distinct pathways for the solute (tracer) to take from the injection to the production well. Three such inter-streamline pathways emanating from the injection well and curving towards the production well (Figure 6.3-14a) are assumed for the partial-recirculation analysis in this section. These pathways, labeled Interstreamline pathway 1, 2, and 3 in Figure 6.3-14a, and the three non-labeled pathways, which are mirror images of them around the horizontal line of symmetry, carry all the tracer mass from injection to production well. Symmetry allows that the analysis be restricted to only three of the six interstreamline pathways emanating from the injection well and curving towards the production well, namely Interstreamline pathway 1, 2, and 3, and that half of the mass of the tracer and half the reinjection flow rate be carried by these three pathways. The Moench (1989 [101146]) single-porosity, purely convergent solution is viewed as the solution of the advection-dispersion equation along a single straight pathway (Figure 6.3-14b). This solution for a particular longitudinal dispersivity value and flow porosity is applied to each of the above three distinct pathways. Because the Moench solution is for a strictly convergent flow field, its application to the first–diverging-then-converging, flow pattern within Interstreamline pathway 1, 2, and 3 in Figure 6.3-14a is an approximation and will introduce some error. A proper delay factor (the advective travel time calculated from the volume of rock of each pathway, the flow rate within the pathway, and the assumed porosity) is used to account for the differences in lengths, or swept volumes, of these pathways relative to the straight purely convergent pathway, and the injected mass is distributed among the three pathways in proportion to the flow in each of them.

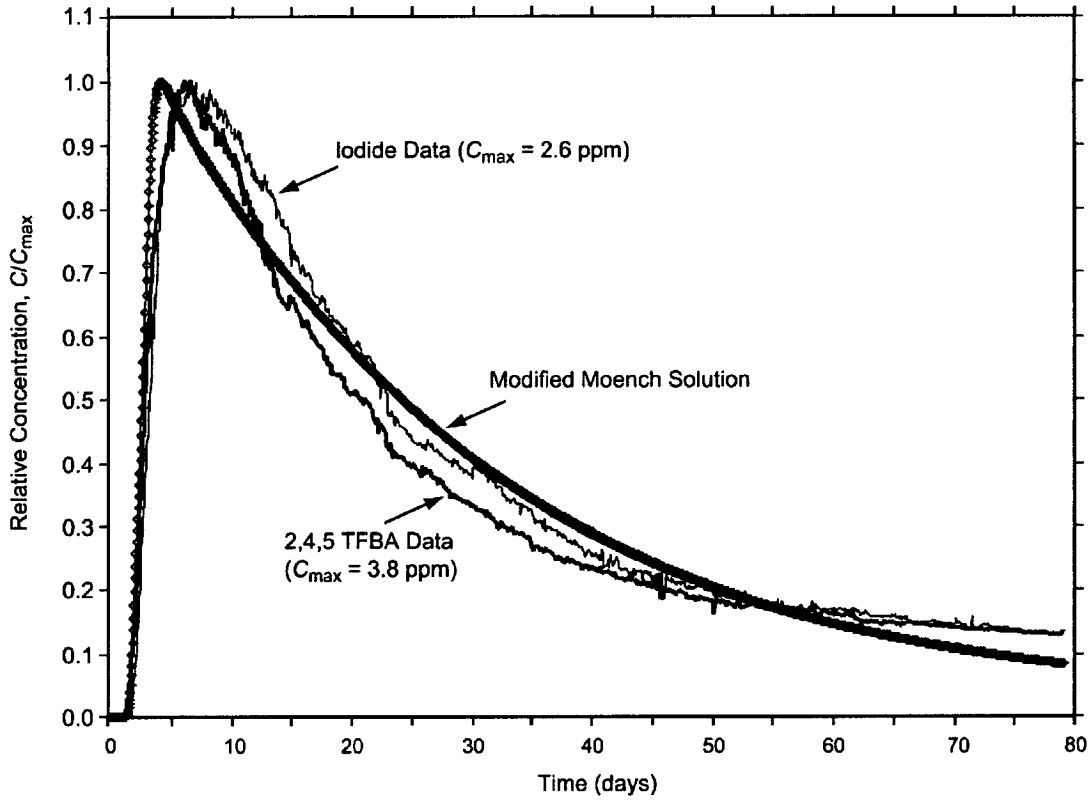

DTN: GS990208312315.001 [159238] (data); Output DTN: GS031008312315.002 (analysis).

NOTE: Three inter-streamline pathways were assumed with delay factors of 2.01 days, 2.99 days, and 3.11 days. The flow porosity = 0.00045, storage porosity was not applicable because a single-porosity solution was assumed, and longitudinal dispersivity = 0.27 m (Pe = 107). Borehole mixing length was 30.5 m.

Figure 6.3-13. Breakthrough Curve for June 17, 1998, 2,4,5 TFBA and Iodide Tracer Test Matched by the Single-Porosity, Partial-Recirculation Solution Derived from Moench

The solutions from Moench (1989 [101146]) for a particular longitudinal dispersivity value, flow porosity, and an instantaneous-slug injection are then superimposed with appropriate delay factors (defined above) to obtain what is considered to be the system's unit response function. The summed curve represents what is seen at the pumped well in response to an instantaneous input function at the injection well in a partial-recirculation flow field.

The second element of partial recirculation is that the reinjected water contains a small amount of tracer; therefore, the tracer is continuously reintroduced into the aquifer. For the calculations presented here, it was assumed that this lag duration is approximately 1 hr, which was the estimated time for travel of the recirculated fluid in the 2.5-cm (1-in) coil-tubing return line (YMP 1998 [104211], Attachment 5, p. 2) from the production well, c#2, to the injection well, c#3 (536 m [1,760 ft] at 5.7 L/min [1.5 gpm]) (Umari 2002 [162858], Binder 10, p. 57). The input concentration curve at the injection well is, therefore, constructed by starting with the breakthrough curve at the pumped (or extraction) well and then lagging it by the "lag duration." The input concentration curve at the injection well is then convolved (Levenspiel 1972 [156839], Chapter 9) with the unit response function to produce the calculated partial-recirculation

breakthrough curve at the production well. Different flow porosity and longitudinal dispersivity values are used in a trial and error process to iteratively repeat the process described above until the calculated partial-recirculation breakthrough curve is as visually close as possible to the measured breakthrough curve.

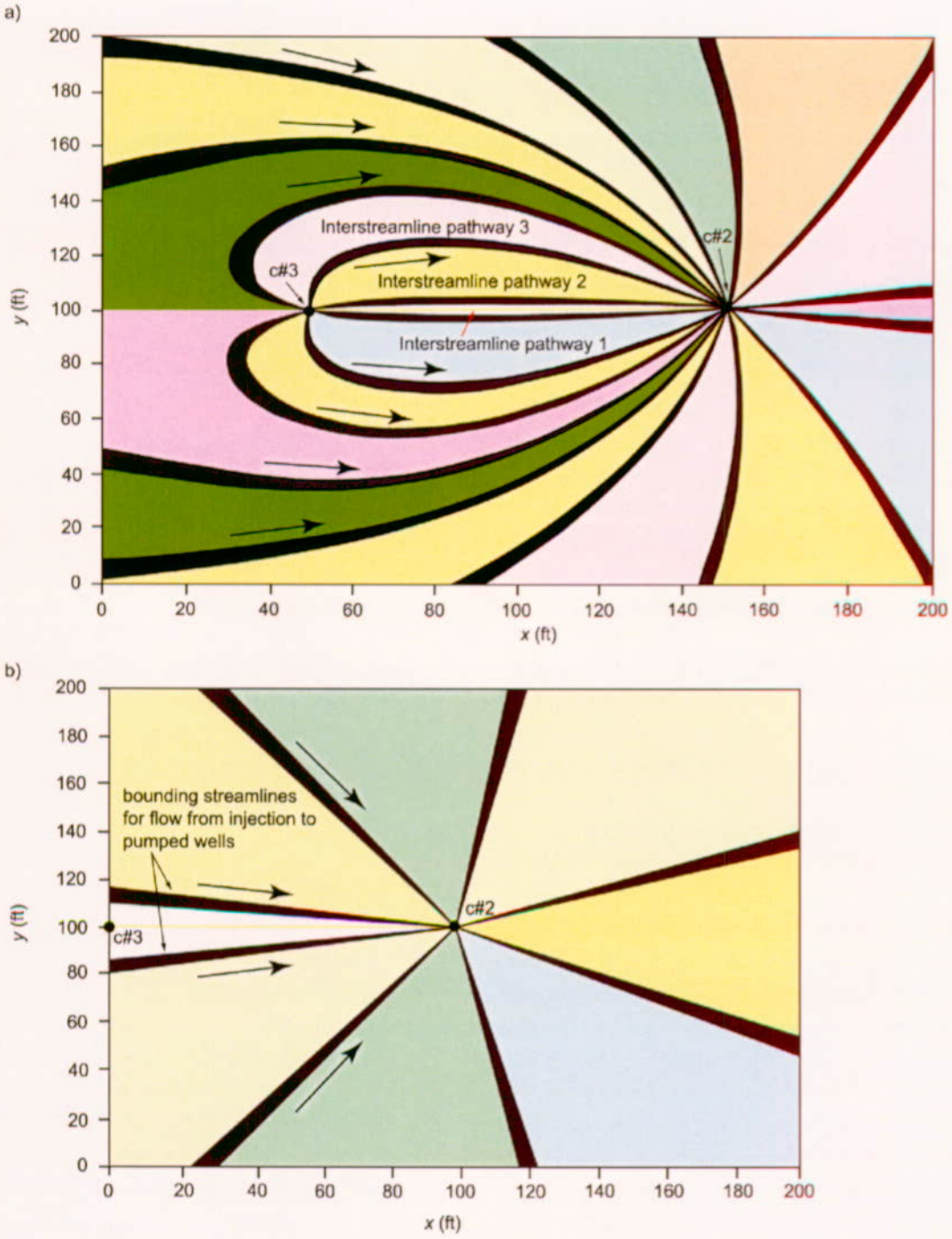

For illustration purposes only

NOTE: English units are shown in the figure because the analysis was conducted in English units.

Figure 6.3-14. Streamlines for a) Partial-Recirculation Flow Field and b) Purely Convergent Flow Field

Using the iterative parameter-matching process described above, a longitudinal dispersivity of 0.27 m (Pe = 107.4) and a flow porosity of 0.00045 were selected as optimal for the single-porosity, partial-recirculation case (as opposed to the 1.45 m and 0.0007 optimal values found earlier for the single-porosity, purely-convergent solution). These parameters result in the calculated partial-recirculation breakthrough curve presented in Figure 6.3-13.

The delay factors for the three inter-streamline pathways inherent in the calculation of the breakthrough curve of Figure 6.3-13 were initially assumed to be 1.83 days for the first pathway, 3.5 days for the second, and 7.5 days for the third (these are the advective travel times calculated from the volume of rock of each pathway, the assumed porosity, and the flow rate within the pathway).

However, use of these delay factors (as defined above) produced a calculated breakthrough curve that did not visually match the actual curve. The visual match was substantially improved by changing the delay factors to 2.01 days, 2.99 days, and 3.11 days, which resulted in the calculated breakthrough curve of Figure 6.3-13. Because these three delay factors are not the ones indicated by the volumes of rock calculated for the three inter-streamline pathways, they are interpreted to represent the uncertainty in either the single-flow porosity value or in the assumed streamline pattern and resulting rock volumes. If the streamline pattern with associated rock volumes is assumed correct, then the delay factors of 2.01, 2.99, and 3.11 days correspond to storage porosities of 0.0005, 0.0004, and 0.0002 for the three inter-streamline pathways, respectively. However, because different porosities for the three pathways are not compatible with the underlying homogeneity assumption, the three porosities provide a range of uncertainty for the single-porosity estimate of 0.00045 used for all partial recirculation cases.

The results shown in Figures 6.3-12 and 6.3-13 indicate that if the breakthrough curves of 2,4,5 TFBA and iodide are analyzed as if they result from a purely-convergent flow field, ignoring that the real flow field is partially recirculating, some error in the derived parameters results. A longitudinal dispersivity of 1.45 m is obtained when purely-convergent conditions are assumed, five times the 0.27 m obtained when the partial-recirculation flow field is recognized. The flow porosity of 0.0007 obtained for purely-convergent conditions is 56% higher than the flow porosity of 0.00045 obtained for partial recirculation.

The partial-recirculation solution shown in Figure 6.3-13, and others in the remainder of Section 6.3.1.2 are not as good fits to the actual tracer breakthrough curves as the purely-convergent solution of Figure 6.3-12, even though the latter ignores the flow field created by partial recirculation. This could either mean that the explicit representation of the partial-recirculation flow field is not important and that the test can be analyzed successfully as a purely-convergent tracer test, or that the homogeneous and isotropic representation of the partial-recirculation flow field presented here does not capture the real partial-recirculation flow field. Perhaps increasing the number of the inter-streamline pathways beyond three to, in effect, "discretize" the flow field more finely would improve the fits. This increased discretization was not attempted.

6.3.1.2.1.3 Dual-Porosity, Partially Recirculating Interpretation

In the dual-porosity case, the medium is comprised of flow and storage components. The flow component is conceptualized as a flow network of (1) continuous fractures and (2) discontinuous fractures with interconnecting segments of matrix. The porosity of the flow component of the medium is referred to as the "flow porosity." The storage component is assumed to consist of dead-end fractures and the part of the matrix not contributing to the flow network. The porosity of the storage component of the medium is referred to as the "storage porosity" (within Section 6.3 of this report, "matrix porosity" means the same thing as "storage porosity"). The flow network is represented by a longitudinal dispersivity and a flow porosity, and the storage component is represented by a storage porosity and a dimensionless matrix diffusion coefficient.

The calculated dual-porosity, partial recirculation solution is predicated upon the single-porosity, partial-recirculation solution presented earlier, i.e., a longitudinal dispersivity of 0.27 m and a flow porosity of 0.00045. Two calculated breakthrough curves obtained for a storage porosity of 0.001 and two dimensionless matrix diffusion coefficients (Gamma), namely 0.000444 and 0.001, are presented in Figure 6.3-15 along with the actual breakthrough curves of 2,4,5 TFBA and iodide.

The free-water molecular diffusion coefficients of 2,4,5 TFBA and iodide are 8.0×10^{-6} cm^2/s and 18.0×10^{-6} cm^2/s, respectively (Bowman 1984, Table 2 [156645]; Skagius and Neretnieks 1986, Tables 2 and 3 [156862]), which corresponds to a ratio of 1:2.25 (TFBA: iodide). When a solution is placed in a porous medium and it diffuses into the matrix, the extent of matrix diffusion is represented by the dimensionless matrix diffusion parameter, Gamma, defined in Moench (1995, Table 1, p. 1826, [148784]). According to Moench (1995 [148784], Table 1, p. 1826), the ratio of the dimensionless matrix diffusion parameter, Gamma, for the two tracers is the same as the ratio of their free-water molecular diffusion coefficients. The Gamma values of 0.000444 and 0.001 were chosen for Figure 6.3-15 because they have the same ratio as the Gamma values of 2,4,5 TFBA and iodide, namely 1:2.25. Figure 6.3-15 shows the effects on matrix diffusion, as represented by the two calculated breakthrough curves, of changing the free-water diffusion coefficient by a factor of 2.25 for a fixed storage porosity of 0.001 and the fixed flow rate of the test. The effect of increasing the free-water diffusion coefficient, which increases Gamma, is a delay of the calculated breakthrough curve for higher Gamma relative to the breakthrough curve for lower Gamma. This "differential matrix diffusion delay" is seen as a horizontal offset between the two calculated breakthrough curves in Figure 6.3-15 and later figures. The larger the difference in Gamma between the two curves, the larger the differential matrix diffusion delay.

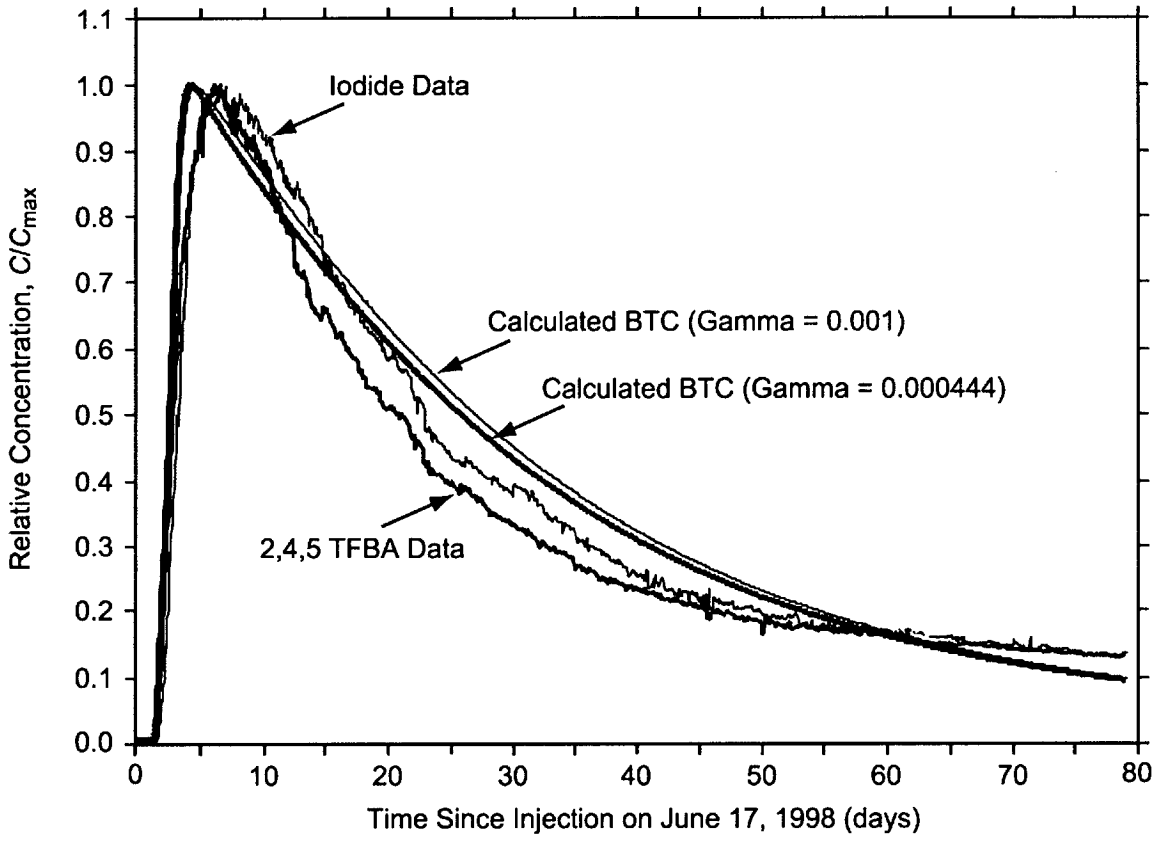

DTN: GS990208312315.001 [159238] (data); Output DTN: GS031008312315.002 (analysis).

NOTE: The breakthrough curves were matched by the dual-porosity, partial-recirculation solution derived from Moench (1995 [148784]) with storage porosity of 0.001 and dimensionless diffusion coefficients, Gamma, of 0.000444 and 0.001. Three inter-streamline pathways were assumed to have delay factors of 2.01 days, 2.9 days, and 3.11 days. Longitudinal dispersivity = 0.27 m (0.9 ft).

Figure 6.3-15. Breakthrough Curve for June 17, 1998, 2,4,5 TFBA and Iodide Tracer Test Matched with a Lower Storage Porosity and a Higher Diffusion Coefficient

In addition, it is seen from a comparison of Figures 6.3-15 and 6.3-16 that this differential matrix diffusion delay for a particular pair of free-water diffusion coefficients (or Gamma values) increases with increasing storage porosity. Figure 6.3-16, which uses the same pair of Gamma values used in Figure 6.3-15, shows that when the storage porosity is increased from the 0.001 value of Figure 6.3-15 to 0.01, the differential matrix diffusion delay is markedly larger than what it is in Figure 6.3-15.

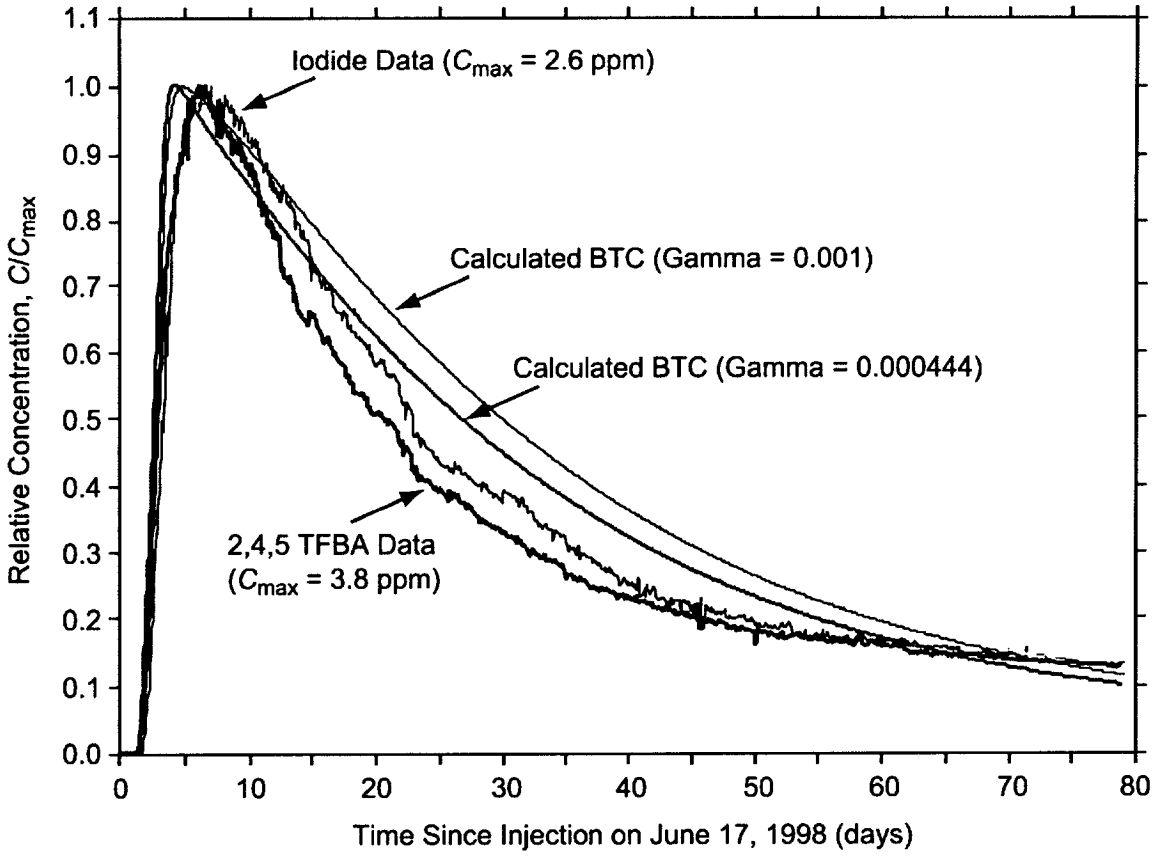

DTN: GS990208312315.001 [159238] (data); Output DTN: GS031008312315.002 (analysis).

NOTE: The breakthrough curves were matched by the dual-porosity, partial-recirculation solution derived from Moench (1995 [148784]) with storage porosity of 0.01 and dimensionless diffusion coefficients, Gamma, of 0.000444 and 0.001. Three inter-streamline pathways were assumed with delay factors of 2.01 days, 2.9 days, and 3.11 days. The flow porosity was 0.00045, and the longitudinal dispersivity was 0.27 m.

Figure 6.3-16. Breakthrough Curve for June 17, 1998, 2,4,5 TFBA and Iodide Tracer Test Matched with a Higher Storage Porosity and a Higher Diffusion Coefficient

The differential matrix diffusion delay between calculated breakthrough curves in Figure 6.3-16 is similar to that between the actual 2,4,5 TFBA and iodide, suggesting a storage porosity value of approximately 0.01. This result is combined with earlier ones to indicate a dual-porosity medium with a flow porosity of 0.00045 (with an uncertainty range of 0.0002 to 0.0005), a storage porosity of 0.01, and a longitudinal dispersivity of 0.27 m. The flow porosity and longitudinal dispersivity characterize a flow network within this medium comprised of (1) continuous fractures and (2) discontinuous fractures with interconnecting segments of matrix. The storage porosity characterizes a storage component of the conceptualized dual-porosity medium consisting of dead-end fractures and the part of the matrix not contributing to the flow network.

6.3.1.2.2 2,3,4,5 Tetrafluorobenzoic Acid Test from c#1 to c#2

On July 31, 1998, the nonsorbing tracer 2,3,4,5 tetrafluorobenzoic acid (2,3,4,5 TeFBA) was injected in the Prow Pass interval of c#1 while c#2 continued to be pumped at the rate of approximately 19.3 L/min (5.1 gpm) (Umari 2002 [162858], Binder 13, Sections M-23 to M-25; Binder 14, Section M-40; Binder 15, Section M-34, pp. 187, 197). Breakthrough of this tracer occurred on August 17, 1998 in the water pumped out of c#2, and the concentration eventually rose to a maximum of around 90 ppb, approximately 65 days after tracer injection (Figure 6.3-17). The results of this tracer test were used to qualitatively assess flow heterogeneity at the C-wells (see Table 6.3-1)

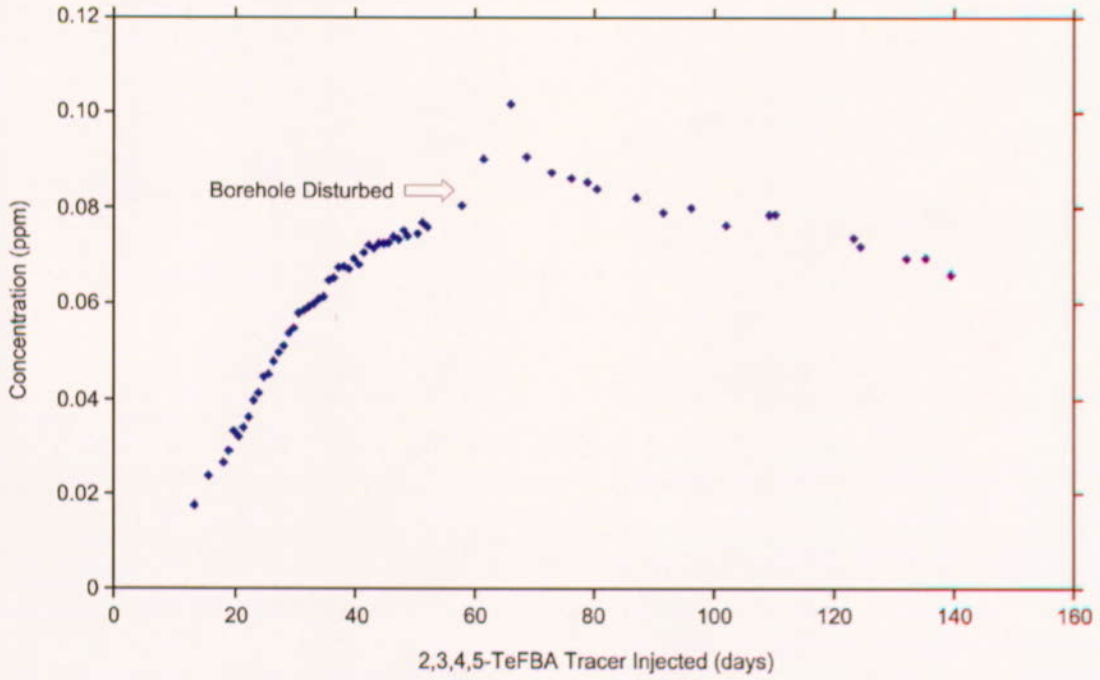

DTN: MO0308SPATRCRC.000 [164821].

Figure 6.3-17. Breakthrough Curve for 2,3,4,5 TeFBA Tracer Test in Prow Pass from UE-25 c#1 to UE-25 c#2

6.3.2 Flow Anisotropy at the Scale of the C-wells from Nonsorbing Tracer Arrival Times

The comparisons of tracer responses resulting from injections into well c#1 and into either well c#2 or c#3 (while pumping the other well) provided some insights into flow heterogeneity/ anisotropy at the scale of the C-wells. Table 6.3-1 lists the ratios of peak arrival times or first arrival times for nonsorbing tracers between c#1 and the production well (either c#2 or c#3) and between c#2 and c#3 for all tests in which a comparison was possible. For a homogeneous, isotropic medium, the arrival times under radial flow conditions are expected to vary as r_L^2, the distance squared between injection and production well (Guimerà and Carrera 2000 [156830], Equation 6). The ratios of r_L^2 values corresponding to each case are also listed in Table 6.3-1. If

the ratio of arrival times is less than the ratio of distances squared, then the direction from c#1 to the production well is a preferred flow orientation; on the other hand, if the ratio of arrival times is greater than the ratio of distances squared, then the direction from c#2 to c#3 is a preferred flow orientation. Furthermore, the ratio of arrival times divided by the ratio of distances squared can be taken as a measure of the flow anisotropy ratio for the two different directions relative to the production well (note that these two directions are not strictly orthogonal). The ratios of tracer arrival times and r_L^2 values are in reasonably good agreement in all three cases, with apparent flow anisotropy ratios (c#1 to production well direction divided by c#2-c#3 direction) varying from 0.77 to 1.42. These relatively small ratios suggest that flow anisotropy at the scale of the C-wells may be relatively small despite the apparent orientation of the fracture network in the general direction of c#1 to c#2 (Geldon 1993 [101045], pp. 43 to 51). The apparent flow anisotropy ratios deduced from the tracer arrival times should be carefully distinguished from the flow anisotropy ratios derived in Section 6.2.6, which were based on drawdown observations over much larger scales.

Table 6.3-1. Ratios of Observed Tracer Arrival Times and Distances Squared, as Well as Apparent Flow Anisotropy Ratios, for C-wells Nonsorbing Tracer Tests

Tests (Injection Well)	$Time_{c\#1}$/ $Time_{c\#2\text{-}c\#3}$[(a)]	$r_L^2{}_{c\#1}$/ $r_L^2{}_{c\#2\text{-}c\#3}$[(a)]	Anisotropy Ratio[(a)]
Bullfrog: PFBA (c#2) and iodide (c#1)[(b)]	6	8.5	1.42
Bullfrog: 2,6-DFBA (c#2) and pyridone (c#1)[(c)]	11	8.5	0.77
Prow Pass: iodide and 2,4,5-TFBA (c#3) and 2,3,4,5-TeFBA (c#1)[(d)]	10	8.3	0.83

DTNs: GS010508312315.001 [155860]; GS990208312315.001 [159238]; LA0007PR831231.001 [156043] (data); GS030508312314.003 [164425], p. 6, Table 1, borehole separations).

NOTE: c#1, c#2, and c#3 are abbreviations for boreholes UE-25 c#1, UE-25 c#2, and UE-25 c#3. r_L^2 is the distance squared between injection and production wells.

(a) $Time_{c\#1}$ and $r_L^2{}_{c\#1}$ are the time and distance, respectively, between c#1 and the production well (either c#2 or c#3, depending on the test), and $Time_{c\#2\text{-}c\#3}$ and $r_L^2{}_{c\#2\text{-}c\#3}$ are the time and distance, respectively between c#2 and c#3. Columns 2 and 3 give the ratios of these times and distances. Ratio is for c#1 to production well direction divided by c#2 to c#3 direction. For the anisotropy ratio, a value greater than 1.0 indicates that the c#1 to production well direction is the preferred flow orientation.

(b) Both tests conducted with 2.5 to 3.5% recirculation into injection well. Peak tracer arrivals compared.

(c) Both tests conducted with no recirculation. First tracer arrivals compared.

(d) c#3-to-c#2 test conducted with 30% recirculation; c#1-to-c#2 test conducted with no recirculation. Peak tracer arrivals compared.

6.3.3 Summary of Conceptual Models and Parameters from Nonsorbing Tracer Tests at the C-wells

Uncertainty in the values of longitudinal dispersivity, flow porosity, and matrix (or storage) porosity result from physical processes, such as the scale-dependence of dispersivity (when

comparing tracer tests conducted from borehole c#1 to those conducted between boreholes c#2 and c#3), as well as from variability in the transport characteristics of the tracer materials. However, there is good agreement in dispersivity values obtained from tracer tests conducted between boreholes c#2 and c#3 in the Bullfrog and Tram intervals. Peclet numbers range from 11 to 15; therefore, the longitudinal dispersivities are similar (Table 6.3-2).

The breakthrough times are identical for the iodide and the DFBA tracer tests (Table 6.3-2), and the advective travel times are within 10 percent. Therefore, the inferred flow porosities are similar, which implies that similar flow pathways are used by the tracers in those tests. These differences can be explained by the different thicknesses of the zones tested: the iodide tracer test was conducted in the combined Bullfrog-Tram zone, and the DFBA tracer test was conducted in the Lower Bullfrog zone.

The parameter estimates are robust because the visual-graphic match is close to the PEST fit (which is based on the dual-porosity analytical model.) The differences are less than 5% for all parameters except matrix porosity, and these estimates vary by only 0.03.

The estimated flow porosities suggest that the pathways between boreholes c#2 and c#3 in the Bullfrog and Tram intervals are not well-connected. This possibility is supported by the interpretation of the higher-than-expected flow porosities for the Bullfrog and Tram Tuffs. The microsphere responses (Section 6.3.4) are consistent with this interpretation. The arrival of the microspheres at the recovery borehole indicates the existence of a connected pathway, somewhere, with an aperture at least 0.36 μm (the diameter of the spheres).

Table 6.3-2. Summary of Results and Transport Properties for the Bullfrog and Tram Tuffs from Nonsorbing Tracer Tests.

	Iodide test from c#2 to c#3 in Bullfrog-Tram	DFBA test from c#2 to c#3 in Lower Bullfrog	Pyridone test from c#1 to c#3 in Lower Bullfrog
Breakthrough (days)	5.07	5.07	56.3
Peak concentration (μg/L)	99.5	251	0.210 (final value)
Peclet number	11	12–15	11
Dispersivity (m)	2.6	2.4–1.9	6.2
Flow porosity, ϕ_f (%)	8.6	9.9–7.2	NA
Matrix (or storage) porosity, ϕ (%)	19	8.8–13.2	NA

DTNs: GS960808312315.001 [159235] (Iodide data) and GS010508312315.001 [155860] (DFBA and Pyridone data); Output DTN: GS031008312315.002 (analysis).

NOTES: NA: the value is not available.
c#1, c#2, and c#3 are abbreviations for boreholes UE-25 c#1, UE-25 c#2, and UE-25 c#3, respectively.

The estimates of flow porosity cannot be separated from the parameter h, which represents a uniform aquifer thickness. In conducting tracer tests in isolated, permeable intervals in fractured rock, it is difficult to identify a meaningful thickness because transport occurs through an interconnected network of fractures. For this report, we have assumed that the appropriate

thickness is the effective thickness as previously reported in Geldon (1996 [100396], pp. 12 to 20).

This report presents the first unequivocal tracer testing from borehole c#1 to c#3 in the Lower Bullfrog test and from c#1 to c#2 in the Prow Pass test. The preliminary results suggest that the arrival time from c#1 to c#3, 56.3 days, is consistent with the arrival time from c#2 to c#3, 5.07 days, because, as implemented in the Moench (1989 [101146]) solution, the arrival time is directly proportional to the square of the distance between injection and production wells (see Section 6.3.2).

Tracer testing in the Prow Pass interval (Table 6.3-3) showed different transport characteristics than those obtained in the Bullfrog and Tram intervals. The flow porosity was found to be 0.00045 in the Prow Pass as opposed to 0.072 to 0.099 in the Bullfrog and Tram Tuffs (Table 6.3-2). This result indicates that the flow network in the Prow Pass is dominated by interconnected fractures (fracture porosity is in the range from 0.00001 to 0.01), whereas in the Bullfrog and Tram, it was dominated by discontinuous fractures with interconnecting segments of matrix. Alternatively, the flow heterogeneity in the Bullfrog and Tram Tuffs may have been such that a vast majority of the water produced from c#3 came from locations that were not in communication with the injection wells (i.e., only a small amount of the production flow rate came from the direction of the injection wells).

Longitudinal dispersivity in the Prow Pass Tuff testing at the scale of the distance between c#2 and c#3 was calculated as 0.27 m, whereas it was 1.9 to 2.6 m in the Bullfrog and Tram intervals at the same scale. A relatively small dispersivity is consistent with a flow network dominated by interconnected fractures (Prow Pass), and a relatively large dispersivity is consistent with a flow network dominated by discontinuous fractures with interconnecting segments of matrix (Bullfrog and Tram) because the more the actual microscopic flow pathways are different from the macroscopic, averaged, flow pathway, the larger is the longitudinal dispersivity. Clearly, a flow network dominated by discontinuous fractures with interconnecting segments of matrix (Bullfrog and Tram) would have more microscopic flow pathways than a flow network dominated by interconnected fractures (Prow Pass).

The storage porosity (or matrix porosity) calculated for the Prow Pass Tuff was 0.01 (Table 6.3-3), whereas it was 0.088 to 0.19 for the Bullfrog and Tram (Table 6.3-2). A small storage porosity is consistent with a dual-porosity medium dominated by interconnected fractures (Prow Pass). In such a medium, the storage component, which is assumed to consist of dead-end fractures and the part of the matrix not contributing to the flow network, would be dominated by fractures, which have very small porosities. Similarly, a large storage porosity is consistent with a dual-porosity medium dominated by discontinuous fractures with interconnecting segments of matrix (Bullfrog and Tram). In such a medium, the porosity of the storage component (dead-end fractures and the part of the matrix not contributing to the flow network) would be dominated by the large porosity of the matrix component of storage.

Table 6.3-3. Summary of Results and Transport Properties in a Partly Recirculating Tracer Test from Borehole c#3 to c#2 and from Borehole c#1 to c#2, Prow Pass Tuff

Parameter	2,4,5 TFBA & Iodide: c#3 to c#2		2,3,4,5 TeFBA: c#1 to c#2
Breakthrough (days)	1.67		17
Peak concentration (ppm)	TFBA : 3.7 Iodide : 2.7		0.09
	Single-Porosity, Partial Recirc. Solution	Dual –Porosity, Partial Recirc. Solution	
Longitudinal dispersivity (m)	0.27	0.27	
Peclet number	107.4	107.4	
Flow porosity, ϕ_f	0.00045	0.00045	
Gamma (dimensionless matrix diffusion coefficient)	N/A	0.000444, 0.001(TFBA and Iodide, respectively)	
Storage porosity, ϕ	N/A	0.01	

DTNs: GS990208312315.001 [159238] and MO0308SPATRCRC.000 [164821] (data); Output DTN: GS031008312315.002 (analysis).

NOTE: c#1, c#2, and c#3 are abbreviations for boreholes UE-25 c#1, UE-25 c#2, and UE-25 c#3, respectively. Borehole mixing length was assumed to be 30.5 m.

N/A stands for "Not Applicable."

6.3.4 Multiple Tracer Tests with Sorbing Solutes and Colloid Tracers at the C-wells

6.3.4.1 Introduction and Objectives

This section describes the conduct and interpretation of two cross-hole tracer tests between c#2 and c#3 in which multiple solute tracers and colloid tracers (carboxylate-modified latex (CML) microspheres) were simultaneously injected. One test was conducted in the Lower Bullfrog Tuff and the other was conducted in the Prow Pass Tuff (referred to as the Bullfrog test and the Prow Pass test, respectively). The objectives of the multiple-tracer tests in the fractured tuffs at the C-wells included the following:

- Testing/validating the applicability of a dual-porosity conceptual transport model (see Section 6.3.4.2) in the saturated, fractured volcanic tuffs that underlie Yucca Mountain.
- Obtaining estimates of key transport parameters in the flow system, including parameters for colloid transport.
- Assessing the applicability of laboratory-derived tracer transport parameters to field-scale transport predictions.

The latter objective is important because radionuclides cannot be tested in the field, so favorable comparisons of laboratory- and field-scale transport of nonradioactive tracers can lend credibility to the practice of using laboratory-derived radionuclide transport parameters in field-scale predictive simulations.

This section also summarizes laboratory experiments that were conducted to support the C-wells field test interpretations and to provide the comparisons between laboratory-derived transport parameters and field-scale transport parameters. Special emphasis is given to the sorption behavior of the lithium ion, which was used as a sorbing tracer in the field tracer tests.

6.3.4.2 Dual-Porosity Conceptual Transport Model

A consistent observation in all hydrogeologic units below the water table at the C-wells is that bulk permeabilities (determined from aquifer tests) exceed matrix permeabilities (determined from laboratory core measurements) by 2 to 6 orders of magnitude (Geldon 1993 [101045], pp. 58 to 64; Geldon 1996 [100396], pp. 69 to 71). This ratio of bulk to matrix permeabilities suggests that flow in the Miocene tuffs at the C-wells occurs predominantly in fractures. However, matrix porosities in the C-wells range from about 0.10 to 0.35 (Geldon 1993 [101045], pp. 58 to 64), so most of the water in these rocks is stored in the pores of the matrix. Radionuclide and tracer transport in fractures, therefore, could be attenuated by diffusive mass transfer between the fractures and the rock matrix, a process known as matrix diffusion. Matrix diffusion in fractured systems has been discussed and modeled at length by Neretnieks (1980 [101148], pp. 4379 to 4397), Grisak and Pickens (1980 [101132]), Tang et al. (1981 [101160], pp. 555 to 564), Maloszewski and Zuber (1984 [156840]; 1985 [148312]), and Moench (1995 [148784]). A system exhibiting fracture and matrix flow frequently is called a "dual-porosity, dual-permeability" system. When the matrix permeability is small compared to the fracture permeability (e.g., smaller by a factor of 100 or more), the matrix permeability can be assumed to be negligible in transport calculations, and the system is often referred to as simply a "dual-porosity" system. It has been suggested elsewhere that the saturated zone in the vicinity of Yucca Mountain should behave as a dual-porosity system (Robinson 1994 [101154]). This concept has important transport implications, particularly for sorbing radionuclides, because it suggests that solutes moving through fractures will have access to a very large surface area for sorption once they diffuse out of fractures and into adjacent matrix pores.

6.3.4.3 Tracer Testing Strategy

To accomplish all of the test objectives mentioned in Section 6.3.4.1 in a reasonable time, cross-hole, forced-gradient tracer tests were conducted in which three different solute tracers having different physical and chemical properties were simultaneously injected into the lower Bullfrog and Prow Pass flow systems. By dissolving the tracers in the same solution and simultaneously introducing them, it was ensured that they all experienced the same flow field and, hence, initially followed identical flow pathways through the system. This assurance is especially important in field tests where it can be extremely difficult to reproduce exactly flow conditions for different tracer injections because of equipment problems and possible irreversible changes in the system (e.g., well development, biofouling, unsteady drawdown, etc.). The test interpretations were then based on comparing the responses of the different tracers. The tracers used in each test included two nonsorbing solutes having different diffusion coefficients (bromide and penta-fluoro-benzoate) and a weakly-sorbing, ion-exchanging solute (lithium ion). The bromide and pentafluorobenzoate were verified to be nonsorbing in a limited set of batch adsorption experiments involving the seven different C-wells tuff lithologies listed in Tables 6.3-16 and 6.3-17 (DTN: LA0302PR831231.001 [162605]). Carboxylate-modified-latex polystyrene (CML) microspheres were also injected in both tests to serve as colloid tracers. These microspheres have negatively charged hydrophilic surfaces at pH > 5, which tends to minimize their attachment to rock surfaces (Reimus 1995 [101474], p. 35, Table 3.6). The properties of all tracers are summarized in Table 6.3-4 along with the injection masses and concentrations used in the tracer tests.

The rationale for using multiple solute tracers in cross-hole tests is illustrated in Figure 6.3-18. The left plot of this figure shows hypothetical solute tracer responses (log normalized concentration versus log time) for a cross-hole tracer test with a short injection pulse in a single-porosity system. Note that there is no distinction between nonsorbing tracers with different diffusion coefficients in this plot because there is no secondary porosity for the tracers to diffuse into and, hence, no separation of their responses. The sorbing tracer response is delayed in time and lower in concentration than the nonsorbing tracers. In contrast, the right plot of Figure 6.3-18 shows hypothetical solute tracer responses for a test in a dual-porosity system. In this case, there is a separation between nonsorbing tracers with different diffusion coefficients, with the higher diffusivity tracer exhibiting a lower peak concentration and a longer tail than the lower diffusivity tracer. This separation occurs because the higher-diffusivity tracer diffuses more readily into the matrix than the lower-diffusivity tracer, resulting in a lower recovery at early times but a longer tail due to subsequent diffusion back out of the matrix after the tracer pulse has passed.

Table 6.3-4. Tracer Characteristics, Injection Masses, and Injection Concentrations in the Two Multiple-Tracer Tests

Solute Tracers			
Parameters	**PFBA**	**Bromide**	**Lithium**
Free water diffusion coefficient, D_f (cm^2/sec) [(a)]	7.2×10^{-6} [(b)]	2.1×10^{-5} [(c)]	1.0×10^{-5} [(c)]
Sorption[(d)]	None[(d)]	None[(d)]	Weak (ion exchange)
Bullfrog test injection mass (kg)	12.1	165.6	14.39
Bullfrog test injection concentration (mg/L) [(e)]	1000	13800	1200
Prow Pass test injection mass (kg)	12.0	30.6	16.0 [(f)]
Prow Pass test injection concentration (mg/L) [(g)]	2000	5100	2670

CML Microsphere Tracers			
Tracer (fluorescent dye color)	**Test**	**Injection Amount[(j)]**	**Injection Concentration[(k)]**
0.36-μm CML microspheres (yellow) [(h)]	Bullfrog	3.6×10^{14} spheres	4.6×10^{10} spheres/L
0.64-μm CML microspheres (blue) [(i)]	Prow Pass	3.0×10^{14} spheres	5.1×10^{10} spheres/L
0.28-μm CML microspheres (orange) [(i)]	Prow Pass	2.1×10^{14} spheres	3.5×10^{10} spheres/L
0.28-μm CML microspheres (yellow)	Prow Pass	2.1×10^{14} spheres	3.5×10^{10} spheres/L

DTNs: LA0007PR831231.001 [156043] (Bullfrog Test), LAPR831231AQ99.001 [140134] (Prow Pass Test); LA0302PR831231.001[162605].

Sources: Reimus (2000 [165125]), Reimus (2000 [162855]), Reimus (2000 [162852]), Reimus (2003 [165129], including Attachment A).

NOTE:
(a) Callahan et al. (2000 [156648], Table 7) found that diffusion coefficients in rock matrices had the same ratio as free water diffusion coefficients for PFBA and bromide.
(b) Benson and Bowman (1994, p. 1125 [122788]; 1996 [153427]).
(c) Newman (1973 [148719], p. 230, Table 75-1); based on ionic conductances at infinite dilution.
(d) Based on results of laboratory batch sorption experiments (DTN: LA0302PR831231.001 [162605]).
(e) Tracers were dissolved in ~12,000 L of groundwater from c#3 (Reimus 2000 [162855]).
(f) Lithium was injected as 33.3 kg LiBr and 80.8 kg LiCl (Reimus 2000 [162855]).
(g) Tracers were dissolved in ~6,000 L of groundwater from c#2 (Reimus 2000 [162852]).
(h) The microsphere injection was initiated 3.5 hours after the start of injection of solute tracers in the Bullfrog test. The microsphere and solute injections ended at the same time. (Reimus 2000 [162855]).
(i) These microspheres were injected 2 days prior to solute tracers in the Prow Pass test (dispersed in ~6,000 L of ground water from c#2) to avoid the possible destabilization of the microspheres in the high-ionic strength injection solution containing the solute tracers (Reimus 2000 [162852]).
(j) Based on average concentration measured in a dilution of a known volume fraction of the microsphere stock solution injected. Sources: concentration measurements (Reimus 2000 [165125]); preparation of dilutions for Bullfrog test (Reimus 2000 [162855]); preparation of dilutions for Prow Pass test (Reimus 2000 [162852]); and summary of calculations (Reimus 2003 [165129], pp. 115 to 116; Attachment A, pp. A-1 to A-6).
(k) Injection concentrations calculated by dividing number of spheres injected by injection volumes of 12,000 L x (6.5/10) = 7,800 L (Bullfrog test) and 6,000 L (Prow Pass test). The factor of 6.5/10 for the Bullfrog test accounts for the fact that the microspheres were injected for only 6.5 hours of the total of 10 hrs that the 12,000 L was injected.

Figure 6.3-18 also shows two possible responses for a sorbing tracer: (1) one with sorption occurring in the matrix and (2) one with sorption occurring in the fractures and the matrix (if the

fractures have sorptive mineral coatings or are filled with sorptive granular material). Note that in the matrix-only case, the sorbing tracer response is attenuated in peak concentration but not significantly in time relative to the nonsorbing tracers, whereas in the latter case both a concentration and a time attenuation are apparent. The minimal time attenuation of the sorbing tracer relative to the nonsorbing tracers in the matrix-only sorption case is primarily a result of the relatively short duration of a typical cross-hole tracer test relative to characteristic times of diffusion into the matrix; as travel times increase, the time and concentration attenuation of a sorbing tracer relative to nonsorbing tracers should increase.

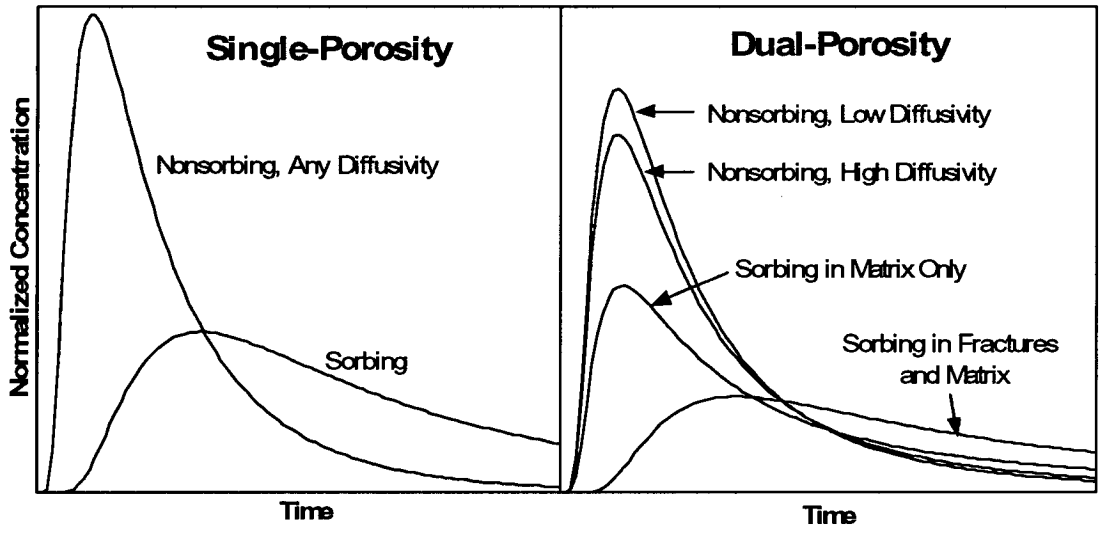

For illustration purposes only

NOTE: The figure illustrates how multiple tracers can be used to distinguish between single- and dual-porosity systems (Reimus 2003 [165129], Attachment A, pp. A-198 to A-208). As cross-hole travel times increase, the "nonsorbing, high diffusivity" and "sorbing, matrix only" peaks on the right-hand plot will begin to arrive later than the "nonsorbing, low diffusivity" peak. The curves were generated using the RELAP V 2.0 code (STN: 10551-2.0-00 [159065]) with arbitrary input parameters intended to qualitatively illustrate the differences between tracer responses in single- and dual-porosity media. The inputs and outputs of the simulations were not submitted to the TDMS and do not have a DTN.

Figure 6.3-18. Hypothetical Cross-Hole Responses of Tracers with Different Physical and Chemical Characteristics in Single- and Dual-Porosity Media

The hypothetical responses in Figure 6.3-18 suggest that a multiple tracer test involving the simultaneous injection of nonsorbing solute tracers with different diffusion coefficients and a sorbing tracer should allow qualitative discrimination between a single-porosity system and a dual-porosity system. That is, if nonsorbing tracers of different diffusion coefficients have different responses and/or if a sorbing tracer has a peak concentration that occurs at about the same time as a nonsorbing tracer but with a lower concentration, then a dual-porosity system is suggested. This approach was taken by Maloszewski et al. (1999 [156841]), although they used only multiple nonsorbing tracers in a fractured sandstone/quartzite/slate system. Furthermore, if a dual-porosity response is observed and one knows the relative diffusion coefficients of the two nonsorbing tracers, it should be possible to determine how much of the apparent dispersion in the responses is due to true hydrodynamic dispersion and how much is due to matrix diffusion. Both

of these processes have the effect of broadening the response curves/increasing the tailing of the tracers, but only matrix diffusion can cause a separation of the responses of the two tracers. The magnitude of the separation can be used to distinguish quantitatively between the effects of matrix diffusion and hydrodynamic dispersion, resulting in unambiguous estimates of mean residence times, dispersion coefficients, and matrix diffusion parameters in a tracer test.

Effective sorption parameters associated with the response of a simultaneously injected sorbing tracer can then be estimated by assuming that the sorbing tracer experiences the same mean residence time, longitudinal dispersivity, and matrix diffusion (subject to its diffusion coefficient) as the nonsorbing tracers. In this case, only the sorption parameter(s) need be adjusted to obtain a model fit/match to the sorbing tracer response. Likewise, colloid filtration/attachment and detachment parameters can be obtained by assuming that the CML microspheres experience the same mean residence times and longitudinal dispersivities as the nonsorbing solute tracers. For the microspheres, matrix diffusion is assumed to be negligible because of their large size and small diffusivity relative to the solutes.

6.3.4.4 Conduct of Tracer Tests

The cross-hole tracer tests were conducted between wells c#2 and c#3, which are separated by about 30 m at the surface (Figure 6.3-2). c#2 was used as the tracer injection well and c#3 as the production well in the lower Bullfrog Tuff (Reimus 2000 [162855]; Reimus 2000 [164624]). In the Prow Pass Tuff, c#3 was the injection well, and c#2 was the production well (Reimus 2000 [162852]). The natural gradient at the C-wells site, though quite flat, is believed to be oriented in the direction from c#3 to c#2 (Figure 6.3-2), so tracer movement in the Bullfrog test was against the gradient, and in the Prow Pass test, it was with the gradient. Prior to injecting tracers, a weak-dipole flow field was established in each test by reinjecting a fraction of the water pumped from the production well into the injection well. The production and recirculation flow rates are summarized in Table 6.3-5. The weak-dipole flow configuration was chosen over a convergent flow configuration (no recirculation) to ensure that tracers were "flushed" out of the injection wellbore instead of relying on the flow field induced by pumping the production well to draw tracers out of the wellbore. Pressure transducers continuously monitored pressures between the packers, above the upper packer, and below the lower packer in each well during the tests. Because of the drastic differences in transmissivity of the two test intervals, the water level drawdown in the Prow Pass interval (62 m) was over an order of magnitude greater than the drawdown in the Bullfrog interval (5 m) despite the fact that the production rate in the Bullfrog test was ~30 times greater than in the Prow Pass test.

After establishing a reasonably steady weak-dipole flow field, as indicated by stable water levels in the packed-off intervals, the recirculation of produced water into the injection well was replaced by the injection of a groundwater solution containing the three solute tracers. The tracer solution was injected at the same flow rate as the recirculation and without any interruption to the flow, and when the injection was complete, recirculation was immediately resumed without interruption. Thus, there were no pressure or flow transients introduced to the system as a result of tracer injection. Recirculation of produced water was discontinued after 40 days in the Bullfrog test, but it was maintained throughout the Prow Pass test. The Bullfrog test was conducted for 337 days, and the Prow Pass test was conducted for 127 days.

Table 6.3-5. Average Production and Recirculation Rates During the Bullfrog and Prow Pass Tracer Tests and Summary of Flow Interruptions During the Prow Pass Test

Test	Production Rate (L/min)	Recirculation Rate (L/min)	Recirculation Ratio
Bullfrog[a]	568	19 (zero after 40 days)	0.033
Prow Pass[b]	19	5.7	0.3
Prow Pass Test Flow Interruptions:[c]			
Interruption	**Flow Shut Off**	**Flow Turned On**	**Duration (hr)**
1	11/14/98, ~9:00 am	11/14/98, ~11:00 pm	~14
2	11/23/98, ~9:00 am	11/30/98, ~4:00 pm	~175
3	12/21/98, ~9:00 am	1/4/99, ~11:00 pm	~337

DTNs: GS981008312314.002 [147068]; GS981008312314.003 [144464] (Bullfrog rates); and DTN: GS010799992315.001 [157067] (Prow Pass rates).

NOTE: (a) Injection well was c#2, production well was c#3. Test initiated in October 1996.
(b) Injection well was c#3, production well was c#2. Test initiated in September 1998.
(c) Microsphere tracers were injected on 9/23/98, and solute tracers were injected on 9/25/98.

The Prow Pass test featured three different flow interruptions (two intentional) during the tailing portion of the test. The times and durations of these interruptions are summarized in Table 6.3-5. The first interruption was unplanned and occurred as a result of a diesel generator failure. The latter two interruptions were intentional and coincided with the Thanksgiving and Christmas-New Year's holiday breaks, respectively. In addition to the practical consideration of not staffing the remote field site over the holidays, these flow interruptions offered the opportunity to obtain independent confirmation of matrix diffusion in the flow system. If a flow interruption is introduced during the tailing portion of a tracer test in a dual-porosity medium when tracers are diffusing back out of the matrix, then an increase in nonsorbing tracer concentrations should result when flow is resumed.

Water samples were collected at the production well throughout both tests using an automatic sampler. The sampling interval was gradually increased as the tests progressed. Sampling of the injection interval was not possible in the Bullfrog test, but a sampling loop that was designed to continuously mix the injection interval in c#3 was implemented in the Prow Pass test. Unfortunately, the submersible pump used to bring water to the surface generated more heat than could be efficiently removed from the loop, so the use of the loop for mixing had to be abandoned to prevent overheating of the downhole instrumentation. However, the loop was used 40 days into the Prow Pass test to obtain samples over a 10-hr period to assess how well the injection wellbore had been purged of tracers by the reinjection of production water.

Groundwater samples were analyzed for bromide (Br^-) by liquid chromatography (with a conductivity detector) and for lithium (Li^+) by inductively-coupled-plasma, atomic-emission-spectroscopy (ICP-AES) at LANL. Pentafluorobenzoate (or PFBA) was analyzed by HPLC (with a UV absorbance detector), also at Los Alamos. The fluorescent CML microspheres were analyzed by flow cytometry.

6.3.4.5 Tracer Test Results

Figure 6.3-19 shows the normalized concentrations of the three solute tracers at the production well as a function of time during the Bullfrog test. All concentrations are normalized to the injection masses of tracers (μg/L-kg injected or L^{-1} x 10^9). The axes in Figure 6.3-19 have logarithmic scales so that the details of the breakthrough curves can be seen throughout the entire test. The fractional recoveries of the tracers over the duration of the test were 0.74 for PFBA, 0.69 for bromide, and 0.39 for lithium (Reimus 2003 [165129], Attachment A, pp. A-36 to A-86). Figure 6.3-20 shows the response of the 360-nm diameter CML microspheres relative to the PFBA response in the Bullfrog tracer test. It is apparent that while the microspheres arrived slightly earlier than the PFBA, they were significantly attenuated relative to the PFBA throughout the test. The fractional recovery of microspheres during the test was 0.145 (Reimus 2003 [165129, Attachment A, pp. A-36 to A-86).

The most striking feature of the tracer breakthrough curves (Figures 6.3-19 and 6.3-20) is their bimodal shape. It is believed that the double-peak responses were the result of at least two distinct fracture-flow pathways between the injection and production wells that were located at different depths within the relatively long (~100 m) test interval. The flow survey information in Figure 6.1-2 suggests that there were probably two principal zones of outflow during tracer injection and recirculation in c#2 (see the triangles indicating percentages of flow during open-hole pumping). Because of the lack of mixing in the injection interval, the tracer solutions, which were injected directly below the top packer and were ~2% more dense than the groundwater, probably sank rapidly to the bottom of the interval (~200 kg of tracers dissolved in ~12,000 L (or kg) of ground water would have resulted in a ~2% increase in water density). Under these conditions, the majority of the tracer mass would be expected to exit c#2 from the lower flow zone; and, indeed, the majority of the tracer mass (60%) was associated with the second tracer peak. The first peak was apparently the result of a small percentage (~12%) of the tracer mass exiting c#2 from the upper flow zone. This zone was apparently more conductive (as suggested by the greater percentage of flow during open-hole pumping) and much better connected hydraulically to c#3 than the lower zone, as the travel time between the wells in this zone was much shorter. Additional evidence to support this hypothesis is obtained by comparing the PFBA response of Figure 6.3-19 with the response of the same tracer injected into c#2 six months prior to the start of the multiple tracer test. Figure 6.3-21 shows that the PFBA breakthrough curve in the earlier test was a more conventional single-peak response with a peak arrival time that coincided with the arrival time of the second peak in the latter test. The earlier test was conducted in the same interval between c#2 and c#3 and under the same flow conditions as the multiple-tracer test. The only noteworthy difference between the two tests, besides the additional tracers in the second test, was that only ~1000 L of tracer solution was injected in the first test, whereas ~12,000 L was injected in the second. The larger volume in the second test was due to the large mass of LiBr that was dissolved to ensure a quantifiable response of lithium ion. Given that the volume of the injection interval (volume between the two packers) was ~4300 L, it seems logical that the ~1000 L of tracer solution injected in the first test would have sunk rapidly and exited the borehole via only the lower flow zone. In contrast, the ~12,000 L of tracer solution injected in the second test (approximately 3 interval volumes) would have eventually "filled up" the interval, and a small fraction of the tracer mass apparently accessed the upper flow zone.

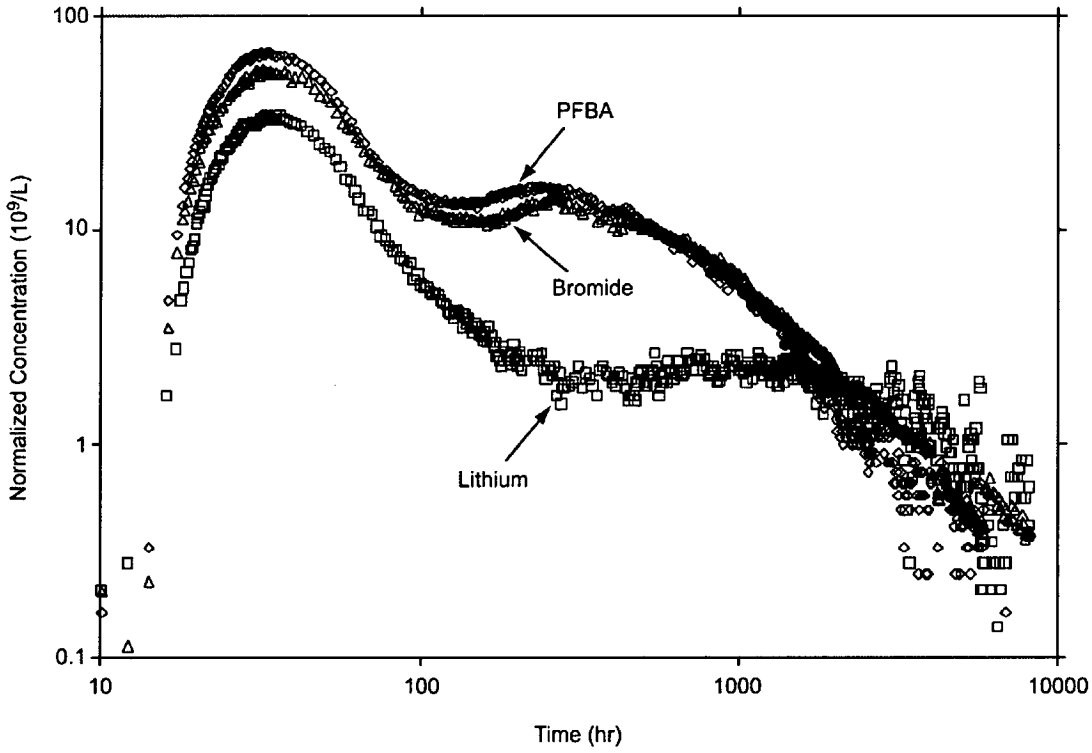

DTN: LA0007PR831231.001 [156043].

NOTE: Log-log scales are used for the axes so that the bimodal nature of the tracer responses can be seen more clearly.

Figure 6.3-19. Normalized Tracer Concentrations Versus Time in the Bullfrog Tuff Tracer Test Conducted from October 1996 to September 1997

PFBA concentrations in the earlier test were monitored for just over 3000 hr with a total fractional recovery of 0.72; at 3000 hr into the second test, the total PFBA fractional recovery was 0.60 (Reimus 2003 [165129], Attachment A, pp. A-7 to A-14, A-36 to A-86). Thus, the tracer recovery in the former test was actually higher than in the latter test despite the early tracer arrival in the latter test. This observation, plus the fact that the shapes of the common peaks of the two tests are different, suggest that a considerable fraction of the mass injected in the latter test followed additional pathways that were not accessed in the first test. Although the possibility of additional recovery of PFBA from the first test in the second test cannot be ruled out, it is not plausible that the PFBA from the first test could have caused either the first or second PFBA peak in the second test because all the other tracers used in the second test (which were not injected in the first test) exhibited a bimodal response.

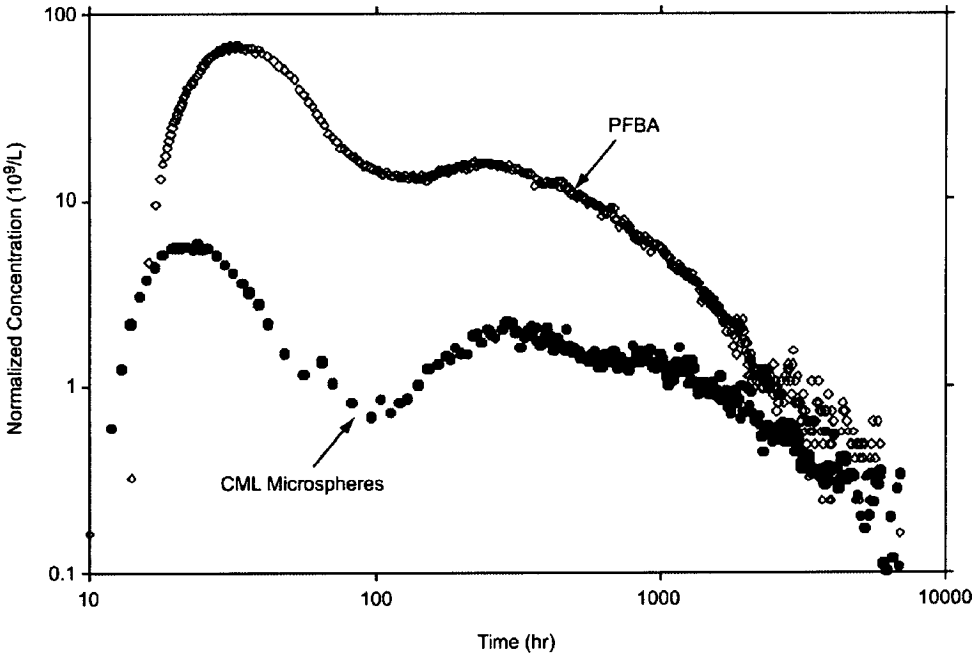

DTN: LA0007PR831231.001 [156043].

NOTE: Log-log scales are used for the axes so that the bimodal nature of the tracer responses can be seen more clearly.

Figure 6.3-20. Normalized Concentrations of PFBA and 360-nm-Diameter Carboxylate-Modified Polystyrene Latex Microspheres in the Bullfrog Tuff Tracer Test

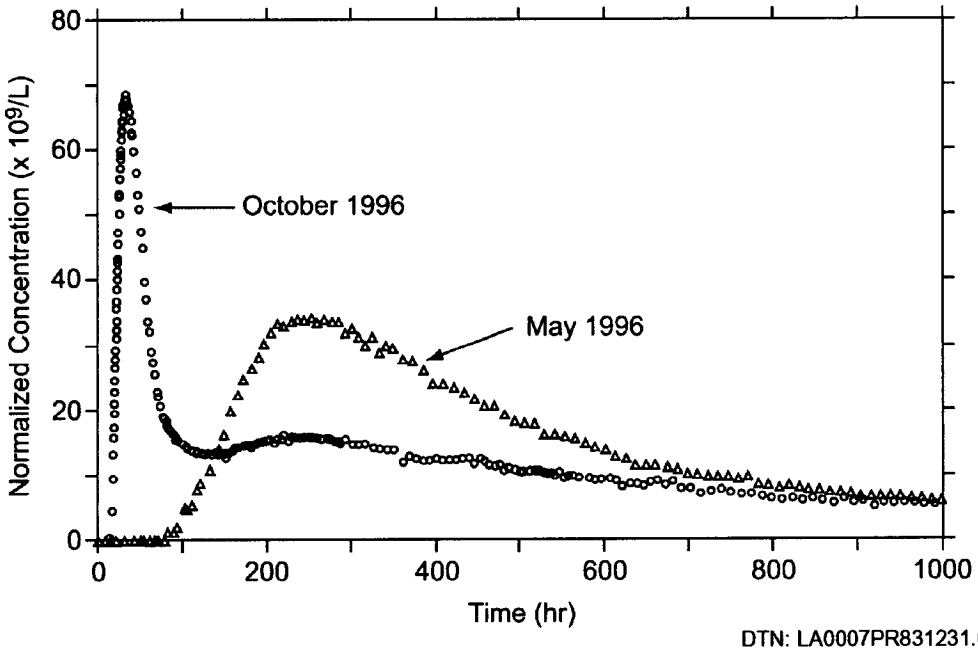

DTN: LA0007PR831231.001 [156043].

NOTE: The test conditions were the same in both tests, but the injection solution volume was ~1000 L in the May test and ~12,000 L in the October test.

Figure 6.3-21. Comparison of Normalized PFBA Responses in the Bullfrog Tuff Resulting from Tracer Injections in May 1996 and October 1996

Figure 6.3-22 shows the normalized concentrations of the three solute tracers at the production well as a function of time during the Prow Pass test. In contrast to the Bullfrog test, the responses in this test had a more conventional single-peak shape. Figure 6.3-22 also shows that there was indeed an increase in the tracer concentrations upon resumption of flow after each of the three interruptions. The fractional recoveries of the solute tracers over the duration of the test were 0.52 for PFBA, 0.43 for bromide, and 0.19 for lithium ion (Reimus 2003 [165129], Attachment A, pp. A-87 to A-144). Note that the axes in Figure 6.3-22 have a linear scale as opposed to the logarithmic scale used in Figure 6.3-19 for the Bullfrog test.

It is apparent in both Figures 6.3-19 and 6.3-22 that there is considerable separation between the peak normalized concentrations of bromide and PFBA in the two tracer tests, with PFBA always having a higher normalized concentration in each peak. It is also apparent that the tails of the responses of these two tracers converge, with a suggestion of a crossover at late times. However, the appearance of a second peak in the Bullfrog test precluded a crossover after the first peak, and the Prow Pass test was not conducted long enough to see a definitive crossover. Referring to Figure 6.3-18, these breakthrough-curve features are qualitatively consistent with a dual-porosity transport system. The lithium responses in the first peak of the Bullfrog test and in the Prow Pass test are highly attenuated in normalized concentration compared to the nonsorbing tracers, although they are not significantly attenuated in time. Again referring to Figure 6.3-18, these responses are qualitatively consistent with a dual-porosity transport system in which most of the sorption is occurring in the matrix (after diffusive mass transfer from the fractures), with possibly a small amount of sorption also occurring on fracture surfaces. In the case of the second peak in the Bullfrog test, the lithium response is attenuated both in concentration and in time, which is consistent with sorption occurring in both the matrix and on fracture surfaces.

The responses of the CML microspheres relative to PFBA in the Prow Pass test are shown in Figure 6.3-23, which has a logarithmic normalized concentration axis because of the very low normalized concentrations of the microspheres. The fractional recoveries of microspheres in this test were 0.0033 for the 640-nm-diameter blue microspheres, 0.0012 for the 280-nm-diameter orange microspheres, and effectively zero for the 280-nm-diameter yellow microspheres (Reimus 2003 [165129], Attachment A, pp. A-145 to A-167). The response of the yellow microspheres is not shown in Figure 6.3-23 because these microspheres effectively never arrived at the production well. The 280-nm-diameter orange and 640-nm-diameter blue microspheres were injected 2 days before the solutes, whereas the 280-nm-diameter yellow microspheres were injected simultaneously with the solutes. It is likely that the high ionic strength of the injection solution (~0.4 M) caused the yellow microspheres to attach to rock surfaces much more readily than the other microspheres, which were injected in untraced groundwater (ionic strength = ~0.003 M). It is also interesting to note that the peak concentrations of blue and orange microspheres occurred at about the same time that solutes began arriving at c#2, and then the microspheres rapidly decreased in concentration as the solute concentrations increased. This behavior may be purely coincidental, or it may hint that the increased ionic strength associated with the solutes caused the remaining microspheres to attach more readily to rock surfaces. The microsphere "spikes" occurring at about 1000 hr into the test (Figure 6.3-23) actually correspond to a few days after the c#3 mixing/sampling loop was run, which suggests that the pressure and flow transients caused by the mixing may have mobilized/detached some microspheres. The timing of this response was consistent with the arrival time of the microspheres after injection into c#3 on September 23, 1998. A second spike in microsphere concentrations occurred the day

after the unplanned flow interruption on November 14, 1998 (Figure 6.3-23), which further supports the hypothesis that flow and pressure transients may have resulted in microsphere detachment.

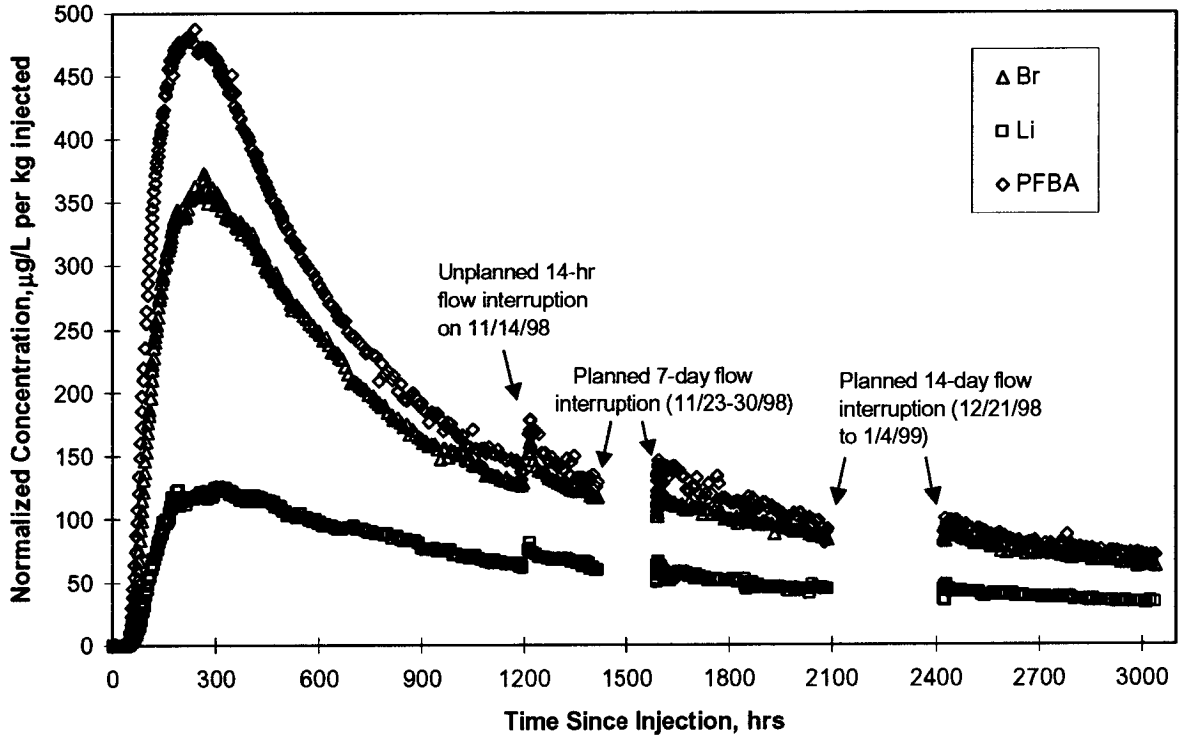

DTN: LAPR831231AQ99.001 [140134].

NOTE: "Spheres" in the legend refers to CML microspheres.

Figure 6.3-22. Normalized Tracer Concentrations Versus Time in the Prow Pass Tracer Test Conducted from September 1998 to January 1999

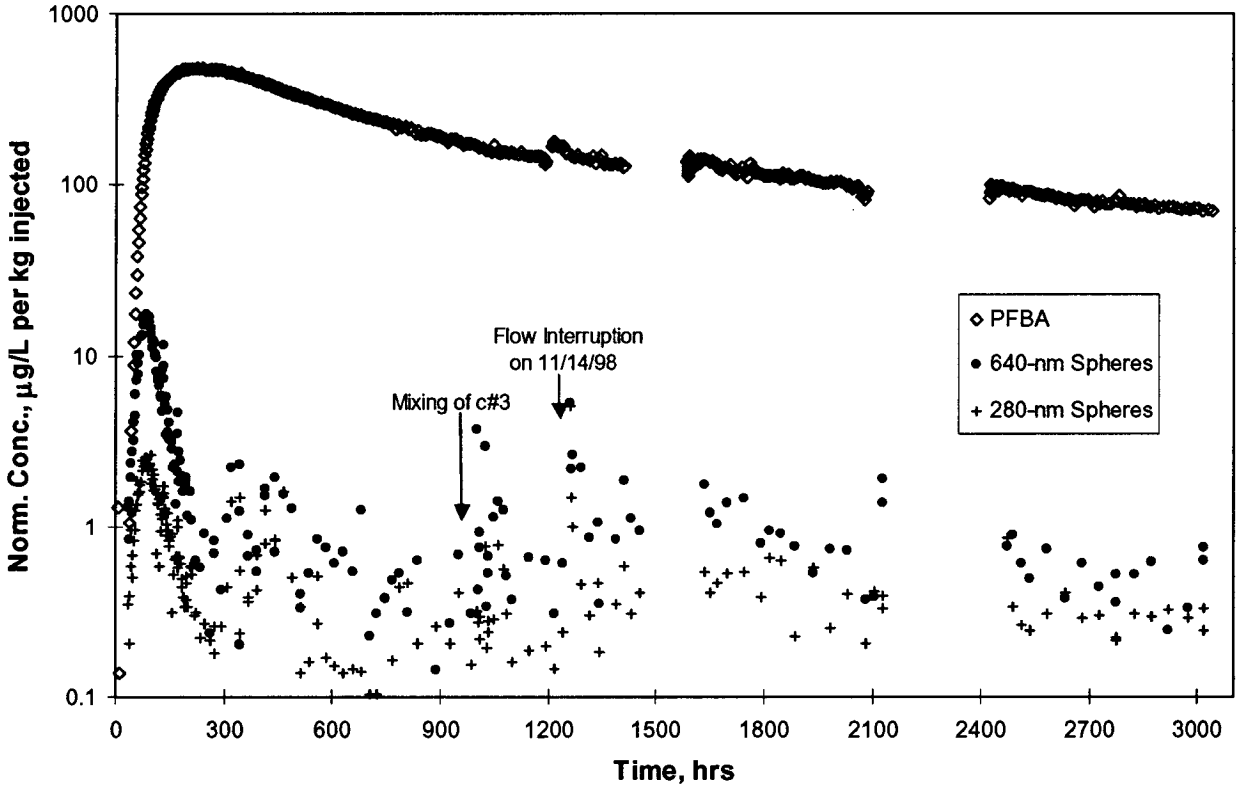

DTN: LAPR831231AQ99.001 [140134].

NOTE: "Spheres" in the legend refers to CML microspheres. The 280-nm-diameter spheres are the orange-dyed microspheres injected two days prior to the solutes. The 280-nm-diameter yellow-dyed spheres that were injected with the solutes were not recovered.

Figure 6.3-23. Normalized Concentrations of PFBA and Carboxylate-Modified Polystyrene Latex Microspheres in the Prow Pass Tracer Test

The sampling loop in c#3 in the Prow Pass test afforded the opportunity to see how well tracers had been "flushed" from the injection borehole after the test had been running for ~40 days. The sampling loop was run for ~11 hr, and over 50 samples were collected at the surface during this time. The "responses" from the injection interval are shown in Figure 6.3-24. These responses clearly indicate that there was a "slug" of concentrated tracer solution remaining in the interval and that this slug circulated around the sampling loop/borehole several times during the 11 hr of loop operation, dispersing as it circulated (indicated by the lowering and broadening of tracer peaks). Interestingly, the microspheres appear to precede the solutes each time the tracers cycle through the loop, which suggests that there was some as yet unexplained spatial separation of microspheres and solutes in the borehole. The total mass of any given tracer associated with the slugs was less than 0.1% of the mass that was injected, so the injection interval had been reasonably well purged of all tracers. This result is important because it shows that the unaccounted-for tracer mass in the overall test is not the result of mass being left behind in the injection borehole, but rather it is mass that is being "lost" by other means (e.g., flow into the

matrix that never makes it to the production borehole, stagnation points, losses due to density-driven flow). Given the flow rate through the sampling loop and the volumes of the injection interval and piping, the timing of the slug(s) suggested that they had been near the bottom of the interval where the pump intake was located. This result is consistent with the expectation that some of the dense tracer solution would have sunk to the bottom of the interval and remained there if there was no flow to push it out.

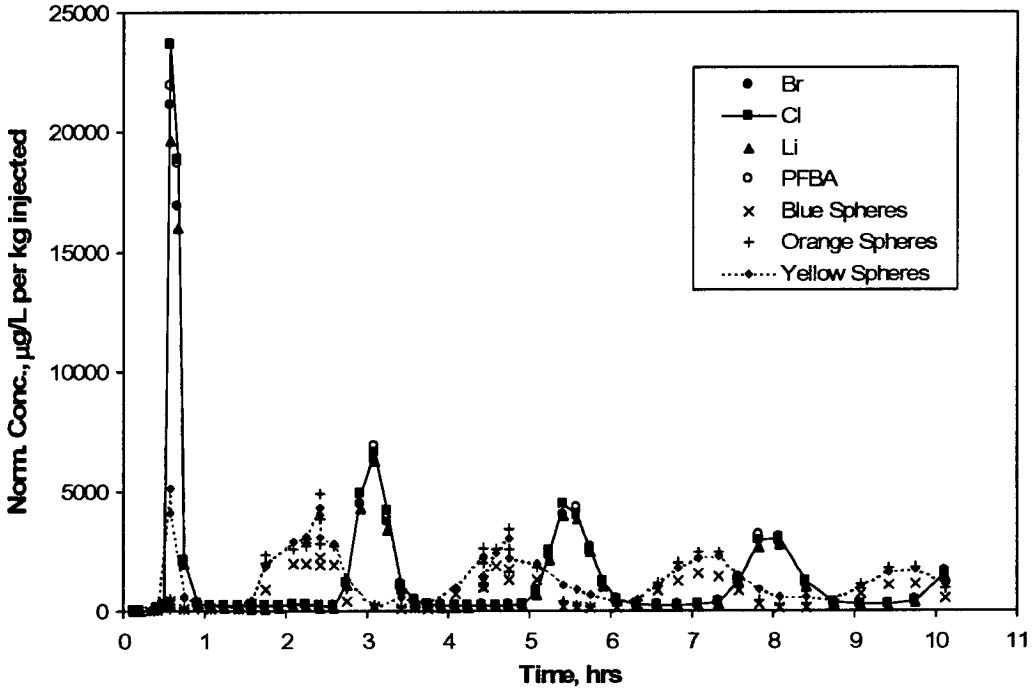

DTN: LAPR831231AQ99.001 [140134].

NOTE: "Spheres" in the legend refers to CML microspheres. The tracers remaining in the injection interval were apparently highly stratified, probably at the bottom of the interval. Total masses remaining in the injection interval were less than 0.1% of the total injection mass of each tracer.

Figure 6.3-24. Tracer Concentrations Mixing Loop 40 Days After Tracer Injection in UE-25 c#3 in the Prow Pass Tracer Test

6.3.4.6 Tracer Test Interpretive Modeling Approach

6.3.4.6.1 Solute Tracers

To obtain estimates of solute transport parameters in the flow system, the semi-analytical dual-porosity transport model RELAP (REactive transport LAPlace transform inversion computer code) V 2.0 (STN: 10551-2.0-00 [159065]) was used to fit simultaneously the solute tracer responses. RELAP, which is described in detail by Reimus and Haga (1999 [154705], Appendix

B), essentially combines the Laplace-domain dual-porosity transport equations derived by Maloszewski and Zuber (1984 [156840], Appendix; 1985 [148312]) (modified to account for linear sorption) with Laplace-domain transfer functions that describe a finite-pulse injection, wellbore mixing, and recirculation. Similar approaches have been used by others (Moench 1989 [101146], 1995 [148784]; Becker and Charbeneau 2000 [156633], pp. 299 to 310). Maloszewski and Zuber (1984 [156840], Appendix; 1985 [148312]) assumed that tracer transport in fractures was described by the one-dimensional (1-D) advection-dispersion equation with 1-D diffusion occurring into the surrounding matrix perpendicular to the flow direction in fractures. This simplified flow-system geometry assumed by RELAP is shown in Figure 6.3-25. The model assumes parallel-plate fractures of constant aperture, 2b, and constant spacing, L, no concentration gradients across the fracture aperture, and a steady flow rate in fractures.

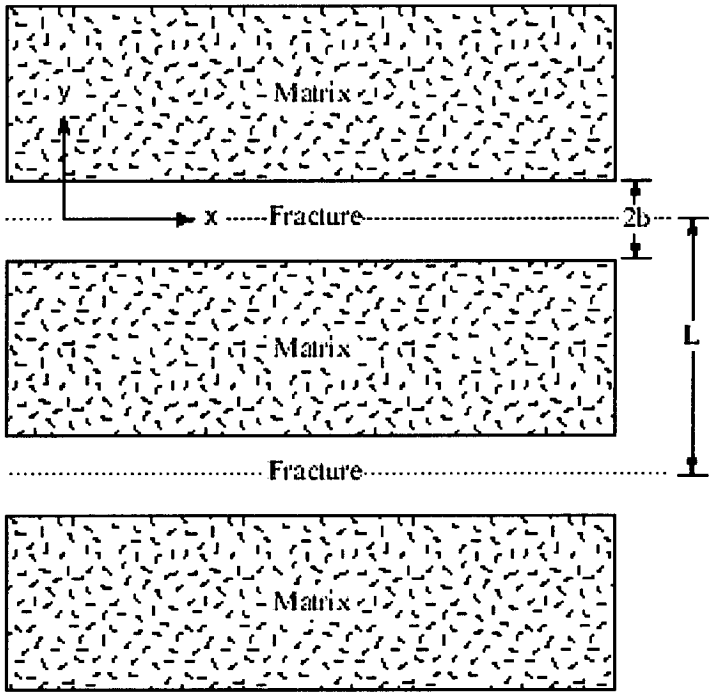

For illustration purposes only.

NOTE: Matrix and fractures extend infinitely in z direction.

Figure 6.3-25. System Geometry Assumed in the RELAP and MULTRAN Codes

The equations describing dual-porosity transport under these conditions are the following (based on Maloszewski and Zuber {1984 [156840], Appendix}).

Fracture:

$$R_f \frac{\partial C_f}{\partial t} + v_f \frac{\partial C_f}{\partial x} - D_f \frac{\partial^2 C_f}{\partial x^2} - \frac{\phi D_m}{b\eta} \frac{\partial C_m}{\partial y}\bigg|_{y=b} = 0 \qquad \text{(Eq. 5)}$$

Matrix:

$$R_m \frac{\partial C_m}{\partial t} - D_m \frac{\partial^2 C_m}{\partial y^2} = 0 \qquad \text{(Eq. 6)}$$

subject to the following initial and boundary conditions

$$C_f(x,0) = 0 \qquad \text{(Eq. 5a)}$$

$$C_f(x,0) = C_p \text{ from } t = 0 \text{ to } t = t_{pulse} \text{ (i.e., Pulse Input)} \qquad \text{(Eq. 5b)}$$

$$C_f(\infty,t) = 0 \qquad \text{(Eq. 5c)}$$

$$C_m(y,x,0) = 0 \qquad \text{(Eq. 6a)}$$

$$C_m(b,x,t) = C_f(x,t) \qquad \text{(Eq. 6b)}$$

$$\frac{\partial C_m}{\partial y}\bigg|_{y=\frac{L}{2}} = 0 \text{ (finite matrix) or } C_m(\infty,x,t) = 0 \text{ (semi - inifinte matrix)} \qquad \text{(Eq. 6c)}$$

where

C_f = tracer concentration in solution in fractures, μg/cm^3

C_m = tracer concentration in solution in matrix, μg/cm^3

C_p = pulse concentration, μg/cm^3

v_f = fluid velocity in fractures (in x direction), cm/sec

D_f = dispersion coefficient in fractures, cm^2/sec

D_m = molecular diffusion coefficient in matrix, cm^2/sec

R_f = retardation factor in fractures = $1 + A_{sp} k_A$ (or $1 + \frac{2}{b} k_A$ for open parallel-plate fractures). Alternatively, for fractures that are filled with aquifer material, $R_f = 1 + \frac{\rho_f}{\eta} K_d$

R_m = retardation factor in matrix = $1 + \frac{\rho_B}{\phi} K_d$

K_d = sorption partition coefficient = mass of tracer sorbed per unit mass of aquifer material divided by solution concentration of tracer at equilibrium, cm^3/g

$k_A = K_d / A_{sp}$ surface-based sorption partition coefficient , cm^3/cm^2

A_{sp} = surface area per unit mass of material in fractures or on fracture walls, cm^2/g

ρ_f = bulk density in fractures, g/cm^3

ρ_B = bulk density in matrix, g/cm^3

η = porosity within fractures

ϕ = matrix porosity

b = fracture half aperture, cm

L = spacing between centerlines of adjacent fractures, cm.

The transformation of Equations 5 and 6 to the Laplace domain and their subsequent solution in the Laplace domain and inversion of the solution back to the time domain are described by Reimus and Haga (1999 [154705], Appendix B). Note that Equations 5 and 6 reduce to a single-porosity system if the matrix porosity, ϕ, (or the matrix diffusion coefficient, D_m) is set equal to zero. RELAP V 2.0 (STN: 10551-2.0-00 [159065]) provides a simultaneous least-squares fit to up to four tracer data sets by automatically adjusting the following model parameters (which arise from the dimensionless forms of the governing equations):

- the mean fluid residence time in fractures (τ)
- the Peclet number ($Pe = r_L/\alpha$, where r_L = distance between wells, m, and α = dispersivity in fractures, m)
- the mass fraction of tracers participating in the test (f)
- a matrix diffusion mass-transfer coefficient, $\frac{\phi}{b}\sqrt{D_m}$, which is obtained from the Laplace transformations of Equations 5 and 6.
- the characteristic fracture spacing, L
- the fracture retardation factor, R_f
- the matrix retardation factor, R_m.

The fractional mass participation (f) is used as an adjustable parameter because low mass recoveries are frequently observed in field tracer tests in fractured rock (e.g., Reimus and Haga 1999 [154705], Appendix B), presumably due to (1) dense tracer solutions "sinking" out of the zone of influence of pumping, (2) a significant volumetric flow of tracer solution into the matrix within the injection wellbore (this tracer mass will not make it to the production well during the tracer test because of the very low flow velocities in the matrix), or (3) the loss of tracer mass due to stagnation points induced either by recirculation or by the superposition of the induced flow field on the ambient flow field. Although these phenomena can affect absolute tracer responses, they should not, in principle, affect the relative responses of different tracers that are injected simultaneously.

The interpretation of the tracer responses in each test involved first fitting the two nonsorbing tracer responses by simultaneously adjusting all of the parameters listed above with the constraint that the matrix diffusion coefficient, D_m, for bromide was three times that of PFBA

(and therefore the matrix diffusion mass transfer coefficient, $\frac{\phi}{b}\sqrt{D_m}$, was ~1.7 times that of PFBA). This factor-of-three difference is based on literature data (Newman 1973 [148719], p. 230, Table 75-1; Benson and Bowman 1994 [122788], p. 1125; 1996 [153427]) and the experimental diffusion cell results discussed in Section 6.3.8. R_f and R_m were held equal to 1 for the two nonsorbing tracers. This fitting procedure implicitly assumed that both tracers had exactly the same mean residence time, Peclet number, mass fraction participation, and characteristic fracture spacing during the tracer tests, which is justified because the tracers were injected simultaneously and, thus, should have experienced the same flow system and same flow conditions.

For the Bullfrog test, the two sets of tracer peaks were fitted sequentially with the second peak being fitted after accounting for the contribution of the tail from the first peak. The model parameters were allowed to vary independently for each peak, as the peaks were assumed to represent different flow pathways with different transport characteristics. Although the tracer injection duration in the Bullfrog test was about 10 hr, it was assumed that for the first peak there was a delay of 4 hr followed by a 6-hr injection of tracer into the pathways that resulted in the first peak. The rationale for this assumption was that there was no early peak in the earlier PFBA test (Figure 6.3-21), which involved an injection of less than one hour, so it seemed logical to assume that the earliest injected tracer solution did not follow the earliest-arriving pathways. A 4-hr delay time was chosen because the injected-tracer-solution volume exceeded the injection-interval volume by this time, and it was felt that this was a reasonable criterion for when at least a portion of the tracer solution should have begun moving through the early arriving pathways.

In contrast to the Bullfrog test, the fitting procedure for the Prow Pass test was very straightforward, as only one set of tracer peaks was observed. However, because RELAP V 2.0 (STN: 10551-2.0-00 [159065]) is based on a semi-analytical Laplace transform inversion method, it was not capable of simulating the flow transients associated with the flow interruptions during the latter part of the test. To simulate these transients, the computer code MULTRAN (multicomponent transport) V 1.0 (STN: 10666-1.0-00 [159068]) was used. MULTRAN is an implicit alternating-direction, two-dimensional (2-D), finite-difference code that accounts for cation exchange (involving up to three exchanging cations), charge balance, and multicomponent diffusion in a dual-porosity transport system (see Section 6.3.9.2.2 for details). The best-fitting transport parameters obtained from RELAP fits to the tracer data up until the time of the flow interruptions were used in MULTRAN to extend the simulations throughout the entire test.

Once best simultaneous fits to the nonsorbing tracer responses in both tests were obtained, the lithium responses associated with each distinct tracer peak were fitted with RELAP V 2.0 (STN: 10551-2.0-00 [159065]) by adjusting R_f and R_m while holding all other parameters equal to the values that provided the best fits to the nonsorbing tracers. However, D_m for lithium was assumed to be two-thirds that of bromide (and ~2 times that of PFBA), rather than about half that of bromide as indicated in Table 6.3-4, because lithium and bromide would tend to diffuse together to maintain local charge balance. Rate-limited sorption was not considered in the field tests because the response times were all quite long relative to typical rates of ion exchange.

RELAP V 2.0 (STN: 10551-2.0-00 [159065]) provided a good match to the lithium response associated with the second peak in the Bullfrog test and also to the lithium response in the Prow Pass test. However, in the case of the first peak in the Bullfrog test, RELAP consistently overestimated the normalized concentrations in the lithium tail when the leading edge of the lithium response was fitted well. The inability to fit the response of an ion-exchanging tracer using a linear equilibrium sorption model (K_d model) had been previously encountered when trying to fit cation responses from both laboratory-scale fracture-transport experiments (Section 6.3.9.2) and crushed-rock column experiments (Section 6.3.9.1). In these previous studies, it was observed that cation-exchanging tracers transport with less apparent sorption than K_d models predict when the tracer injection concentration is high relative to the ionic strength of the groundwater (that is, when the total cation equivalents in the system are dominated by the cation tracer). Under these conditions, some of the cation tracer mass tends to elute with the anion tracers to maintain local charge balance in the system. When tracer concentrations are sufficiently dilute, local charge balance can be maintained by exchanging cations, and a K_d model tends to approximate more closely the observed transport behavior. In the Bullfrog test, the injection concentration of lithium was ~0.1 M, whereas the ionic strength of the C-wells groundwater was ~0.003 M; therefore, the conditions of a very high cation injection concentration relative to the groundwater ionic strength were met. MULTRAN V1.0 (STN: 10666-1.0-00 [159068]) provided much better predictions of cation transport data in laboratory-scale dual-porosity systems under these conditions than RELAP because it explicitly accounts for ion-exchange reactions, multicomponent diffusion, and local charge balance (see Section 6.3.9.2.2). For this reason, MULTRAN was employed to match the lithium data in the first peak of the Bullfrog test using the mean residence time, Peclet number, and matrix-diffusion, mass-transfer coefficient obtained from the best RELAP fit to the nonsorbing tracer data and allowing the lithium ion-exchange parameters to be varied to fit the lithium data. Lithium was assumed to exchange with sodium and calcium ions based on the results of cation exchange capacity (CEC) measurements conducted on C-wells tuffs (Section 6.3.7.2).

It should be noted that the relatively low tracer concentrations observed at the production well in the Bullfrog test do not necessarily reflect the concentrations that existed in the fractures in which transport occurred; it is very likely that a significant amount of dilution occurred in the production borehole. Thus, concentrations could have remained quite high in the fractures that conducted tracers, satisfying conditions for weakly-sorbing transport of the lithium ion. For the second lithium peak of the Bullfrog test and for the Prow Pass test, concentrations in the fractures apparently were dilute enough during the much longer residence times associated with these responses that the lithium transport behavior could be reasonably approximated by a K_d model.

6.3.4.6.2 Colloid Tracers (Microspheres)

As with the solutes, the microsphere responses in the tracer tests were interpreted using the RELAP V 2.0 (STN: 10551-2.0-00 [159065]) code to fit the data. The differential equations used to describe microsphere transport were:

$$\frac{\partial C}{\partial t} + v_f \frac{\partial C}{\partial x} - D\frac{\partial^2 C}{\partial x^2} + k_{filt} C - k_{res} S = 0 \qquad \text{(Eq. 7)}$$

$$\frac{1}{b}\frac{\partial S}{\partial t} - k_{filt}C + k_{res}S = 0 \qquad \text{(Eq. 8)}$$

where

C = colloid concentration in solution, no./L

S = colloid concentration on surfaces, no./cm^2

v_f = flow velocity in fractures, cm/sec

D = dispersion coefficient, cm^2/sec

k_{filt} = filtration rate constant (1/sec) = λv_f, where λ = filtration coefficient (1/cm)

k_{res} = resuspension rate constant, 1/cm-sec

x, t = independent variables for distance and time, respectively.

These equations assume that microspheres are confined to fractures because they are too large to diffuse significantly into the porous rock matrix. The RELAP V 2.0 (STN: 10551-2.0-00 [159065]) semi-analytical model is capable of representing Equations 7 and 8 by making use of its rate-limited sorption features and setting the matrix porosity equal to zero (to eliminate matrix diffusion). It was assumed that the mass fractions, mean residence times, and Peclet numbers that provided the best fits to the nonsorbing solute responses also applied to the microspheres. Any size exclusion chromatography effects (Hiemenz 1986 [117358], pp. 42-45) that would have resulted in a shorter mean residence time for the microspheres compared to the solutes were assumed to be accounted for by not allowing the microspheres to diffuse into the matrix. Thus, the only adjustable parameters in the analysis were a forward first-order filtration-rate constant and a first-order reverse-filtration-rate constant (also called a resuspension or detachment-rate constant).

Initially, attempts to fit the microsphere response associated with the first peak in the Bullfrog test were made by assuming only irreversible filtration with no resuspension/detachment. Although this approach was capable of fitting the timing and normalized concentration of the first microsphere peak, it resulted in a much shorter tail than the data indicated. Therefore, to account for the tail, a small fraction of the filtered microspheres was assumed to detach. A fit to the tail was obtained by adjusting both the fraction of microspheres detaching and the detachment rate constant (only a single-forward filtration-rate constant was assumed for all the microspheres in the first peak).

A fit to the second microsphere peak in the Bullfrog test was obtained in the same manner. However, in this case, the forward filtration rate constant had to be adjusted large enough so that essentially all of the microspheres were filtered as they moved through the system. This approach was necessary because any microspheres moving through the system without being filtered were predicted to arrive too early to match the observed response (note that the second microsphere peak occurred after the second nonsorbing solute peaks; see Figure 6.3-20). Unfiltered microspheres moving through the second set of pathways were predicted to arrive at about the same time as the low point in concentration between the two peaks. Thus, to account for the second microsphere peak, it was necessary to assume that a substantial fraction of the microspheres in the second set of pathways were reversibly filtered. The peak itself was fit by

assuming a fraction of the microspheres experienced one detachment rate, and the tail was fit by assuming a separate fraction experienced another detachment rate. The remaining microspheres were assumed to not detach at all. This approach implies that there is a *distribution* of detachment rate constants, a possibility that has been discussed by Dabros and Ven de Ven (1982 [143278], pp. 232 to 244; 1983 [156652], pp. 576 to 579). The forward rate constant associated with each of these mass fractions was set equal to the minimum rate constant necessary to ensure that nearly all of the microspheres were filtered before making it through the system.

In the Prow Pass test, only a single filtration and detachment-rate constant were needed to fit the responses of each microsphere, provided the "spikes" associated with the flow transients could be ignored. No attempt was made to fit these spikes.

6.3.4.7 Tracer Test Interpretations

6.3.4.7.1 Solute Tracers

The best RELAP/MULTRAN fits to the solute tracer breakthrough curves in the Bullfrog test are shown in Figure 6.3-26. As discussed above, RELAP V 2.0 (STN: 10551-2.0-00 [159065]) was used to fit the nonsorbing tracer responses and the lithium response in the second peak, and MULTRAN V 1.0 (STN: 10666-1.0-00 [159068]) was used to fit the lithium response in the first peak (MULTRAN fits to the bromide and PFBA data are also shown for the first peak in Figure 6.3-26). The RELAP fits were obtained assuming a constant production rate of 568 L/min and a constant recirculation rate of 19 L/min (3.3% of production), despite the fact that recirculation in the field test was stopped after 40 days. Both tracer peaks occurred well before recirculation was terminated, so the only portion of the test that was incorrectly modeled was the latter tailing portion of the second peak. Separate simulations comparing the results of MULTRAN runs with and without recirculation after 40 days indicated that the assumption of continued recirculation after 40 days had negligible effect on the fits or the values of the fitted model parameters.

The best-fitting model parameters from RELAP V 2.0 (STN: 10551-2.0-00 [159065]) for the Bullfrog test are listed in Table 6.3-6. Note that separate estimates of τ and Pe are provided, depending on whether linear flow (constant flow velocity between injection and production well) or radial flow (flow velocity inversely proportional to distance from production well) is assumed to occur in the test interval. RELAP is capable of providing estimates for these parameters under either assumption (the quality of the fits and the other model parameters are not affected). In a heterogeneous, confined aquifer with fully-penetrating wells (i.e., no flow in the vertical direction), the flow velocity to a single production well with no recirculation into an injection well is expected to vary between linear and radial (National Research Council 1996 [139151], pp. 252 to 261). Thus, if it is assumed that the test interval was reasonably confined, presenting the two values of τ and Pe in Table 6.3-6 is a rough way of bounding these model parameter estimates as a result of flow-field uncertainty. Although the Bullfrog flow system was not perfectly confined, this approach should still yield reasonable bounds for τ and Pe, as the flow velocities in pathways carrying tracers from c#2 to c#3 should have started out relatively high due to the recirculation into c#2, gone through a minimum, and then increased again in the vicinity of c#3. Thus, the weak dipole should have resulted in a flow pattern that was intermediate between linear and radial flow.

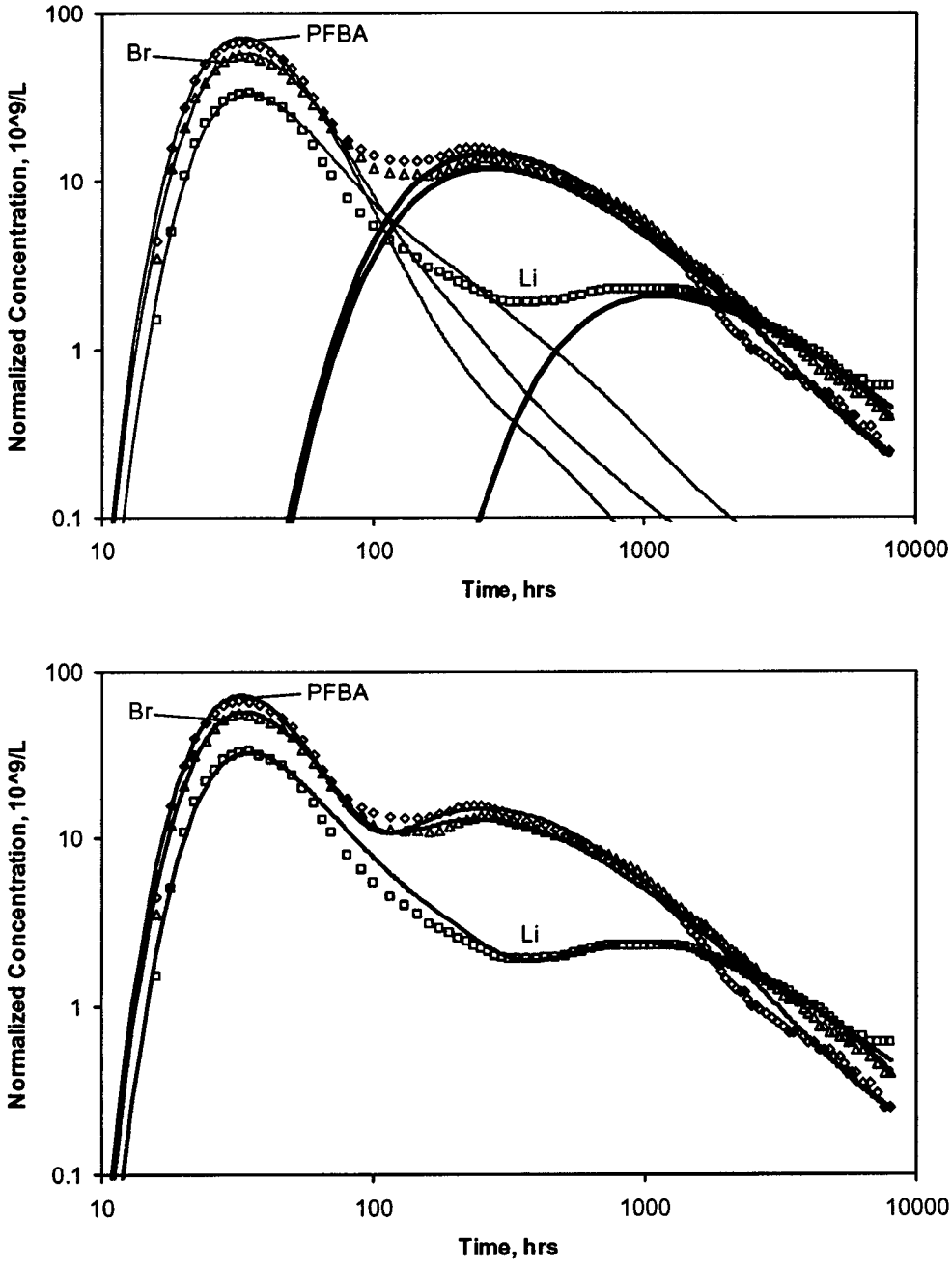

DTN: LA0007PR831231.001 [156043] (data). Output DTN: LA0303PR831231.003 (model).

Sources: Reimus (2000 [162855]), Reimus (2003 [165129], including Attachment A).

NOTE: The upper plot shows individual fits to first and second tracer peaks (MULTRAN V 1.0 (STN: 10666-1.0-00 [159068]) and RELAP V 2.0 (STN: 10551-2.0-00 [159065], respectively), and the lower plot shows composite fits. For clarity, the data points shown are a subset of the actual data. The best-fitting model parameters are provided in Table 6.3-6.

Figure 6.3-26. RELAP and MULTRAN Fits to the Tracer Response Curves in the Bullfrog Tuff Tracer Test

Table 6.3-6. RELAP Model Parameters Providing the Best Fits to the Bullfrog Tracer Test Data

Parameter	Pathway 1	Pathway 2
Mass fraction, f	0.115	0.60
Mean residence time, τ, for linear flow (hr)	36	1020
Peclet number, Pe, for linear flow	6.5	1.6
Mean residence time, τ, for radial flow (hr)	30	630
Peclet number, Pe, for radial flow	9.3	2.8
$\frac{\phi}{b}\sqrt{D_m}$ for bromide ($sec^{-1/2}$) [a]	0.0015	0.000469
Fracture spacing (cm)	∞ (2.4) [b]	4.4
Lithium fracture retardation factor, R_f	1	4
Lithium matrix retardation factor, R_m	7.5 [c]	20

Output DTNs: LA0303PR831231.003; LA0303PR831231.005.

NOTE: Pathway 1 and Pathway 2 are associated with the first and second tracer peaks, respectively. The fits are shown in Figure 6.3-26 (MULTRAN V 1.0 (STN: 10666-1.0-00 [159068]) was used to fit first lithium peak in Figure 6.3-26).

(a) The mass transfer coefficient, $MTC = \frac{\phi}{b}\sqrt{D_m}$, for PFBA is 0.577 times that for bromide.

(b) The number in parentheses is the minimum fracture spacing that yields the same results as an infinite fracture spacing.

(c) Lithium response associated with first tracer peak was poorly fitted by RELAP V 2.0 (STN: 10551-2.0-00 [159065]), so MULTRAN was used to obtain a better fit, which is shown in Figure 6.3-26.

Figure 6.3-27 shows the best RELAP/MULTRAN fits to the Prow Pass solute tracer test data, and Table 6.3-7 gives the best-fitting RELAP V 2.0 (STN: 10551-2.0-00 [159065]) model parameters (obtained by simulating the first 1200 hr of the test, prior to the first flow interruption). MULTRAN V 1.0 (STN: 10666-1.0-00 [159068]) was used after the first flow interruption to model the remainder of the test using the best-fitting parameters from RELAP to extend the simulations. Because the tracer concentrations were significantly higher in this test than in the Bullfrog test, it was possible to determine the responses of the cations (sodium and calcium) that exchanged with lithium during the test. (The background concentrations of the exchanging cations were too high relative to their signals in the Bullfrog test to determine their responses.) Figure 6.3-28 shows the responses of lithium, sodium, and calcium ions in the Prow Pass test, expressed as meq/L versus time. MULTRAN fits to the data are also included in Figure 6.3-28. Although not shown here, it was confirmed that the total cation and anion charges balanced each other, as they must, throughout the test.

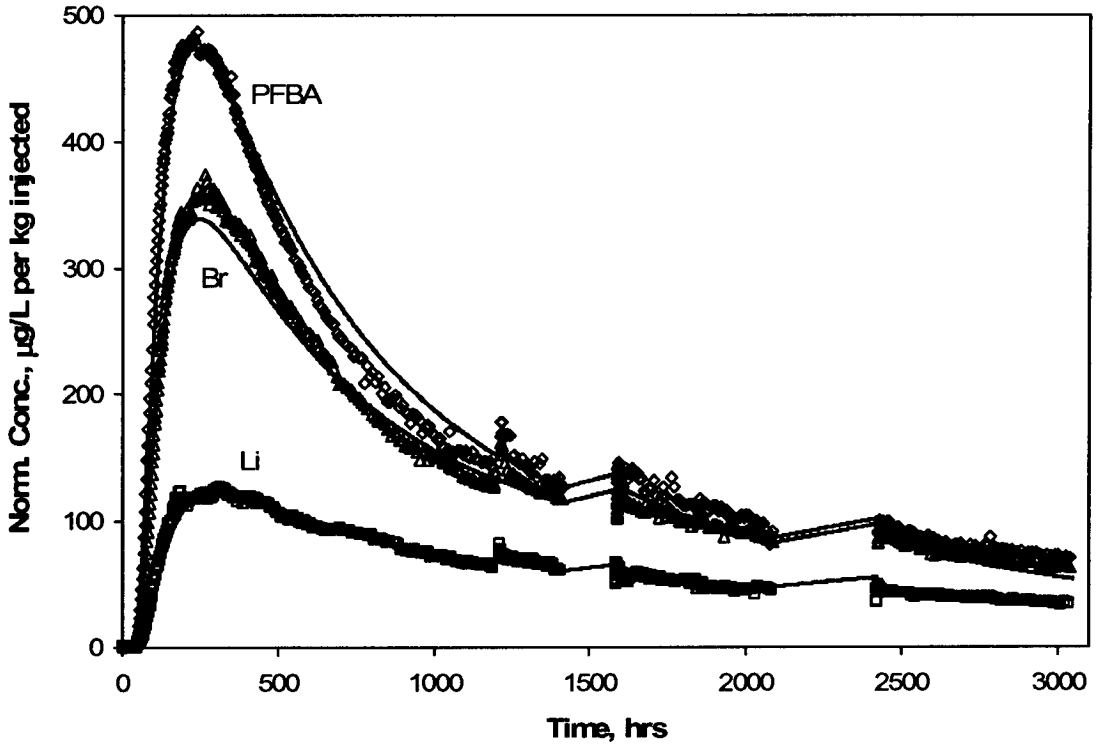

DTN: LAPR831231AQ99.001 [140134] (data). Output DTN: LA0303PR831231.003 (model).

Sources: Reimus (2000 [162852]), Reimus (2003 [165129], including Attachment A).

NOTE: The best-fitting model parameters are provided in Table 6.3-7.

Figure 6.3-27. RELAP/MULTRAN Fits to the Tracer Response Curves in the Prow Pass Tuff Tracer Test

Table 6.3-7. RELAP Model Parameters Providing the Best Fits to the First 1200 Hours of Prow Pass Tracer Test Data

Parameter	Parameter Value
Mass fraction, f	0.72
Mean residence time, τ, for linear flow (hr)	1210
Peclet number, Pe, for linear flow	1.3 [(a)]
Mean residence time, τ, for radial flow (hr)	610
Peclet number, Pe, for radial flow	2.3 [(a)]
$\frac{\phi}{b}\sqrt{D_m}$ for bromide ($sec^{-1/2}$) [(b)]	0.00095
Fracture spacing (cm)	∞ (6.4) [(c)]
Lithium fracture retardation factor, R_f	1
Lithium matrix retardation factor, R_m	12

Output DTNs: LA0303PR831231.003; LA0303PR831231.005.

NOTE: The fits (extended by MULTRAN V 1.0 (STN: 10666-1.0-00 [159068) simulations) are shown in Figure 6.3-27.

(a) The Peclet numbers were adjusted to correct for the theoretical dispersion caused by the partial recirculation flow field (see text). Peclet numbers obtained directly from RELAP V 2.0 (STN: 10551-2.0-00 [159065]) were 0.9 (linear flow) and 1.9 (radial flow).

(b) The mass transfer coefficient, $MTC = \frac{\phi}{b}\sqrt{D_m}$, for PFBA is 0.577 times that for bromide.

(c) The number in parentheses is the minimum fracture spacing that yields the same results as infinite fracture spacing.

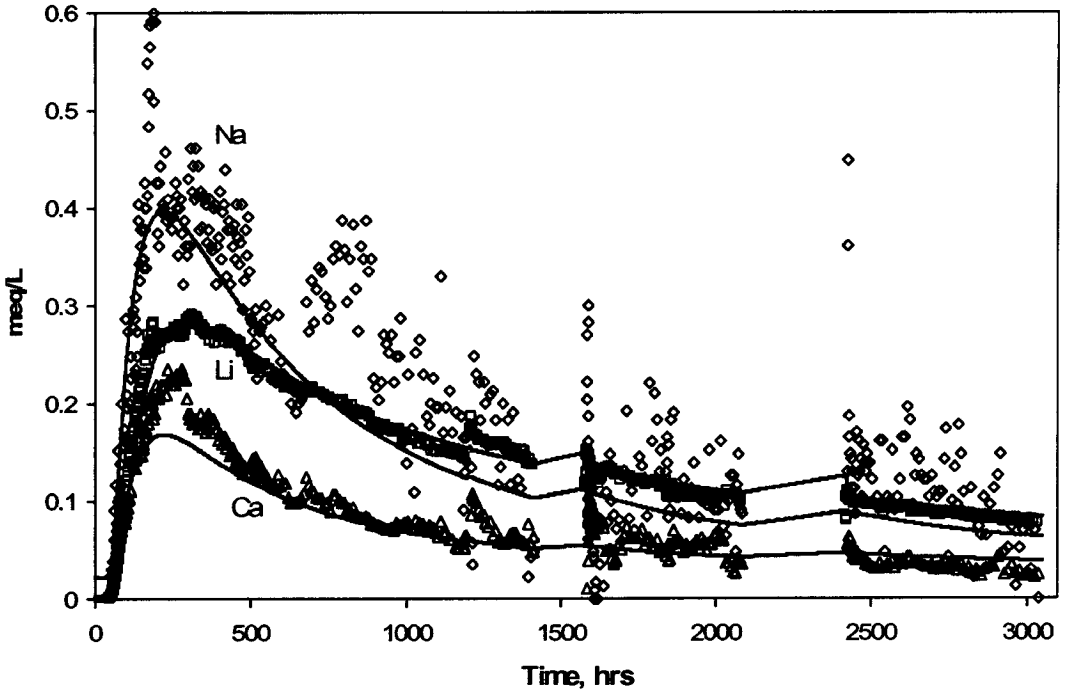

DTN: LAPR831231AQ99.001 [140134] (data); Output DTN: LA0303PR831231.003 (model).

Sources: Reimus (2000 [162852]), Reimus (2003 [165129], including Attachment A).

NOTE: Scatter for sodium is due to the background, which has been subtracted, being large relative to the signal.

Figure 6.3-28. MULTRAN Fits to Cation Responses in the Prow Pass Tracer Test

6.3.4.7.2 Colloid Tracers (Microspheres)

The fit(s) to the Bullfrog test microsphere data are shown in Figure 6.3-29. The "pathways" labeled 1A and 1B represent the nondetaching (or very slowly detaching) and detaching fractions, respectively, of the microspheres following the pathway(s) that resulted in the first solute peak. Pathways 2A, 2B, and 2C in Figure 6.3-29 represent the nondetaching (or very slowly detaching) and the two detaching fractions of the microspheres following the pathway(s) that resulted in the second solute peak. The fitted mass fractions and filtration parameters associated with the "subpathways" in Figure 6.3-29 are given in Table 6.3-8.

Note that the predicted first arrival of microspheres precedes their actual first arrival by 2 to 3 hr. This result can be attributed to the fact that a 4-hr delay was not assumed for the injection of microspheres into the pathways that resulted in the first tracer peaks (as it was for the solutes). No delay was assumed for the microspheres because the microsphere injection began about 3.5 hr after the solutes were injected. If the solutes did not begin entering the pathways resulting in the first tracer peaks until after the microspheres were injected, then it would be reasonable to assume that the microspheres should have entered those pathways at the same time as the solutes.

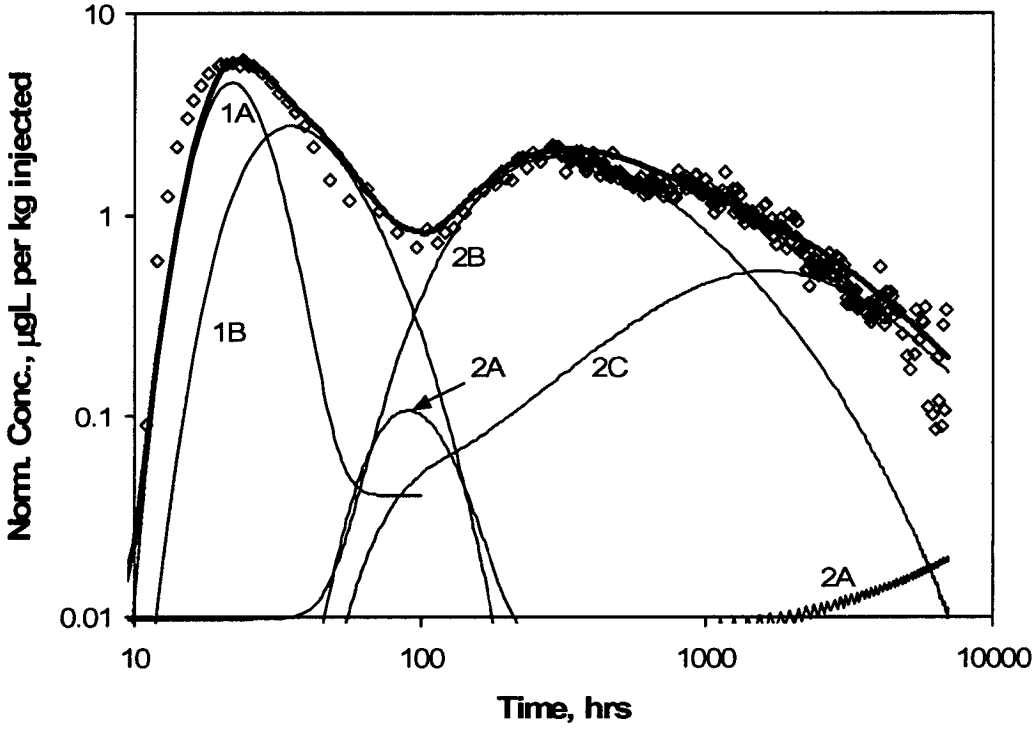

DTN: LA0007PR831231.001 [156043] (data). Output DTN: LA0303PR831231.003 (model).

Sources: Reimus (2000 [165125]), Reimus (2000 [162855]), Reimus (2003 [165129], including Attachment A).

NOTE: Diamonds are microsphere data points. Numbers followed by letters indicate flow pathways discussed in text and listed in Table 6.3-8. Bold line is the sum of all the pathways.

Figure 6.3-29. RELAP Fits to CML Microsphere Response in Bullfrog Tuff Tracer Test

Table 6.3-8. Microsphere Filtration and Detachment Parameters Associated with the Fits Shown in Figure 6.3-29

Parameter	Path 1A	Path 1B	Path 2A	Path 2B	Path 2C
Mass fraction, f	0.111	0.004	0.42	0.07	0.11
k_{filt} (1/hr)	0.175	0.175	0.04	0.04	0.04
λ[a] (1/cm)	0.0017	0.0017	0.0084	0.0084	0.0084
bk_{res}[b] (1/cm-hr)	0.000219[c]	1.08	0.000201[c]	0.211	0.00755

Output DTNs: LA0303PR831231.003; LA0303PR831231.005.

NOTE: Other transport parameters used to obtain the fits are given in Table 6.3-6. Note that subpathways 1A and 1B represent a mass fraction split of Pathway 1 from Table 6.3-6, and subpathways 2A, 2B, and 2C represent a mass fraction split of Pathway 2 from Table 6.3-6.

(a) λ calculated as k_{filt}/v_f, where v_f = average linear velocity determined from mean fluid residence time.

(b) b = fracture half aperture in cm. The fitted detachment rate constant is this lumped parameter.

(c) Maximum detachment rate constant; cannot distinguish between this value and zero, so microspheres could be very slowly detaching or not detaching at all.

However, if the microspheres experienced a delay similar to the solutes, then their predicted first arrival would actually be slightly later than the observed first arrival. In fact, in this case, the first arrival would coincide almost exactly with the first arrival of solutes. Thus, the uncertainty associated with when the microspheres actually began entering the flow system causes uncertainty in the predicted first arrival of the microspheres.

The fits to the Prow Pass test microsphere data are shown in Figure 6.3-30, and the corresponding best-fitting filtration and detachment rate constants are listed in Table 6.3-9. The fits suggest that the small peaks in this test were the result of a very small fraction of microspheres that moved through the flow system unfiltered, and the long tails were the result of small detachment rate constants. The filtration-rate constant listed in Table 6.3-9 for the 280-nm-diameter yellow microspheres was not obtained from fitting, but rather it was the smallest filtration coefficient that resulted in a peak concentration of microspheres that was at or below detection limits. This number can be considered a lower-bound estimate of the yellow-microsphere filtration coefficient because any larger value will result in more filtration and an even lower recovery. Unlike the Bullfrog test, only a single filtration and detachment rate constant were needed to effectively fit the microsphere responses in the Prow Pass test. As mentioned in Section 6.3.4.6.2, no attempt was made to fit the "spikes" in microsphere concentration that occurred after flow transients.

It should be pointed out that the interpretations of the microsphere responses presented in the preceding paragraphs, particularly for the Bullfrog test, are by no means unique. First, it is quite likely that there exists a continuous distribution of filtration and detachment rate constants rather than a few discrete ones, as assumed in the above analyses. Such a distribution could arise from a distribution of colloid surface properties and/or physical and chemical heterogeneities in fracture surfaces (Dabros and Van de Ven 1982 [143278], pp. 232 to 244; 1983 [156652], pp. 576 to 579). It is also possible that colloid filtration and detachment are not linear first-order processes as assumed in Equations 7 and 8. Rather, they might be better described as nonlinear and/or stochastic processes. Finally, as mentioned above, the interpretation of the microsphere

response relative to the solutes is complicated by the fact that, with the exception of the 280-nm-diameter yellow microspheres in the Prow Pass test, the microsphere injections were not started at exactly the same times as the solute injections. In addition to causing uncertainty as to when the microspheres actually began moving into flow pathways (relative to the solutes), the differences in injection times may have resulted in the microspheres not being distributed into flow pathways in exactly the same proportion as the solutes (i.e., a different source term). If different assumptions were made about the distribution of microspheres between the two major sets of pathways in the Bullfrog test, different filtration parameters would be obtained.

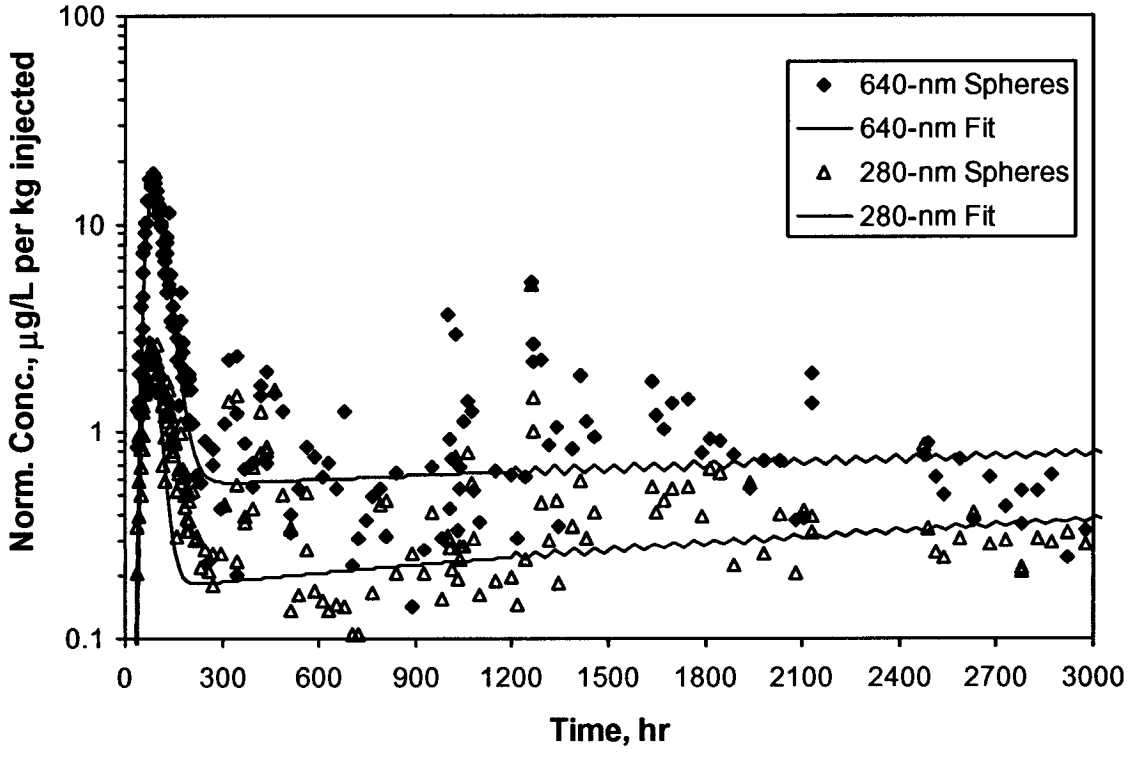

DTN: LAPR831231AQ99.001 [140134] (data). Output DTN: LA0303PR831231.003 (model).

Sources: Reimus (2000 [165125]), Reimus (2000 [162852]), Reimus (2003 [165129], including Attachment A).

NOTE: The jagged appearance of the fits starting at ~1000 hr is the result of instabilities in the Laplace transform inversion algorithm of RELAP V 2.0 (STN: 10551-2.0-00 [159065]). "Spheres" in the legend refers to CML microspheres.

Figure 6.3-30. RELAP Fits to the CML Microsphere Responses in the Prow Pass Tracer Test

Table 6.3-9. Filtration and Detachment Rate Constants for the CML Microspheres in the Prow Pass Tuff Tracer Test

Parameter	Microspheres		
	640-nm Blue	280-nm Orange	280-nm Yellow
k_{filt} (1/hr)	0.043	0.07	0.2[a]
λ (1/cm)	0.0087	0.014	0.041
bk_{res}[b] (1/hr)	0.000154	0.000251	0.0002

Output DTN: LA0303PR831231.003.

NOTE: Mass fractions are assumed to be the same as for solutes (Table 6.3-7).

(a) Minimum value that is consistent with the lack of appearance of these spheres at the production well. The actual filtration rate constant could be much higher.

(b) Maximum values; cannot distinguish between these values and zero. See also footnote (b) of Table 6.3-8.

6.3.4.8 Discussion of Field Tracer Test Results

Estimates of transport parameters that can be used directly in solute transport models were derived from the best-fitting model parameters in Tables 6.3-6 and 6.3-7. These parameter estimates are presented in Table 6.3-10 as ranges of values that are consistent with the tracer test interpretation(s). Additional discussion of these ranges and how they were derived is provided in the following sections. This parameter estimation exercise has several important implications for radionuclide transport in fractured volcanic tuffs near Yucca Mountain.

Table 6.3-10. Transport Parameter Estimates Deduced from the Bullfrog and Prow Pass Multiple-Tracer Tests

Parameter	Prow Pass		Bullfrog	
	Lower Bound	Upper Bound	Lower Bound	Upper Bound
Effective flow porosity (from eq. 22)	0.003	0.006	0.003[a]	0.031[a]
Longitudinal dispersivity, m[b]	13.0	61.5	3.2	62.5
MTC, $\frac{\phi}{b}\sqrt{D_m}$, for radionuclides ($sec^{-1/2}$)[c]	0.00054	0.00095	0.00027	0.0015
Fracture aperture (cm)	0.18	1.05	0.081	1.31
Fracture spacing (cm)	6.4	∞	4.4	∞
Ratio of stagnant to flowing water volumes	3.1	∞	2.1	∞

Output DTN: LA0303PR831231.005.

NOTE: These values above are provided as ranges of values; see text for explanations.

(a) These estimates assume that 75% of the production flow was associated with flow pathways that resulted in the first tracer peak and 25% was associated with the second tracer peak (based on flow survey information (DTN: GS930908312313.008 [166332]), MOL.19951115.0127 through MOL.19951115.0131; see Figure 6.1-2).

(b) Lower bounds assume Peclet numbers for radial flow and 30-m travel distance; upper bounds assume Peclet numbers for linear flow and interval thicknesses as travel distances (see Table 6.1-1 for actual borehole separations and interval thicknesses; also DTN: GS030508312314.003 [164425]), p. 6, Table 1).

(c) Assumes that bromide and PFBA effectively bound molecular sizes and diffusion coefficients of radionuclide solution species.

6.3.4.8.1 Conceptual Transport Model

Even without quantitative parameter estimation, it is clear that the tracer responses in both the Bullfrog and Prow Pass tests are consistent with a dual-porosity conceptual transport model for the fractured volcanic tuffs. It is simply not possible to account for the differences in the bromide and PFBA responses or the relatively small time attenuation but significant concentration attenuation of the lithium response relative to the nonsorbing tracers (in the Prow Pass test and the first peak of the Bullfrog test) without invoking diffusion between flowing fractures and stagnant matrix water. Some diffusion into stagnant water within fractures (e.g., dead-end fractures or along rough fracture walls) cannot be ruled out. However, if the stagnant water were primarily in fractures, the surface area for sorption would be limited, and it is unlikely that there would be as much concentration attenuation of lithium relative to the nonsorbing solutes as observed in the tracer tests. The large surface-area-to-volume ratio necessary to result in the large observed concentration attenuation of lithium seems plausible only if a significant fraction of the stagnant water is in matrix pores.

The quantitative estimates of the lumped mass transfer parameter $\frac{\phi}{b}\sqrt{D_m}$ for bromide in Tables 6.3-6 and 6.3-7 are based on the assumption that bromide has a diffusion coefficient that is a factor of three greater than PFBA. This assumption is based on matrix diffusion coefficients measured in laboratory diffusion cell tests, which are discussed in Section 6.3.8. It is worth noting that RELAP V 2.0 (STN: 10551-2.0-00 [159065]) simulations in which a finite matrix was assumed (i.e., a finite spacing between fractures) offered a slightly better fit to the tracer responses associated with the second peak of the Bullfrog test than simulations assuming an infinite matrix. This result suggests that tracer molecules may have diffused far enough into the matrix to begin encountering molecules from neighboring fractures, which implies a relatively small fracture spacing. Alternatively, the tracers may have encountered diffusion boundaries (no-flux boundaries) within the matrix, which implies a significant increase in tortuosity or a decrease in interconnected porosity at some distance into the matrix from fracture surfaces. For the first peak in the Bullfrog test and for the Prow Pass test, a finite matrix offered no better fits to the tracer data than an infinite matrix. In these cases, it can only be stated that the fracture spacing must have exceeded some threshold value below which the tracer responses would have been significantly different than observed. The applicable threshold values for the first Bullfrog test peak and for the Prow Pass test were estimated by adjusting the fracture spacing in RELAP until the simulated tracer responses began to differ significantly from the simulated responses assuming an infinite matrix. The results are presented in Table 6.3-10 as lower bounds for fracture spacing.

The tracer responses and the qualitative and quantitative conclusions about matrix diffusion that can be drawn from them illustrate very clearly the advantages of using multiple nonsorbing tracers with different diffusion coefficients in tracer tests to distinguish between alternative conceptual transport models. The individual responses of either bromide or PFBA could have been fit reasonably well assuming no matrix diffusion at all. Only when the responses of these tracers are considered together is it obvious that diffusive mass transfer must be invoked to explain the test results. Even long tails that plot linearly on log-log plots of tracer responses (power-law behavior), which are often said to infer matrix diffusion when single tracer responses are analyzed (Haggerty et al. 2000 [156832], pp. 3467 to 3469), do not unequivocally

substantiate diffusive mass transfer. Such responses can also be attributed to hydrodynamic dispersion that scales with residence time (due to the recirculating flow field or effects of density-driven flow), stagnation points, and/or source-term effects (e.g., the slow release of tracers from the injection borehole). Furthermore, the fact that the lithium responses were significantly attenuated in concentration but not in time supports the concept that a significant amount of diffusion occurred into the matrix pores and not simply into stagnant water within the fracture network. This conclusion is very important for Yucca Mountain performance assessment because mass transfer between flowing fractures and the true matrix implies that a large amount of surface area will be available for sorption of radionuclides in the saturated, fractured tuffs.

6.3.4.8.2 Fracture Apertures

An estimate of the average fracture aperture ($2b$) experienced by the tracers in the Bullfrog and Prow Pass tests can be obtained from the estimate of the lumped, diffusive, mass-transfer parameter, $\frac{\phi}{b}\sqrt{D_m}$, provided independent estimates of matrix porosity, ϕ, and matrix diffusion coefficients, D_m, are available. Using estimates of ϕ determined from laboratory measurements and D_m for bromide and PFBA from diffusion cell tests (Section 6.3.8), estimates of $2b$ range from 0.081 to 1.31 cm in the Bullfrog Tuff and from 0.18 to 1.05 cm in the Prow Pass Tuff, as listed in Table 6.3-10. Because the long tracer test intervals in each test both included more than one major lithology (Figure 6.1-2), it was necessary to estimate $2b$ for each major lithologic unit in each interval. The fact that there is a positive correlation between matrix porosity and matrix diffusion coefficient results in a relatively large range of aperture estimates. If it is assumed that the flow pathways associated with the first tracer peak in the Bullfrog test were in the central Bullfrog unit and the pathways associated with the second tracer peak were in the lower Bullfrog unit, then the aperture estimates in these two units correspond to the two extremes listed in Table 6.3-10. These aperture estimates based on tracer responses should be distinguished from friction loss or cubic-law aperture estimates that are obtained from hydraulic responses (Tsang 1992 [113901], pp. 1451 to 1455), although they should be the most appropriate aperture estimates to use for transport calculations.

6.3.4.8.3 Ratios of Stagnant Water to Flowing Water Volumes

Estimates of the ratio of stagnant water volume to flowing water volume in the flow system(s) can be calculated from estimates of fracture spacings obtained from RELAP V 2.0 (STN: 10551-2.0-00 [159065]) simulations and the matrix porosities and fracture apertures used in the RELAP simulations (ratio = $\phi(L/2b - 1)$). Ranges of these estimates are listed in Table 6.3-10. The upper-bound ratios for both tracer tests are listed as infinite because all tracer responses could be fitted reasonably well, assuming infinite fracture spacing. The lower bounds in Table 6.3-10 were obtained using fracture spacings that yielded slightly better fits to the tracer responses than the fits obtained assuming an infinite fracture spacing. These ratios plus one can be considered physical retardation factors for nonsorbing species in the flow system when flow rates are low enough that there is ample time for solutes to diffuse throughout the stagnant water in the system (Robinson 1994 [101154]).

6.3.4.8.4 Lithium Sorption Behavior

Tables 6.3-6 and 6.3-7 list the best-fitting values of the lithium fracture and matrix retardation factors (R_f and R_m, respectively) for the Bullfrog and Prow Pass tests. Note that the R_f values are 1 for both the Prow Pass test and for the first peak in the Bullfrog test, implying negligible retardation within the fractures and sorption only in the matrix. Note that a fracture retardation factor of 1 does not necessarily imply that sorption did not occur on fracture surfaces; it merely suggests that the majority of the lithium sorption occurred after a diffusive mass-transfer step to sorptive surfaces in the matrix. For the second peak in the Bullfrog test, the lithium response was best fitted with $R_f = 4$ and $R_m = 20$, implying some sorption in fractures and a large amount of sorption in the matrix.

Matrix K_d values were deduced from the fitted matrix retardation factors by simple rearrangement of the expression defining the retardation factor:

$$K_d = \frac{\phi}{\rho_B}(R_m - 1) \qquad \text{(Eq. 9)}$$

Because the K_d values depend on the matrix porosity, values are listed in Table 6.3-11 for each lithologic unit that transport may have occurred in for each test (matrix porosities from Section 6.3.8 were used in Equation 9). For a given retardation factor, the corresponding K_d value is always higher in a unit with higher matrix porosity. The R_m value associated with the first lithium peak in the Bullfrog test (Table 6.3-6) was obtained by fitting the rising limb of the lithium response using RELAP V 2.0 (STN: 10551-2.0-00 [159065]). However, because it was necessary to use MULTRAN V 1.0 (STN: 10666-1.0-00 [159068]) to achieve a reasonable fit to the tail of the response (see above), the K_d value for this peak was estimated from the ion-exchange parameters that yielded the best fit to the lithium data (see Section 6.3.9.1.3) rather than from the R_m value obtained from RELAP. The best-fitting, ion-exchange parameters suggested a nonlinear sorption isotherm for lithium in the matrix; hence, K_d values are reported in Table 6.3-11 for lithium concentrations of both ~600 mg/L (low K_d value) and ~0.5 mg/L (high K_d value). This range of concentrations should reasonably bound the concentrations experienced in the field test.

Laboratory batch measurements of lithium sorption onto crushed tuff from C-wells cores indicated a dependence of K_d values on both lithium concentrations and the mineralogy associated with the different lithologies (see Section 6.3.7). The concentration dependence in each case could be represented by a classic nonlinear isotherm in which K_d values decreased as lithium solution concentrations increased. There was also a strong dependence of lithium K_d values on the smectite and zeolite content of the tuffs (Anghel et al. 2002 [164635], pp. 822-824, Section 3.2). The range of laboratory-derived K_d values associated with each unit that could have participated in the Bullfrog and Prow Pass tests is listed in Table 6.3-11 next to each corresponding field-derived K_d value.

Table 6.3-11. Lithium Partition Coefficients Derived from Field Tracer Tests and Laboratory Measurements

Parameter	Field K_d (ml/g)	Laboratory K_d [(a)] (ml/g)
Prow Pass matrix K_d assuming Central Prow Pass Tuff	0.66	0.13 (0.26 at infinite dilution)
Prow Pass matrix K_d assuming Lower Prow Pass Tuff	1.68	0.084 (0.44 at infinite dilution)
Bullfrog matrix K_d in Pathway 1 assuming Central Bullfrog Tuff [(b)]	0.58–4.1 (nonlinear) [(c)]	0.19 (0.44 at infinite dilution)
Bullfrog matrix K_d in Pathway 1 assuming Lower Bullfrog Tuff [(b)]	0.58–4.1 (nonlinear) [(c)]	0.32 (1.64 at infinite dilution)
Bullfrog matrix K_d in Pathway 2 assuming Central Bullfrog Tuff [(b)]	0.74	0.19 (0.44 at infinite dilution)
Bullfrog matrix K_d in Pathway 2 assuming Lower Bullfrog Tuff [(b)]	3.04	0.32 (1.64 at infinite dilution)

Output DTN: LA0303PR831231.005.

NOTE: These lithium partition coefficients (K_d values) were derived from field tracer tests assuming transport in different lithologies within the test intervals.

(a) Values at "infinite dilution" obtained from Langmuir isotherm fits to the data (asymptotic slope at very low concentrations (i.e., $K_L S_{max}$ – see Section 6.3.7.2 for definitions). Other values obtained from a simple linear fit to the entire range of data.

(b) "Pathway 1" refers to pathways that resulted in the first tracer peak in the Bullfrog reactive tracer test, and "Pathway 2" refers to pathways that resulted in the second peak in this test. K_d values were calculated from the smallest matrix retardation factors obtained from alternative interpretations of the test.

(c) The first number corresponds to a K_d value calculated at ~600 mg/L Li^+ using the three-component cation exchange model parameters yielding the best fit to the first lithium peak (see Section 6.3.9.1.3 for description of three-component model); the second number corresponds to a K_d value calculated at 0.5 mg/L Li^+ concentration using the same model parameters. In obtaining the field parameters, a matrix porosity of 0.10 was assumed in the MULTRAN V 1.0 (STN: 10666-1.0-00 [159068]) simulations (approximately equal to that of the Central Bullfrog Tuff). The K_d values for pathway 1 would increase if a greater matrix porosity was assumed, and they would decrease if a smaller matrix porosity was assumed.

The lithium K_d values deduced from the field tracer tests (assuming any given lithologic unit) are consistently higher than the corresponding K_d values measured at the lowest lithium concentrations in the laboratory. These results suggest that the use of laboratory-derived K_d values to predict sorbing species transport in the saturated fractured tuffs near the C-wells location would tend to underpredict the amount of sorption experienced by the species in the field. The fact that the field K_d values tended to be greater than the laboratory K_d values suggests that lithium may have come into contact with alteration minerals in the field that were not present or were depleted in the lab rock samples. Any loosely adhering alteration minerals (e.g., clays) that may have been present in the core samples would very likely have been lost during crushing and wet sieving of the material when it was prepared for the batch sorption experiments.

6.3.4.8.5 Effective Flow Porosity

Contaminant transport predictions are generally very sensitive to assumed flow porosities because transport rates are directly proportional to the specific discharge divided by flow porosity. The effective flow porosity in a cross-hole tracer test without recirculation can be estimated from the following equation, which assumes a steady-state, 2-D (confined with fully-penetrating well), homogeneous and isotropic flow system (Guimera and Carrera 2000 [156830], Equation 6):

$$\eta = \frac{Q\tau}{\pi r_L^2 T} \qquad \text{(Eq. 10)}$$

where

η = effective flow porosity

Q = production flow rate, m^3/hr

τ = mean residence or travel time, hr

r_L = distance between wells, m

T = formation thickness (assumed to be interval length).

With recirculation, the situation is complicated by the fact that there is a hypothetical stagnation point; hence, the mean tracer residence time theoretically approaches infinity. However, the interpretive method described in this report allows for incomplete tracer mass recoveries that could result from stagnation, so a finite estimate of the mean tracer residence time can always be obtained. Guimera and Carrera (2000 [156830]) discuss an alternative method of estimating effective flow porosity from peak, rather than mean, tracer arrival times in tests with partial recirculation. However, their method was derived for system Peclet numbers (r_L/α) ranging from 10 to 100, which are considerably larger than the Peclet numbers obtained in the C-wells multiple-tracer tests (1.3 to 9.3); therefore, their method was not applied here.

For the mean tracer arrival times and flow conditions in the C-wells tracer tests, Table 6.3-10 gives the effective flow porosities calculated using Equation 10 for the Bullfrog and Prow Pass tests. The upper and lower bounds given in Table 6.3-10 were calculated using the mean tracer residence times calculated assuming linear and radial flow, respectively (values in Tables 6.3-6 and 6.3-7). Also, in the Bullfrog test, it was assumed that 75% of the total production flow rate

was associated with the first tracer peak and 25% was associated with the second tracer peak (based on flow survey information suggesting that a large amount of flow occurred in the upper part of the injection interval in c#2 (DTN: GS030508312314.003 [164425], p. 6, Table 1; see Figure 6.1-2).

The relatively large effective porosity estimates obtained from Equation 10 could be due to heterogeneities in the flow field. Flow is undoubtedly not radial, as assumed in the above equations, but rather it very likely follows tortuous pathways between the injection and production wells. Furthermore, it is conceivable that a single high-conductivity feature such as a large, open fracture or fault could transmit the vast majority of the flow to the production well. If this feature does not pass near the injection well, the effective flow rate drawing tracers to the production well will be greatly reduced relative to what would occur in a radial flow field.

6.3.4.8.6 Longitudinal Dispersivity

Longitudinal dispersivity estimates from cross-hole tracer tests generally have considerable uncertainty due to (1) uncertainty in the actual tracer transport distance (the actual flow pathways followed by tracers are unknown), (2) whether the flow field is radial, linear, or some combination, (3) the amount of apparent dispersion caused by nonidealities such as a poorly mixed injection wellbore or density/buoyancy effects, and (4) the amount of apparent dispersion caused by recirculation or the ambient flow field. It is beyond the scope of this report to address in detail the possible effects of each of these uncertainties on the longitudinal dispersivity estimates provided in Table 6.3-10. These estimates can be considered "upper and lower bounds" that were obtained as follows.

1. The maximum transport distance, r_L, was assumed to be the distance from the top of one packed-off interval in the production well to the bottom of the packed-off interval in the injection well (80 to 100 m) while the minimum transport distance was assumed to be the linear distance between the wells (~30 m).

2. The radial and linear Peclet numbers were used to obtain estimates of the dispersivity for the two cases above ($\alpha = r_L/Pe$), and the most extreme values were used for the upper and lower bounds.

3. The RELAP V 2.0 code (STN: 10551-2.0-00 [159065]) simulated a gradual release of tracer from the borehole to the formation by assuming a well-mixed interval, resulting in an exponential decay in tracer concentration in the wellbore. The decay time constant was determined from the volume of the packed-off interval divided by the injection/recirculation rate. Thus, the slow release of tracers from the injection well did not bias the dispersivity (or mean residence time) estimates.

4. An attempt to "subtract out" the apparent dispersion caused by recirculation in the Prow Pass test was made by the following (Reimus 2003 [165129], pp. 123 to 129).

    a. Obtaining a simulated tracer response for a cross-hole test with the appropriate amount of recirculation in a homogeneous, isotropic medium using the 2WELLS_2D V 1.0 computer code (STN: 10665-1.0-00 [159067]).

b. Calculating the variance of the particle residence times in (a).

c. Calculating the variance of tracer response in the actual field test from $\sigma^2 = 2\frac{\tau^2}{Pe}$ where σ^2 is the variance.

d. Subtracting the variance in (b) from the variance in (c) to obtain the variance due to "true hydrodynamic dispersion", σ_T, in the flow system (this assumes that the variance due to recirculation and the variance due to true dispersion are additive, which assumes that the two processes giving rise to the total variance are independent).

e. Rearranging the above expression to obtain the Peclet number and, hence, dispersivity, that represents true hydrodynamic dispersion; i.e., $Pe = 2\frac{\tau^2}{\sigma_T^2}$.

Corrections for dispersion caused by recirculation in the Bullfrog test were assumed to be negligible because 2WELLS_2D V 1.0 (STN: 10665-1.0-00 [159067]) simulations indicated that the variance in tracer travel times for 3.5% recirculation was very small (Reimus 2003 [165129], Attachment A). No attempt was made to account for density/buoyancy effects or the effects of the ambient flow field on the longitudinal dispersivity estimates.

6.3.4.8.7 Colloid Transport

The microsphere filtration and detachment rate constants deduced from the Bullfrog and Prow Pass tracer tests can potentially be used as estimates of filtration and detachment rate constants for natural colloids that could facilitate the transport of radionuclides that are strongly adsorbed to colloids. However, it must be kept in mind that the CML microspheres do not have the same physical and chemical properties as natural inorganic colloids (see the revision of the SZ colloid transport report, BSC 2003 [162729], Section 6.8). The revision to the SZ colloid transport report summarizes laboratory experiments (BSC 2002 [162729], Section 6.8), in which it was shown that 330-nm-diameter CML microspheres transported with the same attenuation or less attenuation through saturated fractures than 100-nm-diameter silica spheres, suggesting that microsphere filtration and detachment rate constants may be conservative if used to predict silica colloid transport in fractured media.

Perhaps of greater importance than the microsphere filtration and detachment rate constants derived from the field tests is the fact that the microsphere responses qualitatively indicate that (1) colloid detachment from fracture surfaces is a process that clearly occurs in fractured tuffs, and (2) colloid detachment is apparently enhanced by flow transients. These qualitative results suggest that it is not sufficient to consider only colloid filtration when assessing colloid-facilitated radionuclide transport, but that colloid detachment and its dependence on other variables must also be considered and could actually dominate the transport behavior of colloids.

6.3.5 Limitations and Uncertainties Associated with Transport Parameter Estimates

6.3.5.1 Limitations and Uncertainties Inherent in Tracer Testing

Several factors contributed to the uncertainty in transport parameters derived from tracer test interpretations. First, there are data uncertainties, which are related to the accuracy and precision of the tracer chemical analyses, including both random and systematic errors. Random errors were estimated to be small because the breakthrough-curve data are not widely scattered and show well-defined trends. The most significant sources of systematic errors would have been day-to-day differences in analytical instrument operation and in analytical standard preparation over extended periods of time. However, repeat measurements on separate days indicate that these errors were also minimal.

During the iodide tracer test in the Bullfrog-Tram interval (February to April 1996), the pump gradually failed, resulting in a decreasing flow rate during the test, which changed from 526 L/min (139 gpm) at the beginning to 371 L/min (98 gpm) at the end (Umari 2002 [162858], Binder 5, Section G-10, pp. 65 to 77). This violated the assumption of a steady-state flow field in the Moench (1989 [101146]) semi-analytic method employed to analyze the tracer test results. This source of uncertainty was eliminated for subsequent tests by replacing the pump.

There was uncertainty regarding the extent to which the tracers were evacuated from the injection intervals to the aquifer in each test. The very long injection intervals (ranging from 75 m to almost 200 m) and the lack of down-hole mixing contributed to this uncertainty. Slow release of tracers from the injection intervals could have contributed to tailing in the solute tracer responses that would have been interpreted as dispersion or matrix diffusion when only one nonsorbing tracer was used. Attempts to reduce this uncertainty in the Prow Pass tests were made by deploying a down-hole system capable of mixing the tracer solution after its injection into the borehole. Although the down-hole mixing system worked only marginally, it is believed that stratification of tracer concentrations in the borehole was minimized. Also, recirculation of 30% of the water produced from c#2 during the Prow Pass test should have served to help "flush" tracers out of the injection interval.

The influence of the natural gradient that exists at the C-wells on tracer recovery at the pumped well is a source of uncertainty. Determinations of the capture zone of the pumped well, and how it is altered by the existence of a natural gradient, depend on the assumptions made regarding flow heterogeneity and anisotropy. Mass that is not recovered by the pumped well is potentially the result of path ways other than the postulated radially convergent or partially recirculating streamlines toward the pumped well. However, it could also be a result of some of the tracer mass moving through the matrix rather than fractures; transport through the matrix would be so slow that the mass would not be expected appear in the production well during the time of the tracer tests.

A limitation of all tracer tests conducted at the C-wells is that they produce estimates only of longitudinal dispersivity, not transverse dispersivity (because sampling occurs only at the production well and is not spatially distributed). In addition, the estimate of flow porosity has the uncertainty of an unknown travel distance between the tracer injection and production points in the boreholes (i.e., the source and the sink locations). This travel distance was bounded by

assuming a minimum of the straight-line distance between the injection and production wells and a maximum of the formation thickness, defined by the distance between packers in the injection and the pumped intervals.

6.3.5.2 Uncertainties Associated with Test Interpretation Methods

When estimating transport parameters using a semi-analytical solution to the advection-dispersion equation, such as the Moench (1989 [101146]) solution or the RELAP V 2.0 computer code (STN: 10551-2.0-00 [159065]) employed in this study, several assumptions are made. The medium is assumed to be homogeneous and isotropic, and the flow regime is assumed to be either radial or linear (i.e., having a velocity that varies as 1/r or having a constant velocity between injection and production well). Also, the aquifer is assumed to be two-dimensional (flow only in the two horizontal dimensions without a vertical component). To the extent that these assumptions do not reflect the true nature of the media, the transport parameter estimates will be erroneous. However, the information necessary to implement more sophisticated models that explicitly account for flow and transport heterogeneity does not exist. Even data to support stochastically-generated hydraulic conductivity distributions in numerical models are scarce to nonexistent. Thus, the interpretive models used in this report, while relatively unsophisticated, reflect the level of knowledge of flow and transport heterogeneity at the scale of the tracer tests. Uncertainty associated with assuming either radial or linear flow (when the actual nature of the flow field could be somewhere in between) is addressed in the multiple tracer-test interpretations by reporting mean residence times and Peclet numbers for both radial and linear flow assumptions.

The Moench (1989 [101146]; 1995 [148784]) and RELAP V 2.0 (STN: 10551-2.0-00 [159065]) semi-analytical models are mathematically very similar. However, differences in the methodologies and assumptions used in the implementation of the models to interpret tracer responses result in differences in the resulting transport parameter estimates. Highlights of the differences in the two approaches are the following.

(1) The first approach (Moench model, Section 6.3.1) involves normalizing tracer concentrations to the maximum (peak) tracer concentration, whereas the second approach (RELAP model, Section 6.3.4.6) involves normalizing tracer concentrations to the injection mass. The first method results in matching the shapes of breakthrough curves (or differences in shapes when there are multiple tracers), while the second is aimed at matching not only shapes, but also peak normalized concentrations and total recoveries. Thus, the second method has some additional fitting constraints that result in different transport parameter estimates compared to the first method.

(2) Both methods use essentially the same mathematical model to account for the tracer residence time in the injection borehole (i.e., a well-mixed interval with an exponential decay in tracer concentration). However, the mean residence time in the borehole was allowed to be much larger when running simulations using the first method (Section 6.3.1) compared to the second method (Section 6.3.4.6). A larger residence time in the injection borehole effectively adds dispersion to the simulated response curves, which results in a smaller flow-system dispersivity when the tracer data are fitted. Thus, the

longitudinal dispersivity estimates from the first method tend to be lower than from the second method.

To assess the different results obtained from the two approaches qualitatively, the RELAP V 2.0 (STN: 10551-2.0-00 [159065]) computer code was used to interpret the iodide and 2,4,5-TFBA tracer test in the Prow Pass Tuff. The Moench model (Moench 1995 [148784]) interpretation of this test is presented in Section 6.3.1.2.1. First, the parameters obtained from the Moench model analysis were used in RELAP to see how well the two models agree when using the same inputs. It can be shown through algebraic manipulations that the mass transfer coefficient $\frac{\phi}{b}\sqrt{D_m}$ in RELAP is equivalent to $6\,b'\sqrt{\frac{\sigma'\gamma'}{\tau}}$ in the Moench model (Moench 1995 [148784]), where b' = radius of spheres that represent matrix blocks (into which diffusion occurs), σ' = dimensionless storage parameter = $\frac{\phi}{\phi_f}$, and $\gamma' = \frac{D_m\tau}{\phi_f(b')^2}$. ϕ_f is the fracture porosity in this case, and τ is defined as $\frac{\pi h\phi_f(r_L^2 - r_w^2)}{Q}$, where h is the aquifer thickness, r_L is the distance between the injection and production wells, r_w is the radius of the production well, and Q is the volumetric flow rate from the production well. Additionally, an injection borehole "mixing length" of 30.5 m was used in the Moench model analysis of Section 6.3.1.2.1. This mixing length can be shown to translate to an injection borehole time constant of ~0.0023 hr^{-1} in the RELAP model (time constant $= \frac{4Q r_i}{2\pi r_L}\left(\frac{1}{\pi r_i^2 h_i}\right)$, where r_i = injection well radius and h_i = mixing length; Moench 1989 [101146]). Using these input parameters, along with a Peclet number of 100 (i.e., a longitudinal dispersivity of 0.29 m), the RELAP model yields the fits shown in Figure 6.3-31 (the mean residence time and mass fraction were adjusted to obtain these fits). The longitudinal dispersivity reported in Section 6.3.1.2.1 was 0.27 m. The tracer responses and fits in Figure 6.3-31 are adjusted so that they all have the same maximum concentration, which is consistent with the analysis used in Section 6.3.1.2.1. A comparison of Figure 6.3-31 and Figure 6.3-16 shows that the two models yield almost indistinguishable results when the same input parameters are used.

The injection borehole time constant of 0.0023 hr^{-1} used in the above analysis translates to a mean tracer residence time in the borehole of 1/0.0023, or ~435 hr. This residence time is at odds with the tracer concentration measurements in the injection borehole described in Section 6.3.1.2.1.1, where it is stated that the borehole was effectively flushed of tracer in ~8.5 hr. The fact that the tracer was flushed from the borehole in such a short time is not surprising given that there was a continuous injection of ~1.5 gpm (~5.7 L/min) of groundwater into the injection zone following the injection of tracers. A mean residence time of ~9 hrs is calculated by dividing the volume of the injection interval (~3,000 L) by the 5.7 L/min flow rate. For these reasons, a second RELAP simulation was conducted in which it was assumed that the injection borehole

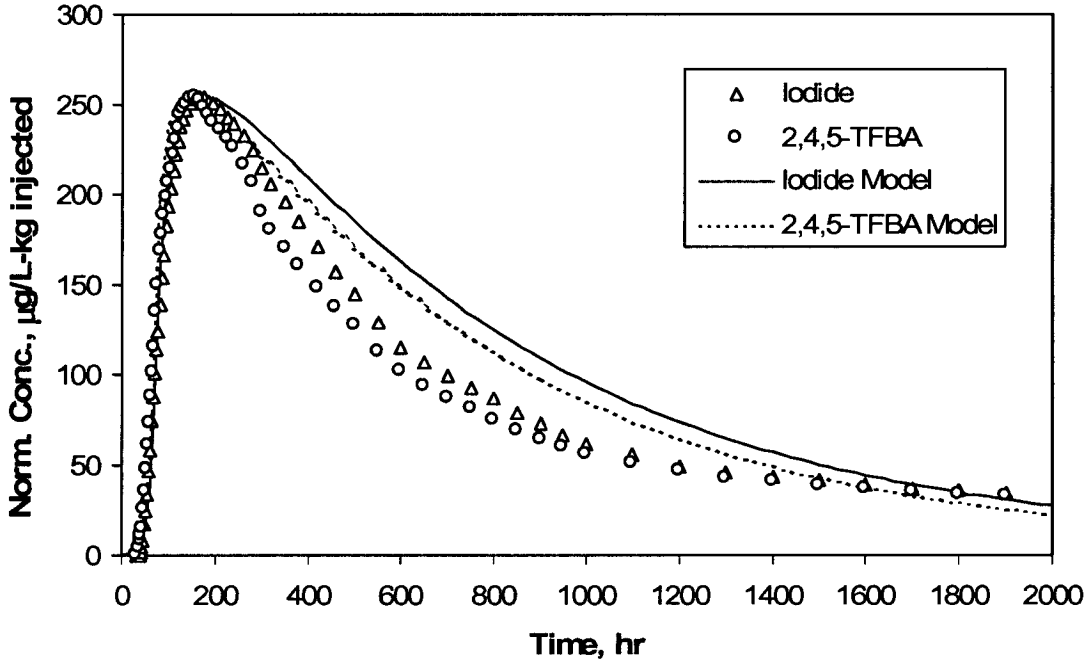

Output DTN: LA0304PR831231.001.

NOTE: Data points represent a subset of the actual data. Data and curves are adjusted so that they all have the same maximum normalized concentration (see Figure 6.3-16 for comparison). The same parameters obtained from the Moench model in Section 6.3.1.2.1 were used.

Figure 6.3-31. RELAP Fits to the Iodide and 2,4,5-TFBA Responses in the Prow Pass Tuff Tracer Test Assuming an Injection Zone Time Constant of 0.0023 hr^{-1}

time constant was 0.11 hr^{-1} ((5.7)(60)/3000). This is the same time constant value that was used in the analysis of the PFBA and bromide tracer test conducted in the Prow Pass Tuff described in Section 6.3.4.7.1. The resulting RELAP fits to the tracer data are shown in Figure 6.3-32, where in this case the tracer concentrations are normalized to tracer injection mass, as in Section 6.3.4. The RELAP transport parameters for the simulations of Figures 6.3-31 and 6.3-32 are listed in Table 6.3-12. Also listed in this table are the parameters obtained from RELAP fits to the PFBA and bromide data in the Prow Pass Tuff, discussed in Section 6.3.4.7. This test was conducted in the same configuration and with the same flow rates as the iodide and 2,4,5-TFBA test, although the volume of the tracer solution injected was considerably larger. Clearly, there is a very large difference in the mean residence times and Peclet numbers of the simulations with significantly different borehole time constants, although the iodide mass transfer coefficients, $\frac{\phi}{b}\sqrt{D_m}$, are in reasonably good agreement in all simulations.

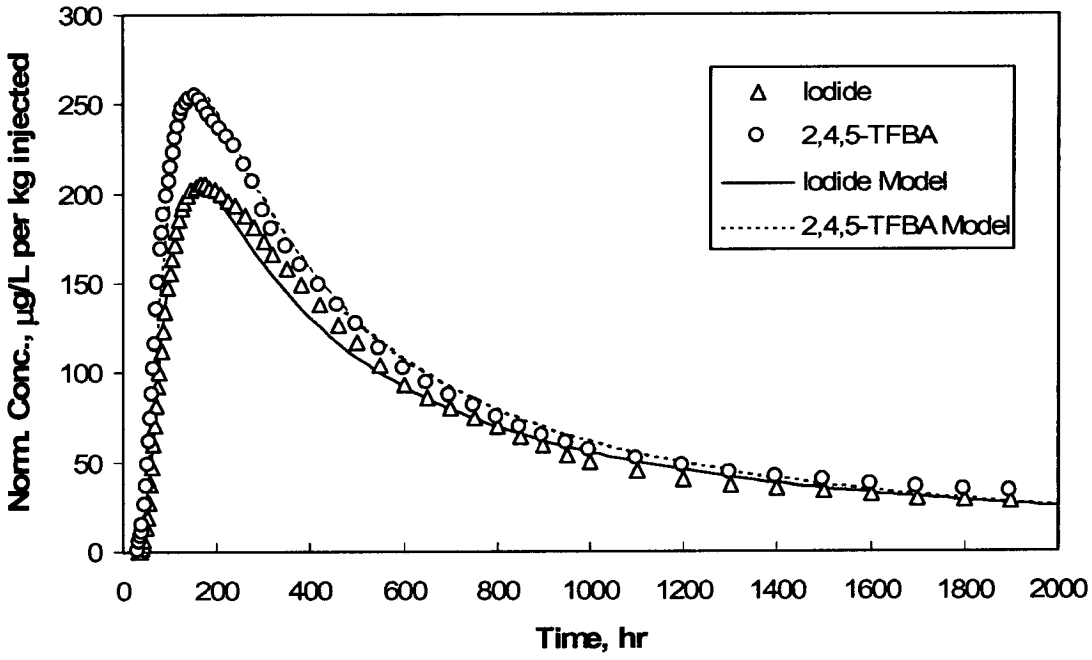

Output DTN: LA0304PR831231.001.

NOTE: Data points represent a subset of the actual data.

Figure 6.3-32. RELAP Fits to the Iodide and 2,4,5-TFBA Responses in the Prow Pass Tuff Tracer Test Assuming an Injection Borehole Time Constant of 0.11 hr^{-1}

The reason for the large differences in mean residence times and Peclet numbers in Table 6.3-12, particularly between the two interpretations of the iodide and 2,4,5-TFBA test, becomes clear when one considers the implications of the different borehole mixing assumptions. Figure 6.3-33 shows tracer responses calculated by RELAP V 2.0 (STN: 10551-2.0-00 [159065]) in a hypothetical system with a mean residence time in the aquifer (not the injection borehole) of 1 hr, a Peclet number of 100, and no matrix diffusion. With this choice of parameters, the responses are due almost entirely to tracer residence time in the injection borehole. The tails of the responses are linear on a semi-log plot because tracer concentrations in a well-mixed region decay exponentially. The curve with the largest time constant corresponds to the tracer residence time distribution in the borehole for the RELAP fits of Figure 6.3-32, and the curve with the smallest time constant shows the residence time distribution associated with the fits of Figure 6.3-31. The iodide response in the Prow Pass tracer test is also shown in Figure 6.3-33. It is apparent that the curve with the smallest time constant has a tail that matches the tracer data quite well. Thus, to match the entire breakthrough curve, it is only necessary to impose a lag on the borehole response (accounted for by a finite residence time in the flow system), with only a very small amount of additional dispersion or matrix diffusion in the flow system necessary to optimize the fit. However, as the borehole time constants get larger, it becomes necessary to impose a greater lag and account for more dispersion or matrix diffusion in the flow system to achieve a match to the data.

Table 6.3-12. Transport Parameters Estimates from RELAP Fits of Figures 6.3-31, 6.3-32, and from the Fits to the PFBA and Bromide Responses in the Prow Pass Tuff

Parameter	I, TFBA Figure 6.3-31	I, TFBA Figure 6.3-32	Br, PFBA Test
Borehole Time Constant, α, hr^{-1}	0.0023	0.11	0.11
Mean Res. Time, τ, hr (linear flow)	55	520	1210
Peclet number, *Pe* (linear flow)	100	1.6	0.9
MTC, $\frac{\phi}{b}\sqrt{D_m}$, $sec^{-1/2}$	0.00161	0.001	0.000949

Output DTN: LA0304PR831231.001.

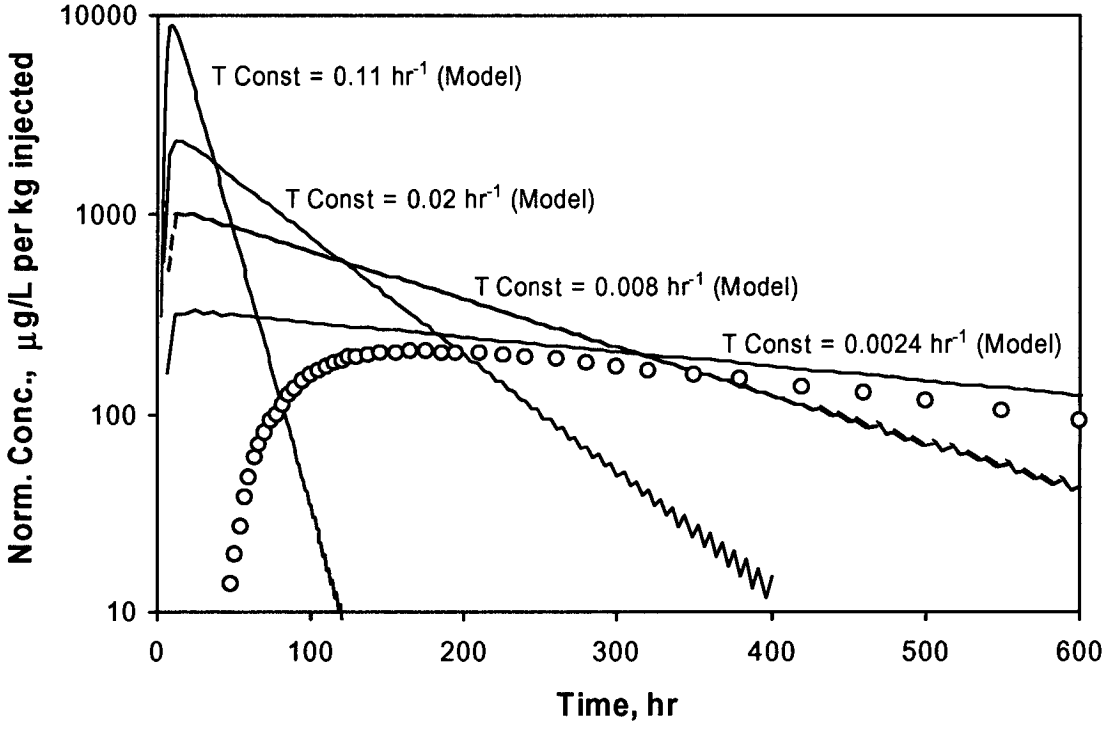

Output DTN: LA0304PR831231.001.

NOTE: Data points represent a subset of the actual data. Iodide data from the Prow Pass Tuff tracer test (Figures 6.3-31 and 6.3-32) are shown for comparison. See Section 6.3.4.7 for discussion.

Figure 6.3-33. Tracer Responses as a Function of Injection Borehole Time Constant in a Hypothetical Flow System with a Mean Residence Time of 1 hr in the Aquifer, a Peclet Number of 100, and No Matrix Diffusion

Figure 6.3-34 shows the mean residence times (in the aquifer), Peclet numbers, and mass transfer coefficients, $\frac{\phi}{b}\sqrt{D_m}$ or MTC, that provided best fits to the combined iodide and 2,4,5-TFBA tracer data sets as a function of borehole time constant. The fits were equally good until the time constant became less than about 0.0025 hr^{-1}, which roughly corresponds to the time constant used in Figure 6.3-31. Note that there is a sharp transition at a time constant of ~0.007 hr^{-1}, where residence times increase and Peclet numbers decrease dramatically. This transition corresponds to the point where the tracer residence time in the borehole can no longer account for the majority of the dispersion in the tracer curves. Figure 6.3-34 shows that the MTC does not vary nearly as much as the mean residence time and Peclet number, although it goes through a maximum at the transition point because of an attempt to account for tracer dispersion with increased matrix diffusion. This result is important because it indicates that despite the dramatic differences in mean residence time and Peclet number as a function of borehole time constant, matrix diffusion is always necessary to explain the tracer responses (at least until borehole residence times become so low that all fits are poor). Furthermore, the estimates of matrix diffusion parameters do not vary all that much. Thus, the various interpretations, while significantly different in mean residence time and Peclet number, are all consistent with a dual-porosity conceptualization of the fractured volcanics.

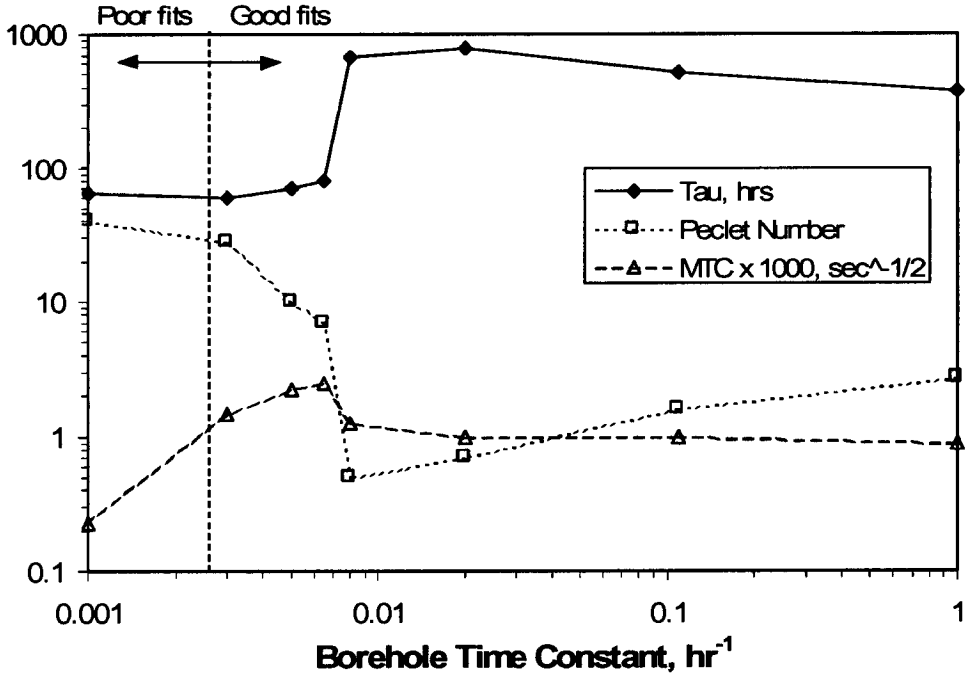

Output DTN: LA0304PR831231.001.

NOTE: Units on y axis depend on the curve.

Figure 6.3-34. Mean Residence Time (τ), Peclet Number, and MTC (x 1000) as a Function of Borehole Time Constant from RELAP Fits to the Iodide and 2,4,5-TFBA Data of Figure 6.3-32

6.3.5.3 Uncertainties Associated with Nonuniqueness of Test Interpretations

Nonuniqueness of tracer test interpretations must be considered before uncertainties in transport parameters derived from tracer tests can be fully addressed. A prime example of nonuniqueness is that long tails in tracer responses can be interpreted as either being the result of large longitudinal dispersion or significant matrix diffusion. In the nonsorbing tracer tests, nonuniqueness was addressed by using PEST V 5.5 (STN: 10289-5.5-00 [161564]) to obtain optimal transport parameter estimates and to estimate confidence intervals associated with the parameters. In the multiple tracer tests, nonuniqueness of interpretations was minimized by simultaneously fitting the tracer responses using known ratios of diffusion coefficients as constraints on the relative matrix diffusion of different tracers. However, even after taking these measures, there is considerable nonuniqueness associated with tracer test interpretations.

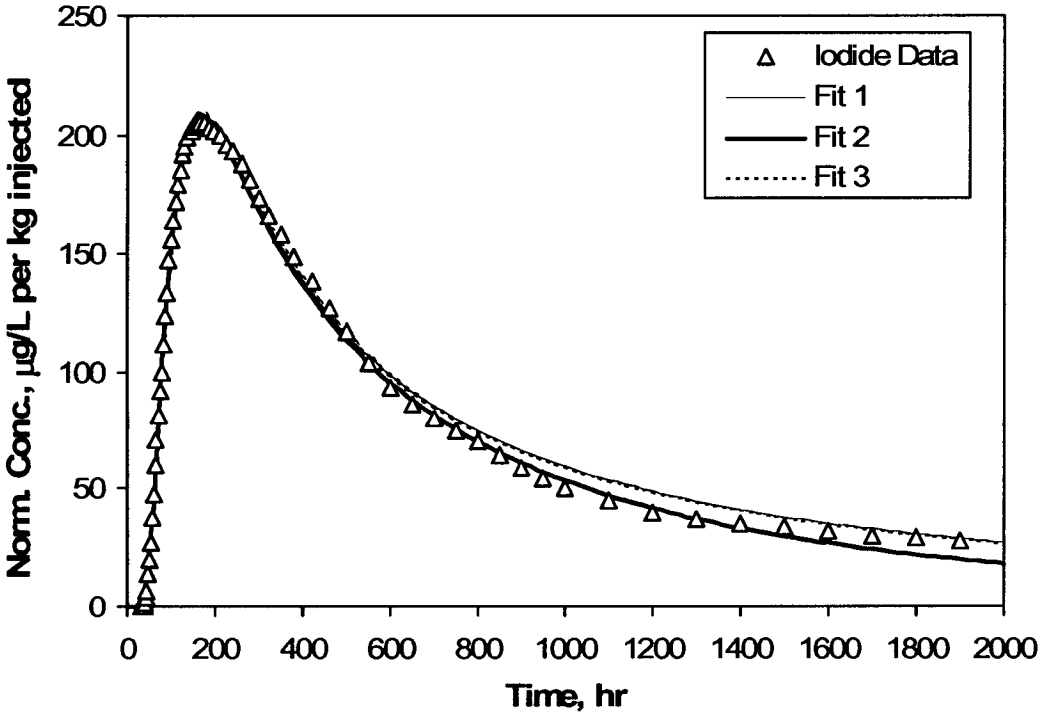

Output DTN: LA0304PR831231.001.

NOTE: Data points represent a subset of the actual data. Model parameters associated with the fits are listed in Table 6.3-13. Note that Fits 1 and 3 essentially fall on top of each other.

Figure 6.3-35. RELAP Fits to Iodide Data from Prow Pass Tracer Test

Table 6.3-13. Transport Parameters Obtained from RELAP Fits to Iodide Data shown in Figure 6.3-35

Parameter	Fit 1	Fit 2	Fit 3
Mass Fraction	0.23	0.11	0.24
Borehole Time Constant, hr^{-1}	0.11	0.11	0.11
Mean Res. Time, τ, hr (linear flow)	50	700	9000
Peclet number, *Pe* (linear flow)	17	1.3	0.1
Iodide MTC, $\frac{\phi}{b}\sqrt{D_m}$, $sec^{-1/2}$	0.01	0.0	0.0001

Output DTN: LA0304PR831231.001.

First, nonuniqueness associated with the interpretation of responses of single tracers is addressed. Figure 6.3-35 shows three RELAP V 2.0 (STN: 10551-2.0-00 [159065]) fits to the iodide response in the Prow Pass tracer test shown in Figure 6.3-32. These fits, which were obtained by arbitrarily fixing the Peclet number and then allowing the mean residence time, mass fraction, and MTC to be adjusted to achieve a fit, are arguably equally good. However, the best-fitting parameters, listed in Table 6.3-13, vary by 2 to 4 orders of magnitude, and it is not even possible to distinguish between a single-porosity and a dual-porosity system (MTC can be zero). Clearly, nonuniqueness associated with interpreting single tracer responses is excessive and probably unacceptable for the purpose of transport parameter estimation.

A similar exercise in determining nonuniqueness of test interpretations was conducted for each of the multiple tracer responses; i.e., two in the Prow Pass Tuff and two in the Bullfrog Tuff (two peaks in this case). Although the absolute best-fitting parameters in each case, as determined by minimizing the sum of squares of differences between model and data, are reported in Sections 6.3.1 and 6.3.4, there is still considerable nonuniqueness of the fits. If we arbitrarily establish a criterion that any sum of squares of differences less than 1.5 times the minimum is an equally good fit to the data, then the ranges of parameter values that provide equally good fits to the data sets are listed in Table 6.3-14. Fits having sum-of-squares differences of less than a factor of 1.5 times the minimum are essentially equally good in appearance; and when one considers that the best fits are dependent on data scatter and on variability in data point density in the breakthrough curves (e.g., more data in tails as opposed to peaks), then a good case can be made that the fits are equally plausible. The parameter ranges were determined by varying each parameter in Table 6.3-14 manually over a wide range of values while letting all other parameters in Table 6.3-14 be adjusted to achieve fits to the data sets. Figure 6.3-36 shows the fits to the iodide and 2,4,5-TFBA data from the Prow Pass tracer test (Figure 6.3-32) that had the lowest and highest optimized sum-of-squares differences (with the highest still being within a factor of 1.5 of the lowest). Another "parameter" that was varied in the exercise was the ratio of the diffusion coefficients of halides (bromide and iodide) and FBAs (PFBA and TFBA) in the multiple tracer tests. This ratio is somewhat uncertain, especially in rock matrices, because most literature values are based on free water measurements. However, the values of the other transport parameters were found to be quite insensitive to this ratio when it was varied over a reasonable range.

Table 6.3-14. Transport Parameter Ranges from Multiple-Tracer Tests at the C-wells

Parameter	BF, Peak 1	BF, Peak 2	PP, I-TFBA	PP, Br-PFBA
Mass Fraction	0.11 – 0.13	0.56 – 0.7	0.17 – 0.3	0.56 – 0.82
Mean Res. Time, τ, hr (linear flow)	320 – 420	700 – 1800	340 – 1340	600 – 1900
Peclet number, *Pe* (linear flow)	5 – 8	0.9 – 2.4	0.6 – 2.6	0.6 – 1.9
Halide MTC, $\frac{\phi}{b}\sqrt{D_m}$, $sec^{-1/2}$	0.000837 – 0.00224	0.000245 – 0.000775	0.000775 – 0.00122	0.000632 – 0.00122

Output DTN: LA0304PR831231.001.

NOTE: BF refers to Bullfrog
PP refers to Prow Pass.

It is important to note that the ranges of parameter values in Table 6.3-14 are not completely independent of each other. That is, when one parameter value is taken from the high end of its range, another may have to be taken from near the low end of its range to achieve a good fit. This is especially true of the mean residence time and Peclet number, which have a very strong inverse correlation. Figure 6.3-37 shows the relationship between best-fitting values of Peclet number and mean residence time for the four multiple-tracer tests at the C-wells. All of the points plotted in this figure are associated with equally good fits to the data according to the criterion stated in the previous paragraph. Note that the range of mean residence times is significantly lower for the data set with the largest Peclet numbers compared to the three data sets with smaller Peclet numbers. This result was found to be true in general; i.e., the range of mean residence times was smaller for hypothetical tracer responses with less longitudinal dispersion.

Figure 6.3-38 shows that the best-fitting mass fractions are positively correlated with the best-fitting mean residence times for the iodide and 2,4,5-TFBA responses in the Prow Pass Tuff. This result and Figure 6.3-37 imply a negative correlation of mass fraction with Peclet number. These same trends were obtained for all other multiple-tracer tests. Interestingly, the MTC, $\frac{\phi}{b}\sqrt{D_m}$, was poorly correlated with any of the other transport parameters. In fact, the extremes of MTC values were generally associated with values of other parameters that were not near the ends of their respective ranges. Also, the range of MTC values never included zero, which indicates that a dual-porosity system is always implied from the fits.

The parameter ranges in Table 6.3-14 reflect considerable uncertainty associated with the nonuniqueness of interpretive model fits for multiple tracer tests. These ranges, in general, are comparable in magnitude to the ranges of derived parameter values provided in Table 6.3-10, which were based on uncertainties in tracer travel distances and radionuclide diffusion coefficients, as well as the range of parameter values obtained from different tests in the same interval. The ranges in Table 6.3-10 would have to be expanded somewhat to account for the additional uncertainty associated with the nonuniqueness of model fits. Expanding these ranges by multiplying the lower value of any parameter in Table 6.3-10 by 0.5 and the upper value by 2 would effectively capture this additional uncertainty.

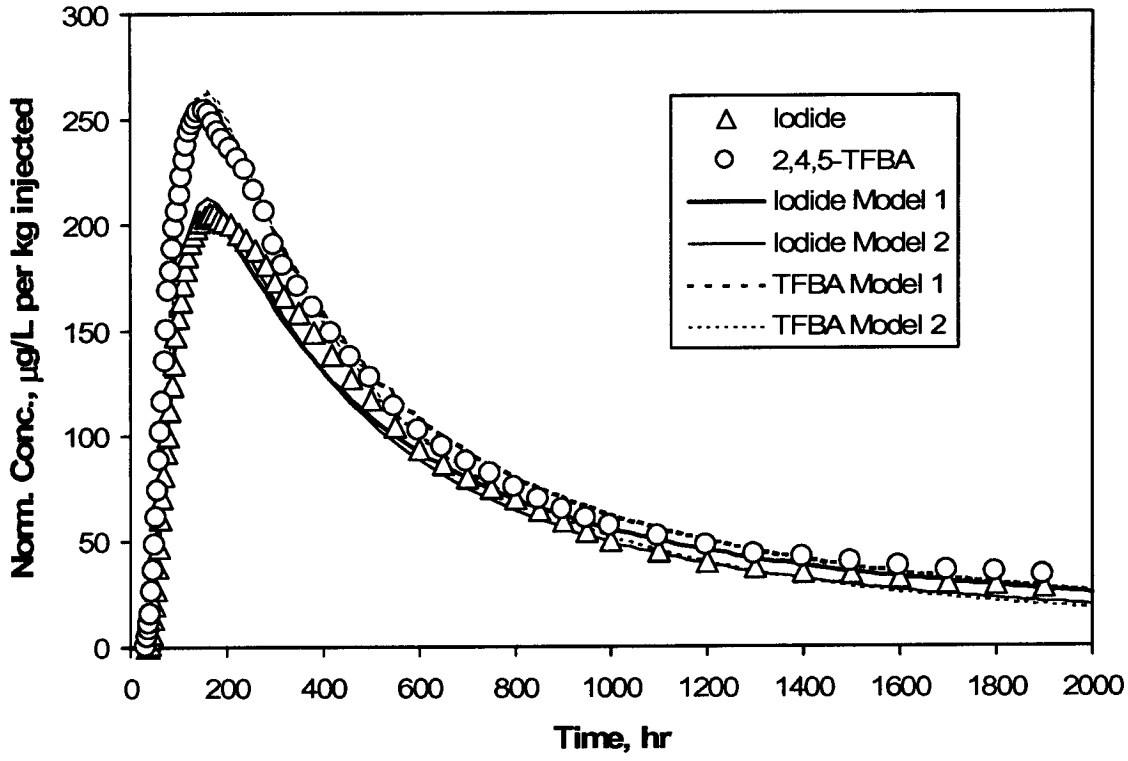

Output DTN: LA0304PR831231.001.

NOTE: Data points represent a subset of the actual data. Bold curves represent the best fits to data. The sum of squares differences between data and models are within a factor of 1.5 of each other.

Figure 6.3-36. RELAP Fits to the Iodide and 2,4,5-TFBA Data from the Prow Pass Tracer Test

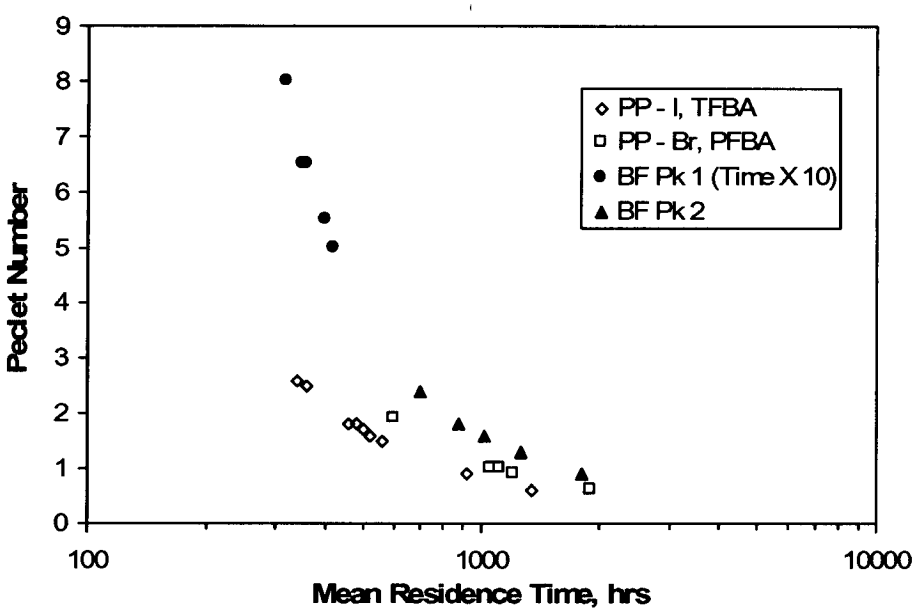

Output DTN: LA0304PR831231.001.

NOTE: PP refers to Prow Pass; BF refers to Bullfrog. Note that the residence times (but not Peclet numbers) are multiplied by 10 for peak 1 of the Bullfrog Tuff tracer test.

Figure 6.3-37. Correlation Between Best-fitting Peclet Numbers and Mean Residence Times for the Multiple-Tracer Tests at the C-wells

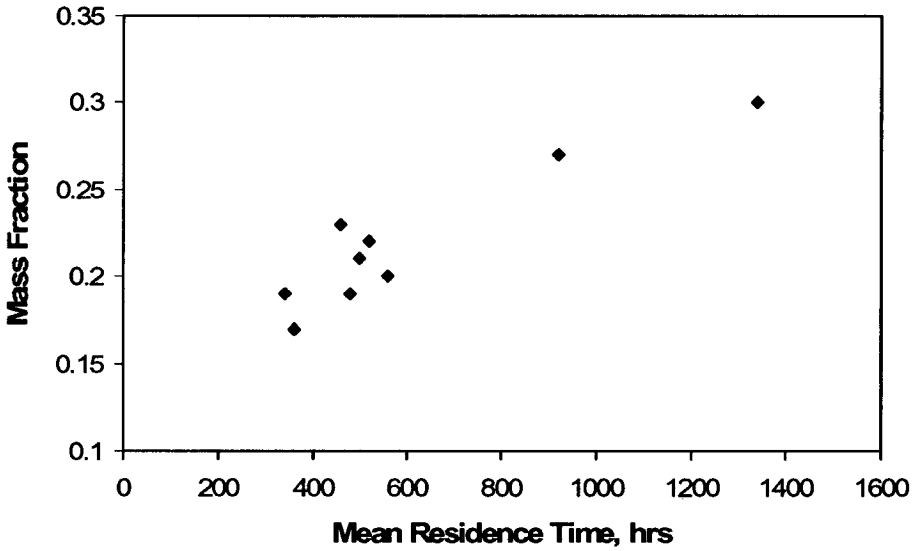

Output DTN: LA0304PR831231.001.

Figure 6.3-38. Correlation Between Best-fitting Mass Fractions and Mean Residence Times for the Multiple-Tracer Tests at the C-wells

A few points are worthy of mention regarding uncertainty associated with nonuniqueness of model fits to obtain transport parameter estimates:

1. Although there is considerable uncertainty associated with model fits to multiple-tracer data sets, the uncertainty is far less than the uncertainty associated with fits to single-tracer data sets (compare Tables 6.3-13 and 6.3-14). Also, all the fits to multiple-tracer data sets indicated a dual-porosity system, while fits to single-tracer data sets cannot effectively distinguish between a single- and dual-porosity transport system.

2. This uncertainty analysis and discussion is by no means complete. Other factors must be considered when doing a rigorous uncertainty analysis. A couple of additional considerations that go beyond the scope of this analysis report are:

   - When fitting multiple data sets, one must be careful to not inadvertently give one set more weight than the others in the fitting procedure. Inappropriate weighting can occur, for instance, when one data set has significantly more data points than the other(s) or when one set has much larger numerical values than the other(s). Approaches to dealing with this problem include (1) various weighting schemes, (2) making the number of data points the same for all data sets (by dropping some data from the larger data sets), or (3) normalizing the sum-of-squares errors for each data set by dividing by the number of points fitted for each set. Each of these approaches introduces some arbitrary bias into the fitting procedure, which introduces bias into the errors associated with the parameter estimates. In this analysis report, we use approach (3).

   - The fitting criteria (or objective function) are very important and can have a significant influence on both parameter estimates and error estimates. For instance, one will obtain different answers if the sum-of-squares differences between model and data are minimized vs. minimizing the sum-of-squares differences between the log of the data and the model. In this analysis report, it was chosen to minimize the straight sums-of-squares differences rather than the differences in any transformations of the data and model values.

6.3.6 Concluding Remarks About Field Tracer Tests

It is recognized that the tracer-test interpretations using primarily semi-analytical solution methods that assume an idealized geometry and steady flow rates are a considerable simplification of reality. Numerical models could certainly be used to account for greater system heterogeneity. Also, more sophisticated semi-analytical representations of dual-porosity systems, such as the multirate-diffusion model of Haggerty and Gorelick (1995 [156831], pp. 2383 to 2400), could be applied. However, the information available to support these more sophisticated representations of the flow and transport system is sparse to nonexistent. Furthermore, the agreement between the relatively simple semi-analytical models (either the Moench 1989 [101146]; 1995 [148784]) model or RELAP (LANL 2002 [159065]) and the tracer responses are considered to be very good. The only additional model complexity needed to explain any portion of the tracer-test data sets was the multicomponent transport and ion exchange capabilities of the MULTRAN V 1.0 (STN: 1066-1.0-00 [159068]) model needed to match the lithium response in the first peak of the Bullfrog tracer test. Although the introduction

of additional model complexity could improve the agreement between model and data, it appears that all of the critical features of the tracer responses are effectively captured, and the introduction of additional complexity, especially in light of the minimal information to support it, is not justified.

One must also keep in mind that the tracer-test results are intended to support predictive calculations that span much larger time and distance scales than represented by the test. With this in mind, it is desirable to capture the important transport processes with as concise a model as possible so that others can incorporate a relatively simple model on a local scale into a more sophisticated flow model that captures the important hydraulic features of the larger-scale flow system. It is believed that the C-wells tracer tests and their interpretations presented in this report accomplish this objective.

6.3.7 Batch Testing of Lithium Sorption to C-wells Tuffs

6.3.7.1 Materials and Methods

The batch lithium sorption experiments were conducted as follows (full details of the sorption measurements are provided in Reimus 2000 [164625]).

- C-wells core from a stratigraphic unit of interest was crushed, pulverized, and passed through a 500-μm sieve but retained on a 75-μm sieve.
- A specified amount of crushed tuff was added to polycarbonate (polyallomer) Oak Ridge centrifuge tubes. In some experiments, the tuff and centrifuge tubes were autoclaved prior to contacting the tuff with the lithium solution.
- The tuff was preconditioned with filter-sterilized (0.2-μm filter) J-13 water.
- A specified amount of lithium-bearing water (either from well J-13 or well c#3) was added to the preconditioned tuff, and the mixture was continuously shaken for 24 to 72 hr at either 25°C or 38°C. Previous studies had indicated that lithium sorption equilibrium onto C-wells tuffs was reached in ~1 hour (Newman et al. 1991 [156849], so 24 hours should have been sufficient to achieve equilibration between solid and solution.
- After equilibration, the tubes were centrifuged and a portion of the supernate was filtered (0.2- or 0.4-μm filter) for tracer analysis to determine the tracer concentration remaining in solution. Lithium was analyzed by inductively-coupled plasma-atomic emission spectrometry (ICP-AES).

- The mass of tracer sorbed to the tuff was determined by mass balance, with corrections, if necessary, to account for sorption to the container walls, which was measured in control experiments in which tuff was omitted.

- All measurements were made in duplicate or triplicate.

Sorption isotherms were determined under several different experimental conditions:

- 1:1 solution:solid ratio in J-13 water at 25°C
- 1:1 solution:solid ratio in J-13 water at 38°C
- 2:1 solution:solid ratio in J-13 water at 25°C
- 4:1 solution:solid ratio in C-3 water at 38°C
- 4:1 solution:solid ratio in J-13 water at 25°C
- 4:1 solution:solid ratio in J-13 water at 38°C.

The two temperatures were intended to approximate the range of conditions under which sorption would occur in either the laboratory or the field (the groundwater temperature in the Bullfrog Tuff at the C-wells ranges from about 38°C to 45°C {Geldon 1993 [101045], pp. 68 to 70, Figures 31 to 33}).

At the time of these studies, groundwater from the C-wells complex was not consistently available, so groundwater from well J-13, located 4 km southeast of the C-wells complex, was used as a surrogate in most tests. J-13 water is well-characterized and has become a *de facto* standard groundwater for use in Yucca Mountain sorption studies (Harrar et al. 1990 [100814], pp. 6.6 to 6.7; Triay et al. 1997 [100422], pp. 11, 16, 45). A comparison of J-13 and C-wells groundwater chemistry shows that the two waters are both sodium bicarbonate dominated and, in all regards, quite similar (Table 6.3-15). Lithium solutions for sorption tests were prepared by dissolving reagent-grade lithium bromide in either c#3 or J-13 water. All solutions were filter-sterilized before use.

Table 6.3-15. Comparison of Major Ion Chemistry of J-13 and c#3

Species	Concentration (µg/mL)	
	J-13	C-wells
Ca	12	11
Cl	7.1	7.2
K	5	1.9
Mg	2.1	0.4
Na	42	55
SiO_2	47	53
SO_4	17	22
HCO_3	124	137
pH	7.2	7.7

DTNs: MO0007MAJIONPH.013 [151530] (J-13); MO0007MAJIONPH.011 [151524] (c#3).

A few tests were conducted in a sodium bicarbonate solution having the same ionic strength as J-13 water but without the calcium and other cations present in J-13 water. Lithium sorption in this solution was noticeably greater than in J-13 water, presumably because of the absence of cations that compete with lithium for sorption sites (primarily calcium). The results of these experiments are not reported here (Callahan 2001 [165123]).

Ion-exchange theory suggests that the actual ion-exchange process is rapid and will reach equilibrium quickly; in natural systems, apparent equilibration rates are limited by diffusion of ions through the solution to the mineral surface (Bolt et al. 1978 [113856], pp. 54 to 90). In a well-mixed system, such as a shaken centrifuge tube, diffusion is not limiting, and equilibration should be achieved quickly. A previous study of lithium sorption to the Prow Pass member of the Crater Flat Tuff found that sorption equilibrium was reached within 1 hr, confirming this hypothesis (Newman et al. 1991 [156849]). For consistency with other sorption studies and for scheduling convenience, a minimum equilibration period of 24 hr was adopted for these studies.

Tuffs from seven different lithologies were tested, including two samples of the same unit (the central Bullfrog Tuff) from two different holes (c#1 and c#2) to allow an assessment of spatial heterogeneity in lithium-sorption parameters. The experimental matrix of tuffs, groundwaters, temperatures, and solid-solution ratios is summarized in Table 6.3-16. Figure 6.3-39 shows the sampling locations of the C-wells core used in the experiments. This figure is essentially identical to Figure 6.1-2 except that the triangles indicating flow zones in the wells have been replaced with triangles identifying locations of core samples used in the batch experiments.

Batch-sorption experiments were also conducted on each of the tuffs to determine whether PFBA and bromide sorbed to them. The bromide experiments were actually conducted simultaneously with the lithium experiments, as lithium was added to the solutions as lithium bromide. The starting bromide concentrations ranged from ~10 ppm to ~1000 ppm. The PFBA experiments were conducted at a single concentration (1 ppm). These experiments were conducted on each rock type at 25°C. There was no measurable sorption of PFBA or bromide on any of the tuffs (DTN: LA0302PR831231.001 [162605]).

Table 6.3-16. Summary of C-wells Experimental Batch Lithium Sorption Test Matrix

Tuff* (Lithology, Borehole, Depth (m))	Water (Well ID)	Solution: Solid (mL:g)	Temperature (°C)
Central Bullfrog, c#1, 715 m (1)	J-13	2:1	25
	J-13	2:1	38
Central Bullfrog, c#2, 734 m (2)	J-13	1:1	25
	J-13	1:1	38
	c#3	4:1	38
Lower Bullfrog, c#1, 795 m (3)	J-13	4:1	25
	J-13	4:1	38
	J-13	2:1	25
Upper Prow Pass, c#2, 533 m (4)	J-13	4:1	25
	J-13	4:1	38
	J-13	2:1	25
Central Prow Pass, c#2, 553 m (5)	J-13	4:1	25
	J-13	4:1	38
	J-13	2:1	25
Lower Prow Pass, c#1, 573 m (6)	J-13	4:1	25
	J-13	4:1	38
	J-13	2:1	25
Bedded Prow Pass, c#2, 643 m (7)	J-13	4:1	25
	J-13	4:1	38
	J-13	2:1	25
Upper Tram, c#2, 839 m (8)	J-13	4:1	25
	J-13	4:1	38
	J-13	2:1	25

Source: This table shows the test matrix.

NOTE: *The numbers in parentheses correspond to the numbers in Figure 6.3-39 (the locations where core was collected from the C-wells).

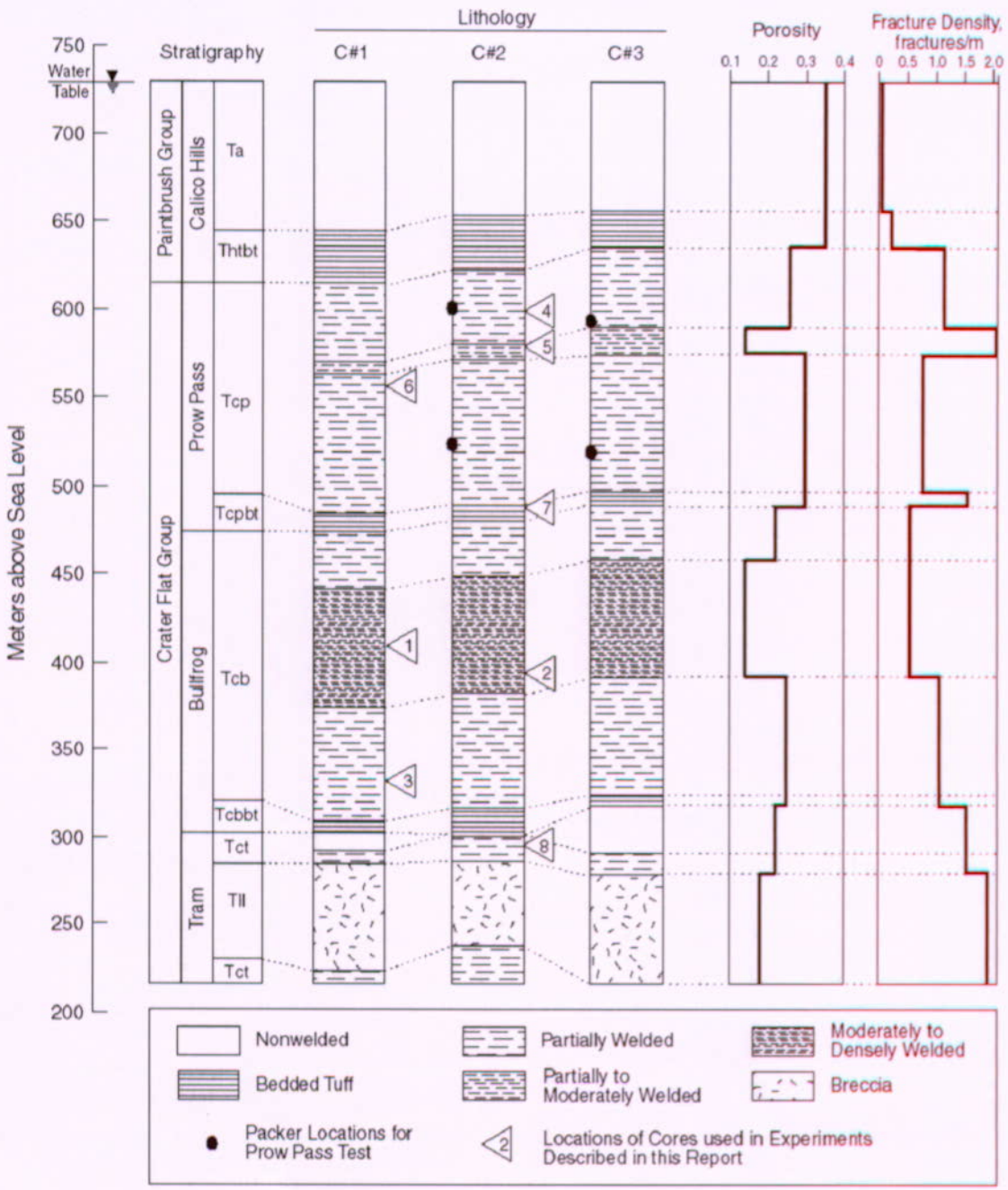

Source: Geldon (1993 [101045], pp. 35 to 37, 43 to 51, 58 to 64) for lithology, stratigraphy, porosity, and fracture density information. DTN: GS990408312315.002 [140115] for packer locations. Reimus (2000 [165124], pp. E1 to E10, M1 to M14, Q1 to Q20, W1 to W15, X1 to X14, AB1 to AB11, AC1 to AC17) for locations of core samples.

NOTE: The numbers in the figure correspond to the numbers in Table 6.3-16. Also shown are approximate locations of packers for the tracer tests in the Prow Pass Tuff.

Figure 6.3-39. C-wells Hydrogeology Showing Sampling Locations of All Core Used in the Laboratory Experiments Described in Sections 6.3.7, 6.3.8, and 6.3.9

The mineralogy of the tuffs used in the batch-sorption experiments is listed in Table 6.3-17. The mineralogy was determined from quantitative X-ray diffraction (XRD) analyses. The tuffs differ primarily in their smectite and zeolite (clinoptilolite and mordenite) content, both of which have high cation-exchange capacities and would be expected to sorb lithium quite strongly compared to other minerals present in the rocks (Anghel et al. 2002 [164635], pp. 822-824, Section 3.2).

Table 6.3-17. X-Ray Diffraction Results for Tuffs from Prow Pass, Bullfrog, and Tram Units

Tuff	Depth (m)	Concentration (wt %)				
		Smectite	Clinoptilolite	Mordenite	Analcime	Calcite
Central Bullfrog, c#1	715	2 ± 1	—	—	—	2 ± 1
Central Bullfrog, c#2	734	5 ± 2	—	—	—	—
Lower Bullfrog, c#1	795	9 ± 3	4 ± 1	3 ± 1	12 ± 1	4 ± 1
Upper Prow Pass, c#2	533	—	—	—	—	Trace
Central Prow Pass, c#2	553	2 ± 1	—	—	—	2 ± 1
Lower Prow Pass, c#1	573	2 ± 1	—	—	—	—
Bedded Prow Pass, c#2	643	—	—	20 ± 4	39 ± 2	—
Upper Tram, c#2	839	1 ± 1	—	—	—	—

DTN: MO0012MINLCHOL.000 [153370]; LA9909PR831231.004 ([129623] for Central Bullfrog c#2 only (non-Q data).

NOTE: c#1, c#2, and c#3 are abbreviations for boreholes UE-25 c#1, UE-25 c#2, and UE-25 c#3, respectively.
Trace: trace abundance of < 0.5 wt%.
Only the main sorptive mineral fractions are listed; the balance of the tuffs was mostly quartz and feldspar with small amounts of hematite, mica/illite, and/or kaolinite.
Dashes indicate "not measured."

A Li-specific CEC method was developed to quantify the Li affinity for the selected tuffs. The method involved two steps: saturation of the exchange sites with Li, followed by displacement of the Li and other cations with Cs. The mineralogical composition of the samples was preserved as close as possible to the field conditions; therefore, no pretreatment was applied to remove carbonate or organic matter. The method involved the following steps (Anghel et al. 2002 [164635], pp. 822 to 824, Section 3.2).

- The tuff samples were crushed and wet-sieved with J-13 water to a particle-size range between 75 to 500 μm. Then ~5 g of each tuff was weighed into a 50-mL centrifuge Teflon tube. Each tuff sample was tested in triplicate.

- The samples were saturated three times with 30 mL of 0.8 N LiBr–0.2 N LiOAc solution to ensure replacement of cations present on mineral surface sites with Li. The pH of the solution was maintained at ~8.2 to prevent dissolution of calcite. After each LiBr addition, the tubes were sonicated to disperse the centrifuged sediment, and then the samples were shaken for 30 min.

- The samples were centrifuged at 10,000 rpm for 15 minutes to achieve a good separation of solids and solution. The supernatant from each Li-sorption step was combined and analyzed for Na, K, Ca, and Mg.

- After the Li-sorption steps, the tuff present in each centrifuge tube was washed three times with 30 mL of 1 N CsCl to remove the sorbed Li. The combined supernate from centrifuging was analyzed for Li, Na, Ca, K, and Mg. Residual Li saturating solution remaining in the centrifuge tubes was accounted for by analyzing for Br and making the appropriate correction. Cs has more affinity for zeolites, and it should, therefore, displace more cations than Li. In many cases, Cs sorption gives a measure of the total CEC (Li measurements of the aliquots give the CEC for Li-Cs exchange).

The method described yields two different CEC results: (1) *CEC-Li*$_T$, the total CEC available to Li, estimated from the total cations displaced by Li in the saturation step, and (2) *CEC-Cs*$_T$, the total CEC available to Cs, estimated from the total cations displaced by Cs in the displacement step. *CEC-Cs*$_T$ can be further subdivided into CEC-*Cs*$_{Li}$, based on the Li displaced by Cs, and *CEC-Cs*$_{Nat}$, based on the native cations (Na, K, Ca, Mg) displaced by Cs. Each of these results is expressed in milliequivalents per 100 g of dry tuff.

6.3.7.2 Results and Discussion

During the course of the experiments, it became apparent that lithium sorption was essentially independent of solution:solid ratio, temperature, and water composition (J-13 or c#3) over the range of conditions studied. Therefore, the data sets for a given tuff lithology were combined to estimate sorption parameters. Three common isotherm models, defined as follows, were fitted to the data for each tuff.

(1) *Linear Isotherm:*

$$S = K_d C \qquad \text{(Eq. 11)}$$

where

S = equilibrium sorbed concentration (μg/g)
C = equilibrium solution concentration (μg/mL)
K_d = linear distribution coefficient (mL/g).

(2) *Freundlich Isotherm:*

$$S = K_F C^n \qquad \text{(Eq. 12)}$$

where

K_F = Freundlich coefficient $(mL/\mu g)^n(\mu g/g)$
n = Freundlich exponent (dimensionless).

(3) *Langmuir Isotherm:*

$$S = \frac{K_L S_{max} C}{1 + K_L C} \qquad \text{(Eq. 13)}$$

where

K_L = Langmuir coefficient (mL/μg)
S_{max} = maximum attainable solid sorption capacity (μg/g).

Figures 6.3-40 to 6.3-46 show the experimental data for each tuff plotted as log-equilibrium-sorbed concentration, S (μg/g) versus log-solution concentration, C (μg/mL). A Langmuir isotherm consistently yielded better visual fits to the data than the other isotherms, so a fitted Langmuir isotherm is also shown in each figure. The Langmuir isotherm is the only isotherm that captures the curvature of the data when graphed on log-log axes. Furthermore, only the Langmuir isotherm recognizes the finite sorptive capacity of the solid matrix; the other models imply potential infinite sorption. A previous study of lithium sorption to the Prow Pass member of the Crater Flat Tuff also revealed Langmuir behavior (Newman et al. 1991 [156849]). The Langmuir, Freundlich, and linear isotherm parameters associated with the data in Figures 6.3-40 to 6.3-46 are given in Table 6.3-18. It is concluded that a Langmuir isotherm provides the best representation of lithium sorption onto C-wells tuffs. However, a detailed statistical analysis to quantify how much better this representation is relative to the other isotherms (or whether it is statistically better) was not conducted. Statistical analyses were not conducted to determine whether there were significant isotherm differences as a function of temperature, solid-solution ratio, or core taken from different locations in the same lithological unit (i.e., the Central Bullfrog Tuff from c#1 or c#2). However, it appears from Figures 6.3-40 to 6.3-46 that any of these differences should have been minimal.

The error bounds shown in Figures 6.3-40 to 6.3-46 reflect the propagation of analytical errors associated with lithium concentration measurements in the solutions before and after contact with the sorbing tuffs (Reimus 2003 [165129], p. 126). These bounds are shown relative to the fitted Langmuir isotherms, not relative to individual data points. The bounds were calculated assuming a 10% relative standard deviation in the lithium concentration measurements, which is high for ICP-AES measurements but it also serves to account for other experimental errors, such as imperfect separations of solid and solution phases during centrifugation. Errors increase as concentrations increase because there is a lower percentage of lithium sorbing at higher concentrations and, hence, a smaller relative difference between measured initial and final solution concentrations. It is apparent that the scatter in the data sets often exceeds the analytical error bounds, suggesting greater than 10% error in some of the measurements.

In Figures 6.3-40 to 6.3-44, the lithium isotherm associated with the ion-exchange parameters used in MULTRAN V 1.0 (STN: 1066-1.0-00 [159068]) to obtain a good match to either the first lithium peak in the Bullfrog Tuff tracer test (Figure 6.3-26) or the lithium response in the Prow Pass Tuff tracer test (Figure 6.3-27) are plotted along with the laboratory data and the Langmuir isotherm fits to the laboratory data. In all cases, the isotherms derived from the simulations of the field data indicate greater lithium sorption in the field than in the laboratory experiments. "Field" isotherms are not shown in Figures 6.3-45 and 6.3-46 because the Bedded Prow Pass and Upper Tram Tuff lithologies were not part of the packed-off intervals in the reactive tracer tests.

The fitted Langmuir isotherms corresponding to all seven C-wells tuff lithologies are plotted together in Figure 6.3-47. By comparing Figure 6.3-47 to the XRD results of Table 6.3-17, it is apparent that the two tuffs demonstrating the greatest affinity for lithium (Bedded Prow Pass and Lower Bullfrog) are also the tuffs that have the greatest smectite and/or zeolite contents. A quantitative relationship between lithium sorption and tuff mineralogy is discussed further below.

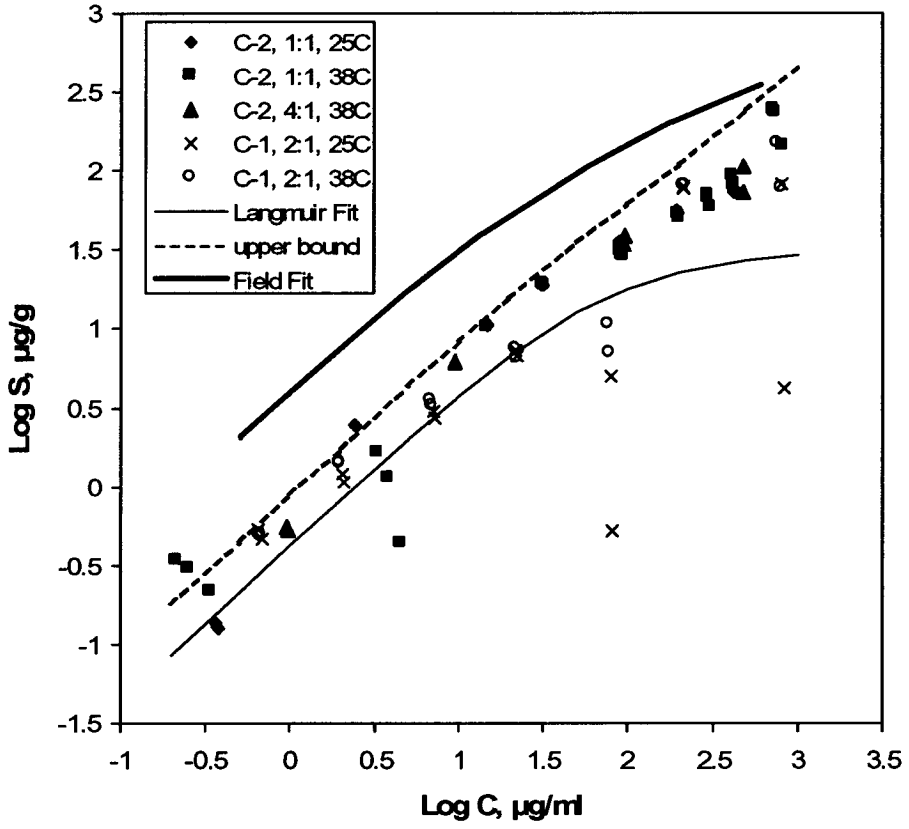

DTN: MO0012SORBCHOL.000 [153375] (data). Output DTN: LA0303PR831341.003 (model).

NOTE: C-1 and C-2 refer to UE-25 c#1 and c#2, respectively. The legend indicates the borehole (c#1 or c#2) from which the tuff came, the solution:solid ratio (mL:g), and the temperature of the experiments. The dashed line is an upper error bar associated with a 10% experimental error (this error bar is plotted relative to the Langmuir isotherm line – lower error bound is off-scale over the entire range of data). The method for calculating the error bars is described in Reimus (2003 [165129], p. 126). J-13 water was used in all experiments except for "C-2, 4:1, 38C." Water from c#3 was used for "C-2, 4:1, 38C." The lithium concentration range in the Bullfrog Tuff field test spanned from less than 0.1 µg/mL up to 1200 µg/mL. The line labeled "Field Fit" is the isotherm corresponding to the MULTRAN V 1.0 (STN: 1066-1.0-00 [159068]) "fit" to the first lithium peak in the Bullfrog Tuff field tracer test (see Figure 6.3-26).

Figure 6.3-40. Lithium Sorption Data and Fitted Langmuir Isotherm for the Central Bullfrog Tuff

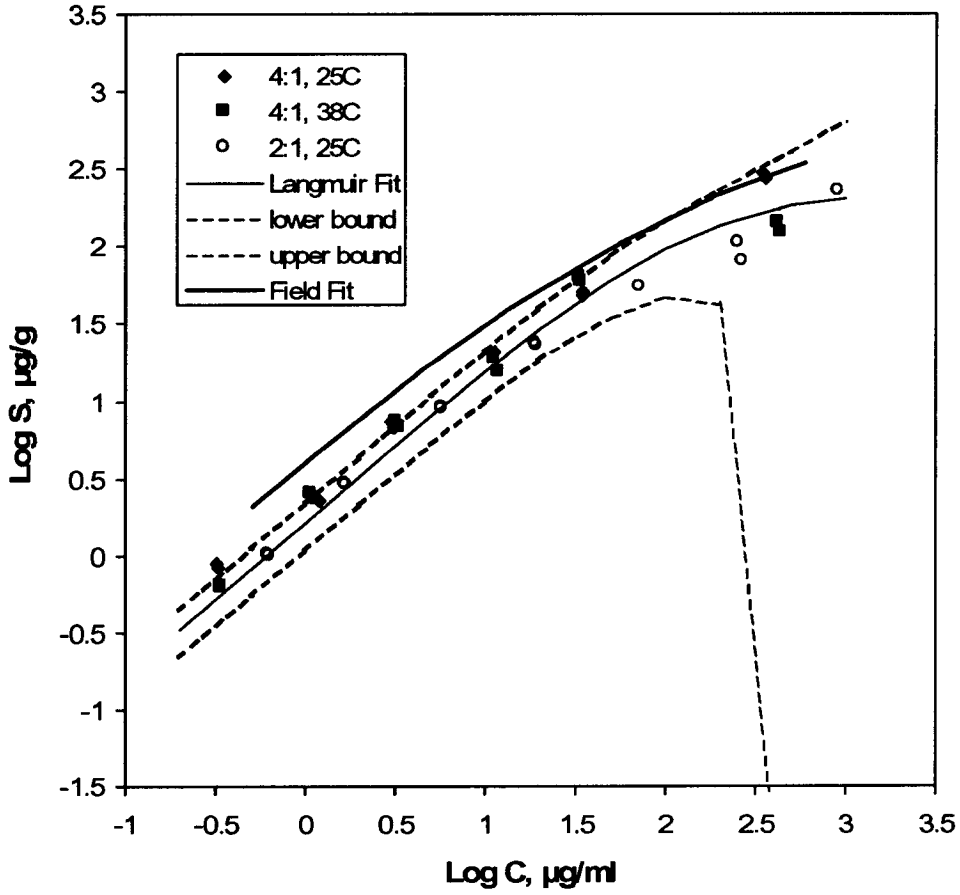

DTN: MO0012SORBCHOL.000 [153375] (data). Output DTN: LA0303PR831341.003 (model).

NOTE: The legend indicates the solution:solid ratio (mL:g) and the temperature of the experiments. The dashed lines are error bars associated with a 10% experimental error (these error bars are plotted relative to the Langmuir isotherm line). The method for calculating the error bars is in Reimus (2003 [165129], p. 126). J-13 water was used in all experiments. The lithium concentration range in the Bullfrog Tuff field test spanned from less than 0.1 µg/mL up to 1200 µg/mL. The line labeled "Field Fit" is the isotherm corresponding to the MULTRAN V 1.0 (STN: 1066-1.0-00 [159068]) "fit" to the first lithium peak in the Bullfrog Tuff field tracer test (see Figure 6.3-26).

Figure 6.3-41. Lithium Sorption Data and Fitted Langmuir Isotherm for the Lower Bullfrog Tuff (c#1, 795 m below land surface).

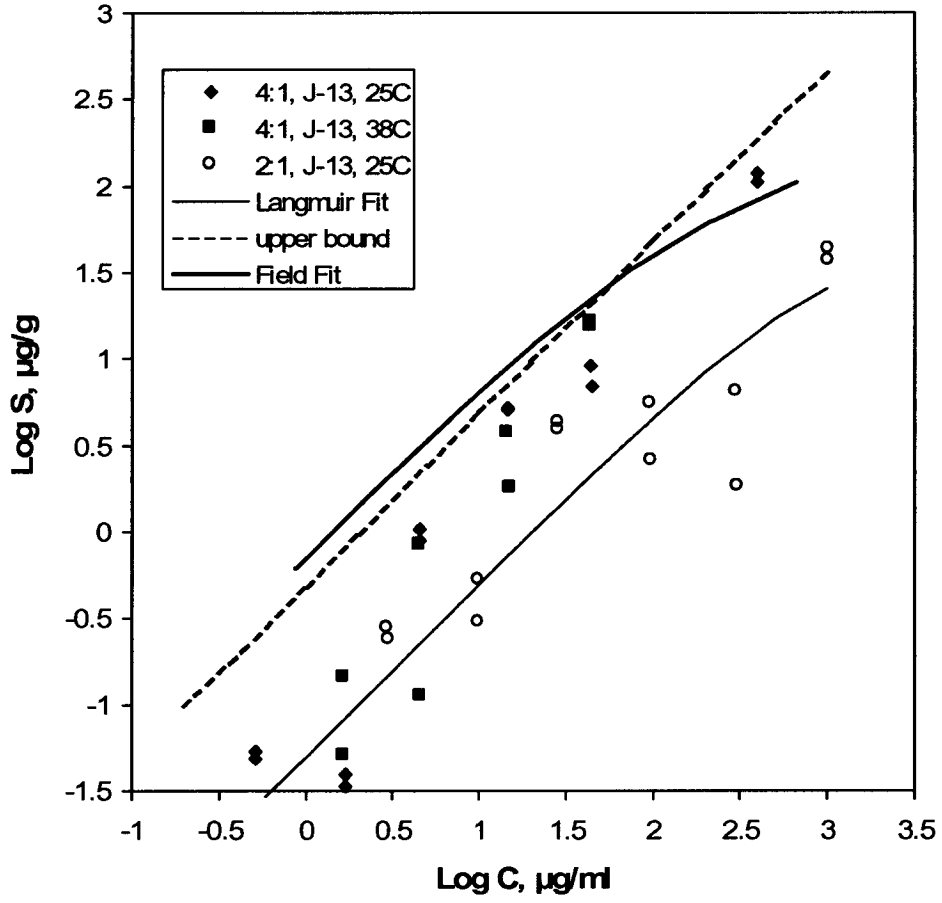

DTN: MO0012SORBCHOL.000 [153375] (data). Output DTN: LA0303PR831341.003 (model).

NOTE: The legend indicates the solution:solid ratio (mL:g) and the temperature of the experiments. The dashed line is an upper error bar associated with a 10% experimental error (this error bar is plotted relative to the Langmuir isotherm line – lower error bound is off-scale over entire range of data). The method for calculating the error bars is in Reimus (2003 [165129], p. 126). J-13 water was used in all experiments. The lithium concentration in the Prow Pass Tuff field test ranged from less than 0.1 µg/mL up to 2700 µg/mL. The line labeled "Field Fit" is the isotherm corresponding to the MULTRAN V 1.0 (STN: 1066-1.0-00 [159068]) "fit" to the lithium data in the Prow Pass Tuff field tracer test (see Figure 6.3-27).

Figure 6.3-42. Lithium Sorption Data and Fitted Langmuir Isotherm for the Upper Prow Pass Tuff (c#2, 533 m below land surface)

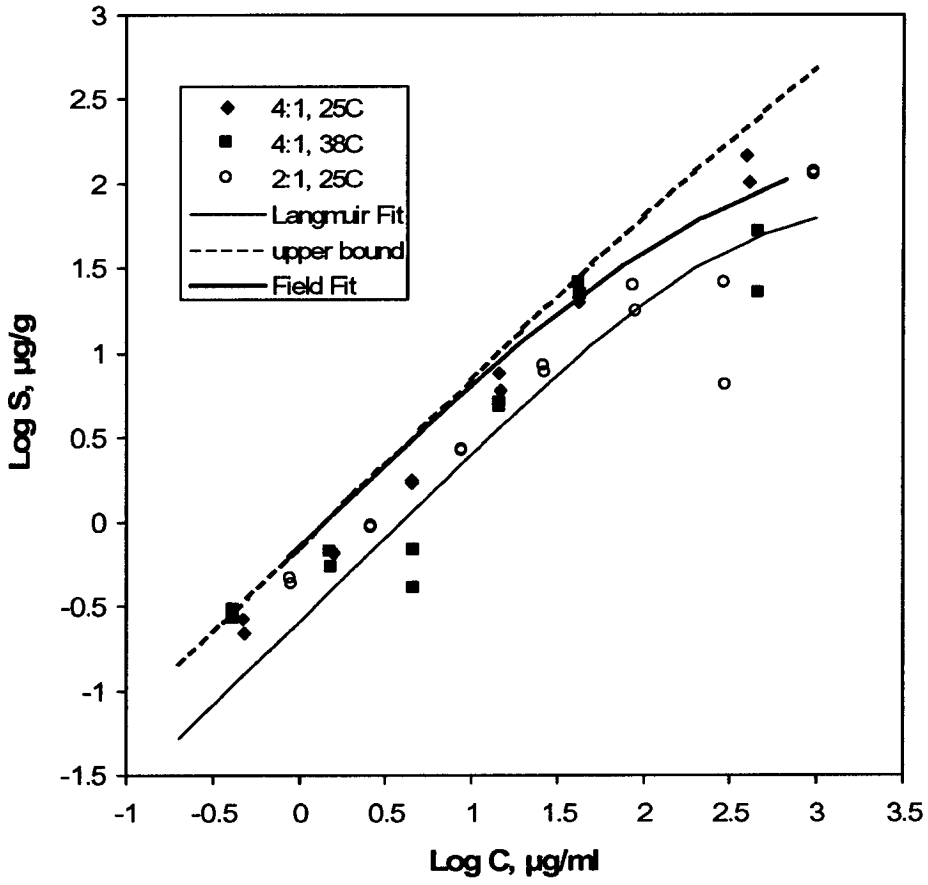

DTN: MO0012SORBCHOL.000 [153375] (data). Output DTN: LA0303PR831341.003 (model).

NOTE: The legend indicates the solution:solid ratio (mL:g) and the temperature of the experiments. The dashed line is an upper error bar associated with a 10% experimental error (this error bar is plotted relative to the Langmuir isotherm line – lower error bound is off-scale over entire range of data). The method for calculating the error bars is in Reimus (2003 [165129], p. 126). J-13 water was used in all experiments. The lithium concentration in the Prow Pass Tuff field test ranged from less than 0.1 µg/mL up to 2700 µg/mL. The line labeled "Field Fit" is the isotherm corresponding to the MULTRAN V 1.0 (STN: 1066-1.0-00 [159068]) "fit" to the lithium data in the Prow Pass Tuff field tracer test (see Figure 6.3-27).

Figure 6.3-43. Lithium Sorption Data and Fitted Langmuir Isotherm for the Central Prow Pass Tuff (c#2, 553 m below land surface)

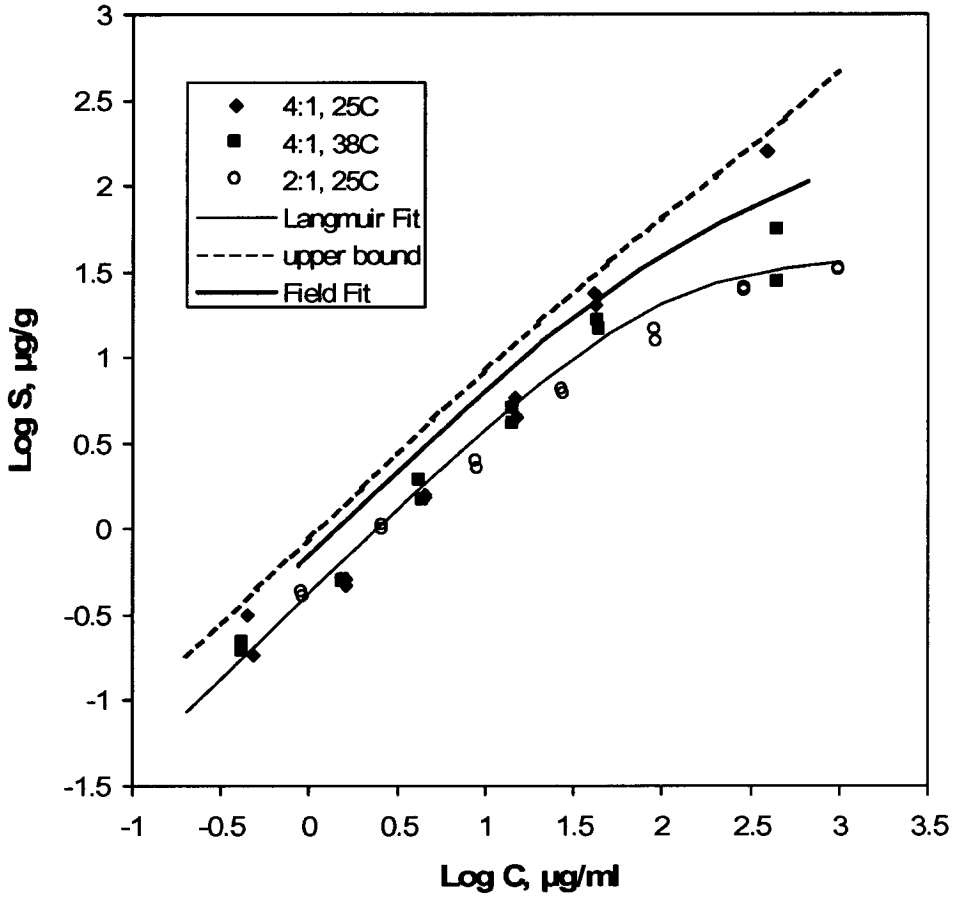

DTN: MO0012SORBCHOL.000 [153375] (data). Output DTN: LA0303PR831341.003 (model).

NOTE: The legend indicates the solution:solid ratio (mL:g) and the temperature of the experiments. The dashed line is an upper error bars associated with a 10% experimental error (this error bar is plotted relative to the Langmuir isotherm line – lower error bound is off-scale over entire range of data). The method for calculating the error bars is in Reimus (2003 [165129], p. 126). J-13 water was used in all experiments. The lithium concentration in the Prow Pass Tuff field test ranged from less than 0.1 µg/mL up to 2700 µg/mL. The line labeled "Field Fit" is the isotherm corresponding to the MULTRAN V 1.0 (STN: 1066-1.0-00 [159068]) "fit" to the lithium data in the Prow Pass Tuff field tracer test (see Figure 6.3-27).

Figure 6.3-44. Lithium Sorption Data and Fitted Langmuir Isotherm for the Lower Prow Pass Tuff (c#1, 573 m below land surface)

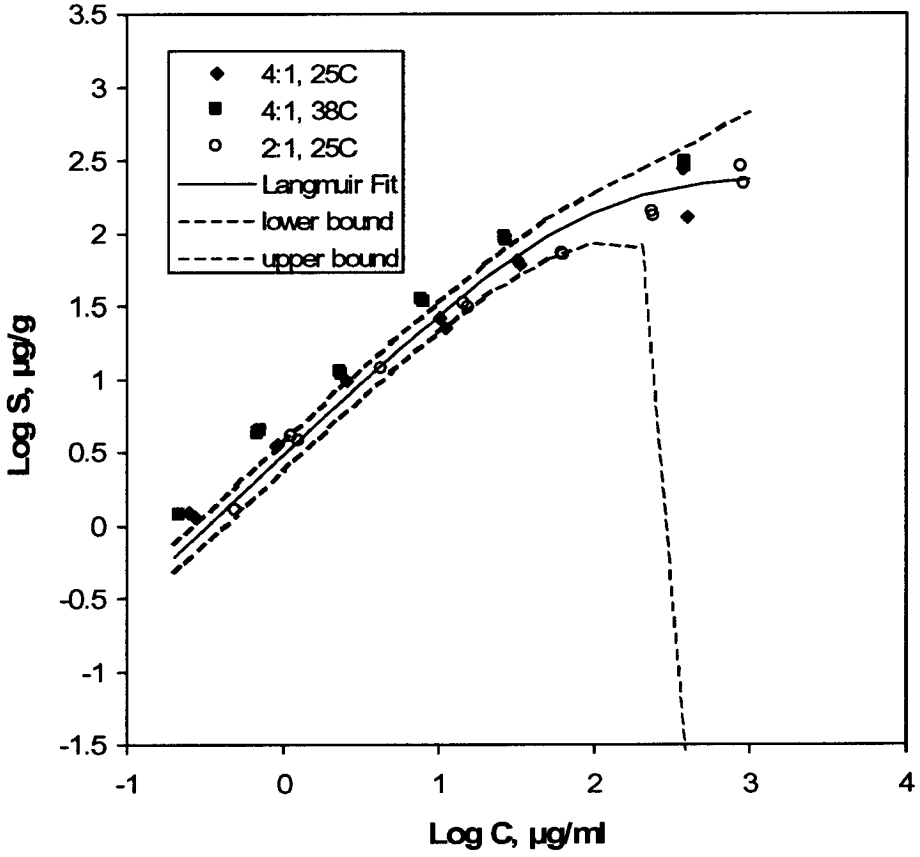

DTN: MO00012SORBCHOL.000 [153375] (data). Output DTN: LA0303PR831341.003 (model).

NOTE: The legend indicates the solution:solid ratio (mL:g) and the temperature of the experiments. The dashed lines are error bars associated with a 10% experimental error (these error bars are plotted relative to the Langmuir isotherm line). The method for calculating the error bars is in Reimus (2003 [165129], p. 126). J-13 water was used in all experiments.

Figure 6.3-45. Lithium Sorption Data and Fitted Langmuir Isotherm for the Bedded Prow Pass Tuff (c#1, 643 m below land surface)

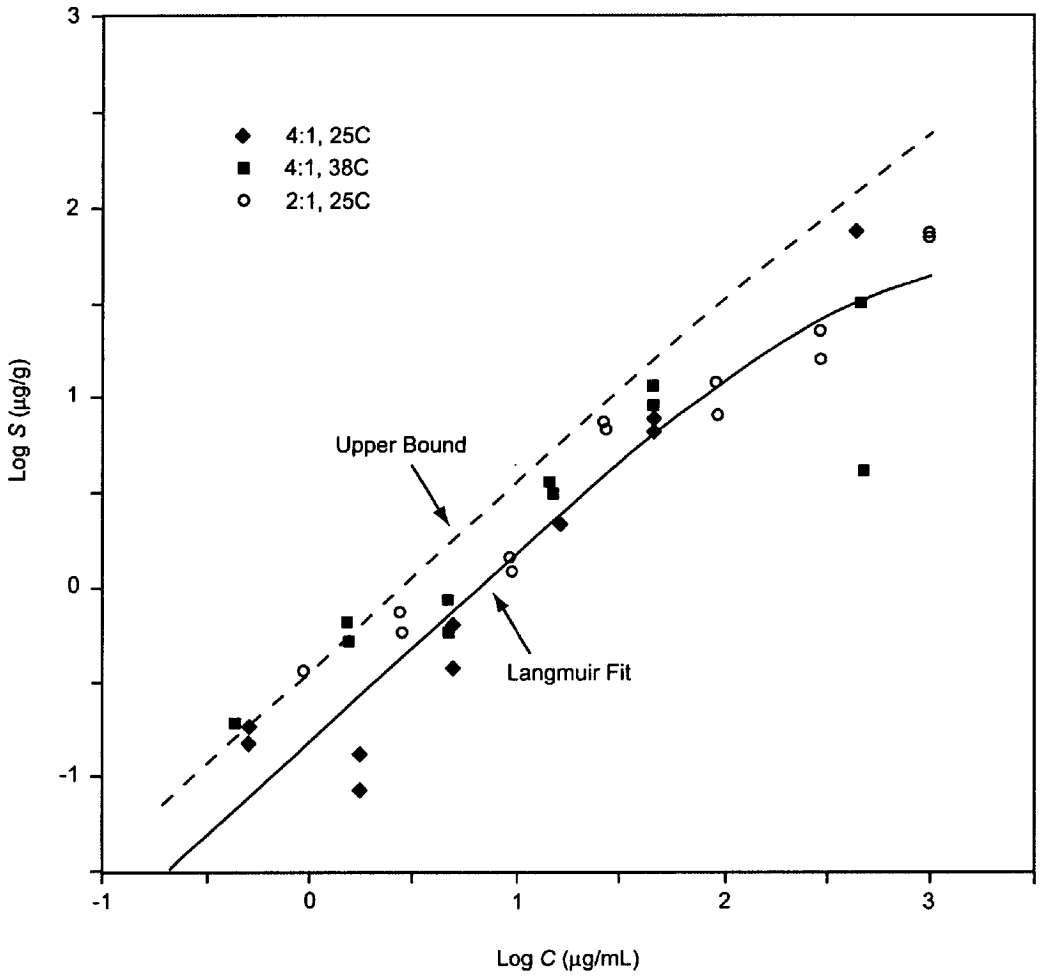

DTN: MO0012SORBCHOL.000 [153375] (data). Output DTN: LA0303PR831341.003 (model).

NOTE: The legend indicates the solution:solid ratio (mL:g) and the temperature of the experiments. The dashed line is an upper error bar associated with a 10% experimental error (these error bars are plotted relative to the Langmuir isotherm line - lower error bound is off-scale over entire range of data). The method for calculating the error bars is described in Reimus (2003 [165129], p. 126). J-13 water was used in all experiments.

Figure 6.3-46. Lithium Sorption Data and Fitted Langmuir Isotherm for the Upper Tram Tuff (c#2, 839 m below land surface)

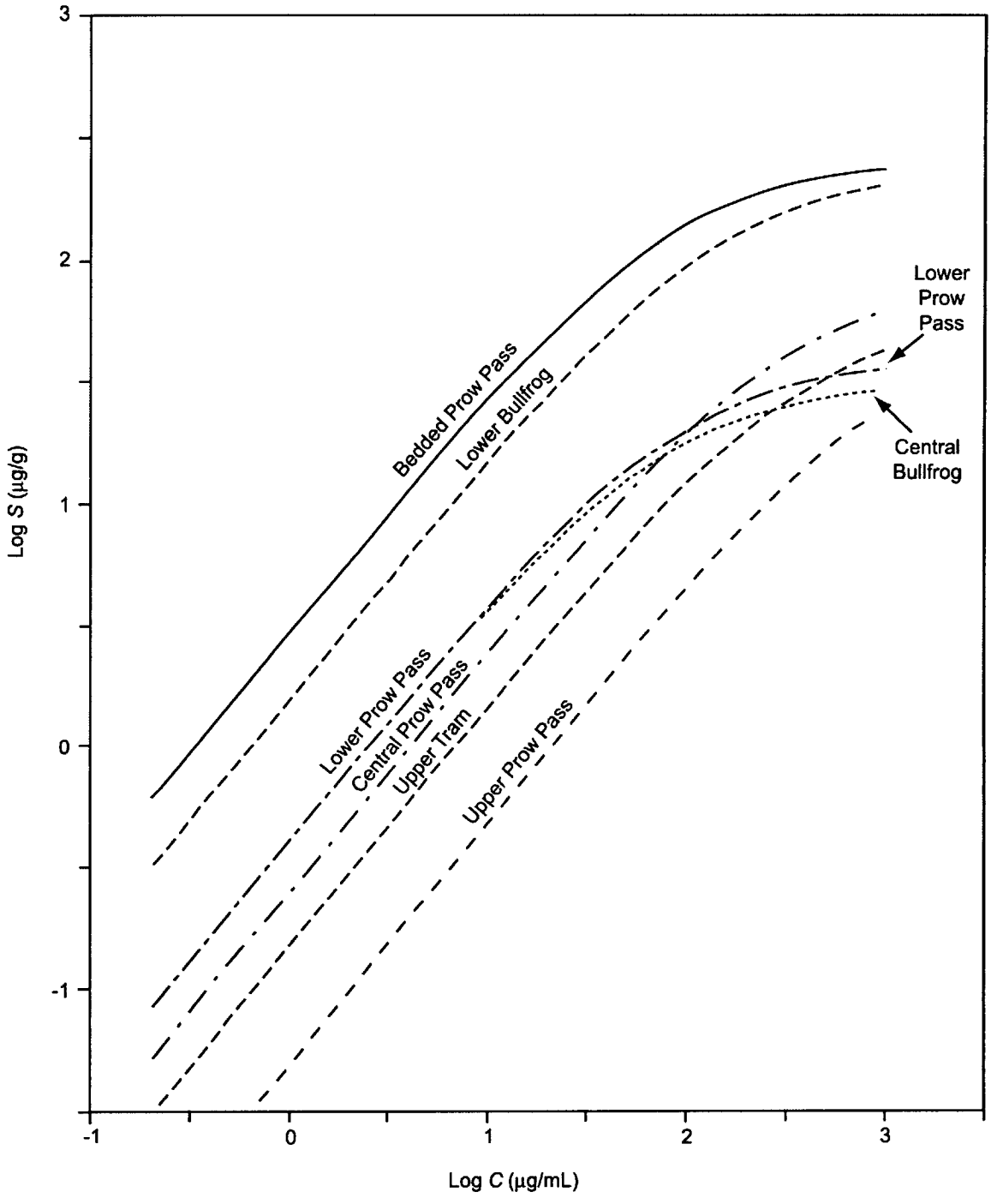

Output DTN: LA0303PR831341.003.

NOTE: The lithium concentration range in the field test in the central and lower Bullfrog Tuff spanned from less than 0.1 µg/mL up to 1200 µg/mL. The concentration range in the Prow Pass Tuff field test ranged from less than 0.1 µg/mL up to 2700 µg/mL.

Figure 6.3-47. Fitted Langmuir Isotherms for the Seven C-wells Tuffs

Table 6.3-18. Lithium Sorption Isotherm Parameters Associated with the Different C-wells Tuffs

Unit	Langmuir		Freundlich		Linear
	K_L (L/mg)	S_{max} (µg/g)	K_F	n	K_d (mL/g)
Central Bullfrog, c#1 + c#2 [(a)]	0.014	31.4	0.70	0.79	0.186
Lower Bullfrog, c#1	0.0070	233.9	2.26	0.75	0.321
Upper Prow Pass, c#2	0.00094	53.1	0.075	1.03	0.068
Central Prow Pass, c#2	0.0031	83.3	0.48	0.80	0.131
Lower Prow Pass, c#1	0.011	39.8	0.48	0.78	0.084
Bedded Prow Pass, c#2	0.012	254.9	4.17	0.69	0.383
Upper Tram, c#2	0.0026	59.8	0.27	0.78	0.072

Output DTN: LA0303PR831341.003 (also from Anghel et al. 2002 [164635], Section 3.2, pp. 822 to 824).

NOTE: c#1 and c#2 are abbreviations for boreholes UE-25 c#1 and UE-25 c#2, respectively.

(a) Sorption data from c#1 and c#2 tuffs are lumped together to obtain parameter estimates. K_L and S_{max} were 0.0053 L/mg and 110 µg/g, respectively, for the Central Bullfrog Tuff from c#2 alone (used in crushed tuff column experiments of Section 6.3.9).

Results of the four CEC measurements on the seven tuff samples are presented in Figure 6.3-48 and Table 6.3-19. In all cases, the total CEC available to Cs ($CEC\text{-}Cs_T$) exceeds that available to Li ($CEC\text{-}Li_T$). This result is not surprising; the hydrated ionic radius of Cs (0.33 nm) is smaller than that of Li (0.38 nm) (Israelachvili 2000 [156835], p. 55), which permits Cs access to internal exchange sites in zeolites that are not available to Li. More surprising is the consistent observation that Cs displaces more Li during the displacement step than Li displaced other cations during initial saturation (i.e., $CEC\text{-}Cs_{Li} > CEC\text{-}Li_T$). This phenomenon, a "lithium excess" during the displacement step, was also reported by Eckstein et al. (1970 [156653], pp. 341-342). They attributed this Li excess to a separate process that occurs in addition to normal cation exchange: selective and specific adsorption of Li, particularly to amorphous silicates and to edges and broken bonds of non-expanding clay minerals. They state that "it [is] difficult or even doubtful that a 'true' value for the exchange capacity can be given for any specific clay." They further conclude that "the sum of cations replaced by Li will usually give a better value for the exchange capacity than the amount of Li retained and replaced by $Ca(OAc)_2$."

Inspection of the mineralogy of the samples, presented in Table 6.3-17, indicates that the primary minerals likely to participate in cation exchange include smectite and the zeolite minerals clinoptilolite and mordenite. (Although analcime has a high theoretical CEC (Ming and Mumpton 1995 [156843], pp. 873 to 911), kinetic factors prevent significant cation exchange at normal environmental temperatures, (Vaughan 1978 [156867], pp. 353 to 371)). To test whether a simple two-mineral model could explain the observed measurements, a multivariable linear regression was conducted on the CEC results, using measured smectite and (clinoptilolite + mordenite) fractions (f_{smec}, $f_{clin/mord}$) as independent variables, and three CEC estimates as the dependent variables. In all cases, the model yielded the following results:

$$CEC\text{-}Li_T = 106\pm8 \text{ meq/100g} \cdot f_{smec} + 99\pm3 \text{ meq/100g} \cdot f_{clin/mord} + 1.5\pm0.3 \text{ meq/100g}, R^2 = 0.997.$$

$$CEC\text{-}Cs_{Li} = 103\pm13 \text{ meq/100g} \cdot f_{smec} + 95\pm5 \text{ meq/100g} \cdot f_{clin/mord} + 6.1\pm0.5 \text{ meq/100g}, R^2 = 0.990.$$

$$CEC\text{-}Cs_T = 90\pm13 \text{ meq/100g} \cdot f_{smec} + 199\pm5 \text{ meq/100g} \cdot f_{clin/mord} + 7.7\pm0.5 \text{ meq/100g}, R^2 = 0.997.$$

where R^2 = coefficient of regression (sum of squares regression divided by sum of squares total).

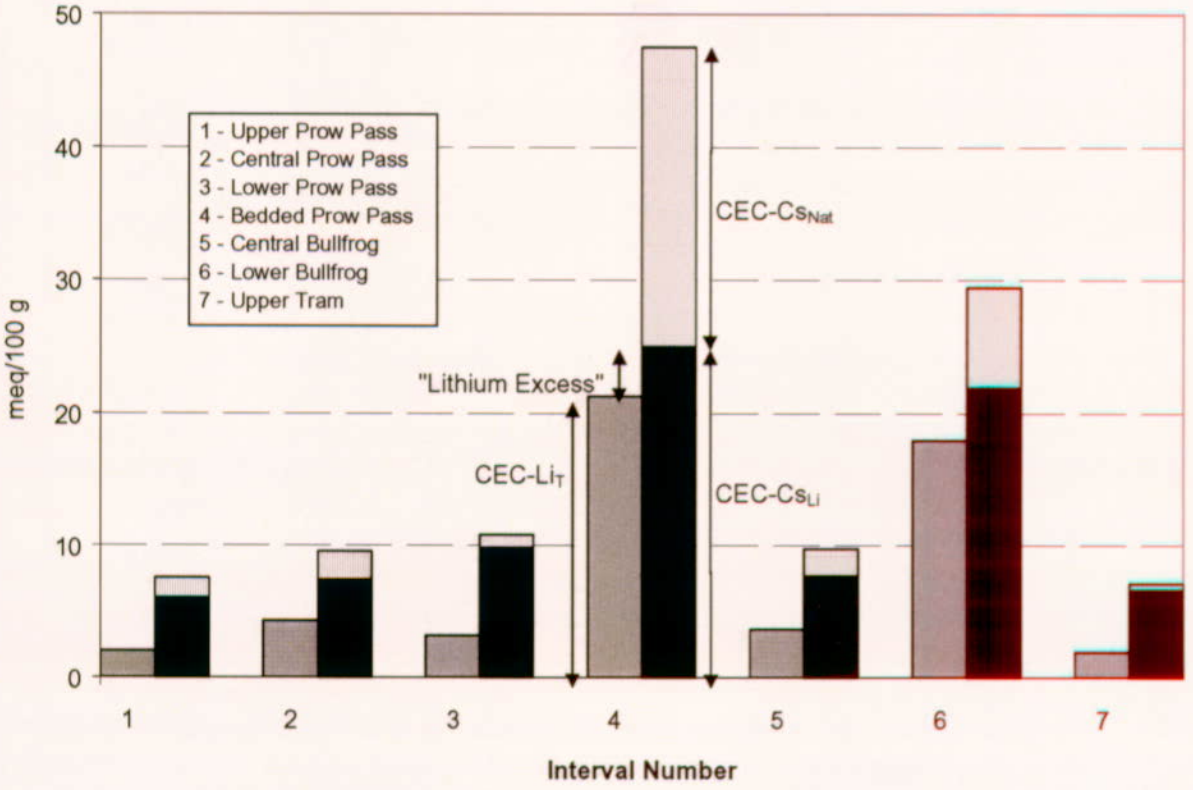

DTNs: MO0012CATECHOL.000 [153371] (CEC-Li data); LA0302PR831341.001 [162604] (CEC-Cs data); Output DTN: LA0303PR831341.001.

NOTE: Interval numbers in legend do not correspond to numbers in Table 6.3-16 or Figure 6.3-39.

Figure 6.3-48. Cation Exchange Capacity Results for the Seven Different C-wells Tuff Intervals

Table 6.3-19. Cation Exchange Capacity Measurements for C-wells Tuffs

Sample[a]	Cation Exchange Capacity (meq/100g)				
	CEC-Li$_T$	*CEC-Cs*$_{Nat}$	*CEC-Cs*$_{Li}$	*CEC-Cs*$_T$	Li Excess
Upper Prow Pass (1)	2.0 ± 0.5	1.5 ± 0.1	6.1 ± 0.8	7.5	4.1
Central Prow Pass (2)	4.3 ± 0.1	2.1 ± 0.0	7.4 ± 0.4	9.5	3.1
Lower Prow Pass (3)	3.2 ± 0.4	1.0 ± 0.9	9.8 ± 1.9	10.8	6.6
Bedded Prow Pass (4)	21.3 ± 0.1	22.5 ± 0.4	25.0 ± 1.4	47.5	3.8
Central Bullfrog (5)[b]	3.7 ± 0.1	2.0 ± 0.5	7.7 ± 0.6	9.7	4.1
Lower Bullfrog (6)	18.0 ± 0.2	7.5 ± 0.4	21.9 ± 0.2	29.5	4.0
Upper Tram (7)	1.9 ± 0.1	0.5 ± 0.2	6.6 ± 0.5	7.1	4.7

DTNs: MO0012CATECHOL.000 [153371] (CEC-Li data); LA0302PR831341.001 [162604] (CEC-Cs data). Output DTN: LA0303PR831341.001.

NOTE: Range shown is ± one standard deviation. Refer to text for definitions.
(a) Numbers correspond to numbers in Figure 6.3-48.
(b) Only the Central Bullfrog Tuff from c#1 was analyzed for CEC.

The exchange factors for the individual minerals can be compared to literature values of 110 ± 23 meq/100 g for smectite (Borchardt 1995 [156639], Chapter 14) and 220 meq/100 g for both clinoptilolite and mordenite (Ming and Mumpton 1995 [156843]). Starting with the model for *CEC-Li*$_T$, we see that the specific exchange capacity for smectite matches reported value from Borchardt (1995 [156639], Chapter 14), whereas the modeled capacity for the zeolite minerals is less than half that reported by Ming and Mumpton (1995 [156843]). This discrepancy is consistent with the inaccessibility of some of the internal zeolite exchange sites to the relatively large Li ion. The *CEC-Li*$_T$ model includes a relatively small constant term, indicating that almost all of the observed behavior can be explained by smectite and clinoptilolite/mordenite cation exchange. Comparing this model to the *CEC-Cs*$_{Li}$ model, we see that the major difference lies in the constant term; the larger constant term in the second model reflects the observed Li excess. The similarity of the other two terms demonstrates that the Li-excess effect is not a result of exchange onto either smectite or clinoptilolite/mordenite; additional correlation analysis shows that the Li excess is not proportional to any of the mineral phases identified by quantitative x-ray diffraction (QXRD). These observations, combined with the overall uniformity of the Li excess among these widely varying tuff samples, lead one to agree with Eckstein et al. (1970 [156653], pp. 341, 342) and attribute the Li excess to a noncation exchange sorption process.

The final model for *CEC-Cs*$_T$ reveals a similar specific CEC for smectite as found in the literature and the previous models but shows a much higher specific CEC for the zeolite minerals, which is more in line with published values (Ming and Mumpton 1995 [156843]). This demonstrates the accessibility to the smaller Cs ion of internal exchange sites that were apparently unavailable to Li.

To a first approximation, it can be seen that the two samples that sorb Li most strongly have the highest isotherms in Figure 6.3-47 and the largest K_d and K_F values in Table 6.3-18. These two rocks also showed the highest CEC values. To quantify the sorption relationships more rigorously, the linearization of the nonlinear Freundlich isotherm was undertaken, and K_{lin} was

calculated. K_{lin} is an effective distribution coefficient with uniform units, identical to those of K_d. For this purpose, the equal-area linearization of van Genuchten et al. (1977 [156868], pp. 278 to 285) was used:

$$K_{lin} = \frac{2K_F C_{max}^{n-1}}{n+1} \quad \text{(Eq. 14)}$$

where C_{max} is the maximum solution concentration of interest; in this case, 1000 mg/L, and K_F and n are taken from Table 6.3-18. Using the same multivariate linear regression methods described above, K_{lin} can be modeled as a function of smectite and clinoptilolite/mordenite content:

$$K_{lin} = 2.28\pm0.45 \text{ L/kg}\cdot f_{smec} + 2.46\pm0.18 \text{ L/kg}\cdot f_{clin/mord} + 0.09\pm0.02 \text{ L/kg}, r^2 = 0.981.$$

This model does not fit the data quite as well as the CEC models described above but, nevertheless, demonstrates that Li sorption can be estimated fairly accurately for these tuffs, given smectite, clinoptilolite, and mordenite concentrations. The small constant term in the model indicates that the contribution of other minerals to Li sorption is quite low.

6.3.7.3 Conclusions from Batch Lithium Sorption Studies

Lithium ion sorption onto devitrified tuffs from the saturated zone near Yucca Mountain follows nonlinear isotherm behavior. Both the lithium sorption parameters and the lithium-specific cation exchange capacities of the tuffs are highly correlated with the clay (smectite) content and the zeolite (clinoptilolite + mordenite) content of the tuffs. Multiple linear regression analyses shows that these two classes of minerals account for the majority of the observed lithium exchange. Regression of cesium cation-exchange data yields results that are consistent with the accessibility of the smaller cesium ion to internal zeolite exchange sites that lithium cannot access. The cesium CEC data also suggest that some of the lithium sorption to the tuffs can be attributed to a noncation exchange process. The results of this study support the development and use of mineralogy-based models for predicting cation sorption in the saturated zone near Yucca Mountain.

6.3.8 Diffusion Cell Experiments

6.3.8.1 Materials and Methods

Six diffusion cell experiments were conducted to determine diffusion coefficients of PFBA and bromide ion in five different C-wells tuff matrices (details are in Reimus 2000 [165121]). Estimates of matrix diffusion coefficients are important because they can greatly reduce uncertainty in interpreting and predicting both field-scale and laboratory-scale tracer experiments. One of the tests was a repeat experiment using a different core from the same interval as another test (the lower Prow Pass Tuff). This test was conducted to determine the reproducibility and variability of the experiments. The five different intervals tested in the diffusion cell experiments represented all of the major lithologies in either the Bullfrog field tracer test or the Prow Pass field tracer test (see Table 6.3-20 for specific intervals tested).

A schematic drawing of the experimental diffusion cell apparatus is illustrated in Figure 6.3-49. The apparatus consists of two Plexiglas reservoirs, one large and one small, separated by a "pellet" of tuff, which is cut/cored from C-wells core and incorporated into either a flat epoxy cast or a room-temperature vulcanizing (RTV) silicone cast of the same thickness as the pellet. After saturating the tuff, experiments were initiated by carefully pouring a solution containing PFBA and LiBr into the large reservoir and tracer-free solution into the small reservoir. The pressures in the two reservoirs were kept approximately equal to minimize advective flow through the tuff, thus ensuring that tracer movement through the tuff was by diffusion only. The small reservoir was kept well mixed with a magnetic stir bar and flushed continuously at a relatively low flow rate. The flush water was collected in an automatic fraction collector, and fractions were analyzed for tracers to establish breakthrough curves through the tuff from which diffusion coefficients could be estimated. As in the other laboratory experiments, PFBA and bromide were analyzed by liquid chromatography, and lithium was analyzed by ICP-AES. Filtered J-13 water or synthetic J-13 water (a sodium/calcium bicarbonate solution having the same ionic strength as J-13 water – see Reimus 2000 [165121] for details) were used in all experiments.

The porosities of the tuffs were measured by subtracting dry weights from saturated weights of intact tuff samples and dividing by the volumes of the samples (measured by water displacement). Porosity measurements were used to obtain unambiguous estimates of diffusion coefficients in the tuff matrices (see equations below). Hydraulic conductivities/permeabilities of the tuffs were also measured by imposing a known head difference across the tuff pellets, either before or after a diffusion experiment was conducted. The flow through the pellets at the imposed head difference was measured by weighing the water that flowed through the pellet over a specified amount of time.

Hydraulic conductivities were then calculated from the following equation:

$$K = -\frac{Q\,L}{A\,\Delta H} \qquad \text{(Eq. 15)}$$

where

K = hydraulic conductivity, cm/sec

ΔH = water height (head) difference across pellet, cm

A = surface area of pellet, cm^2

Q = volumetric flow rate through pellet, ml/sec

L = thickness of pellet, cm.

Permeabilities were calculated from hydraulic conductivities using the following well-known formula (Freeze and Cherry 1979 [101173], pp. 26 to 30):

$$k = \left(1.013 \times 10^{11}\right)\frac{K\,\mu}{\rho\, g} \qquad \text{(Eq. 16)}$$

where

k = permeability, millidarcys (mD)

μ = water viscosity, g/cm-sec (1.00 centipoise or 0.01 g/cm-sec at 20°C (Weast and Astle 1981 [100833], p. F-42))

ρ = water density, g/cm^3 (0.998 g/cm^3 at 20°C (Weast and Astle 1981 [100833], p. F-11))

g = acceleration due to gravity, cm/sec^2 (980 cm/sec2 on Earth (Weast and Astle 1981 [100833], p. F-144))

and the constant 1.013×10^{11} has units of mD/cm^2.

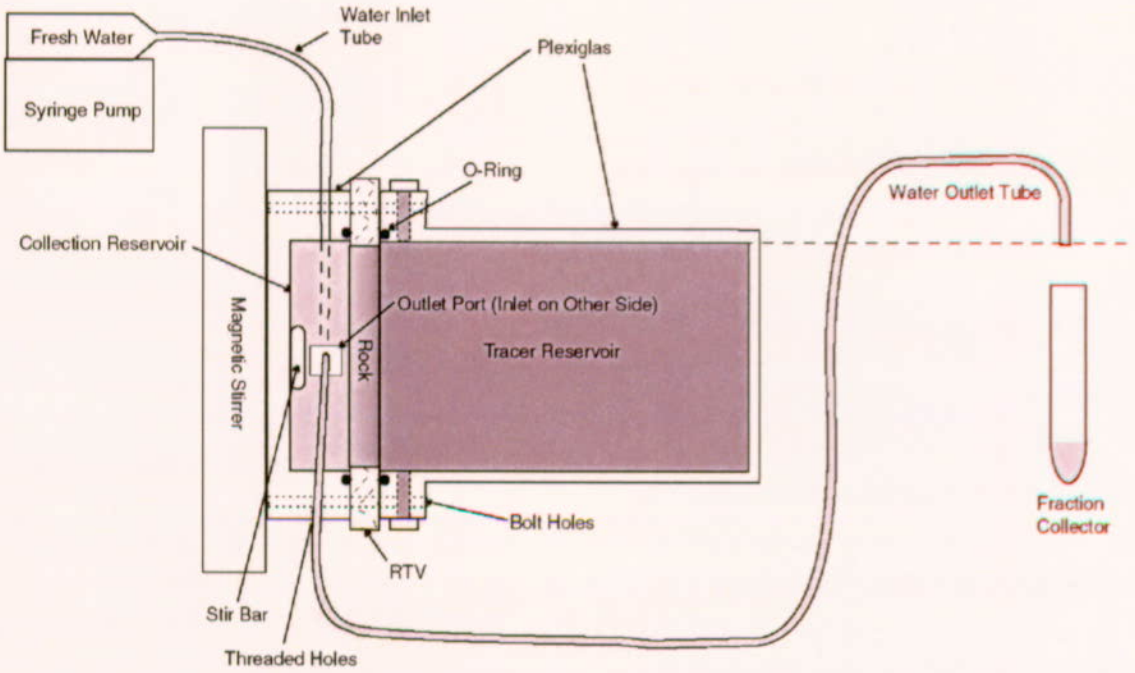

For illustration purposes only

Figure 6.3-49. Diffusion Cell Experimental Apparatus

To estimate diffusion coefficients, it was assumed that the tracers moved according to 1-D diffusive transport through the tuff pellets. The 1-D diffusion equation is:

$$\frac{\partial c}{\partial t} = \frac{D}{R}\frac{\partial^2 c}{\partial x^2} \qquad \text{(Eq. 17)}$$

where

c = tracer concentration in tuff pellet, µg/mL
D = diffusion coefficient, cm^2/sec
R = retardation factor (1 for nonsorbing solutes),
x = position within tuff pellet (x = 0 at inlet reservoir), cm
t = time, sec.

Although analytical solutions to this simple partial differential equation exist for simple boundary conditions (Jenson and Jeffreys 1977 [156836], pp. 291 to 295), the time-dependent concentration boundary conditions at the inlet and outlet reservoirs in the diffusion cell experiments demand a numerical solution. Thus, Equation 17 was solved using an implicit finite-difference technique. The equations describing the tracer concentrations in the inlet and the outlet reservoirs (the first and last finite difference nodes), respectively, were:

$$\frac{\partial c_i}{\partial t} = \frac{\phi \pi r^2 D}{V_i}\left.\frac{\partial c}{\partial x}\right|_{x=0} \qquad \text{(Eq. 18)}$$

$$\frac{\partial c_o}{\partial t} = -\frac{\phi \pi r^2 D}{V_o}\left.\frac{\partial c}{\partial x}\right|_{x=L} - \frac{q}{V_o}c_o \qquad \text{(Eq. 19)}$$

where

c_i = tracer concentration in inlet reservoir, µg/mL
c_o = tracer concentration in outlet reservoir, µg/mL
V_i = volume of inlet reservoir, mL
V_o = volume of outlet reservoir, mL
q = flush rate of outlet reservoir, mL/sec
ϕ = porosity of tuff
r = radius of tuff "pellet", cm
L = thickness of tuff "pellet", cm.

The numerical solution of Equations 17, 18, and 19 was obtained using computer code DIFFCELL 2.0 (STN: 10557-2.0-00 [159063]). This code allows the user to specify changes in the flush rate, q, with time, which was necessary to simulate the manner in which the experiments were conducted.

6.3.8.2 Results and Discussion

Figures 6.3-50 through 6.3-55 show the breakthrough curves of the bromide and PFBA in each of the six diffusion cells along with "fits" to the data obtained using DIFFCELL 2.0 (STN: 10557-2.0-00 [159063]). The "fits" are not actual least-squares fits; rather, they were obtained by manual adjustment of the diffusion coefficients until a reasonable match to the data was obtained. The apparent discontinuities in some of the data sets and the corresponding model predictions are a consequence of changes in the flush rate through the outlet reservoirs. A decrease in concentration occurs when the flush rate is increased and vice-versa.

The resulting estimates of tracer diffusion coefficients in each diffusion cell are given in Table 6.3-20 (measured tuff porosities, pellet thicknesses, and tuff permeabilities are also listed in this table). It is apparent that there is about an order of magnitude range of diffusion coefficients in the various tuff lithologies. Figures 6.3-56 and 6.3-57 show the bromide diffusion coefficients in the tuff matrices as a function of porosity and permeability, respectively, for the five different C-wells tuffs. Although the diffusion coefficients are not well correlated with porosity, they are quite well correlated with permeability (on a log-log scale). This result suggests that permeability may be a good predictor of matrix diffusion coefficients. Such correlations could prove useful for estimating matrix diffusion coefficients, as diffusion coefficients are typically more difficult to measure than matrix properties such as permeabilities.

Table 6.3-20 shows that excellent agreement was obtained between the two diffusion cell experiments conducted for the same lithology (the lower Prow Pass Tuff). This result suggests that the experiments have reasonably good reproducibility, although certainly more experiments should be conducted in the same lithologies before measurement uncertainty and tuff variability can be properly assessed.

It is interesting to note that although the PFBA and bromide diffusion coefficients are significantly different in the different tuffs, the ratios of the diffusion coefficients are approximately the same in each tuff. This result suggests that advection through the tuff pellets was successfully eliminated, as any advection would result in different ratios in different tests. The factor of ~3 difference in the diffusion coefficients of the PFBA and bromide is the basis for assuming a factor of 3 difference in all of the field and laboratory tracer-test interpretations in this report.

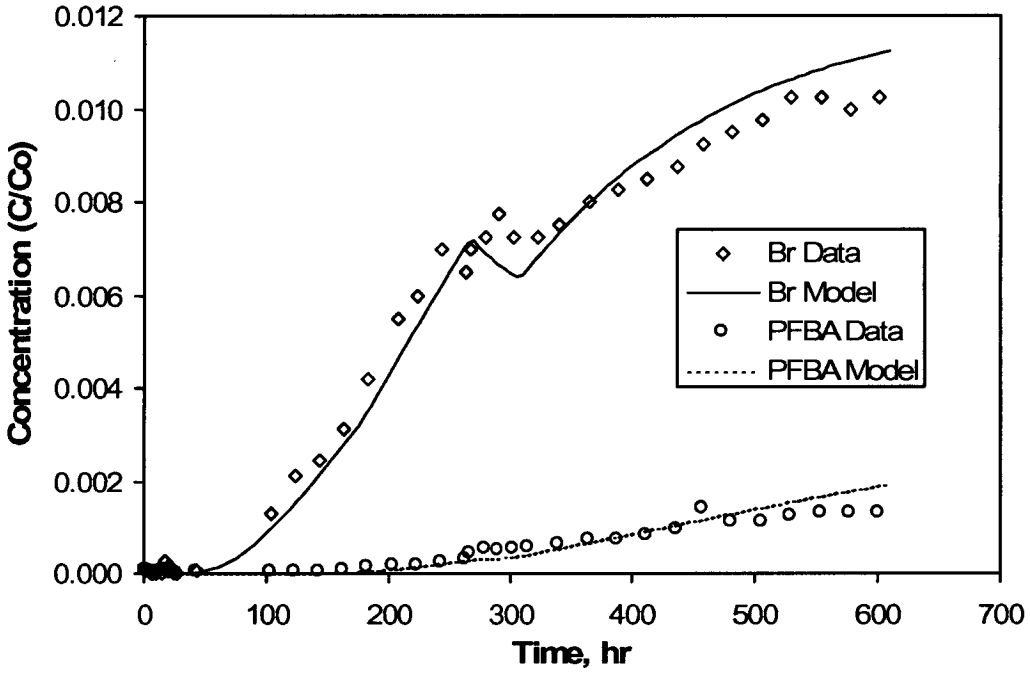

DTN: MO0012DIFFCHOL.000 [159243] (data). Output DTN: LA0303PR831362.001 (model).

NOTE: Diffusion coefficients are given in Table 6.3-20.

Figure 6.3-50. Diffusion Cell Data (Tracer Concentrations in Outlet Reservoir Normalized to Starting Concentrations in Inlet Reservoir, C_o) and DIFFCELL Model Fits for Bromide and PFBA in the Central Bullfrog Tuff

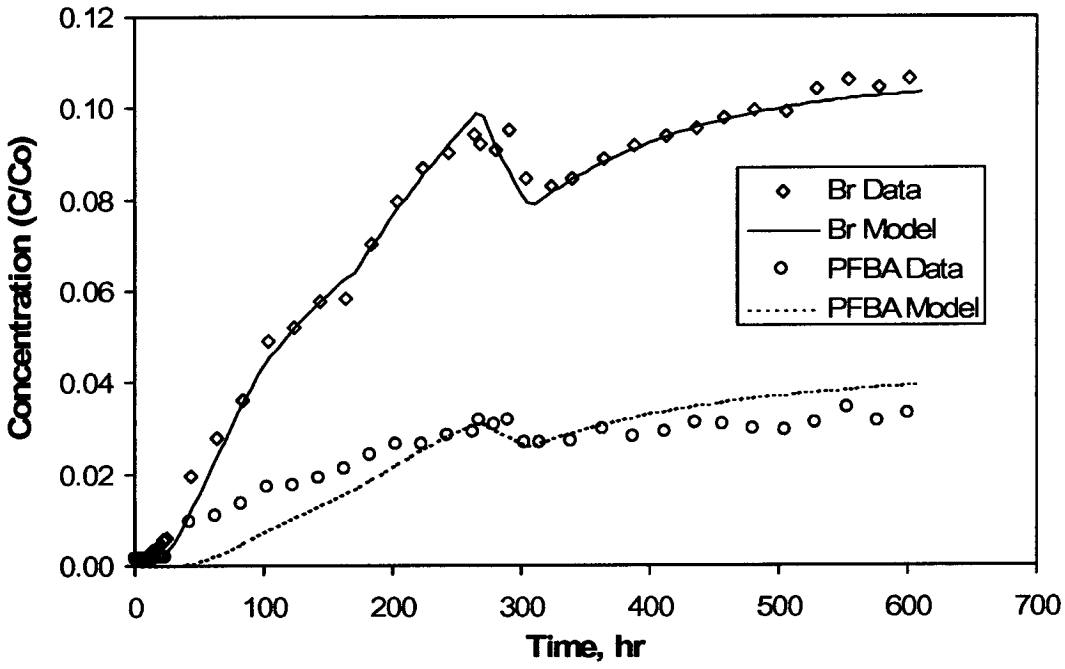

DTN: MO0012DIFFCHOL.000 [159243] (data). Output DTN: LA0303PR831362.001 (model).

NOTE: Diffusion coefficients are given in Table 6.3-20.

Figure 6.3-51. Diffusion Cell Data (Tracer Concentrations in Outlet Reservoir Normalized to Starting Concentrations in Inlet Reservoir, C_o) and DIFFCELL Model Fits for Bromide and PFBA in the Lower Bullfrog Tuff

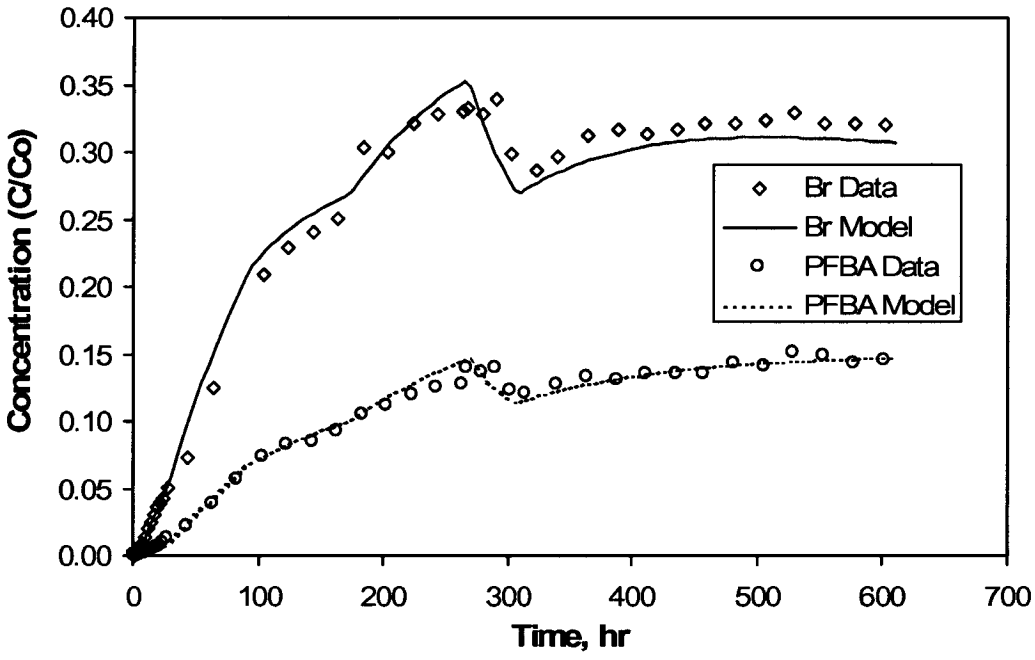

DTN: MO0012DIFFCHOL.000 [159243] (data); Output DTN: LA0303PR831362.001 (model).

NOTE: Diffusion coefficients are given in Table 6.3-20.

Figure 6.3-52. Diffusion Cell Data (Tracer Concentrations in Outlet Reservoir Normalized to Starting Concentrations in Inlet Reservoir, C_o) and DIFFCELL Model Fits for Bromide and PFBA in the Upper Prow Pass Tuff

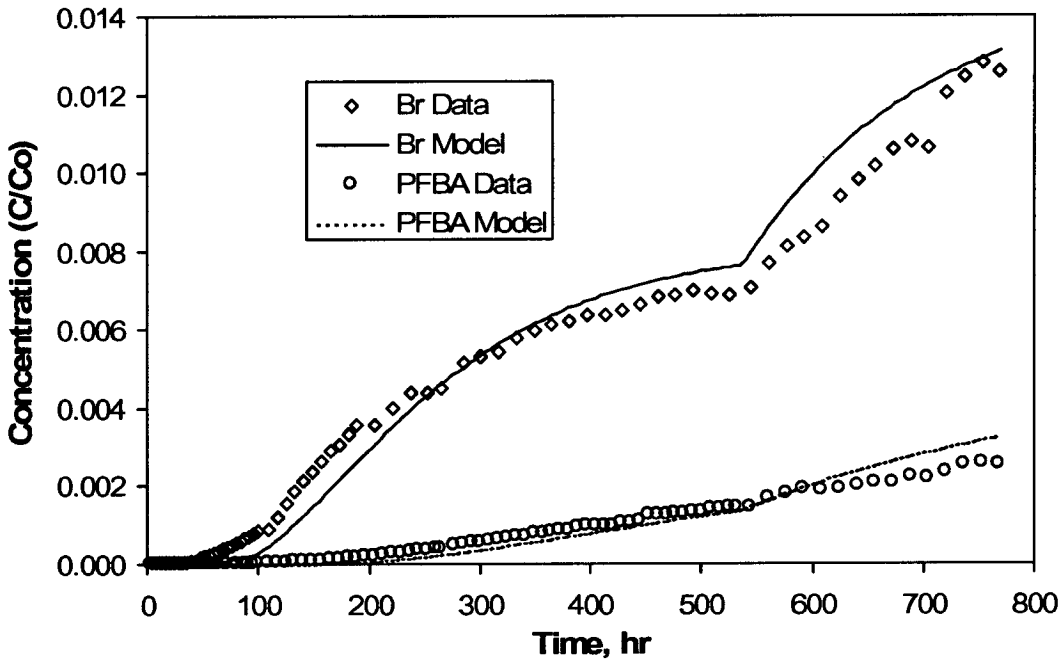

DTN: MO0012DIFFCHOL.000 [159243] (data). Output DTN: LA0303PR831362.001 (model).

NOTE: Diffusion coefficients are given in Table 6.3-20.

Figure 6.3-53. Diffusion Cell Data (Tracer Concentrations in Outlet Reservoir Normalized to Starting Concentrations in Inlet Reservoir, C_o) and DIFFCELL Model Fits for Bromide and PFBA in the Central Prow Pass Tuff

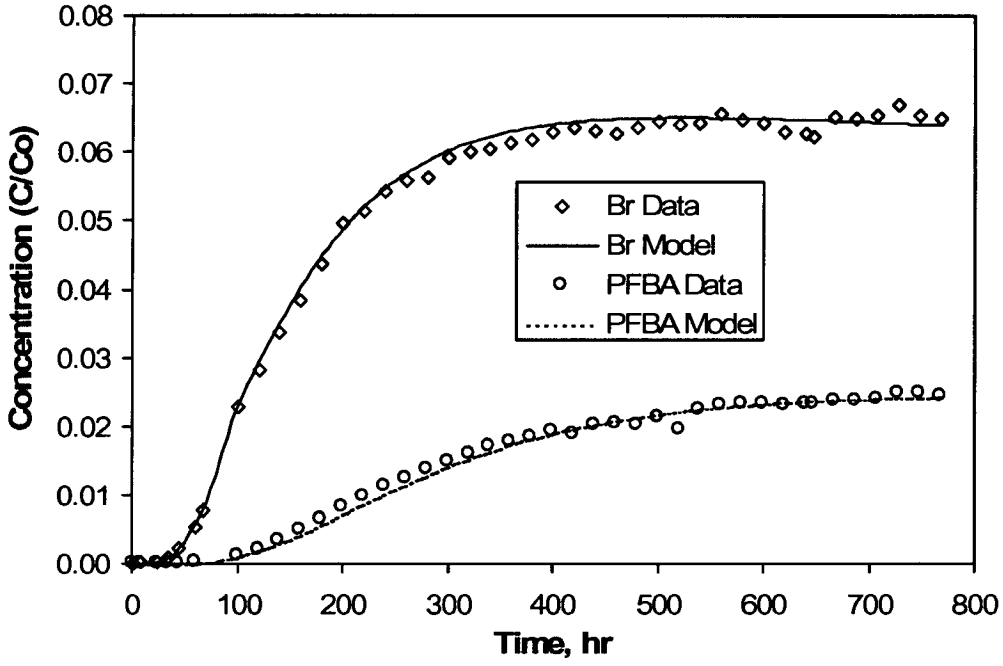

DTN: MO0012DIFFCHOL.000 [159243] (data). Output DTN: LA0303PR831362.001 (model).

NOTE: Diffusion coefficients are given in Table 6.3-20.

Figure 6.3-54. First Diffusion Cell Data (Tracer Concentrations in Outlet Reservoir Normalized to Starting Concentrations in Inlet Reservoir, C_o) and DIFFCELL Model Fits for Bromide and PFBA in the Lower Prow Pass Tuff

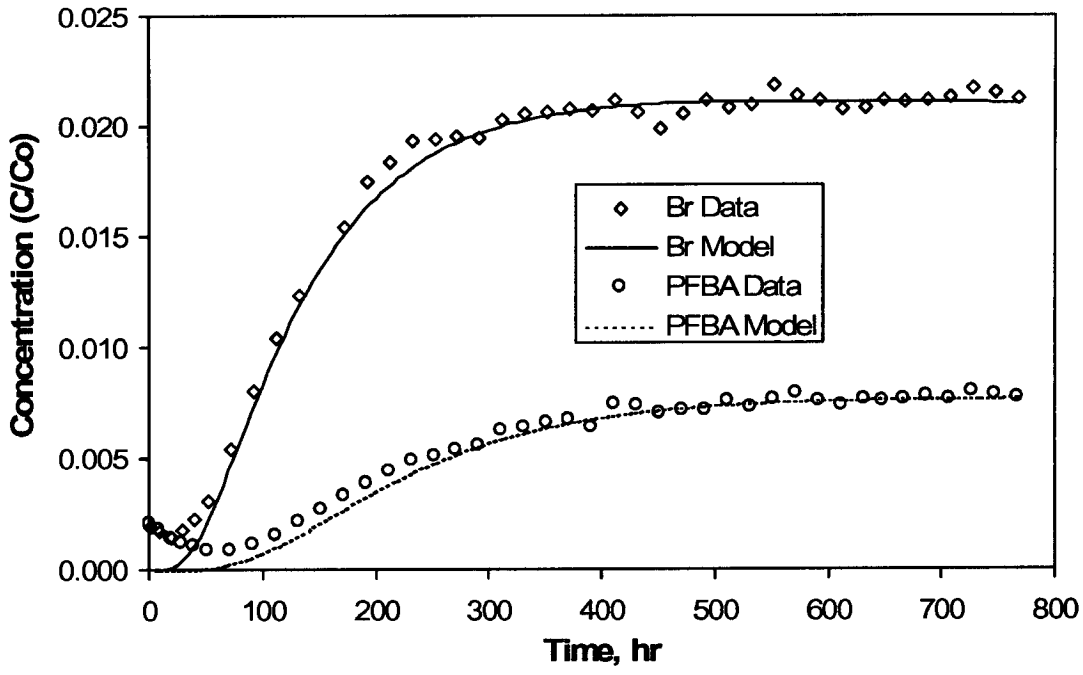

DTN: MO0012DIFFCHOL.000 [159243] (data). Output DTN: LA0303PR831362.001 (model).

NOTE: Diffusion coefficients are given in Table 6.3-20.

Figure 6.3-55. Second Diffusion Cell Data (Tracer Concentrations in Outlet Reservoir Normalized to Starting Concentrations in Inlet Reservoir, C_o) and DIFFCELL Model Fits for Bromide and PFBA in the Lower Prow Pass Tuff

Table 6.3-20. Measured Porosities, Permeabilities, and Matrix Diffusion Coefficients of Bromide and PFBA in C-wells Tuffs

Tuff [a]	Porosity	Permeability (mDarcy)	Thickness [b] (cm)	Diffusion Coefficient ($cm^2/s \times 10^6$)		
				Br	PFBA	Br/PFBA
Central Bullfrog (1)	0.094	0.00107	1.12	0.42	0.12	3.5
Lower Bullfrog (3)	0.298	0.0949	0.79	1.0	0.35	2.86
Upper Prow Pass (4)	0.272	4.72	0.98	6.2	2.0	3.1
Central Prow Pass (5)	0.138	0.000786	1.23	0.38	0.13	2.92
Lower Prow-1 (6) [c]	0.288	0.455	2.27	3.0	1.1	2.73
Lower Prow-2 (6) [c]	0.288	0.455	1.82	2.8	1.0	2.8

DTNs: MO0012POROCHOL.000 [153376] (porosity); MO0012PERMCHOL.000 [153368] (permeability); MO0012DIFFCHOL.000 [159243] (diffusion cells). Output DTN: LA0303PR831362.001 (model results – diffusion coefficients).

NOTE: Synthetic J-13 water was used for the experiments involving the first three tuffs. Filtered J-13 water was used in the other three experiments.

(a) Numbers in parentheses correspond to numbers in Figure 6.3-39 (locations where core was collected from the C-wells) and in Table 6.3-16 (where actual depths associated with the cores are listed).

(b) Thickness, *L*, of tuff pellet.

(c) Experiments were conducted using two separate tuff pellets from the Lower Prow Pass Tuff.

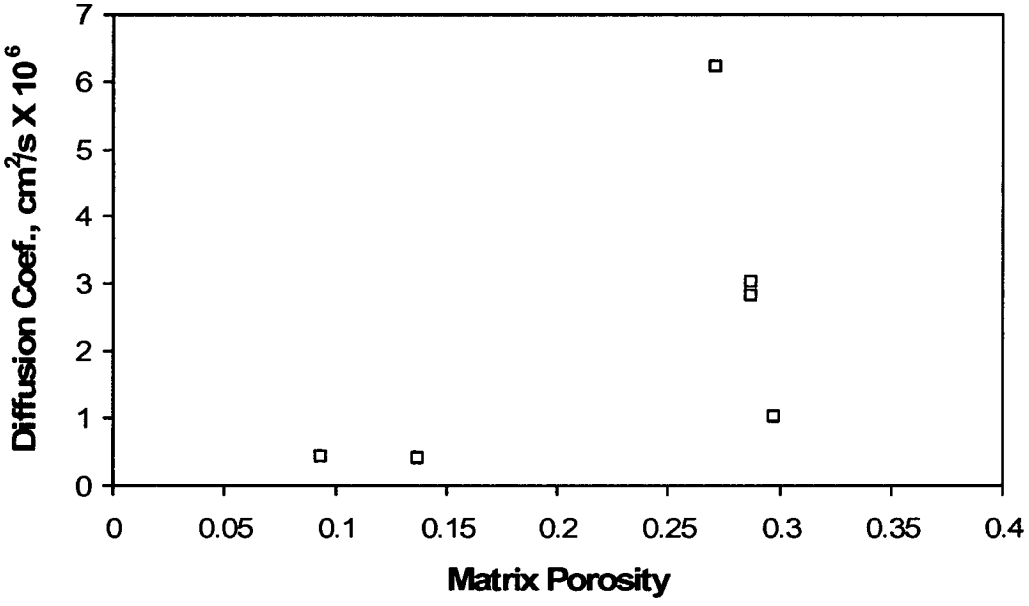

DTN: MO0012POROCHOL.000 [153376] (porosity data). Output DTN: LA0303PR831362.001 (diffusion coefficients).

NOTE: Porosity and diffusion coefficient for bromide are listed in Table 6.3-20.

Figure 6.3-56. Bromide Diffusion Coefficients Versus Tuff Porosity for all C-wells Diffusion Cell Experiments

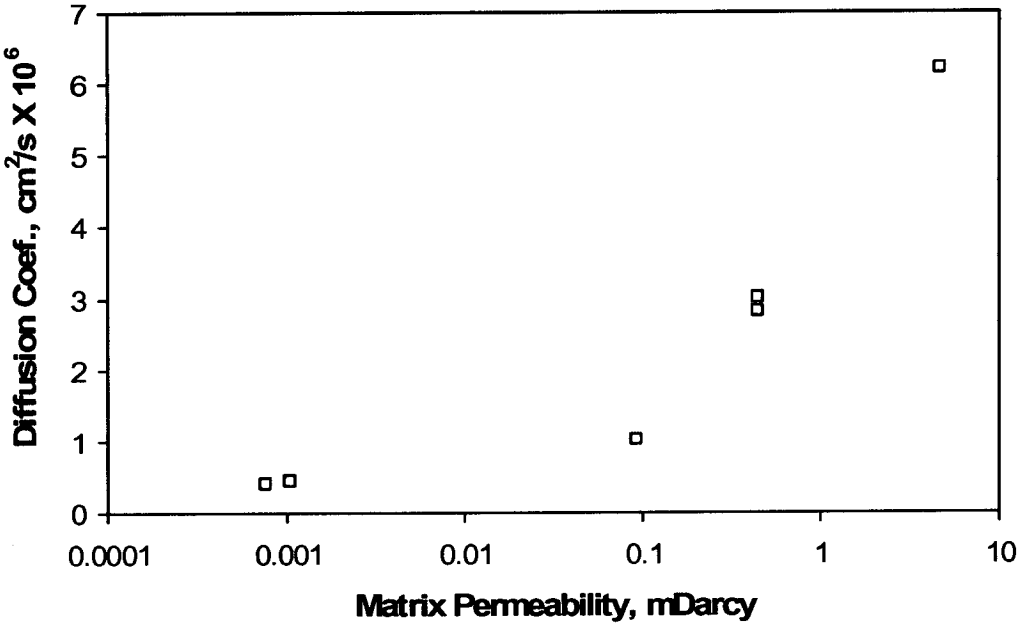

DTN: MO0012PERMCHOL.000 [153368] (permeability data). Output DTN: LA0303PR831362.001 (diffusion coefficients).

NOTE: Permeability and diffusion coefficient are listed in Table 6.3-20.

Figure 6.3-57. Bromide Diffusion Coefficients Versus Tuff Permeability for all C-wells Diffusion Cell Experiments

6.3.9 Laboratory Studies of Lithium Transport in Crushed Tuff Columns and Fractured Cores

Several laboratory transport experiments were conducted to study lithium transport under flowing conditions in both columns packed with crushed C-wells tuff and fractured C-wells cores (Reimus 2003 [163760], Attachments A, B1, and B2). The crushed-tuff column experiments were conducted to compare lithium sorption parameters under flowing conditions to batch-sorption measurements. The fractured-core experiments were conducted to study lithium transport under more realistic fracture flow conditions where matrix diffusion and sorption in the matrix should also influence transport. The crushed-tuff experiments are described in Section 6.3.9.1, and the fractured-core experiments are described in Section 6.3.9.2.

6.3.9.1 Crushed-Tuff Column Experiments

6.3.9.1.1 Experimental Methods

A series of transport experiments was conducted in plexiglass columns 91.44 cm in length and 0.62 cm in diameter (Reimus 2003 [163760], Attachment A). The columns were packed with crushed central Bullfrog Tuff (from location number 2 in Figure 6.3-39) that had been wet-sieved to a size range between 75 and 500 μm. A wet slurry technique was used to pack the

columns. Column porosity was measured at ~57% (average of two columns), and dry bulk density was calculated at 1.14 g/mL by assuming a mineral density of 2.65 g/mL, which are typical values for columns prepared in this fashion (e.g., Treher and Raybold 1982 [125967], pp. 8 to 9; Thompson 1989 [100830], pp.353 to 364). Two columns were prepared identically. The column apparatus included a constant-rate pump, a valve to switch between a reservoir containing J-13 "background" water and a solution of lithium bromide in J-13 water, and an automatic fraction collector at the downstream end of the column. Each experiment began by pumping approximately 180 mL (roughly 12 pore volumes) of J-13 water through the column at a specified flow rate to equilibrate the tuff with the groundwater. The input was then switched to a lithium bromide solution, which was maintained for approximately three pore volumes before being switched back to tracer-free groundwater. Effluent samples were analyzed for lithium and bromide using liquid chromatography (detection limits were 0.10 mg L^{-1} for Li^+ and 0.005 mg L^{-1} for Br^-). Bromide was used as a nonsorbing tracer to determine mean residence times and dispersivities in the columns as well as to serve as a nonsorbing tracer against which lithium retardation could be gauged.

A total of five experiments were conducted in the two columns, with the tracer concentrations and flow rate both being varied. In three of the five column experiments, the responses of Li^+ and Br^- were monitored until concentrations returned to background levels; in the other two experiments, concentrations were monitored only until they leveled off at the inlet concentrations. The experimental conditions are summarized in Table 6.3-21. The different tracer concentrations were intended to investigate potential effects of lithium sorption nonlinearity, and the different flow rates were intended to reveal rate-limited effects such as sorption nonequilibrium or diffusion-controlled sorption rates. All tests were conducted at 25°C.

Table 6.3-21. Results of RELAP Fits to Rising Limbs of Lithium and Bromide Breakthrough Curves in Crushed Tuff Columns

Column	Figure	Flow Rate (mL/hr)	Li Conc. (mg/L)	τ (hr)	*Pe*	R_F	k_f (1/hr)	*Da*
1*	6.3-58	2.2	23.5	7.6	250	2.0 (2.0)	3.1	24
1	6.3-59	1.6	23.5	10.3	260	2.0 (2.0)	3.7	38
1*	6.3-60	9.7	20.1	1.8	580	1.8 (1.7)	8.8	16
2*	6.3-61	2.2	5.9	7.7	870	2.3 (2.3)	22	169
2	6.3-62	1.6	5.9	10.4	750	2.3 (2.25)	4.6	48

DTN: LA0301PR831231.001 [162603] (for flow rates and concentrations). Output DTN: LA0303PR831361.003 (model results).

NOTE: *Denotes experiments in which tracer concentrations were monitored until background levels were reached.

In this table, τ is residence time; *Pe* is the Peclet number; R_f is the retardation factor; k_f is the rate constant for sorption onto the column material; and *Da* is the Damkohler number (= $k_f\tau$), which represents the ratio of reaction rate to advection rate in the columns. R_f values in parentheses indicate the best-fitting retardation factors when equilibrium sorption was assumed (i.e., very fast sorption kinetics).

6.3.9.1.2 Interpretive Methods

The bromide responses in the experiments were interpreted using the RELAP V 2.0 computer code (STN: 10551-2.0-00 [159065]) to obtain estimates of mean residence times and dispersivities/Peclet numbers in the columns. RELAP was also used to fit the rising limbs of the lithium responses in each experiment to obtain an estimate of the lithium retardation factor in the columns. The rate-limited sorption features of RELAP were also used to obtain an estimate of the rate constant (k_f) describing lithium sorption onto the column packing material. The rate constants were obtained by relaxing the equilibrium sorption assumption and adjusting the rate constants for each data set until the RELAP fits were optimized. Damkohler numbers ($k_f\tau$), which represent the ratio of reaction rate to advection rate in the columns, were calculated for each experiment. Damkohler numbers significantly greater than one indicate a system that can be treated as being at equilibrium locally (Valocchi 1985 [144579], pp. 808 to 820).

It was apparent that while RELAP V 2.0 (STN: 10551-2.0-00 [159065]) could fit the arrival of lithium, it could not fit the tails of the lithium responses when concentrations were monitored until they returned to background levels. The tails exhibited a behavior suggesting that a portion of the lithium eluted with the bromide as if it were a nonsorbing tracer. This behavior can occur when an ion-exchanging cation such as lithium comprises the majority of the cation equivalents in the tracer solution, which was certainly the case in the higher-concentration LiBr experiments. Essentially, if the CEC of the tuff and the exchange equilibria are not sufficient to exchange all of the lithium injected into a column, then some of the lithium must elute with the bromide to maintain charge balance in the solution exiting the column. Thus, for the tests in which the lithium was fully eluted from the columns, the MULTRAN V 1.0 computer code ([STN: 10666-1.0-00 [159068]), which is capable of explicitly modeling cation exchange and maintaining solution charge balance, was used to interpret the lithium responses (see Section 6.3.9.2.2 for description of the code).

6.3.9.1.3 Results and Interpretations

The rising limbs of the breakthrough curves for the five experiments along with the RELAP V 2.0 (STN: 10551-2.0-00 [159065]) fits to the data are shown in Figures 6.3-58 through 6.3-62. The best-fitting model parameters are listed in Table 6.3-21. Although significant improvements to the RELAP fits of the lithium breakthrough curves were obtained by assuming finite sorption rates, the relatively large Damkohler numbers listed in Table 6.3-21 suggest that the local equilibrium assumption is reasonably valid in the columns. Furthermore, this assumption should be even more valid in field experiments where tracer residence times are much longer than in the columns. Figure 6.3-58 shows the results of fitting the lithium response curve from one of the experiments assuming a nonlinear (Langmuir) sorption isotherm with parameters obtained from batch sorption testing (K_L = 0.0058 mL/μg and S_{max} = 106 μg/g for the Bullfrog Tuff from c#2 used in these columns). It is apparent that the model fits are not improved by assuming a nonlinear isotherm. The RETRAN V 2.0 computer code (STN: 10552-2.0-00 [159066]) was used for the nonlinear simulations.

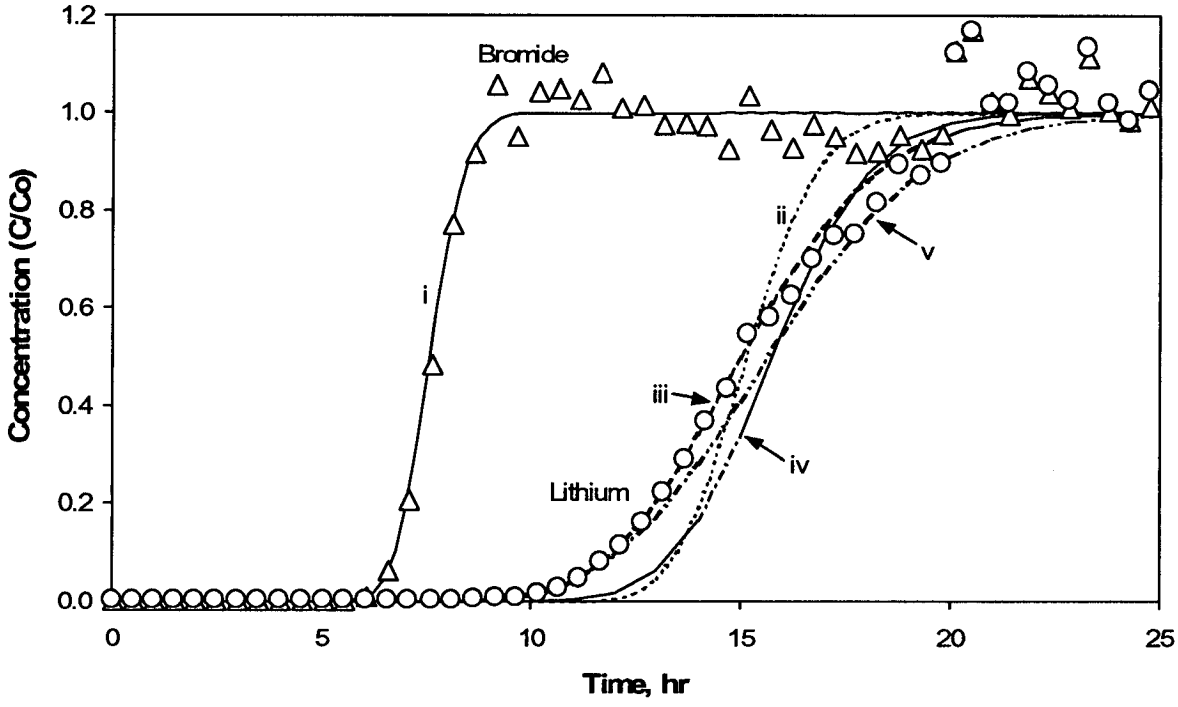

DTN: LA0301PR831231.001 [162603] (data). Output DTN: LA0303PR831361.003 (models).

NOTE: The curves above are numbered as follows:

(i) fit to bromide data with a Peclet number of 250
(ii) fit to lithium data assuming linear isotherm (R_F = 2.0) with equilibrium sorption
(iii) fit to lithium data assuming linear isotherm with a forward rate constant of 3.1 1/hr (and R_F = 2.0)
(iv) fit to lithium data assuming a Langmuir isotherm with equilibrium sorption
(v) fit to lithium data assuming a Langmuir isotherm with a forward rate constant of 3.2 1/hr.

Langmuir isotherm parameters: K_L = 0.0058 mL/µg and S_{max} = 105.8 µg/g (batch isotherm values obtained for lithium on central Bullfrog Tuff from UE-25 c#2).

Figure 6.3-58. Bromide and Lithium Breakthrough Curves in Column 1 at a Flow Rate of 2.2 mL/hr and Corresponding RELAP and RETRAN Fits to Data

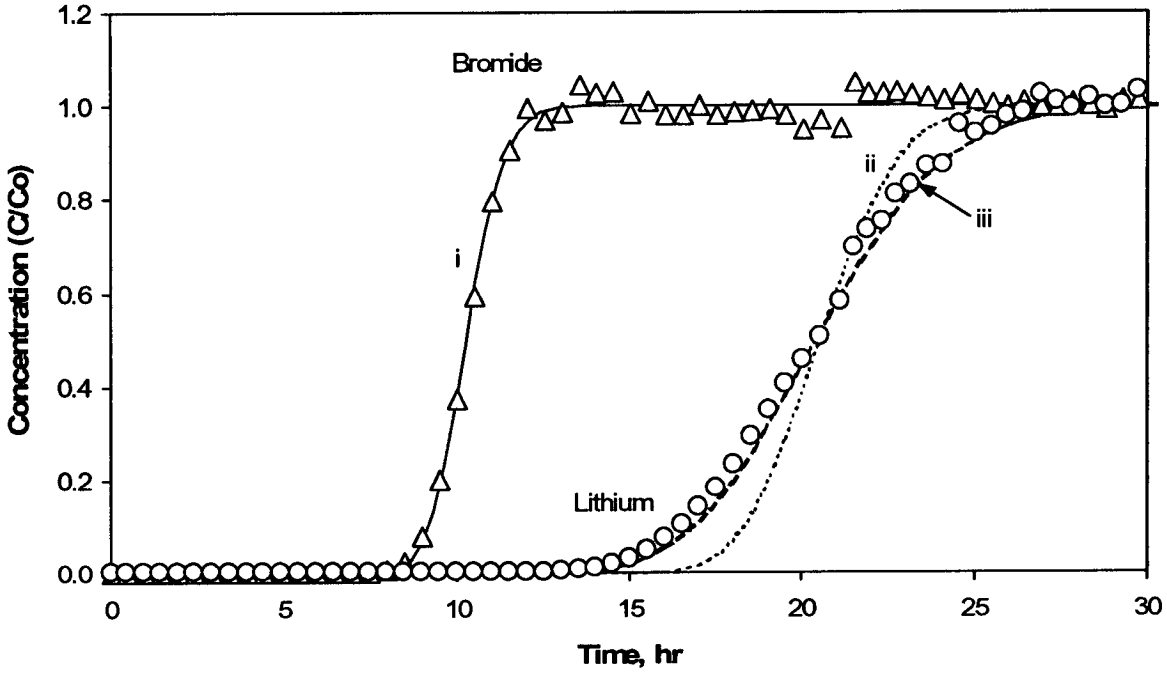

DTN: LA0301PR831231.001 [162603] (data). Output DTN: LA0303PR831361.003 (models).

NOTE: The curves above are numbered as follows:

(i) fit to bromide data with a Peclet number of 260

(ii) fit to lithium data assuming linear isotherm (R_F = 2.0) with equilibrium sorption

(iii) fit to lithium data assuming linear isotherm with a forward rate constant of 3.7 1/hr (and R_F = 2.0).

Figure 6.3-59. Bromide and Lithium Breakthrough Curves in Column 1 at a Flow Rate of 1.6 mL/hr and Corresponding RELAP Fits to Data

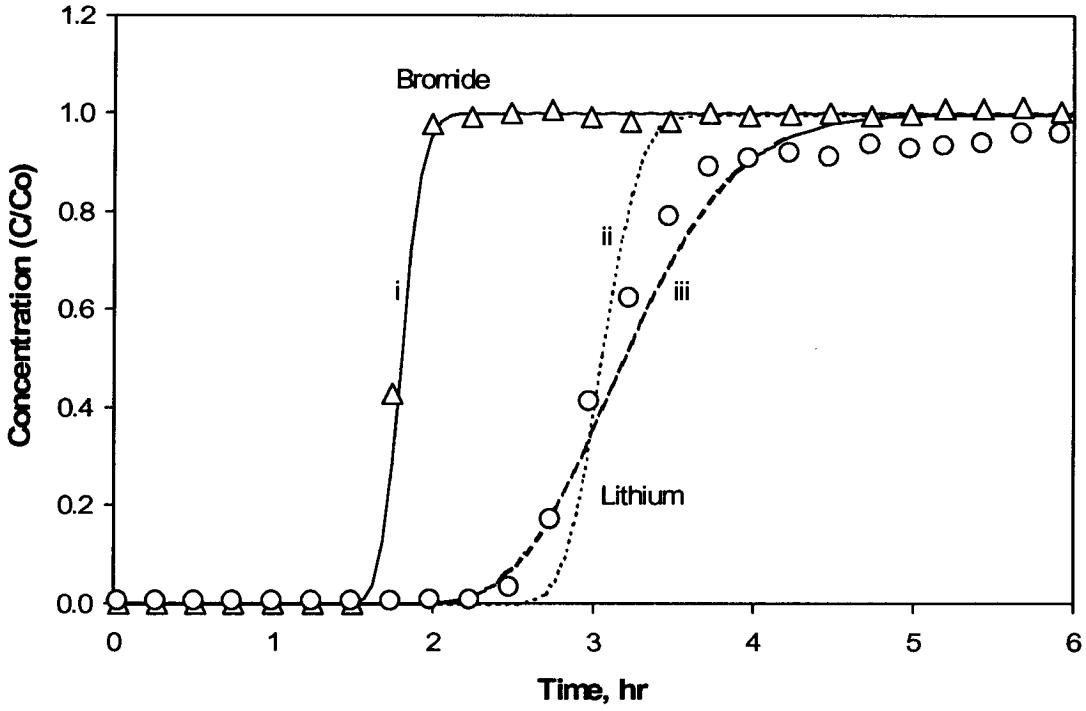

DTN: LA0301PR831231.001 [162603] (data). Output DTN: LA0303PR831361.003 (models).

NOTE: The curves above are numbered as follows:

(i) fit to bromide data with a Peclet number of 580

(ii) fit to lithium data assuming linear isotherm (R_F = 1.7) with equilibrium sorption

(iii) fit to lithium data assuming linear isotherm with a forward rate constant of 8.8 1/hr (and R_F = 1.8).

Figure 6.3-60. Bromide and Lithium Breakthrough Curves in Column 1 at a Flow Rate of 9.7 mL/hr and Corresponding RELAP Fits to Data

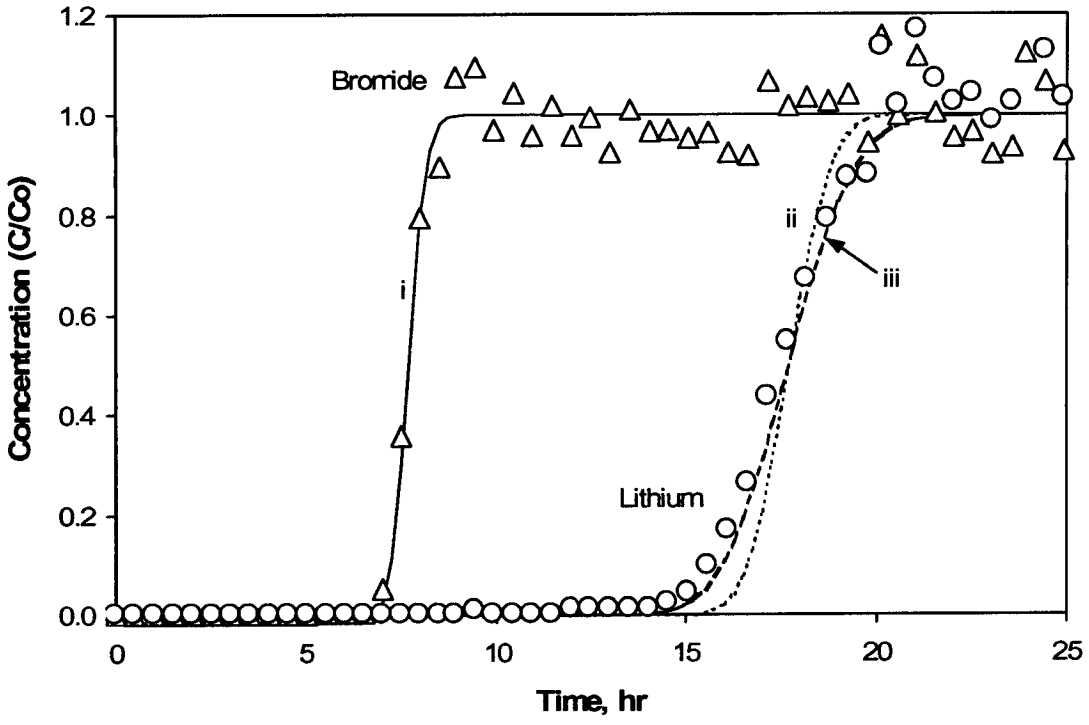

DTN: LA0301PR831231.001 [162603] (data). Output DTN: LA0303PR831361.003 (models).

NOTE: The curves above are numbered as follows:

(i) fit to bromide data with a Peclet number of 870

(ii) fit to lithium data assuming linear isotherm (R_F = 2.3) with equilibrium sorption

(iii) fit to lithium data assuming linear isotherm with a forward rate constant of 22 1/hr (and R_F = 2.3).

Figure 6.3-61. Bromide and Lithium Breakthrough Curves in Column 2 at a Flow Rate of 2.2 mL/hr and Corresponding RELAP Fits to Data

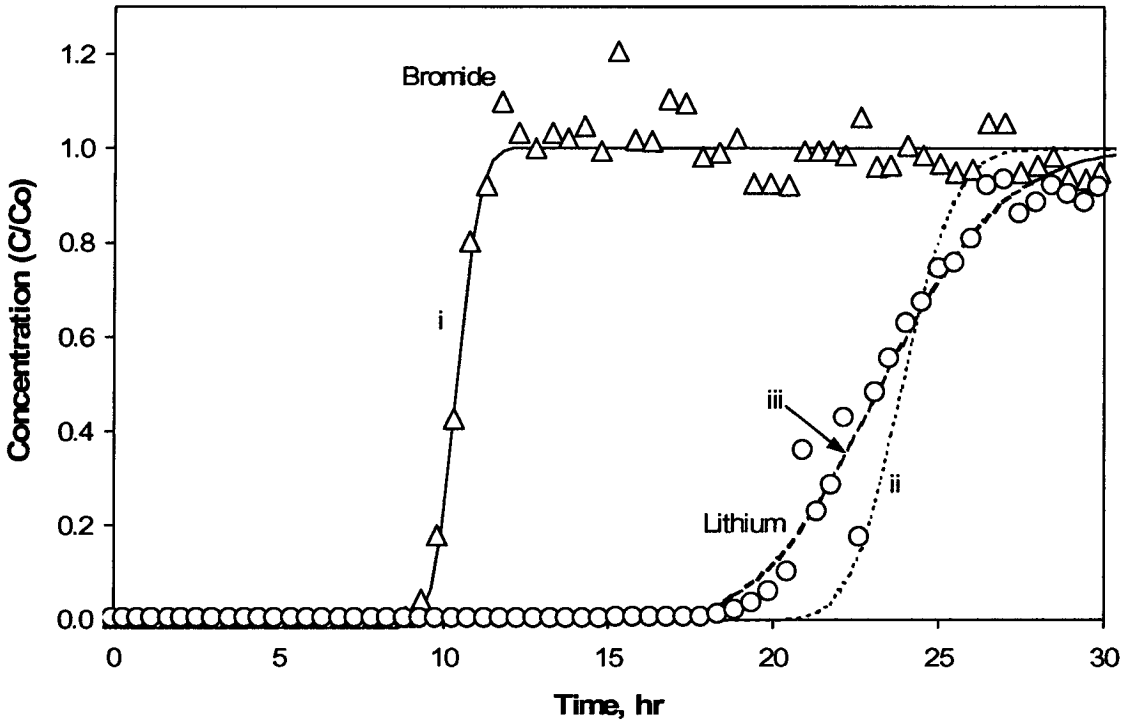

DTN: LA0301PR831231.001 [162603] (data). Output DTN: LA0303PR831361.003 (models).

NOTE: The curves above are numbered as follows:
(i) fit to bromide data with a Peclet number of 750
(ii) fit to lithium data assuming linear isotherm (R_F = 2.3) with equilibrium sorption
(iii) fit to lithium data assuming linear isotherm with a forward rate constant of 4.6 1/hr (and R_F = 2.25).

Figure 6.3-62. Bromide and Lithium Breakthrough Curves in Column 2 at a Flow Rate of 1.6 mL/hr and Corresponding RELAP Fits to Data

Table 6.3-21 shows that lithium retardation factors (R_Fs) for the tests with lower tracer concentrations ranged from 2.2 to 2.3, with a mean of 2.25; whereas R_Fs for the higher concentration tests ranged from 1.7 to 2.0, with a mean of 1.87. The observed decreased R_F at higher concentrations is consistent with a nonlinear sorption isotherm. For the Langmuir isotherm, the R_F can be shown to be (Fetter 1993 [102009], pp. 122 to 123):

$$R_F = 1 + \frac{\rho_B}{\theta}\left(\frac{K_L S_{max}}{(1+K_L C)^2}\right) \quad \text{(Eq. 20)}$$

where

ρ_B is the dry bulk density of the medium (g/mL)

θ is the volumetric moisture content, or porosity for a saturated medium.

By solving Equation 20 with the batch Langmuir parameters obtained for the Central Bullfrog Tuff used in the column experiments (K_L = 0.0053 mL/μg and S_{max} = 110 μg/g – see Table 6.3-18 footnote) and column values for ρ_B and θ, retardation factor predictions of 2.11 are obtained for the lower concentration tests and 1.95 for the higher concentration tests. Overall these predictions match the R_F values of Table 6.3-21 very well, differing by 7% or less for both concentration levels. The MULTRAN V 1.0 (STN: 10666-1.0-00 [159068]) fits to the full data sets for the three experiments in which tracer concentrations were monitored until they returned to background levels are shown in Figures 6.3-63 to 6.3-65. The Q_1 and Q_2 values listed in these figures correspond to the "selectivity coefficients" for the following cation exchange reactions:

$$Li^+ + NaX \leftrightarrow LiX + Na^+ \quad Q_1 = \frac{[LiX][Na^+]}{[NaX][Li^+]} \quad \text{(Eq. 21)}$$

$$2Li^+ + CaX_2 \leftrightarrow 2LiX + Ca^{2+} \quad Q_2 = \frac{[LiX]^2[Ca^{2+}]}{[CaX_2][Li^+]^2} \quad \text{(Eq. 22)}$$

where X = a negatively charged surface site.

In addition to these reactions, MULTRAN V 1.0 (STN: 10666-1.0-00 [159068]) also accounts for the exchange between sodium and calcium ions, and it solves the surface cation-exchange balance equation for a three-component system:

$$2Na^+ + CaX_2 \leftrightarrow 2NaX + Ca^{2+} \quad \frac{Q_2}{Q_1^2} = \frac{[NaX]^2[Ca^{2+}]}{[CaX_2][Na^+]^2}, \quad \text{(Eq. 23)}$$

$$CEC = \frac{\rho_B}{\phi}([LiX]+[NaX]+2[CaX_2]) \quad \text{(Eq. 24)}$$

The measured CEC for the Bullfrog Tuff (Section 6.3.7.2) was used as the CEC value in the model simulations, and the selectivity coefficients Q_1 and Q_2 were adjusted to fit the lithium

data. However, without sodium and calcium concentration data, it was not possible to obtain a unique fit to the lithium responses. In fact, the lithium responses could be fit equally well assuming lithium exchange with only sodium or only calcium. Thus, the Q_1 and Q_2 values presented in Figures 6.3-63 through 6.3-65 should be considered as only one of many possible combinations that could fit the lithium data equally well. However, it is not the values of these parameters that are important but rather the recognition that cation-exchange equilibria must be explicitly accounted for to explain the observed transport behavior of the lithium. For comparison, a RELAP V 2.0 (STN: 10551-2.0-00 [159065]) "fit" to the data from Figure 6.3-63 is shown in Figure 6.3-66. It is clear that the single-component equilibrium K_d-model fit cannot capture the tailing behavior of the lithium. These results could have important implications for field tracer tests conducted in porous media that have a small sorption capacity for cation-exchanging tracers.

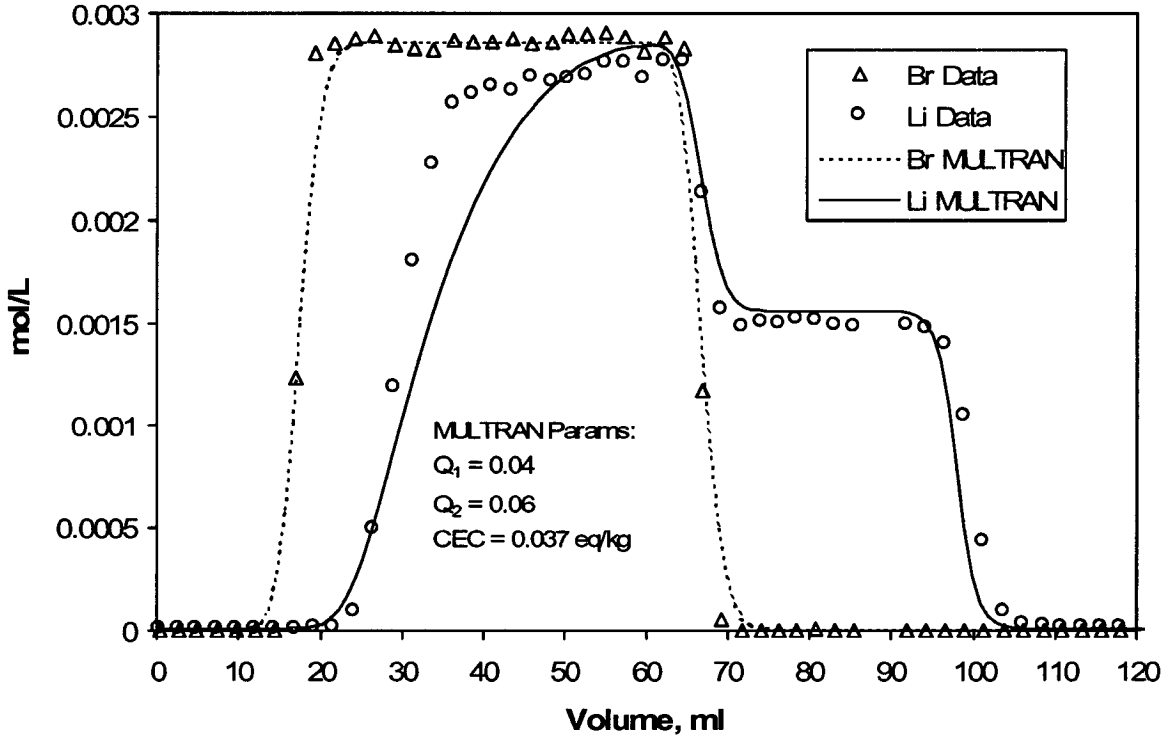

DTN: LA0301PR831231.001 [162603] (data). Output DTN: LA0303PR831361.003 (model).

NOTE: "MULTRAN Params" refers to the parameter values used in MULTRAN V 1.0 (STN: 10666-1.0-00 [159068]) to obtain the simulated curves.

Figure 6.3-63. MULTRAN Fits to Complete Bromide and Lithium Breakthrough Curves from High-Concentration Experiment Conducted at 9.7 mL/hr in Column 1 (Figure 6.3-60)

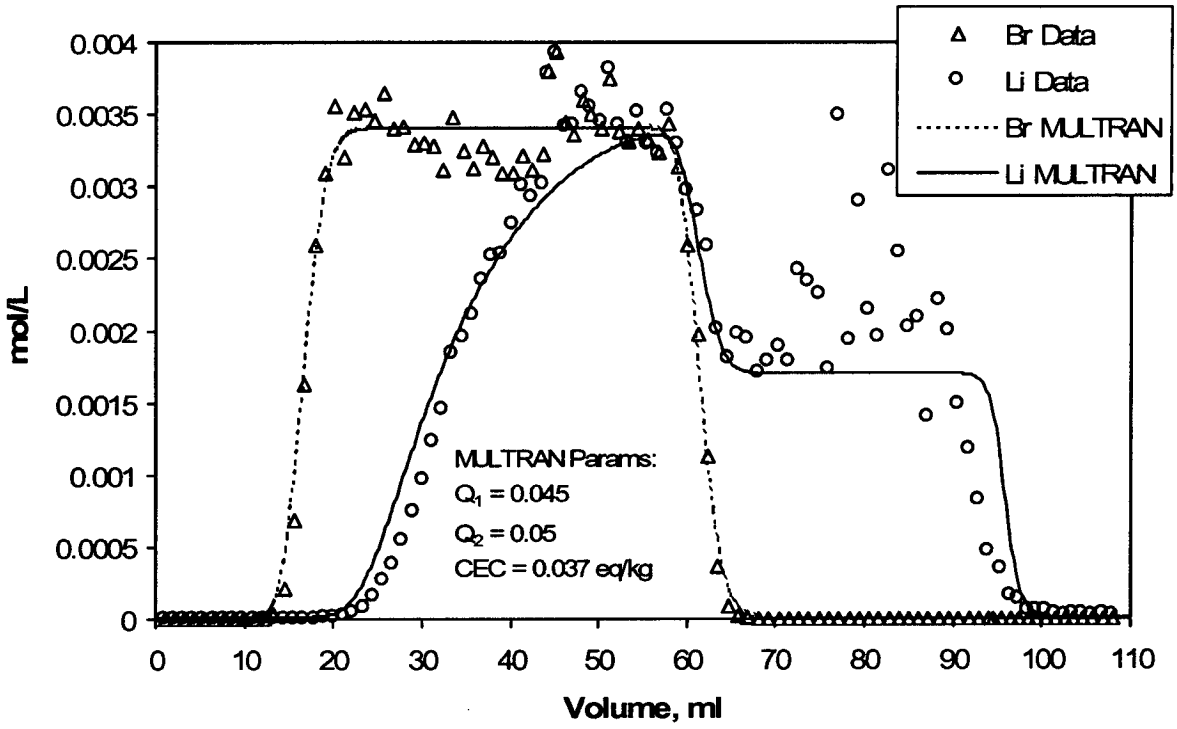

DTN: LA0301PR831231.001 [162603] (data). Output DTN: LA0303PR831361.003 (model).

NOTE: "MULTRAN Params" refers to the parameter values used in MULTRAN V 1.0 (STN: 10666-1.0-00 [159068]) to obtain the simulated curves.

Figure 6.3-64. MULTRAN Fits to Complete Bromide and Lithium Breakthrough Curves from High-Concentration Experiment Conducted at 2.2 mL/hr in Column 1 (Figure 6.3-58)

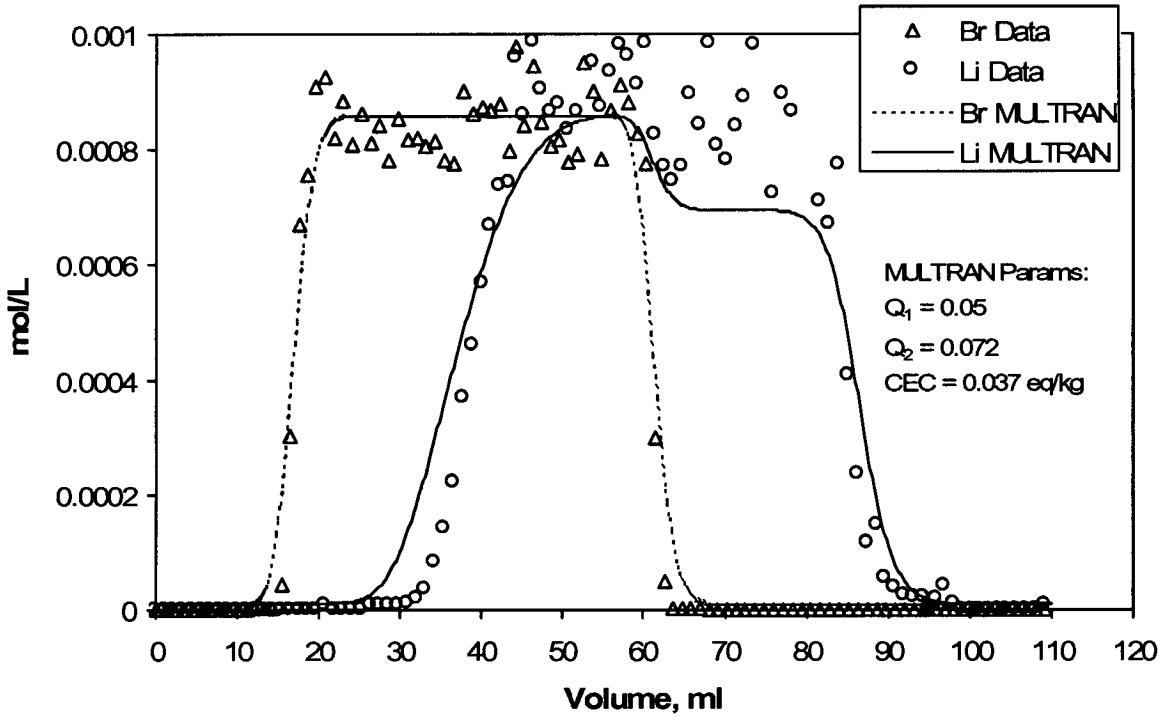

DTN: LA0301PR831231.001 [162603] (data). Output DTN: LA0303PR831361.003 (model).

NOTE: "MULTRAN Params" refers to the parameter values used in MULTRAN V 1.0 (STN: 10666-1.0-00 [159068]) to obtain the simulated curves.

Figure 6.3-65. MULTRAN Fits to Complete Bromide and Lithium Breakthrough Curves from Low-Concentration Experiment Conducted at 2.2 mL/hr in Column 2 (Figure 6.3-61)

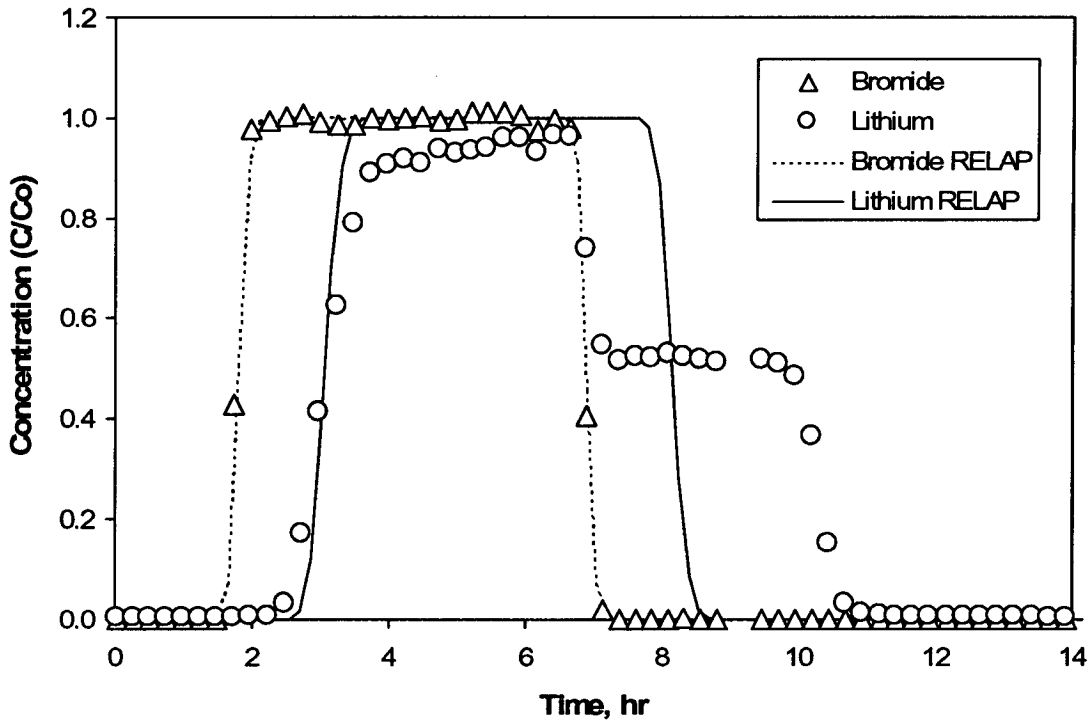

DTN: LA0301PR831231.001 [162603] (data). Output DTN: LA0303PR831361.003 (model).

Figure 6.3-66. RELAP Fits to Complete Bromide and Lithium Breakthrough Curves from Experiment Conducted at 9.7 mL/hr in Column 1 (Figure 6.3-63 shows the MULTRAN fits)

6.3.9.2 Fractured-Core Experiments

6.3.9.2.1 Experimental Methods

Fractured-core transport experiments were conducted on four separate cores obtained from the C-wells following the procedure of Callahan et al. (2000 [156648], pp. 3547 to 3558). The experiments are documented in detail in Reimus (2003 [163760], Attachments B1 and B2). The cores were obtained from locations 3, 4, 5, and 6 in Figure 6.3-39. In the following discussion, the cores from the upper, central, and lower flow zones of the Prow Pass Tuff (locations 4, 5, and 6, respectively) will be referred to as cores 1, 2, and 3, respectively. The core from the lower flow zone of the Bullfrog Tuff will be referred to as core 4. The mineralogy of the cores is given in Table 6.3-17. Core 4 (lower flow zone of the Bullfrog Tuff) contained the highest percentage of clay and zeolite minerals, 9 ± 3 wt. % smectite, 4 ± 1 wt % clinoptilolite, and 13 ± 1 wt. % analcime. A single fracture was mechanically induced in each of the four cores. The cores were laid on a cement floor and a four-pound hammer and chisel were used to induce an axial fracture running the length of the core. The cores were then encased in an epoxy and Plexiglas column apparatus following the procedure of Callahan et al. (2000 [156648]). Figure 6.3-67 shows a schematic illustration of a column experimental system.

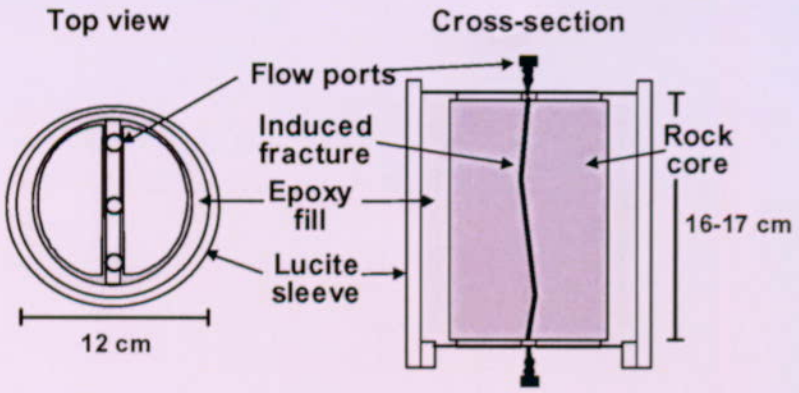

For illustration purposes only

NOTE: Three flow ports on each end of the core allowed access to the inlet and outlet regions; the central flow ports were used to connect the cores to a syringe pump and fraction collector via a 0.8-mm diameter tubing. The lengths of the cores varied, but the diameters of all cores were 9.5 cm.

Figure 6.3-67. Schematic Illustration of a Fractured Rock Core Experimental System

The tracer experiments conducted in each core are summarized in Tables 6.3-22 through 6.3-27. As described by Callahan et al. (2000 [156648]), cores 1 and 2 each featured three experiments in which iodide was used as a nonsorbing tracer at three different flow rates. The objective of these experiments was to obtain estimates of matrix-diffusion, mass-transfer parameters in the cores by using RELAP to fit simultaneously the iodide responses at each flow rate. All four cores also featured at least two multiple-tracer experiments that were conducted and interpreted very similarly to the C-wells field tracer tests. Each experiment involved the injection of a pulse containing PFBA, lithium bromide (LiBr), and, in some cases, sodium iodide (NaI). Five multiple-tracer experiments were conducted in core 1. Two of these experiments were intended to be replicates, and they yielded very similar results, indicating good experimental reproducibility. Only two multiple-tracer tests were conducted in each of the other three cores. The flow rate in at least one of the multiple-tracer experiment in each core was approximately an order of magnitude lower than the flow rate(s) in the other multiple-tracer experiment(s). Flow rates were varied over this large range so that the effect of experiment time scale on matrix diffusion processes could be assessed in fracture systems of constant geometry. The fractures were thoroughly flushed after each experiment so that residual tracer concentrations were minimized in subsequent experiments.

A steady-state flow field was established in each core by continuously injecting degassed, filtered groundwater obtained from well J-13. A pulse of tracer solution (tracers dissolved in J-13 water) was then injected. After injection of the tracer pulse, continuous injection of tracer-free J-13 well water was resumed. The effluent was monitored for the tracer ions as well as for Na^+ and Ca^{2+} using ion chromatography for Br^- and PFBA and ICP-AES for analysis of Li^+, Na^+, and Ca^{2+}. Iodide was analyzed either using an ion-selective electrode or ion chromatography. The quantitative detection limits were 0.05 mg/L for Li^+, Na^+, and Ca^{2+}, 0.04 mg/L for Br^-, 0.02 mg/L for I^-, and 0.02 mg L^{-1} for PFBA. Na^+ and Ca^{2+} were analyzed so that cation exchange

equilibria could be more rigorously quantified than in the crushed-tuff column experiments described in Section 6.3.9.1. Cu-EDTA (copper complexed with ethylenediamine tetraacetic acid) was used as a tracer in some of the experiments to determine its potential to serve as a weakly sorbing tracer in field tests. In some of the tests (Tables 6.3-23 through 6.3-27), flow was interrupted for a time after the tracer concentrations had been tailing to verify diffusive mass transfer in the cores (Brusseau et al. 1997 [156647], pp. 205 to 219; Callahan et al. 2000 [156648]). This strategy was similar to that used in the Prow Pass multiple-tracer field test (Section 6.3.4.4).

Table 6.3-22. Experimental Conditions for the Iodide Fracture Transport Tests, Upper Prow Pass Tuff Core (Core 1)

Experimental Parameters			
Core length, L (m)		0.161	
Core width, w (m)		0.095	
Matrix porosity, n_m		0.272	
Hydraulic aperture, B_h (m) [(a)]		0.14×10^{-3}	
Iodide tests:	**Test 1**	**Test 2**	**Test 3**
Volumetric flow rate, Q (mL/hr)	2.2	19.6	8.7
Injection duration, t_p (hr)	28.02	3.08	7.23
Injection concentration, C_o (mg/L)	1000	1000	1000
Flow interruption period, time since start of injection (hr)	N/A [(b)]	N/A [(b)]	N/A [(b)]
Flow rate after restart, Q (mL/hr)	N/A [(b)]	N/A [(b)]	N/A [(b)]
Mass recovery (%)	86	96	94

Source: Reimus (2003 [163760], Attachment B1).

NOTE: (a) Determined from a constant head permeameter method.

(b) N/A: Not applicable; flow was not interrupted during these tests.

Table 6.3-23. Experimental Conditions for the Multiple-Tracer Fracture Transport Tests, Upper Prow Pass Tuff Core (Core 1)

Experimental Parameters	Test 1	Test 2
Volumetric flow rate, Q (mL/hr)	3.8	3.9
Injection duration, t_p (hr)	14.97	15.22
Injection concentration, C_o (mg/L)	192 (Li^+) 0 (Na^+) 0 (Ca^{2+}) 1728 (Br^-) 300 (I^-) 635 (PFBA)	192 (Li^+) 0 (Na^+) 0 (Ca^{2+}) 1728 (Br^-) 300 (I^-) 635 (PFBA)
Background groundwater concentration, C_i (mg/L)	0.64 (Li^+) 46.7 (Na^+) 12.8 (Ca^{2+}) 3.63 (Br^-) 1.8 (I^-) 1.11 (PFBA)	1.79 (Li^+) 45.4 (Na^+) 12.8 (Ca^{2+}) 10.7 (Br^-) 0.55 (I^-) 3.86 (PFBA)
Flow interruption period, time since start of injection (hr)	87.3–137.3	87.1–137.2
Flow rate after restart, Q (mL/hr)	3.96	3.99
Mass recovery (%)	89 (Li^+) 89 (Br^-) 92 (I^-) 95 (PFBA)	89 (Li^+) 89 (Br^-) 86 (I^-) 95 (PFBA)

Experimental Parameters	Test 3	Test 4	Test 5
Volumetric flow rate, Q (mL hr^{-1})	0.51	7.9	6.3
Injection duration, t_p (hr)	156.85	19.0	10.5
Injection concentration, C_o (mg/L)	159 (Li^+) 394 (Na^+) 0 (Ca^{2+}) 1870 (Br^-) 296 (I^-) 641 (PFBA) 145 (Cu^{2+}) 699 (EDTA [b])	1010 (Li^+) 59.1 (Na^+) 0 (Ca^{2+}) 11400 (Br^-) N/A [a] (I^-) 766 (PFBA)	216 (Li^+) 250 (Na^+) 0 (Ca^{2+}) 2528 (Br^-) N/A [a] (I^-) 766 (PFBA) 192 (Cu^{2+}) 1131 (EDTA [b])
Background groundwater concentration, C_i (mg/L)	0.08 (Li^+) 51.8 (Na^+) 13.2 (Ca^{2+}) 10.87 (Br^-) < 0.4 (I^-) 2.07 (PFBA)	0.08 (Li^+) 45 (Na^+) 13.3 (Ca^{2+}) < 0.02 (Br^-) < 0.4 (I^-) < 0.005 (PFBA)	0.53 (Li^+) 45 (Na^+) 13.3 (Ca^{2+}) 0.98 (Br^-) < 0.4 (I^-) < 0.005 (PFBA)
Flow interruption period, time since start of injection (hr)	689–904	19.8–21.2, 49.9–64.2	44.0–64.0
Flow rate after restart, Q (mL/hr)	0.51	8.05, 8.04	6.46
Mass recovery (%)	83 (Li^+) 94 (Br^-) 82 (I^-) 94 (PFBA)	89 (Li^+) 89 (Br^-) N/A [a] (I^-) 95 (PFBA)	89 (Li^+) 89 (Br^-) N/A [a] (I^-) 95 (PFBA)

Source: Reimus (2003 [163760], Attachment B1).

NOTE: (a) N/A: not applicable; iodide was not injected in these tests.

(b) EDTA: ethylenediamine tetraacetic acid.

Table 6.3-24. Experimental Conditions for the Iodide Fracture Transport Tests, Central Prow Pass Tuff Core (Core 2)

Experimental Parameters			
Core length, L (m)	0.173		
Core width, w (m)	0.095		
Matrix porosity, n_m	0.138		
Hydraulic aperture, B_h (m) [(a)]	0.13×10^{-3}		
	Test 1	**Test 2**	**Test 3**
Volumetric flow rate, Q (mL/hr)	19.7	49.3	11.3
Injection duration, t_p (hr)	4.0	1.47	6.05
Injection concentration, C_o (mg/L)	1000	1000	1000
Flow interruption period, time since start of injection (hr)	N/A [(b)]	N/A [(b)]	N/A [(b)]
Flow rate after restart, Q (mL/hr)	N/A [(b)]	N/A [(b)]	N/A [(b)]
Mass recovery (%)	89	98	84

Source: Reimus (2003 [163760], Attachment B2).

NOTE: (a) Determined from a constant head permeameter method.

(b) N/A: not applicable; flow was not interrupted during these tests.

Table 6.3-25. Experimental Conditions for the Multiple-Tracer Fracture Transport Tests, Central Prow Pass Tuff Core (Core 2)

Experimental Parameters	Test 1	Test 2
Volumetric flow rate, Q (mL/hr)	5.9	0.44
Injection duration, t_p (hr)	12.3	170
Injection concentration, C_o (mg/L)	216 (Li^+) 205 (Na^+) 0 (Ca^{2+}) 2528 (Br^-) N/A [(a)] (I^-) 766 (PFBA) 192 (Cu^{2+}) 1131 (EDTA [(b)])	159 (Li^+) 301 (Na^+) 0 (Ca^{2+}) 1870 (Br^-) 296 (I^-) 641 (PFBA) 145 (Cu^{2+}) 699 (EDTA [(b)])
Background groundwater concentration, C_i (mg/L)	0.08 (Li^+) 45 (Na^+) 13.3 (Ca^{2+}) < 0.02 (Br^-) < 0.4 (I^-) < 0.005 (PFBA)	0.55 (Li^+) 75.1 (Na^+) 10.0 (Ca^{2+}) 1.97 (Br^-) 0.9 (I^-) 0.98 (PFBA)
Flow interruption period, time since start of injection (hr)	42.9–62.9	799–999
Flow rate after restart, Q (mL/hr)	5.95	0.44
Mass recovery (%)	84 (Li^+) 90 (Br^-) N/A [(a)] (I^-) 95 (PFBA)	68 (Li^+) 97 (Br^-) 97 (I^-) 102 (PFBA)

Source: Reimus (2003 [163760], Attachment B2).

NOTE: (a) N/A: not applicable; iodide was not injected in these tests.

(b) EDTA: ethylenediamine tetraacetic acid.

Table 6.3-26. Experimental Conditions for the Multiple-Tracer Fracture Transport Tests, Lower Prow Pass Tuff Core (Core 3)

Experimental Parameters		
Core length, L (m)	0.116	
Core width, w (m)	0.095	
Matrix porosity, n_m	0.288	
Hydraulic aperture, B_h (m) [(a)]	0.16×10^{-3}	
	Test 1	**Test 2**
Volumetric flow rate, Q (mL/hr)	11.4	0.46
Injection duration, t_p (hr)	14.5	340
Injection concentration, C_o (mg/L)	159 (Li^+) 331 (Na^+) 1.2 (Ca^{2+}) 1870 (Br^-) 296 (I^-) 641 (PFBA) 145 (Cu^{2+}) 699 (EDTA [(b)])	165 (Li^+) 310 (Na^+) 0 (Ca^{2+}) 1930 (Br^-) 299 (I^-) 681 (PFBA) 150 (Cu^{2+}) 699 (EDTA [(b)])
Background groundwater concentration, C_i (mg/L)	0.08 (Li^+) 44.6 (Na^+) 13.3 (Ca^{2+}) < 0.02 (Br^-) < 0.35 (I^-) < 0.005 (PFBA)	4.41 (Li^+) 67.2 (Na^+) 16.4 (Ca^{2+}) 60.1 (Br^-) 9.49 (I^-) 16.2 (PFBA)
Flow interruption period, time since start of injection (hr)	43.6–68.6	792–992
Flow rate after restart, Q (mL/hr)	11.4	0.47
Mass recovery (%)	97.2 (Li^+) 95.7 (Br^-) 98.4 (I^-) 99.3 (PFBA)	72.4 (Li^+) 87.3 (Br^-) 84.2 (I^-) 80.1 (PFBA)

Source: Reimus (2003 [163760], Attachment B1).

NOTES: (a) Determined from a constant head permeameter method.

(b) EDTA: ethylenediamine tetraacetic acid.

Table 6.3-27. Experimental Conditions for the Multiple-Tracer Fracture Transport Tests, Lower Bullfrog Tuff Core (Core 4)

Experimental Parameters	Test 1	Test 2
Volumetric flow rate, Q (mL/hr)	5.0	0.47
Injection duration, t_p (hr)	34.0	335.0
Injection concentration, C_o (mg/L)	165 (Li^+) 342 (Na^+) 0 (Ca^{2+}) 1930 (Br^-) 299 (I^-) 681 (PFBA) 150 (Cu^{2+}) 699 (EDTA*)	192 (Li^+) 0 (Na^+) 0 (Ca^{2+}) 1728 (Br^-) 300 (I^-) 635 (PFBA)
Background groundwater concentration, C_i (mg/L)	0.04 (Li^+) 51.1 (Na^+) 11.0 (Ca^{2+}) 0.14 (Br^-) 0.07 (I^-) 0.14 (PFBA)	4.41 (Li^+) 67.2 (Na^+) 16.4 (Ca^{2+}) 60.1 (Br^-) 9.49 (I^-) 16.2 (PFBA)
Flow interruption period, time since start of injection (hr)	67.2–87.2	79–992
Flow rate after restart, Q (mL/hr)	5.05	0.47
Mass recovery (%)	57 (Li^+) 96 (Br^-) 86 (I^-) 99 (PFBA)	85 (Li^+) 103 (Br^-) 86 (I^-) 91 (PFBA)

Source: Reimus (2003 [163760], Attachment B2).

NOTE: *EDTA: ethylenediamine tetraacetic acid.

6.3.9.2.2 Interpretive Methods

The RELAP V 2.0 (STN: 10551-2.0-00 [159065]) code was used to interpret the nonsorbing iodide, bromide, and PFBA tracer responses. For the iodide-only experiments conducted in cores 1 and 2, the responses at the three different flow rates were simultaneously fitted, assuming the same Peclet number and matrix diffusion mass transfer coefficient ($MTC = \frac{\phi}{b}\sqrt{D_m}$) in each test, and a mean residence time (τ) that was inversely proportional to flow rate. This procedure assumes that the *MTC* and Peclet number have no flow rate or time scale dependence.

For the multiple-tracer tests, the bromide and PFBA responses were simultaneously fitted, assuming that bromide had a matrix diffusion coefficient a factor of three greater than PFBA (this same assumption was used in the field tracer-test interpretations). However, because of the difficulties encountered in fitting the lithium responses in the crushed-tuff column experiments, and the fact that Na^+ and Ca^{2+} were analyzed in addition to Li^+ in the fractured-core experiments, it was decided to use the MULTRAN V 1.0 (STN: 10666-1.0-00 [159068]) model (described below) rather than RELAP V 2.0 (STN: 10551-2.0-00 [159065]) to interpret the lithium responses. The values of τ, *Pe*, and *MTC* that provided the best RELAP fits to the bromide and PFBA responses were used as inputs to MULTRAN (note that for tests conducted at different flow rates in the same core, τ was adjusted such that it was inversely proportional to flow rate and *Pe* was held constant for all tests). The parameters Q_1 and Q_2 were then adjusted to fit the Li^+, Na^+, and Ca^{2+} data while holding the CEC values equal to the measured CEC values.

MULTRAN V 1.0 (STN: 10666-1.0-00 [159068]) is a 2-D numerical model that employs an implicit-in-time, alternating-direction, finite-difference method to solve the equations describing multicomponent transport of sorbing and nonsorbing solutes in a single- or dual-porosity medium. Figure 6.3-68 illustrates the assumed model domain and shows an example spatial discretization. Advective transport, simulated by solving the advection-dispersion equation, is assumed to occur only in the *x*-direction in Region I. The first and last nodes in the *x*-direction in this region are modeled as well-mixed regions that simulate either boreholes in field experiments or flow manifolds in laboratory experiments. Reinjection of part or all of the solution entering the last node back into the first node can be specified to simulate recirculating conditions in tracer experiments. Only diffusive transport is assumed to occur in the *y*-direction in both regions I and II, with the model having the capability to simulate different diffusion coefficients in the different regions. Finally, within each region, additional diffusive transport can be simulated into "grains," which are assumed to be spherical. These grains can be assigned a lognormal distribution of diameters with specified mean and variance. The user can control the spatial discretization within each region and within the grains.

The user also can eliminate certain portions of the model domain shown in Figure 6.3-68 simply by specifying that they have zero porosity. For instance, if one wishes to simulate a single-porosity medium, it is only necessary to specify a zero porosity for region II and zero porosity for the grains in region I. This approach was taken to simulate the crushed-tuff column transport experiments described in Section 6.3.9.1 because the columns were packed with a relatively uniform material that had no apparent secondary porosity. Reducing the model effectively to a 1-D system (region I) greatly simplifies numerical computations.

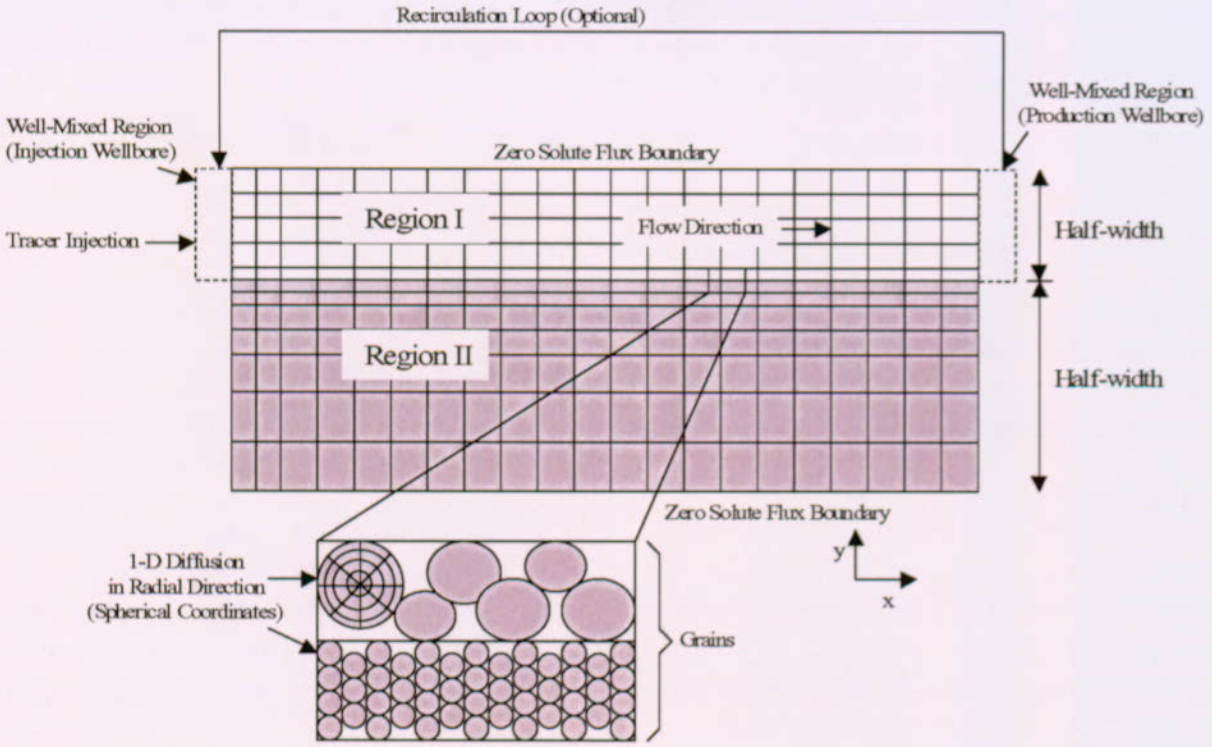

For illustration purposes only.

NOTE: Blocks are finite-difference cells that are solved at their midpoints. Region I is the high-permeability layer (advective transport in *x*-direction, diffusive in *y*-direction); region II is the low-permeability layer (diffusive transport in *y*-direction only).

Figure 6.3-68. Schematic Illustration of MULTRAN Model Domain

Each time-step of a MULTRAN V 1.0 (STN: 10666-1.0-00 [159068]) simulation is broken into four computational segments that are conducted sequentially, as follows.

(1) Solution of the advection-dispersion equation in the *x*-direction in region I

$$\frac{\partial c}{\partial t} = -v_x \frac{\partial c}{\partial x} + D \frac{\partial^2 c}{\partial x^2} \qquad \text{(Eq. 25)}$$

where

c = molar concentration, moles/L

v_x = velocity in x direction, cm/sec

D = dispersion coefficient, cm^2/sec ($D = \alpha v_x$, α = dispersivity, cm).

(2) Solution of the multicomponent diffusion equation(s) and the local electroneutrality equation in the y-direction in regions I and II (coupled)

a. *Multicomponent diffusion equation for all species except species n (Newman 1973 [148719], p. 228):*

$$\frac{\partial c_i}{\partial t} = D_i \nabla^2 c_i - \sum_j \frac{z_j}{z_i}(D_j - D_n)\nabla \cdot (t_i \nabla c_i) \qquad \text{(Eq. 26)}$$

where

c_i = molar concentration of species i, moles/L

D_i = diffusion coefficient of species i, cm^2/sec

∇ = del operator

∇^2 = Laplacian operator

$t_i = \dfrac{z_i^2 u_i c_i}{\sum_j z_j^2 u_j c_j}$ = transference number of species i

z_i = charge of species i

$u_i = \dfrac{D_i}{RT}$ = mobility of species i, where R = gas constant and T = temperature (K)

n = species being determined using electroneutrality equation,

b. *Electroneutrality equation for species n:*

$$z_n c_n = -\sum_{j \neq n} z_j c_j \qquad \text{(Eq. 27)}$$

(3) Solution of the multicomponent diffusion equation(s) and the local electroneutrality equation in the radial direction in the grains of both regions I and II (same as step 2, but using spherical coordinates).

(4) Chemical re-equilibration of the entire system with respect to cation exchange. This step is accomplished by solving Equations 21 through 24 at each node in the model domain to ensure that the equilibrium expressions and the surface cation balance are locally satisfied. The system is assumed to always be at chemical equilibrium (i.e., reaction kinetics assumed to be fast relative to transport rates).

6.3.9.2.3 Results and Interpretations

The experimental data and modeling fits for the iodide-only tests conducted in cores 1 and 2 (three in each core) are shown in Figures 6.3-69 and 6.3-70, respectively. Tables 6.3-28 and 6.3-29 list the model parameters associated with the fits shown in these figures. It is apparent that RELAP offered good simultaneous fits to the three data sets.

The experimental data and associated MULTRAN V 1.0 (STN: 10666-1.0-00 [159068]) fits for Tests 1 and 3 in the Upper Prow Pass Tuff core (Core 1) are shown in Figure 6.3-71. MULTRAN fits to the multiple-tracer tests in Cores 2, 3, and 4 (two tests in each core) are shown in Figures 6.3-72, 6.3-73, and, 6.3-74, respectively. Table 6.3-30 lists the model parameters associated with the fits to the tracer responses in Cores 1 and 2, and Table 6.3-31 lists the parameters associated with the fits to the responses in Cores 3 and 4. The Br^- and PFBA responses in the two tests in each core were first fitted simultaneously using RELAP V 2.0 (STN: 10551-2.0-00 [159065]) (i.e., a total of four responses were fitted simultaneously, two from each test). The RELAP fits were executed only up to the time of a flow interruption (which was introduced in several of the tests). For these fits, the Peclet numbers and tracer matrix-diffusion parameters were constrained to be the same for both tests, and the mean residence times were constrained to be inversely proportional to the flow rates in the tests. The fracture spacing was also manually varied to improve the simultaneous fits to the tracer responses; this was justified because the residence times in the low-flow-rate tests were long enough for tracers to potentially diffuse to the epoxy sealing the periphery of the fractured cores, which should serve as a diffusion boundary. The parameters resulting from the RELAP fits were then used in MULTRAN with only the ion-exchange parameters, Q_1 and Q_2, being varied to achieve a match to the Li^+, Na^+, and Ca^{2+} responses.

Figures 6.3-71 through 6.3-74 indicate that MULTRAN V 1.0 (STN: 10666-1.0-00 [159068]) was able to simulate very effectively the responses of all tracers in each multiple-tracer test in each core. The finite fracture spacing used in both the RELAP V 2.0 (STN: 10551-2.0-00 [159065]) and MULTRAN simulations was found to be essential for obtaining a reasonable simultaneous fit to the tracer responses at the two significantly different flow rates in each core, suggesting that diffusion boundaries played an important role at the lower flow rates.

The matrix-diffusion, MTCs for Br^- in the first two cores were surprisingly much smaller than the MTCs obtained for iodide in these two cores. In theory, these two halides should have very similar diffusion properties. However, the apparent dispersivities and deduced fracture apertures in the two cores were both larger in the multiple-tracer tests than in the iodide-only tests. Larger apertures directly decrease MTCs, and larger dispersivities indirectly decrease MTCs because greater dispersion results in longer-tailed and lower-peaked tracer responses, both of which matrix diffusion also produces. The greater apparent dispersion and lower apparent matrix diffusion in the multiple-tracer tests relative to the iodide-only tests cannot be explained. However, it is speculated that microbial growth or small geometry changes in the flow systems could have played a role because the iodide-only tests were conducted well before the multiple-tracer tests in both cores. An inherent fundamental difference in the transport behavior of Br^- and iodide can be ruled out because these two tracers behaved almost identically in the multiple-tracer tests in which both were injected simultaneously (8 of the 11 multiple tracer tests – see Tables 6.3-23 and 6.3-25 to 6.3-27). Another more subtle explanation could be that the iodide

tests were conducted only at what would be considered the higher flow rates in the multiple-tracer tests, raising the possibility that tests conducted at higher flow rates could be biased toward greater apparent matrix diffusion because of a greater influence of diffusion into stagnant free water in the fractures or other time-scale effects (see next section).

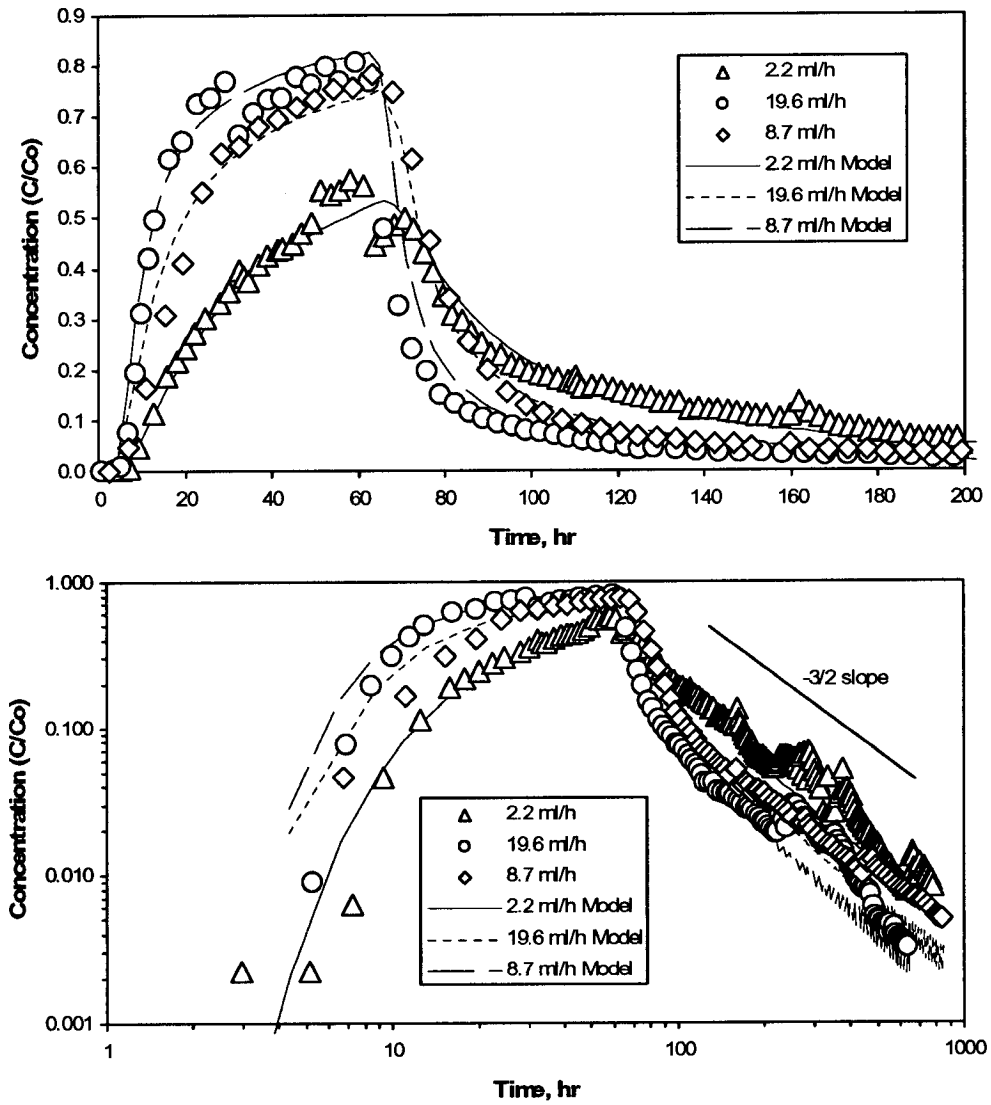

DTN: LA0212PR831231.001 [162607] (data). Output DTN: LA0303PR831361.004 (models).

NOTE: All three data sets were used to simultaneously fit τ, *Pe*, and *MTC*. Concentrations are normalized to injection concentration. Lower plot is same as upper plot except with log scales for the x- and y-axes. The –3/2 slope on the log-log plot is the expected slope for a system experiencing single-rate matrix diffusion.

Figure 6.3-69. Experimental and Modeling Results from the Three Iodide-Only Transport Tests in Core 1

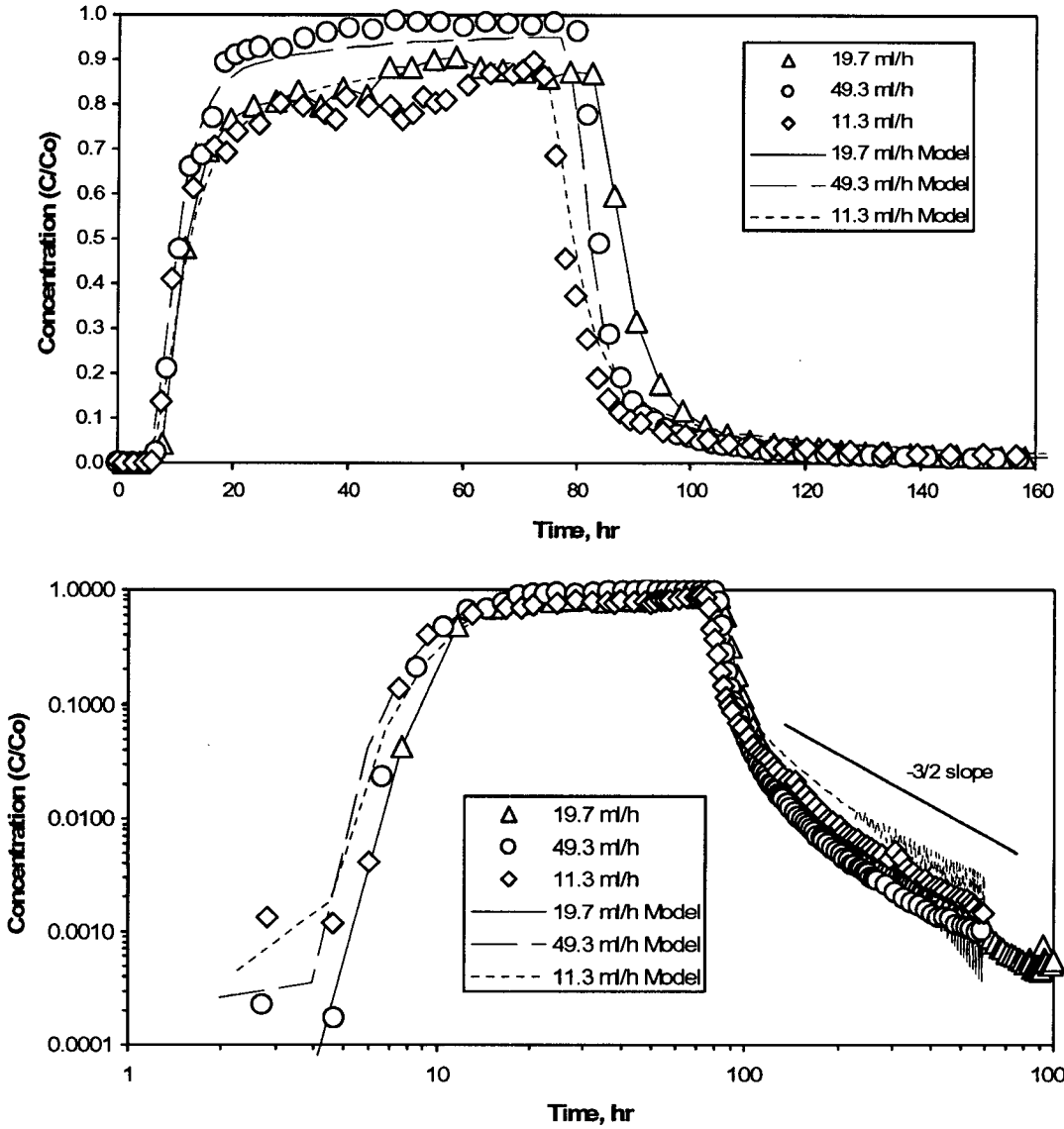

DTN: LA0212PR831231.001 [162607] (data). Output DTN: LA0303PR831361.004 (models).

NOTE: All three data sets were used to simultaneously fit τ, *Pe*, and *MTC*. Concentrations are normalized to injection concentration. Lower plot is same as upper plot except with log scales for the x- and y-axes. The –3/2 slope on the log-log plot is the expected slope for a system experiencing single-rate matrix diffusion.

Figure 6.3-70. Experimental and Modeling Results from the Three Iodide-Only Transport Tests in Core 2

Table 6.3-28. Modeling Results for the Three Iodide Tracer Tests in Upper Prow Pass Tuff Core (Core 1)

Modeling Parameters [a]	Test 1	Test 2	Test 3
Solute mean residence time, τ (hr)	3.0	0.34	0.76
Peclet number, *Pe*		18	
Mass transfer coefficient, $MTC = \frac{\phi}{b}\sqrt{D_m}$ ($hr^{-0.5}$)		1.56 (I^-)	
Fracture aperture, 2*b* (cm) [b]		0.043	
Dispersivity in fracture, $\alpha = \frac{L}{Pe}$ (cm)		0.89	
Matrix diffusion coefficient, D_m (x 10^{-10} m^2/s) [c]		4.3 (I^-)	

Output DTNs: LA0303PR831361.004; LA0303PR831231.005.

NOTES: (a) The three I^- data sets were fit simultaneously assuming *Pe* was the same for the three tests and τ was inversely proportional to the volumetric flow rate.

(b) Based on the relationship $b = \frac{Q\tau}{Lw}$, where τ is the solute mean residence time.

(c) Determined from the *MTC* using the measured ϕ and the calculated *b*.

Table 6.3-29. Modeling Results for the Three Iodide Tracer Tests in Central Prow Pass Tuff Core (Core 2)

Modeling Parameters [a]	Test 1	Test 2	Test 3
Solute mean residence time, τ (hr)	0.48	0.19	0.84
Peclet number, *Pe*		24	
Mass transfer coefficient, $MTC = \frac{\phi}{b}\sqrt{D_m}$ ($hr^{-0.5}$)		0.518 (I^-)	
Fracture aperture, 2*b* (cm) [b]		0.058	
Dispersivity in fracture, $\alpha = \frac{L}{Pe}$ (cm)		0.72	
Matrix diffusion coefficient, D_m (x 10^{-10} m^2/s) [c]		3.2 (I^-)	

Output DTNs: LA0303PR831361.004; LA0303PR831231.005.

NOTE: (a) The three I^- data sets were fit simultaneously assuming *Pe* was the same for the three tests and τ was inversely proportional to the volumetric flow rate.

(b) Based on the relationship $b = \frac{Q\tau}{Lw}$, where τ is the solute mean residence time.

(c) Determined from the *MTC* using the measured ϕ and the calculated *b*.

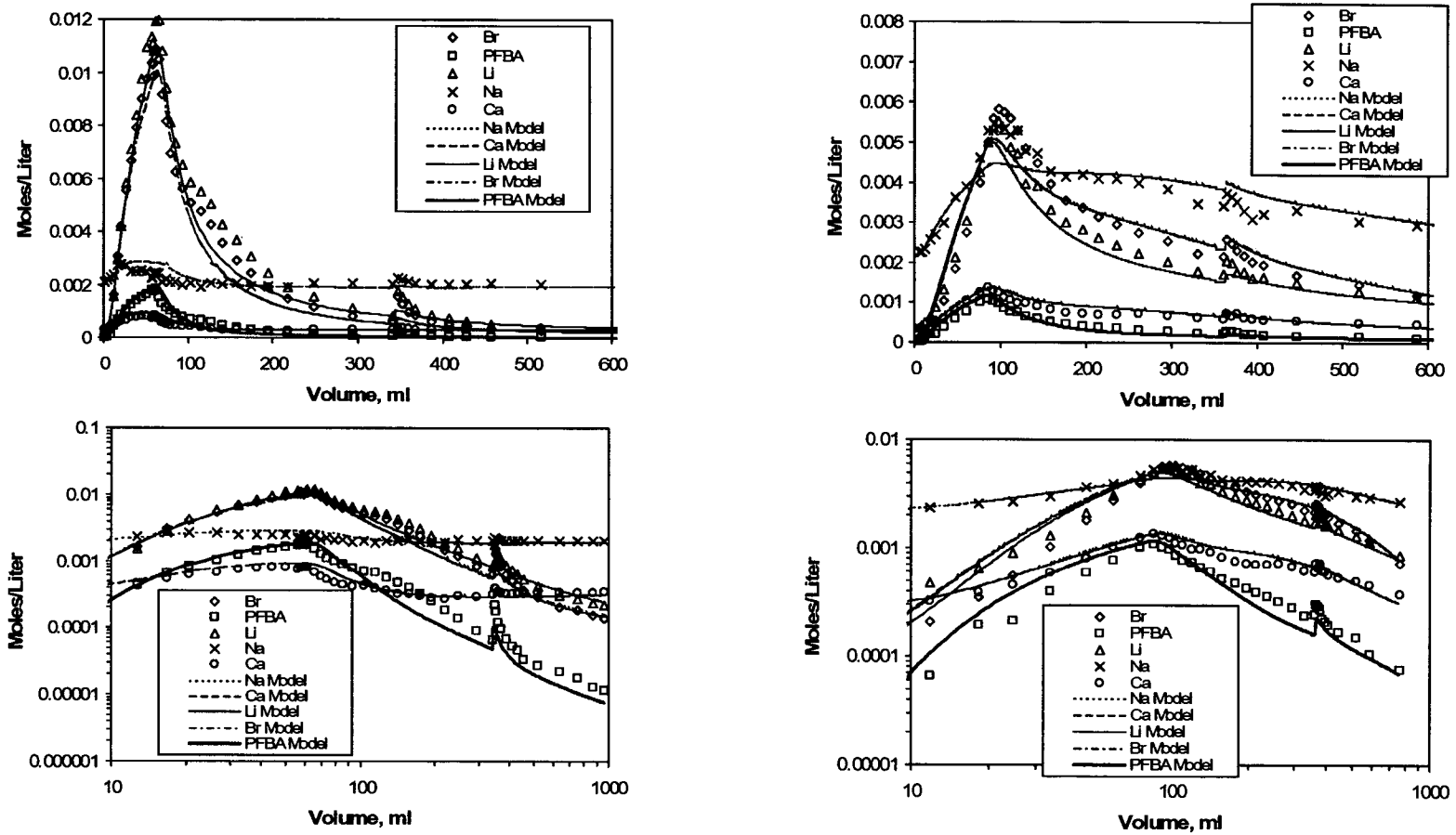

DTNs: LA0212PR831231.003 [162609] (Li, Br, PFBA data); LA0212PR831231.005 [166215] (Na, Ca data); Output DTN: LA0303PR831361.004 (models).

NOTE: The jumps in the concentrations and in the model curves correspond to flow interruptions in the tests. The flow rate in Test 1 (left) was 3.9 ml/h, and the flow rate in Test 3 (right) was 0.51 ml/h. The Br^- and PFBA data were fit simultaneously by constraining the D_m ratio for Br:PFBA to 3:1.

Figure 6.3-71. Experimental Data and MULTRAN Modeling Results for Multiple Tracer Tests 1 and 3 in the Upper Prow Pass Tuff Core (Core 1)

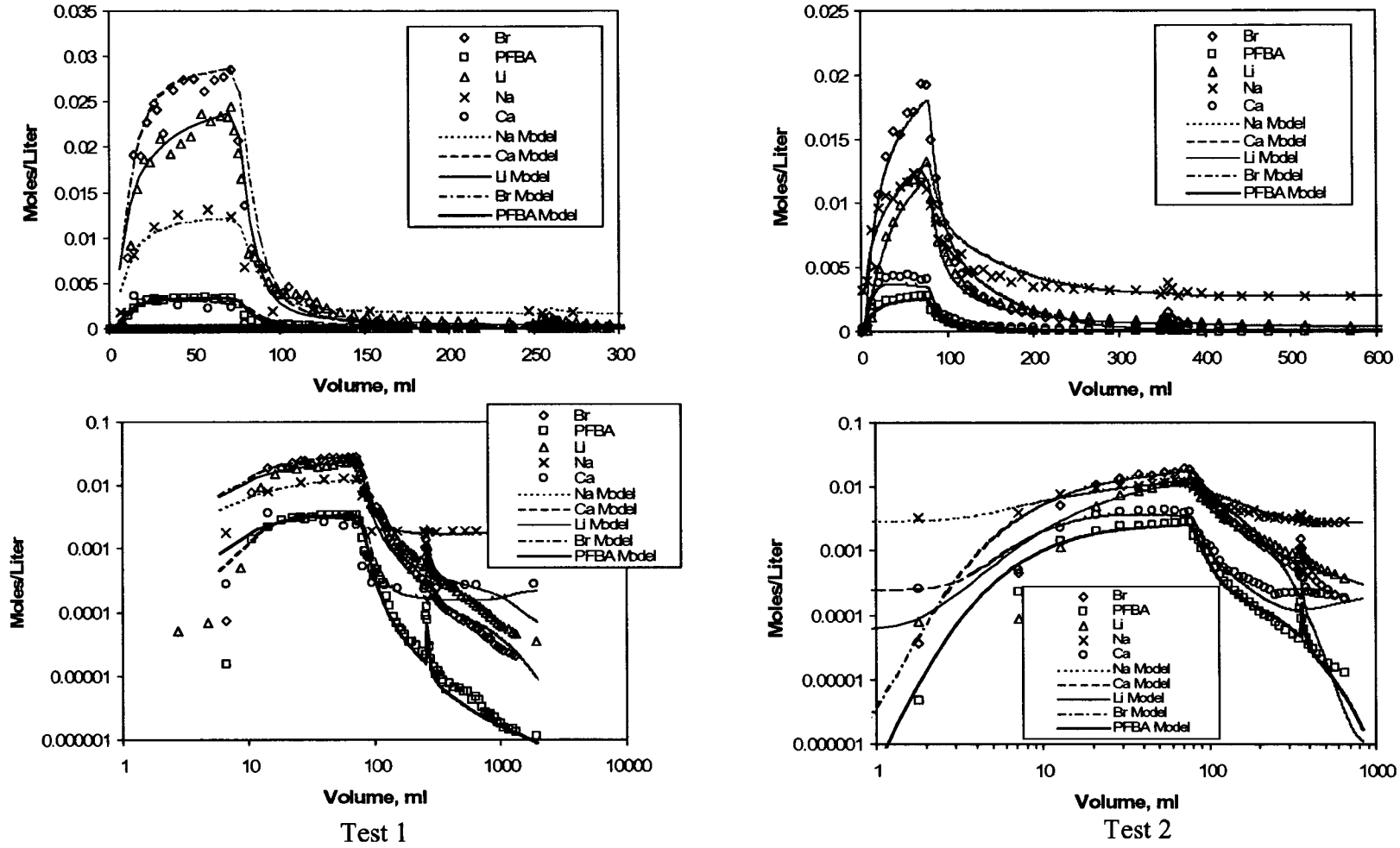

DTNs: LA0212PR831231.002 [162608] (Na, Ca data); LA0212PR831231.005 [166215] (Li, Br, PFBA data); Output DTN: LA0303PR831361.004 (models).

NOTE: The jumps in the concentrations and in the model curves correspond to flow interruptions in the tests. The flow rate in Test 1 (left) was 5.9 ml/h, and the flow rate in Test 2 (right) was 0.44 ml/h. The Br^- and PFBA data were fit simultaneously by constraining the D_m ratio for Br:PFBA to 3:1.

Figure 6.3-72. Experimental Data and MULTRAN Modeling Results for Multiple Tracer Tests 1 and 2 in the Central Prow Pass Tuff Core (Core 2)

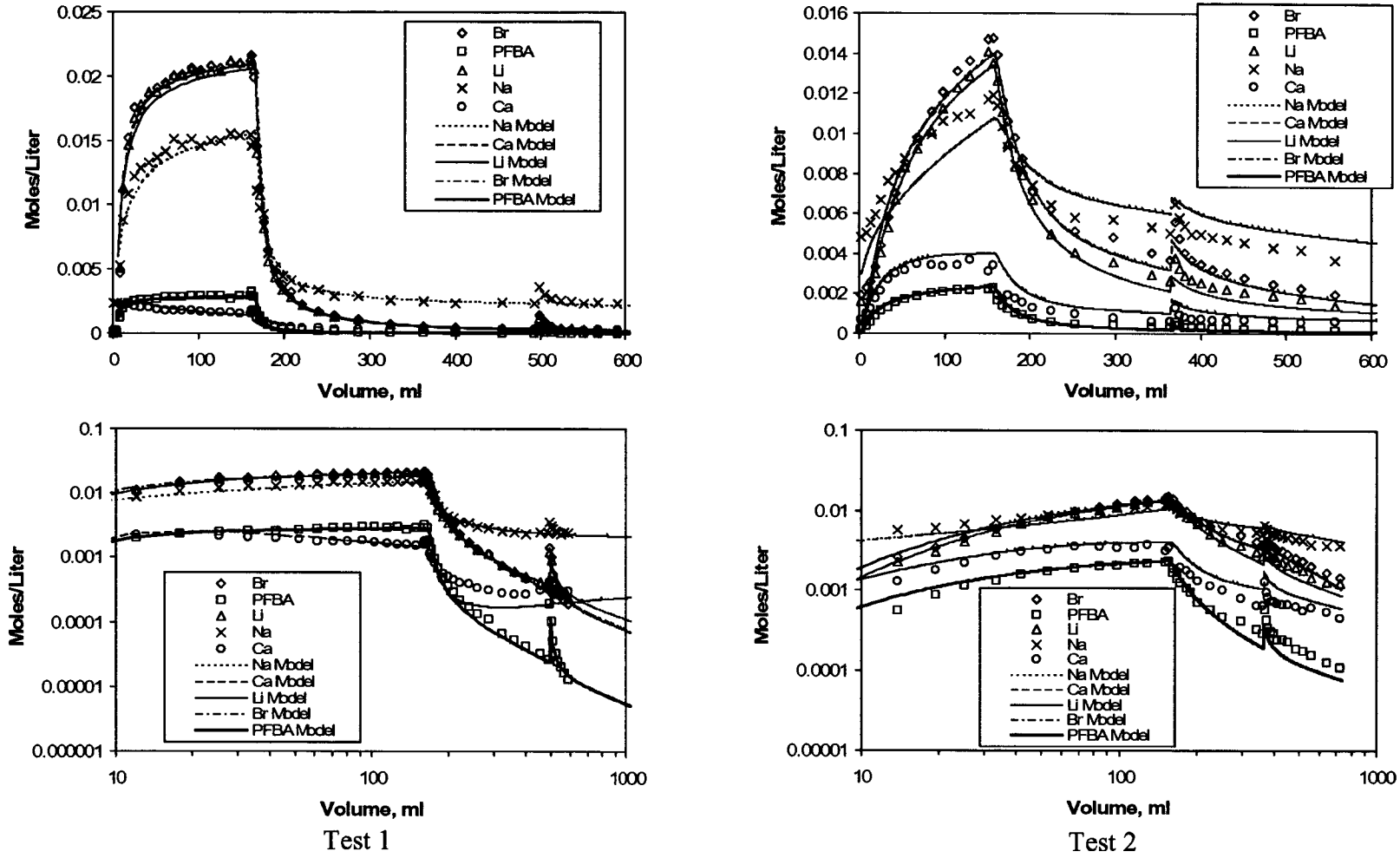

DTNs: LA0212PR831231.002 [162608] (Na, Ca data); LA0212PR831231.003 [162609] (Li, Br, PFBA data); Output DTN: LA0303PR831361.004 (models).

NOTE: The jumps in the concentrations and in the model curves correspond to flow interruptions in the tests. The flow rate in Test 1 (left) was 11.4 ml/h, and the flow rate in Test 2 (right) was 0.46 ml/h. The Br^- and PFBA data were fit simultaneously by constraining the D_m ratio for Br:PFBA to 3:1.

Figure 6.3-73. Experimental Data and MULTRAN Modeling Results for Multiple Tracer Tests 1 and 2 in the Lower Prow Pass Tuff Core (Core 3)

Table 6.3-30. Best-Fit Model Parameters for the Multiple-Tracer Tests Conducted in Cores 1 and 2

Modeling Parameters	Core 1, Test 1	Core 1, Test 3	Core 2, Test 1	Core 2, Test 1
Porosity of matrix	0.27	0.27	0.14	0.14
Solute mean residence time, τ (hr) [(a)]	5.4	40.2	1.95	26.1
Peclet number, Pe [(a)]	4.0	4.0	3.5	3.5
Dispersivity in fracture, $\alpha = \frac{L}{Pe}$ (cm)	4.0	4.0	5.0	5.0
Li^+ Retardation factor, R [(a)]	2.25	1.1	4.2	5.9
Li^+ Partition coefficient, K_d (L/kg)	0.17	0.014	0.19	0.30
Mass transfer coefficient[(a)], $MTC = \frac{\phi}{b}\sqrt{D_m}$ ($hr^{-0.5}$)	0.80 (Br^-) 0.46 (PFBA)	0.80 (Br^-) 0.46 (PFBA)	0.21 (Br^-) 0.12 (PFBA)	0.21 (Br^-) 0.12 (PFBA)
Fracture aperture, $2b$ (cm) [(b)]	0.134	0.134	0.07	0.07
Distance to diffusion boundary (fracture half spacing), (cm)	1.9	1.9	0.9	0.9
Matrix diffusion coefficient[(c)], D_m (x 10^{-10} m^2/s)	11.0 (Br^-) 3.7 (PFBA)	11.0 (Br^-) 3.7 (PFBA)	0.8 (Br^-) 0.27 (PFBA)	0.8 (Br^-) 0.27 (PFBA)
CEC (meq/kg), Measured	19.9	19.9	43.2	43.2
Q_1 [(d)]	0.05	0.025	10.2	6.0
Q_2 [(d)]	0.079	0.04	3.0	0.45

DTN: MO00012POROCHOL.000 [153376] (for porosity); Output DTNs: LA0303PR831361.004 (model results); LA0303PR831231.005.

NOTE: Cores 1 and 2 are shown in Figures 6.3-69 through 6.3-72.

(a) Parameters obtained using RELAP to fit simultaneously the Br^- and PFBA data from the two tests for a given core with the constraint that the D_m ratio for Br^-:PFBA was 3:1. The matrix diffusion coefficient for Li^+ was assumed to be two-thirds the value for Br^-.

(b) Based on the relationship $b = \frac{Q\tau}{Lw}$, where τ is the solute mean residence time.

(c) Determined from the *MTC* using the measured ϕ and the calculated b.

(d) Equilibrium ion-exchange coefficients, obtained using MULTRAN to manually "fit" the Li^+, Na^+, and Ca^{2+} data for each test.

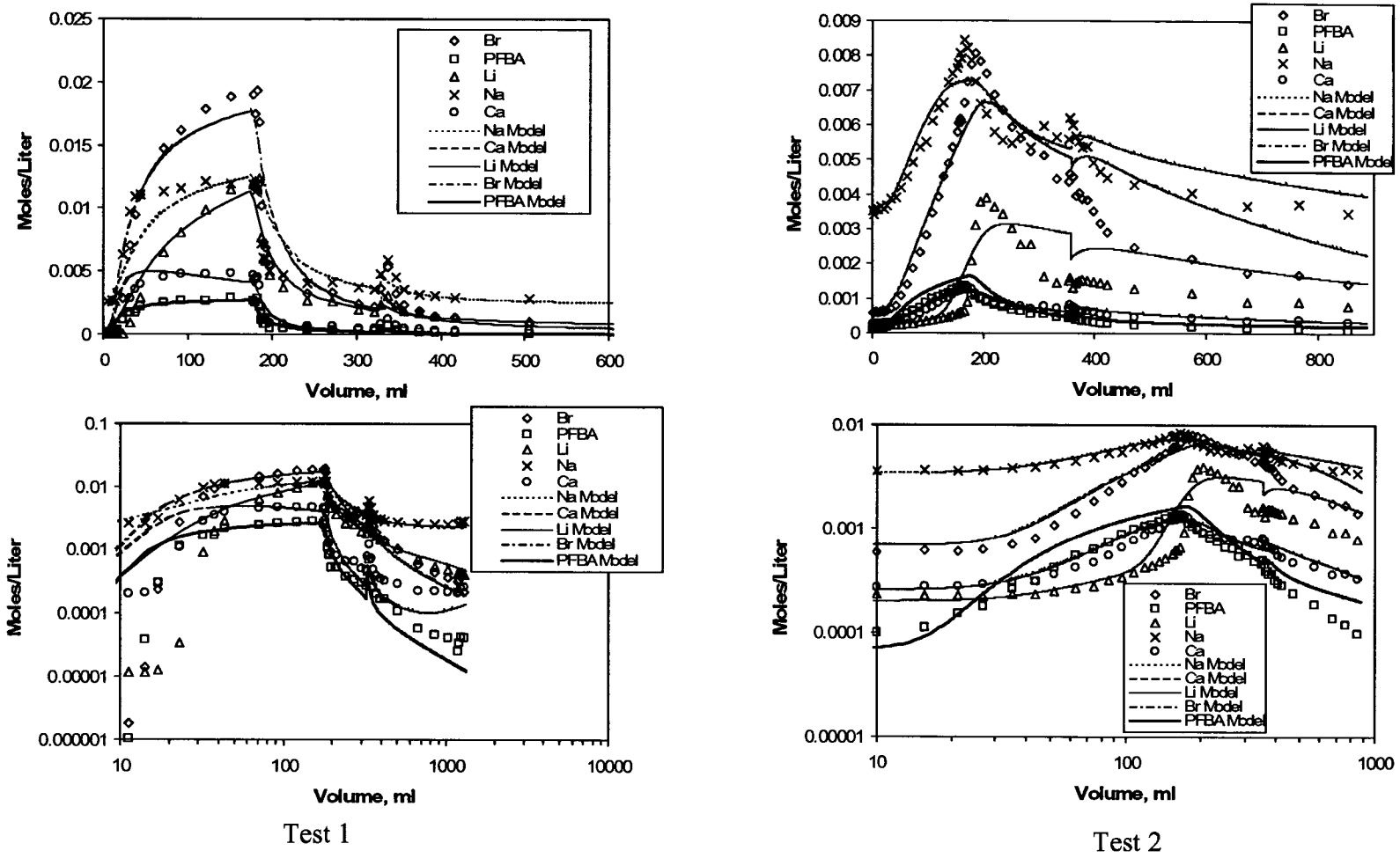

DTNs: LA0212PR831231.002 [162608] (Na, Ca data – Test 1); LA0212PR831231.005 [166215] (Na, Ca data – Test 2); LA0212PR831231.003 [162609] (Li, Br, PFBA data). Output DTN: LA0303PR831361.004 (models).

NOTE: The jumps in the concentrations and in the model curves correspond to flow interruptions in the tests. The flow rate in Test 1 (left) was 4.85 ml/h, and the flow rate in Test 2 (right) was 0.47 ml/h. The Br^- and PFBA data were fit simultaneously by constraining the D_m ratio for Br:PFBA to 3:1.

Figure 6.3-74. Experimental Data and MULTRAN Modeling Results for Multiple Tracer Tests 1 and 2 in the Lower Bullfrog Tuff Core (Core 4).

The ion exchange parameters, Q_1 and Q_2, exhibited a curious decreasing trend from the first to the second multiple-tracer test in each core, suggesting that some Li^+ may have become irreversibly sorbed in the first test and reduced the sorption capacity for Li^+ in subsequent tests. This speculation is consistent with the incomplete recovery of Li^+ in each test. In any case, the Li^+ sorption isotherms calculated from the ion-exchange parameters deduced from MULTRAN V 1.0 (STN: 10666-1.0-00 [159068]) fits were generally higher than or comparable to the sorption isotherms derived from batch Li^+ sorption experiments (Figure 6.3-75).

It is important to point out that the best-fitting values of the ion-exchange parameters Q_1 and Q_2 in the MULTRAN V 1.0 (STN: 10666-1.0-00 [159068]) simulations were somewhat sensitive to the background concentrations specified for all three cations in the system. These background concentrations were chosen to match the concentrations measured in the first one or two samples collected in each experiment (prior to the arrival of the tracers), which generally differed slightly from one experiment to the next in a given core. There were also significant differences in the relative amounts of cations and the overall ionic strengths of the tracer solutions used in different experiments, which could have affected the experimental and modeling results. One notable difference in the cation mix occurred as a result of using either NaOH or LiOH to neutralize the PFBA in the tracer solutions (if a stoichiometric amount of OH^- was not added, the pH of the tracer solutions was <2). These differences in cation mix and ionic strength were accounted for in the MULTRAN inputs, but any "memory" effects resulting from the use of significantly different tracer solutions in consecutive experiments, which could affect the pre-experiment mix of cations sorbed to mineral surfaces, were not accounted for. It is possible that if these factors had been accounted for, the Q_1 and Q_2 values from consecutive experiments may have been in better agreement.

It was also found that reasonable matches to the cation responses in the cores could be obtained using almost any value of the CEC greater than some threshold, provided that Q_1 and Q_2 were both adjustable. This nonuniqueness problem was avoided by setting the CEC values in all MULTRAN V 1.0 (STN: 10666-1.0-00 [159068]) simulations equal to the laboratory measurements for each tuff. However, if the effective CEC value had been reduced for each subsequent experiment in each core (because of some irreversible sorption of Li^+), then the Q_1 and Q_2 values would have been higher in the later experiments, which would have brought them into better agreement with the values in earlier experiments.

Although not all of the experimental and modeling results can be completely explained, Figure 6.3-76 shows that the use of the multicomponent ion-exchange MULTRAN V 1.0 (STN: 10666-1.0-00 [159068]) model offers a significant improvement over the single-component RELAP V 2.0 (STN: 10551-1.0-00 [159065]) model in simulating the responses of ion-exchanging tracers in dual-porosity systems. This improvement is especially pronounced when there is a large amount of sorption in the matrix, as there is for the Lower Bullfrog Tuff core (Figure 6.3-76).

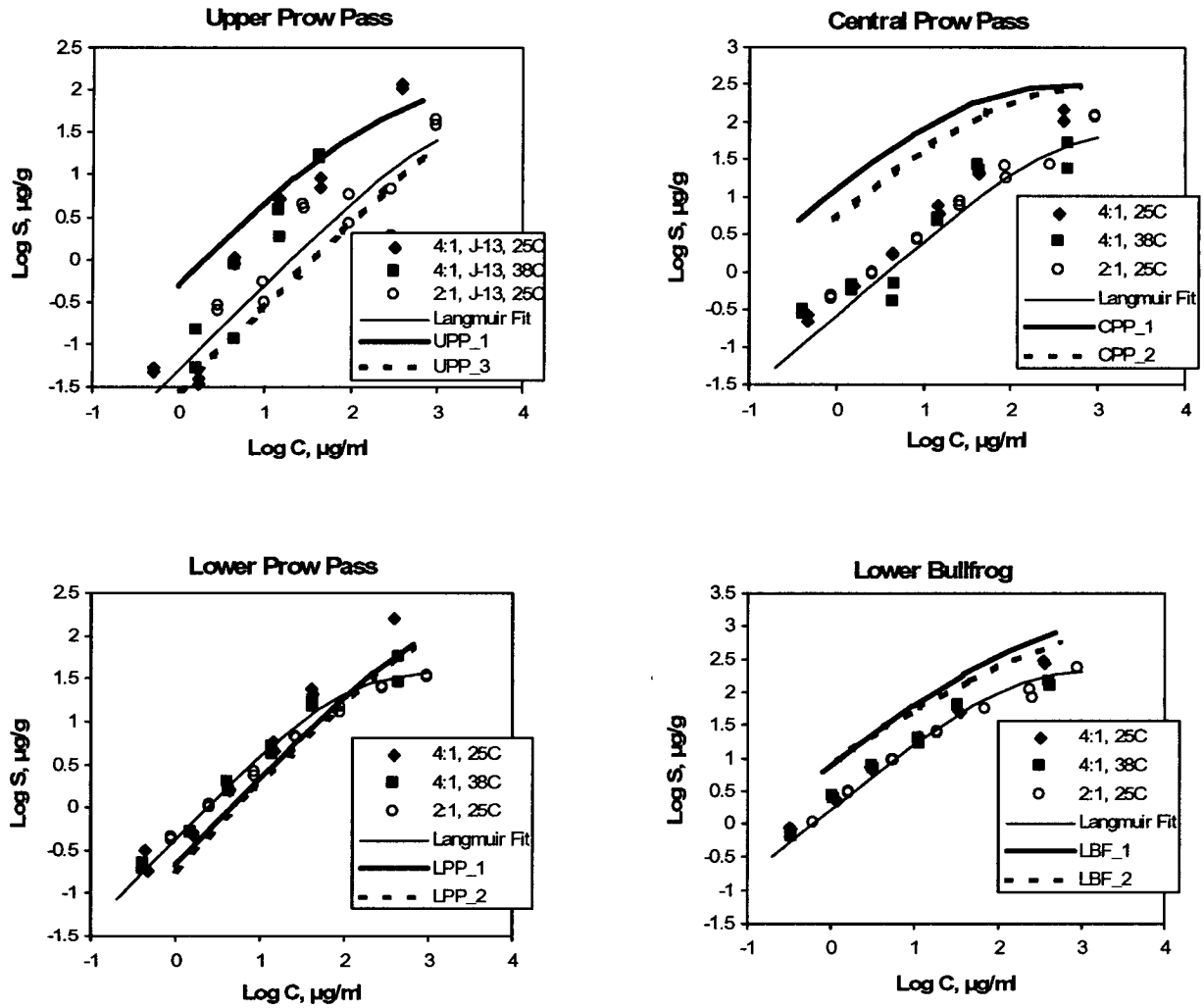

DTN: MO0012SORBCHOL.000 [153375] (data). Output DTN: LA0303PR831341.003 (models) .

Figure 6.3-75. Comparison of Li^+ Isotherms Calculated from Best-Fitting MULTRAN Parameters (Designated by XXX_Y, where Y is the Fractured Core Test Number) and Obtained in Batch Sorption Experiments for the Four Different C-wells Tuffs Used in the Fracture Experiments

Table 6.3-31. Best-Fit Model Parameters for the Multiple-Tracer Tests Conducted in Cores 3 and 4

Modeling Parameters	Core 3, Test 1	Core 3, Test 2	Core 4, Test 1	Core 4, Test 2
Porosity of matrix	0.29	0.29	0.30	0.30
Solute mean residence time, τ (hr) [(a)]	0.55	13.6	2.0	21.3
Peclet number, Pe [(a)]	4.5	4.5	130	130
Dispersivity in fracture, $\alpha = \frac{L}{Pe}$ (cm)	2.6	2.6	0.09	0.09
Li^+ Retardation factor, R [(a)]	1.3	1.6	9.2	8.2
Li^+ Partition coefficient, K_d (L/kg)	0.046	0.092	1.33	1.16
Mass transfer coefficient[(a)], $MTC = \frac{\phi}{b}\sqrt{D_m}$ ($hr^{-0.5}$)	1.32 (Br^-) 0.76 (PFBA)	1.32 (Br^-) 0.76 (PFBA)	1.45 (Br^-) 0.84 (PFBA)	1.45 (Br^-) 0.84 (PFBA)
Fracture aperture, $2b$ (cm) [(b)]	0.057	0.057	0.049	0.049
Distance to diffusion boundary (fracture half spacing), (cm)	4.4	4.4	4.6	4.6
Matrix diffusion coefficient[(c)], D_m (x 10^{-10} m^2/s)	4.6 (Br^-) 1.5 (PFBA)	4.6 (Br^-) 1.5 (PFBA)	3.8 (Br^-) 1.3 (PFBA)	3.8 (Br^-) 1.3 (PFBA)
CEC (meq/kg), Measured	31.9	31.9	179.7	179.7
Q_1 [(d)]	0.1	0.085	6.0	0.2[(d)]
Q_2 [(d)]	0.08	0.035	0.3	0.12[(d)]

DTN: MO00012POROCHOL.000 [153376] (for porosity). Output DTNs: LA0303PR831361.004 (model results), LA0303PR831231.005.

NOTE: Cores 3 and 4 are shown in Figures 6.3-73 and 6.3-74.

(a) Parameters obtained using RELAP V 2.0 (STN: 10551-2.0-00 [159065]) to simultaneously fit the Br^- and PFBA data from the two tests for a given core with the constraint that the D_m ratio for Br^-:PFBA was 3:1. The matrix diffusion coefficient for Li^+ was assumed to be 2/3 the value for Br^-.

(b) Based on the relationship $b = \frac{Q\tau}{Lw}$, where τ is the solute mean residence time.

(c) Determined from the *MTC* using the measured ϕ and the calculated b.

(d) Equilibrium ion exchange coefficients, obtained using MULTRAN V 1.0 (STN: 10666-1.0-00 [159068]) to manually "fit" the Li^+, Na^+, and Ca^{2+} data for each test.

(e) The MULTRAN V 1.0 (STN: 10666-1.0-00 [159068]) "fit" shown for Core 4, Test 2 in Figure 6.3-74 was actually obtained assuming sorption in both the fracture and the matrix. The fracture was assumed to have a porosity of 0.9, a CEC of 200 meq/kg, K_1 = 5.0, and K_2 = 50.0. The matrix had a CEC of 179.7 meq/kg, and K_1 = K_2 = 0.0223. The resulting fit was somewhat better than the fit assuming sorption only in the matrix.

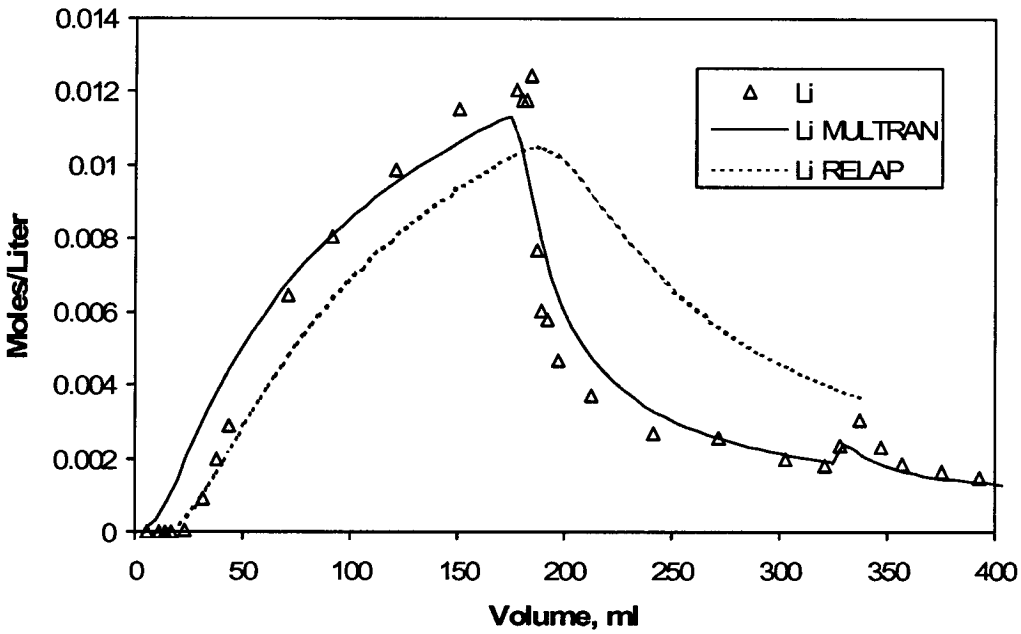

DTN: LA0212PR831231.003 [162609] (Li data). Output DTN: LA0303PR831361.003 (models).

Figure 6.3-76. Comparison of the Fits of the MULTRAN Multicomponent Ion-Exchange Model and the Single-Component RELAP Model to the Lithium Transport Data in the First Multiple-Tracer Test in Core 4

6.3.10 Scale-Dependence of Transport Parameters in Fractured Tuffs

6.3.10.1 Scale-Dependence of Longitudinal Dispersivity

A plot of the longitudinal dispersivity values as a function of test scale for several NTS fractured-rock, tracer-test programs is shown in Figure 6.3-77. The plot indicates that the longitudinal dispersivity increases with test scale that ranges from less than one meter to over 100 meters. Figure 6.3-78 shows the range of longitudinal dispersivities as a function of scale derived from the C-wells multiple-tracer tests (darkened area) superimposed on a plot of dispersivity versus scale prepared by Neuman (1990 [101464], Figure 1). Note that the lower end of the range of length scales associated with the darkened area corresponds to the interwell separation in the tracer tests, and the upper end corresponds to the test interval thickness (used as an upper bound for the transport distance).

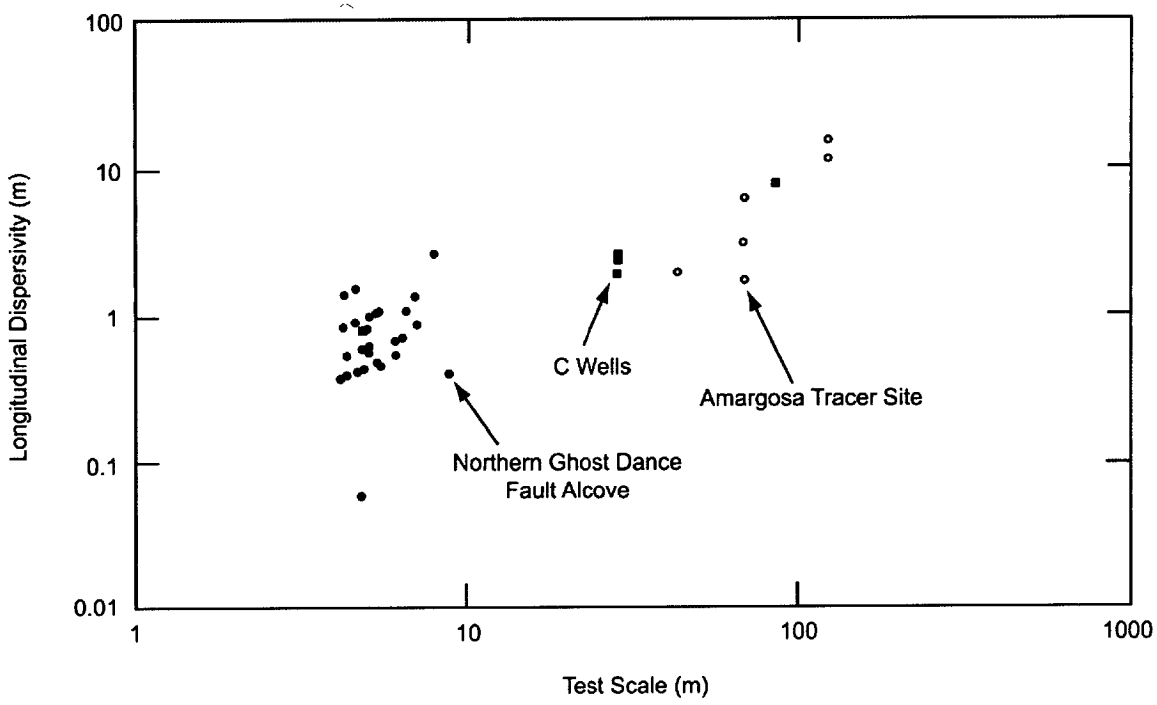

Source: LeCain et al. (2000 [144612], Figure 19).

Figure 6.3-77. Longitudinal Dispersivity as a Function of Test Scale in Several Tracer Tests Conducted in the Vicinity of Yucca Mountain

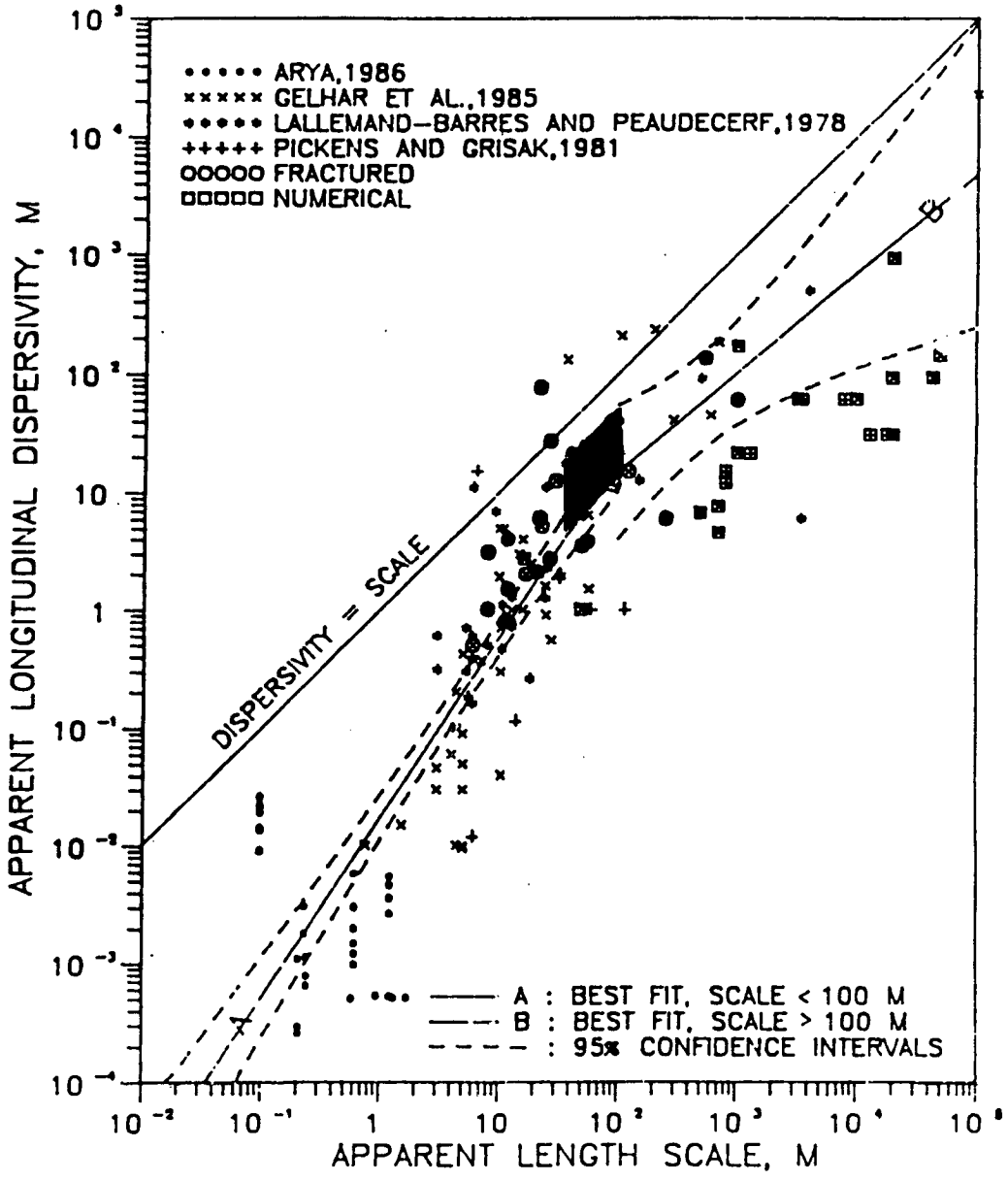

Source: Plot taken from Neuman (1990 [101464], Figure 1). Output DTN: LA0303PR831231.003 (dispersivities from C-wells).

NOTE: The darkened box shows the range of values derived from the multiple-tracer field tests at the C-wells in which lithium ion was used as a sorbing tracer. The right edge of the box corresponds to the interwell separation distance, and the left edge of the box corresponds to the test interval thickness (taken to be the upper limit of transport distance).

Figure 6.3-78. Plot of Longitudinal Dispersivity Versus Length Scale Showing the Range of C-wells Values Derived from Interpretations of the Prow Pass and Bullfrog Multiple Tracer Tests in which Lithium Ion was Used as a Sorbing Tracer

6.3.10.2 Scale-Dependence of Matrix Diffusion

There is some question about whether matrix diffusion parameters measured in laboratory-scale experiments can be used reliably in field-scale transport predictions. To address this issue, it is first of interest to compare the matrix diffusion coefficients measured in the diffusion cell tests of Section 6.3.8 with the diffusion coefficients calculated from the fractured-core tests of Section 6.3.9.2. Table 6.3-32 shows that the Br^- matrix diffusion coefficients deduced from the fractured-core experiments (from simultaneous RELAP V 2.0 (STN: 10551-2.0-00 [159065]) fits to the Br^- and PFBA responses at two different flow rates in each fracture) were consistently greater than the Br^- diffusion coefficients obtained from the diffusion cell experiments. This result could be explained by the fact that matrix diffusion in the fractured cores was really a combination of diffusion into stagnant free water in the fractures (e.g., into voids along the rough walls of the fracture surfaces or into stagnant regions between flowing channels) and true diffusion into the matrix, whereas diffusion in the diffusion cell experiments, by design, occurred only in the matrix. The RELAP computer code interprets both free-water and matrix diffusion as matrix diffusion, so any free-water diffusion will tend to increase estimates of matrix diffusion coefficients (Callahan 2001 [156649], Chapter 5). The time scales of the diffusion cell measurements also tended to be longer than in the fractured cores, which would have resulted in greater tracer penetration of the matrices and, hence, a more representative measurement of true matrix diffusion.

It is also of interest to compare matrix-diffusion MTCs derived from the fractured-core experiments (Section 6.3.9.2) with MTCs derived from the C-wells field tracer tests (Section 6.3.4.7). Such a comparison is provided in Figure 6.3-79, which shows the laboratory and field MTCs plotted as a function of time scale in the tests. The MTCs derived from the laboratory experiments are plotted as lines that span the range of tracer residence times in the cores. It is apparent that the residence times in the iodide-only core experiments were shorter than in the multiple-tracer experiments, and there is a corresponding increase in the deduced MTC values in the iodide experiments. The MTCs from the field experiments are also plotted as lines that span the range of tracer residence times obtained assuming either linear or radial flow fields. Separate lines are plotted for the two pathways that resulted in the two tracer peaks in the Bullfrog Tuff field test.

It is clear that the MTCs collectively exhibit a decreasing trend with tracer residence times in Figure 6.3-79. This trend is consistent with the notion that as time scales increase, more of the apparent diffusion will be true matrix diffusion and less will be diffusion into stagnant free water. However, it is also likely that effective fracture apertures over the 30-meter scales of the field tests were much larger than in the ~0.2-meter-scale laboratory tests. Intuitively, one would expect that, as distance scales increase, there will be a higher probability of encountering larger-aperture fractures in which flow can occur. Larger apertures would have contributed to the decreasing trend of Figure 6.3-79 because fracture apertures appear in the denominator of the MTC. Alternatively, matrix diffusion coefficients, which appear as a square-root term in the numerator of the MTC, would have to be nearly two orders of magnitude smaller in the field than in the lab to explain the trend of Figure 6.3-79 if fracture apertures were held constant, which seems implausible. Similarly, matrix porosities, which appear in the numerator of the MTC, would have to be smaller by about a factor of 10 in the field to explain the observed trend if

fracture apertures were held constant and matrix diffusion coefficients were assumed to be the same as in the lab experiments – also seemingly implausible.

One would expect an asymptotic lower limit to be reached eventually for the *MTC* in saturated fractured systems, given a long enough travel time or distance. However, for the C-wells field system, the transport data suggest that this asymptotic value, if it exists, was not reached for characteristic travel times of up to ~1200 hrs or travel distances of ~30 m (Figure 6.3-79).

All of the test results discussed here are consistent with diffusive mass transfer having a strong influence on the migration of solutes in fractured volcanic tuffs. However, at short time and distance scales, there may be a significant influence of diffusion into stagnant free water within fractures in addition to "true" matrix diffusion. Thus, matrix diffusion parameters obtained from laboratory tracer experiments should be used cautiously when predicting contaminant migration at larger scales in fractured media.

Table 6.3-32. Comparison of Matrix Diffusion Coefficients Calculated from Fractured-Core Tracer Tests and from Diffusion-Cell Experiments

Core	Fractured Core D_m (Br^-) (m^2/s) [(a)]	Diffusion Cell D_m^* (Br^-) (m^2/s)
Upper Prow Pass (1)	11.0×10^{-10}	6.2×10^{-10}
Central Prow Pass (2)	0.8×10^{-10}	0.38×10^{-10}
Lower Prow Pass (3)	4.6×10^{-10}	2.9×10^{-10} [(b)]
Lower Bullfrog (4)	3.8×10^{-10}	1.0×10^{-10}

Output DTNs: LA0303PR831362.001 (diffusion cells); LA0303PR831361.004 (fractured cores).

NOTE: (a) Determined from MTC using the measured matrix porosity and b determined from $b = Q\tau$ (see Tables 6.3-30 and 6.3-31).

(b) Average of two measurements.

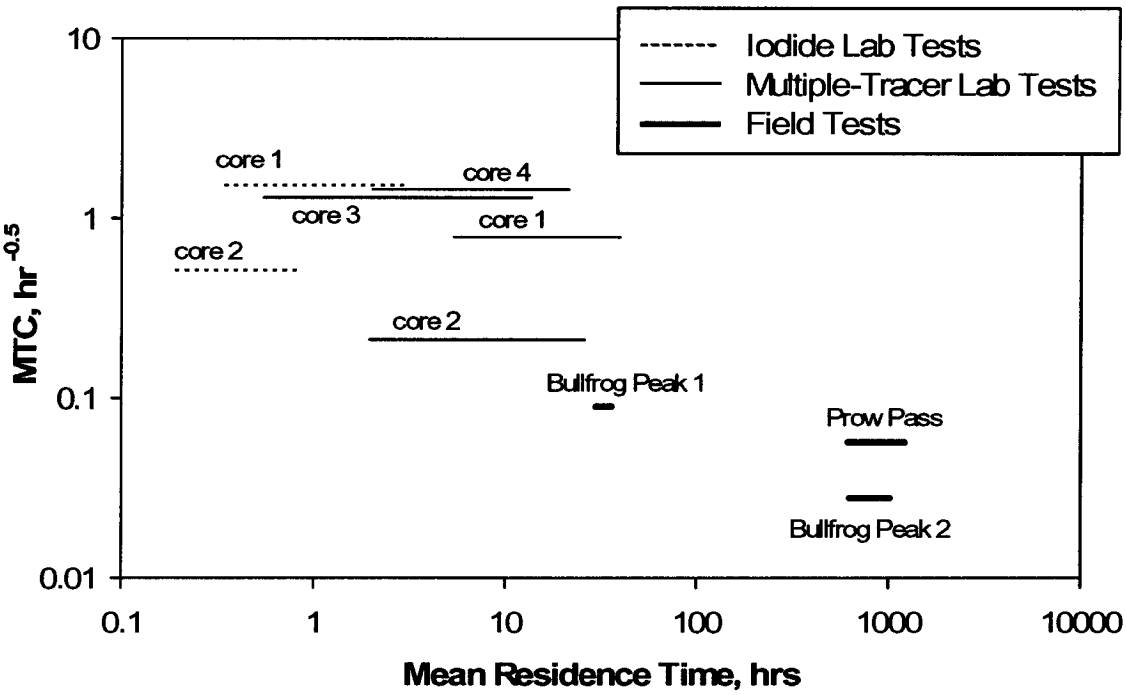

Output DTNs: LA0303PR831231.003 (field data); LA0303PR831361.004 (lab data); LA0303PR831231.005.

NOTE: The lines represent the field tests; endpoints of the lines reflect the uncertainty in the mean residence time depending on whether radial or linear flow is assumed.

The matrix diffusion mass transfer coefficient, MTC, is defined as $\frac{\phi}{b}\sqrt{D_{\mathrm{m}}}$.

The experimental time scale here is the mean residence time.

Figure 6.3-79. Matrix Diffusion Mass Transfer Coefficient as a Function of Experimental Time Scale in All of the C-wells Laboratory and Field Multiple Tracer Tests

6.4 HYDRAULIC PROPERTIES OF THE ALLUVIUM (ATC)

6.4.1 ATC Single-Well Hydraulic Tests

Single-well hydraulic testing of the saturated alluvium in well NC-EWDP-19D1 was conducted between July 2000 and November 2000. This section presents the results and interpretations of those tests. Detailed documentation of the tests is contained in Umari (2003 [164573]).

6.4.1.1 Hydraulic Test of the Four Combined Alluvium Intervals in NC-EWDP-19D1

On July 7, 2000, a single-well hydraulic test of the alluvium aquifer to a depth of 247.5 m (812 ft) below land surface was initiated in NC-EWDP-19D1 (referred to as 19D1 in the remainder of this document) to determine the transmissivity and hydraulic conductivity of the entire alluvium system at the 19D1 location. The construction of this well, including the location of all the screens discussed in this section, is summarized in Figure 6.1-8. The well was pumped for seven days, with production coming from the upper four screened intervals in 19D1, for all of the intervals completed in the alluvium (a packer was inflated below the fourth screen to isolate the alluvium from the underlying tuffs). Prior to the completion of 19D1, Nye County and USGS/LANL representatives agreed to install screens 5, 6, and 7 in the tuffaceous units encountered by the well bore to allow for possible testing of these intervals in the future. Depth to water just before the test was ~106 m (~349 ft) below land surface, and the effective alluvium thickness tested was ~136 m (446 ft), which is the distance from the water table to the bottom of the fourth screened interval; the total saturated alluvium thickness is 141 m (463 ft). Recovery data were collected for 14 days after pumping stopped. The test was used, along with the isolated-interval tests that followed, to obtain preliminary estimates of transmissivity and horizontal hydraulic conductivity that were then improved with cross-hole testing. Also, during this test, distant wells (NC-EWDP-15P, NC-EWDP-4PA, NC-EWDP-4PB, and Washburn-1x) were monitored. The nearby piezometer NC-EWDP-19P was also monitored. No responses were detected at these wells. (Note that the wells discussed in this report will be referred to by their abbreviated forms).

During the combined-interval test, 19D1 was pumped at the rate of approximately 564 L/min (149 gpm); after seven days of pumping, the drawdown was approximately 33.5 m (110 ft). Comparable pumping rates in the Nye County 48-hour (hr) well-development aquifer test in which all seven screened intervals in 19D1 were allowed to produce water caused an order of magnitude less drawdown. This result indicates that the Tertiary volcanics and tuff below the alluvium had contributed significantly to that test.

Figure 6.4-1 presents the drawdown data for the entire combined-interval test, including both the pumping and recovery periods. Pumping was started at 12:00 P.M. on July 7, 2000, and ended at 12:00 P.M. on July 14, 2000. The open alluvium interval was allowed to recover until 1:00 P.M. on July 28, 2000. The average pumping rate during the test was 564 L/min (149.11 gpm). The day markers in Figure 6.4-1 are at 12:00 P.M., so the day-1 marker indicates 12:00 P.M. on July 8, 2000; the day-2 marker indicates 12:00 P.M. on July 9, 2000, and so forth. There were no changes in the pumping rate or any other configuration changes to cause the jump in drawdown seen at the 6-day marker. All drawdown values were calculated relative to the starting pressure head at 12:00 P.M. on July 7, 2000, registered by one of the two pressure transducers placed

above the packer isolating the alluvium from the underlying tuffs (there were two transducers for redundancy; only one was used for drawdown measurements). Negative drawdown values during recovery indicate pressure heads higher than the starting pressure head. These negative drawdowns indicate that when the test was started on July 7, 2000, there was some residual drawdown relative to background water levels due to pumping associated with preparations for the test, including a step-drawdown test on July 6, 2000.

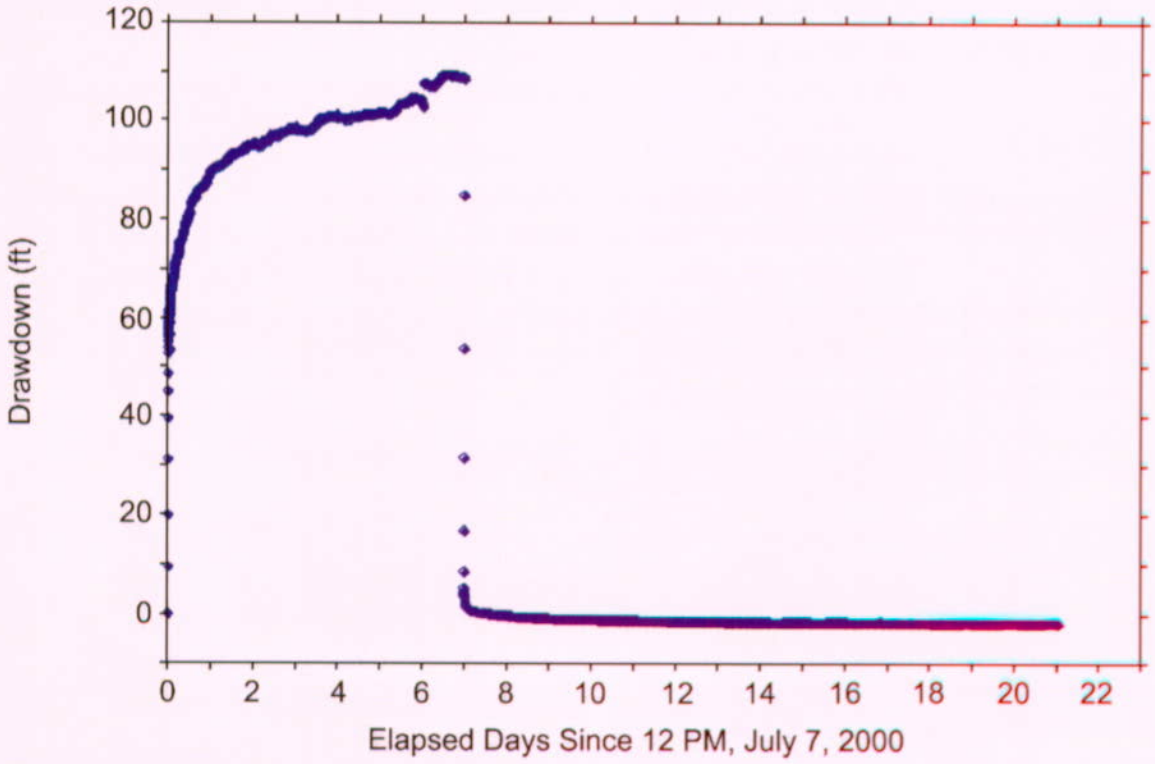

DTN: GS020708312316.001 [162678] (data).

NOTE: English units are shown in the figure because the analysis was conducted in English units. However, parameter estimates are reported in metric units to downstream users.

Figure 6.4-1. Drawdown and Recovery Data Associated with the Pump Test of the Four Combined Alluvium Intervals in NC-EWDP-19D1, July 2000

Figure 6.4-2 presents a fit of the Neuman (1975 [150321]) (Neuman.vi V 1.0, STN: 10972-1.0-00 [162754]) fully-penetrating unconfined aquifer analytic solution to the combined-interval test data. The Neuman solution gives a transmissivity value of 20.7 m^2/day (223 ft^2/day). If the thickness of the saturated alluvium from the water table to the bottom of the fourth screened interval 136 m (446 ft) is used, a hydraulic conductivity of approximately 0.5 ft/day is calculated. The type-curve matching procedure for the Neuman unconfined aquifer solution involves matching both the early and late portions of the drawdown data. In Figure 6.4-2, these two portions of the matching type curve are graphically spliced together (the late portion of the type curve match is horizontally shifted to the left) to give the appearance of a single type curve. The latter portion of the early curve match and the early portion of the late curve match are not shown in Figure 6.4-2. Both portions of this match are consistent with the transmissivity and hydraulic conductivity reported above. The slope of 1 for the early-time data (less than 2 minutes) in

Figure 6.4-2 (log-log scale) is indicative of borehole storage (Papadopulos and Cooper 1967 [150323]), so these very early time data were not considered in the curve-matching procedure.

6.4.1.2 Hydraulic Tests of Isolated Alluvium Intervals in NC-EWDP-19D1

After the combined interval test, each of the four intervals in the alluvium in NC-EWDP-19D1 were isolated and hydraulically tested to obtain transmissivity and associated hydraulic conductivity. This interval testing program was initiated in an effort to evaluate heterogeneity in hydraulic properties over the thickness of the alluvium at the NC-EWDP-19D1 location to help determine the conceptual model of flow in the saturated alluvium south of Yucca Mountain.

The following description of the isolated-interval hydraulic tests is presented in order of screen depth, starting with screen #1, the top screen, and ending with screen #4, the bottom screen. The chronological order in which the tests were conducted was screens #4, #3, #1, and #2.

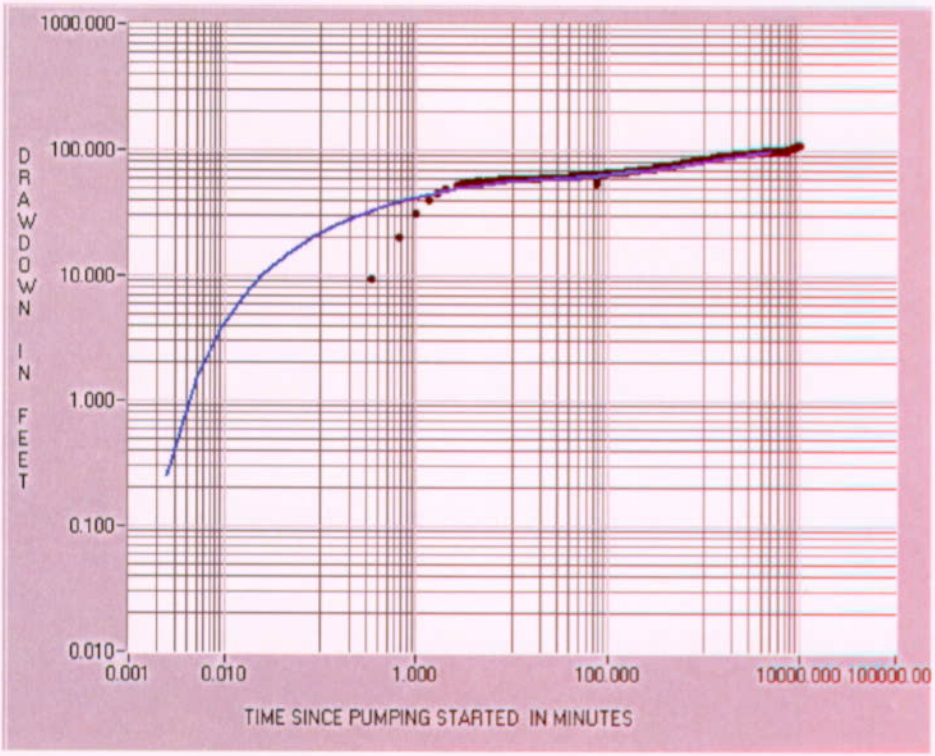

DTN: GS020708312316.001 [162678] (data); Output DTN: GS031008312316.002 (analysis).

NOTE: The blue line is a composite curve showing both early- and late-time fits of July 7, 2000, open-hole drawdown data to Neuman's (1975 [150321]) beta = 0.001 type curve (latter portion of early-time type curve and beginning portion of late-time type curve are truncated so that the two curves are joined into one continuous type curve). A value of beta = 0.001 in the Neuman (1975 [150321]) solution translates to a transmissivity of 20.7 m^2/day (223 ft^2/day). The early-time data (less than 2 minutes) were not considered in the type-curve analysis because this early-time response was attributed to borehole storage, not aquifer response. English units are shown in the figure because the analysis was conducted in English units. However, parameter estimates are reported in metric units to downstream users.

Figure 6.4-2. Drawdown as a Function of Elapsed Time for the Combined Interval Hydraulic Test in NC-EWDP-19D1 Overlaid with the Neuman Unconfined Aquifer Type Curve Solution

On October 24, 2000, a hydraulic test in the top interval in the alluvium, screen #1, was started in 19D1. Pumping continued at a nominal rate of 61 L/min (16 gpm), with an average of 61.7 L/min (16.3 gpm), until October 27, 2000. Recovery was monitored until October 30, 2000. Figure 6.4-3 presents the drawdown data from the test. Figure 6.4-4 presents a fit of the Neuman (1975 [150321]) (Neuman.vi V 1.0, STN: 10972-1.0-00 [162754]) fully-penetrating unconfined aquifer analytic solution to the data, which was obtained following the same procedure of matching the early- and late-time drawdown responses as in the combined-interval test, but with no horizontal shift required. The fully-penetrating Neuman solution gives a transmissivity value of 6.1 m^2/day (66 ft^2/day) (see Section 6.4.1.3 for correction needed because screen #1 only partially penetrates the total saturated alluvium section).

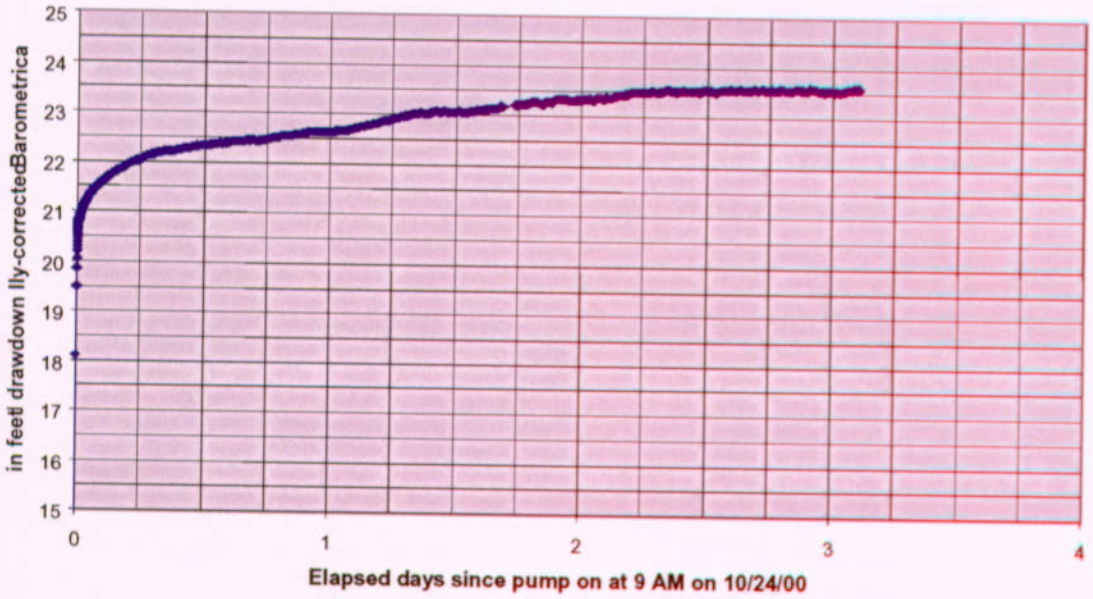

DTN: GS020708312316.001 [162678].(data).

NOTE: English units are shown in the figure because the analysis was conducted in English units. However, parameter estimates are reported in metric units to downstream users.

Figure 6.4-3. Drawdown as a Function of Time for the Hydraulic Test in Screen #1 of NC-EWDP-19D1, October 24 to October 27, 2000

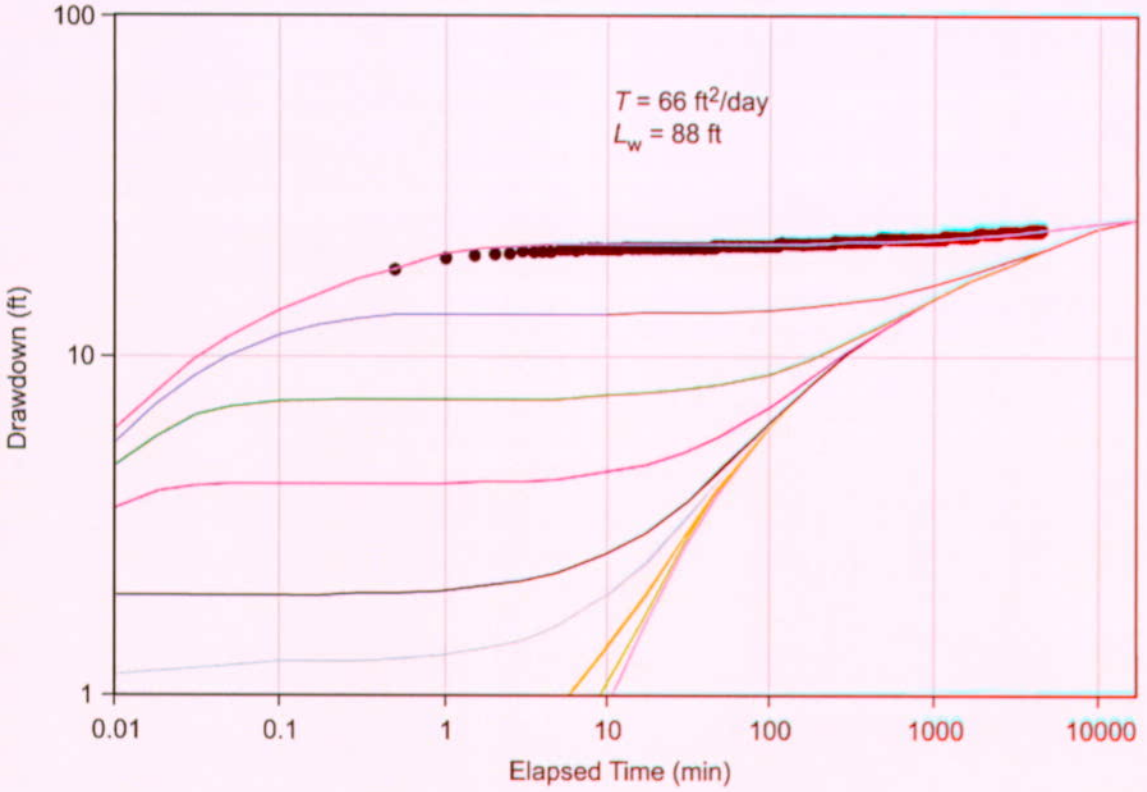

DTN: GS020708312316.001 [162678] (data); Output DTN: GS031008312316.002 (analysis).

NOTE: The chosen type curve fits early- and late-time data simultaneously. L_w is defined in Section 6.4.1.3. English units are shown in the figure because the analysis was conducted in English units. However, parameter estimates are reported in metric units to downstream users.

Figure 6.4-4. Drawdown Versus Elapsed Time for the Hydraulic Test in Screen #1 of NC-EWDP-19D1 Overlaid with the Neuman Unconfined Aquifer Type Curves

On October 31, 2000, a hydraulic test in the second interval from the top in the alluvium, screen #2, was started in 19D1. Pumping continued at a nominal rate of 17 L/min (19 gpm) until November 6, 2000. Recovery was monitored until November 9, 2000. Figure 6.4-5 presents the drawdown data from the test. It is apparent that, unlike the other isolated interval hydraulic tests in 19D1, the drawdown in screen #2 increased at a relatively constant rate. This interval was completed just below a clay-rich layer in the alluvium, and there is a possibility (unconfirmed) that the screen and gravel pack may have been gradually clogging with fines during the test. Figure 6.4-6 presents a fit of the Neuman (1975 [150321]) (Neuman.vi V 1.0, STN: 10972-1.0-00 [162754]) fully-penetrating unconfined aquifer analytic solution to the drawdown data from screen #2, which was obtained following the same procedure of matching the early- and late-time drawdown responses as in the combined-interval test, but with no horizontal shift required. The fully-penetrating Neuman solution gives a transmissivity value of 0.70 m^2/day (7.5 ft^2/day) (Output DTN: GS031008312316.002) (see Section 6.4.1.3 for correction needed because screen #2 only partially penetrates the total saturated alluvium section).

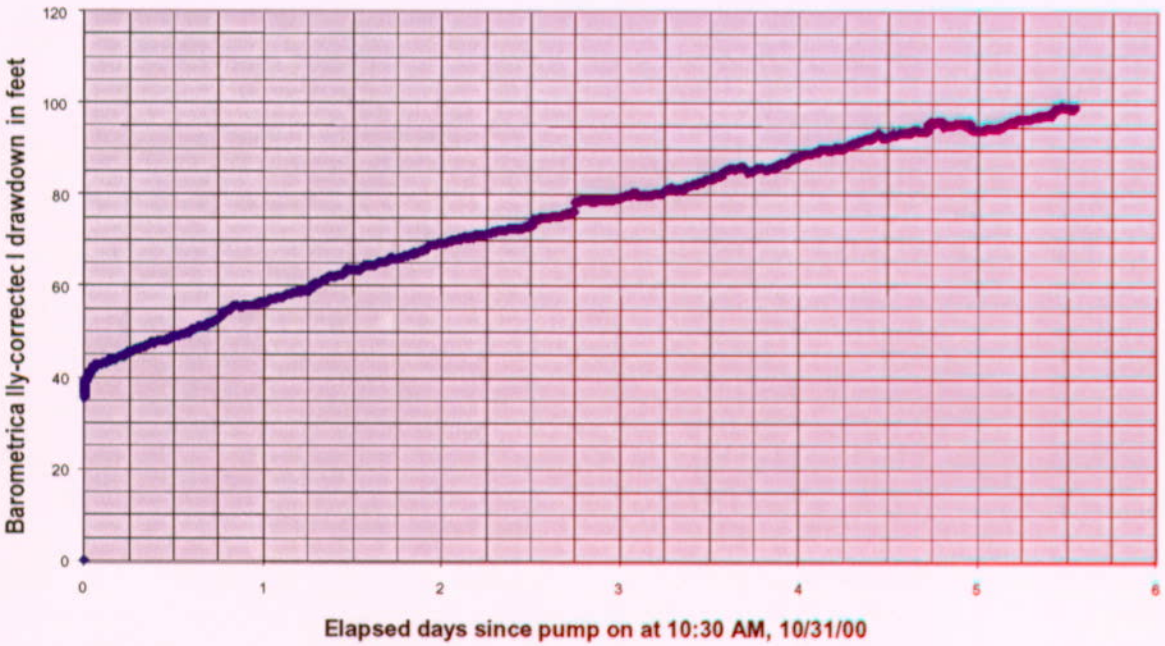

DTN: GS020708312316.001 [162678] (data); Output DTN: GS031008312316.002 (analysis)

NOTE: English units are shown in the figure because the analysis was conducted in English units. However, parameter estimates are reported in metric units to downstream users.

Figure 6.4-5. Drawdown as a Function of Time for the Hydraulic Test in Screen #2, NC-EWDP-19D1, October 31 to November 6, 2000

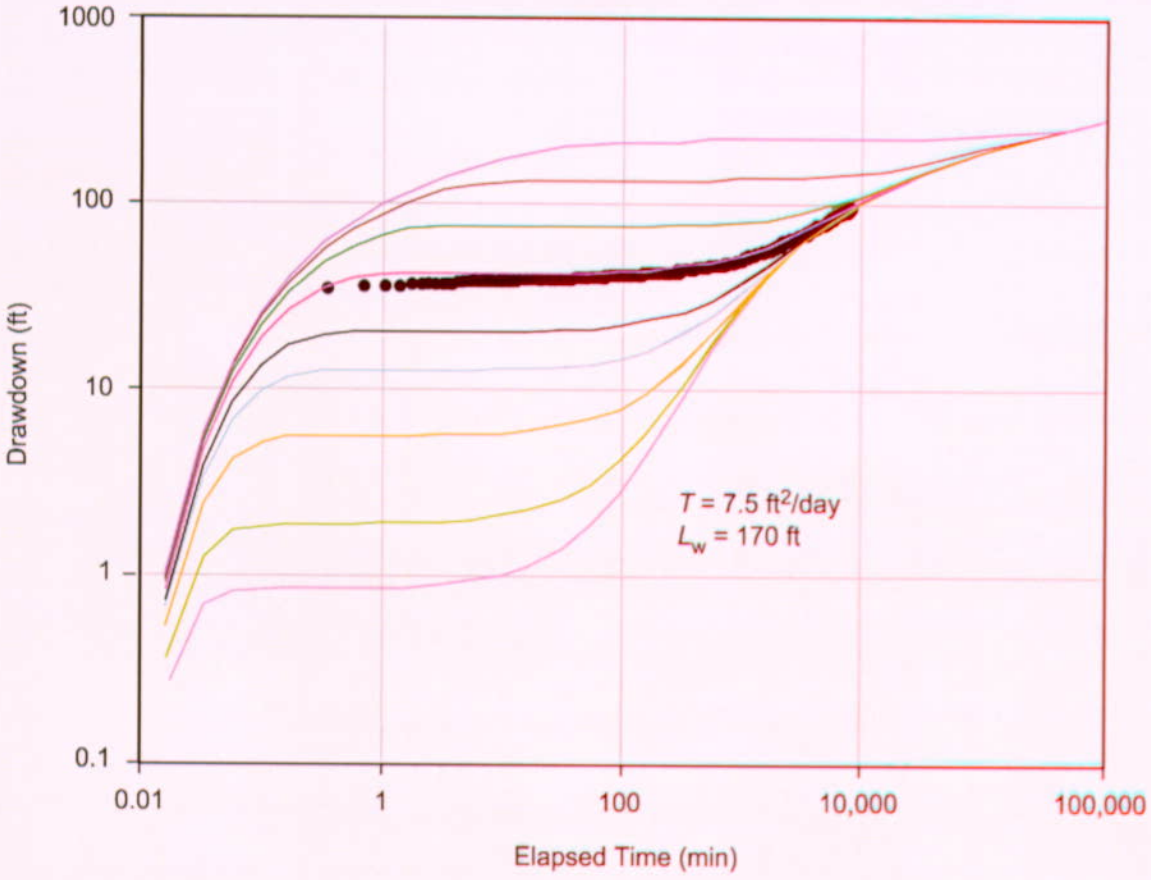

DTN: GS020708312316.001 [162678] (data); Output DTN: GS031008312316.002 (analysis).

NOTE: The chosen type curve fits early- and late-time data simultaneously. L_w is defined in Section 6.4.1.3. English units are shown in the figure because the analysis was conducted in English units. However, parameter estimates are reported in metric units to downstream users.

Figure 6.4-6. Drawdown as a Function of Time During the Hydraulic Test in Screen #2, NC-EWDP-19D1, Overlaid with the Neuman Unconfined Aquifer Type Curves

On September 9, 2000, a hydraulic test in the second interval from the bottom in the alluvium, screen #3, was started in 19D1. Pumping continued at a nominal rate of 314 L/min (83 gpm), with an average of 309.3 L/min (81.7 gpm), until September 16, 2000. Recovery was monitored until September 21, 2000. Figure 6.4-7 presents the drawdown data from this test. The stair-step shape of the drawdown versus time curve suggests that the gravel pack was compacting at discrete times during this test, thus causing nearly instantaneous jumps in the drawdown. Figure 6.4-8 presents a fit of the Neuman (1975 [150321]) (Neuman.vi V 1.0, STN: 10972-1.0-00 [162754]) fully-penetrating unconfined aquifer analytic solution to the drawdown data from screen #3, which was obtained following the same procedure of matching the early- and late-time drawdown responses as in the combined-interval test, but with no horizontal shift required. The fully-penetrating Neuman (1975 [150321]) solution gives a transmissivity value of 20.7 m^2/day (223 ft^2/day) (see Section 6.4.1.3 for correction needed because screen #3 only partially penetrates the total saturated alluvium section).

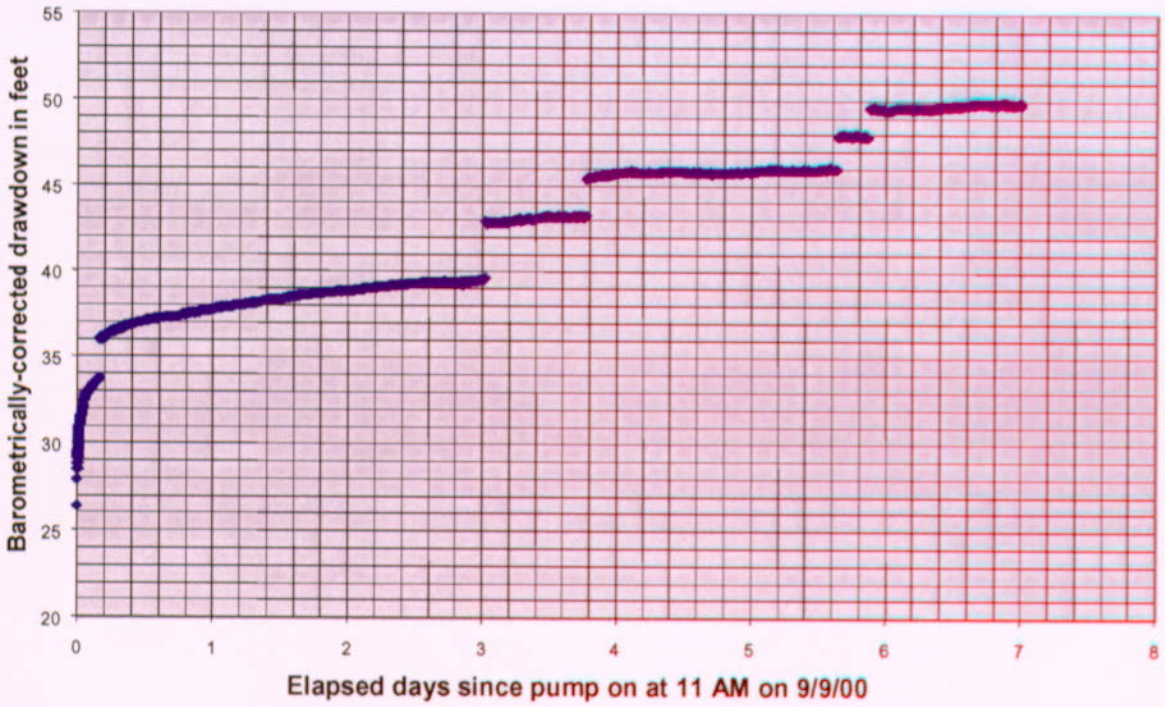

DTN: GS020708312316.001 [162678] (data); Output DTN: GS031008312316.002 (analysis).

NOTE: English units are shown in the figure because the analysis was conducted in English units. However, parameter estimates are reported in metric units to downstream users.

Figure 6.4-7. Drawdown as a Function of Elapsed Time for the Hydraulic Test in Screen #3 of NC-EWDP-19D1, September 9 to September 16, 2000

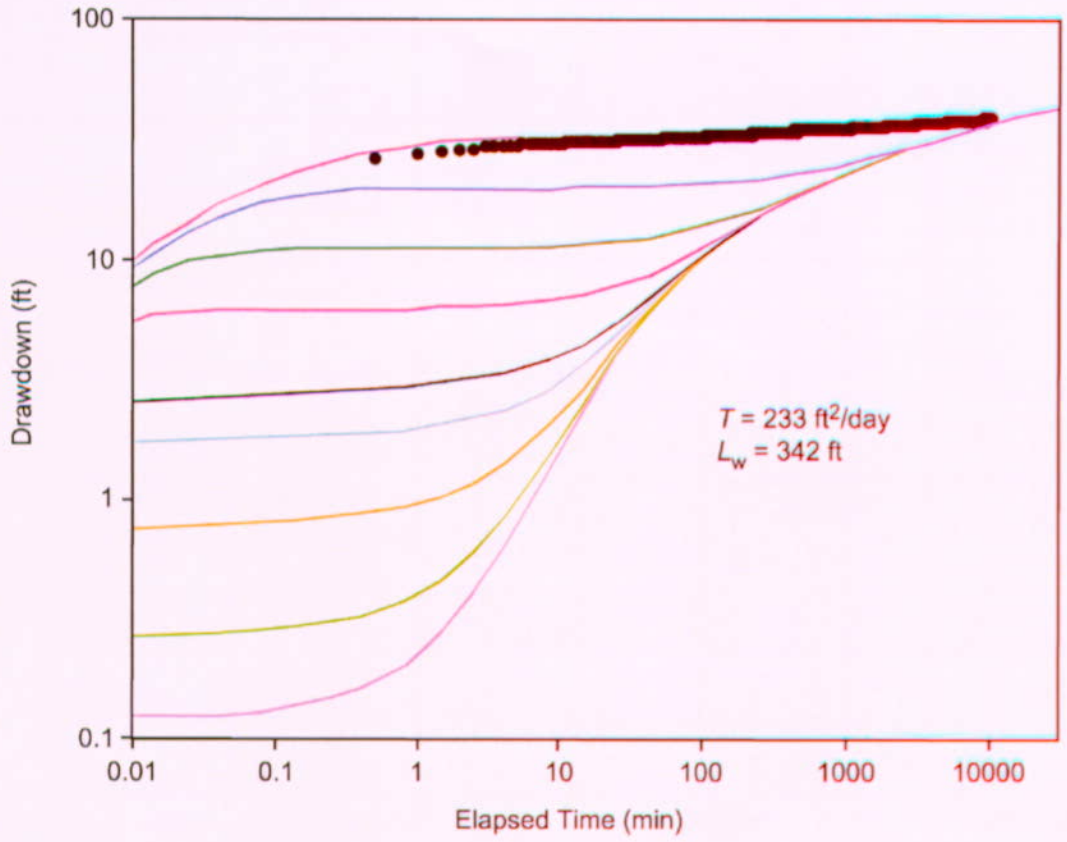

DTN: GS020708312316.001 [162678] (data); Output DTN: GS031008312316.002 (analysis).

NOTE: The chosen type curve fits early- and late-time data simultaneously. L_w is defined in Section 6.4.1.3. English units are shown in the figure because the analysis was conducted in English units. However, parameter estimates are reported in metric units to downstream users.

Figure 6.4-8. Drawdown as a Function of Time During the Hydraulic Test in Screen #3, NC-EWDP-19D1, Overlaid with the Neuman Unconfined Aquifer Type Curves

On August 24, 2000, a hydraulic test in the lower-most screen in the alluvium section of 19D1, screen #4, was started. Pumping continued at the nominal rate of 299 L/min (79 gpm) until August 31, 2000, with an average of 299.8 L/min (79.2 gpm). Recovery was monitored from August 31, 2000, to September 7, 2000. Figure 6.4-9 presents the drawdown data from this test, including both the pumping and recovery periods. Figure 6.4-10 presents a fit of the Neuman (1975 [150321]) (Neuman.vi V 1.0, STN: 10972-1.0-00 [162754]) fully-penetrating unconfined aquifer analytic solution to the drawdown data from screen #4, which was obtained following the same procedure of matching the early- and late-time drawdown responses as in the combined-interval test. The fully-penetrating Neuman solution gives a transmissivity value of 28 m^2/day (300 ft^2/day) (Output DTN: GS031008312316.002) (see Section 6.4.1.3 for correction needed because screen #4 only partially penetrates the total saturated alluvium section).

The drawdown in the combined screens #5, #6, and #7 interval as a function of elapsed time during the above test in screen #4 beginning on August 24, 2000, is presented in Figure 6.4-19 in Section 6.4.1.5, where it is used to calculate the rate of leakage from below the alluvium into the screen #4 interval.

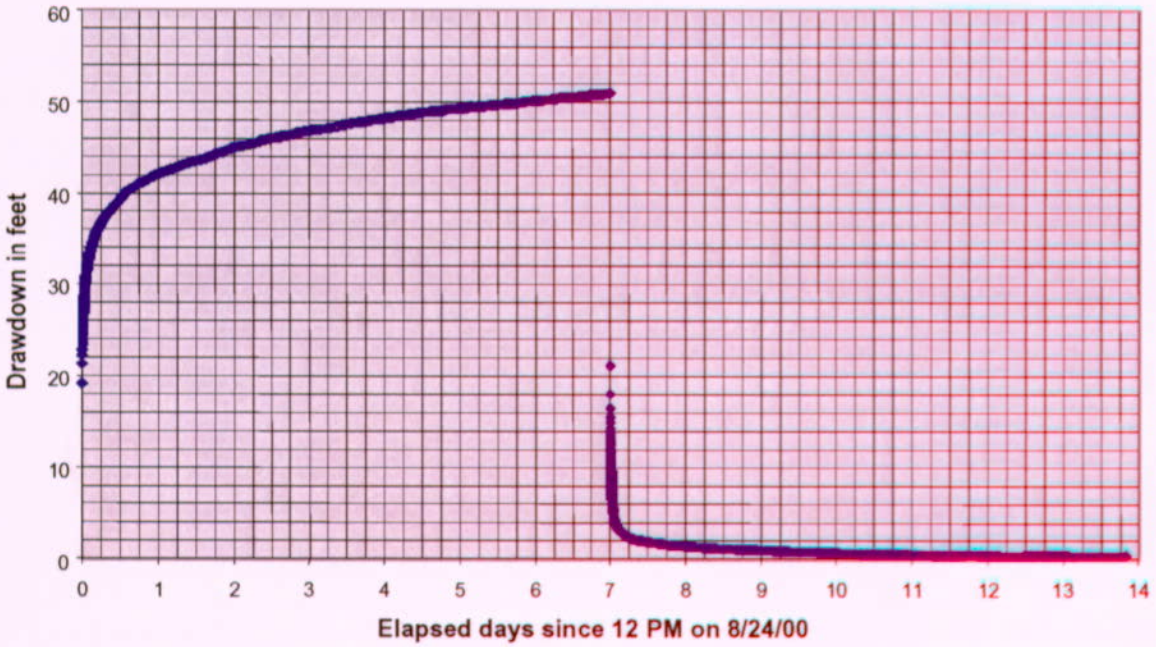

DTN: GS020708312316.001 [162678] (data).

NOTE: English units are shown in the figure because the analysis was conducted in English units. However, parameter estimates are reported in metric units to downstream users.

Figure 6.4-9. Drawdown as a Function of Time for the Hydraulic Test in NC-EWDP-19D1, Screen #4, August 24 to August 31, 2000

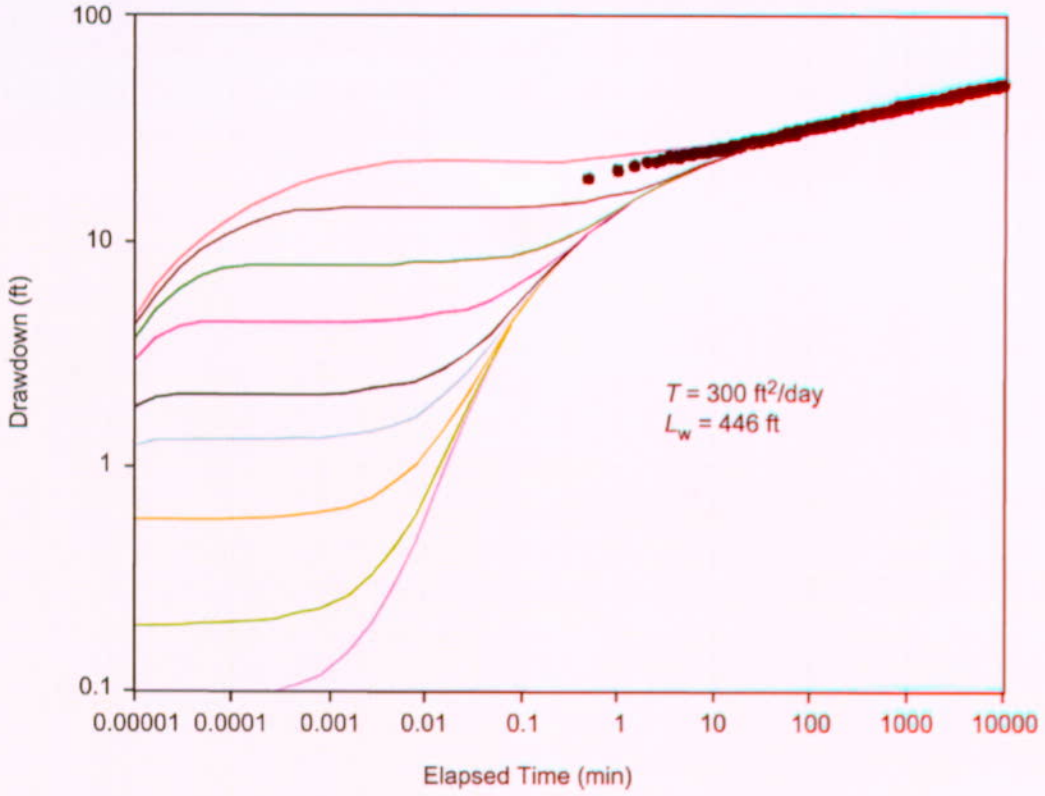

DTN: GS020708312316.001 [162678] (data); Output DTN: GS031008312316.002 (analysis)

NOTE: The matching type curve has been shifted horizontally to emphasize the match to the late-time data. The early time data were also matched by this type curve, although, unlike in Figure 6.4-2, the early-time and late-time type curve (Neuman 1975 [150321]) matches are not "spliced " together to show a single composite fit. L_w is defined in Section 6.4.1.3. English units are shown in the figure because the analysis was conducted in English units. However, parameter estimates are reported in metric units to downstream users.

Figure 6.4-10. Drawdown as a Function of Time During the Hydraulic Test in Screen #4, NC-EWDP-19D1, Overlaid with the Neuman Unconfined Aquifer Type Curves

6.4.1.3 Summary of Single-Well Hydraulic Tests in Alluvium in NC-EWDP-19D1

The hydraulic tests in 19D1, screens 1 through 4, were analyzed using the fully-penetrating Neuman (1975 [150321]) (Neuman.vi V 1.0, STN: 10972-1.0-00 [162754]) unconfined aquifer solution because all 4 individual screens, as well as the combined intervals, exhibited characteristic unconfined aquifer responses. Because each of the screens did not fully penetrate the unconfined alluvial aquifer, they should be analyzed by the partially-penetrating Neuman solution. However, there is no YMP-qualified software to perform this analysis, so the transmissivity, T, values resulting from the Neuman fully-penetrating solution should be corrected to account for the length of the screen, L_e, and the depth from the water table to the bottom of the screen being tested, L_w (see, for example, Bouwer 1978 [162675], pp. 79 to 82, 114 to 117). An empirical relationship was sought between T and each of L_e and L_w by plotting

T versus L_e (Figure 6.4-11) and T versus L_w/b in Figure 6.4-12, where b is the total unconfined alluvial aquifer thickness (136 m or 446 ft). The results from screen #2 are not included in Figures 6.4-11 and 6.4-12 because they don't follow the trend of the results from the other screens, probably because the screen #2 interval is highly affected by a clay layer at the same horizon. Figure 6.4-13 is a plot of T versus L_w/b showing results from all four screens.

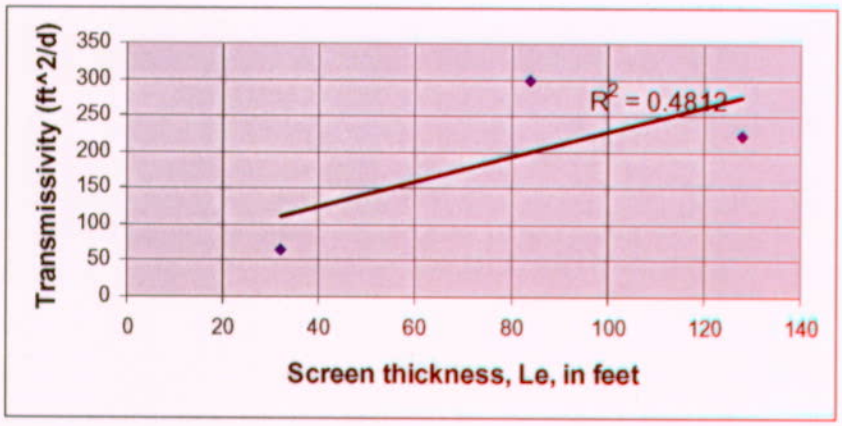

DTN: GS020708312316.001 [162678] (data); Output DTN: GS031008312316.002 (analysis).

NOTE: English units are shown in the figure because the analysis was conducted in English units. However, parameter estimates are reported in metric units to downstream users.

Figure 6.4-11. Transmissivity of Screens #1, #3, and #4 of NC-EWDP-19D1 as a Function of Screen Thickness

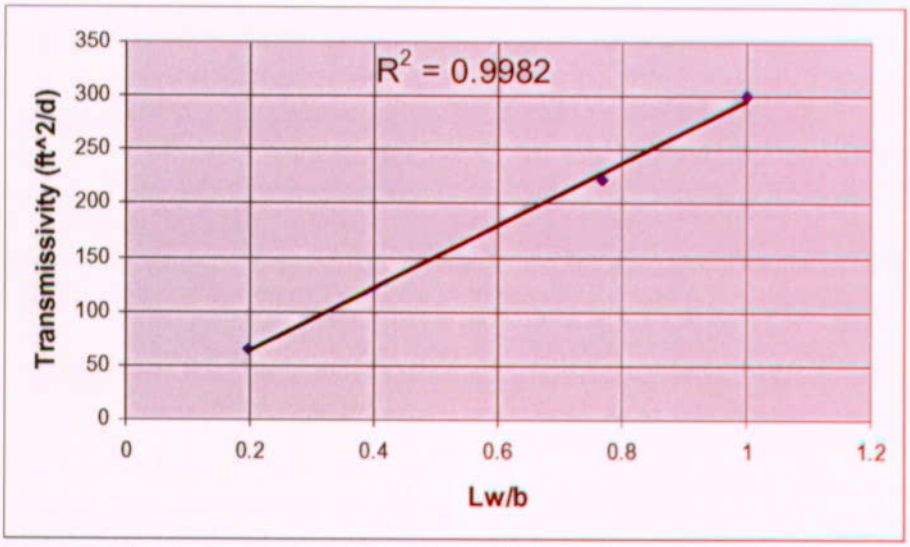

DTN: GS020708312316.001 [162678] (data); Output DTN: GS031008312316.002 (analysis).

NOTE: English units are shown in the figure because the analysis was conducted in English units. However, parameter estimates are reported in metric units to downstream users.

Figure 6.4-12. Transmissivity of Screens #1, #3, and #4 of NC-EWDP-19D1 as a Function of Distance from Water Table to Bottom of Screen Divided by Distance from Water Table to Bottom of Screen #4

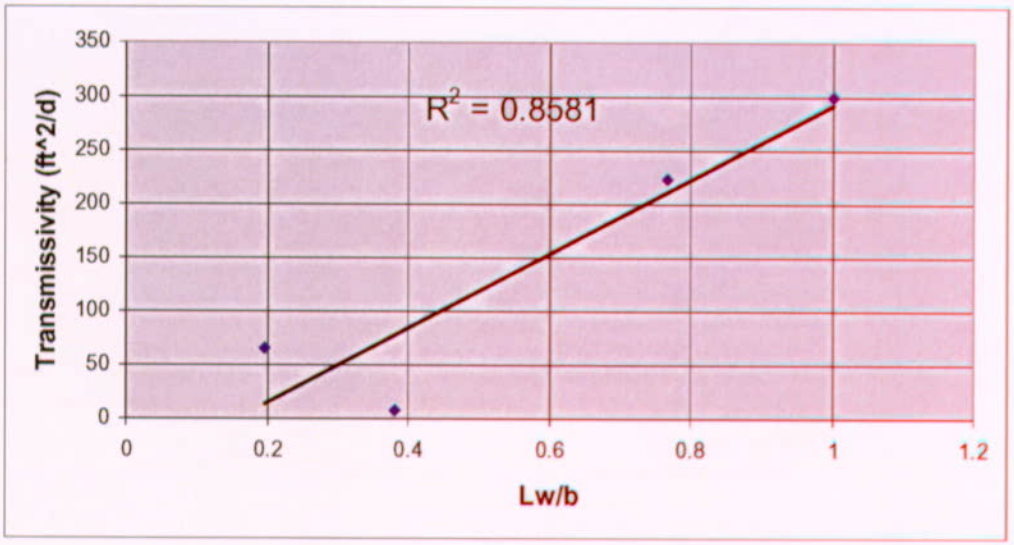

DTN: GS020708312316.001 [162678] (data); Output DTN: GS031008312316.002 (analysis).

NOTE: English units are shown in the figure because the analysis was conducted in English units. However, parameter estimates are reported in metric units to downstream users.

Figure 6.4-13. Transmissivity of Screens #1, #2, #3, and #4 of NC-EWDP-19D1 as a Function of Distance from Water Table to Bottom of Screen Divided by Distance from Water Table to Bottom of Screen #4

It can be seen from Figures 6.4-11 and 6.4-12 that the hydraulic test results from screens #1, #3, and #4 indicate that T calculated with the fully-penetrating solution is a very weak function of L_e ($R^2 = 0.4812$) but is very strongly correlated ($R^2 = 0.9982$) with L_w/b, and, therefore, with L_w. In fact, Figure 6.4-12, and even Figure 6.4-13, can be viewed as an empirical relationship derived from ATC single-well hydraulic testing for correction of the partially-penetrating T values that give a value for T of 28 m^2/day (300 ft^2/day) as their upper limit when the aquifer is fully penetrated, i.e. at $L_w/b = 1$. Thus, the transmissivity values obtained in the hydraulic tests of screens #1, #3, and #4 are all consistent with an overall transmissivity of 28 m^2/day (300 ft^2/day) for the saturated alluvium at 19D1 (Output DTN: GS031008312316.002). The T value of 28 m^2/day (300 ft^2/day) from the 8/24/00 screen #4 test is essentially the same as the transmissivity from the fully-penetrating open-hole test started on July 7, 2000 (20.7 m^2/day or 223 ft^2/day), considering that the borehole was slugged to increase its capacity between the two tests. Using an aquifer thickness equal to the distance from the water table to the bottom of screen #4 (136 m or 446 ft), an overall transmissivity value of 28 m^2/day (300 ft^2/day) represents a hydraulic conductivity of 0.20 m/day (0.67 ft/day) (Output DTN: GS031008312316.002).

Because of the large head losses discussed in the next section, the results from single-well hydraulic testing at 19D1 are considered to have a high degree of uncertainty in their absolute values. It is recommended instead that values of transmissivity, and associated hydraulic conductivity, obtained from cross-hole testing at the ATC, which is discussed in Section 6.4.2, be used for the saturated alluvium.

6.4.1.4 Step-Drawdown Tests to Determine Head Losses

A step-drawdown test was conducted prior to the hydraulic test in each interval. On July 6, 2000, prior to the open-alluvium hydraulic test starting on July 7, a step-drawdown test was conducted in the open-alluvium in well 19D1. Two methods were attempted to analyze the data as presented below.

The drawdown in the well itself (as opposed to the drawdown in the aquifer at the well wall) is given by the following equation (modified from Bouwer 1978 [162675], p. 83, Equation 4.38):

$$s = B \cdot Q + C \cdot Q^n \qquad \text{(Eq. 28)}$$

where

s = the drawdown
Q = the pumping rate
B, C, and n are coefficients.

$B \cdot Q$ represents the laminar flow that describes groundwater flow movement occurring in the aquifer and $C \cdot Q^n$ represents the turbulent flow and associated head losses caused by water entering the borehole on its way from the aquifer to the pump intake. Jacob assumed $n = 2$ (Bouwer 1978 [162675], p. 83, Equation 4.39) to obtain:

$$s = B \cdot Q + C \cdot Q^2. \qquad \text{(Eq. 29)}$$

The idea is to calculate B and C and then to calculate the fractional efficiency as the laminar drawdown divided by total (laminar plus turbulent) drawdown. Efficiency would, thus, be $B \cdot Q/(B \cdot Q + C \cdot Q^n)$, if Equation 28 is used, and $B \cdot Q/(B \cdot Q + C \cdot Q^2)$, if Equation 29 is used.

Calculations based on both equations were carried out on the data from the July 6, 2000, step-drawdown test in the open alluvium that indicate a negative value of B (a similar result is obtained when analyzing a step-drawdown test conducted in screen #4 on January 7, 2002). This result, of course, is incorrect because a negative B leads to an indeterminate efficiency calculation. Calculation of B is demonstrated below for the July 6, 2000, step-drawdown test.

Dividing Equation 29 by Q to obtain

$$\frac{s}{Q} = B + C \cdot Q \qquad \text{(Eq. 30)}$$

indicates that a plot of s/Q versus Q yields a linear relationship with an intercept of B and a slope of C. Figure 6.4-14 is such a plot for the above step-drawdown test. It can be seen from the figure that the intercept B is -0.1027 and the slope C is 0.004. Since the laminar flow component, $B \cdot Q$, cannot be negative, the negative value for B is taken to indicate that $B \cdot Q$ is approximately zero.

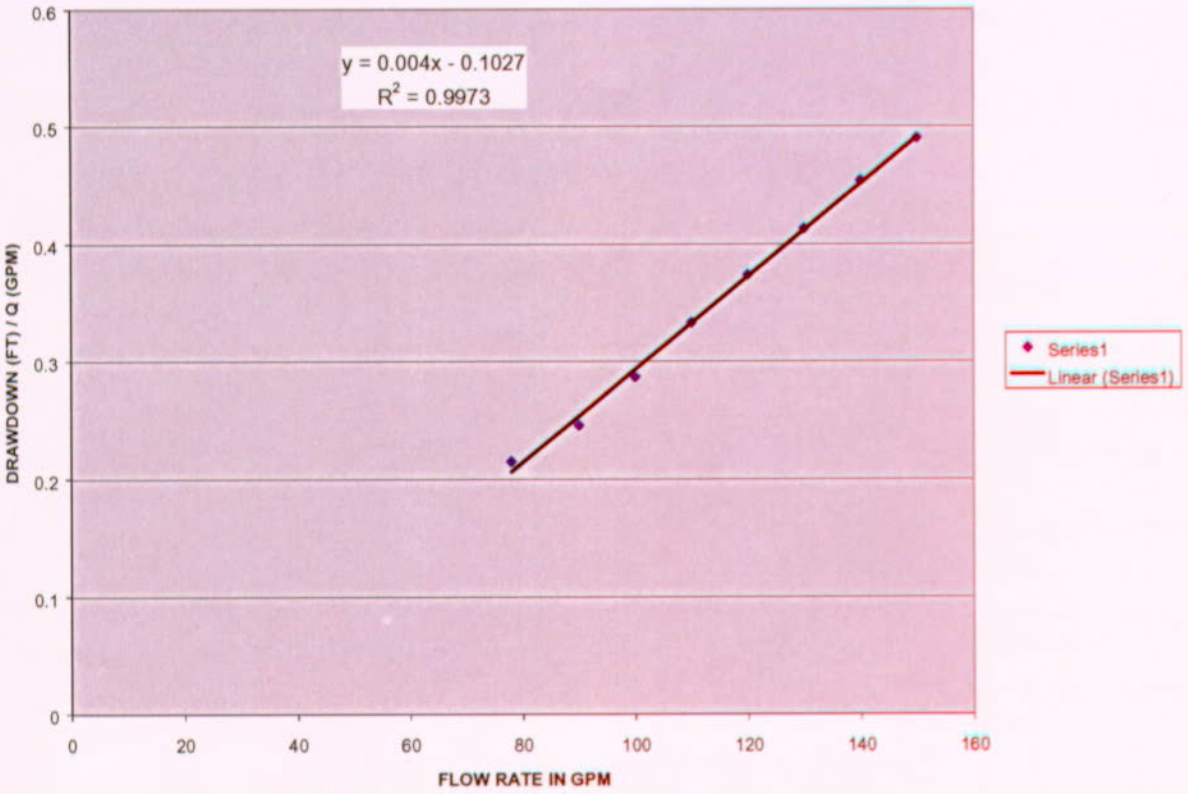

DTN: GS0207083123316.001 [162678] (data).

NOTE: Each data point represents an average of several drawdown and flow rate measurements at each nominal pump rate. English units are shown in the figure because the analysis was conducted in English units. However, parameter estimates are reported in metric units to downstream users.

Figure 6.4-14. Step-Drawdown Test in the Open Alluvium of NC-EWDP-19D1, July 6, 2000

The cause of this problem is believed to be that the step-drawdown test was carried out at a flow-rate range too high to permit calculation of the laminar groundwater flow component, $B \cdot Q$. In the flow-rate range for the test, 295 to 568 L/min (78 to 150 gpm), the turbulent head losses, $C \cdot Q^2$, were so large that they dominated the much smaller laminar-flow-caused drawdown, $B \cdot Q$, which, at the accuracy of the test results, is approximately zero. To have been able to calculate the laminar component and, therefore, quantify well efficiency, the step-drawdown test would have had to be run at a much lower range of flow rates than the range used, namely 295 to 568 L/min (78 to 150 gpm). However, the pump used, which was required for pumping up to 606 L/min (160 gpm) in the open-alluvium test and which was used in the screens #4 and #3 isolated interval tests, had a minimum operational rate of approximately 291 L/min (77 gpm).

Because the 19D1 well efficiency could not be calculated from the step-drawdown tests conducted in it, the efficiency was estimated by comparing results from single-well hydraulic tests in that well with those of cross-hole tests. Single-well tests indicated a transmissivity of 28 m^2/day (300 ft^2/day) for the saturated alluvium at 19D1 (Output DTN: GS031008312316.002)

(Section 6.4.1.3), whereas cross-hole testing indicated a transmissivity of 306 m^2/day (3,300 ft^2/day) (Output DTN: GS031008312316.002) by analyzing the response in observation well 19IM2 (Section 6.4.2).

Drawdown is related to Q and transmissivity, T, by the relationship:

$$s = \frac{Q}{4\pi T} W(u) \qquad \text{(Eq. 31)}$$

where

$u = r^2S/4Tt$ in which:

r[L] = radial distance from the pumping well

S[L^0] = storativity

t[T] = elapsed time from the beginning of pumping

and

$W(u) = \int_u^\infty \{(e^{-u}/u)\, du$; $W(u)$ is the well function, which can be a confined, unconfined, or leaky well function.

Equation 31 is the same relationship as in Theis (1935 [150327], p. 520, Equation 4) except that s is used for drawdown instead of v, and Q is used for the discharge rate instead of F.

Assuming that head losses in observation well 19IM2 in the cross-hole test when well 19D1 was being pumped (Section 6.4.2) to be negligible relative to those in the pumped well, the value of 306 m^2/day (3,300 ft^2/day) is considered to be the true transmissivity value of the alluvium aquifer at the ATC (Output DTN: GS031008312316.002). Therefore, in the single-well tests at well 19D1, by substituting 306 m^2/day (3,300 ft^2/day) into Equation 31, the drawdown in the aquifer itself due to laminar flow is:

$$s_{\text{laminar}} = \frac{Q}{4\pi(306)} W(u) \qquad \text{(Eq. 32)}$$

The actual drawdown in well 19D1 is the total drawdown (laminar plus turbulent) that was used to calculate a T of 28 m^2/day (300 ft^2/day), which when substituted into Equation 31 yields:

$$s_{\text{laminar}} + s_{\text{turbulent}} = \frac{Q}{4\pi(28)} W(u) \qquad \text{(Eq. 33)}$$

The well function, $W(u)$, in both Equations 32 and 33 is the same because it pertains to the same well and time history. Q is also the same; it is the actual pumping rate for the single-well testing.

The well efficiency for 19D1 (Output DTN: GS031008312316.002) is now calculated by dividing Equation 32 by Equation 33:

$$\text{Efficiency} = \frac{s_{\text{laminar}}}{s_{\text{laminar}} + s_{\text{turbulent}}} = \frac{28}{306} = 0.091 = 9.1\% \qquad \text{(Eq. 34)}$$

6.4.1.5 Determination of Leakage From Screens #5, #6, and #7 to Screen #4

After single-well hydraulic and tracer tests in well 19D1, screen #4 had been selected to conduct cross-hole tracer testing by pumping 19D1 and injecting tracers into 19IM1 and 19IM2. For that reason, it was desirable to determine the upward contribution of the intervals below the alluvium (screens #5, #6, and #7 in 19D1) to the water withdrawn from screen #4 in 19D1 during such a cross-hole tracer test (see Figure 6.1-8 for location of screens and other lithologic information). Such contribution from the intervals below the alluvium would be promoted by the natural upward gradient at the site and the creation of a substantial additional vertical gradient by pumping screen #4 in 19D1 and lowering its hydraulic head. Knowledge of this contribution is necessary for the correct analysis of the results from cross-hole tracer testing in screen #4, especially for effective porosity. The flow rate that should be used in calculating the effective porosity when analyzing the results of cross-hole tracer testing should be the portion of the pumped rate that is actually provided by screen #4 of the alluvium, that is, excluding the portion contributed by the intervals below the alluvium.

To determine the component of flow from below screen #4, three "confirmatory" hydraulic tests were conducted in 19D1. The results from these three tests will first be presented below, followed by an analysis to determine the leakage rate from below the screen #4 interval.

In the first confirmatory test from December 18 to 20, 2001, the combined interval below the alluvium containing screens #5, #6, and #7 was pumped at the nominal rate of 356 L/min (94 gpm) for 48 hr. During the test, the screen #4 interval and the combined interval containing screens #1, #2, and #3 were monitored. The drawdown in the combined screens #5, #6, and #7 interval as a function of elapsed time is shown in Figure 6.4-15.

In the second confirmatory test from January 4 to 6, 2002, the screen #5 interval also (like the screens #5, #6, and #7 interval test) was pumped at the nominal rate of 356 L/min (94 gpm) for 48 hr. During the test, the combined screens #6 and #7 interval, the screen #4 interval, and the combined screens #1, #2, and #3 interval were monitored. The drawdown in the screen #5 interval as a function of elapsed time is shown in Figure 6.4-16.

In the third confirmatory test from January 8 to 10, 2002, the screen #4 interval was pumped at the nominal rate of 254 L/min (67 gpm) for 48 hr. During the test, the combined screens #5, #6, and #7 interval, the screen #3 interval, and the combined screens #1 and #2 interval were monitored. The drawdown in the screen #4 interval as a function of elapsed time is shown in Figure 6.4-17.

Also for this confirmatory test in screen #4, the recovery for the screens #5, #6, and #7 interval is shown in Figure 6.4-18 because it is needed in the following analysis of leakage.

To determine the component of flow from below screen #4 to withdrawal from screen #4, a comparison was made of the drawdown in screens #5, #6, and #7 when they were pumped at 356 L/min (94 gpm) in the December 18, 2001, test (Figure 6.4-15) with the drawdown in screens #5, #6, and #7 in response to pumping screen #4 in the August 24, 2000, "screen #4" test (Figure 6.4-19).

Figure 6.4-20 presents the comparison. The responses are very similar with a ratio of 153 in the drawdown values. These are both drawdowns in the same intervals (i.e., screens #5, #6, and #7): one in response to direct pumping at 356 L/min (94 gpm) and the other in response to an unknown leakage rate from screens #5, #6, and #7 to screen #4. Thus,

$$\frac{s_{5,6,7(12/18/01)}}{s_{5,6,7(8/24/00)}} = 153 \qquad \text{(Eq.35)}$$

where $s_{5,6,7(12/18/01)}$ is the drawdown for the combined screens #5, #6, and #7 interval on December 18, 2001, and so forth.

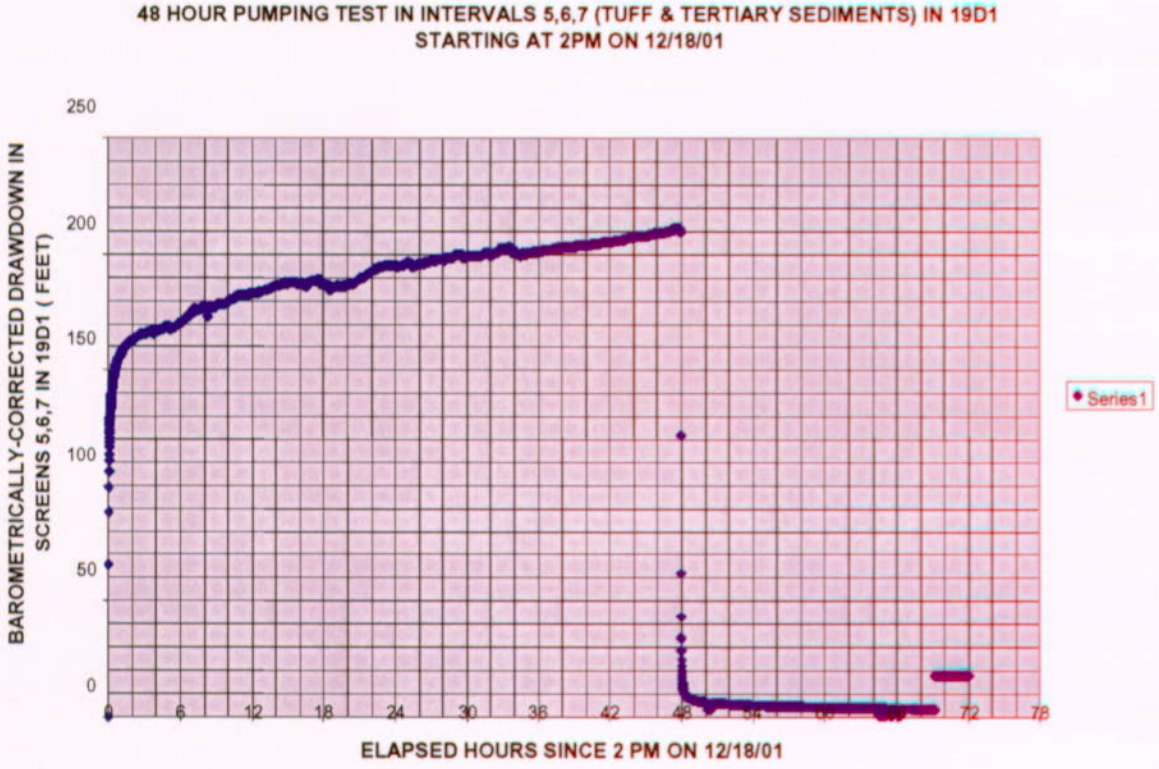

DTN: GS020908312316.002 [162679] (data).

NOTE: English units are shown in the figure because the analysis was conducted in English units. However, parameter estimates are reported in metric units to downstream users

Figure 6.4-15. Drawdown Versus Elapsed Time Since Pumping Started for the Confirmatory Hydraulic Test in Which the Combined Screens #5, #6, and #7 Interval in NC-EWDP-19D1 Was Pumped

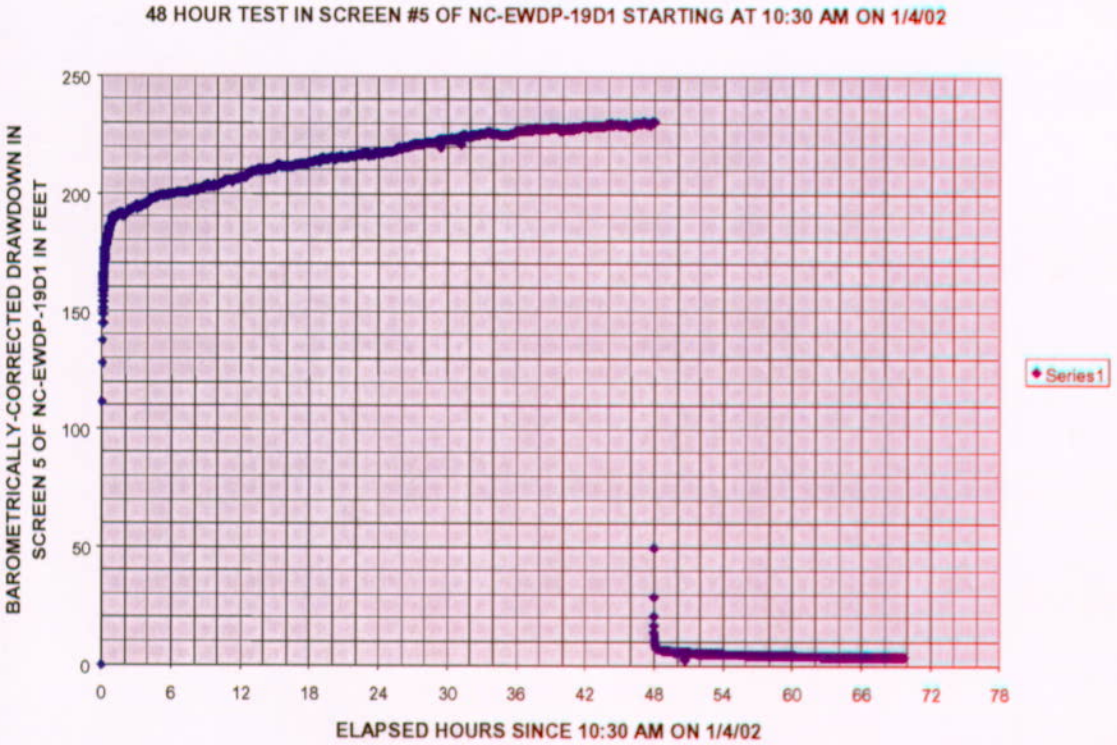

DTN: GS020908312316.002 [162679] (data).

NOTE: English units are shown in the figure because the analysis was conducted in English units. However, parameter estimates are reported in metric units to downstream users.

Figure 6.4-16. Drawdown as a Function of Elapsed Time for the Confirmatory Hydraulic Test in Which the Screen #5 Interval in NC-EWDP-19D1 Was Pumped

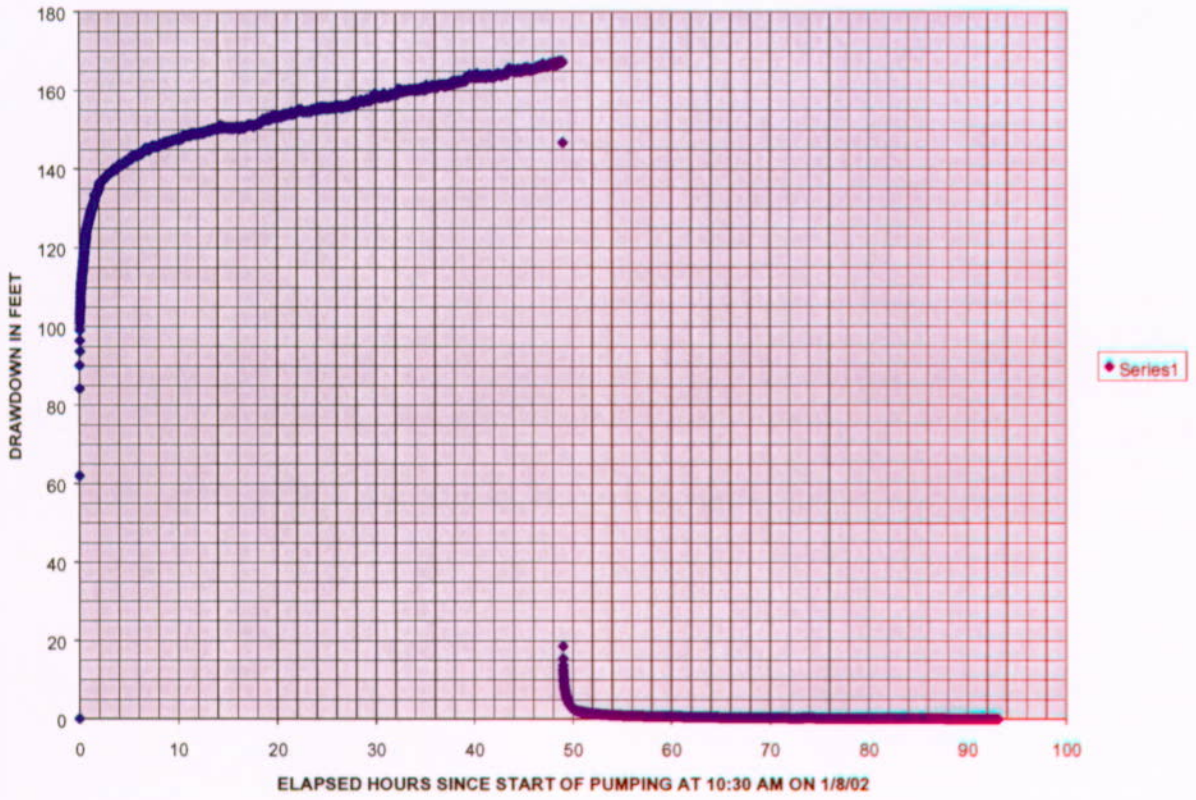

DTN: GS020908312316.002 [162679] (data).

NOTE: English units are shown in the figure because the analysis was conducted in English units. However, parameter estimates are reported in metric units to downstream users.

Figure 6.4-17. Drawdown as a Function of Elapsed Time in Screen #4 During Pumping and Recovery in the Confirmatory Hydraulic Test in That Screen, January 8 to 10, 2002

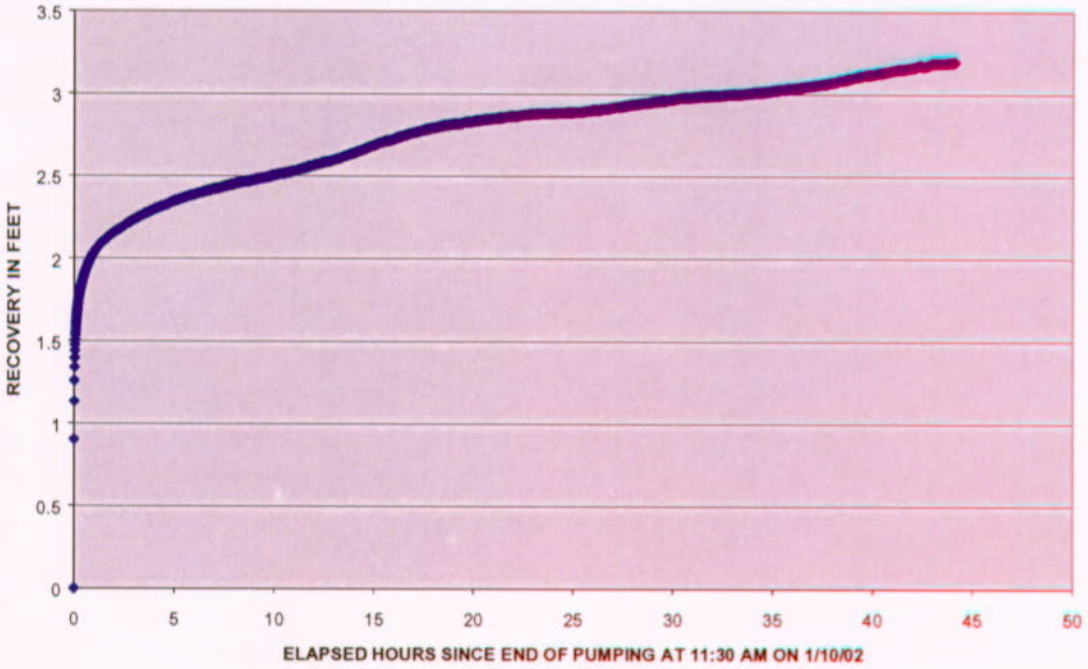

DTN: GS020908312316.002 [162679] (data).

NOTE: English units are shown in the figure because the analysis was conducted in English units. However, parameter estimates are reported in metric units to downstream users.

Figure 6.4-18. Recovery Versus Elapsed Time for the Screens #5, #6, and #7 Interval During the Confirmatory Hydraulic Test in Screen #4 of NC-EWDP-19D1, January 8 to 10, 2002

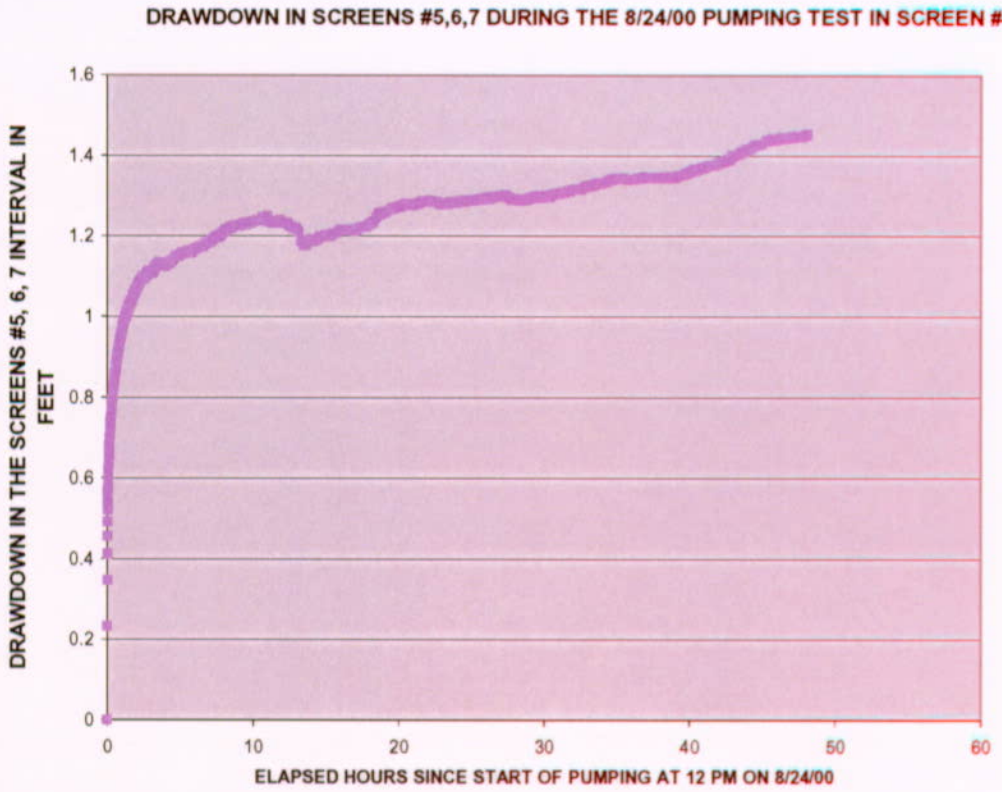

DTN: GS020708312316.001 [162678] (data).

NOTE: English units are shown in the figure because the analysis was conducted in English units. However, parameter estimates are reported in metric units to downstream users.

Figure 6.4-19. Drawdown in the Screens #5, #6, and #7 Interval During the August 24 to 31, 2000, Pumping Test in Screen #4

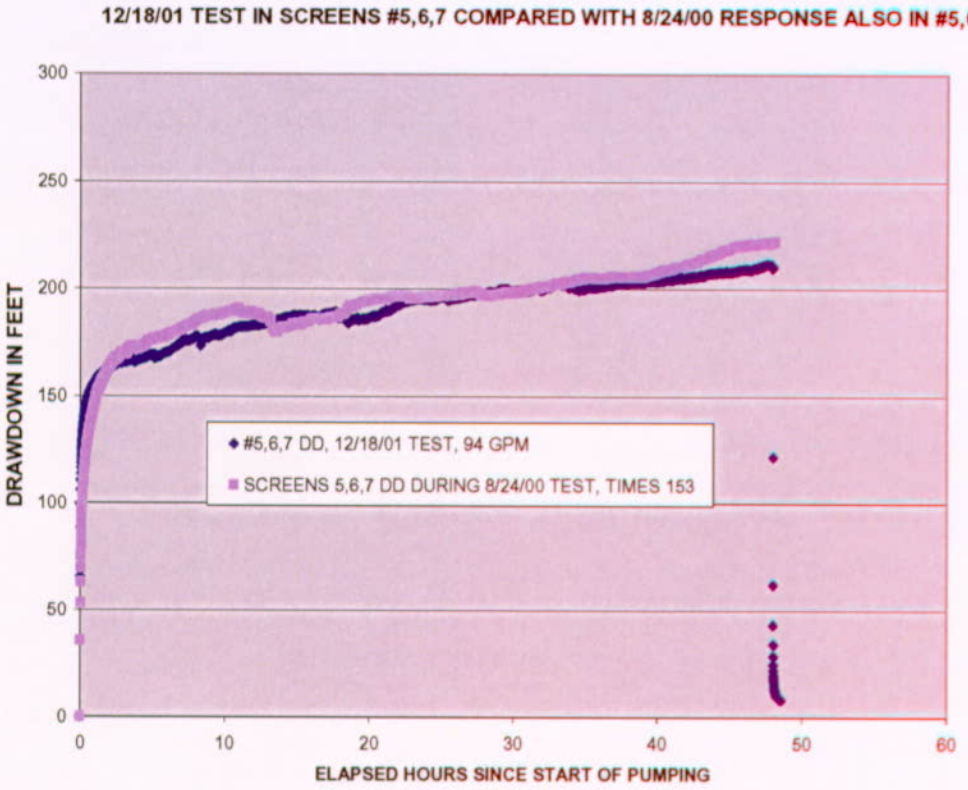

DTNs: GS020708312316.001 [162678] and GS020908312316.002 [162679] (data).

NOTE: English units are shown in the figure because the analysis was conducted in English units. However, parameter estimates are reported in metric units to downstream users

Figure 6.4-20. Comparing Drawdown in the Screens #5, #6, and #7 Interval While It Was Pumped During the December 18, 2001, Test With the Drawdown in the Same Interval During the August 24 to 31, 2000, Pumping Test in Screen #4

A correction should be made, however, to the drawdown in the screens #5, #6, and #7 interval during the December 18, 2001, test, based on the approximately 9% well efficiency of 19D1, as determined by Equation 34. This efficiency indicates that the laminar component of the drawdown occurring in the aquifer is only 9% of the total drawdown recorded in the screens #5, #6, and #7 interval of 19D1 when that interval was directly pumped during the December 18, 2001, test. In other words, using a prime to indicate laminar drawdown in the aquifer and multiplying the drawdown by the well efficiency (decimal equivalence 0.09) in order to calculate 9 percent of drawdown is mathematically expressed as,

$$s'_{5,6,7(12/18/01)} = (0.09)s_{5,6,7(12/18/01)} \qquad \text{(Eq. 36)}$$

On the other hand, negligible head losses are assumed in the screens #5, #6, and #7 interval when it was not pumped directly but leaked to the screen #4 interval when the latter was pumped in the

August 24, 2000, test—that is, if we do not subtract any drawdown for well inefficiency, then *s* prime equals *s*, which is mathematically expressed as

$$s'_{5,6,7(8/24/00)} = s_{5,6,7(8/24/00)}. \quad \text{(Eq. 37)}$$

Therefore, the ratio of drawdowns occurring in the aquifer itself for the above two contrasted tests is

$$\frac{s'_{5,6,7(12/18/01)}}{s'_{5,6,7(8/24/00)}} = (0.09)\frac{s_{5,6,7(12/18/01)}}{s_{5,6,7(8/24/00)}} = (0.09)(153) = 13.77 \quad \text{(Eq. 38)}$$

Assuming that the transmissivity of the screens #5, #6, and #7 interval is the same during the August 24, 2000, and December 18, 2001, tests, the ratio of the two drawdown responses, which is 13.77, should be the same as the ratio of the flow rates that produced them—that is, from Equation 31 (Theis 1935 [150327]),

$$s'_{5,6,7(12/18/01)} = \frac{356}{4\pi T}W(u) \quad \text{(Eq. 39)}$$

and

$$s'_{5.6.7(8/24/00)} = \frac{Q_{5,6,7(8/24/00)}}{4\pi T}W(u) \quad \text{(Eq. 40)}$$

where $Q_{5,6,7(8/24/00)}$ is the "withdrawal" rate from the screens #5, #6, and #7 interval that occurred while pumping screen #4, that is, the leakage from screens #5, #6, and #7 to screen #4 during the August 24 to 31, 2000 test. Dividing Equation 39 by Equation 40 gives

$$\frac{s'_{5,6,7(12/18/01)}}{s'_{5,6,7(8/24/00)}} = \frac{356}{Q_{5,6,7(8/24/00)}} \quad \text{(Eq. 41)}$$

or, using the value for the ratio of 13.77 from Equation 38, we find that

$$Q_{5,6,7(8/24/00)} = \frac{356}{13.77} = 25.8 \text{ L/min or } (6.83 \text{ gpm}). \quad \text{(Eq. 42)}$$

In other words, when screen #4 was pumped at the rate of 299 L/min (79 gpm) during the August 24, 2000 test, 25.8 L/min (6.83 gpm) of the 299 L/min (79 gpm) withdrawn (or 8.65%) actually came from the screens #5, #6, and #7 interval.

The same analysis can be done by comparing the drawdown in the screens #5, #6, and #7 interval when it was pumped in the December 18, 2001 test (Figure 6.4-15) with the recovery in the same interval in response to pumping the screen #4 interval in the January 8, 2002, test (Figure 6.4-18).

Figure 6.4-21 presents the comparison. The responses are very similar with a ratio of 69 in the drawdown values—that is,

$$\frac{S_{5,6,7(12/18/01)}}{S_{5,6,7(1/8/02)}} = 69. \qquad \text{(Eq. 43)}$$

These are both drawdowns in the same intervals (i.e., the combined screens #5, #6, and #7)—one in response to direct pumping at 356 L/min (94 gpm) and the other in response to an unknown leakage rate from screens #5, #6, and #7 to screen #4.

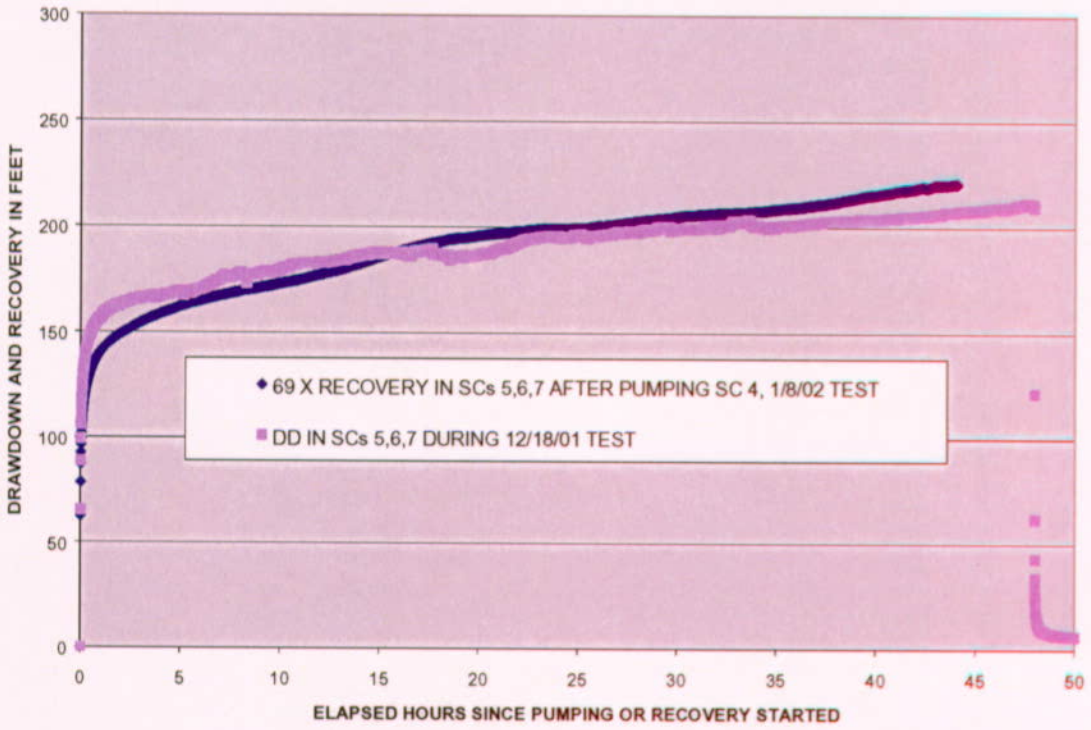

DTN: GS020908312316.002 [162679] (data).

NOTE: English units are shown in the figure because the analysis was conducted in English units. However, parameter estimates are reported in metric units to downstream users.

Figure 6.4-21. Comparing Drawdown in the Screens #5, #6, and #7 Interval While It Was Pumped During the December 18, 2001 Test with the Recovery in the Same Interval After Cessation of Pumping in Screen #4 During the January 8, 2002 Test

Negligible head losses are assumed in the screens #5, #6, and #7 interval when it was not pumped directly but leaked to the screen #4 interval when the latter was pumped in the January 8, 2002 test—that is,

$$s'_{5,6,7(1/8/02)} = s_{5,6,7(1/8/02)}. \quad \text{(Eq. 44)}$$

Assuming that the transmissivity of screens #5, #6, and #7 is the same during the December 18, 2001 and January 8, 2002 tests, the ratio of the two drawdown responses, which is 38.8, should be the same as the ratio of the flow rates that produced them—that is, from Equation 31 (Theis 1935 [150327], p. 520, Equation 4),

$$s'_{5,6,7(12/18/01)} = \frac{356}{4\pi T} W(u), \quad \text{(Eq. 45)}$$

which is the same as Equation 39 (Theis 1935 [150327], p. 520, Equation 4), and

$$s'_{5,6,7(1/8/02)} = \frac{Q_{5,6,7(1/8/02)}}{4\pi T} W(u), \quad \text{(Eq. 46)}$$

where $Q_{5,6,7(1/8/02)}$ is the "withdrawal" rate from the screens #5, #6, #7 interval that was occurring during the pumping of screen #4 (that is, the leakage from screens #5, #6, and #7 to screen #4) during the January 8, 2002, test. Dividing Equation 45 by Equation 46 (Theis 1935 [150327], p. 520, Equation 4) gives

$$\frac{s'_{5,6,7(12/18/01)}}{s'_{5,6,7(1/8/02)}} = \frac{356}{Q_{5,6,7(1/8/02)}}. \quad \text{(Eq. 47)}$$

Substituting 0.09 $s_{5,6,7(12/18/01)}$ for $s'_{5,6,7(12/18/01)}$ from Equation 36, and $s_{5,6,7(1/8/02)}$ for $s'_{5,6,7(1/8/02)}$ from Equation 44, into Equation 47, and then further substituting 69 from Equation 43 for the resulting ratio of $s_{5,6,7(12/18/01)} / s_{5,6,7(1/8/02)}$, we obtain:

$$Q_{5,6,7(1/8/02)} = 356 / (0.09 \times 69) = 57.3 \text{ L/min (15.14 gpm)} \quad \text{(Eq. 48)}$$

In other words, when screen #4 was pumped at the rate of 254 L/min (67 gpm) during the January 8, 2002 test, 57.3 L/min (15.14 gpm) of the 254 L/min (67 gpm) withdrawn (or 22.6%) actually came from the screens #5, #6, and #7 interval.

The increase in calculated leakage from screens #5, #6, and #7 to screen #4 in the January 8, 2002 test, 22.6%, compared to the calculated leakage in the August 24, 2000 test, 8.65%, is a result of the drop of efficiency of borehole 19D1 (at least in screen #4) in the time period between the two tests. When the screen #4 drawdown of the January 8, 2002 test is analyzed by the Neuman (1975 [150321] (Neuman.vi V 1.0, STN: 10972-1.0-00 [162754]) solution, a transmissivity of 4.4 m^2/day (48 ft^2/day) is obtained compared with the 28 m^2/day (300 ft^2/day) obtained by analyzing the August 24, 2000, screen #4 interval test. Both of these transmissivities were estimated without accounting for leakage from screens #5 to #7 to screen #4; the transmissivities would be somewhat smaller if leakage were accounted for. This result indicates

that the 19D1 (screen #4) well efficiency during the January 8, 2002, test could have been as low as 16% (4.4/28) of the well efficiency during the August 24, 2000, test. Loss of well efficiency causes increased drawdown in the pumped interval, screen #4, which causes an increase in the upward gradient, and resultant leakage, from screens #5, #6, and #7 to screen #4.

Based on the two analyses above that compare the drawdown in the screens #5, #6, and #7 interval when it was directly pumped during the December 18, 2001, test with the drawdown in the screens #5, #6, and #7 interval in response to pumping screen #4 in both the August 24, 2000, and January 8, 2002, tests, it is concluded that up to 23% (upper envelope of 8.65% and 22.6%) of the flow rate may have been a contribution from the screens #5, #6, and #7 interval when pumping screen #4 in 19D1 (DTN: GS020708312316.001 [162678]; DTN: GS020908312316.002 [162679]; Output DTN: GS031008312316.002).

6.4.2 ATC Cross-Hole Hydraulic Testing

Two cross-hole hydraulic tests were conducted at the ATC in January 2002. In both tests, borehole 19D1 was pumped in the open-alluvium section while 19IM1 and 19IM2 were used as monitoring wells. The surface configuration of the three wells is shown in Figure 6.1-7, and Figure 6.1-8 shows the construction/completion of the wells. Cross-hole hydraulic responses in 19IM1 were not analyzed quantitatively for this scientific analysis report because data collection in this well was not conducted in strict accordance with YMP QA procedures.

In the first cross-hole hydraulic test, conducted from January 26 to 28, 2002, in 19D1, both 19IM1 and 19IM2 were packed off, each isolating four intervals in the alluvium section. In the January 29 to February 4, 2002, test, 19IM1 was packed off while 19IM2 had only one packer inflated isolating the alluvium section from the intervals below it. Only results from the January 29 to February 4, 2002, test are presented in this report because the total transmissivity of the alluvium is less ambiguously obtained in this test than in the earlier test with isolated intervals in the observation wells.

The drawdown in the alluvium section of 19IM2 resulting from pumping the same section in well 19D1 at 109 gpm from January 29 to February 4, 2002, is presented in Figure 6.4-22. This drawdown exhibits the characteristics of a confined aquifer, and the fit to the type curve of Theis (1935 [150327]) (Neuman.vi V 1.0, STN: 10972-1.0-00 [162754]) is presented in Figure 6.4-23. The fact that the response at 19IM2 is that of a confined aquifer whereas the response of single-well testing in 19D1 conformed to the Neuman (1975 [150321]) unconfined response indicates that there may be a unit causing confinement at 19IM2 that pinches out at 19D1. The possibility was considered that the drawdown in 19IM2 was so small relative to the saturated thickness at this observation well (~2%) that the response followed that of a confined aquifer even though the aquifer was unconfined. However, attempts to fit the Neuman (1975 [150321]) (Neuman.vi V 1.0, STN: 10972-1.0-00 [162754]) unconfined aquifer solution to the drawdown response indicated that the test had been conducted long enough to exhibit the flattening in drawdown at late times that would be expected if the aquifer were unconfined. Because this flattening did not occur, it appears likely that a confining layer influenced the response near 19IM2.

The fit to the Theis (1935 [150327]) curve presented in Figure 6.4-23 results in an estimated transmissivity value of 306 m^2/day (3,300 ft^2/day) (Output DTN: GS031008312316.002) and a storativity of 0.00045 (Output DTN: GS031008312316.002). The transmissivity estimate is approximately an order-of-magnitude higher than the 28 m^2/day (300 ft^2/day) value obtained from single-well testing in 19D1 (Section 6.4.1.2). This difference is the result of large head losses in the single-well testing, and the ratio of the single-well to the cross-hole transmissivities is shown in the discussion leading to Equation 34 to be the efficiency of well 19D1. The tested interval in 19IM2 from the water table to the bottom of screen #4 is approximately 133 m (437 ft). Therefore, the hydraulic conductivity is 306 m/day/133 m (3,300 ft^2/day/437 ft), which is approximately 2.3 m/day (7.5 ft/day) (Output DTN: GS031008312316.002).

The storativity estimate above allows calculation of the specific storage that is needed for calculation of total porosity in Section 6.4.3. The above storativity estimate of 0.00045 is for the entire open-alluvium thickness at 19IM2, which is 133.1 m (436.6 ft) (depth to bottom of sand at the bottom of screen #4, 242.5 m [795.6 ft], minus depth to water, 109 m [359 ft]). These numbers give a value for the specific storage, S_s, of 0.00045/ 133.1 m = 0.00000338 m^{-1} (0.00045/436.6 ft = 0.000001031 ft^{-1}) (Output DTN: GS031008312316.002).

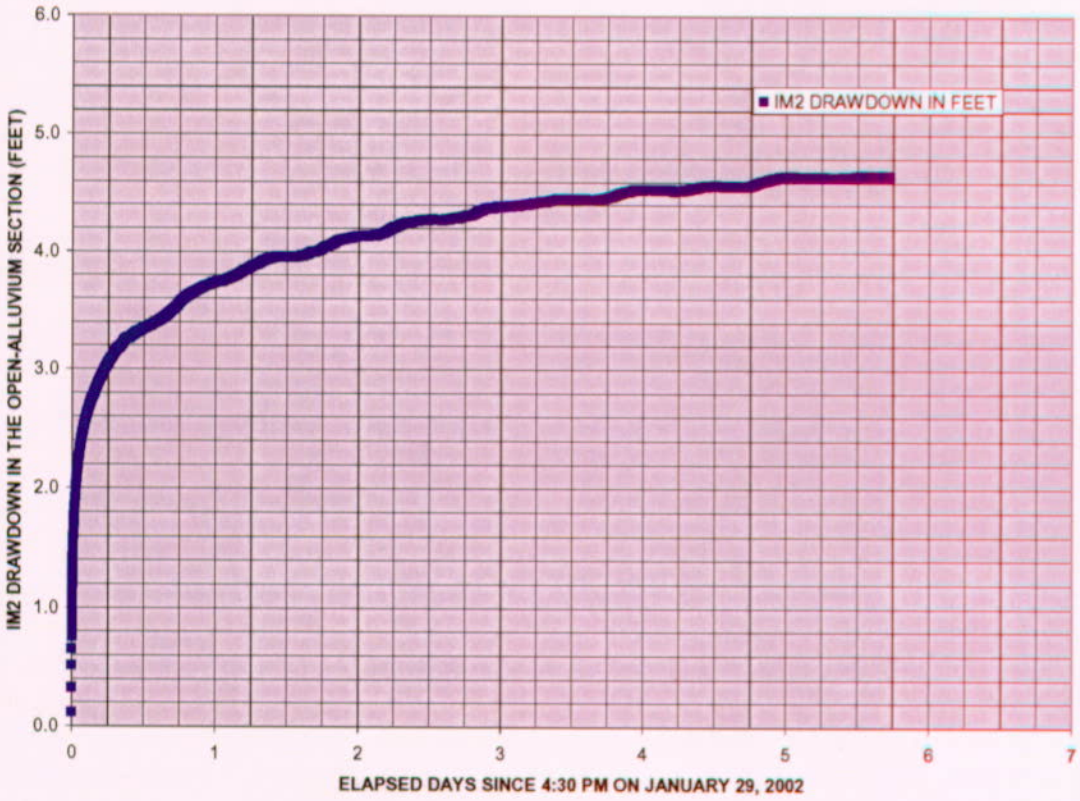

DTN: GS020908312316.002 [162679] (data).

NOTE: English units are shown in the figure because the analysis was conducted in English units. However, parameter estimates are reported in metric units to downstream users.

Figure 6.4-22. Drawdown in the Open-Alluvium Section of Observation Well NC-EWDP-19IM2 While Pumping NC-EWDP-19D1 at the Nominal Rate of 109 gpm

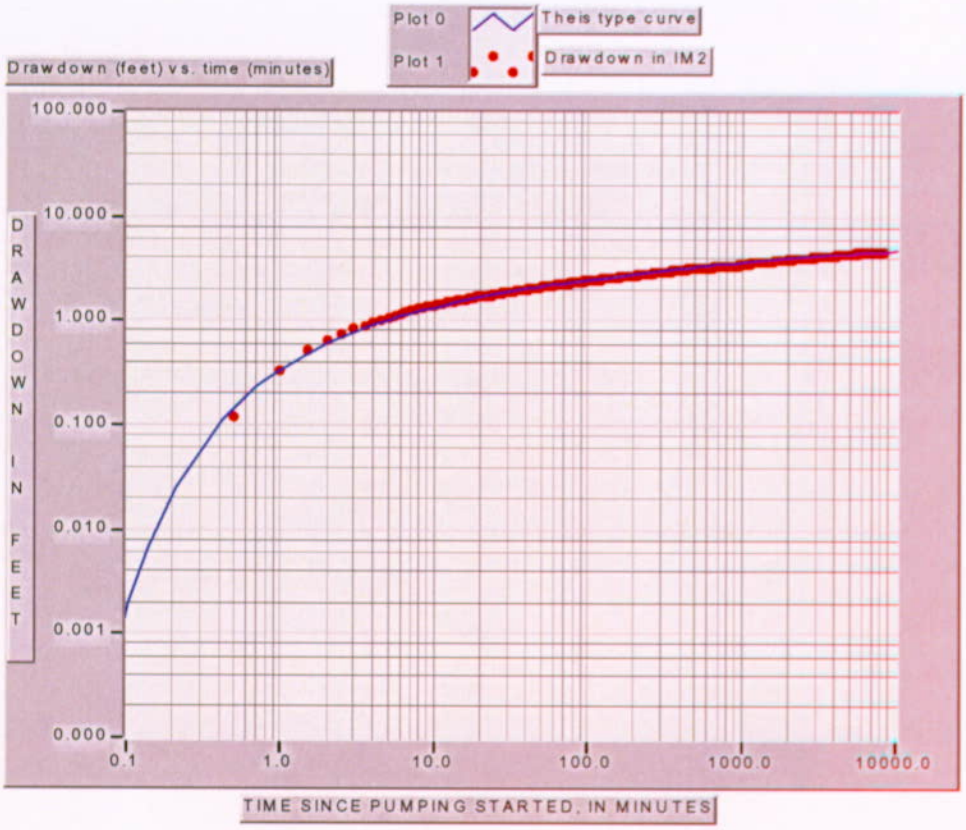

DTN: GS020908312316.002 [162679] (data); Output DTN: GS031008312316.002 (analysis).

NOTE: English units are shown in the figure because the analysis was conducted in English units. However, parameter estimates are reported in metric units to downstream users.

Figure 6.4-23. Fit to the Theis (1935) Confined-Aquifer Solution of the Drawdown in NC-EWDP-19IM2 Resulting from Pumping NC-EWDP-19D1 at 109 gpm

6.4.2.1 Qualitative Discussion of Horizontal Anisotropy of the Hydraulic Conductivity

The drawdown pattern at 19IM1 and 19IM2 in response to pumping 19D1 in both of the above cross-hole tests clearly indicated anisotropy in the horizontal hydraulic conductivity. It showed that the direction of the major principal hydraulic conductivity tensor is oriented in the northeast to southwest direction (Output DTN: GS031008312316.002). With only two observation wells, however, the degree of horizontal anisotropy and its precise orientation cannot be quantified. It should be noted that because the apparent transmissivity between 19D1 and IM2 was greater than the transmissivity between -19D1 and 19IM1, the estimate of well efficiency in Section 6.4.1.5 would have been greater if the transmissivity between 19D1 and 19IM1 had been used instead of the transmissivity between 19D1 and 19IM2.

6.4.3 Obtaining Total Porosity from Specific Storage and Barometric Efficiency

An estimate of total porosity was obtained by combining the specific storage value from cross-hole testing, namely S_s = 0.00000338 m^{-1} (0.000001031 ft^{-1}) (Section 6.4.2), with a value of barometric efficiency, *BE*, obtained from analyzing background water-level monitoring. Calculation of total porosity is done through use of a relationship derived for a confined aquifer in De Wiest (1965 [162674], p. 191, Equation 4.77). This equation is also presented in Geldon et al. (1997 [156827], p. 15, Equation 14) and attributed to Jacob. Using the notation of Geldon et al. (1997 [156827]) and rearranging terms of his equation, an expression for total porosity, θ, can be written as:

$$\theta = \frac{S_s(BE)}{\gamma\beta} \qquad \text{(Eq. 49)}$$

where

γ = the unit weight of water = = 1000 kg/m^3 (0.434 $lb/in^2/ft$ [62.496 lb/ft^3]) (Lohman 1972 [150250], Constants in Equations 20 and 21).

β = the compressibility of water = 4.69 x 10^{-9} m^2/kg (3.3 x 10^{-6} in^2/lb [2.29167 x 10^{-8} ft^2/lb]) (Lohman 1972 [150250], Constants in Equations 20 and 21).

The barometric efficiency, *BE*, was obtained by analyzing background water-level monitoring conducted between May 1 and July 3, 2002 (DTN: GS020908312316.003 [162680]).

The atmospheric pressure is first subtracted from the absolute-pressure transducer values to obtain the hydraulic pressure (represented in equivalent feet of water.) The hydraulic pressure and atmospheric pressure (also represented as equivalent feet of water) records for the period of monitoring (DTN: GS020908312316.003 [162680]) are then filtered (Output DTN: GS031008312316.002; Software: Filter.vi V 1.0, STN: 10970-1.0-00 [162668]) to remove all oscillations with frequencies higher than 0.8 cycles/day. This step removes the effects of all semidiurnal atmospheric pressure changes and all earth tides on the hydraulic-pressure record. It also removes the semidiurnal atmospheric pressure fluctuations from the atmospheric-pressure record. What remains are the low-frequency atmospheric pressure fluctuations associated with weather systems and the oscillations they cause in the hydraulic pressure record. The changes in the low-frequency hydraulic pressure record is then plotted against the changes in the low-frequency atmospheric pressure record as shown in Figure 6.4-24.

The slope of the best-fit line through the data in Figure 6.4-24 is -56.54%, indicating that for any incremental change in the atmospheric pressure at the 19D1 location, a corresponding change in the hydraulic pressure occurs, which is opposite in sign to the atmospheric pressure change and equal to 56.54% of its magnitude. In other words, the barometric efficiency, *BE*, of the aquifer at the 19D1 location is 56.54%, or 0.5654 (Output DTN: GS031008312316.002).

Substituting $BE = 0.5654$ from above and $S_s = 0.00000338\ m^{-1}$ ($0.000001031\ ft^{-1}$) (from Section 6.4.2) into Equation 49 (along with the values for γ and β listed under that equation) gives (Output DTN: GS031008312316.002):

$$\theta = \frac{(0.00000338\ m^{-1})(0.5654)}{(1000\ kg/m^3)(4.69 \times 10^{-9}\ m^2/kg)} = 0.407 = 40.7\% \qquad \text{(Eq. 50)}$$

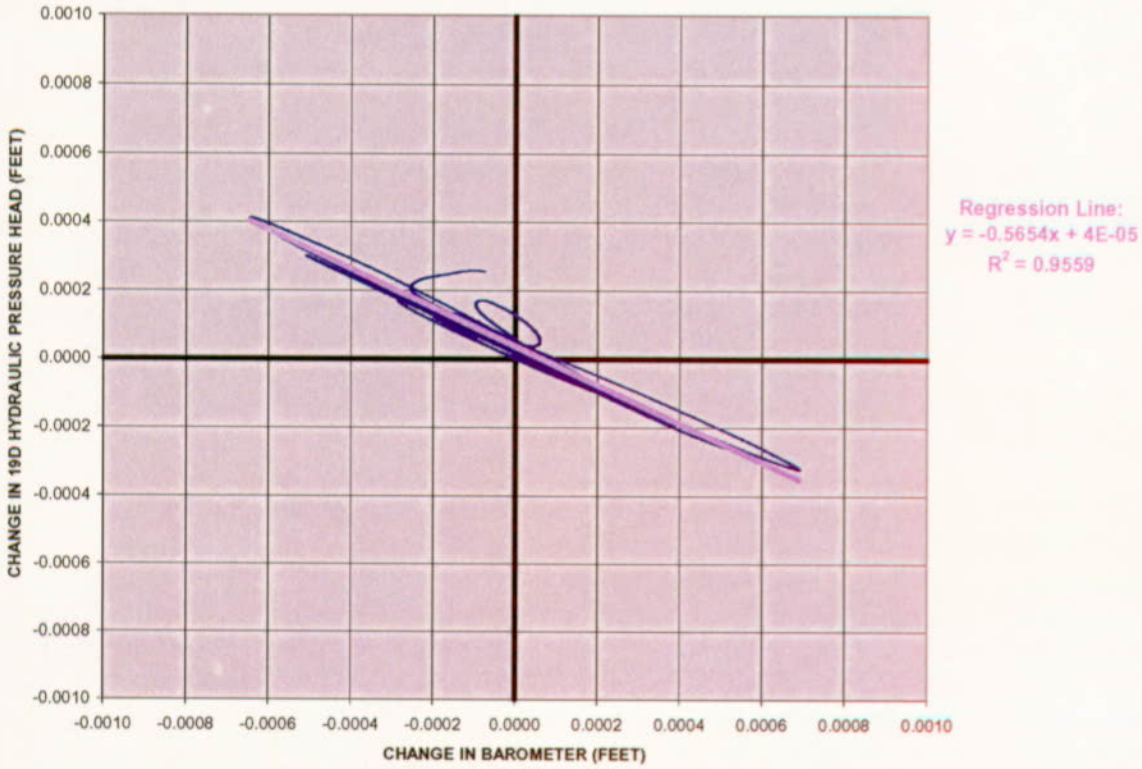

DTN: GS020908312316.003 [162680]. (data); Output DTN: GS031008312316.002 (analysis).

NOTE: English units are shown in the figure because the analysis was conducted in English units. However, parameter estimates are reported in metric units to downstream users.

Figure 6.4-24. Relation of Low-Frequency Hydraulic-Pressure Change in NC-EWDP-19D1 to Low-Frequency Atmospheric-Pressure Change at the NC-EWDP-19D1 Location: Data and Regression Line

The largest total porosity value obtained from grain-size distributions in well 19D1 is 0.33, occurring at the 152- to 154-m (500- to 505-ft) depth interval (DTN: LA0201JS831421.001 [162613], Output DTN: GS031008312316.002). The largest total porosity value obtained from the Borehole Gravity Meter survey done in NC-EWDP-19D1, presented in Section 6.5.5, is 0.29, occurring at approximately 198 m (650 ft) of depth. The above values would indicate that the upper limit for total porosity in the alluvium at the 19D1 location ranges from 29% to approximately 40%. (The total porosity from grain-size distribution is obtained through the

relation, Porosity = 0.255 $(1 + 0.83^{C})$, where C, the coefficient of uniformity, is the ratio of the 60th grain-size percentile to the 10th percentile.) (Kasenow 2002 [164666], p. 72).

There are many assumptions involved in the derivation of Equation 49 (De Wiest 1965 [162674], pp. 189 to 191). Uncertainties in the estimate of total porosity using this equation depend primarily on the extent to which these assumptions hold true in the saturated alluvium. Unfortunately, the data and information necessary to evaluate the validity of these assumptions were not available. Barometric efficiency was believed to be determined quite accurately from the large number of barometer and water-level measurements, and the storativity estimate obtained from cross-hole hydraulic testing at the ATC is considered less uncertain than the assumptions inherent in Equation 49. A formal analysis of uncertainty in the porosity estimate was not conducted.

6.4.4 Summary of Hydraulic Parameters in Alluvium

The single-hole testing indicated an overall transmissivity for the alluvium of 28 m^2/day (300 ft^2/day) with an associated hydraulic conductivity of 0.20 m/day (0.67 ft/day) (Output DTN: GS031008312316.002). This is a horizontal hydraulic conductivity value with no directional dependence. The transmissivity and hydraulic conductivity estimates were also estimated without assuming any near-wellbore head losses, which apparently were very significant, possibly because of the narrow slots in the well screens and the relatively small particle size of the sand packs in 19D1, among other reasons (well efficiency is determined to be 9.1% [Output DTN: GS031008312316.002]; see Section 6.4.1.4, Equation 34). Thus, the true transmissivity and hydraulic conductivity are believed to be approximately an order-of-magnitude higher than the single-hole *apparent* values.

Vertical hydraulic conductivities could not be estimated from the single-well testing, although they were presumably small, because none of the intervals above or below the isolated intervals in the hydraulic tests showed any pressure response during pumping (with the exception of interval #5 in the tuffs, which responded slightly to pumping interval #4). Also, there was minimal response in 19P when pumping any of the intervals in 19D1 except for screen #1 and the combined-interval test.

Estimates of transmissivity and horizontal hydraulic conductivity were greatly improved after cross-hole hydraulic testing was conducted at the 19D1 location (Section 6.4.2). The cross-hole tests indicated a transmissivity of 306 m^2/day (3,300 ft^2/day) (hydraulic conductivity of 2.0 m/day [6.7 ft/day]), which is about an order of magnitude higher than the transmissivity and hydraulic conductivity values obtained from single-well hydraulic tests. Because of well losses in 19D1 (well efficiency of 9.1%), the cross-hole transmissivity value of 306 m^2/day (3,300 ft^2/day) is considered to be much more representative of the saturated alluvium in the vicinity of 19D1 than the single-well transmissivity values of ~28 m^2/day (~300 ft^2/day). The cross-hole tests also provided storativity estimates as well as qualitative information on horizontal anisotropy of hydraulic conductivity in the saturated alluvium.

6.5 TRANSPORT PROPERTIES OF THE ALLUVIUM (ATC)

6.5.1 Introduction and Alternative Conceptual Transport Models

Three single-well injection-withdrawal tracer tests were conducted in screen #1 (the uppermost screened interval) of NC-EWDP-19D1 between December 2000 and April 2001 (see Figure 6.1-8 for diagram showing well completion and lithology; note that well NC-EWDP-19D1 will be referred to by its abbreviated form (19D1) in the remainder of this document; see Table 1). The primary objective of these tests was to distinguish between alternative conceptual transport models for the saturated alluvium south of Yucca Mountain. A secondary objective was to obtain estimates of key transport parameters associated with the appropriate conceptual model. A fourth single-well injection-withdrawal tracer test was conducted in screen #4 of 19D1 in February and March of 2002. This test is only briefly discussed in this report (Section 6.5.4.5) because it was conducted for the purposes of comparing and contrasting parameter estimates obtained from single-well and cross-hole tests, but the cross-hole tests were not conducted. Detailed documentation of the tracer tests is contained in Umari (2003 [164573]) and Reimus (2003 [165128]).

The three conceptual transport models that were considered for the saturated valley-fill deposits located south of Yucca Mountain prior to single-well tracer testing at 19D/D1 are depicted in Figure 6.5-1 (with some additional variations/combinations). The first model assumes purely advective transport through a porous medium with no diffusive mass transfer into either the grains of the medium or between advective and nonadvective regions of the aquifer. This model does not necessarily imply a homogeneous flow field, but it does preclude a system with alternating layers of relatively narrow thickness and significant permeability contrasts. Such a conceptual model might be valid in a sandy aquifer with grains of relatively low porosity. The second model is similar to the first except that it assumes diffusive mass transfer into the grains of the porous medium. These grains have significant internal porosity, but the porosity is not well-connected over the scale of the grains; therefore, the grains transmit negligible flow. The third model assumes diffusive mass transfer between advective and nonadvective layers in the aquifer. In this model, the flow system is assumed to alternate between high and low conductivity layers, a simplified representation that is consistent with some depositional scenarios. Diffusive mass transfer in this case is only between the two layers, not into grains within the layers. However, one variation of this model is to assume that diffusion also occurs into grains in both the advective and nonadvective layers. This variation is essentially a combination of the second and third conceptual models, with an additional level of complexity allowing for diffusion in the nonadvective layer into both the inter- and intragranular pore spaces.

Pre-test predictions of the single-well injection-withdrawal tracer tests conducted at 19D1 are presented in Section 6.5.2. Pre-test predictions of cross-hole tracer test responses in the alluvium are provided in Section 6.5.3. The results and preliminary interpretations of the three single-well injection-withdrawal tests conducted in FY 2001 are presented in Section 6.5.4. Finally, Section 6.5.5 presents the results and interpretations of several laboratory experiments that have been conducted to support the ATC testing effort.

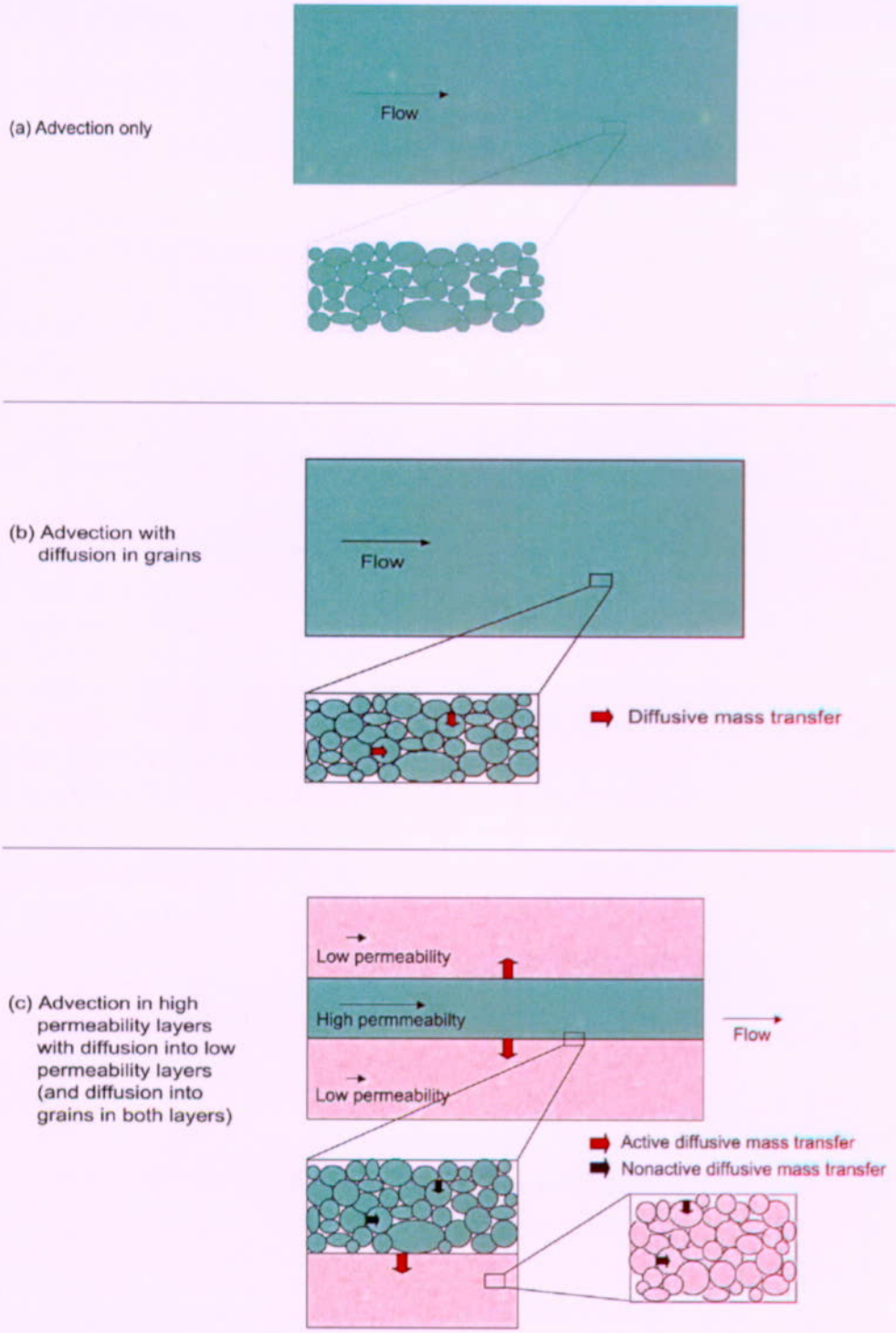

For illustration purposes only

NOTE: Red arrows in (c) indicate diffusive mass transfer options that were exercised in this scientific analysis, and black arrows indicate options that were not exercised.

Figure 6.5-1. Schematic Illustration of Alternative Conceptual Transport Models for the Valley-Fill Deposits South of Yucca Mountain

6.5.2 Pre-Test Predictions of Single-Well Tracer Responses for Each Conceptual Model

Prior to conducting the single-well tracer tests in 19D1, the MULTRAN model (Section 6.3.9.2.2) was used to simulate tracer responses, assuming each of the three alternative conceptual models of Figure 6.5-1. Simulations were conducted for each of three planned single-well tests: a zero rest-period test, a 2-day rest-period test, and a 30-day rest-period test (where "rest period" refers to the time period after injection that is allowed to elapse before starting to pump the well). In each of these tests, it was anticipated that approximately 11,000 L (3,000 gallons) of tracer solution would be injected into the test interval followed by approximately 95,000 L (25,000 gallons) of tracer-free "chase" water to push the tracer solution out of the wellbore and gravel pack into the formation. The well would then be pumped for several days to several weeks after the prescribed rest period. Each of the three tracer tests was to include both a halide (bromide, chloride, or iodide) and a fluorinated benzoate (FBA) so that any diffusion from flowing water into stagnant water could be identified from differences in the tracer responses.

In single-well simulations using MULTRAN V 1.0 (STN: 10666-1.0-00 [159068]), only one end of the domain is modeled as a well-mixed borehole; the other end becomes a zero-concentration-gradient boundary. However, to minimize boundary effects, an initial calculation establishes a node spacing in the radial (r) direction that results in a tracer "plume" that never reaches the edge of the domain. Furthermore, the numerical calculations are carried out assuming cylindrical coordinates with flow only in the radial direction (with a flow velocity that varies as $1/r$), instead of Cartesian coordinates. Ambient flow during single-well tests, which is superimposed on the radial flow induced by injection into and pumping of the well, is not accounted for in the current version of MULTRAN. Thus, the advection-dispersion equation in the flow direction solved by MULTRAN for single-well tests is (Bear 1979 [105038], p. 247):

$$\frac{\partial c}{\partial t} = -V(r)\frac{\partial c}{\partial r} + \frac{1}{r}\frac{\partial}{\partial r}\left(rD\frac{\partial c}{\partial r}\right) \qquad \text{(Eq. 51)}$$

where

c = tracer concentration (mol/L)
r = radial coordinate, cm
$V(r)$ = flow velocity as a function of r (cm/hr)
D = dispersion coefficient (cm^2/hr).

Single-well tracer test responses for all three single-well tests were simulated for both a generic halide (bromide or iodide) and a generic fluorinated benzoate, with the assumption that the halide has a factor-of-three larger diffusion coefficient than the benzoate. The response of a counter cation (potassium was assumed in all cases) was also simulated, as well as the responses of the cations with which it exchanges. Also, a flow interruption of several hours was simulated for the test with zero rest period to illustrate the additional information that can be obtained by doing a planned flow interruption during the latter portion of the test.

The MULTRAN V 1.0 (STN: 10666-1.0-00 [159068]) simulations associated with the different conceptual transport models illustrate how the appropriate conceptual transport model can be best determined by comparing the responses of the nonsorbing tracers with different diffusion coefficients for each of the different rest periods. The differences in the responses of the tracers with different diffusion coefficients as a function of rest period can provide information on the relative volumes of flowing and stagnant water in the system, which is very important for determining the ability of the alluvium to attenuate the transport of nonsorbing radionuclides. The MULTRAN simulations also illustrate how cation responses (both injected and exchanged cations) could potentially provide useful information on CEC and, hence, cation sorption in the system. The flow system parameters that were assumed for the three different conceptual models are listed in Table 6.5-1. Other input parameters that do not pertain to the flow system are listed in Table 6.5-2.

Figure 6.5-2 illustrates the tracer responses that can be expected in each of the three tracer tests if an homogeneous single-porosity medium is assumed (conceptual model of Figure 6.5-1a). Only one response is shown because there is no difference between the predicted responses of the nonsorbing tracers of different diffusion coefficients or the predicted responses after the different rest periods. Although not shown in Figure 6.5-2, there is also no change in predicted tracer concentrations immediately after a flow interruption. The lack of a difference between tracers, and between tracer responses for different rest periods, as well as the lack of a response after a flow interruption are all indications of very little or no diffusive mass transfer in the flow system.

Table 6.5-1. Flow System Parameters Used in the Single-Well Simulations

Parameter	Figure 6.5-1a Model	Figure 6.5-1b Model	Figure 6.5-1c Model
Porosity in advective layers	0.25	0.25	0.25
Porosity in nonadvective layers	N/A	N/A	0.25
Porosity of grains	N/A	0.15	N/A
Width of advective layers (cm)	N/A	N/A	10.0
Width of nonadvective layers (cm)	N/A	N/A	24.0
Grain diameter in advective layers (mm)	N/A	3.0 (2.2) [(b)]	N/A
Grain diameter in nonadvective layers (mm)	N/A	N/A	N/A
Halide diffusion coefficient in advective Layers (cm^2/sec) [(a)]	N/A	3×10^{-6}	3×10^{-6}
Halide diffusion coefficient in nonadvective layers (cm^2/sec) [(a)]	N/A	N/A	1×10^{-6}
Halide diffusion coefficient in grains (cm^2/sec) [(a)]	N/A	1×10^{-6}	N/A
Drift velocity (cm/sec)	0 [(c)]	0 [(c)]	0 [(c)]

Output DTN: LA0303PR831231.001.

NOTE: (a) The FBA diffusion coefficient is always assumed to be one-third of the halide diffusion coefficient (Section 6.3.8).

(b) The number in parentheses is the standard deviation of ln (diameter) used for a lognormal distribution of grain sizes in one set of simulations (see text).

(c) Drift velocity is assumed to be zero because of the small apparent hydraulic gradient in the vicinity of NC-EWDP-19D/D1.

Table 6.5-2. Non-Flow-System Input Parameters for the Single-Well Simulations

Parameter	Value
Volume of injection interval (including gravel pack) (L)	500
Radius of gravel pack (cm)	18
Duration of injection pulse (hr)	3
Duration of chase (hr)	28
Flow interruption duration (zero-rest-period test only) (hr)	24
Flow rate during injection and pumping (L/min [gpm])	~57 (~15)

Output DTN: LA0303PR831231.001.

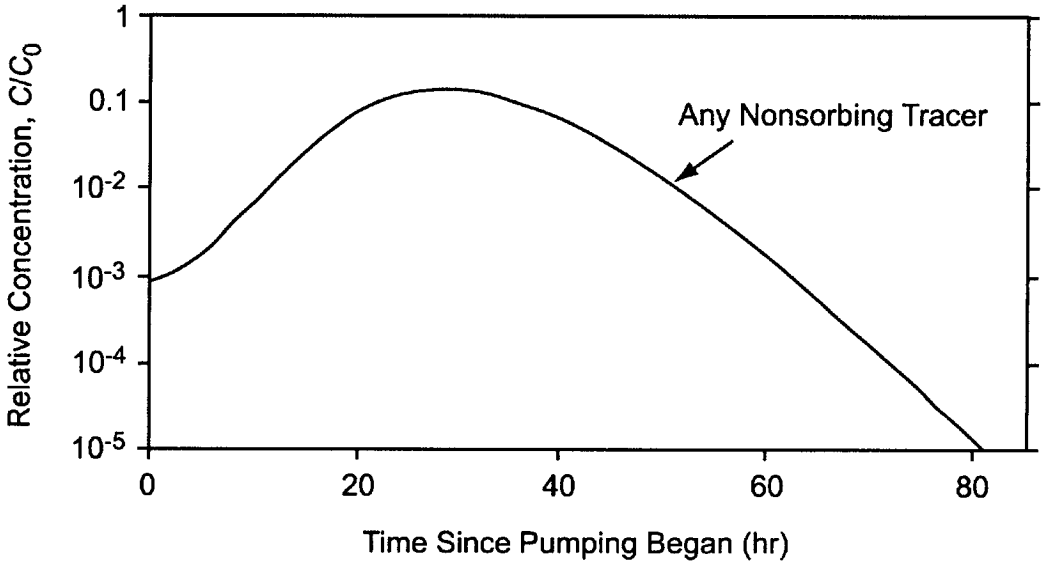

Output DTN: LA0303PR831231.001.

Figure 6.5-2. Normalized Concentration Response of Any Nonsorbing Tracer in a Single-Well Test in a Porous Medium with No Diffusive Mass Transfer and/or No Stagnant Water (the conceptual model of Figure 6.5-1a).

Figure 6.5-3 shows the tracer responses (normalized to injection concentrations) that can be expected in each of the three single-well tracer tests if a homogeneous system with porous grains is assumed (conceptual model of Figure 6.5-1b). In this case, a uniform grain diameter of 3 mm was assumed, which corresponds to the mass-weighted mean diameter of the material collected from four different intervals in 19P. A mass-weighted mean diameter was used because tracer storage capacity in grains is proportional to mass, not number of grains. Cuttings collected from 19D (D1) were not used for grain-size analysis because the mud-rotary-drilling method used in this hole tended to truncate the upper and lower ends of the size range. Figure 6.5-3 shows that there is a slight difference in the responses of the halide and FBA in each test, with the halide having a slightly higher peak concentration and a shorter tail than the FBA. These differences qualitatively indicate that there is some diffusion into stagnant water in the system. However, the fact that the halide has a higher peak concentration and a shorter tail than the FBA indicates that the characteristic diffusion lengths must be relatively short. Both tracers effectively diffused throughout the grains during the time that they were injected and chased into the system, so the responses primarily reflect the diffusion rates of the tracers back out of the grains, which is faster for the halide. The tracer mass recoveries (not presented) were very high (over 95%) in all of these simulations, with the recoveries of the two tracers being essentially the same at the end of the simulations. The halide initially had a higher recovery than the FBA (during the peak) because it diffused more rapidly out of the grains, but the FBA recovery approached that of the halide as pumping continued into the tails of the responses. Given a long enough pumping period, the recoveries of both tracers would have approached 100%.

Another indication of the short diffusion lengths is the lack of an increase in tracer concentrations after the flow interruption in the test with no rest period. If a significant amount of tracer remained in the grains at the time of the flow interruption, an increase in concentration would be expected upon resumption of flow due to the tracer diffusing out of the grains during the rest period. An additional indication of the relatively short diffusion distances in the system is the fact that both the halide and the FBA have essentially the same response in the 2-day rest period test as the 30-day rest period test. This result suggests that the tracers were able to effectively diffuse throughout the grains during the 2-day rest period so that very little additional diffusion occurred during the 30-day rest period.

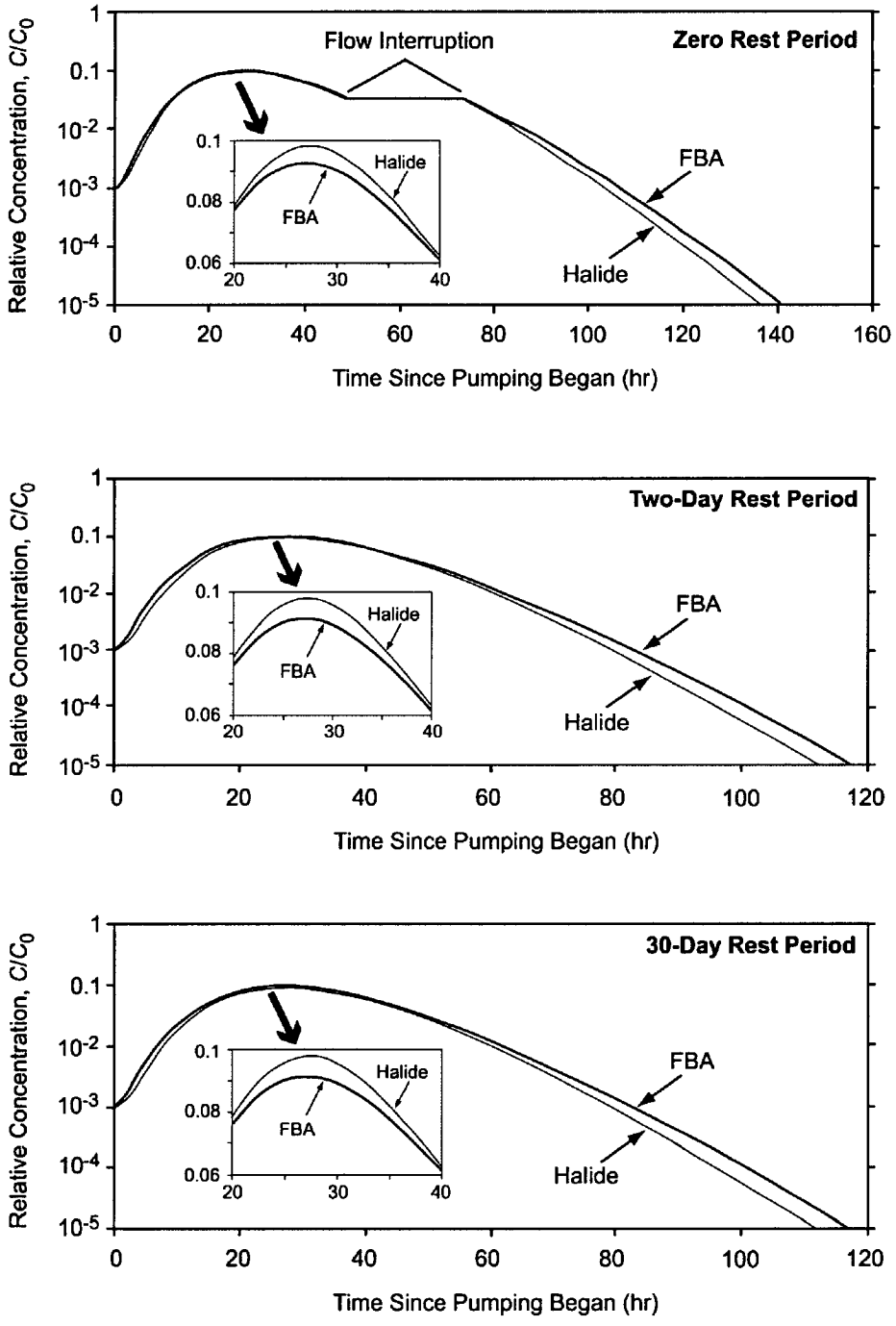

Output DTN: LA0303PR831231.001.

NOTE: The rest periods are zero (top), 2 days (middle), and 30 days (bottom); a 3-mm fixed grain diameter was used. X axis extends to 160 hr for zero-rest-period test because of 24 hours flow interruption.

Figure 6.5-3. Normalized Concentration Responses of a Halide and a FBA in Single-Well Tests for the Conceptual Transport Model of Figure 6.5-1b Using a Fixed Grain Diameter

Figure 6.5-4 shows the measured grain-size distribution of the material collected from 19P. A qualitative fit of a lognormal distribution to the data is also shown. Clearly, there is a relatively wide distribution of grain sizes that are not accounted for when a single mean grain size is assumed, as in the simulations that generated the tracer responses shown in Figure 6.5-3. Figure 6.5-5 shows the results of incorporating the lognormal distribution of grain sizes shown in Figure 6.5-4 into the MULTRAN V 1.0 (STN: 10666-1.0-00 [159068]) simulations. The only difference between Figures 6.5-3 and 6.5-5 is that the grain size in the former is uniform (equal to the mean), whereas in the latter, it is varied over the lognormal distribution of Figure 6.5-5. It is apparent that the inclusion of larger grain sizes in the simulations greatly increases the length of the tails of both tracers. Additional simulations confirmed that the elimination of the smaller grain sizes in the lognormal distribution had very little effect on the tracer responses. The increase in the lengths of the tails is a result of the greater diffusion distances associated with the larger grains. Because of the greater distances, it takes longer for the tracer mass to diffuse back out into the advective pathways, resulting in the extended tailing. The longer diffusion distances are also indicated by the noticeable increase in tracer concentrations after the flow interruption in the test with no rest period. Note that in all cases the FBA still has a longer/higher tail than the halide, indicating that the responses are still dominated by diffusion back out of the grains. The mass recoveries of both tracers were slightly lower than in the simulations of Figure 6.5-3 (for the same pumping time). However, by the end of the simulations, both tracer recoveries were well over 95%.

Figure 6.5-6 shows the tracer responses that can be expected in each of the three single-well tracer tests if a layered dual-porosity system is assumed (Figure 6.5-1c). Grains in both the advective and nonadvective regions were assumed to be nonporous for these simulations. The differences in the responses of the halide and the FBA in the tests and the fact that the peak concentrations decrease while the lengths of the tails increase as the rest period increases all indicate relatively long diffusion lengths. However, in contrast to the results shown in Figures 6.5-3 and 6.5-5, the FBA has a higher peak concentration and a shorter/lower tail than the halide during the pumpback phase. This result is primarily due to the relatively wide advective flow pathways (10 cm), which tracers can only slowly diffuse out of because of the long distance to the nonadvective region. It is the slower diffusion of the FBA out of these advective pathways that is primarily responsible for the higher peak concentrations and lower tails of the FBA relative to the halide.

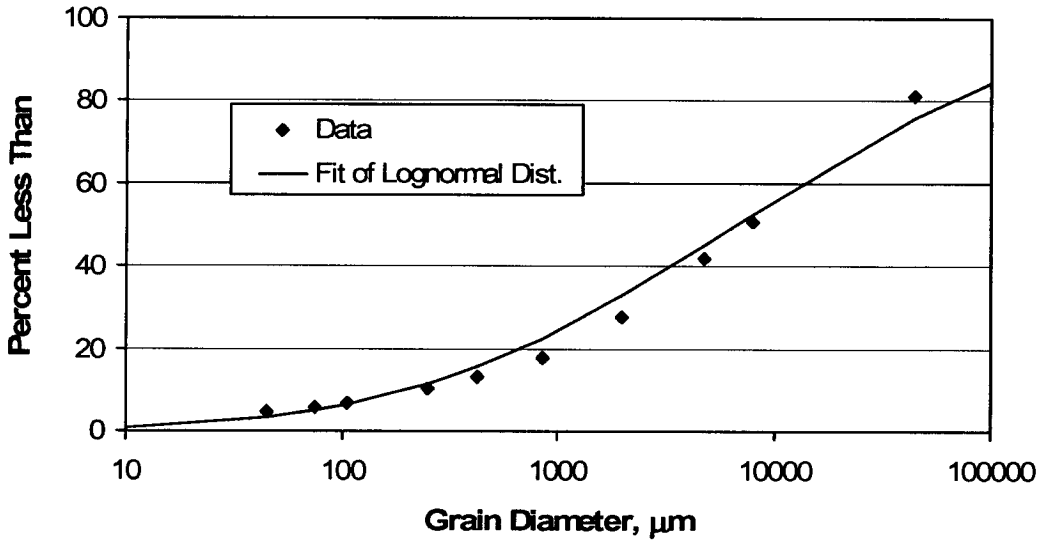

DTN: LA0201JS831421.001 [162613].

NOTE: The above data are a composite of four depth intervals.

Figure 6.5-4. Measured and Fitted Grain Size Distributions from NC-EWDP-19P

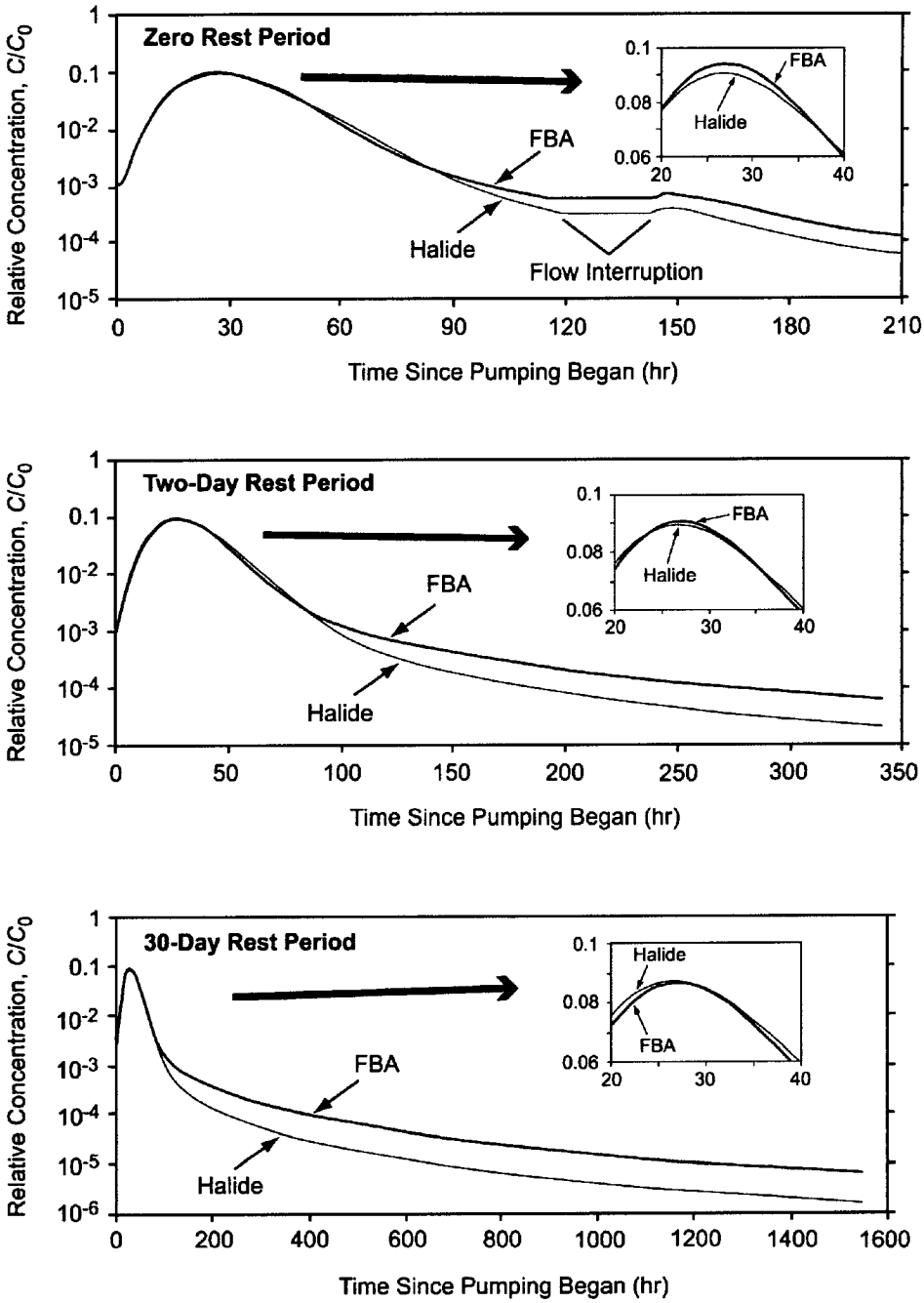

Output DTN: LA0303PR831231.001.

NOTE: The rest periods are zero (top) days, 2 days (middle), and 30 days (bottom); a mean grain diameter of 3 mm was used with a standard deviation for ln (diameter) of 2.2. X axes have different scales to reflect the different pumping durations planned for the three tests.

Figure 6.5-5. Normalized Concentration Responses of a Halide and a FBA in Single-Well Tests for the Conceptual Transport Model of Figure 6.5-1b Using a Grain Size Distribution

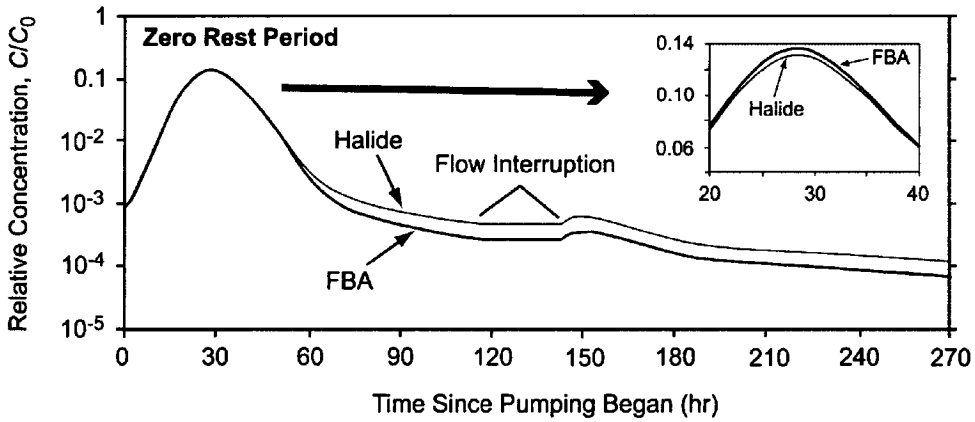

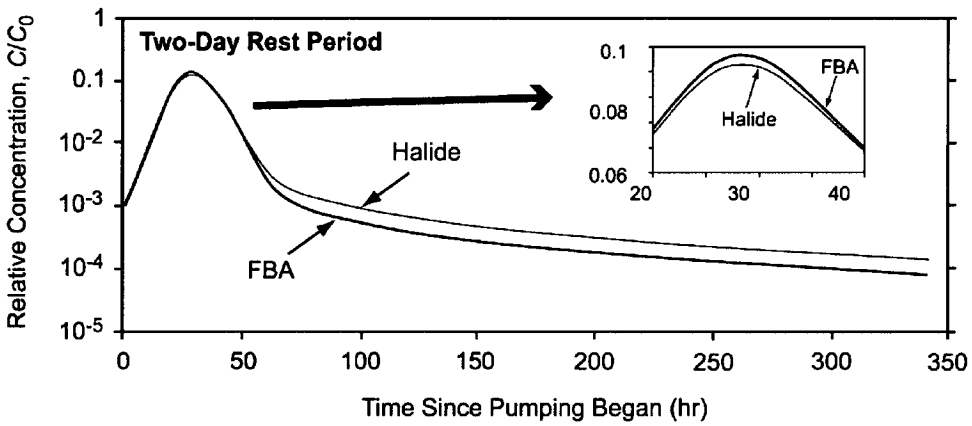

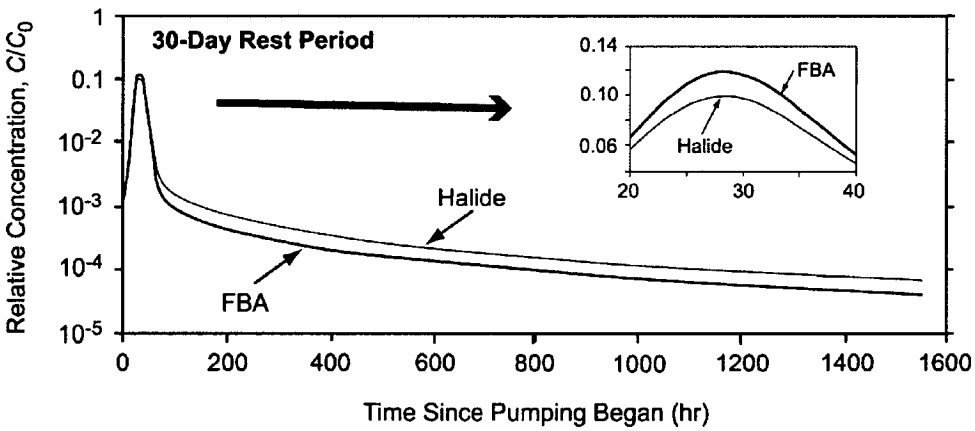

Output DTN: LA0303PR831231.001.

NOTE: The rest periods are zero (top) days, 2 days (middle), and 30 days (bottom). X axes have different scales to reflect the different pumping durations planned for the three tests.

Figure 6.5-6. Normalized Concentration Responses of a Halide and an FBA in Single-Well Tests for the Conceptual Transport Model of Figure 6.5-1c

The value of comparing the responses of the FBA and halide to help distinguish between alternative conceptual models is made apparent in Figure 6.5-7, which shows the simulated responses of the FBA in the 2-day-rest period tests with the diffusion-into-grains model (Figure 6.5-5) and the diffusion-into-layers model (Figure 6.5-6). Other than a slightly broader peak in the diffusion-into-grains response (which could be attributed to hydrodynamic dispersion or tracer drift with the natural gradient), the two responses are very similar, and it would be difficult to distinguish between the two models on the basis of either one of these responses alone. However, by knowing whether the halide has a higher or lower tail, it will be possible to make a distinction between the models. The additional information obtained from the test with a longer rest period will also help in making this distinction. Also, quantitative estimates of diffusive mass-transfer rates and diffusion distances can be best made using the MULTRAN V 1.0 (STN: 10666-1.0-00 [159068]) model to fit simultaneously the tracer responses from each test with the constraint that the halide has a factor-of-three larger diffusion coefficient than the FBA.

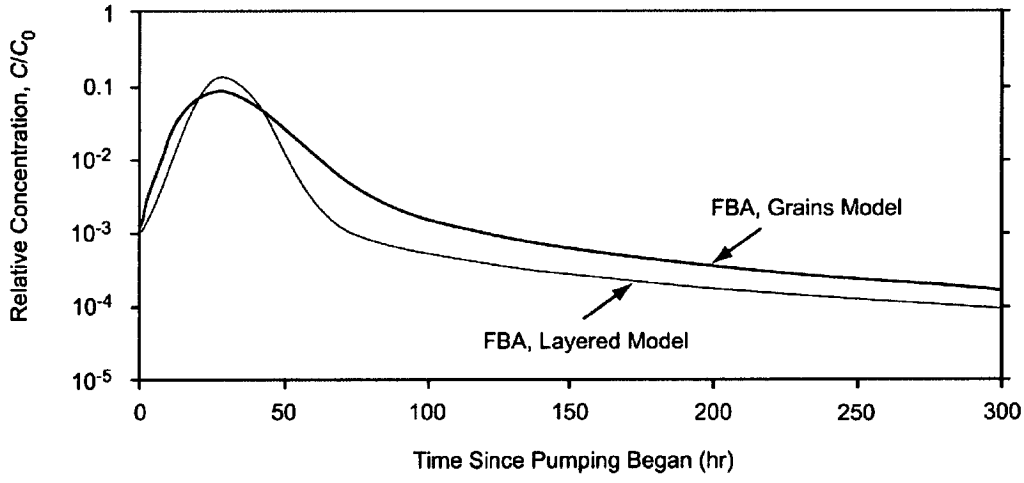

Output DTN: LA0303PR831231.001.

NOTE: The rest period was 2 days.

Figure 6.5-7. Comparison of FBA Responses for the Layered Conceptual Model (Figure 6.5-1c) and the Grain-Diffusion Model (Figure 6.5-1b) with a Lognormal Distribution of Grain Sizes

Table 6.5-3 summarizes the tracer-response characteristics from single-well tracer tests that are consistent with the different conceptual transport models of Figure 6.5-1, including a diffusion-into-grains model (Figure 6.5-1b) with a relatively wide distribution of grain sizes (see Figure 6.5-4 and 6.5-5). This table serves as a guide for how the appropriate conceptual transport model can be identified from the qualitative nature of the tracer responses in the three planned single-well tracer tests.

Table 6.5-3. Single-Well Tracer Test Response Characteristics that are Consistent with the Conceptual Models of Figure 6.5-1

Conceptual Model	Single-Well Tracer Test Response Characteristics
Single-Porosity (Figure 6.5-1a)	• All nonsorbing tracers have the same normalized concentration responses • Response curves are independent of rest period (unless there is significant tracer drift during the rest period, but even then, there will be little or no difference in the response curves of different nonsorbing tracers) • No increase in tracer concentrations after a flow interruption in the tail of the response curves
Diffusion into Small Grains —Short Diffusion Distances (Figure 6.5-1b)	• Tracer with larger diffusion coefficient will tend to have higher peak concentration and lower tail concentration than tracer with smaller diffusion coefficient • Relatively minor differences in response curves of each individual tracer as a function of rest period (unless there is significant tracer drift during the rest period) • Relatively minor increase in tracer concentrations after a flow interruption in the tail of the response curves
Diffusion into Variable-Sized Grains—Combination of Short and Long Diffusion Distances, but Relatively Narrow Advective Flow Pathways (Figure 6.5-1b, with grain size distribution of Figure 6.5-4)	• Either tracer (large or small diffusion coefficient) could have the higher peak concentration, with the larger diffusion coefficient tracer tending to have the higher peak concentration as grain sizes decrease or rest periods increase • Tracer with smaller diffusion coefficient will tend to have the higher concentration in the tails of the responses • Noticeable differences in response curves of each individual tracer as a function of rest period, with longer, higher tails as rest period increases • Significant increase in tracer concentrations after a flow interruption in the tail of the response curves
Diffusion into Layers— Long Diffusion Distances and Relatively Wide Advective Flow Pathways (Figure 6.5-1c)	• Tracer with smaller diffusion coefficient will tend to have higher peak concentration and lower tail concentration than tracer with larger diffusion coefficient • Significant differences in response curves as a function of rest period, with longer, higher tails as rest period increases • Significant increase in tracer concentrations after a flow interruption in the tail of the response curves

Output DTN: LA0303PR831231.001.

NOTE: The characteristics in this table apply when tracer concentrations are normalized to injection concentrations.

Although sorption parameters for sorbing tracers are much more easily obtained from cross-hole tracer tests, Figure 6.5-8 shows how information on cation sorption can also be obtained from a single-well tracer test. In this case, the counter-cation (assumed to be potassium ion) injected with the nonsorbing anion tracers exchanges with sodium and calcium, the two predominant cations in the system. The potassium ion initially responds more quickly than the nonsorbing anions because it traveled a shorter distance into the system during injection (due to ion exchange). This behavior results in an initial depression of the sodium and calcium concentrations because they displace potassium as the system is pumped back and also because

charge balance must be maintained. As the anions respond, the concentrations of sodium and calcium increase and peak at the same time as the anions. In principle, the magnitude of the fluctuations of the sodium and calcium concentrations, as well as the response of the counter-cation, can provide qualitative estimates of ion-exchange parameters for the counter-cation in the system.

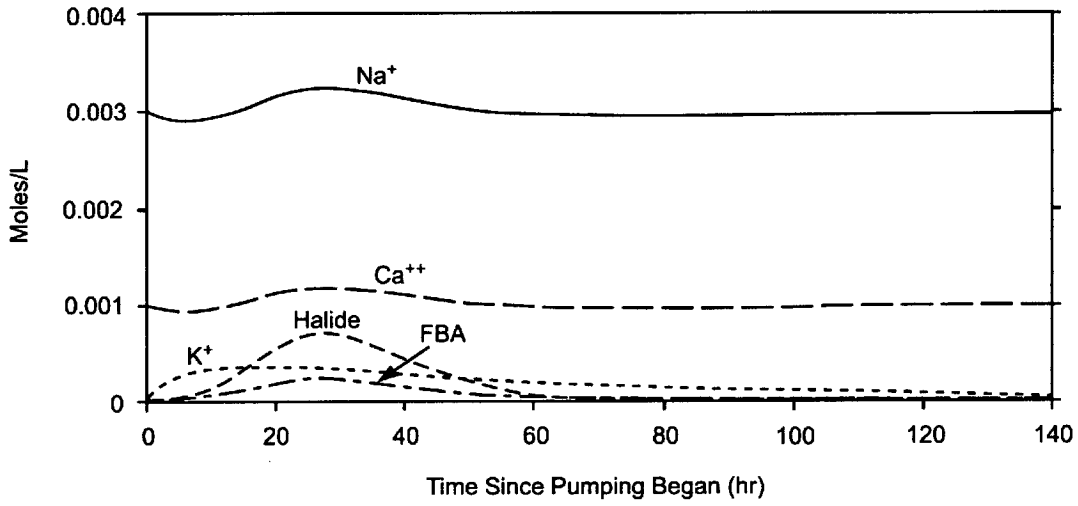

Output DTN: LA0303PR831231.001.

NOTE: The Na^+ and Ca^{++} responses are the result of cation exchange with K^+.

Figure 6.5-8. Molar Responses of Injected Tracers (K^+, halide, FBA) and Naturally Occurring Cations (Na^+ and Ca^{++}) in the 2-Day-Rest-Period Test Assuming the Model of Figure 6.5-1b

6.5.3 Pre-Test Predictions of Cross-Hole Tracer Test Responses

After the single-well tracer tests were completed, Nye County drilled two additional wells (NC-EWDP-19IM1 and NC-EWDP-19IM2, known as 19IM1 and 19IM2) in the immediate vicinity of 19D1 to allow for cross-hole hydraulic and tracer testing. These wells were completed similarly to 19D1 so that they could be used interchangeably as production, injection, or observation wells. Cross-hole tracer tests were to be conducted immediately after cross-hole hydraulic testing was completed (Section 6.4.2). However, water discharge and tracer injection permits issued by the State of Nevada were rescinded before tracer testing could be initiated.

In lieu of presenting results from the planned cross-hole tracer tests, this section provides a summary of the plans for testing as well as pre-test predictions of tracer responses in the cross-hole tests, with emphasis on (1) expected tracer arrival times under various assumptions, and (2) predicted lithium transport behavior given results of lithium sorption testing onto alluvium in the laboratory. The pre-test predictions served to satisfy environmental permitting requirements and address a key technical issue (KTI) raised by the NRC (KTI RT 2.04).

The cross-hole tracer tests were expected to provide additional information on diffusive mass-transfer properties and the appropriate conceptual transport model for the saturated valley-fill system. They were also expected to provide field estimates of several transport parameters for performance-assessment calculations that cannot be obtained from single-well tracer testing, including effective flow porosity, longitudinal dispersivity, sorption parameters, and colloid transport parameters. Because sorbing radionuclides of interest to Yucca Mountain performance assessments cannot be used in field tests, sorption parameters were to be obtained for a weakly sorbing cation tracer, lithium ion. Although lithium transport is not of immediate interest to the project, its field-sorption behavior was to be compared to its laboratory-sorption behavior to determine whether laboratory-derived parameters provide reasonable estimates of field-scale retardation. If that proved to be the case, or if the laboratory parameters resulted in underestimation of field-scale sorption, the Project would gain credibility in its approach of using laboratory-derived radionuclide sorption parameters in performance-assessment calculations. On the other hand, if the field transport behavior of lithium indicated that lithium was sorbing less than predicted from laboratory experiments, then conceptual models and parameterizations of radionuclide sorption might have to be revisited to account for differences between lab and field observations.

Cross-hole testing would have involved the simultaneous injection of several tracers into a screened interval of one well while a nearby well was continuously pumped. The plan was to establish a partial-recirculation flow pattern between the injection well and the production well prior to tracer injection and then maintain that recirculation pattern for at least one month after the injection. Partial recirculation means that a portion of the produced water would be recirculated into the injection well. This type of flow pattern ensures that the injected tracers are pushed out into the formation and do not linger in the injection well, which would result in biased estimates of transport parameters.

The tracer mixture would have included two nonsorbing solute tracers (probably bromide ion and an FBA), a weakly sorbing tracer (lithium ion), and at least one type of polystyrene microsphere as a colloid tracer. The sorption parameters for lithium and filtration parameters for the microspheres were to be determined by comparing the cross-hole responses of these tracers to that of the two nonsorbing solutes.

Cross-hole tracer-test predictions were conducted primarily to estimate how long a cross-hole test may take to conduct for scheduling and budgeting reasons. However, pre-test predictions were also a requirement imposed by the State of Nevada to obtain an environmental permit for tracer injections. Emphasis was placed on the sensitivity of the predictions to variables such as interwell separation, interval thickness, flow porosity, production rate, longitudinal dispersivity, 2-D vs. 3-D flow conditions, and most importantly, lithium sorption parameters. 2-D flow conditions refers to a situation where a well fully penetrates a confined aquifer and, therefore,

there is no flow in the vertical direction, whereas 3-D flow conditions refer to a situation in which a well is open to only a small fraction of the thickness of an aquifer so that flow occurs in all three dimensions without being influenced by upper and lower boundaries (e.g., confining layers). These represent two extremes of flow conditions (in a homogeneous, isotropic medium) with respect to cross-hole tracer travel times.

Many of these sensitivities can be effectively captured using a simple analytical expression for nonsorbing tracer travel times in radial convergent flow to a pumping well in a 2-D homogeneous, isotropic medium (i.e., a rearrangement of Equation 10) (Guimera and Carrera 2000 [156830], Equation 6):

$$\tau = \frac{\eta \pi r_L^2 T}{Q} \qquad \text{(Eq. 52)}$$

where

τ = mean travel time, hr

η = effective flow porosity

r_L = distance between injection and production wells, m

T = formation thickness, m

Q = production flow rate, m^3/hr.

Of course, any real flow system will never be completely homogeneous or isotropic, but this equation serves as a useful starting point for estimating travel times. It is clear that, all other things being equal, mean travel times will vary linearly with effective flow porosity and formation thickness, with the square of the distance between wells, and inversely with the production flow rate. Equation 52 does not account for any delays associated with diffusion into stagnant water in the system, although these delays are not expected to affect first arrival times and peak arrival times of tracers significantly in the valley-fill deposits, which are of greater practical interest than the mean arrival time.

The first arrival times and peak arrival times of tracers were estimated as a function of mean travel time and dispersivity using the RELAP V 2.0 computer code (STN: 10551-2.0-00 [159065]). A set of response curves showing the effect of dispersivity (or, more specifically, Peclet number, which is equal to the travel distance/dispersivity) on the first and peak arrival times for a given mean tracer residence time is shown in Figure 6.5-9. The ratio of first arrival time to mean arrival time and the ratio of peak arrival time to mean arrival time were both found to have a relatively smooth dependence on the Peclet number of the system. By obtaining a polynomial fit to these ratios as a function of Peclet number, the first and peak arrival times could be estimated from the mean arrival time obtained from Equation 52 for any assumed value of dispersivity. Plots of these ratios and the polynomial fits as a function of Peclet number are shown in Figure 6.5-10.

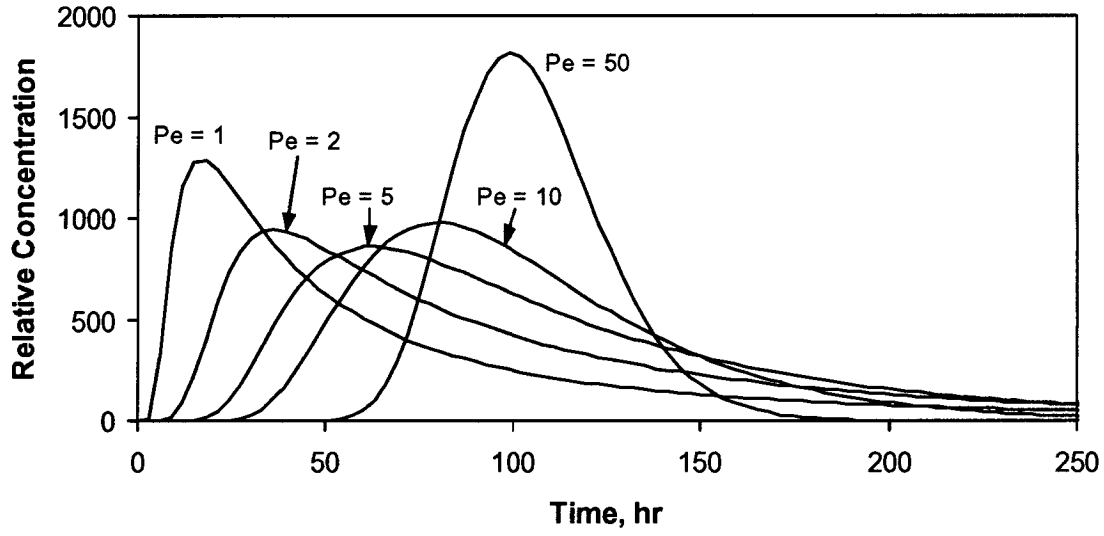

Output DTN: LA0303PR831231.004.

NOTE: Peclet number is travel distance/dispersivity; mean arrival time is 100 hr; and flow is assumed to be linear, not radial.

Figure 6.5-9. Relative Responses in a Single-Porosity Medium to a Pulse Function Input for Different Peclet Numbers

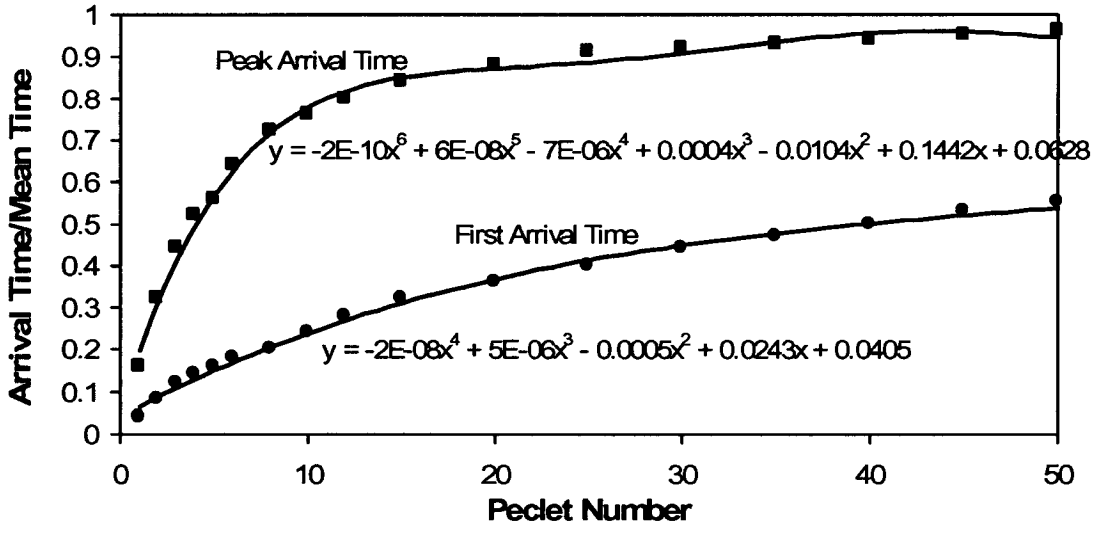

Output DTN: LA0303PR831231.004.

NOTE: Equations are polynomial fits to the "data." First arrival time is defined as the arrival time corresponding to 1% of the peak concentration.

Figure 6.5-10. Ratios of First Arrival Time to Mean Arrival Time and Peak Arrival Time to Mean Arrival Time for Different Peclet Numbers

To obtain estimates of the mean, first, and peak arrival times for a sorbing tracer, the corresponding arrival times for a nonsorbing tracer can be multiplied by the retardation factor, R, given by (Freeze and Cherry 1979 [101173], p. 404, Equation 9.14):

$$R = 1 + \frac{\rho_B}{\phi} K_d \qquad \text{(Eq. 53)}$$

where

K_d = linear partition coefficient, mL/g

ρ_B = bulk density of medium, g/cm^3

ϕ = porosity of medium

To obtain an estimate of travel times in an unbounded 3-D flow system, the 2WELLS_3D V 1.0 computer code was used (STN: 10667-1.0-00 [159036]). 2WELLS_3D is a particle-tracking code that simulates tracer transport between two wells in a homogeneous, isotropic medium. It assumes that flow streamlines between the injection and production well follow trajectories given by the prolate spheroidal coordinate system, shown in Figure 6.5-11. This coordinate system reduces to spherical coordinates in the limit of $a = 0$ (i.e., a point source instead of a line source). A number of 2WELLS_3D simulations with zero dispersion were conducted to determine mean nonsorbing tracer residence times as a function of the ratio of well separation to interval length (i.e., length of screen or gravel pack). Because 2WELLS_3D superimposes tracer movement (as particles) onto an analytical solution of the 3-D flow field, there is effectively no numerical dispersion in the simulated tracer responses. In the limit of a very large interval length relative to well separation, the arrival times approached those given by Equation 52 for radial flow in cylindrical coordinates; and in the limit of a very small interval length relative to well separation, the arrival times approached what would be expected for spherical flow (derivation found in Reimus 2003 [165129], pp. 116 to 122):

$$\tau = \frac{4\eta\pi r_L^3}{3Q} \qquad \text{(Eq. 54)}$$

where the symbols are defined the same as in Equation 52.

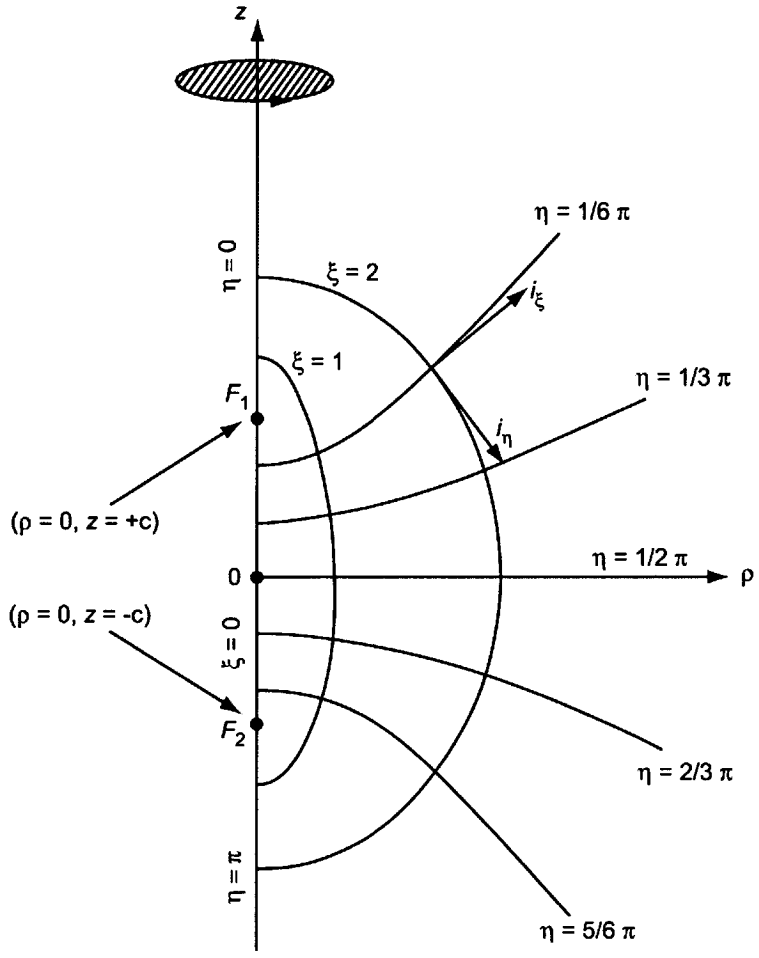

Source: Happel and Brenner (1965 [156833], Appendix A, Figure A-17.1(a)).

NOTE: η and ξ are coordinate designations by Happel and Brenner; they have no relation to η and ξ elsewhere in this report.

Figure 6.5-11. Prolate Spheroidal Coordinate System Used for Unbounded 3-D Flow and Transport Calculations Using the 2WELLS_3D Code

The ratio of mean arrival time in unbounded 3-D flow to mean arrival time in 2-D flow was found to have a relatively smooth dependence on the ratio of well separation to interval length. This dependence and a piecewise fit to the simulated data are shown in Figure 6.5-12. Using the piecewise fit, it was possible to "correct" the mean arrival times obtained from Equation 52 to obtain corresponding arrival times for unbounded 3-D flow. The relationship shown in Figure 6.5-12 was obtained from 2WELLS_2D V 1.0 (STN: 10665-1.0-00 [159067]) and 2WELLS_3D V 1.0 (STN: 10667-1.0-00 [159036]) simulations, assuming zero longitudinal and transverse dispersivity. However, the same correction factors were assumed to apply to the first and peak arrival times in cases where the dispersivity was not zero.

A final "correction" applied to the calculations described above was to account for shifts in first and peak tracer arrival times due to recirculation of produced water. Recirculation establishes a dipole flow pattern (Figure 6.5-13) that causes some of the tracer mass to arrive earlier and some later than in the case of no recirculation. A correction factor for various recirculation ratios (ratios of recirculation flow rate to production flow rate) was obtained by simulating a series of tracer responses with different recirculation ratios using the 2WELLS_2D V 1.0 code (STN: 10665-1.0-00 [159067]). This code is very similar to the 2WELLS_3D V 1.0 code (STN: 10667-1.0-00 [159036]) except that it simulates cross-hole responses in two-dimensional (2-D) flow using a cylindrical coordinate system instead of three-dimensional (3-D) flow. These simulations assumed no longitudinal or transverse dispersion, so the travel-time shifts reflected only the changing flow patterns. As in the case of 2WELLS_3D, 2WELLS_2D superimposes tracer movement (as particles) onto an analytical solution of the 2-D flow field, so there is effectively no numerical dispersion in the simulated tracer responses. A subset of the resulting response curves is shown in Figure 6.5-14. In reality, the response curves for the larger amounts of recirculation (greater than about 20%) should all have multiple tracer peaks that are equally spaced in time due to tracer recirculation. However, all but the first peak for each response curve was suppressed from the 2WELLS_2D output to clarify Figure 6.5-14. With typical amounts of dispersion, these secondary peaks would be highly damped relative to the first peak anyway. Note that because there was no dispersion assumed for the simulations associated with Figure 6.5-14, the first and peak arrival times nearly coincide. The correction factor for both first arrival times and peak arrival times was taken to be the ratio of peak recirculation arrival time to the peak arrival time without recirculation. These correction factors as a function of recirculation ratio, as well as a polynomial fit to the simulated data, are plotted in Figure 6.5-15.

The methods described above for estimating first and peak arrival times while accounting for dispersion, sorption, unbounded 3-D flow, and recirculation ratio in cross-hole tracer tests are amenable to simple spreadsheet calculations once adequate expressions/fits are obtained for the dependence of the correction factors on the appropriate input parameters. A Microsoft Excel spreadsheet was set up for this purpose (Output DTN: LA0303PR831231.001). It should be noted that the spreadsheet calculations assume that the correction factors are linearly independent and commutative. That is, corrections are made by multiplying the mean arrival time (given by Equation 52) by each of the appropriate correction factors for a given set of test conditions.

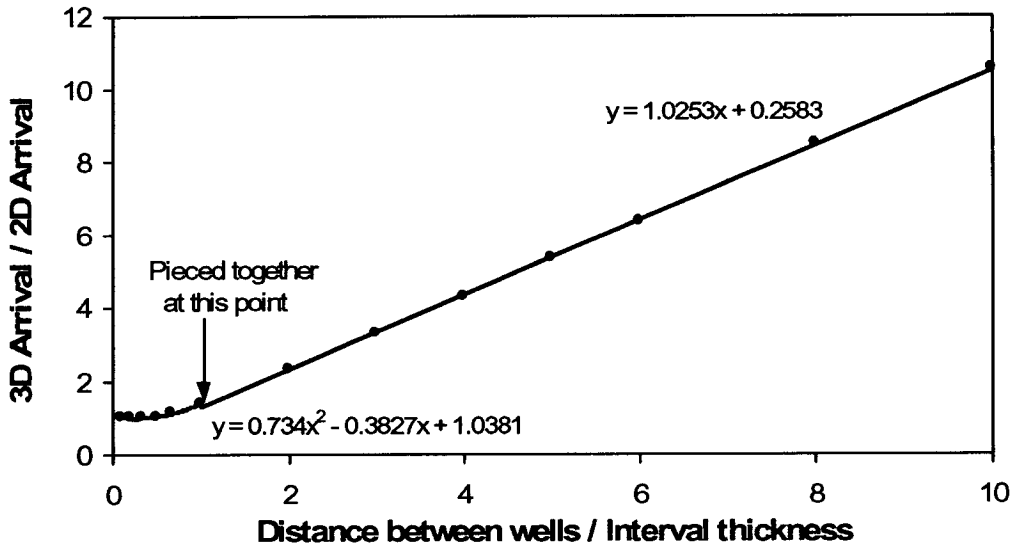

Output DTN: LA0303PR831231.004.

NOTE: A piecewise polynomial fit to the "data" is shown.

Figure 6.5-12. Ratio of Mean Arrival Time in Unbounded 3-D Flow to Mean Arrival Time in 2-D Flow as a Function of Distance Between Wells Divided by Interval Thickness

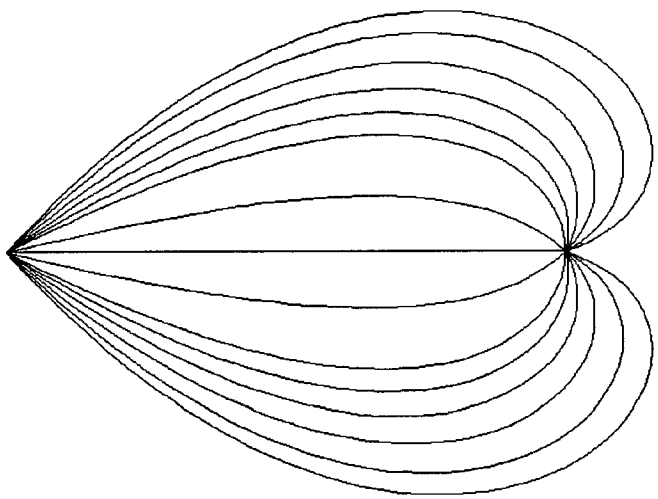

For illustration purposes only

NOTE: In the above pattern, the injection well is on the right, the production well is on the left, and the injection flow rate is 30% of the production flow rate. A homogeneous isotropic medium is assumed.

Figure 6.5-13. Tracer Streamlines in a Weak Dipole Flow Pattern

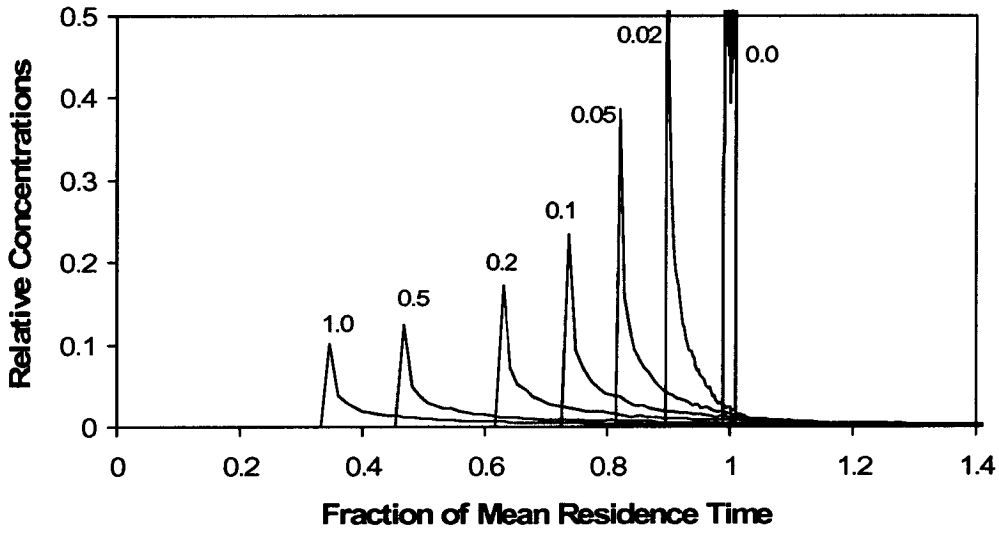

Output DTN: LA0303PR831231.004.

NOTE: The numbers next to the curves above are the recirculation fractions; local dispersivity was set equal to zero; and secondary tracer peaks associated with tracer recirculation are not shown. The sharp early arrivals occur because of the zero longitudinal and transverse dispersion assumed in the simulations. The long tails are the result of a small number of flow streamlines having very long residence times.

Figure 6.5-14. Predicted Nonsorbing Tracer Responses in a 2-D Homogeneous Isotropic Medium as a Function of the Recirculated Fraction of Produced Water

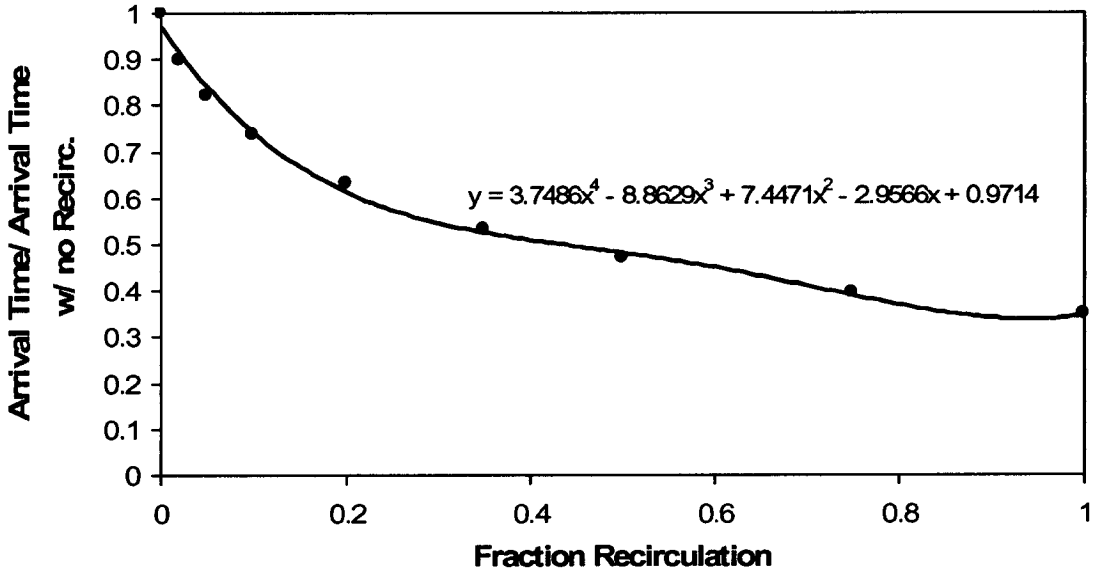

Output DTN: LA0303PR831231.004.

Figure 6.5-15. Tracer Arrival Times as a Function of Fraction Recirculation in a 2-D Homogeneous Isotropic Medium

A final feature added to the Excel spreadsheet was the propagation of uncertainties of two key input parameters: flow porosity and well separation. Flow porosity is an uncertain parameter because it is an unknown property of the flow system, and well separation is uncertain because of vertical deviations that can occur during well drilling, which can result in significantly different separations at depth than planned. The propagation of these uncertainties was accounted for using standard error propagation methods and assuming that the uncertainties were not correlated (i.e., linearly independent). Without derivation, when these methods are applied to Equation 52, they yield the following result for the relative standard deviation of the travel time of a nonsorbing tracer as a function of standard deviation of the flow porosity and well separation (flow derivation found in Reimus 2003 [165129]):

$$\frac{\sigma_\tau}{\tau} = \sqrt{\frac{\sigma_\eta^2}{\eta^2} + 4\frac{\sigma_{r_L}^2}{r_L^2}} \qquad \text{(Eq. 55)}$$

where

σ_i = standard deviation of variable i

τ = mean residence time, hr

η = flow porosity

r_L = well separation, m.

To provide a measure of travel time uncertainties, the Excel spreadsheet calculates mean, first, and peak tracer travel times associated with $\pm \sigma_\tau \tau$ (i.e., travel times that are plus and minus one standard deviation from the best estimate).

An additional parameter of considerable uncertainty is the K_d sorption parameter for sorbing tracers. However, a formal propagation of uncertainty calculation for this parameter was not included in the spreadsheet. Rather, it is left to the analyst to evaluate this uncertainty by manually entering different K_d values and determining what effect these have on predicted travel times.

As mentioned at the beginning of this section, all simulations using the RELAP V 2.0 (STN: 10551-2.0-00 [159065]), 2WELLS_2D V 1.0 (STN: 10665-1.0-00 [159067]), and 2WELLS_3D V 1.0 (STN: 10667-1.0-00 [159036]) codes assumed a single-porosity system with no diffusive mass transfer into nonadvective water. Two sets of paired MULTRAN V 1.0 (STN: 10666-1.0-00 [159068]) simulations were conducted to illustrate the impact of relaxing this assumption on predicted cross-hole responses. One set used sorption parameters corresponding to the strongest lithium sorption that has been observed in laboratory batch sorption tests with 19P or 19D material, and the other set used parameters corresponding to the weakest lithium sorption observed. Of the two simulations in each pair, one used parameters corresponding to the single-porosity system for the single-well tracer test simulations (conceptual model of Figure 6.5-1a)

and the other used parameters corresponding to the layered flow system for the single-well simulations (Figure 6.5-1c). The latter system had the greatest predicted mass loss from advective flow pathways of the three conceptual models shown in Figure 6.5-1 in the single-well simulations. The predicted cross-hole responses of a halide, an FBA, and lithium ion for each type of flow system are shown in Figures 6.5-16 and 6.5-17 for the cases of weak and strong lithium sorption, respectively. A mean tracer residence time of 150 hr (for nonsorbing tracers) and a Peclet number of 10 were arbitrarily chosen for the simulations. There was no recirculation in the simulations. The 150-hr mean residence time corresponds to a relatively low effective flow porosity or a relatively high production flow rate in the valley-fill deposits if a well separation of 20 to 25 m is assumed and if the flow intervals are assumed to be 8 to 40 m thick, which is approximately the range of gravel-pack thicknesses in the valley-fill deposits in 19D. Table 6.5-4 provides combinations of flow system parameters and production flow rates that result in mean nonsorbing tracer residence times of 150 hr based on Equation 52.

It is apparent in Figures 6.5-16 and 6.5-17 that the differences in first and peak arrival times of any given tracer as a function of the system conceptualization (single porosity vs. layered system) are trivial. However, the first and peak arrival times for lithium are quite different in the two figures depending on whether weak (Figure 6.5-16) or strong (Figure 6.5-17) sorption is assumed. Also, the tails of the tracer responses are significantly different for the different system conceptualizations because the layered system has a secondary porosity that tracers diffuse into and out of, which results in the long tailing behavior typical of a dual-porosity system. The parameters assumed for the layered system are the same as those listed in Table 6.5-1. The single-porosity system was assumed to have the same geometry and parameters as the layered system except that the nonadvective region was assigned a porosity of zero so that it played no part in tracer transport. The parameters used to describe cation exchange between lithium, sodium, and calcium are listed in the figure captions (see Equations 21 and 22). These parameters are representative of the smallest (Figure 6.5-16) and largest (Figure 6.5-17) amounts of lithium exchange observed in laboratory batch-sorption experiments conducted to date (see Section 6.5.6).

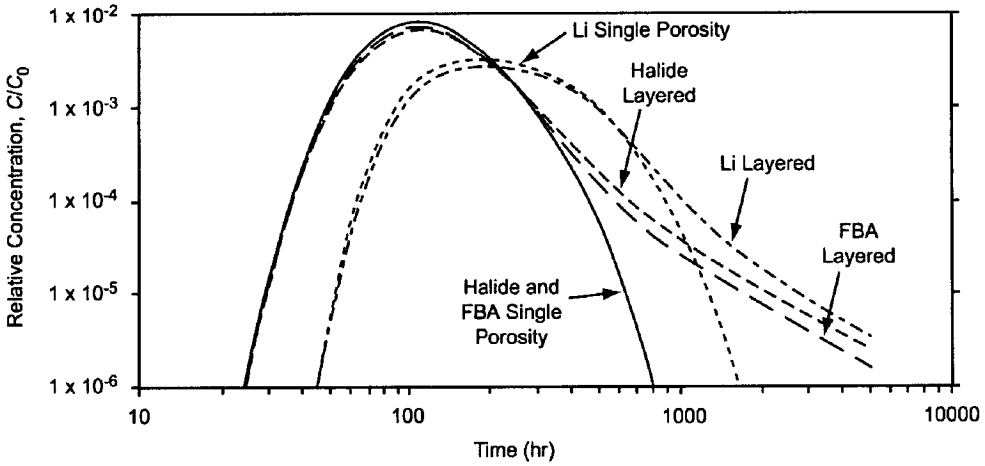

Output DTN: LA0303PR831231.001.

NOTE: Lithium sorption parameters are Q_1 = 0.17, Q_2 = 0.019 L/kg, *CEC* = 0.024 eq/kg (see Equations 21, 22, and 24); the two systems have the same mean tracer residence time of 150 hr; and the peak lithium concentration occurs at about 190 hr, whereas the peak FBA and halide concentrations occur at about 110 hr.

Figure 6.5-16. Predicted Cross-Hole Responses for a Halide, FBA, and Lithium Ion in a Single-Porosity System and a Layered System with Weak Lithium Sorption

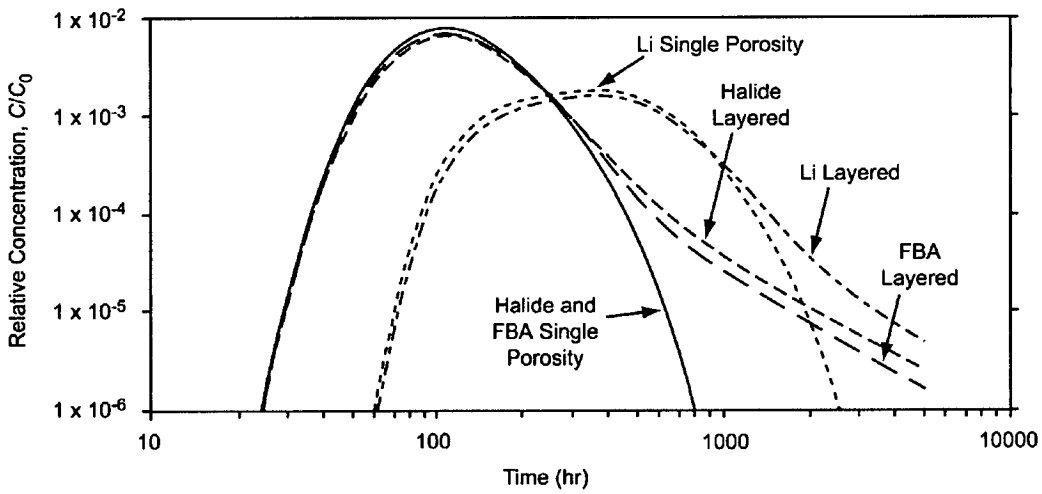

Output DTN: LA0303PR831231.001.

NOTE: Lithium sorption parameters are Q_1 = 0.35, Q_2 = 0.005 L/kg, *CEC* = 0.345 eq/kg (see Equations 21, 22, and 24); the two systems have the same mean tracer residence time of 150 hr; the peak lithium concentration occurs at about 390 hr, whereas the peak FBA and halide concentrations occur at about 110 hr; and the peak lithium concentration is ~1.75 times lower than in Figure 6.5-16.

Figure 6.5-17. Predicted Cross-Hole Responses for a Halide, FBA, and Lithium Ion in a Single-Porosity System and a Layered System with Strong Lithium Sorption

Table 6.5-4. Combinations of Flow-System Parameters and Production Flow Rate that Result in a Mean Nonsorbing Tracer Residence Time of 150 Hours in a Cross-Hole Tracer Test

Well Separation (m)	Interval Thickness (m)	Flow Porosity	Production Flow Rate (L/min [gpm])
25	40	0.1	874 [231]
25	40	0.3	2,619 [692]
20	40	0.1	560 [148]
20	40	0.3	1,677 [443]
25	8	0.1	174 [46]
25	8	0.3	522 [138]
20	8	0.1	114 [30]
20	8	0.3	337 [89]

Output DTNs: LA0303PR831231.004; LA0303PR831231.005.

6.5.4 Results and Interpretation of Single-Well Tracer Tests in Alluvium

Three single-well injection-withdrawal tracer tests were conducted in the saturated alluvium at NC-EWDP-19D1 between December 2000 and April 2001. Detailed documentation of these tracer tests is contained in Umari (2003 [164573]) and Reimus (2003 [165128]). In each of the three tracer tests, two nonsorbing solute tracers with different diffusion coefficients were simultaneously injected (a halide and an FBA dissolved in the same solution). The three tests were conducted in essentially the same manner except for the time that was allowed to elapse between the cessation of tracer and chase water injection and the initiation of pumping, that is, the so-called "rest" or "shut-in" period. The rest period was systematically varied from ~0.5 hr, to ~2 days, to ~30 days in the tests to vary the time allowed for tracers to diffuse into stagnant water in the flow system and for the tracers to migrate with the natural groundwater flow. Test interpretations were based on comparing the responses of the different tracers in the same test and in different tests ("responses" refers to tracer concentrations normalized to injection mass as a function of time or volume pumped). As demonstrated in Section 6.5.2, the differences between the responses of two tracers with different diffusion coefficients in the same test and in tests with different rest periods can yield valuable information on diffusive mass transfer between flowing and stagnant water in the flow system and on the relative volumes of flowing and stagnant water in the system. In this section, it will be shown that differences in the responses of tracers with the same (or similar) diffusion coefficients in tests with different rest periods can provide information on ambient groundwater flow velocities in the flow system.

All three tests were conducted in the uppermost screened interval of 19D1, which ranges from approximately 15 to 21 m (50 to 70 ft) below the water table (gravel pack from approximately 14 to 23 m [45 to 75 ft] below the water table). The static water table is approximately 107 m (350 ft) below land surface at this location. The tracer solution volume injected in each test was approximately 11,000 L (2,900 gallons), and the volume of chase water (untraced water injected immediately after the tracer solution) was approximately 83,000 L (22,000 gallons). The chase water was intended to push the tracers into the formation so as to minimize the influence of the wellbore and gravel pack on the test results. Actual distances penetrated by the tracer solution

into the formation ultimately depend on the effective porosity of the formation and its spatial variability in hydraulic conductivity, which are uncertain quantities at this time.

The tracers used in each test and their injection concentrations and recoveries, the injection and withdrawal flow rates (averages), and the volumes pumped during each test are listed in Table 6.5-5. Tracer solutions were prepared by adding tracers to groundwater that had been withdrawn from 19D1 prior to any of the tests. Tracer concentrations were kept low and the solutions were heated to roughly match the ambient groundwater temperature to minimize density contrasts between the injection and chase solutions and the groundwater.

Table 6.5-5. Summary of Tracers and Test Conditions in the Three Single-Well Tracer Tests in NC-EWDP-19D1

Rest Period (Test)	0.5 hr	2 days	30 days
Dates	1/5/01–1/12/01	12/1/00–12/18/00	1/27/01–4/25/01
Tracers (concentration)*	2,4-DFBA (0.46 g/L) Cl^- (0.62 g/L NaCl) 640-nm microspheres	2,6-DFBA (0.46 g/L) I^- (0.64 g/L KI)	PFBA (0.46 g/L) Br^- (0.64 g/L NaBr)
Injection rate (L/min [gpm])	56.8 [15.0]	56.8 [15.0]	56.8 [15.0]
Average pumping rate (L/min [gpm])	50.3 [13.3]	41.3 [10.9]	51.67 [13.65]
Pumping duration (days)	7	14	54
Total liters (gallons) pumped	510,600 [134,900]	833,000 [220,000]	4,024,000 [1,063,000]
Tracer recovery (FBA)	0.864	0.928	0.913

DTNs: GS020708312316.001 [162678] (data); UN0109SPA008IF.006 [162442] (data); UN0109SPA008KS.005 [162681] (data); UN0109SPA008KS.007 [162615] (data); UN0109SPA008KS.008 [162616] (data).

NOTE: *DFBA = difluorobenzoate, PFBA = pentafluorobenzoate

6.5.4.1 Single-Well Tracer Test Results

Figures 6.5-18, 6.5-19, and 6.5-20 show the normalized tracer responses in the each of the three tracer tests. The two solute tracers had essentially identical responses (within experimental error) in each test. This result is consistent with very little diffusive mass transfer between flowing and stagnant water in the aquifer over the time scales of the tests. It is, therefore, consistent with a single-porosity conceptualization of the saturated alluvium. The flow interruptions during the tailing portions of the two longer tests provided additional evidence for very little diffusive mass transfer in the aquifer. If diffusive mass transfer were an important process, the tracer concentrations would have increased significantly immediately after the flow interruptions due to tracers diffusing out of stagnant water and into flowing water during the interruptions. The microspheres used in the shortest rest period test (Figure 6.5-18) provided information on colloid filtration and detachment rates in the flow system (see Section 6.5.4.6).

Figure 6.5-21 shows how the responses of the FBAs differed as a function of volume pumped in each of the three tracer tests. Because diffusion can be ruled out as having caused these differences, the most plausible explanation is that the differences are due to drift during the different rest periods. These different responses and the assumption that they are due to drift form the basis of three separate methods of estimating drift or seepage velocities in the aquifer.

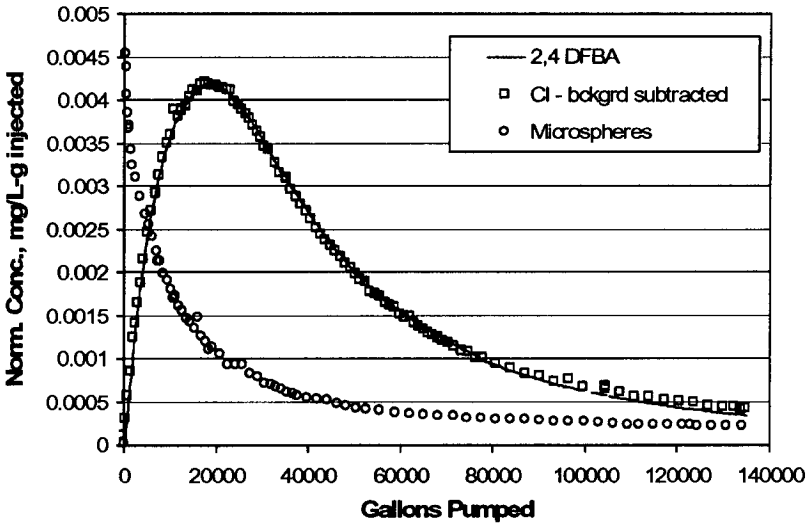

DTNs: UN0109SPA008IF.006 [162442] (2,4-DFBA and Cl), LA0207PR831352.001 [162431] (microspheres).

NOTE: Microspheres were 640-nm diameter carboxylate-modified latex (CML) polystyrene spheres tagged with a UV-excited fluorescent dye for detection. The figure is plotted in English units because the data were obtained in those units. However, parameter estimates are reported in metric units to downstream users.

Figure 6.5-18. Normalized Concentrations of Tracers in Production Water from NC-EWDP-19D1 as a Function of Gallons Pumped After a Rest Period of ~0.5 Hours

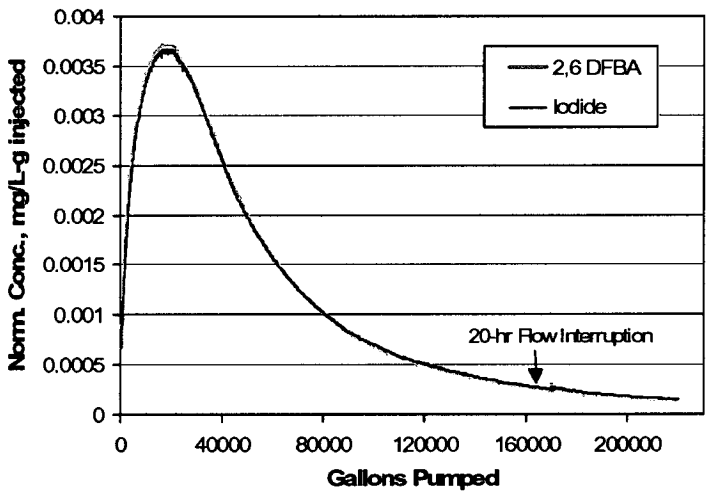

DTN: UN0102SPA008KS.003 [162614]. Output DTN: LA0303PR831231.002 (volumes).

NOTE: The tracer responses are almost identical, so it is difficult to distinguish between the two responses. The figure is plotted in English units because the data were obtained in those units. However, parameter estimates are reported in metric units to downstream users.

Figure 6.5-19. Normalized Concentrations of Tracers in Production Water from NC-EWDP-19D1 as a Function of Gallons Pumped After a Rest Period of ~2 Days

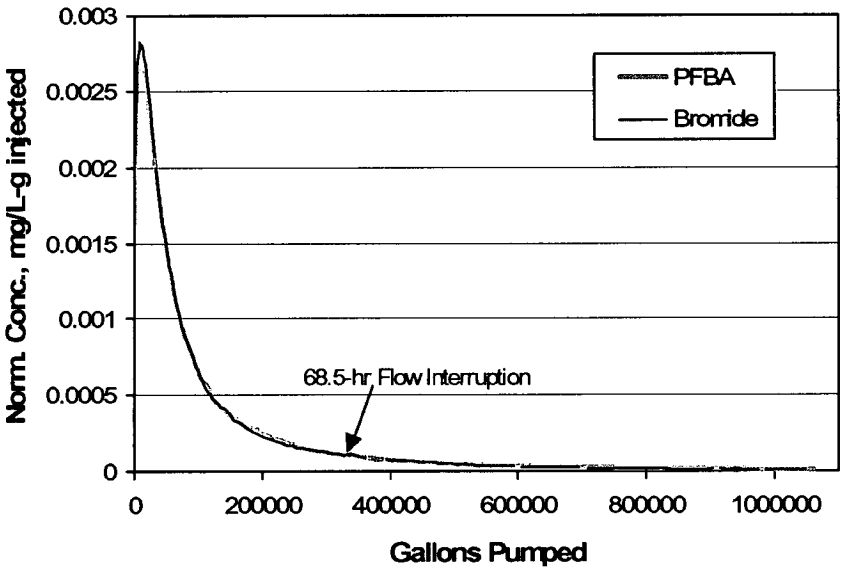

DTNs: UN0109SPA008KS.007 [162615] (PFBA), UN0109SPA008KS.008 [162616] (Br). Output DTN: LA0303PR831231.002. (volumes).

NOTE: The tracer responses are almost identical, so it is difficult to distinguish between the two responses. The figure is plotted in English units because the data were obtained in those units. However, parameter estimates are reported in metric units to downstream users.

Figure 6.5-20. Normalized Concentrations of Tracers in Production Water from NC-EWDP-19D1 as a Function of Gallons Pumped After a Rest Period of ~30 Days

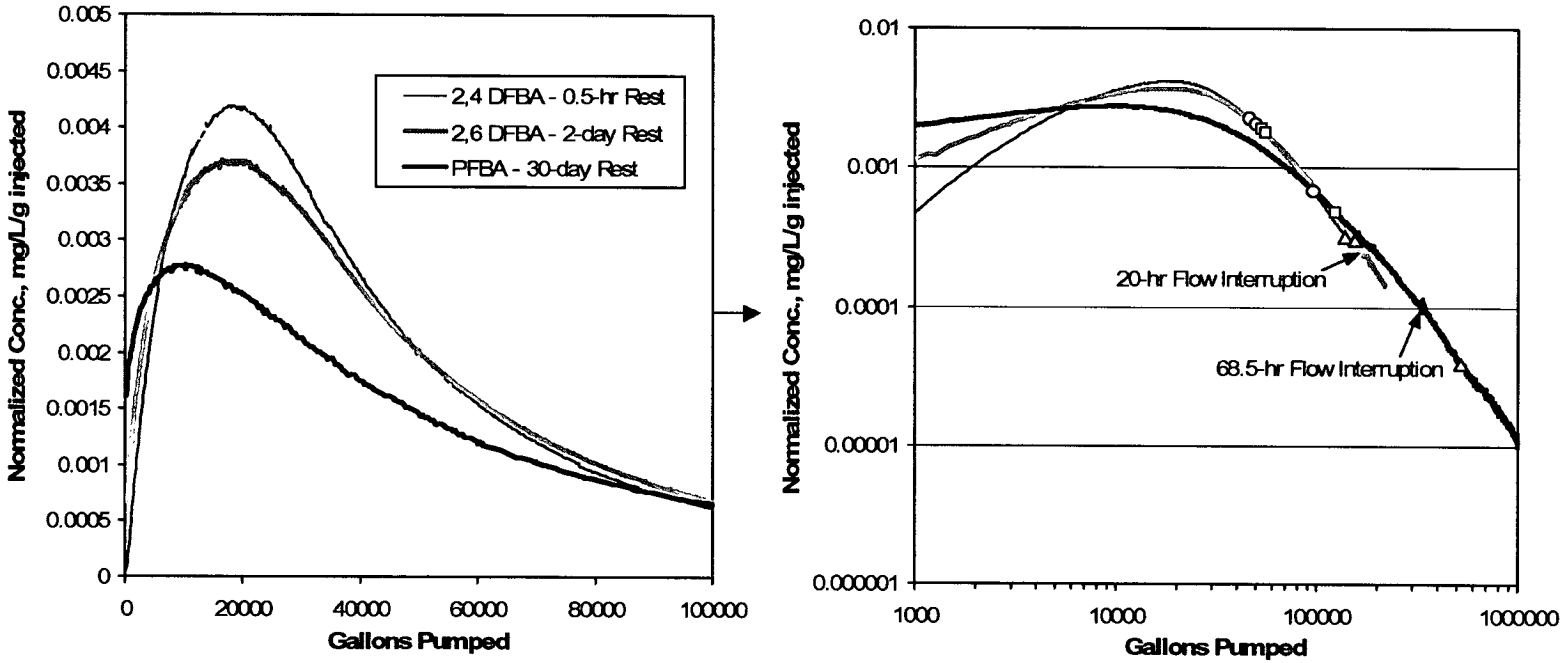

DTNs: UN0109SPA008IF.006 [162442] (2,4-DFBA), UN0102SPA008KS.003 [162614] (2,6-DFBA), UN0109SPA008KS.007 [162615] (PFBA). Output DTN: LA0303PR831231.002. (volumes).

NOTE: On the right-hand plot, circles indicate volumes associated with mean arrival times (for each tracer response), squares indicate volumes associated with alternate mean arrival times, and triangles indicate volumes associated with "late" arrival times. The left-most symbol is always associated with the 0.5-hr rest-period test, and the right-most symbol is associated with the 30-day rest-period test. The bases for these different arrival times/volumes are discussed in detail in Section 6.5.4.2. The figure is plotted in English units because the data were obtained in those units. However, parameter estimates are reported in metric units to downstream users.

Figure 6.5-21. Normalized Concentrations of Fluorinated Benzoates as a Function of Gallons Pumped in Each of the Three Single-Well Tracer Tests in NC-EWDP-19D1

6.5.4.2 Estimation of Groundwater Velocity

Four methods were used to obtain groundwater velocity estimates from the single-well tracer tests. The first three methods involve relatively simple spreadsheet calculations that, given various simplifying assumptions, solve for groundwater velocities that are consistent with the observed differences in the following:

(1) Peak tracer concentration arrival times.

(2) "Late" arrival times, defined as the times in each test when the fractional tracer mass recovery was equal to the final recovery in the test having the lowest overall mass recovery. Given that the total mass recoveries in the three tests were 0.864, 0.928, and 0.913 (Table 6.5-5), then the late arrival time in each test was the time at which the mass recovery was 0.864.

(3) "Mean" arrival times of tracer mass recovered at the same arbitrarily-selected high fractional recovery in each test. Two different fractional recoveries were selected to calculate mean arrival times: 0.864, the lowest fractional recovery in any of the tests, and 0.913, the fractional recovery in the 30-day-rest-period test. In the latter case, the tracer responses in the test with a mass recovery of 0.864 were extrapolated to 0.913 (see Section 6.5.4.2.3 for details) to allow a calculation of the mean arrival time. This alternative method of calculating the mean arrival time was employed because the 30-day test had the largest calculated mean arrival time, and it was therefore considered to have the greatest amount of information pertinent to groundwater velocity estimates.

Note that these three times also correspond to volumes pumped, and because the pumping rates varied in the different tests, the relationship between times and volumes is different for each test. The peak, late, and mean arrival times (and corresponding volumes) for each test are listed in Table 6.5-6. The points on the tracer breakthrough curves corresponding to the mean and late arrival times in each test are identified in the right-hand plot of Figure 6.5-21. The fourth method involved detailed analytical calculations of tracer migration during the tests by linking together solute transport solutions that assume a 2-D homogeneous and isotropic aquifer.

Because the peak tracer concentration occurred earliest in the test with the longest rest period, the tracer mass corresponding to the peak probably moved upgradient during injection and then drifted back toward the well during the rest period. In contrast, the tracer mass corresponding to times at which fractional recoveries were high (i.e., mass recovered far out in the tails of the responses) probably moved downgradient during injection and arrived late because of the competing effects of drift that moved the tracer further from the well and pumping the tracers toward the well. The mean tracer arrival time represents a compromise between these two cases, as the mean is influenced by both early- and late-arriving tracer mass. However, for asymmetric long-tailed distributions, the mean is more strongly influenced by late-arriving mass than early-arriving mass, so it was assumed that the differences in mean arrival times were due mainly to tracer mass that had moved downgradient during injection.

Table 6.5-6. Times and Pumped Volumes Associated with Each of the Arrival Times Used in the Different Methods of Estimating Groundwater Velocities

Rest Period (Test):	Arrival Time (hr)/Volume (L [gal])		
	0.5 hr	2 days	30 days
Peak arrival	24 / 76,000 [20,000]	30.5 / 76,000 [20,000]	12.2 / 38,600 [10,200]
Late arrival [(a)]	168 / 511,000 [135,000]	225 / 556,000 [147,000]	639 / 1,780,000 [471,000]
Mean arrival [(b)]	52 / 161,000 [42,500]	71 / 178,000 [46,500]	109 / 344,000 [91,000]
Alternate mean arrival [(c)]	61.5 / 189,000 [50,000]	81 / 201,000 [53,000]	149 / 469,000 [124,000]

DTNs: UN0109SPA008IF.006 [162442] (0.5 hr); UN0102SPA008KS.003 [162614] (2 days); UN0109SPA008KS.007 [162615] (30 days). Output DTN: LA0303PR831231.002 (volumes).

NOTE: (a) Time/volume associated with ~86.4% mass recovery in each test (the final recovery in the 0.5-hr rest period test, which had the lowest final recovery of any test).

(b) Mean arrival time calculated by truncating all tracer response curves at ~86.4% recovery in each test.

(c) Alternate mean arrival time calculated by extrapolating the tracer response curves in the 0.5-hr rest period test to 91.3% and truncating the response curves in the 2-day rest period test to 91.3% recovery (the final recovery in the 30-day rest period test).

In all four estimation methods, it is assumed that injection into and pumping from the well results in a 2-D radial flow field in which the flow velocity varies as 1/r:

$$v(r) = \frac{Q}{2h\eta\pi r} \qquad \text{(Eq. 56)}$$

where

$v(r)$ = linear velocity as a function of radial position, m/hr

Q = injection or production flow rate, m^3/hr (negative number for production)

h = interval thickness, m

η = flow porosity

r = radial distance from the well, m.

For the first three methods, the ambient groundwater flow is superimposed on the radial flow induced by injection or pumping, and it is present during the rest period when there is no radial flow component. The ambient flow is assumed to be unidirectional.

Flow fields resulting from injection and pumping will not be ideally radial unless the aquifer is perfectly homogeneous, isotropic, and 2-D. Figure 6.5-22 shows a hypothetical representation of how injected tracer solution and chase water might be distributed in the aquifer immediately after injection. Figure 6.5-22 represents only one of many possibilities for how heterogeneity might affect tracer distribution in the system, and all of these possibilities must be considered equally likely given the present knowledge of the flow system. Although it may not be strictly correct, the radial flow assumption is qualitatively consistent with the picture of heterogeneity shown in Figure 6.5-22 because the flow velocity will maintain a ~1/r dependence as long as the flow cross-sectional area "fans out" such that it increases approximately linearly with r. Only highly

channelized flow that does not increase significantly in cross-sectional area with r will have a velocity that does not decrease as ~1/r. In pipeline flow, the extreme case of channelized flow, there is no dependence of velocity on r.

Alternatively, if the system is not 2-D (confined aquifer will fully-penetrating well), the flow cross-sectional area could increase with more than a linear dependence on r, with the extreme case being spherical flow where the velocity decreases as $1/r^2$ (at sufficiently large distances from the well). However, this latter possibility was ignored because (1) there is qualitative evidence (both lithologic and from hydraulic testing) of layering in the aquifer that could cause considerable vertical confinement, and (2) the injection volumes were small enough relative to the interval thickness and potential flow porosities that the tracer injection distances into the formation should have been relatively short compared to what it would take to approximate a spherical flow condition.

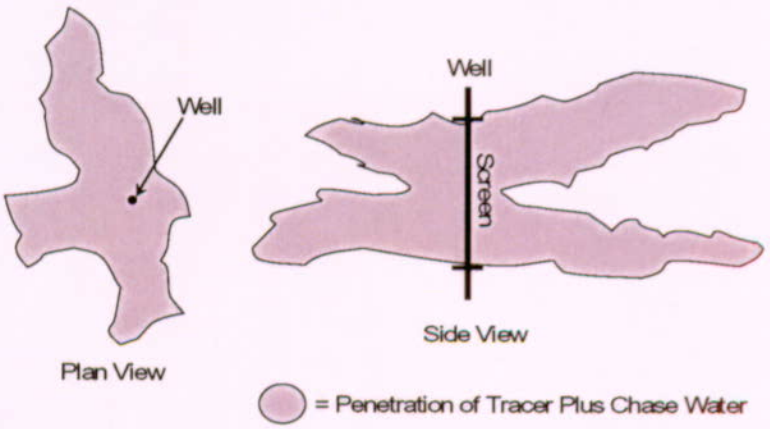

For illustration purposes only

Figure 6.5-22. Depiction of How Tracer and Chase Water Might be Distributed after Injection into a Heterogeneous Porous Medium

6.5.4.2.1 Peak-Arrival-Time Analysis

For the analysis comparing the peak tracer arrival times, the mass contributing to the peak was assumed to move directly upgradient during injection. That is, the radial flow pushing the mass was assumed to be in the exact opposite direction as the ambient groundwater flow (Figure 6.5-23). Any estimate of groundwater drift velocity using this assumption should be considered a lower bound because the peak mass will have the *greatest decrease* in arrival time as the rest period is increased when the mass is injected directly upgradient. Trigonometric calculations show that if the tracer mass corresponding to the peak concentration were injected at some angle relative to the ambient gradient direction, the groundwater velocity would have to be greater to result in the same decrease in arrival time (assuming a reasonably homogeneous system).

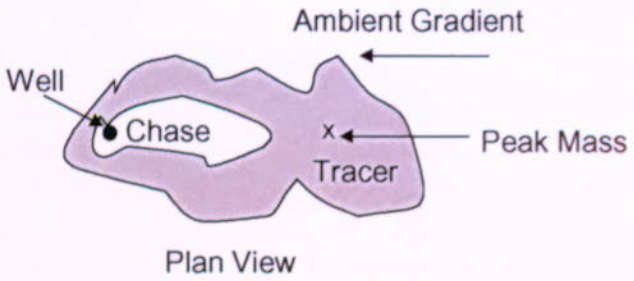

For illustration purposes only

NOTE: The shape of the distribution is not important; the key assumption is that the tracer mass associated with the peak concentration is located directly up-gradient.

Figure 6.5-23. Depiction of Assumed Tracer Mass Distribution Immediately After Injection

Given the assumption of the peak tracer mass moving strictly upgradient, the distance that the tracer mass moved into the formation during the injection and chase phase is given by (derivations of Equations 57 to 66 are documented in Reimus 2003 [165129]):

$$r_{inj} = \sqrt{\frac{(0.5\ V_{tracer} + V_{chase})}{\pi \eta\ h}} - v_{GW} \frac{(0.5\ V_{tracer} + V_{chase})}{Q_{inj}} \qquad \text{(Eq. 57)}$$

where

r_{inj} = upgradient injection distance, m
V_{tracer} = volume of tracer solution injected, m^3
V_{chase} = volume of chase water injected, m^3
v_{GW} = ground water velocity (seepage velocity), m/hr
Q_{inj} = injection flow rate, m^3/hr
h = interval thickness, m
η = flow porosity

The first term in Equation 57 accounts for the distance injected under pure radial flow conditions, and the second term accounts for the drift back toward the well during injection. Only half of the tracer solution volume is used in Equation 57 because it is assumed that the tracer mass resulting in the peak should have corresponded to approximately the midpoint of the injection volume. However, the calculations are not sensitive to this assumption because the tracer solution volume in all tests was small relative to the chase volume. Because the tracer and chase volumes and the injection rates were essentially the same in the three tests, the injection distance given by Equation 57 is the same for all three tests.

The radial distance, r_{rest}, between the peak tracer mass and the well at the end of the rest period is given by:

$$r_{rest} = r_{inj} - v_{GW}\, t_{rest} \qquad \text{(Eq. 58)}$$

where t_{rest} = duration of the rest period, hr.

The time required to pump the peak tracer mass back to the well after the rest period, t_{pump}, is calculated from the following integral:

$$t_{pump} = \int_{r_{rest}}^{0} \frac{dr}{v(r)} \qquad \text{(Eq. 59)}$$

where

$$v(r) = -\frac{|Q_{pump}|}{2h\eta\pi\, r} - v_{GW}$$

Q_{pump} = production flow rate, m^3/hr.

The solution to this integral (with v(r) from Equation 56 inserted and using the appropriate upper and lower limits) is (Weast and Astle 1981 [100833], p. A-36, Equations 84 and 85):

$$t_{pump} = \left[-\frac{r}{v_{GW}} + \frac{|Q_{pump}|}{2\pi\eta\, h\, v_{GW}^{\,2}} \ln\left(\frac{|Q_{pump}|}{2\pi\eta\, h} + v_{GW} r \right) \right]_{r=r_{rest}}^{r=0} \qquad \text{(Eq. 60)}$$

t_{pump} can be converted to a volume corresponding to the arrival time of the peak concentration using:

$$V_{pump} = t_{pump} |Q_{pump}| . \qquad \text{(Eq. 61)}$$

The pertinent equations above were encoded into an Excel spreadsheet for the analysis (Output DTN: LA0303PR831231.002). The only unknown variables for each of the three tests were the ground-water velocity, v_{GW}, and the flow porosity, η, both of which were assumed to be the same in all three tests. The procedure for obtaining an estimate of v_{GW} involved selecting η and then varying v_{GW} by trial-and-error until the calculated peak arrival volumes in the three tests had approximately the same ratios as in the actual field tests. It was considered more important to match the ratios of times rather than to match the actual times, although the calculated times were generally in reasonable agreement with the actual times, once the ratios were matched. Also, greater emphasis was placed on matching the volume ratio between the 30-day-rest-period test and the ~0.5-hr-rest-period test than on matching the volume ratios in any other pair of tests, particularly the two shorter tests. The uncertainty associated with a groundwater velocity estimate obtained from the two shorter duration tests was considered to be far greater than estimates obtained using the 30-day test results because of the much greater time allowed for drift to take place in the 30-day test.

The process of estimating v_{GW} was repeated for three different values of η - 0.05, 0.18, and 0.3. These values are approximately the lowest, expected (mean), and highest values, respectively, used for alluvium flow porosity in Yucca Mountain performance assessment simulations. The value of v_{GW} was different in each case because of the dependence of Equations 57 and 60 on η. For each case, a specific discharge, v_S, was calculated from v_{GW} using $V_S = \eta\ v_{GW}$.

6.5.4.2.2 Analysis of Late Arrival Times (Associated With High Fractional Tracer Recoveries)

The analysis of late arrival times (arrival times associated with high fractional tracer recoveries) was similar to the analysis of peak arrival times except that the tracer mass associated with the late arrival time was assumed to have been injected downgradient rather than upgradient. This assumption seems reasonable, given that any mass injected upgradient should arrive earlier than the mean tracer arrival time, not later. Analogous to the peak arrival-time analysis, it was assumed that the mass was injected directly downgradient (in the same direction as the ambient groundwater flow). Any estimate of groundwater velocity using this assumption should be considered an upper bound because the late-arriving mass will have the *greatest increase* in arrival time as the rest period is increased when the mass is injected directly downgradient.

The times/volumes associated with the final recovery in the ~0.5-hr-rest-period test (0.864), which had the lowest recovery of the three tests, were used as the basis of comparison of the late arrival times for the three tests. Although this is a somewhat arbitrary definition of the late arrival time because it depends on when pumping was stopped in the ~0.5-hr-rest-period test, it was considered to be the most objective measure because times associated with recoveries greater than 0.864 would require an extrapolation of the tracer responses in the 0.5-hr test. Clearly, if the 0.5-hr test had been pumped longer, the late arrival times in the tests would have all been greater, and the estimates of groundwater velocities would be slightly different. However, the pumped volumes associated with the arrival times would also have been greater, which would tend to have a moderating effect on the changes in velocity estimates.

The analysis requires that Equations 57, 58, and 59 be modified as shown in Equations 62, 63, and 64, respectively.

$$r_{inj} = \sqrt{\frac{(V_{tracer} + V_{chase})}{\pi \eta\, h}} + v_{GW} \frac{(V_{tracer} + V_{chase})}{Q_{inj}} \qquad \text{(Eq. 62)}$$

$$r_{rest} = r_{inj} + v_{GW}\, t_{rest} \qquad \text{(Eq. 63)}$$

$$t_{pump} = \left[\frac{r}{v_{GW}} + \frac{|Q_{pump}|}{2\pi \eta\, h\, v_{GW}^{\,2}} \ln\left(\frac{|Q_{pump}|}{2\pi \eta\, h} - v_{GW} r \right) \right]_{r = r_{rest}}^{r = 0} \qquad \text{(Eq. 64)}$$

The modifications are primarily changes in sign associated with the v_{GW} terms because the groundwater drift velocity is now assumed to push the tracer mass further from the well during injection and slow down the movement of the mass toward the well during pumping. Also, the mass associated with the high fractional recovery is assumed to be on the leading edge of the tracer injection volume rather than at the midpoint of the volume (Equation 62). One additional difference between the peak- and late-arrival analyses that does not involve equation modifications is that the flow interruption times were added to t_{rest} for the late-arrival analyses because the tracer mass associated with the latter analyses arrived after the flow interruptions.

As with the peak arrival time analyses, v_{GW} was varied to achieve matches to the ratios of the arrival volumes, rather than the actual volumes. However, unlike the peak analyses, the calculated volumes were typically much smaller than the actual volumes associated with the late recoveries. The most likely reason for this discrepancy is that this simple analysis does not account for any hydrodynamic dispersion during any of the three test phases (injection, rest period, withdrawal). Dispersion during each of these three phases could have significantly increased late-recovery arrival times relative to those calculated without dispersion because a fraction of the tracer mass should always disperse further away from the well at any given time. However, if it is assumed that dispersion during each test had approximately the same effect on the tracer plume (disregarding the expected slight increase in dispersion for the longest test), then a comparison of the ratios of the late arrival times should still yield a reasonable estimate of groundwater velocity.

6.5.4.2.3 Mean-Arrival-Time Analysis

The mean tracer arrival-time analysis was essentially identical to the analysis of the late-recovery arrival time, with the only exception being that the mass associated with the mean tracer mass was assumed to be at the midpoint of the tracer injection volume rather than at the leading edge. Thus, Equation 62 was modified to

$$r_{inj} = \sqrt{\frac{(0.5\,V_{tracer} + V_{chase})}{\pi \eta\ h}} + v_{GW}\frac{(0.5\,V_{tracer} + V_{chase})}{Q_{inj}} \qquad \text{(Eq. 65)}$$

The primary difference between the mean and late arrival time analyses was in how the times/volumes used for comparison with the calculations were obtained from the actual field tracer data. For the late-recovery time analysis, it was a simple matter to extract the times/volumes associated with a specific (though arbitrary) tracer recovery. However, for the mean analysis, it was necessary to calculate a meaningful estimate of the mean arrival time/volume from the data. Without 100% tracer recovery, it is impossible to calculate a true mean, so a mean for comparison purposes was calculated by truncating the tracer responses in the two longer-rest-period tests at the final recovery of the ~0.5-hr-rest-period test (0.864). The mean volume was calculated by:

$$\mu = \frac{\sum_i (f_i - f_{i-1})\, V_{pump\ i}}{\sum_i (f_i - f_{i-1})} \qquad \text{(Eq. 66)}$$

where

μ = mean volume, m^3

f_i = mass fraction recovered at volume $V_{pump\ i}$

f_{i-1} = mass fraction recovered at volume $V_{pump\ i-1}$.

However, because the mean times/volumes are sensitive to the tails of the tracer response curves, an alternative method of calculating the mean arrival time was devised to include all the data from the 30-day-rest-period test, which had the largest mean of the three tests and, therefore, was considered to contain the greatest amount of information pertinent to ambient groundwater velocities. Although this method required that the data from the ~0.5-hr rest-period-test be extrapolated until the fractional recovery in that test matched the final recovery in the 30-day test (0.913), the extrapolation was considered justified in light of the additional information contained in the tracer responses from the 30-day test. Also, it was desirable to determine the sensitivity of the ambient groundwater velocity estimates to different methods of calculating the mean arrival time.

The extrapolation of the ~0.5-hr test data was accomplished by doing the mathematical equivalent of linearly extending the tail of the tracer response curve on a log-log plot. The means were then recalculated using Equation 66. The recalculated means for all three tests increased significantly relative to the means calculated from the breakthrough curves that were truncated at a fractional tracer recovery of 0.864. However, the mean for the 30-day test increased by the greatest percentage (about 36% compared to 18% and 15% for the ~0.5-hr and 2-day tests, respectively). The (re)calculated mean for the ~0.5-hr test was found to be relatively insensitive to the slope of the line used to extrapolate the tracer data. This insensitivity was probably due to the relatively steep slope of the tail of the response curve in this test.

6.5.4.2.4 Linked Analytical Solutions

Three different analytical solutions of the advection-dispersion equation, with appropriate boundary conditions representing the three distinct single-well tracer test phases (injection/chase, drift, and pump back) were combined into one Personal Computer-based Windows program with a user interface, called Injection-Pumpback.vi V 1.0 (STN: 10675-1-00 [162749]). Injection-Pumpback.vi is a "LabView" program, where LabView is the graphical-programming language "G" as implemented by National Instruments, Inc. The linked analytical solutions were intended to provide an alternative, more rigorous, method of estimating groundwater drift velocities in the alluvium from single-well tracer tests than the analytical approaches described in Sections 6.5.4.2.1 through 6.5.4.2.3. This method was also intended to provide estimates of other transport parameters derived from single-well tracer testing in the alluvium (flow porosity, dispersivity) given an assumption of a homogeneous and isotropic flow system. The method was chosen instead of numerical modeling approaches because of the relative simplicity of the analysis and the desire to avoid numerical dispersion that occurs in numerical models. A description of the three analytical solutions that constitute the program Injection-Pumpback.vi and the application of the program to analyze the three injection-pumpback tracer tests conducted in borehole 19D1 follows.

The tracer injection and chase phase was analyzed using simple flow displacement calculations combined with a 1-D uniform-flow solution of the advection-dispersion equation by Crank (Bear 1979 [105038], p. 266, Equation 7-123) to determine the location and width of the "tracer ring" resulting from the outward radial flow. The inner radius of the ring was calculated directly from the volume of chase water injected, and the 1-D solution was then used to determine the width and, hence, outer radius, of the ring. This approach is only approximate because the 1-D column solution assumes a constant velocity flow field whereas a divergent radial flow field has a decreasing velocity with increasing distance from the injection well. In the 1-D column solution, dispersion of the "plume" results in the leading and trailing edges of the plume being essentially equidistant from the plume center of mass. However, in an outward radial flow field, the leading edge will tend to be closer to the center of mass than the trailing edge because of the velocity decrease in the radial direction. Given this approximation, the analysis of the tracer injection and chase phase is conducted as follows.

The column solution by Crank (Bear 1979 [105038]) is given by:

$$C_{CR}(x,t) = \frac{M/\eta}{(4\pi D_h t)^{1/2}} \exp\left\{-\frac{x'^2}{4D_h t}\right\} \qquad \text{(Eq. 67)}$$

where

$C_{CR}(x,t)$ = concentration of solute at a point x meters from the point of tracer injection (top of the column) at t minutes after injection (kg/m^3)

M = mass of tracer injected per unit cross-sectional area in kilograms (kg/m^2)

η = flow porosity

D_h = coefficient of hydrodynamic dispersion (longitudinal) as given by Equation 68 (m^2/sec)

x' = distance in meters from the top of the column (where the tracer slug is introduced at time t=0) to the centroid of the slug at time t as given by Equation 69 (m)

t = 27.6 hours (for this application), the time it took to inject the tracer volume, 10,600 L (2,800 gallons), followed by the chase volume, 83,000 L (22,000 gallons), at an injection rate of 56.8 L/min (15 gpm).

If molecular diffusion is ignored, D_h (m^2/min) is given by (Bear 1979 [105038], p.264):

$$D_h = \alpha_L |q| / \eta \qquad \text{(Eq. 68)}$$

where

α_L = longitudinal dispersivity (m)

q = specific discharge in cubic meters per minute for a unit area of one meter squared (m/sec).

For 1-D flow in a column, x' is given by Bear (1979 [105038], p. 266, Equation 7-120):

$$x' = x - (q/\eta)\, t\,. \qquad \text{(Eq.69)}$$

where x = distance from top of column (m).

Equations (67 to 69), representing movement of a tracer slug in a 1-D column experiment, were modified to represent outwardly-divergent flow from an injection well as follows. The radial distance from the center of the well, r, was converted to an equivalent linear column length x by calculating the length of a column whose volume is equivalent to that of a cylinder centered at the well with height equal to the test-interval thickness, h, and with radius r. This cylinder has radial cross-sectional areas increasing from a minimum of $2\pi r_w h$ at the well, (where $r = r_w$ (the well radius, m)), to $2\pi rh$ at a radius of r from the center of the well. The equivalent column is defined as having a constant cross-sectional area of $2\pi r_w h$ (representing the cross-sectional area of the aquifer in contact with the well) and a volume equal to that of the cylinder. For the same porosity, this equivalent column would contain the same volume of water as the cylinder.

The volume of the above cylinder, V_{CYL}, is given by:

$$V_{CYL} = \pi r^2 h \qquad \text{(Eq. 70)}$$

where h = interval thickness (m).

The volume of the equivalent linear column, V_{COL}, is:

$$V_{COL} = A_{COL}\, x \qquad \text{(Eq. 71)}$$

where A_{COL} = cross-sectional area of the column (m^2), which is $2\pi r_w h$, by definition.

Setting V_{CYL} equal to V_{COL} and A_{COL} equal to $2\pi r_w h$ in Equations 70 and 71, and solving for x, results in Equation 72:

$$x = \pi r^2 h / 2\pi r_w h = r^2 / (2r_w) \qquad \text{(Eq. 72)}$$

where r_w = injection well radius (m).

So, for a particular radius r, Equation 72 is used to calculate the equivalent linear column distance, x. This value of x is used to calculate x' in Equation 69, and then Equation 67 is used to calculate the concentration $C_{CR}(x,t)$ (kg/m^3), according to Crank (Bear 1979 [105038], p. 266, Equations 7-120 and 7-123). $C_{CR}(x,t) = C_{CR}(r,t)$, obtained in this manner, describes the change of concentration as a function of radial distance from the injection well.

The specific discharge, q (m/sec), used in Equations 68 and 69 is obtained by dividing the injection rate, Q_{INJ} = 56.8 L/min (15 gpm), by the cross-sectional area of the aquifer in contact with the well, $2\pi r_w h$:

$$q = Q_{INJ} / (2\pi r_w h) \qquad \text{(Eq. 73)}$$

By defining a threshold concentration at which a sharp edge of the tracer ring starts at its inner circumference and ends at its outer circumference (5 mg/L or 5 x 10^{-9} kg/m^3 for this analysis), a width can be determined for the tracer ring from the modified Equation 67. In summary, the modified solution has been used to define the width of the tracer ring (formed by the chase fluid pushing the tracer outward from the well) as a function of the assumed effective porosity and longitudinal dispersivity. The tracer ring is then positioned with its inner radius at a distance r_C (radius of chase zone) calculated from the assumed effective porosity and known volume of chase water, Vc (r_C from Vc = 83,000 L [22,000 gallons] = $\pi r_C^2 h\eta$) and with its width as determined from the analytical solution by Crank (Bear 1979 [105038], p. 266, Equation 7-123). The superposition of the ambient groundwater flow on the outward-radial flow caused by tracer injection and chase was ignored (i.e., it was assumed that the injection and chase dominated the flow field). Given that the tracer injection and chase phase in all the single-well tests was relatively short compared to the drift plus pumpback phase, this approximation should not preclude obtaining reasonable estimates of groundwater velocity for the purposes of comparing with the analytical methods of Sections 6.5.4.2.1 through 6.5.4.2.3. Figure 6.5-24 shows a LabView depiction of the tracer "plume" after injection and chase.

A 2-D analytical solution of the advection-dispersion equation for a tracer slug injected in a uniform flow field (Bear 1979 [105038], as given in Bachmat et al. (1988 [162534], p. 149, Equation 11) was used to calculate tracer movement during the "drift" phase of each single-well test:

$$C_i(x_1, y_1, t_1) = \frac{M_1 / h\eta}{4\pi(\alpha_L \alpha_T)^{1/2} V_o t_1} \exp\left\{ -\frac{1}{4V_o t_1}\left[\frac{(x_1 - V_o t_1)^2}{\alpha_L} + \frac{y_1^2}{\alpha_T}\right]\right\} \qquad \text{(Eq. 74)}$$

where

$C_i(x_1,y_1,t_1)$ = concentration at one of the grid blocks (with transformed coordinates (x_1, y_1) – see below) in Figure 6.5-25 resulting from drift of a mass M_1 kg initially positioned at the centroid of the particular wedge, wedge i (i = 1 through 18) of Figure 6.5-24. Wedge numbering is not unique and the index "i" is only used here to indicate enumeration of wedges.

x_1 and y_1 are the coordinates of this grid block relative to an orthogonal system centered at the centroid of wedge i. For this orthogonal coordinate system, the positive x_1 axis is oriented parallel to streamlines of the ambient flow field and in the direction of flow.

α_L = longitudinal dispersivity (m)

α_T = transverse dispersivity (m)

V_o = interstitial velocity caused by the ambient gradient (m/sec)

t_1 = duration of drift allowed before pumpback (hr).

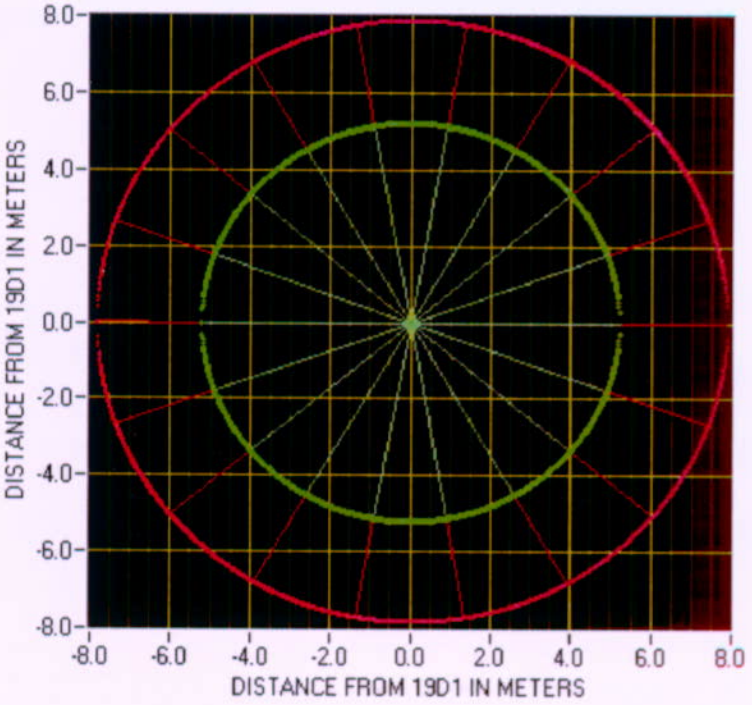

DTNs: GS020708312316.001 [162678] (data); GS020908312316.002 [162679] (data). Output DTN: GS031008312316.003 (analysis).

Figure 6.5-24. Tracer Ring (red-hatched area) and Chase Ring (green-hatched area) Around the Injection Well NC-EWDP-19D1

In essence, Equation 74 is solved in the transformed coordinate system to obtain the distribution of tracer mass resulting from the drift of tracer initially located in each of the wedge-shaped volume elements of Figure 6.5-24. Then, the solutions for all 18 wedge-shaped volume elements are superimposed to obtain the overall distribution of tracer mass after the drift phase. The relatively coarse discretization of the tracer mass at the centroid of the 18 wedges of Figure 6.5-24 at the beginning of the drift phase is an inherent approximation in the method. The resultant concentration field representing the drifted plume is shown in Figure 6.5-25.

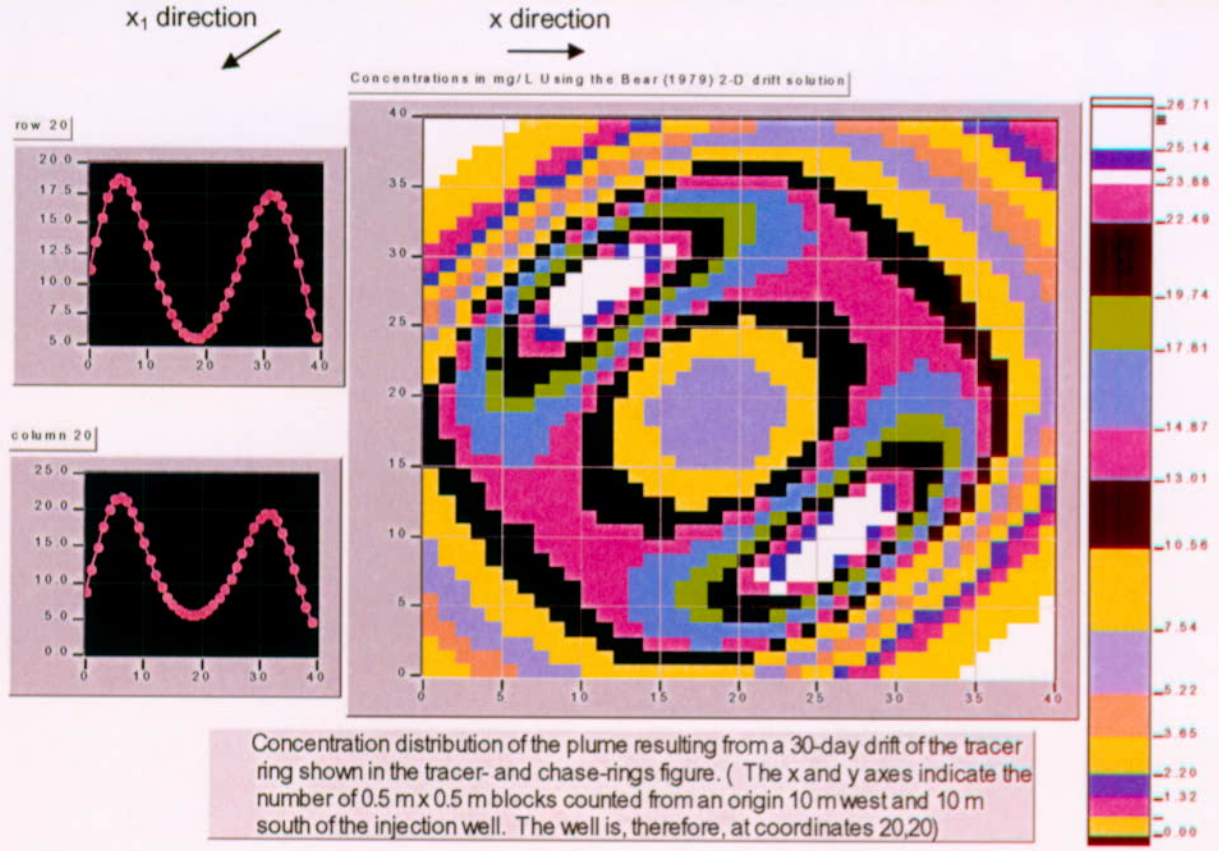

Concentration distribution of the plume resulting from a 30-day drift of the tracer ring shown in the tracer- and chase-rings figure. (The x and y axes indicate the number of 0.5 m x 0.5 m blocks counted from an origin 10 m west and 10 m south of the injection well. The well is, therefore, at coordinates 20,20)

DTNs: GS020708312316.001 [162678] (data); GS020908312316.002 [162679] (data); UN0109SPA008IF.006 [162442] (conc.); UN0109SPA008KS.005 [162681] (conc.) UN0109SPA008KS.007 [162615] (conc.); UN0109SPA008KS.008 [162616] (conc.);Output DTN: GS031008312316.003 (analysis).

NOTE: The x and y axes indicate the number of blocks counted from an origin 10 m west and 10 m south of the injection well; the blocks are 0.5 m on a side; and the well is, therefore, at coordinate (20, 20). Concentrations are calculated using the Bear (1979 [105038]) two-dimensional drift solution.

The x-y plots to the left of the main 2-D plot show the tracer concentration distribution along linear profiles in the east-west (top) and north-south (bottom) directions through the grid point corresponding to the location of the well (20,20).

The x_1 direction is the direction of ambient flow.

Figure 6.5-25. Concentration Distribution of Tracer Plume Resulting from a 30-Day Drift of the Tracer Ring Shown in Figure 6.5-24

For each block, the total concentration, $C_1 + C_2 + C_3 + \ldots + C_{18}$, is multiplied by the volume of the block, 0.5m x 0.5m x h, times the porosity, η, to obtain the mass of the tracer slug, M_{slug}, used at that block for the pumpback phase. A radial solution of the advection-dispersion equation for a cross-hole convergent tracer test with slug injection (Moench 1989 [101146], pp. 440 to 443; 1995 [148784], pp. 1824 to 1827) was then used to calculate tracer movement during the pumpback phase of each test.

The mass in each of the 0.5 m x 0.5 m blocks of the calculation grid of Figure 6.5-25 was considered a slug injection in a convergent flow field towards the pumped well located at coordinates 20, 20 of the figure.

Moench (1989 [101146], pp. 440 to 443; 1995 [148784], pp 1824 to 1827) used the Laplace transform method to solve the following dimensionless governing advection-dispersion equation for horizontal, radial flow in an homogeneous, double-porosity aquifer:

$$\frac{1}{Pe\, r_D}\frac{\partial^2 C_D}{\partial r_D^2}+\frac{1}{r_D}\frac{\partial C_D}{\partial r_D}-\frac{2R}{(1-r_{wD}^2)}q'_D=\frac{2R}{(1-r_{wD}^2)}\frac{\partial C_D}{\partial t_D} \qquad \text{(Eq. 75)}$$

where

$Pe = r_L/\alpha_L$, the Peclet number, and r_L = distance from the tracer injection point (normally a well) to the pumped well

$r_D = r/r_L$ is the dimensionless radial distance from the pumping well, where r is the dimensional distance from the pumping well

C_D = dimensionless concentration, which for a slug injection is given by $C_D = C/C_i$, where C = concentration at r, and C_i = reference concentration given by $C_i = M_{slug} / [\pi h \eta (r_L^2 - r_w^2)]$ in which r_w = radius of the pumping well

$r_{wD} = r_w/r_L$, the dimensionless well radius

t_D = dimensionless time, t/t_a, where t_a is the advection travel time given by $t_a = (\pi r_L^2 h \eta)/Q$ in which Q = pumping rate

R = retardation factor

q'_D = dimensionless distributed sources or sinks of tracer due to diffusion of the tracer into stagnant porosity.

Moench (1989 [101146] , pp. 440 to 443; 1995 [148784], 1824 to 1827) provided a FORTRAN program, rcv2amos.exe V 1.0 (STN: 10583-1.0-00 [162750]), that computes the Laplace transform of Equation 75 and then the inverse Laplace transform to finally give dimensionless concentration, C_D, versus dimensionless time, t_D, at the pumped well in the form of two numerical arrays. The C_D versus t_D dimensionless theoretical breakthrough curve is then converted to a dimensional curve of C versus t using the above relation. Injection-Pumpback.vi V 1.0 (STN: 10675-1-00 [162749]) uses rcv2amos.exe to obtain the effect at the pumping well of a slug of mass M_{slug} placed at each block of the calculation grid of Figure 6.5-25. It then superposes all of these solutions to obtain the final effect at the pumping well of a slug of mass M_{slug} placed at each block of the calculation grid of Figure 6.5-25, and then superposes all of these solutions to obtain the final calculated breakthrough. The superposition of the ambient groundwater flow on the radial flow caused by the pumping well was ignored (i.e., it was assumed that the pumping dominated the flow field). This approximation clearly introduces some error to the analysis. However, given that the curve-matching procedure discussed below is heavily influenced by tracer data obtained early in the pumpback phase of each test (the tracer peaks occur within a day), the error should not preclude reasonable estimates of groundwater velocity for the purposes of comparing with the analytical methods of Sections 6.5.4.2.1 through 6.5.4.2.3.

The complete analysis involves adjusting the flow porosity, longitudinal dispersivity, transverse dispersivity, and specific discharge in all three computational stages (keeping them the same in each stage) until simulated tracer responses offer a reasonable match to the observed tracer responses in each single-well test. The results of such a match to the three injection-pumpback tracer responses in well 19D1 are shown in Figure 6.5-26. The analysis indicates a flow porosity value of 0.10, a longitudinal dispersivity of 5 m, and a specific discharge of 1.5 m/yr (Output DTN: GS031008312316.003). Although a rigorous sensitivity analysis to evaluate the uniqueness of the solution was not conducted, many combinations of parameter values were considered, and there appeared to be qualitative convergence to these values. The top three plots in Figure 6.5-26 present dimensional (actual) concentrations, whereas the bottom three plots present concentrations normalized relative to maximum concentrations. The assumed input parameter combination yields a reasonable fit to all three single-well tracer data sets.

The flow porosity value of 0.10 should be less than the total porosity and is, therefore, consistent with three estimates of total porosity presented in different sections of this report: (1) a value of 0.29 obtained from the Borehole Gravity Meter survey in 19D1, presented in Section 6.5.5; (2) a value of 0.41 obtained from estimates of barometric efficiency and specific storage, presented in Section 6.4.3; and (3) a value of 0.33 obtained from grain-size-distribution analysis, presented in Section 6.4.3.

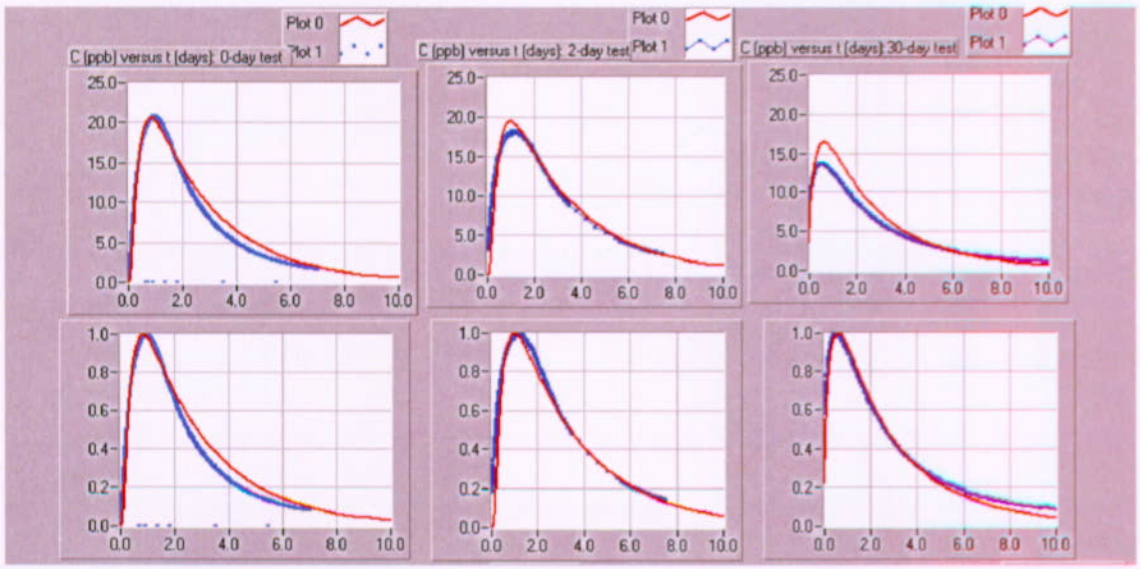

DTN: UN0109SPA008IF.006 [162442] (0-day test), UN0102SPA008KS.003 [162614] (2-day test), UN0109SPA008KS.007 [162615] (30-day test); Output DTN: GS031008312316.003 (analysis).

NOTE: The plots are fits of three injection-pumpback tracer tests with theoretical curves that result from three solutions to the advection-dispersion equation for the three phases of injection, drift, and pumpback. The red curves are the model fits and the blue curves are the data curves. The three top graphs are actual concentrations versus elapsed days, and the bottom three graphs are normalized concentrations versus elapsed days. The parameters used in the calculations are: flow porosity = 0.1, matrix porosity = 0.0, longitudinal dispersivity = 5.05 m, transverse dispersivity = 1.00 m, test interval thickness = 9.75 m (32.0 ft), tracer volume injected = 10,600 L (2,800 gal), chase volume injected = 83,000 L (22,000 gal), injection rate 56.8 L/min = (15.0 gpm), mass injected = 5.0 kg, natural gradient = 0.002 m/m, T for gradient = 20.0 m^2/d, specific discharge = 1.5 m/yr, the Q values for the 0-, 2-, and 30-day tests are 13.41, 11.00, and 13.50, respectively.

Figure 6.5-26. Fitting the Injection-Pumpback Tracer Tests in Screen #1 of NC-EWDP-19D1 Using the Linked-Analytical Solutions Method

6.5.4.3 Groundwater Velocity Analysis Results

Table 6.5-7 lists the results obtained for both v_{GW} and the specific discharge, v_S ($=\eta v_{GW}$), as a function of assumed flow porosity (η) by all four methods of estimation. As expected, of the first three methods, the peak analysis method offers the smallest estimates, and the analysis of late-arriving mass (high recovery) offers the largest. The range of the estimates from the four methods spans about a factor of three for a given assumed value of flow porosity. The velocity estimate from the linked analytical solutions is in very good agreement with the peak analysis method. The peak-analysis method yields a velocity estimate of 17.5 m/yr (specific discharge of 1.75 m/yr), as compared to 15 m/yr (1.5 m/yr specific discharge) from the linked analytical solutions, when a flow porosity of 0.10 is assumed (the flow porosity obtained from the linked analytical solutions).

The specific discharge estimates of Table 6.5-7 are in good agreement with the range of 1.9 to 3.2 m/yr derived from SZ flow-model calibrations (to head and hydraulic conductivity data), which assume a wide range of potential anisotropy in horizontal hydraulic conductivity (BSC 2003 [164870], Table 6-6). The range of values in Table 6.5-7 has been factored into the probability distribution used for specific discharge in the alluvium in Yucca Mountain performance assessment simulations (BSC 2003 [164870], Figure 6-7).

Table 6.5-7. Specific Discharges and Seepage Velocities Estimated from the Different Drift Analysis Methods as a Function of Assumed Flow Porosity

	Specific Discharge (m/yr) / Seepage Velocity (m/yr)		
Assumed Flow Porosity[a]	**0.05**	**0.18**	**0.3**
Peak Arrival Analysis	1.2 / 24.5	2.4 / 13.1	3.0 / 9.9
Late Arrival Analysis[b]	3.9 / 77.1	7.3 / 40.4	9.4 / 31.3
Mean Arrival Analysis[c]	2.0 / 40.3	3.8 / 20.9	4.9 / 16.4
Mean Arrival Analysis[d]	2.5 / 49.1	4.6 / 25.8	6.0 / 20.2
Linked Analytical Solutions	1.5 / 15 with a flow porosity of 0.10 and a longitudinal dispersivity of 5 m.		

Output DTN: LA0303PR831231.002.

NOTE: [a]The three values are approximately the lowest, expected, and highest values of the alluvium flow porosity used in Yucca Mountain performance assessments (BSC 2003 [164870]).

[b]Time/Volume associated with ~86.4% recovery in each test (the final recovery in the 0.5-hr rest period test, which had the lowest final recovery of any test).

[c]Mean arrival time calculated by truncating all tracer response curves at ~86.4% recovery in each test.

[d]Alternative mean arrival time calculated by extrapolating the tracer response curves in the 0.5-hr rest period test to 91.3% and truncating the response curves in the 2-day rest period test to 91.3% recovery (the final recovery in the 30-day rest period test).

6.5.4.4 Discussion of Groundwater-Velocity Analyses

Some significant uncertainties are associated with each of the estimation methods for v_{GW} and v_S described in this report. Although it would be of interest to determine which of the methods provides the best estimate, a detailed analysis of uncertainties was not conducted. In the

discussion that follows, qualitative comments are provided on several uncertainties, and some advantages and potential pitfalls of the different methods are discussed.

The linked-analytical-solution method offers the advantage of providing estimates of flow porosity and longitudinal dispersivity, which are very important parameters for repository performance assessment, in addition to providing flow velocity estimates. Although the parameter estimates in Table 6.5-7 for this method were obtained after many trials using various values of flow porosity, dispersivity, and groundwater flow velocity to fit the three tracer responses simultaneously, an exhaustive sensitivity analysis to evaluate the uniqueness of the matches was not conducted. With such an analysis, it is possible that other combinations of flow porosity, dispersivity, and groundwater-flow velocity could yield essentially equally good matches to the tracer responses.

The value of longitudinal dispersivity obtained from the linked analytical solutions (5 m) intuitively seems large given that calculated injection distances from the well should have been only about 5 to 6 m with a flow porosity of 0.1. This large dispersivity probably reflects that the aquifer was not truly homogeneous and isotropic as assumed, and a large dispersivity was the only way the analytical solutions could account for tracer plume spreading that occurred due to flow heterogeneity.

The impact of ignoring tracer drift during the injection and pumpback phases of testing for the linked-analytical-solution method is not clear. The error introduced by this assumption may be important for the two tests with the shortest rest periods, as the injection and pumpback phases were collectively longer than the rest period in both tests. The remaining discussion is focused on the other three estimation methods, although some aspects of it also apply to the linked-analytical-solution method.

The peak-analysis method would intuitively seem to have considerable uncertainty associated with it because of the inability to determine whether the tracer mass associated with the peak remained upgradient of the well during the rest period or if it drifted back downgradient of the well during the rest phase. The former case was assumed here, as it provides the lowest estimate of groundwater velocity and specific discharge. If the latter case were assumed, the estimated velocity would have been about twice the estimates obtained by the other methods instead of about half the other estimates. Another uncertainty associated with the peak-analysis method is that at least part of the shift in the peak-arrival time/volume may have been due to hydrodynamic dispersion in the system rather than pure advection (as was assumed). A considerable amount of dispersion during the rest phase could have shifted the peak-arrival time without significant translation of the tracer plume's "center of mass" due to advection. However, some advection is necessary for dispersion to occur.

Both the analyses of late-arrival times and mean-arrival times are potentially highly sensitive to diffusion into stagnant water and to density-driven flow resulting from density contrasts between the injection solution and the ambient groundwater. Both of these phenomena can dramatically increase tailing in the tracer response curves and, hence, increase the late-arrival or mean-arrival times/volumes. Although the nearly identical responses of the tracers with different diffusion coefficients in all three tests provide strong evidence that diffusion did not play an important role in the observed tailing behavior in the tests, density contrasts cannot be ruled out. If the tracer

solution was more or less dense than the ambient groundwater during injection (due to either concentration or temperature differences), a portion of the tracer mass could have moved upward or downward into nearly stagnant regions of the aquifer by density-driven flow. Under these conditions, a portion of the tracer mass could remain in the aquifer for an extended period of time because pumping will not rapidly "draw" the tracer out of the nearly-stagnant regions. Despite the disadvantages mentioned above, the peak-analysis method offers an advantage in this situation because the peak-arrival time should be relatively unaffected by such "artificial" tailing behavior.

Assuming that diffusion can either be neglected or corrected for and that the effects of density contrasts are negligible, the mean-arrival-time analysis would intuitively seem to be the method least affected by hydrodynamic dispersion in the system. In theory, dispersion should not affect the mean-arrival time, whereas it will affect the other arrival times. However, the mean-arrival-analysis method has the disadvantage that complete recoveries are seldom achieved in field tracer tests, so the mean must generally be estimated somewhat arbitrarily from either a truncated or an extrapolated distribution, as in the analyses described in this report.

Finally, some practical considerations associated with hypothetically possible test results are worth discussing. Consider a case in which the heterogeneity in aquifer hydraulic conductivity in the vicinity of the well is such that the entire tracer mass moves upgradient of the well during injection. In this situation, it is possible that both the mean and late arrival volumes could be *less* than the sum of the injection and chase volumes. Under these circumstances, the test analyst will have to recognize that the equations used in both the late- and mean-arrival analyses should be modified to account for groundwater flow moving the tracer mass back toward the well. The late-arrival-analysis method will also be sensitive to dispersion in this case.

If the tracer mass moves primarily perpendicular to the direction of ambient ground-water flow during injection but slightly upgradient, the peak-, late-, and mean-arrival methods all have the potential to underestimate groundwater velocities because drift may only slightly alter the separation distance between the tracer mass and the well before pumping starts (Figure 6.5-27). Each of the first three methods will work best if the "center of mass" of the tracer plume is injected either directly upgradient or downgradient. Intuitively, it also seems likely that the uncertainty associated with all the methods should decrease as the difference between the rest periods of the tests, and, hence, the difference in the amount of drift in the tests, increases. An increase in the difference in drift should result in a greater difference in each of the arrival times, which should make the analyses less sensitive to subtle differences in the injection/withdrawal procedures or other non-idealities in the tests.

Additional insights into uncertainties associated with the estimation methods could probably be obtained by (1) generating random-stochastic-hydraulic-conductivity fields having statistics consistent with the current knowledge of the alluvium, and then (2) numerically simulating injection-withdrawal tests in these fields (for various assumed drift velocities). These methods could ultimately yield more refined estimates of groundwater velocities in the alluvium.

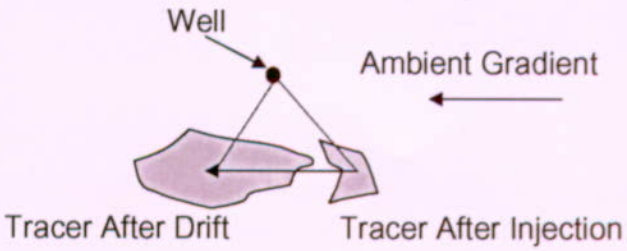

For illustration purposes only

NOTE: The dashed lines connect the well with the center of mass of the tracer "plume" before and after the rest period.

Figure 6.5-27. Depiction of a Tracer Injection Scenario that Could Result in Underestimation of Groundwater Velocity

6.5.4.5 Conclusions From Groundwater-Velocity Analyses

Four methods of estimating groundwater velocities from multiple single-well injection-withdrawal tracer tests conducted with varying rest periods in the saturated alluvium south of Yucca Mountain, Nye County, Nevada are presented in this report. The resulting estimates of groundwater velocity and specific discharge vary over a range of about a factor of 3 for a given assumed flow porosity and by about a factor of 8 for a reasonable range of flow porosities. The estimates of specific discharge range from 1.3 to 9.4 m per year, which falls within the range of specific discharges being used in Yucca Mountain performance assessments (obtained using potentiometric head and hydraulic conductivity data). Flow porosity and longitudinal dispersivity estimates of 0.10 and 5 m, respectively (Output DTN: GS031008312316.003), were obtained using a linked-analytical-solution method.

The same aquifer parameter values obtained from analyzing the three injection-pumpback tracer tests in screen #1 above were used to fit the theoretical breakthrough curve of the above linked-analytical-solutions method to the actual breakthrough curve from the screen #4 injection-pumpback tracer test (detailed documentation contained in Umari (2003 [164573]). The results are shown in Figure 6.5-28. The close fit indicates that the same aquifer parameters that were suitable for screen #1 in well 19D1 are also suitable for screen #4 in the same well.

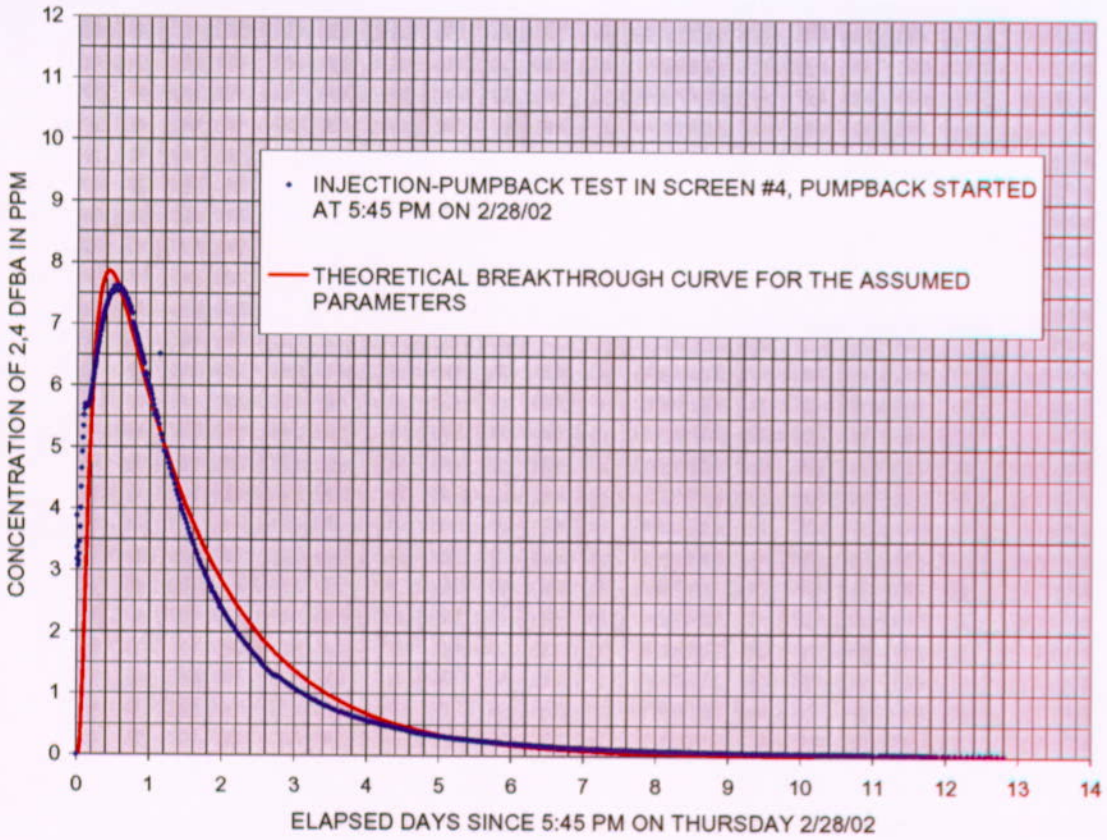

DTNs: MO0205UCC008IF.001 [162617] (data); Output DTN: GS031008312316.003 (analysis).

Figure 6.5-28. Fitting the Theoretical Breakthrough Curve from the Linked-Analytical-Solutions Method to the Actual Breakthrough Curve from the Injection-Pumpback Tracer Test in Screen #4 of NC-EWDP-19D1

6.5.4.6 Estimate of Colloid Detachment Rate Constant from Microsphere Response in Single-Well Test

A rough estimate of the effective detachment rate constant for the 640-nm-diameter polystyrene microspheres that were injected in the zero-rest-period single-well tracer test at 19D1 (Figure 6.5-18) was made as follows. First, the assumption was made that after 90 hr of pumping, the microsphere response is entirely the result of detachment from the alluvium. At this time, about 72% of the solutes had been recovered but only 26% of the microspheres (the final recoveries were 87% and 32%, respectively). In fact, there may have been some spheres recovered after 90 hr that were not truly detaching (they were just making their way out of the system without ever having become attached), so counting these as being detached spheres increases the estimate of the detachment rate constant.

The following simple mass action equation was assumed to apply:

$$Q\,C = k_r M[(1-f_{\text{sphere}})-(1-f_{\text{solute}})] \qquad \text{(Eq. 76)}$$

where

C = concentration of spheres in water produced from well, number/L
Q = production rate from well = 3066 L/hr
k_r = detachment rate constant, 1/hr
M = total number of spheres injected (a known value)
f_{sphere} = fraction of spheres recovered (so $(1-f_{\text{sphere}})$ is the fraction not recovered)
f_{solute} = fraction of solutes recovered.

Equation 76 assumes that the spheres remaining on the alluvium surfaces are equal to the total number of spheres injected times the fraction of spheres not recovered $(1-f_{\text{sphere}})$ minus the fraction of solutes not recovered $(1-f_{\text{solute}})$. Subtracting $(1-f_{\text{solute}})$ from $(1-f_{\text{sphere}})$ is a correction that accounts for the fraction of spheres that would not have been recovered at a given time even if they did not interact with alluvium surfaces. The quantity $[(1-f_{\text{sphere}})-(1-f_{\text{solute}})]$ averages about 0.5 over the last 77 hr of the test (0.46 at 90 hr and 0.545 at 167 hr).

Rearranging Equation 76 to solve for k_r yields the following:

$$k_r = \left(\frac{Q}{[(1-f_{\text{sphere}})-(1-f_{\text{solute}})]}\right)\left(\frac{C}{M}\right) \qquad \text{(Eq. 77)}$$

The quantity C/M is the normalized concentration plotted in Figure 6.5-18. It has a value of approximately 0.0000002/L during the latter portion of the test. Using the average pumping rate during the test of 3066 L/hr, Equation 77 yields a value of 0.0012/hr for k_r (Output DTN: LA0303PR831352.001). This estimate of the detachment-rate constant can be considered high (upper bound) because dC/dt slowly decreased as the test proceeded and the fractional recovery of solutes increased faster than the microsphere recovery (which means that the estimate of the number of spheres remaining on the surfaces according to Equations 76 and 77 actually increased with time—a physical impossibility). The latter contradiction could be remedied by simply setting $(1 - f_{solute})$ equal to zero, which would lower the detachment-rate constant estimate by about 30%.

6.5.4.7 Conclusions from Single-Well Tracer Testing in Alluvium

The fact that there was virtually no difference in the normalized responses of the halide and FBA tracers in the three single-well tracer tests conducted in 19D1 strongly suggests that a single-porosity conceptual model is appropriate for modeling radionuclide transport in the saturated alluvium south of Yucca Mountain. Differences in the tracer responses for the different rest periods in the three tests were apparently the result of groundwater drift during the rest periods, not the result of diffusion between flowing and stagnant water. Further evidence for a single-porosity flow/transport system was provided by the lack of an increase in tracer concentrations after flow interruptions during the tailing portions of the tracer responses in two of the tests. This lack of increase in tracer concentrations indicates a lack of diffusive mass transfer between flowing and stagnant water in the flow system.

Four methods were used to estimate groundwater drift velocities from the three single-well tracer tests. The resulting estimates of groundwater velocity and specific discharge vary over a range of about a factor of three. The estimates are in reasonably good agreement with estimates obtained using potentiometric head and hydraulic conductivity data. It is doubtful that these estimates would be improved significantly by more sophisticated modeling without more detailed information on the distribution of tracer mass after the injection and rest phases of the single-well tests. However, the generation of random-stochastic-hydraulic-conductivity fields having statistics consistent with the current knowledge of the alluvium, followed by the numerical simulation of injection-withdrawal tests within these fields (for various assumed drift velocities), would probably yield considerable additional information on the uncertainties associated with the estimation methods.

6.5.5 Total Porosity Obtained from Borehole Gravimetry at NC-EWDP-19D1

Standard suites of geophysical logs were conducted during, and after, completion of all wells at the ATC. In addition, borehole gravimetry (BHGM) logging of 19D1 was conducted by EDCON, Inc. in September 2000 (DTN: MO0105GPLOG19D.000 [163480]). BHGM logs provide bulk density as a function of depth, from which total porosity as a function of depth can be estimated if grain density is known or assumed. The total porosities deduced from BHGM logging are reported here because they serve as useful upper bounds for effective flow porosity in the alluvium. These estimates can be compared with the estimates of flow porosity obtained from analysis of single-well tracer tests in the alluvium, which are presented in Section 6.5.4. Other estimates of total porosity in the alluvium, obtained from specific storage and barometric efficiency and from grain size distributions, are discussed in Section 6.4.3.

For a water-saturated sample of alluvium, the mass of solids plus the mass of water is equal to the total mass of the sample, i.e.:

$$V_s \rho_s + V_v \rho_w = \rho_b V_T \quad \text{(Eq. 78)}$$

where

V_s is the volume of solids

ρ_s is the density of solids (grain density)

V_v is the volume of voids (filled with water for a saturated medium)

ρ_w is the density of water, ρ_b is the saturated (wet) bulk density of the sample

V_T is the total volume of the sample.

By algebraic manipulation, the porosity, ϕ, which is defined as V_v/V_T, can be obtained from Equation 78 as:

$$\phi = V_v/V_T = (\rho_s - \rho_b)/(\rho_s - \rho_w) \quad \text{(Eq. 79)}$$

Using Equation 79 with $\rho_s = 2.52$ g/cm^3 (USGS n.d. [154495]) and $\rho_w \cong 1.0$ g/cm^3 (ranges from 0.9986 g/cm^3 at 18°C to 0.9959 g/cm^3 at 29°C; (Dean 1992 [100722], p. 5.87)), one can calculate ϕ from various values of ρ_b. For the minimum ρ_b of 2.082 g/cm^3 and the maximum ρ_b of 2.244 g/cm^3 in the alluvium section at 19D1 (DTN: MO0105GPLOG19D.000 [163480]), a maximum porosity of 0.29 and a minimum porosity of 0.18 (Output DTN: GS031008312316.003) are obtained from Equation 79.

Using the entire set of bulk densities for the entire section of 19D1 logged by the BHGM (DTN: MO0105GPLOG19D.000 [163480]) for ρ_b in Equation 79 and the values of ρ_s and ρ_w, given above, total porosities as a function of depth are obtained as shown in Figure 6.5-29.

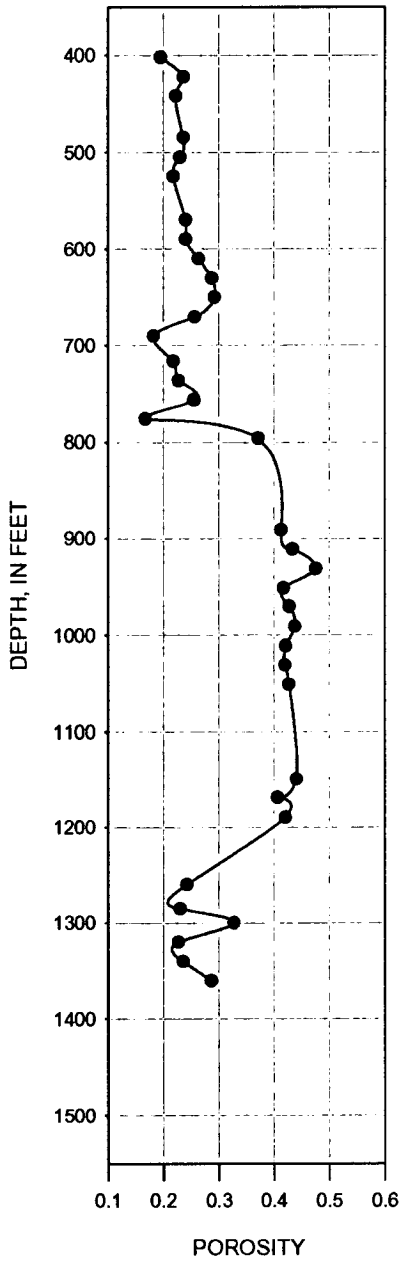

DTN: MO0105GPLOG19D.000 [163480]. Output DTN: GS031008312316.003.

NOTE: The figure is plotted in English units because the data were obtained in those units. However, parameter estimates are reported in metric units to downstream users.

Figure 6.5-29. Total Porosities as a Function of Depth Below Land Surface at NC-EWDP-19D1, Obtained from the Borehole Gravity Meter (BHGM) Survey Conducted in September 2000

6.5.6 Laboratory Transport Tests in the Alluvium

Laboratory measurements of lithium-ion sorption onto alluvium material and tracer transport tests in alluvium-packed columns were carried out in parallel with field tracer testing at the ATC. The objectives of the laboratory tests are the same as for the laboratory testing conducted to support C-wells tracer testing in fractured tuffs: (1) to obtain transport parameter estimates that can help constrain interpretations of the field tracer tests, and (2) to obtain laboratory estimates of lithium sorption parameters that can be compared to field-derived sorption parameter estimates. The latter will allow an assessment of the ability to predict field-scale sorption in the alluvium using laboratory-derived sorption parameters, which is important because laboratory-scale sorption parameters must be used for field-scale predictions of radionuclide transport. Detailed documentation of both the batch and column laboratory tests (the remainder of Section 6.5) is contained in Sullivan (2002 [164623]).

6.5.6.1 Alluvium Cation-Exchange-Capacity Measurements and Lithium Batch-Sorption Experiments

6.5.6.1.1 Alluvium Samples and Their Characteristics

CEC and lithium batch-sorption measurements were conducted on alluvium samples collected from several different depth intervals in wells 19D1 and 19P. The intervals from which material was collected were (in meters [feet] below land surface) 123 to 125 m (405 to 410 ft), 128 to 130 m (420 to 425 ft), 152 to 154 m (500 to 505 ft), 177 to 178 m (580 to 585 ft), 201 to 203 m (660 to 665 ft), 207 to 209 m (680 to 685 ft), 219 to 221 m (720 to 725 ft), and 238 to 239 m (780 to 785 ft) in 19D1, and 125 to 126 m (410 to 415 ft) and 128 to 130 m (420 to 425 ft) in 19P. Particle-size distributions of samples collected from 123 to 125 m and 128 to 130 m in 19D1 and from 125 to 126 m and 128 to 130 m in 19P were determined by a wet-sieve method. Particle-size distributions in all other intervals (all of which were in 19D1) were determined by dry sieving. Well 19P was drilled by a reverse-circulation air hammer method, so the high and low ends of the particle size distribution were considered more representative than in the samples from 19D1, which was drilled using a rotary bit with water as the lubricant. The rotary bit probably broke up the larger particles, and the water washed out most of the smaller particles from the 19D1 samples. Figure 6.5-30 shows a size distribution comparison for material from approximately the same depth intervals in wells 19D1 and 19P.

For the CEC and lithium batch-sorption experiments, measurements were made on material that had been wet- or dry-sieved to a size range between 75 and 2000 μm and also on material that was wet or dry-sieved to less than 75 μm in size. The materials from 19P and from the two uppermost intervals in 19D1 (123 to 125 m and 128 to 130 m) were wet-sieved, and all of the remaining material was dry-sieved. Quantitative minerals abundance analysis using x-ray diffraction (QXRD) (Chipera and Bish 1995 [105075]) was conducted on each fraction used for testing (Table 6.5-8). Not surprisingly, the samples sieved to the smaller size range tended to be richer in smectite clays and zeolites, which have higher CECs than the other minerals listed in Table 6.5-8. Specific surface areas of the samples were measured by a single-point Brunauer-Emmet-Teller (BET) nitrogen adsorption/desorption method (Brunauer et al. 1938 [156646], pp. 309 to 319). The BET surface areas are listed in Table 6.5-9 for each sample. Table 6.5-9 also lists the lithium and cesium CECs of the samples, which are discussed in Section 6.5.6.1.5.

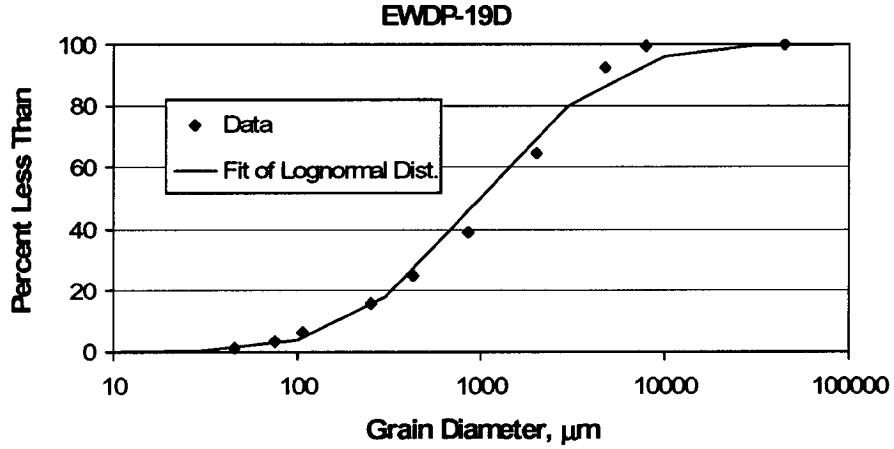

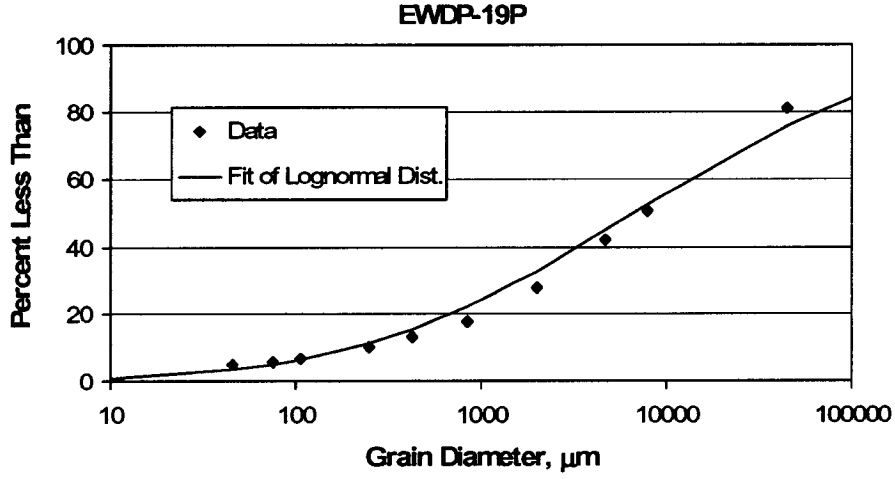

DTN: LA0201JS831421.001 [162613].

NOTE: The mass-weighted particle size distributions above for the two wells are from the same depth interval of 123 to 130 m (405 to 425 ft) below land surface; and the size distributions were determined by dry-sieve analyses.

Figure 6.5-30. Particle Size Distributions of Material in NC-EWDP-19D and NC-EWDP-19P

Table 6.5-8. Mineralogy of Alluvium Samples Used in the Cation-Exchange-Capacity and Lithium Batch-Sorption Experiments Determined by Quantitative X-ray Diffraction

Sample Label*	Smectite	Clinoptilolite	Kaolinite	Mica	Tridymite	Cristobalite	Quartz	Feldspar	Calcite	Hematite	Hornblende	Total
19D 405-410 <75 μm	20 ± 6	10 ± 1	1 ± 1	Trace	3 ± 1	7 ± 2	14 ± 1	39 ± 6	1 ± 1	1 ± 1	—	96 ± 9
19D 405-410 >75 μm	**4 ± 1**	**7 ± 1**	**1 ± 1**	**1 ± 1**	**5 ± 1**	**13 ± 1**	**17 ± 1**	**53 ± 8**	**—**	**1 ± 1**	**—**	**102 ± 8**
19P 410-415 <75 μm	34 ± 10	26 ± 2	1 ± 1	Trace	3 ± 1	5 ± 1	8 ± 1	28 ± 5	1 ± 1	—	Trace	106 ± 12
19P 410-415 >75 μm	5 ± 2	7 ± 1	1 ± 1	1 ± 1	4 ± 1	15 ± 1	18 ± 1	49 ± 7	—	Trace	—	100 ± 8
19D 420-425 <75 μm	16 ± 5	8 ± 1	1 ± 1	Trace	5 ± 1	8 ± 2	13 ± 1	42 ± 6	2 ± 1	1 ± 1	Trace	96 ± 8
19D 420-425 >75 μm	**6 ± 2**	**6 ± 1**	**1 ± 1**	**Trace**	**6 ± 1**	**16 ± 1**	**20 ± 2**	**44 ± 6**	**1 ± 1**	**Trace**	**—**	**100 ± 7**
19P 420-425 <75 μm	40 ± 12	24 ± 2	1 ± 1	Trace	2 ± 1	4 ± 1	8 ± 1	24 ± 4	—	Trace	—	103 ± 13
19P 420-425 >75 μm	11 ± 3	6 ± 1	1 ± 1	Trace	4 ± 1	11 ± 1	22 ± 2	45 ± 7	—	1 ± 1	1 ± 1	102 ± 8
19D 500-505 <75 μm	10 ± 3	10 ± 1	1 ± 1	Trace	5 ± 1	9 ± 3	16 ± 1	43 ± 6	1 ± 1	1 ± 1	—	96 ± 8
19D 500-505 >75 μm	5 ± 2	6 ± 1	1 ± 1	Trace	5 ± 1	15 ± 1	20 ± 2	43 ± 6	—	Trace	—	95 ± 7
19D 580-585 <75 μm	7 ± 2	24 ± 2	1 ± 1	Trace	3 ± 1	7 ± 2	16 ± 1	44 ± 7	1 ± 1	1 ± 1	Trace	104 ± 8
19D 580-585 >75 μm	5 ± 2	10 ± 1	1 ± 1	Trace	4 ± 1	14 ± 1	18 ± 1	45 ± 7	—	Trace	—	97 ± 8
19D 660-665 <75 μm	21 ± 6	24 ± 2	1 ± 1	1 ± 1	2 ± 1	5 ± 1	10 ± 1	36 ± 6	—	Trace	1 ± 1	101 ± 9
19D 660-665 >75 μm	3 ± 1	10 ± 1	1 ± 1	1 ± 1	4 ± 1	12 ± 1	18 ± 1	49 ± 7	—	Trace	Trace	98 ± 7
19D 680-685 <75 μm	12 ± 4	41 ± 2	Trace	Trace	3 ± 1	6 ± 1	8 ± 1	29 ± 5	—	—	1 ± 1	100 ± 7
19D 680-685 >75 μm	4 ± 1	14 ± 1	1 ± 1	1 ± 1	3 ± 1	14 ± 1	19 ± 1	48 ± 7	—	Trace	—	104 ± 7
19D 725-730 <75 μm	17 ± 5	42 ± 3	1 ± 1	Trace	2 ± 1	5 ± 1	11 ± 1	21 ± 4	Trace	—	Trace	99 ± 7
19D 725-730 >75 μm	5 ± 2	15 ± 1	1 ± 1	Trace	3 ± 1	14 ± 1	24 ± 2	41 ± 6	—	Trace	—	103 ± 7
19D 780-785 <75 μm	16 ± 5	31 ± 2	Trace	Trace	2 ± 1	8 ± 2	12 ± 1	34 ± 6	1 ± 1	—	Trace	104 ± 8
19D 780-785 >75 μm	6 ± 2	11 ± 1	Trace	—	3 ± 1	14 ± 1	21 ± 2	47 ± 7	—	Trace	Trace	102 ± 8

DTN: LA0201JS831321.001 [162623].

NOTE: Bold entries denote material used in column experiments.

Mineral abundances are in weight percent.

Errors are 2-sigma values.

— = not detected; Trace = trace amount at less than 0.5 wt%.

Materials from NC-EWDP-19P and the two uppermost intervals in NC-EWDP-19D1 (123 to 125 m [405 to 410 ft] and 128 to 130 m [420 to 425 ft]) were wet-sieved; all other materials were dry-sieved.

*Sample Labels include the interval in feet because the data were collected using English units.

Table 6.5-9. Surface Areas and Lithium and Cesium Cation Exchange Capacities (CEC) of Alluvium Samples Used in the Lithium Batch-Sorption Experiments

Interval † (Well, ft below land surface, size)	BET Surface Area* (m^2/g)	Li CEC (meq/kg)	Cs CEC (meq/kg)
19D, 405-410, < 75 μm	15.96	183	258
19D, 405-410, > 75 μm	**5.34**	**70**	**99**
19P, 410-415, < 75 μm	NM	360	559
19P, 410-415, > 75 μm	NM	126	141
19D, 420-425, < 75 μm	9.80	175	231
19D, 420-425, > 75 μm	**5.64**	**89**	**119**
19P, 420-425, < 75 μm	NM	395	667
19P, 420-425, > 75 μm	8.67	171	186
19D, 500-505, < 75 μm	10.15	125	171
19D, 500-505, > 75 μm	6.17	137	229
19D, 580-585, < 75 μm	NM	204	285
19D, 580-585, > 75 μm	5.17	132	279
19D, 660-665, < 75 μm	NM	303	130**
19D, 660-665, > 75 μm	5.16	119	368
19D, 680-685, < 75 μm	11.16	257	663
19D, 680-685, > 75 μm	3.99	118	439
19D, 720-725, < 75 μm	NM	424	620
19D, 720-725, > 75 μm	5.66	114	433
19D, 780-785, < 75 μm	NM	237	131**
19D, 780-785, > 75 μm	4.43	78	366

DTNs: LA0201JS831421.002 [162625] (BET data); LA0201JS831341.001 [162627] (CEC data).

NOTE: *Surface areas were determined using the nitrogen BET technique.
**Suspected erroneous measurements.
Bold denotes material used in column experiments.
NM: not measured, generally because of insufficient material quantity.
Materials from NC-EWDP-19P and the two uppermost intervals in NC-EWDP-19D1 (123 to 125 m [405 to 410 ft] and 128 to 130 m [420–425 ft]) were wet-sieved; all other materials were dry-sieved.
† The interval is listed in feet because the data were collected using English units.

6.5.6.1.2 Cation-Exchange-Capacity Measurements

CECs of the alluvium from the different depth intervals in well 19D1 were measured using a three-step process of saturating the alluvium surface sites with lithium ion, modified from that of Ming and Dixon (1987 [156842]). Half-gram samples of alluvium were placed in contact with ~30 mL of 1 M LiBr solution prepared in deionized water. The alluvium-solution mixture was shaken for at least 1 hr, centrifuged, and the supernatant was decanted off into a collection container. This treatment was repeated two more times, with the supernatant from each step

being combined with that from the previous steps. The final solution (~90 mL) was analyzed for Na^+, Ca^{++}, K^+, and Mg^{++} using ICP-AES to determine the total number of equivalents of cations that lithium had displaced from the alluvium surfaces. This total number of equivalents divided by the mass of the alluvium sample is the CEC of the alluvium, expressed as eq/kg or meq/g.

It is well known that CECs of materials are dependent on the cation used to saturate the material surfaces (Anghel et al. 2002 [164635], Section 3.1, pp. 821 to 822). The Cs^+ ion is often used to obtain a measure of the "total" CEC of a material because Cs^+ sorbs very strongly to mineral surfaces and will displace most exchangeable cations encountered in nature. To obtain an estimate of the Cs^+-exchangeable CEC, the above procedure was repeated on each of the half-gram alluvium samples that had been subjected to LiBr solution treatments using 1 M CsCl as the saturating solution. However, the CEC determined from the lithium saturation steps was the value used in subsequent modeling of the batch-sorption and column experiments (Section 6.5.6.2) because only cations displaced by lithium are of practical interest when lithium is the sorbing species.

6.5.6.1.3 Batch-Sorption Experiments

Lithium batch-sorption experiments were conducted on each of the sieved alluvium samples. Duplicate measurements were conducted at starting lithium concentrations of approximately 1, 3, 10, 30, 100, and 300 mg/L Li^+ for each material to obtain a sorption isotherm over a 2.5-order-of-magnitude range of concentrations. Starting solutions were prepared by dissolving a known mass of LiBr in a known volume of 19D1 well water and then diluting by weight with well water to the desired starting concentrations. In all of the batch tests, 20 mL of lithium solution was placed in contact with approximately 5 g of alluvium material in 50-mL polycarbonate Oak Ridge centrifuge tubes that were shaken for 48 hr on an orbital shaker. Separate control samples (lithium-spiked solutions in centrifuge tubes without any alluvium material) and blanks (nonspiked well water in contact with alluvium) were processed in parallel with the tubes containing both lithium and alluvium. The controls were used to verify that lithium sorption to tube walls was insignificant, and the blanks were used to measure any lithium background that might be leached out of the alluvium samples. After shaking, the tubes were centrifuged at 30,000 xg for 1 hr, and then an aliquot of supernatant was pipetted off for cation and bromide analyses. Cations (Li, Na, K, Ca, and Mg) were analyzed by inductively-coupled ICP-AES, and bromide (nonsorbing tracer) was analyzed by liquid chromatography with a conductivity detector.

The starting lithium concentration for each measurement was determined from both the corresponding bromide and lithium concentrations in the control samples. In general, lithium concentrations measured in the control samples were in good agreement with those determined from the bromide measurements, indicating that lithium sorption to centrifuge tube walls was negligible. The mass of lithium sorbed per unit mass of alluvium material was determined from:

$$S = \frac{V(C_0 - C)}{M} \qquad \text{(Eq. 80)}$$

where

S = lithium mass sorbed per unit mass of alluvium, mg/g

V = volume of solution in contact with alluvium, L

M = mass of alluvium in contact with solution, g

C_0 = initial concentration of lithium in solution prior to sorption, mg/L

C = final concentration of lithium in solution after sorption, mg/L.

6.5.6.1.4 Interpretation of Batch-Sorption Experiments

It became apparent very early in the batch-sorption experiments that only two cations, Na^+ and Ca^{++}, exchanged significantly with Li^+. K^+ was exchanged to a minor degree, but the amount was so small relative to Na^+ and Ca^{++} that it was considered reasonable to lump the K^+ with the Na^+ as a generic "monovalent cation." Thus, a simplified three-component cation-exchange model analogous to the three-component exchange model used in the MULTRAN V 1.0 code (STN: 10666-1.0-00 [159068]) (Equations 21 through 24 in Section 6.3.9.1.3) was used to interpret the batch experiments.

A simple FORTRAN program called EQUIL_FIT V 1.0 (STN: 10668-1.0-00 [159064]) was developed to obtain the best simultaneous fit to the Li^+, Na^+, and Ca^{++} data obtained in the batch-sorption experiments using Q_1 and Q_2 from Equations 21 and 22 as adjustable parameters. The CEC was set equal to the measured lithium CEC of the alluvium samples. The fits were optimized by minimizing the sum of squares of the differences between the logarithms of the model-predicted concentrations and the experimental concentrations. Logarithms were used in the optimization algorithm so that the fits would not be biased toward the data obtained at the highest lithium concentrations.

6.5.6.1.5 Results of Cation-Exchange-Capacity Measurements

The lithium and cesium CECs of the materials from the sampled alluvium intervals in wells 19D1 and 19P are listed in Table 6.5-9. Only the lithium CEC results were used to interpret the lithium batch-sorption and column transport tests (Section 6.5.6.2) because only cations displaced by lithium are of practical interest in these experiments. It is apparent that the smaller-size fraction material generally had a larger CEC value than the larger-size fraction material from each interval that was tested. Also, the wet-sieved 75- to 2000-μm material from the two uppermost intervals in 19D1 had relatively low CECs compared to the other samples, presumably because the wet-sieving procedure removed many of the clays and zeolite minerals that have high CEC values.

6.5.6.1.6 Results of Batch-Sorption Experiments

The Q_1 and Q_2 values yielding the best simultaneous fits to the Li^+, $[Na^+ + K^+]$, and Ca^{++} data obtained in the lithium batch-sorption experiments are listed in Table 6.5-10 along with the lithium CEC values for each alluvium material tested. Two sets of Q_1 and Q_2 values are listed for each material: (1) one obtained using a direct measurement of the starting lithium concentration as the initial lithium concentration in each experiment and (2) one obtained by using a bromide concentration measurement to determine the starting lithium concentration (the

lithium was introduced as LiBr). The differences between these two sets of values are sometimes quite large for a given alluvium interval. These differences reflect the uncertainty in the Q_1 and Q_2 values due to analytical errors in tracer concentration measurements, and they also reflect the relative insensitivity of the fits to the Q values. Table 6.5-10 also lists the Freundlich isotherm parameters (Equation 12) that yielded the best fits to the lithium sorption data. Larger values of the K_F parameter tend to reflect greater lithium sorption.

Table 6.5-10. Cation Exchange Coefficients (CEC) and Freundlich Isotherm Parameters Resulting in Best Fits to the Li^+, Na^+, and Ca^{++} Data from the Lithium Batch-Sorption Experiments for Alluvium Material

Interval* (well, ft below land surface, size)	i CEC meq/kg)	Li as Starting Conc.		Br as Starting Conc.		Li as Starting Conc.		Br as Starting Conc.	
		Q_1	Q_2 (L^2/kg^2)	Q_1	Q_2 (L^2/kg^2)	K_F (mL/µg) ^{n}(µg/g)	n	K_F (mL/µg) ^{n}(µg/g)	n
19D, 405-410, < 75 µm	183	0.06	0.22	0.06	0.22	0.58	0.82	0.41	0.78
19D, 405-410, > 75 µm	**70**	0.07	0.03	0.06	0.02	0.35	0.85	0.26	0.82
19P, 410-415, < 75 µm	360	0.13	0.004	0.22	0.003	1.48	0.86	0.82	0.81
19P, 410-415, > 75 µm	126	0.11	0.003	0.17	0.003	0.47	0.84	0.26	0.77
19D, 420-425, < 75 µm	175	0.05	0.15	0.04	0.09	0.75	0.89	0.31	0.78
19D, 420-425, > 75 µm	**89**	0.05	0.07	0.04	0.04	0.58	0.94	0.23	0.84
19P, 420-425, < 75 µm	395	0.04	0.5	0.04	0.5	1.25	0.84	1.08	0.82
19P, 420-425, > 75 µm	171	0.05	0.01	0.07	0.002	0.77	0.90	0.38	0.82
19D, 500-505, < 75 µm	125	0.07	0.03	0.06	0.02	0.44	0.79	0.55	0.85
19D, 500-505, > 75 µm	137	0.05	0.03	0.04	0.012	0.43	0.83	0.20	0.78
19D, 580-585, < 75 µm	204	0.07	0.63	0.06	0.49	0.32	0.71	0.56	0.78
19D, 580-585, > 75 µm	132	0.07	0.09	0.06	0.06	0.05	0.55	0.13	0.66
19D, 660-665, < 75 µm	303	0.28	0.002	0.24	0.002	0.47	0.74	0.74	0.80
19D, 660-665, > 75 µm[(1)]	119	0.13	0.09	0.13	0.05	3.67	1.03	2.99	1.01
19D, 680-685, < 75 µm	257	0.16	0.1	0.14	0.04	1.31	0.80	1.10	0.77
19D, 680-685, > 75 µm	118	0.17	0.05	0.16	0.03	0.64	0.78	0.46	0.74
19D, 720-725, < 75 µm	424	0.13	0.011	0.14	0.009	1.25	0.78	1.10	0.77
19D, 720-725, > 75 µm	114	0.21	0.017	0.23	0.01	0.67	0.78	0.48	0.73
19D, 780-785, < 75 µm	237	0.09	0.27	0.09	0.27	0.71	0.77	0.50	0.73
19D, 780-785, > 75 µm	78	0.26	0.03	0.26	0.013	0.52	0.75	0.38	0.74

DTN: LA0201JS831341.001 [162627] (CEC values). Output DTN: LA0303PR831341.002 (sorption parameters).

NOTE: Bold denotes material used in column experiments.

Materials from NC-EWDP-19P and the two uppermost intervals in NC-EWDP-19D1 (123 to 125 m [405 to 410 ft] and 128 to 130 m [420 to 425 ft]) were wet-sieved; all other materials were dry-sieved.

Estimates of the uncertainties in the parameter values listed in this table were not rigorously obtained because these uncertainties are not critical for Performance Assessment calculations. Values represent best estimates only.

Q_1 is dimensionless.

(1) The sorption parameters derived for this alluvium material are suspect because there were very few data points to analyze.

*The interval is given in feet because the data were collected using English units.

Figures 6.5-31 and 6.5-32 show the best fits to the Li^+, $[Na^+ + K^+]$, and Ca^{++} data obtained for the wet-sieved 75- to 2000-μm material from the two uppermost intervals in NC-EWDP-19D1 (123 to 125 m [405 to 410 ft] and 128 to 130 m [420 to 425 ft], respectively). These two materials were combined in a 50:50 mass ratio and used to pack the columns described in Section 6.5.6.2. The data and fits to the data for both the lithium-based starting concentrations; the bromide-based starting concentrations are shown in these figures.

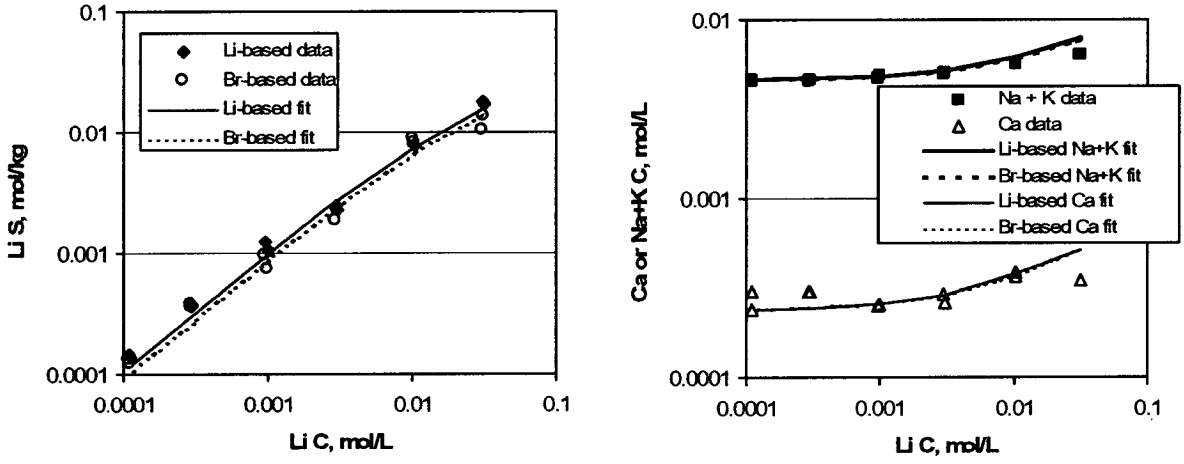

DTN: LA0302JS831341.001 [162628]. (data). Output DTN: LA0303PR831361.002 (model results).

NOTE: The alluvium material is from a depth below the land surface of 123 to 125 m (405 to 410 ft) with a size distribution of 75 to 2000 μm; parameters yielding the fits are listed in Table 6.5-10.

Figure 6.5-31. Best Fits of the Three-Component Cation-Exchange Model to the Lithium Sorption Isotherm (left) and the $[Na^+ + K^+]$ and Ca^{++} Concentration Data (right) for Alluvium Material from NC-EWDP-19D1 at 123 to 125 m (405 to 410 ft)

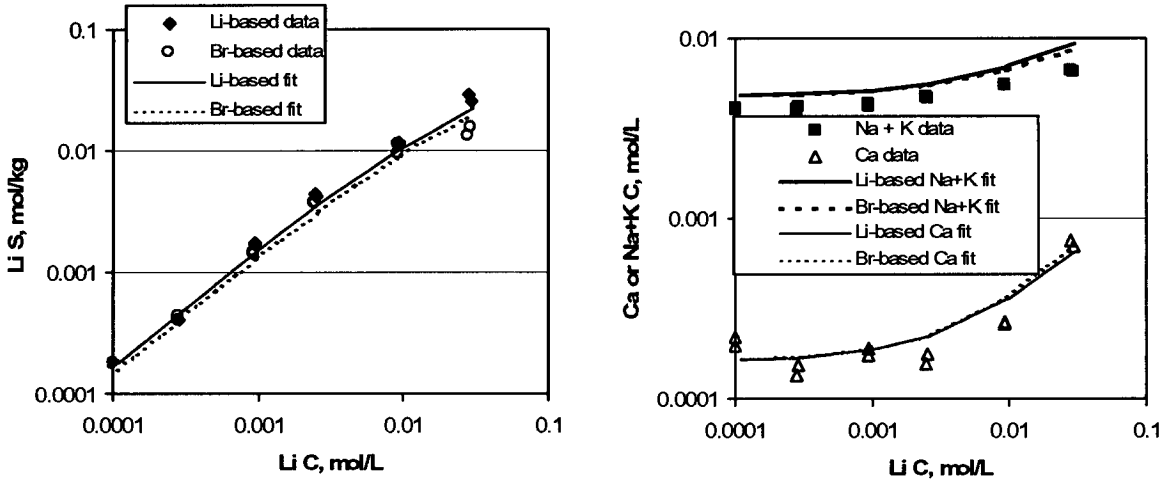

DTN: LA0302JS831341.001 [162628] (data). Output DTN: LA0303PR831341.002 (model results).

NOTE: The alluvium material is from a depth below the land surface of 128 to 130 m (420 to 425 ft) with a size distribution of 75 to 2000 µm; and parameters yielding the fits are listed in Table 6.5-10.

Figure 6.5-32. Best Fits of the Three-Component Cation-Exchange Model to the Lithium Sorption Isotherm (left) and the [Na^+ + K^+] and Ca^{++} Concentration Data (right) for Alluvium Material from NC-EWDP-19D1 at 128 to 130 m (420 to 425 ft)

6.5.6.2 Transport Tests in Alluvium-Packed Columns

This section presents the results and interpretations of several column transport experiments using groundwater and alluvium obtained from the site of the ATC well 19D1 (Figures 6.1-6). These experiments involved injecting lithium bromide as pulses at three different concentrations spanning the range of concentrations expected in the field. The multicomponent numerical transport model, MULTRAN V 1.0 (STN: 10666-1.0-00 [159068]) (see Section 6.3.9.2.2), was used to describe lithium transport through the columns. Companion batch lithium sorption and CEC measurements are discussed in Section 6.5.6.1.

6.5.6.2.1 Materials and Methods

All experiments were conducted using groundwater batches collected from well 19D1 in June 2000 or November 2000. The batches had slightly different chemistries because they were collected from different depth intervals (Table 6.5-11). Batch 1 was used for all experiments except the column experiments with the intermediate LiBr injection concentration. Both waters are essentially sodium-bicarbonate waters that are nearly saturated with respect to silica and with a pH > 8. The groundwater was filter-sterilized using a 0.2-µm filter before use.

The alluvium used in the experiments was obtained from well 19D1 at the depth intervals of 123 to 125 m (405 to 410 ft) and 128 to 130 m (420 to 425 ft) below ground surface (bgs), approximately 15 to 23 m (50 to 75 ft) below the water table. Cuttings samples were wet-sieved

(using 19D1 well water) in the laboratory, and the size range between 75 μm and 2000 μm was retained for testing. Material from the two intervals was combined in a 50:50 mass ratio for the column experiments because there was not enough material from the individual intervals to pack the columns. Table 6.5-8 gives the bulk mineralogy of the alluvium from the two intervals (in bold) as determined by QXRD (Chipera and Bish 1995 [105075]). Table 6.5-9 lists the surface area of the samples (again, in bold) determined by a single-point BET nitrogen adsorption/desorption method (Brunauer et al. 1938 [156646]).

Table 6.5-11. Major Ion Chemistry of NC-EWDP-19D1 Water Used in the Experiments

Species	Batch 1 [(a)] (mg/L)	Batch 2 [(b)] (mg/L)
Ca^{++}	2.2	7.5
Na^{+}	118	75.5
K^{+}	5.2	4.1
Mg^{++}	1.13	0.65
Li^{+}	0.15	0.09
Si	52.5	27.1
HCO_3^{-}	193	168
CO_3^{2-}	43.8	0
SO_4^{2-}	25.9	23.0
Cl^{-}	5.7	5.6
F^{-}	2.1	1.8
pH	9.2	8.1

DTN: LA0303PR831232.001 [162781].

NOTE: (a) Batch 1 was collected in June 2000 from an open borehole.
(b) Batch 2 was collected from two isolated screened intervals in the upper 46 m (150 ft) of the saturated zone. This batch was used only for the 0.006 M LiBr column experiments.

Column experiments were conducted in duplicate using separate 30-cm long by 2.5-cm diameter glass columns equipped with polytetrafluoroethylene (PTFE) end fittings, including a 20-μm end frit and PTFE tubing. Each column was presoaked in deionized water to remove any residual ions. The columns were packed dry with a 50:50 mass ratio of the wet-sieved alluvium from the two intervals that were used in batch-sorption and CEC testing. The columns then were saturated by flushing with deaerated groundwater until air bubbles were no longer visible. They also were packed in ice for 8 hr to promote oxygen and nitrogen dissolution in the water. The saturated versus dry weights of the columns indicated a final porosity of about 40% with a pore volume of about 60 mL in each column.

Three transport experiments were conducted in each column at a flow rate of approximately 10 mL/hr with the two columns run in parallel. Each experiment involved the injection of approximately one pore volume of a tracer solution containing LiBr and 2 mg/L of an FBA (either PFBA or 2,4-difluorobenzoate) dissolved in 19D1 groundwater. The experiments

differed in the concentrations of LiBr in the injection pulses. The first duplicate set of experiments was conducted using an injection concentration of 0.0275 M LiBr (190 mg/L Li^+), the second set had a concentration of 0.006 M LiBr (42 mg/L Li^+), and the third set had a concentration of 0.0013 M LiBr (9 mg/L Li^+). These concentrations were selected so that Li^+ dominated the cation equivalents in solution in the first case (91% of total cation equivalents), accounted for about half of the cation equivalents in the second case (61%), and were a relatively minor fraction of the total cation equivalents in the third case (24%). These three situations represent a range of conditions that will likely occur during field testing, with relatively high concentrations present near the injection well immediately after injection and concentrations decreasing as the tracer pulse advects and disperses through the flow system.

The tracer solutions were injected simultaneously into the two columns using a syringe pump (Harvard Systems). After one pore volume of tracer was injected, tracer-free groundwater was injected at 10 mL/hr using a piston pump (SciLog). Column effluent samples were collected using an automatic fraction collector (Gilson) set up to collect samples simultaneously from both columns in pre-weighed test tubes at pre-set time intervals. The samples were analyzed for the same cations (Li, Na, K, Ca, and Mg) that were analyzed in the batch-sorption experiments using ICP-AES. Bromide and the FBAs were analyzed by liquid chromatography, with the latter being quantified by UV absorption. Samples were diluted as necessary for the tracer analyses.

6.5.6.2.2 Interpretive Modeling Approach

The column transport experiments were simulated using the MULTRAN V 1.0 (STN: 10666-1.0-00 [159068]) multicomponent ion-exchange transport model (Section 6.3.9.2.2). The columns were modeled as single-porosity systems because the FBAs and bromide had essentially identical normalized concentration responses in all experiments, indicative of a system that lacks secondary (stagnant) storage porosity (see Section 6.5.2). The mean residence time and Peclet number (dispersivity) were adjusted to achieve a qualitative fit to the bromide responses in each experiment. The lithium responses were then fitted by adjusting the CECs, Q_1 and Q_2 (see Section 6.5.6.1.3) while setting the CEC of the alluvium equal to the average CEC of the two materials used to pack the columns (80 meq/kg; see Table 6.5-9).

6.5.6.2.3 Experimental Results and Analyses

The breakthrough curves of Br^-, Li^+, Na^+, and Ca^{++}, expressed as meq/L versus volume eluted through the columns, are shown in Figures 6.5-33, 6.5-34, and 6.5-35, for the experiments conducted at each of the three LiBr injection concentrations, respectively. These figures also show the MULTRAN V 1.0 (STN: 10666-1.0-00 [159068]) fits to each data set. The FBA data are not shown in these figures because it was essentially identical to the bromide data when normalized to the injection concentration. However, the FBA concentrations were accounted for in the MULTRAN modeling. A negligible concentration shift of the tracers after a flow interruption in test 2 (Figure 6.5-34, at ~ 500 mL eluted) verified the lack of diffusive mass transfer into secondary storage porosity in the system that was suggested by the identical normalized concentration responses of the bromide and FBA. The apparent slight perturbation in Na^+ concentrations after the flow interruption, with column A showing a minor decrease and column B showing an minor increase, is unexplained. Analyses of additional cations and anions would have been necessary to better understand this phenomenon.

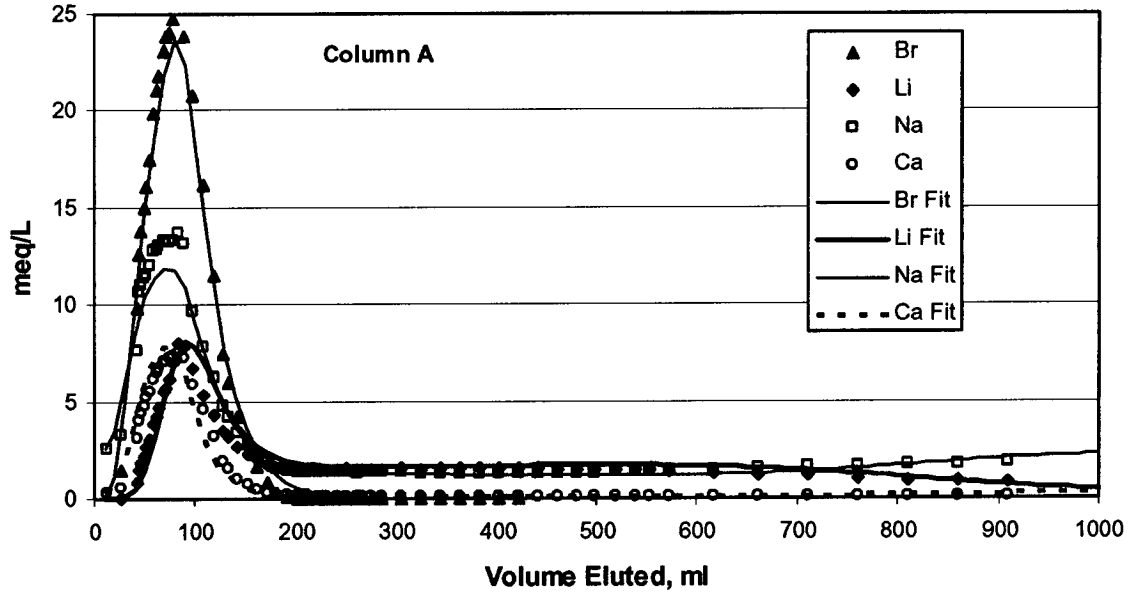

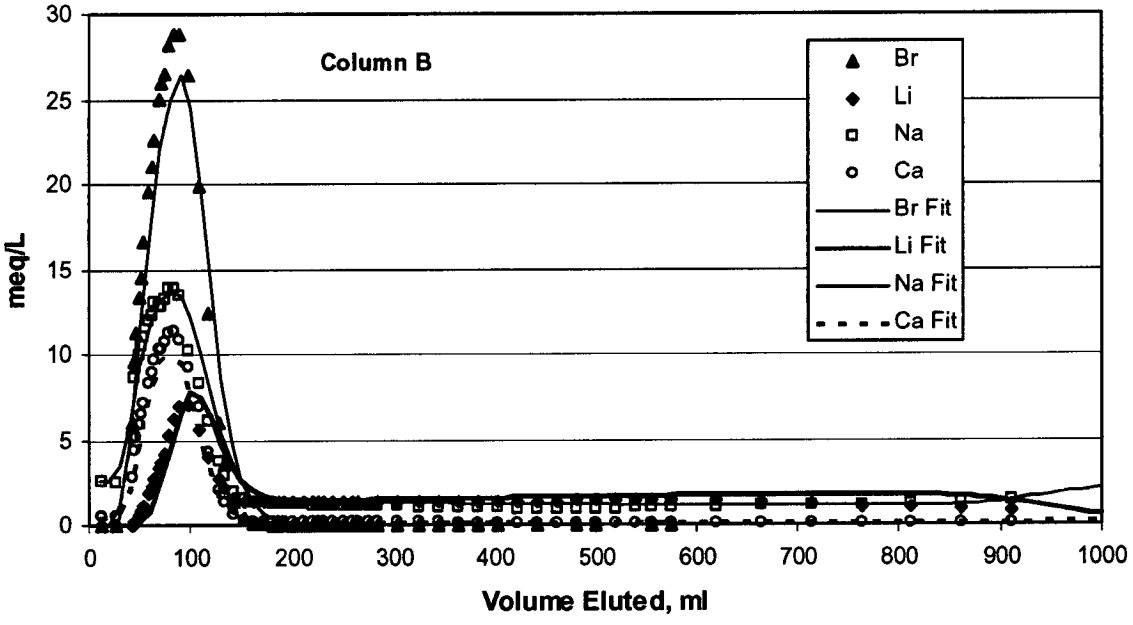

DTN: LA0201JS831361.001 [162629] (data). Output DTN: LA0303PR831361.002 (model results).

Figure 6.5-33. Column Data and MULTRAN Fits for Experiments with a LiBr Injection Concentration of 0.0275 M

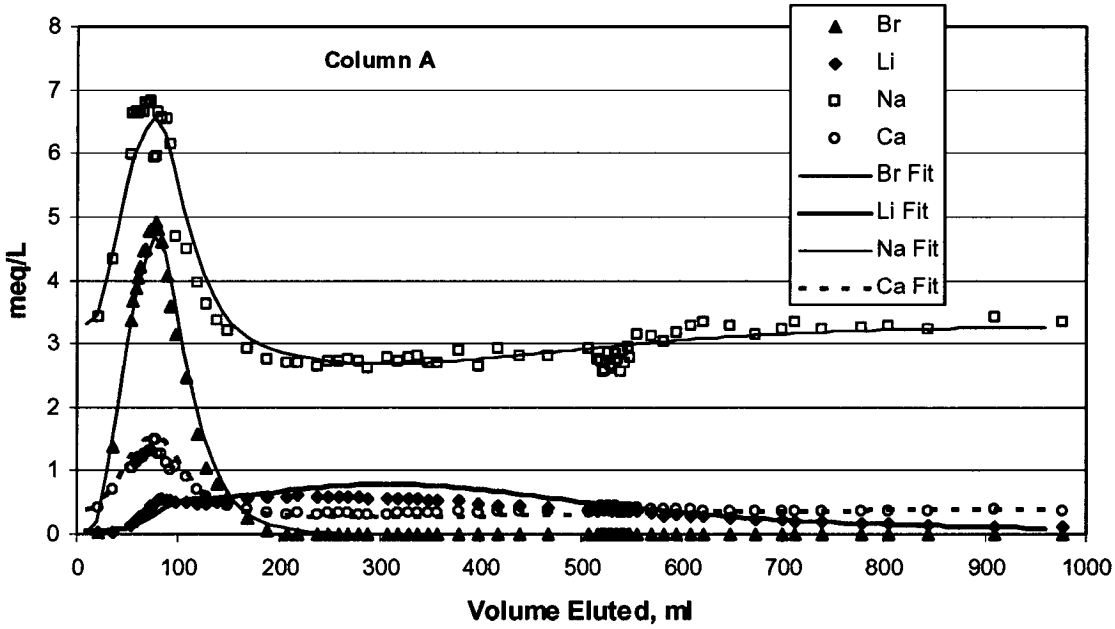

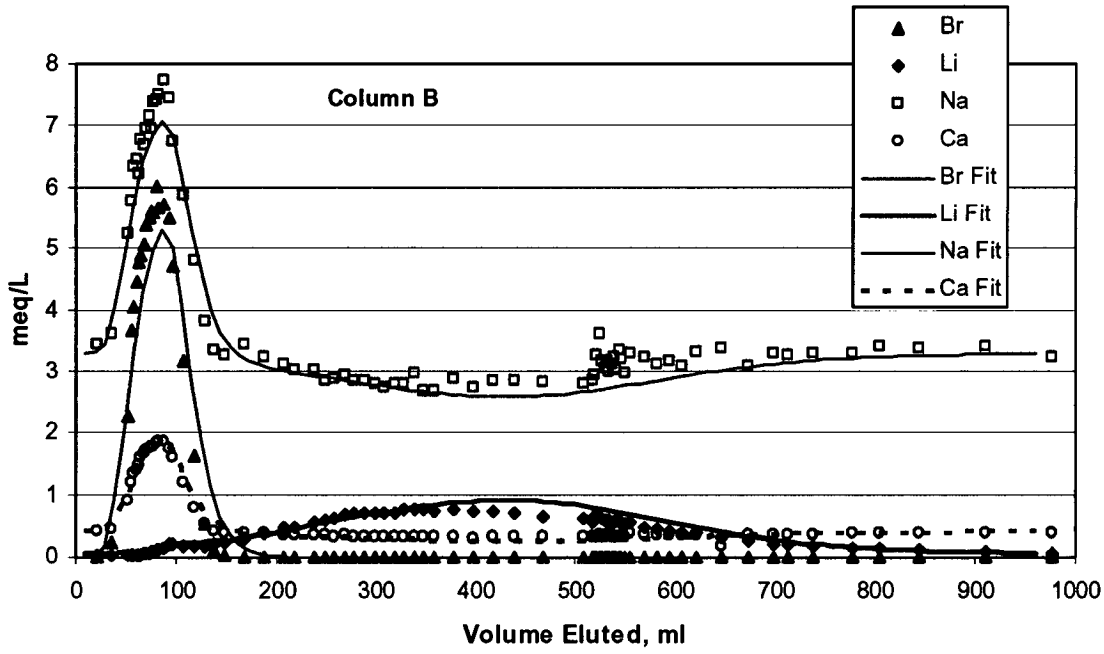

DTN: LA0201JS831361.007 [162630] (data). Output DTN: LA0303PR831361.002 (model results).

Figure 6.5-34. Column Data and MULTRAN Fits for Experiments with a LiBr Injection Concentration of 0.006 M

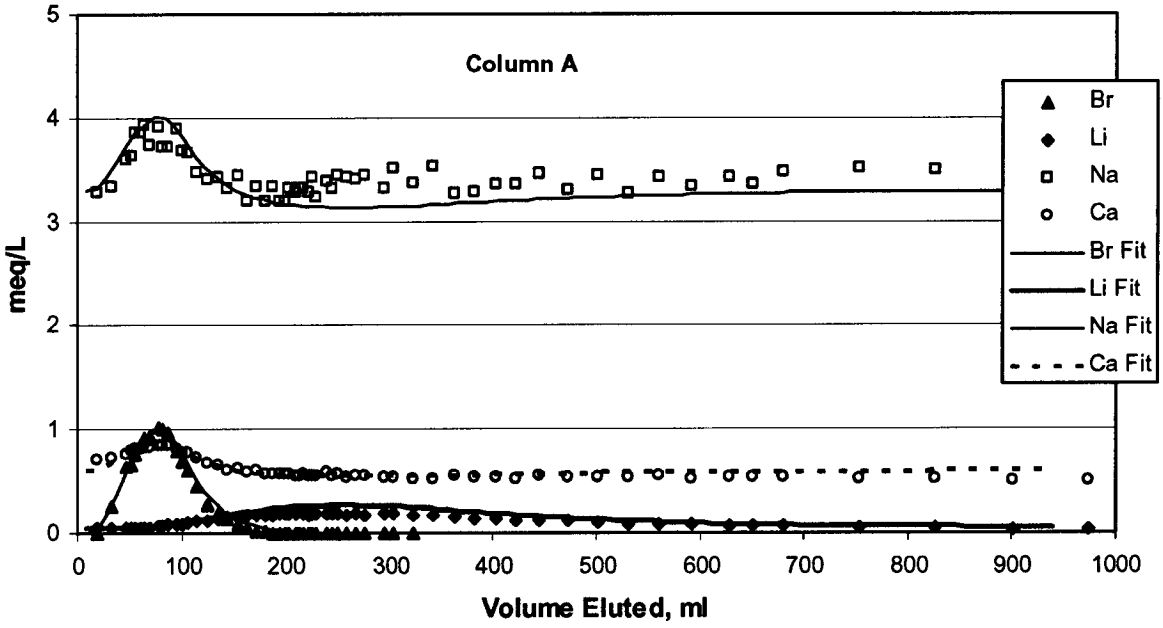

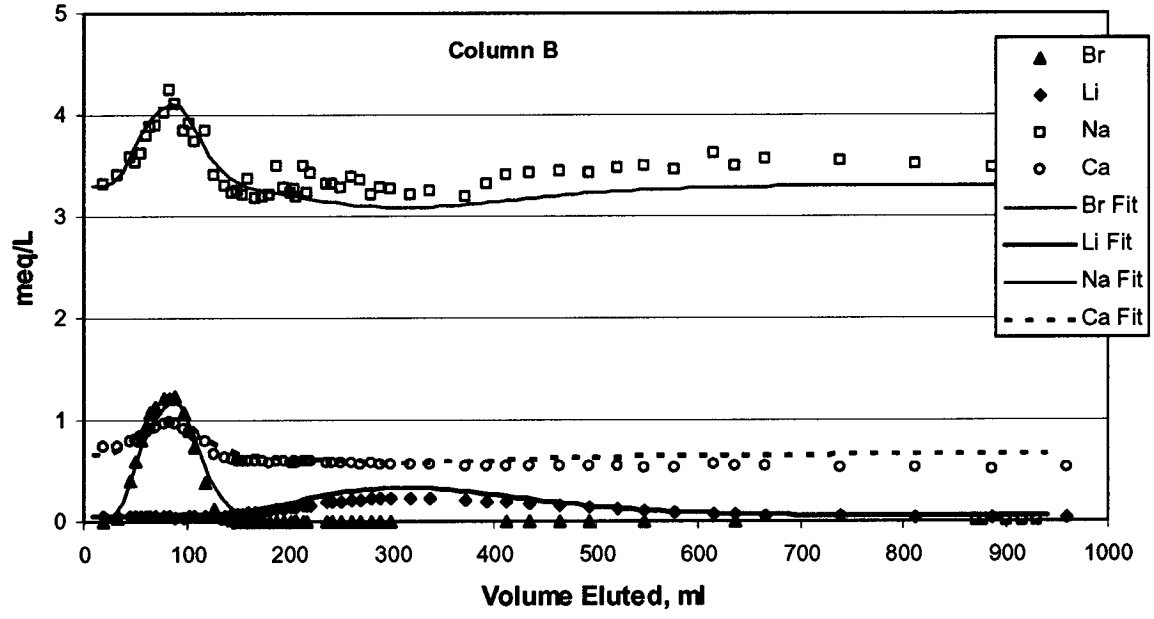

DTN: LA0201JS831361.005 [166205] (data). Output DTN: LA0303PR831361.002 (model results).

Figure 6.5-35. Column Data and MULTRAN Fits for Experiments with a LiBr Injection Concentration of 0.0013 M

The MULTRAN V 1.0 (STN: 10666-1.0-00 [159068]) model parameters resulting in the best fits shown in Figures 6.5-33, 6.5-34, and 6.5-35 are listed in Table 6.5-12. As with the interpretation of the batch-sorption experiments, the lithium CEC was fixed to 0.08 eq/kg for all of the experiments, and Q_1 and Q_2 were adjusted to fit the data. The dispersivity in the column was also adjusted to obtain a reasonable fit to the bromide response curve. The fits were found to be quite sensitive to the background concentrations assumed in the simulations, which were variable in the experiments because the columns were re-used to conduct subsequent experiments, and residual concentrations of the cations varied somewhat. As Tables 6.5-10 and 6.5-12 indicate, the best-fitting ion-exchange constants for lithium exchange with both sodium/potassium (Q_1) and calcium (Q_2) were generally higher in the column experiments than in the batch experiments. The use in MULTRAN of the Q_1 and Q_2 values obtained from the batch experiments consistently overpredicted lithium responses and underpredicted sodium and calcium responses than were observed.

Table 6.5-12. MULTRAN Model Parameters Associated with the Fits to the Column Transport Data

Experiment	Dispersivity (cm)	Q_1	Q_2 (L^2/kg^2)
0.0275 M LiBr, Column A (Figure 6.5-33)	5.4	0.06	0.12
0.0275 M LiBr, Column B (Figure 6.5-33)	1.8	0.045	0.22
0.006 M LiBr, Column A (Figure 6.5-34)	5.4	0.104	0.083
0.006 M LiBr, Column B (Figure 6.5-34)	1.8	0.104	0.083
0.0013 M LiBr, Column A (Figure 6.5-35)	5.4	0.104	0.083
0.0013 M LiBr, Column B (Figure 6.5-35)	1.8	0.104	0.083

Output DTNs: LA0303PR831361.002; LA0303PR831231.005.

NOTE: The model parameters above do not include mean residence times. The column transport data are shown in Figures 6.5-33, 6.5-34, and 6.5-35. The lithium CEC value was assumed to be 0.08 eq/kg for all simulations.

Estimates of the uncertainties in the parameter values listed in this table were not rigorously obtained because these uncertainties are not critical for Performance Assessment calculations. Values represent best estimates only.

Q_1 is dimensionless.

The Q_1 and Q_2 values obtained for each experiment within a given column or for the different columns at a given LiBr injection concentration were in reasonably good agreement, especially after the first set of tests (Table 6.5-12). In principle, these values should not change from column to column or from experiment to experiment because the columns contained exactly the same material. The MULTRAN V 1.0 (STN: 10666-1.0-00; [159068]) fits were not obtained using a least-squares minimization or optimization algorithm, but rather they were obtained by manually adjusting parameters to obtain a good visual fit to the data.

6.5.6.2.4 Discussion

Examination of the MULTRAN V 1.0 (STN: 10666-1.0-00 [159068]) model fits shown in Figures 6.5-33, 6.5-34, and 6.5-35, indicates that the model describes well the transport behavior of the cations through the columns, even though the response curves varied significantly for the three different LiBr injection concentrations. Furthermore, the model parameters did not have to be changed significantly for the different injection concentrations to achieve good fits. This result suggests that the model accurately represented the transport processes occurring in the columns.

The partial nonsorbing transport behavior of lithium ion at high injection concentrations (e.g., Figure 6.5-33) is a consequence of both the limited lithium sorption capacity of the alluvium and the requirement that local charge balance must be maintained throughout the columns. When the concentration of lithium ion was a significant fraction of the total cation concentrations in the injection solution (in eq/L), some of the lithium was forced to move without sorbing through the columns with the nonsorbing anion tracers to maintain charge balance. This phenomenon occurred because the CEC and the cation exchange constants (Q_1 and Q_2) of the alluvium were not so large that all of the injected lithium could be exchanged for sodium and calcium ions to balance the anion tracer charge. The fraction of early-arriving lithium in the column tests decreased as the LiBr injection concentration decreased; and when the Li^+ concentration was only 24% of the total cation eq/L, the lithium was essentially completely retarded (Figure 6.5-35). The lithium responses at the lowest LiBr injection concentration were the only responses that could be adequately modeled when a simple linear partition coefficient, (K_d = mass sorbed per unit mass of solid/solution concentration) was assumed (fits not shown). Such a model assumes that lithium transport is independent of all other species in solution, which is clearly inaccurate at higher injection concentrations for which it becomes a significant fraction of the total cation equivalents in solution.

6.5.6.2.5 Implications of Column Experiment Results for Field Testing

The lithium transport behavior observed in the column experiments and depicted in Figures 6.5-33 through 6.5-35 has important implications for potential cross-hole field tracer testing in the alluvium south of Yucca Mountain. It is common practice to inject large masses and, hence, high concentrations of sorbing tracers in field tests because the combination of sorption, dispersion, and dilution can result in very low concentrations at the production well. Large tracer injection masses and concentrations would, therefore, be used in cross-hole field tests to ensure adequate detection and quantification of lithium concentrations at the production well. This strategy means that lithium concentrations could tend to remain quite high for some time (and distance) near the injection well, which could result in some of the lithium moving without sorbing through the flow system until the tracer "slug" became dispersed and diluted.

There are two possible extremes of sorbing tracer transport in a cross-hole field tracer test that could result in the same observed concentrations at the production well. The first is that the injected tracer slug could disperse and dilute rapidly near the injection well, resulting in a low average concentration throughout the flow system. The second is that the tracer slug could remain relatively concentrated as it moves to the production well and then be diluted in the well bore as a result of mixing with tracer-free water that is also being drawn into the well. There is

no way to distinguish between these two extremes, or any intermediate situation, when nonsorbing tracer responses are analyzed. However, the results and interpretations of the column experiments in this scientific analysis report suggest that the shape of a lithium breakthrough curve in a cross-hole field tracer test may provide a good indication of whether dilution is occurring early or late in the flow system. If dilution occurs early, a lithium response curve similar to those in Figure 6.5-35 can be expected. However, if dilution occurs late, the lithium response curve may look more like those of Figures 6.5-33 or 6.5-34, where there is some asymmetry and nonsorbing transport, even though measured concentrations are quite low because of dilution in the production wellbore. Knowing whether dilution occurs early or late is important when making comparisons between laboratory and field transport behavior. If concentrations remain high in the field test (late dilution), then the lithium may appear to be transporting with less sorption than would be inferred from laboratory batch-sorption measurements, even though the field transport behavior is consistent with the laboratory data if the existence of high concentrations is recognized.

The ability to distinguish between early and late dilution could help refine or constrain estimates of effective flow porosities derived from cross-hole tracer tests. When nonsorbing tracer responses are analyzed, flow porosity estimates are typically based on first, mean, or peak arrival times of nonsorbing tracers. Under ideal radial flow conditions in a 2-D aquifer, Equation 10 can be used to estimate effective flow porosity. Equation 10 (which is a rearrangement of Equation 6 of Guimera and Carrera 2000 [156830]) and the definitions of its variables are repeated here for convenience:

$$\eta = \frac{Q\tau}{\pi L^2 T} \qquad \text{(Eq. 10)}$$

where

η = flow porosity

Q = production flow rate, m^3/hr

τ = mean residence time of a nonsorbing tracer, hr

L = distance between wells, m

T = formation thickness (assumed to be well screen length).

If flow heterogeneity exists, causing the flow field to not be radial, then estimates using Equation 10 will be erroneous. For instance, if most of the flow to the production well is channeled from a direction that does not intersect the tracer slug, then the interwell travel time for the slug can be very long, even if flow occurs in only a small fraction of the system volume. In this case, a considerable amount of dilution will occur late in the system (in the production well), and a misleadingly high flow porosity will be deduced from Equation 10. If an asymmetric lithium response curve with some apparent nonsorbing transport is detected at the production well, the degree of asymmetry in the response can, in principle, be used to estimate the volume that the tracer pulse flowed through within the system. Such an estimate can be obtained by first using MULTRAN V 1.0 (STN: 10666-1.0-00 [159068]) in inverse mode to match the shape of the response curve, given a known injection pulse concentration, injection duration, alluvium CEC (estimated from laboratory tests), and a longitudinal dispersivity (estimated from the nonsorbing

tracer responses). Once a curve shape is matched given these constraints, the flow system volume can be estimated by multiplying the volume of the injection pulse in the field test by the ratio of flow system volume to injection pulse volume assumed in the MULTRAN simulations. An estimate of flow porosity can then be obtained from:

$$Q = \frac{V}{\pi L^2 T} \qquad \text{(Eq. 81)}$$

where V = volume determined from MULTRAN matches to lithium response.

The flow porosity estimate given by Equation 81 is independent of tracer travel times and, therefore, is not biased by flow channeling resulting from flow system heterogeneity. Of course, if the lithium response curve shows no asymmetry, then the method described above can only be used to establish a lower bound for the effective flow porosity. The method relies on the assumption of fast ion exchange kinetics relative to travel times in the flow system (i.e., the local equilibrium assumption), which should be satisfied unless travel times are less than a few hours. Six-hour residence times in the laboratory columns were apparently long enough that the local equilibrium assumption was satisfied.

INTENTIONALLY LEFT BLANK

7. CONCLUSIONS

7.1 SUMMARY OF SCIENTIFIC ANALYSIS

This scientific analysis report documents the results of numerous in-situ field hydraulic and tracer tests conducted in the saturated zone near Yucca Mountain over the past 10 years. These tests were conducted to verify/validate conceptual models of flow and transport in the SZ and to obtain field-scale estimates of flow and transport parameters to support the development of parameter distributions used in process and TSPA models. This analysis report also documents the results of several laboratory experiments conducted to help constrain field tracer test interpretations and to provide comparisons between field- and laboratory-derived sorption parameters for the lithium ion, which is a weakly-sorbing tracer.

The most significant conclusions from in-situ field testing with regard to barrier capability of the saturated zone are the following.

- For flow modeling purposes, the saturated volcanic tuffs in the vicinity of Yucca Mountain can be treated as an equivalent porous medium (at least locally). The fracture networks in the tuffaceous rocks are apparently well enough connected that hydraulic responses are similar to those observed in porous media. However, the flow system exhibits layered heterogeneity with layers of high permeability often associated with relatively narrow fractured intervals. Also, larger-scale hydraulic characteristics of the saturated tuffs are strongly influenced by structural features such as faults. Hydraulic parameters derived from cross-hole testing in the fractured volcanics are summarized in Section 6.2, Tables 6.2-7 through 6.2-9.

- Horizontal anisotropy in hydraulic conductivity in the saturated fractured volcanic tuffs near Yucca Mountain, as determined from drawdown responses in distant wells during the 1996-1997 long-term pumping test in UE-25 c#3, is oriented roughly north-south (direction of greatest conductivity) with an anisotropy ratio of about 4:1. A cumulative distribution function for anisotropy ratio assuming a north-south orientation of anisotropy is provided in Section 6.2.6, Figure 6.2-46.

- Solute tracer responses in cross-hole tracer tests at the C-wells were consistent with a dual-porosity conceptual transport model. In this model, solute migration occurs primarily in flowing fractures, but the solutes are effectively attenuated by diffusion into stagnant water in the porous rock matrix (matrix diffusion). Solute transport parameters derived from cross-hole tracer testing at the C-wells are summarized in Section 6.3, Tables 6.3-2, 6.3-3, and 6.3-10.

- Apparent sorption of an ion-exchanging tracer (lithium) was generally greater in field tracer tests in the volcanic tuffs than in laboratory tests using the same materials. These results lend credibility to the practice of using laboratory-derived radionuclide sorption parameters in performance assessment simulations, as they suggest that laboratory parameters will tend to yield conservative predictions of radionuclide transport in the tuffs. Comparisons of field and laboratory lithium sorption parameters are provided in Section 6.3, Table 6.3-11.

- Polystyrene microsphere responses in cross-hole tracer tests at the C-wells suggest that filtration processes effectively attenuate a large percentage of the microspheres over relatively short distances. However, some of the filtered microspheres later detach from fracture surfaces and continue to migrate. Also, flow transients appear to be capable of initiating detachment. Estimates of microsphere transport parameters derived from the C-wells tracer tests are provided in Section 6.3, Tables 6.3-8 and 6.3-9.

- Single-well hydraulic testing in the saturated alluvium at the NC-EWDP-19D1 location south of Yucca Mountain has indicated that the alluvium behaves as an unconfined aquifer. Preliminary horizontal hydraulic conductivity estimates from the hydraulic testing in the alluvium are 0.15 to 0.23 m/day (0.5 to 0.75 ft/day) in Section 6.4.

- Single-well injection-withdrawal tracer testing in the saturated alluvium in the uppermost screened interval of NC-EWDP-19D1 has indicated that the saturated alluvium at this location behaves as a single-porosity medium. The tracer tests have yielded preliminary detachment rate constants for polystyrene microspheres. They have also yielded estimates of specific discharge that range from about 1 to 10 m/yr (see Section 6.5.4).

- All of these conclusions indicate that the saturated zone beneath and downgradient of the Yucca Mountain repository should serve as an effective barrier to radionuclide transport. In the context of the over-all predicted performance of the engineered and natural barrier systems, the results documented in this analysis report and the uncertainties associated with these results support the adequacy of the saturated zone to meet its performance expectations. Section 7.3 lists specific locations in Section 6 where the reader can find discussions of uncertainties associated with hydrologic and transport parameters that are derived from SZ in-situ testing. These uncertainties are incorporated into probability distributions for parameters that are documented primarily in the SZ transport model abstraction report (BSC 2003 [164870]).

The SZ included Features, Events, and Processes (FEPs) supported by this scientific analysis report are: 1.2.02.01.0A Fractures, 1.2.02.02.0A Faults, 2.2.03.02.0A Rock Properties of Host Rock and Other Units, 2.2.07.13.0A Water-Conducting Features in the SZ, and 2.2.07.15.0A Advection and Dispersion in the SZ. These FEPs are addressed in more detail in Section 6.1.3.

The specific acceptance criteria that relate to this report are discussed in Section 4.2.

7.2 OUTPUTS

Table 7-1 lists the output data for this scientific analysis report. The data will be used primarily to support the development of cumulative distribution functions (CDFs) for various flow and transport parameters used in TSPA simulations. These CDFs are documented in the SZ flow and transport abstraction model report (BSC 2003 [164870]). The horizontal hydraulic conductivity anisotropy ratio described in Section 6.2.6 will also be used to support flow model calibrations described in the revision to the SZ flow model report, MDL-NBS-HS-000011 (BSC 2003 [162649]). Also, transport parameters and tracer breakthrough curves from C-wells tracer testing (Section 6.3) will be used in the model validation section of the revision to the SZ transport model report MDL-NBS-HS-000010 (BSC 2003 [162419]) and in the development of colloid

transport parameter distributions in the revision to the SZ colloid transport scientific analysis report, ANL-NBS-HS-000031 (BSC 2003 [162729]).

Table 7-1. Output Data

Data Description	Data Tracking Number	Location of Output DTNs in This Report
Filtered UE-25 ONC-1 water levels, April, 1995 to December, 1997.	GS030208312314.001	Section 6.2.6.1.2 Section 6.2.6.2.1
Filtered UE-25 WT#3, UE-25 WT#14, and USW H-4 water levels, April, 1995 to December, 1997.	GS030208312314.002	Section 6.2.6.1.2 Section 6.2.6.2.1
PDF and CDF for in north-south/east-west anisotropy ratio in fractured volcanics.	SN0302T0502203.001	Figure 6.2-46 Section 6.2.6.3
Analysis of hydrologic properties of fractured tuffs (C-wells complex).	GS031008312314.004	Figures 6.2-1 to 6.2-45 Tables 6.2-1 to 6.2-10 Table 6.2-12
Analysis of hydraulic testing, ATC.	GS031008312316.002	Figure 6.4-2 Figures 6.4-4 to 6.4-8 Figures 6.4-10 to 6.4-13 Figures 6.4-23 to 6.4-24 Sections 6.4.1.2 to 6.4.1.5 Sections 6.4.2, 6.4.2.1 Sections 6.4.3, 6.4.4
Analysis of tracer testing, C-wells, Bullfrog, and Tram.	GS031008312315.002	Figure 6.3-1 Figures 6.3-3 to 6.3-9 Figures 6.3-12 to 6.3-13 Figures 6.3-15 to 6.3-16 Tables 6.3-2 to 6.3-3
Analysis of tracer testing, ATC.	GS031008312316.003	Figures 6.5-24 to 6.5-26 Figures 6.5-28 to 6.5-29 Sections 6.5.4.2.4, 6.5.4.5 Section 6.5.5
Simulations/modeling of field tracer tests.	LA0303PR831231.003	Figures 6.3-26 to 6.3-30 Figures 6.3-78 to 6.3-79 Tables 6.3-6 to 6.3-9
Fitting or simulations of lithium sorption to C-wells tuffs.	LA0303PR831341.003	Figures 6.3-40 to 6.3-47 Figure 6.3-75 Table 6.3-18
Cation exchange capacity calculations for C-wells tuffs.	LA0303PR831341.001	Figure 6.3-48 Table 6.3-19
DIFFCELL V 2.0 (STN: 10557-2.0-00 [159063]) simulations of diffusion cell data.	LA0303PR831362.001	Figures 6.3-50 to 6.3-57 Tables 6.3-20; 6.3-32
Simulations of crushed C-wells tuff column experiments.	LA0303PR831361.003	Figures 6.3-58 to 6.3-66 Figure 6.3-76 Table 6.3-21
Simulations of C-wells fractured core experiments.	LA0303PR831361.004	Figures 6.3-69 to 6.3-74 Figure 6.3-79 Tables 6.3-28 to 6.3-32

Table 7-1 (Continued). Output Data

Data Description	Data Tracking Number	Location of Output DTNs in This Report
Calculations to obtain values reported in tables and figures (generally combinations of other values reported or unit conversions)	LA0303PR831231.005	Figure 6.3-79 Tables 6.3-6 to 6.3-8 Tables 6.3-10 to 6.3-11 Tables 6.3-28 to 6.3-31 Table 6.5-4 Table 6.5-12
Predictions of transport behavior in single-well and cross-hole tracer tests in the saturated alluvium at the ATC.	LA0303PR831231.001	Figures 6.5-2 to 6.5-3 Figures 6.5-5 to 6.5-8 Figures 6.5-16 to 6.5-17 Tables 6.5-1 to 6.5-3 Section 6.5-3
Predictions of transport behavior in cross-hole tracer tests in single-porosity media.	LA0303PR831231.004	Figures 6.5-9 to 6.5-10 Figure 6.5-12 Figures 6.5-14 to 6.5-15 Table 6.5-4
Calculations to estimate ambient groundwater velocity at NC-EWDP-19D1 from single-well tracer test responses.	LA0303PR831231.002	Figures 6.5-19 to 6.5-21 Tables 6.5-6 to 6.5-7 Section 6.5.4.2.1
Calculations to determine microsphere detachment rate constant in a single-well tracer test in saturated alluvium at NC-EWDP-19D1.	LA0303PR831352.001	Section 6.5.4.6
Determination of cation exchange parameters from EQUIL_FIT V 1.0 (STN: 10668-1.0-00 [159064]) fits to cation concentration data from lithium batch sorption measurements onto alluvium from different intervals in NC-EWDP-19P and -19D.	LA0303PR831341.002	Figure 6.5-32 Table 6.5-10
Simulations of column transport experiments in alluvium from NC-EWDP-19D.	LA0303PR831361.002	Figure 6.5-31 Figures 6.5-33 to 6.5-35 Table 6.5-12
C-wells tracer test sensitivity calculations.	LA0304PR831231.001	Figures 6.3-31 to 6.3-38 Tables 6.3-13 to 6.3-14

7.3 UNCERTAINTIES

Discussions of uncertainties associated with the flow and transport parameters presented in this analysis report can be found in the following sections.

- Uncertainties associated with hydraulic testing and test interpretations in saturated fractured volcanics at the C-wells are discussed in detail in Section 6.2.5.
- Uncertainties associated with anisotropy of horizontal hydraulic conductivity in the fractured volcanics are discussed in Section 6.2.6.
- Uncertainties associated with tracer testing and test interpretations at the C-wells are discussed in detail in Section 6.3.5.

- Uncertainties associated with hydraulic testing and test interpretations in the saturated alluvium at NC-EWDP-19D1 are discussed in Section 6.4.4.

- Uncertainties associated with single-well tracer testing and test interpretations at the ATC are discussed in detail in Section 6.5.4.4.

With the exception of the north-south/east-west anisotropy ratio of horizontal hydraulic conductivity in the fractured volcanics (presented in Section 6.2.6), this scientific analysis report does not provide uncertainty distributions for SZ flow or transport parameters. Uncertainty distributions for these parameters are provided in the SZ transport model abstraction report (BSC 2003 [164870]). The rationale for documenting the uncertainty distributions in the latter report rather than this scientific analysis report is that the distributions are based only in part on the parameters (and their uncertainties) presented in this report. Literature data, expert elicitation input, and peer review input were also considered in the development of parameter distributions because of the limited spatial representation of the SZ offered by the C-wells and ATC hydraulic and tracer tests. Also, the time and distance scales of the C-wells and ATC tests were relatively small compared to time and distance scales of performance assessment calculations (with the exception of the long-term C-wells hydraulic test that led to the uncertainty distribution for hydraulic conductivity anisotropy ratio over a ~21 km^2 area). Thus, it was recognized that the flow and transport parameters derived from the C-wells and ATC tests represent only discrete points in continuous distributions of parameter values that are spatially distributed throughout the SZ and that potentially have scale dependencies that would not be revealed by C-wells and ATC testing. The parameter uncertainty distributions in the SZ model abstraction report (BSC 2003 [164870]) are consistent with and supported by the parameters presented in this analysis report, but they generally consist of a much wider range of potential values because of these issues of representativeness and scale of the field tests.

INTENTIONALLY LEFT BLANK

8. INPUTS AND REFERENCES

8.1 DOCUMENTS CITED

The following is a list of the references cited in this document. Column 1 below contains the unique six-digit numerical identifier (the Document Input Reference System [DIRS] number), which is placed in the text following the reference callout (e.g., BSC 2002 [158198]). The purpose of these numbers is to assist the reader in locating a specific reference in the DIRS database. Within the reference list, multiple sources by the same author or date (e.g., BSC 2002) are sorted alphabetically by title.

164635 Anghel, I.; Turin, H.J.; and Reimus, P.W. 2002. "Lithium Sorption to Yucca Mountain Tuffs." *Applied Geochemistry, 17,* (6), 819-824. New York, New York: Pergamon Press. TIC: 254046.

162534 Bachmat, Y.; Mandel, S.; and Bugayevski, M. 1988. "A Single-Well Tracer Technique for Evaluating Aquifer Parameters, I. Theoretical Work." *Journal of Hydrology,* 99, (1-2), 143-163. Amsterdam, The Netherlands: Elsevier. TIC: 254194.

105038 Bear, J. 1979. *Hydraulics of Groundwater.* New York, New York: McGraw-Hill. TIC: 217574.

156633 Becker, M.W. and Charbeneau, R.J. 2000. "First-Passage-Time Transfer Functions for Groundwater Tracer Tests Conducted in Radially Convergent Flow." *Journal of Contaminant Hydrology, 40,* (4), 299-310. New York, New York: Elsevier. TIC: 251009.

122788 Benson, C.F. and Bowman, R.S. 1994. "Tri- and Tetrafluorobenzoates as Nonreactive Tracers in Soil and Groundwater." *Soil Science Society of America Journal, 58,* (4), 1123-1129. Madison, Wisconsin: Soil Science Society of America. TIC: 246741.

153427 Benson, C.F. and Bowman, R.S. 1996. "Erratum, Tri- and Tetrafluorobenzoates as Nonreactive Tracers in Soil and Groundwater." *Soil Science Society of America Journal, 60,* (4), 1780. Madison, Wisconsin: Soil Science Society of America. TIC: 246741.

113856 Bolt, G.H. and Bruggenwert, M.G.M. 1978. *Soil Chemistry, A. Basic Elements.* Developments in Soil Science 5A. 2nd Revised Edition. New York, New York: Elsevier. TIC: 243742.

156639 Borchardt, G. 1995. "Smectites." Chapter 14 of *Minerals in Soil Environments.* 2nd Edition. Dixon J.B. and Weed, S.B., eds. SSSA Book Series, No. 1. Madison, Wisconsin: Soil Science Society of America. TIC: 237222.

162675 Bouwer, H. 1978. *Groundwater Hydrology.* McGraw-Hill Series in Water Resources and Environmental Engineering. New York, New York: McGraw-Hill. TIC: 244844.

156645 Bowman, R.S. 1984. "Evaluation of Some New Tracers for Soil-Water Studies." *Soil Science Society of America Journal, 48,* (5), 987-993. Madison, Wisconsin: Soil Science Society of America. TIC: 251011.

156646 Brunauer, S.; Emmett, P.H.; and Teller, E. 1938. "Adsorption of Gases in Multimolecular Layers." *Journal of American Chemical Society, 60,* 309-319. Washington, D.C.: American Chemical Society. TIC: 224534.

156647 Brusseau, M.L.; Hu, Q.; and Srivastava, R. 1997. "Using Flow Interruption to Identify Factors Causing Nonideal Contaminant Transport." *Journal of Contaminant Hydrology, 24,* (3-4), 205-219. New York, New York: Elsevier. TIC: 250759.

158198 BSC (Bechtel SAIC Company) 2002. *Test Plan for Alluvial Testing Complex – Single-Well, Multi-Well, and Laboratory Studies.* SITP-02-SZ-003 REV 01. Las Vegas, Nevada: Bechtel SAIC Company. ACC: MOL.20020404.0081.

158966 BSC (Bechtel SAIC Company) 2002. *The Enhanced Plan for Features, Events, and Processes (FEPs) at Yucca Mountain.* TDR-WIS-PA-000005 REV 00. Las Vegas, Nevada: Bechtel SAIC Company. ACC: MOL.20020417.0385.

163128 BSC (Bechtel SAIC Company) 2003. *Features, Events, and Processes in SZ Flow and Transport.* ANL-NBS-MD-000002 REV 02A. Las Vegas, Nevada: Bechtel SAIC Company. ACC: MOL.20030823.0129. TBV-5651

162657 BSC (Bechtel SAIC Company) 2003. *Geochemical and Isotopic Constraints on Groundwater Flow Directions and Magnitudes, Mixing, and Recharge at Yucca Mountain.* ANL-NBS-HS-000021 REV 01A. Las Vegas, Nevada: Bechtel SAIC Company. ACC: MOL.20030604.0164. TBV-5592.

163228 BSC (Bechtel SAIC Company) 2003. *Radionuclide Transport Models Under Ambient Conditions.* MDL-NBS-HS-000008 REV 01. Las Vegas, Nevada: Bechtel SAIC Company. ACC: DOC.20031201.0002.

162729 BSC (Bechtel SAIC Company) 2003. *Saturated Zone Colloid Transport.* ANL-NBS-HS-000031 REV 01. Las Vegas, Nevada: Bechtel SAIC Company. ACC: DOC.20030916.0008. TBV-5652.

162649 BSC (Bechtel SAIC Company) 2003. *Site-Scale Saturated Zone Flow Model.* MDL-NBS-HS-000011 REV 01A. Las Vegas, Nevada: Bechtel SAIC Company. ACC: MOL.20030626.0296. TBV-5203.

162419 BSC (Bechtel SAIC Company) 2003. *Site-Scale Saturated Zone Transport.* MDL-NBS-HS-000010 REV 01A. Las Vegas, Nevada: Bechtel SAIC Company. ACC: MOL.20030626.0180.

164870 BSC (Bechtel SAIC Company) 2003. *SZ Flow and Transport Model Abstraction.* MDL-NBS-HS-000021 REV 00. Las Vegas, Nevada: Bechtel SAIC Company. ACC: DOC.20030818.0007.

166034 BSC (Bechtel SAIC Company) 2003. *Technical Work Plan for: Saturated Zone Flow and Transport Modeling and Testing.* TWP-NBS-MD-000002 REV 01 ICN 01. Las Vegas, Nevada: Bechtel SAIC Company. ACC: DOC.20031203.0002.

165179 BSC (Bechtel SAIC Company) 2003. *Q-List.* TDR-MGR-RL-000005 REV 00. Las Vegas, Nevada: Bechtel SAIC Company. ACC: DOC.20030930.0002.

165123 Callahan, T. 2001. LA-CST-NMTECHA-NBK-96-001, Laboratory Investigation YMP C-Wells Reactive Tracers Test. Scientific Notebook SN-LANL-SCI-028-V1. ACC: MOL.20010830.0384.

156649 Callahan, T.J. 2001. *Laboratory Investigations and Analytical and Numerical Modeling of the Transport of Dissolved Solutes Through Saturated Fractured Rock.* Ph.D. dissertation. Socorro, New Mexico: New Mexico Institute of Mining and Technology. TIC: 251010.

156648 Callahan, T.J.; Reimus, P.W.; Bowman, R.S.; and Haga, M.J. 2000. "Using Multiple Experimental Methods to Determine Fracture/Matrix Interactions and Dispersion in Saturated Fractured Volcanic Tuff." *Water Resources Research, 36,* (12), 3547-3558. Washington, D.C.: American Geophysical Union. TIC: 250760.

161770 Canori, G.F. and Leitner, M.M. 2003. *Project Requirements Document.* TER-MGR-MD-000001 REV 01. Las Vegas, Nevada: Bechtel SAIC Company. ACC: DOC.20030404.0003.

102046 Carr, M.D.; Waddell, S.J.; Vick, G.S.; Stock, J.M.; Monsen, S.A.; Harris, A.G.; Cork, B.W.; and Byers, F.M., Jr. 1986. *Geology of Drill Hole UE-25 p #1: A Test Hole into Pre-Tertiary Rocks near Yucca Mountain, Southern Nevada.* Open-File Report 86-175. Menlo Park, California: U.S. Geological Survey. ACC: HQS.19880517.2633.

105075 Chipera, S.J. and Bish, D.L. 1995. "Multireflection RIR and Intensity Normalizations for Quantitative Analyses: Applications to Feldspars and Zeolites." *Powder Diffraction, 10,* (1), 47-55. Newtown Square, Pennsylvania: Joint Committee on Powder Diffraction Standards. TIC: 222001.

156651 Cohen, A.J.B.; Najita, J.; Karasaki, K.; and Simmons, A. 1996. *Conceptual Model Development of Saturated Zone Flow in the Vicinity of C-holes, Yucca Mountain, Nevada.* Berkeley, California: Lawrence Berkeley National Laboratory. ACC: MOL.19961122.0314.

150245 Cooper, H.H., Jr. and Jacob, C.E. 1946. "A Generalized Graphical Method for Evaluating Formation Constants and Summarizing Well-Field History."

Transactions, American Geophysical Union, 27, (IV), 526-534. Washington, D.C.: American Geophysical Union. TIC: 225279.

101040 Craig, R.W. and Robison, J.H. 1984. *Geohydrology of Rocks Penetrated by Test Well UE-25 p #1, Yucca Mountain Area, Nye County, Nevada.* Water-Resources Investigations Report 84-4248. Denver, Colorado: U.S. Geological Survey. ACC: NNA.19890905.0209.

153246 CRWMS M&O 2000. *Total System Performance Assessment for the Site Recommendation.* TDR-WIS-PA-000001 REV 00 ICN 01. Las Vegas, Nevada: CRWMS M&O. ACC: MOL.20001220.0045.

100131 D'Agnese, F.A.; Faunt, C.C.; Turner, A.K.; and Hill, M.C. 1997. *Hydrogeologic Evaluation and Numerical Simulation of the Death Valley Regional Ground-Water Flow System, Nevada and California.* Water-Resources Investigations Report 96-4300. Denver, Colorado: U.S. Geological Survey. ACC: MOL.19980306.0253.

143278 Dabros, T. and Van de Ven, T.G. 1982. "Kinetics of Coating by Colloidal Particles." *Journal of Colloid and Interface Science, 89,* (1), 232-244. Orlando, Florida: Academic Press. TIC: 224945.

156652 Dabros, T. and Van de Ven, T.G. 1983. "On the Effects of Blocking and Detachment on Coating Kinetics." *Journal of Colloid and Interface Science, 93,* (2), 576-579. New York, New York: Academic Press. TIC: 224944.

100027 Day, W.C.; Dickerson, R.P.; Potter, C.J.; Sweetkind, D.S.; San Juan, C.A.; Drake, R.M., II; and Fridrich, C.J. 1998. *Bedrock Geologic Map of the Yucca Mountain Area, Nye County, Nevada.* Geologic Investigations Series I-2627. Denver, Colorado: U.S. Geological Survey. ACC: MOL.19981014.0301.

101557 Day, W.C.; Potter, C.J.; Sweetkind, D.S.; Dickerson, R.P.; and San Juan, C.A. 1998. *Bedrock Geologic Map of the Central Block Area, Yucca Mountain, Nye County, Nevada.* Miscellaneous Investigations Series Map I-2601. Washington, D.C.: U.S. Geological Survey. ACC: MOL.19980611.0339.

162674 De Wiest, Roger J.M. 1965. *Geohydrology.* New York, New York: John Wiley & Sons, Inc. TIC: 254221.

100722 Dean, J.A. 1992. *Lange's Handbook of Chemistry.* 14th Edition. New York, New York: McGraw-Hill. TIC: 240690.

102781 Dickerson, R.P. and Drake, R.M., II. 1998. "Structural Interpretation of Midway Valley, Yucca Mountain, Nevada." *High-Level Radioactive Waste Management, Proceedings of the Eighth International Conference, Las Vegas, Nevada, May 11-14, 1998.* Pages 254-256. La Grange Park, Illinois: American Nuclear Society. TIC: 237082.

156653 Eckstein, Y.; Yaalon, D.H.; and Yariv, S. 1970. "The Effect of Lithium on the Cation Exchange Behaviour of Crystalline and Amorphous Clays." *Israel Journal of Chemistry, 8*, 335-342. Jerusalem, Israel: Laser Pages Publishing. TIC: 251012.

100633 Ervin, E.M.; Luckey, R.R.; and Burkhardt, D.J. 1994. *Revised Potentiometric-Surface Map, Yucca Mountain and Vicinity, Nevada.* Water-Resources Investigations Report 93-4000. Denver, Colorado: U.S. Geological Survey. ACC: NNA.19930212.0018.

162811 Fahy, M. 1997. "Masses Recovered from Tracer Testing at C-Wells." E-mail from M. Fahy to A. Randall, July 21, 1997. ACC: . MOL.20030515.0196.

137456 Fahy, M.F. 1997. "Dual-Porosity Analysis of Conservative Tracer Testing in Saturated Volcanic Rocks at Yucca Mountain in Nye County, Nevada." *International Journal of Rock Mechanics and Mining Science, 34*, (3-4). Amsterdam, The Netherlands: Elsevier. TIC: 237601.

157319 Farrell, D.A.; Armstrong, A.; Winterle, J.R.; Turner, D.R.; Ferrill, D.A.; Stamatakos, J.A.; Coleman, N.M.; Gray, M.B.; and Sandberg, S.K. 1999. *Structural Controls on Groundwater Flow in the Yucca Mountain Region.* San Antonio, Texas: Center for Nuclear Waste Regulatory Analyses. TIC: 254265.

100146 Faunt, C.C. 1997. *Effect of Faulting on Ground-Water Movement in the Death Valley Region, Nevada and California.* Water-Resources Investigations Report 95-4132. Denver, Colorado: U.S. Geological Survey. ACC: MOL.19980429.0119.

118941 Ferrill, D.A.; Winterle, J.; Wittmeyer, G.; Sims, D.; Colton, S.; Armstrong, A.; and Morris, A.P. 1999. "Stressed Rock Strains Groundwater at Yucca Mountain, Nevada." *GSA Today, 9*, (5), 1-8. Boulder, Colorado: Geological Society of America. TIC: 246229.

102009 Fetter, C.W. 1993. *Contaminant Hydrogeology.* Upper Saddle River, New Jersey: Prentice Hall. TIC: 240691.

165394 Freeze, G. 2003. *KTI Letter Report, Response to Additional Information Needs on TSPAI 2.05 and TSPAI 2.06.* REG-WIS-PA-000003 REV 00 ICN 04. Las Vegas, Nevada: Bechtel SAIC Company. ACC: DOC.20030825.0003.

154365 Freeze, G.A.; Brodsky, N.S.; and Swift, P.N. 2001. *The Development of Information Catalogued in REV00 of the YMP FEP Database.* TDR-WIS-MD-000003 REV 00 ICN 01. Las Vegas, Nevada: Bechtel SAIC Company. ACC: MOL.20010301.0237.

101173 Freeze, R.A. and Cherry, J.A. 1979. *Groundwater.* Englewood Cliffs, New Jersey: Prentice-Hall, Inc. TIC: 217571.

105454 Frizzell, V.A., Jr. and Shulters, J. 1990. *Geologic Map of the Nevada Test Site, Southern Nevada.* Miscellaneous Investigations Series Map I-2046. Denver, Colorado: U.S. Geological Survey. TIC: 200459.

156826 Galloway, D. and Rojstaczer, S. 1988. "Analysis of the Frequency Response of Water Levels in Wells to Earth Tides and Atmospheric Loading." *Proceedings, Fourth Canadian/American Conference on Hydrogeology, Fluid Flow, Heat Transfer, and Mass Transport in Fractured Rocks, Banff, Alberta, Canada, June 21-24, 1988.* Hitchon, B. and Bachu, S., eds. Pages 100-113. Dublin, Ohio: National Water Well Association. TIC: 222289.

101045 Geldon, A.L. 1993. *Preliminary Hydrogeologic Assessment of Boreholes UE-25c #1, UE-25c #2, and UE-25c #3, Yucca Mountain, Nye County, Nevada.* Water-Resources Investigations Report 92-4016. Denver, Colorado: U.S. Geological Survey. ACC: MOL.19960808.0136.

100396 Geldon, A.L. 1996. *Results and Interpretation of Preliminary Aquifer Tests in Boreholes UE-25c #1, UE-25c #2, and UE-25c #3, Yucca Mountain, Nye County, Nevada.* Water-Resources Investigations Report 94-4177. Denver, Colorado: U.S. Geological Survey. ACC: MOL.19980724.0389.

156827 Geldon, A.L.; Earle, J.D.; and Umari, A.M.A. 1997. *Determination of Barometric Efficiency and Effective Porosity, Boreholes UE-25 c #1, UE-25 c #2, and UE-25 c #3, Yucca Mountain, Nye County, Nevada.* Water-Resources Investigations Report 97-4098. Denver, Colorado: U.S. Geological Survey. ACC: MOL.19980226.0570.

129721 Geldon, A.L.; Umari, A.M.A.; Earle, J.D.; Fahy, M.F.; Gemmell, J.M.;and Darnell, J. 1998. *Analysis of a Multiple-Well Interference Test in Miocene Tuffaceous Rocks at the C-Hole Complex, May-June 1995, Yucca Mountain, Nye County, Nevada.* Water-Resources Investigations Report 97-4166. Denver, Colorado: U.S. Geological Survey. TIC: 236724.

161163 Geldon, A.L.; Umari, A.M.A.; Fahy, M.F.; Earle, J.D.; Gemmell, J.M.; and Darnell, J. 2002. *Results of Hydraulic Tests in Miocene Tuffaceous Rocks at the C-hole Complex, 1995 to 1997, Yucca Mountain, Nye County, Nevada.* Water-Resources Investigations Report 02-4141. Denver, Colorado: U.S. Geological Survey. TIC: 253755.

101046 Graves, R.P.; Tucci, P.; and O'Brien, G.M. 1997. *Analysis of Water-Level Data in the Yucca Mountain Area, Nevada, 1985-95.* Water-Resources Investigations Report 96-4256. Denver, Colorado: U.S. Geological Survey. ACC: MOL.19980219.0851.

101132 Grisak, G.E. and Pickens, J.F. 1980. "Solute Transport Through Fractured Media. 1. The Effect of Matrix Diffusion." *Water Resources Research, 16,* (4), 719-730. Washington, D.C.: American Geophysical Union. TIC: 222056.

156830 Guimerà, J. and Carrera, J. 2000. "A Comparison of Hydraulic and Transport Parameters Measured in Low-Permeability Fractured Media." *Journal of*

Contaminant Hydrology, 41, (3-4), 261-281. New York, New York: Elsevier. TIC: 251013.

156831 Haggerty, R. and Gorelick, S.M. 1995. "Multiple-rate Mass Transfer for Modeling Diffusion and Surface Reactions in Media with Pore-scale Heterogeneity." *Water Resources Research, 31,* (10), 2383-2400. Washington, D.C.: American Geophysical Union. TIC: 244502.

156832 Haggerty, R.; McKenna, S.A.; and Meigs, L.C. 2000. "On the Late-time Behavior of Tracer Test Breakthrough Curves." *Water Resources Research, 36,* (12), 3467-3479. Washington, D.C.: American Geophysical Union. TIC: 250770.

165169 Hantush, M.S. 1956. "Analysis of Data from Pumping Tests in Leaky Aquifers." *Transactions, 37,* (6), 702-714. Washington, D.C.: American Geophysical Union. TIC: 255072.

161160 Hantush, M.S. 1966. "Analysis of Data from Pumping Tests in Anisotropic Aquifers." *Journal of Geophysical Research, 71,* (2), 421-426. [Washington, D.C.: American Geophysical Union]. TIC: 225281.

156833 Happel, J. and Brenner, H. 1965. *Low Reynolds Number Hydrodynamics with Special Applications to Particulate Media* (Appendix A). Englewood Cliffs, New Jersey: Prentice-Hall. TIC: 251939.

100814 Harrar, J.E.; Carley, J.F.; Isherwood, W.F.; and Raber, E. 1990. *Report of the Committee to Review the Use of J-13 Well Water in Nevada Nuclear Waste Storage Investigations*. UCID-21867. Livermore, California: Lawrence Livermore National Laboratory. ACC: NNA.19910131.0274.

117358 Hiemenz, P.C. 1986. *Principles of Colloid and Surface Chemistry*. 2nd Edition, Revised and Expanded. Undergraduate Chemistry Volume 9. Lagowski, J.J., ed. New York, New York: Marcel Dekker. TIC: 246392.

156835 Israelachvili, J.N. 2000. *Intermolecular and Surface Forces*. 2nd Edition. San Diego, California: Academic Press. TIC: 251020.

156836 Jenson, V.G. and Jeffreys, G.V. 1977. *Mathematical Models in Chemical Engineering*. 2nd Edition. Orlando, Florida: Academic Press. TIC: 251165.

156837 Johnson, G.W. 1994. *Labview Graphical Programming, Practical Applications in Instrumentation and Control.* New York, New York: McGraw-Hill. TIC: 251938.

164666 Kasenow, M. 2002. *Determination of Hydraulic Conductivity from Grain Size Analysis, Grain-Size Analysis Supplements this Book, with Errata.* Highlands Ranch, Colorado: Water Resources Publications. TIC: 254721.

101049 Lahoud, R.G.; Lobmeyer, D.H.; and Whitfield, M.S., Jr. 1984. *Geohydrology of Volcanic Tuff Penetrated by Test Well UE-25b #1, Yucca Mountain, Nye County,*

Nevada. Water-Resources Investigations Report 84-4253. Denver, Colorado: U.S. Geological Survey. ACC: NNA.19890511.0117.

144612 LeCain, G.D.; Anna, L.O.; and Fahy, M.F. 2000. *Results from Geothermal Logging, Air and Core-Water Chemistry Sampling, Air-Injection Testing, and Tracer Testing in the Northern Ghost Dance Fault, Yucca Mountain, Nevada, November 1996 to August 1998.* Water-Resources Investigations Report 99-4210. Denver, Colorado: U.S. Geological Survey. TIC: 247708.

156839 Levenspiel, O. 1972. *Chemical Reaction Engineering*, Second edition. New York, New York: John Wiley and Sons. TIC: 224877.

150250 Lohman, S.W. 1972. *Ground-Water Hydraulics.* Professional Paper 708. Washington, D.C.: U.S. Geological Survey. TIC: 237291.

100465 Luckey, R.R.; Tucci, P.; Faunt, C.C.; Ervin, E.M.; Steinkampf, W.C.; D'Agnese, F.A.; and Patterson, G.L. 1996. *Status of Understanding of the Saturated-Zone Ground-Water Flow System at Yucca Mountain, Nevada, as of 1995.* Water-Resources Investigations Report 96-4077. Denver, Colorado: U.S. Geological Survey. ACC: MOL.19970513.0209.

156840 Maloszewski, P. and Zuber, A. 1984. "Interpretation of Artificial and Environmental Tracers in Fissured Rocks with a Porous Matrix." *Isotope Hydrology 1983, Proceedings of an International Symposium on Isotope Hydrology in Water Resources Development, Organized by the International Atomic Energy Agency in Co-operation with the United Nations Educational, Scientific, and Cultural Organization and Held in Vienna, 12-16 September 1983.* Vienna, Austria: International Atomic Energy Commission. TIC: 236592.

148312 Maloszewski, P. and Zuber, A. 1985. "On the Theory of Tracer Experiments in Fissured Rocks with a Porous Matrix." *Journal of Hydrology, 79,* (3-4), 333-358. Amsterdam, The Netherlands: Elsevier. TIC: 222390.

156841 Maloszewski, P.; Herrmann, A.; and Zuber, A. 1999. "Interpretation of Tracer Tests Performed in Fractured Rock of the Lange Bramke Basin, Germany." *Hydrogeology Journal, 7,* (2), 209-218. New York, New York: Springer-Verlag. TIC: 250778.

156842 Ming, D.W. and Dixon, J.B. 1987. "Quantitative Determination of Clinoptilolite in Soils by a Cation-Exchange Capacity Method." *Clays and Clay Minerals, 35,* (6), 463-468. New York, New York: Pergamon Press. TIC: 251015.

156843 Ming, D.W. and Mumpton, F.A. 1995. "Zeolites in Soils." Chapter 18 of *Minerals in Soil Environments.* 2nd Edition. Dixon, J.B. and Weed, S.B., eds. *Soil Science Society of America Book Series No. 1.* Madison, Wisconsin: Soil Science Society of America. TIC: 237222.

101146 Moench, A.F. 1989. "Convergent Radial Dispersion: A Laplace Transform Solution for Aquifer Tracer Testing." *Water Resources Research, 25*, (3), 439-447. Washington, D.C.: American Geophysical Union. TIC: 238283.

148784 Moench, A.F. 1995. "Convergent Radial Dispersion in a Double-Porosity Aquifer with Fracture Skin: Analytical Solution and Application to a Field Experiment in Fractured Chalk." *Water Resources Research, 31*, (8), 1823-1835. Washington, D.C.: American Geophysical Union. TIC: 233132.

139151 National Research Council. 1996. *Rock Fractures and Fluid Flow, Contemporary Understanding and Applications*. Washington, D.C: National Academy Press. TIC: 235913.

101148 Neretnieks, I. 1980. "Diffusion in the Rock Matrix: An Important Factor in Radionuclide Retardation?" *Journal of Geophysical Research, 85*, (B8), 4379-4397. Washington, D.C.: American Geophysical Union. TIC: 221345.

150321 Neuman, S.P. 1975. "Analysis of Pumping Test Data from Anisotropic Unconfined Aquifers Considering Delayed Gravity Response." *Water Resources Research, 11*, (2), 329-342. Washington, D.C.: American Geophysical Union. TIC: 222414.

101464 Neuman, S.P. 1990. "Universal Scaling of Hydraulic Conductivities and Dispersivities in Geologic Media." *Water Resources Research, 26,* (8), 1749-1758. Washington, D.C.: American Geophysical Union. TIC: 237977.

156849 Newman, B.D.; Fuentes, H.R.; and Polzer, W.L. 1991. "An Evaluation of Lithium Sorption Isotherms and Their Application to Ground-Water Transport." *Ground Water, 29,* (6), 818-824. Worthington, Ohio: Water Well Journal Publishing. TIC: 203790.

148719 Newman, J.S. 1973. *Electrochemical Systems*. Englewood Cliffs, New Jersey: Prentice-Hall, Inc. TIC: 210201.

163274 NRC (U.S. Nuclear Regulatory Commission) 2003. *Yucca Mountain Review Plan, Final Report*. NUREG-1804, Rev. 2. Washington, D.C.: U.S. Nuclear Regulatory Commission, Office of Nuclear Material Safety and Safeguards. TIC: 254568.

165947 NWRPO (Nye County Nuclear Waste Repository Project Office) 2003. "Program Management." [Pahrump], Nevada: Nuclear Waste Repository Project Office. Accessed December 12, 2003. ACC: MOL.20031212.0014. http://www.nyecounty.com/Program_mgmnt.htm.

156859 Nye County Nuclear Waste Repository Project Office. 1995. *Borehole UE-25 ONC #1 and USW NRG-4 Drilling and Instrumentation Report, Yucca Mountain, Nevada.* Pahrump, Nevada: Nye County Nuclear Waste Repository Program. ACC: MOL.19960910.0231.

101279 O'Brien, G.M.; Tucci, P.; and Burkhardt, D.J. 1995. *Water Levels in the Yucca Mountain Area, Nevada, 1992*. Open-File Report 94-311. Denver, Colorado: U.S. Geological Survey. ACC: NNA.19940627.0003.

150265 Papadopulos, I.S. 1967. "Nonsteady Flow to a Well in an Infinite Aquifer." *Hydrology of Fractured Rocks, Proceedings of the Dubrovnik Symposium, October 1965. I,* 21–31. Gentbrugge, Belgium: Association Internationale d'Hydrologie Scientifique. TIC: 223152.

150323 Papadopulos, S.S. and Cooper, H.H., Jr. 1967. "Drawdown in a Well of Large Diameter." *Water Resources Research, 3,* (1), 241-244. Washington, D.C.: American Geophysical Union. TIC: 225288.

165125 Reimus, P. 2000. General C-Wells Notebook and Microsphere Analyses for C-Wells. Scientific Notebook SN-LANL-SCI-214-V1. ACC: MOL.20000413.0220; MOL.20000824.0084.

165124 Reimus, P. 2000. LA-CST-CW-NBK-98-001, YMP C-Wells Rocks. Scientific Notebook SN-LANL-SCI-146-V1. ACC: MOL.20010308.0191.

164625 Reimus, P. 2000. LA-CST-CW-NBK-98-003, YMP C-Wells Sorption. Scientific Notebook: SN-LANL-SCI-006-V1. ACC: MOL.20010308.0193.

165121 Reimus, P. 2000. YMP C-Wells Diffusion Cells. Scientific Notebook: SN-LANL-SCI-007-V1 (LA-CST-CW-NBK-98-004). ACC: MOL.20010308.0195.

162852 Reimus, P. 2000. LANL C-Wells Prow Pass Field Notebook. Scientific Notebook SN-LANL-SCI-233-V1. ACC: MOL.20000824.0066.

165129 Reimus, P. 2003. LA-CST-NBK-98-011, Modeling and Interpretation of Transport Tests. Scientific Notebook SN-LANL-SCI-255-V1. ACC: MOL.20020206.0093; MOL.20031027.0086; MOL.20031027.0087.

163760 Reimus, P. 2003. Laboratory Testing in Support of Saturated Zone Investigations. Scientific Notebook SN-LANL-SCI-280-V1. ACC: MOL.20030227.0286.

101474 Reimus, P.W. 1995. *The Use of Synthetic Colloids in Tracer Transport Experiments in Saturated Rock Fractures*. Ph.D. dissertation, University of New Mexico. LA-13004-T. Los Alamos, New Mexico: Los Alamos National Laboratory. TIC: 240694.

162855 Reimus, P.W. 2000. C-Wells Bullfrog Multiple Tracer Test Notebook. Scientific Notebook SN-LANL-SCI-223-V1. ACC: MOL.20000818.0075.

164624 Reimus, P. 2000. LA-EES-4-NBK-96-003(b), C-Wells Bullfrog Multiple Tracer Test. Scientific Notebook for SN-LANL-SCI-224-V1. ACC: MOL.20000824.0094.

165126 Reimus, P.W. 2000. QA Notebook for C-Wells Tracer Testing (PFBA/C#2 Test). Scientific Notebook SN-LANL-SCI-217-V1. ACC: MOL.20000818.0063.

165127 Reimus, P.W. 2000. QA Notebook Iodide/C#1 Tracer Test. Scientific Notebook SN-LANL-SCI-218-V1. ACC: MOL.20000818.0071.

165128 Reimus, P.W. 2003. Single-Well and Cross-Hole Alluvial Tracer Testing. Scientific Notebook: SN-LANL-SCI-251-V1. ACC: MOL.20030213.0331 through MOL.20030313.0334.

154705 Reimus, P.W. and Haga, M.J. 1999. *Analysis of Tracer Responses in the BULLION Forced-Gradient Experiment at Pahute Mesa, Nevada.* LA-13615-MS. Los Alamos, New Mexico: Los Alamos National Laboratory. TIC: 249826.

101154 Robinson, B. A. 1994. "A Strategy for Validating a Conceptual Model for Radionuclide Migration in the Saturated Zone Beneath Yucca Mountain." *Radioactive Waste Management and Environmental Restoration, 19*, (1-3), 73-96. Yverdon, Switzerland: Harwood Academic Publishers. TIC: 222513.

156862 Skagius, K. and Neretnieks, I. 1986. "Porosities and Diffusivities of Some Nonsorbing Species in Crystalline Rocks." *Water Resources Research, 22*, (3), 389-398. Washington, D.C.: American Geophysical Union. TIC: 225291.

156863 Stetzenbach, K.J. and Thompson, G.M. 1983. "A New Method for Simultaneous Measurement of Cl^-, Br^-, NO_3^-, SCN^-, and I^- at sub-ppm Levels in Ground Water." *Ground Water, 21*, (1), 36-41. Worthington, Ohio: Water Well Journal Publishing. TIC: 252098.

150754 Streltsova-Adams, T.D. 1978. "Well Hydraulics in Heterogeneous Aquifer Formations." Volume 11 of *Advances in Hydroscience.* Chow, V.T., ed. Pages 357-423. New York, New York: Academic Press. TIC: 225957.

164623 Sullivan, E.J. 2002. Laboratory Testing in Support of Alluvial Tracer Testing. Scientific Notebook SN-LANL-SCI-213-V1. ACC: MOL.20021015.0198.

101160 Tang, D.H.; Frind, E.O.; and Sudicky, E.A. 1981. "Contaminant Transport in Fractured Porous Media: Analytical Solution for a Single Fracture." *Water Resources Research, 17*, (3), 555-564. Washington, D.C.: American Geophysical Union. TIC: 225358.

150327 Theis, C.V. 1935. "The Relation Between the Lowering of the Piezometric Surface and the Rate and Duration of Discharge of a Well Using Ground-Water Storage." *Transactions of the American Geophysical Union Sixteenth Annual Meeting, April 25 and 26, 1935, Washington, D.C.* Pages 519-524. Washington, D.C.: National Academy of Science, National Research Council. TIC: 223158.

100830 Thompson, J.L. 1989. "Actinide Behavior on Crushed Rock Columns." *Journal of Radioanalytical and Nuclear Chemistry—Articles, 130* (2), 353-364. Lausanne, Switerzerland: Elsevier. TIC: 222698.

125967 Treher, E.N. and Raybold, N.A. 1982. *The Elution of Radionuclides Through Columns of Crushed Rock from the Nevada Test Site.* LA-9329-MS. Los Alamos, New Mexico: Los Alamos National Laboratory. ACC: NNA.199920922.0021.

100422 Triay, I.R.; Meijer, A.; Conca, J.L.; Kung, K.S.; Rundberg, R.S.; Strietelmeier, E.A.; Tait, C.D.; Clark, D.L.; Neu, M.P.; and Hobart, D. E. 1997. *Summary and Synthesis Report on Radionuclide Retardation for the Yucca Mountain Site Characterization Project.* Eckhardt, R.C., ed. LA-13262-MS. Los Alamos, New Mexico: Los Alamos National Laboratory. ACC: MOL.19971210.0177.

113901 Tsang, Y. W. 1992. "Usage of 'Equivalent Apertures' for Rock Fractures as Derived from Hydraulic and Tracer Tests." *Water Resources Research, 28,* (5), 1451-1455. Washington, D.C.: American Geophysical Union. TIC: 245891.

101060 Tucci, P. and Burkhardt, D.J. 1995. *Potentiometric-Surface Map, 1993, Yucca Mountain and Vicinity, Nevada.* Water-Resources Investigations Report 95-4149. Denver, Colorado: U.S. Geological Survey. ACC: MOL.19960924.0517.

164543 Umari, A.M.J.; Geldon, A.; Patterson, G.; Gemmell, J.; Earle, J.; and Darnell, J. 1994. "Use of an Analog Site Near Raymond, California, to Develop Equipment and Methods for Characterizing a Potential High-Level, Nuclear Waste Repository Site at Yucca Mountain, Nevada." *High Level Radioactive Waste Management, Proceedings of the Fifth Annual International Conference, Las Vegas, Nevada, May 22-26, 1994. 4,* 2413-2422. La Grange Park, Illinois: American Nuclear Society. TIC: 210984.

162858 Umari, M.J. 2002. Performing Various Hydraulic and Tracer Tests Using Prototype Pressure Transducer and Packer Assemblies. Scientific Notebook SN-USGS-SCI-036-V1. ACC: MOL.20020520.0364; MOL.20020520.0368; through MOL.20020520.0382.

164573 Umari, M.J.; Earle, J.; and Darnell, J. 2003. Alluvium Testing Complex. SN-USGS-SCI-123-V1 through V8. ACC: MOL.20010613.0239; MOL.20010613.0240; MOL.20010613.0241; MOL.20021028.0352; MOL.20030821.0216; MOL.20030821.0217; MOL.20030821.0218; MOL.20030821.0219; MOL.20031021.0281; MOL.20031021.0282; MOL.20031021.0284.

154495 USGS (U.S. Geological Survey) n.d. Bulk Density. [Denver, Colorado: U.S. Geological Survey]. ACC: NNA.19940406.0076.

144579 Valocchi, A.J. 1985. "Validity of the Local Equilibrium Assumption for Modeling Sorbing Solute Transport through Homogeneous Soils." *Water Resources Research, 21,* (6), 808-820. Washington, D.C.: American Geophysical Union. TIC: 223203.

156868 van Genuchten, M.T.; Wierenga, P.J.; and O'Connor, G.A. 1977. "Mass Transfer Studies in Sorbing Porous Media: III. Experimental Evaluation with 2,4,5-T." *Soil Science Society of America Journal, 41*, 278-285. Madison, Wisconsin: Soil Science Society of America. TIC: 251016.

156867 Vaughan, D.E.W. 1978. "Properties of Natural Zeolites." *Natural Zeolites, Occurrence, Properties, Use, A Selection of Papers Presented at Zeolite, 76, an International Conference on the Occurrence, Properties, and Utilization of Natural Zeolites, Tucson, Arizona, June 1976.* Sand, L.B. and Mumpton, F.A., eds. Pages 353-371. New York, New York: Pergamon Press. TIC: 206755.

100833 Weast, R.C. and Astle, M.J., eds. 1981. *CRC Handbook of Chemistry and Physics.* 62nd Edition. Boca Raton, Florida: CRC Press. TIC: 240722.

101366 Whitfield, M.S., Jr.; Thordarson, W.; and Eshom, E.P. 1984. *Geohydrologic and Drill-Hole Data for Test Well USW H-4, Yucca Mountain, Nye County, Nevada.* Open-File Report 84-449. Denver, Colorado: U.S. Geological Survey. ACC: NNA.19870407.0317.

129796 Winterle, J.R. and La Femina, P.C. 1999. *Review and Analysis of Hydraulic and Tracer Testing at the C-Holes Complex Near Yucca Mountain, Nevada.* San Antonio, Texas: Center for Nuclear Waste Regulatory Analyses. TIC: 246623.

110491 Zyvoloski, G.A.; Robinson, B.A.; Dash, Z.V.; and Trease, L.L. 1997. *Summary of the Models and Methods for the FEHM Application—A Finite-Element Heat- and Mass-Transfer Code.* LA-13307-MS. [Los Alamos, New Mexico]: Los Alamos National Laboratory. TIC: 235587.

104211 YMP (Yucca Mountain Site Characterization Project) 1998. *Saturated Zone C-Hole Tracer Testing.* Field Work Package FWP-SB-97-008, Rev. 1 Las Vegas, Nevada: Yucca Mountain Site Characterization Office. ACC: MOL.19981029.0058.

8.2 CODES, STANDARDS, REGULATIONS, AND PROCEDURES

165855 10 CFR 50. 2002. Energy: Domestic Licensing of Production and Utilization Facilities. Readily available.

156605 10 CFR 63. Energy. Disposal of High-Level Radioactive Wastes in a Geologic Repository at Yucca Mountain, Nevada. Readily available.

164786 AP-2.22Q, Rev. 1, ICN 0. *Classification Analyses and Maintenance of the Q-List.* Washington, D.C.: U.S. Department of Energy, Office of Civilian Radioactive Waste Management. ACC: DOC.20030807.0002.

165023 AP-SI.1Q REV 5, ICN 2, *Software Management.* Washington, D.C.: Department of Energy, Office of Civilian Radioactive Waste Management. ACC: DOC.20030902.0003.

166252 AP-SIII.9Q, REV. 1 ICN 2. *Scientific Analyses.* Washington, D.C.: U.S. Department of Energy, Office of Civilian Radioactive Waste Management. ACC: DOC.20031126.0001.

165687 AP-SV.1Q, Rev. 1, ICN 0. *Control of the Electronic Management of Information.* Washington, D.C.: U.S. Department of Energy, Office of Civilian Radioactive Waste Management. ACC: DOC.20030929.0004.

8.3 SOFTWARE

159064 LANL (Los Alamos National Laboratory) 2002. *Software Code: EQUIL_FIT.* V 1.0. PC, Windows 2000/NT 4.0/98. 10668-1.0-00.

159067 LANL (Los Alamos National Laboratory) 2002. *Software Code: 2WELLS_2D.* V 1.0. PC, Windows 2000/NT 4.0/98. 10665-1.0-00.

159036 LANL (Los Alamos National Laboratory) 2002. *Software Code: 2WELLS_3D.* V 1.0. PC, Windows 2000/NT 4.0/98. 10667-1.0-00.

159063 LANL (Los Alamos National Laboratory) 2002. *Software Code: DIFFCELL.* V 2.0. PC, Windows 2000/NT. 10557-2.0-00.

161725 LANL (Los Alamos National Laboratory) 2003. *Software Code: FEHM.* V 2.20. SUN, PC. 10086-2.20-00. (Used as reference only.)

159068 LANL (Los Alamos National Laboratory) 2002. *Software Code: MULTRAN.* V 1.0. PC, Windows 2000/NT 4.0. 10666-1.0-00.

159065 LANL (Los Alamos National Laboratory) 2002. *Software Code: RELAP.* V 2.0. PC, Windows 2000/NT. 10551-2.0-00.

159066 LANL (Los Alamos National Laboratory) 2002. *Software Code: RETRAN.* V 2.0. PC, Windows 2000/NT. 10552-2.0-00.

162668 USGS (U.S. Geological Survey) 2002. *Software Code: Filter.vi.* V 1.0. PC, Windows 2000/NT 4.0/98. 10970-1.0-00.

162749 USGS 2003. *Software Code: Injection_Pumpback.vi.* V 1.0. PC, Windows 2000/NT. 10675-1.0-00.

162750 USGS 2002. *Software Code: Rcv2amos.exe* and *MOENCH.vi, Function(1).* V 1.0. PC, Windows 2000/NT. 10583-1.0-00.

162752 USGS 2002. *Software Code: MOENCH.vi, Function(2).* V 1.0. PC, Windows 2000/NT. 10582-1.0-00.

162754 USGS 2002. *Software Code: Neuman.vi.* V 1.0. PC, Windows 2000/NT. 10972-1.0-00.

164432 USGS 2003. *Software Code: RECIRC.vi.* V. 1.0. PC. Windows 98/NT 4.0/2000. 10673-1.0-00.

162756 USGS 2003. *Software Code: Streltsova-Adams.vi.* V 1.0. PC, Windows 2000/NT. 10971-1.0-00.

162758 USGS 2002. *Software Code: Theis.vi.* V 1.0. PC, Windows 2000/NT. 10974-1.0-00.

161564 Watermark Computing 2002. *Software Code: PEST.* V 5.5. SUN, PC, Linux, Windows 2000. 10289-5.5-00.

8.4 SOURCE DATA, LISTED BY DATA TRACKING NUMBER

155860 GS010508312315.001. Concentrations of Difluorobenzoic Acid and Pyridone from Tracer Tests Conducted at the C-Well Complex, 1/8/97 – 7/11/97. Submittal date: 06/01/2001.

157067 GS010799992315.001. Injection and Production Flow Rates for the LANL Prow Pass Test, 11/30/98 through 1/27/99. Submittal date: 07/25/2001.

158690 GS011008314211.001. Interpretation of the Lithostratigraphy in Deep Boreholes NC-EWDP-19D1 and NC-EWDP-2DB Nye County Early Warning Drilling Program. Submittal date: 01/16/2001.

162678 GS020708312316.001. NC-EWDP-19D, ATC Single-Hole Hydraulic Testing Associated with the July 7, 2000 to April 26, 2001 Tracer Study. Submittal date: 09/10/2002.

162679 GS020908312361.002. Flow Rates, Pressures, and Temperatures for Hydraulic and Tracer Testing at the NC-EWDP-19D, NC-EWDP-19IM1, and NC-EWDP-19IM2 Alluvial Testing Complex from December 18, 2001 to March 22, 2002. Submittal date: 09/30/2002.

162680 GS020908312361.003. Background Pressures and Temperatures During Barometric Monitoring at the NC-EWDP-19D, NC-EWDP-19IM1, and NC-EWDP-19IM2 Alluvial Testing Complex from May 1, 2002 through July 3, 2002. Submittal date: 10/15/2002.

164425 GS030508312314.003. Results of Hydraulic Tests in Miocene Tuffaceous Rocks at the C-Hole Complex, 1995 to 1997, Yucca Mountain, Nevada. Submittal date: 05/08/2003.

166332 GS930908312313.008. Hydrologic Information from the C-hole Complex and the Yucca Mountain Area. Submittal date: 09/16/1993.

164801 GS960108312313.001. 280 Gallon per Minute Pump Test at the C-Hole Complex. Submittal date: 01/24/1996. (Used as reference only.)

159228 GS960108312313.002. 6/12/95 356 GPM Test in UE-25 C#3 with C#1 and C#2 Packed Off. Submittal date: 01/23/1996. (Used as reference only.)

159235 GS960808312315.001. Data Obtained from the Analysis of the Iodide-Tracer-Test Water Samples Collected During the 2/13/96 Convergent-Tracer Test Conducted at the C-Well Complex. Submittal date: 08/12/1996.

161273 GS970308312314.002. Water-Level Altitude Data from Four Wells in the Continuous Network, May through December, 1996. Submittal date: 03/13/1997.

107024 GS980608314221.002. Revised Bedrock Geologic Map of the Yucca Mountian Area, Nye County, Nevada. Submittal date: 06/09/1998.

147068 GS981008312314.002. Pump Test Data Collected at the C-Wells Complex 1/8/97-3/31/97. Submittal date: 10/28/1998.

144464 GS981008312314.003. Pumping Test Data Collected at the C-Well Complex, 5/7/96 – 12/31/96. Submittal date: 10/28/1998.

159238 GS990208312315.001. Tracer Recovery Data from Testing in the Prow Pass Interval. Submittal date: 02/11/1999.

140115 GS990408312315.002. Transducer, Barometric Pressure, and Discharge Data Collected from 4/18/98 through 11/24/98 in Support of the Ongoing Hydraulic and Tracer Tests Being Conducted at the UE-25 C-Well Complex, Nevada. Submittal date: 04/06/1999.

156043 LA0007PR831231.001. Bullfrog Reactive Tracer Test Data. Submittal date: 07/21/2000.

162623 LA0201JS831321.001. Alluvial Test Complex X-ray Diffraction Results. Submittal date: 01/16/2002.

162627 LA0201JS831341.001. Alluvial Test Complex Cation Exchange Capacity Batch Study, Wells 19D and 19P Alluvium; 10/31/00, 06/12/01, 08/12/01. Submittal date: 01/16/2002.

162629 LA0201JS831361.001. Alluvial Test Complex Column Study, Well 19D Alluvium and Water, 12/13/00. Submittal date: 01/24/2002.

166205 LA0201JS831361.005. Alluvial Test Complex Column Study, Well 19D Alluvium and Water, 02/22/01. Submittal date: 01/29/2002.

162630 LA0201JS831361.007. Alluvial Test Complex Column Study, Well 19D Alluvium and Water, 04/02/01. Submittal date: 01/29/2002.

162613 LA0201JS831421.001. Grain Size Analysis of Alluvium Samples from Wells 19D and 19P of the Alluvial Testing Complex. Submittal date: 01/30/2002.

162625 LA0201JS831421.002. BET Surface Area Measurements for 19D and 19P Alluvium Samples. Submittal date: 01/30/2002.

162431 LA0207PR831352.001. Microsphere Data from Single-Well Tracer Testing at NC-EWDP 19D1 (ATC). Submittal date: 07/30/2002.

162607 LA0212PR831231.001. Breakthrough Curves of Iodide in Saturated Fractured Cores from the C-Wells. Submittal date: 01/30/2003.

162608 LA0212PR831231.002. Breakthrough Curves of Sodium, Calcium, Copper, Iodide, and Chloride in Saturated Fractured Cores from the C-wells. Submittal date: 01/21/2003.

162609 LA0212PR831231.003. Breakthrough Curves of Lithium, Bromide, and PFBA in Saturated Fractured Cores from the C-wells. Submittal date: 01/21/2003.

166215 LA0212PR831231.005. Breakthrough Curves of Sodium, Iodide, Calcium, and Chloride in Saturated Fractured Cores from the C Wells. Submittal date: 01/21/2003.

162603 LA0301PR831231.001. Bromide and Lithium Abundance Data from Column Studies of Crushed Central Bullfrog Tuff, UE-25 C#2 at 2406 ft. with Filtered J-13 Water. Submittal date: 02/25/2003.

162628 LA0302JS831341.001. Final Cation Concentrations in Li/Br Batch Sorption Experiments Involving Alluvium from Wells NC-EWDP-19D and NC-EWDP-19P. Submittal date: 03/06/2003.

162605 LA0302PR831231.001. Batch Experiments to Measure Bromide and PFBA Sorption onto C-Wells Tuffs. Submittal date: 03/06/2003.

162604 LA0302PR831341.001. Cation Exchange Capacity Measurements on C-wells Tuffs Involving Displacement of Li and Other Cations by Cs. Submittal date: 03/06/2003.

162781 LA0303PR831232.001. Major Ion Chemistry of NC-EWDP-19D1 Waters Used in Batch Sorption and Column Transport Experiments. Submittal date: 03/12/2003.

129623 LA9909PR831231.004. Laboratory Data from C-Wells Core. Submittal date: 09/02/1999.

140134 LAPR831231AQ99.001. Prow Pass Reactive Tracer Test Field Data. Submittal date: 02/10/1999.

151524 MO0007MAJIONPH.011. Major Ion Content of Groundwater from Selected Yucca Mountain Project Boreholes Extracted from ANL-NBS-HS-000021, Geochemical and Isotopic Constraints on Groundwater Flow Directions, Mixing and Recharge at Yucca Mountain, Nevada. Submittal date: 07/27/2000. (Used as reference only.)

151530 MO0007MAJIONPH.013. Major Ion Content of Groundwater from Selected YMP and Other Boreholes Extracted from ANL-NBS-HS-000021, Geochemical and Isotopic Constraints on Groundwater Flow Directions, Mixing and Recharge at Yucca Mountain, Nevada. Submittal date: 07/27/2000. (Used as reference only.)

153371 MO0012CATECHOL.000. Cation Exchange Capacity Data of C-wells Tuff from UE-25 C#1 and UE-25 C#2. Submittal date: 12/05/2000.

159243 MO0012DIFFCHOL.000. Tracer Movement Measured in C/CO. The Unit C/CO Represents the Effluent Concentration Divided by the Injection Concentration. Submittal date: 12/05/2000.

153370 MO0012MINLCHOL.000. Mineral Abundance Data Using X-Ray Diffraction Analyses of C-Well Tuffs from UE-25 C#1 and UE-25 C#2. Submittal date: 12/05/2000.

153368 MO0012PERMCHOL.000. Permeability Data (Using Filtered J-13 Water) from UE-25 C#1, UE-25 C#2, and UE-25 C#3. Submittal date: 12/05/2000.

153376 MO0012POROCHOL.000. Porosity Data (Using Deionized Water) from UE-25 C#1, UE-25 C#2, and UE-25 C#3. Submittal date: 12/05/2000.

153375 MO0012SORBCHOL.000. Sorbing Element Concentration Data of J-13 and C-3 Well Water from UE-25 C#1 and UE-25 C#2. Submittal date: 12/05/2000.

163480 MO0105GPLOG19D.000. Geophysical Log Data from Borehole NC EWDP 19D. Submittal date: 05/31/2001.

157194 MO0107COV01057.000. Coverage: NCEWDPS. Submittal date: 07/18/2001. (Used as reference only.)

157184 MO0112DQRWLNYE.014. Well Completion Diagram for Borehole NC-EWDP-19P. Submittal date: 12/04/2001.

157187 MO0112DQRWLNYE.018. Well Completion Diagram for Borehole NC-EWDP-19D. Submittal date: 12/05/2001.

162617 MO0205UCC008IF.001. Concentration Dataset for 2,4-Difluorobenzoic Acid (2,4-DFBA) Tracer Used for the Feb/Mar 2002 Single-Well Tracer Test at the Alluvial Tracer Complex. Submittal date: 05/01/2002.

161274 MO0212SPANYESJ.149. Nye County Well ONC-1 Temperature and Pressure Data 03/01/1996 Through 12/22/1997. Submittal date: 12/09/2002.

165876 MO0306NYE05259.165. Revised NC-EWDP-19IM1 Well Completion Diagram. Submittal date: 07/02/2003.

165877 MO0306NYE05260.166. Revised NC-EWDP-19IM2 Well Completion Diagram. Submittal date: 07/02/2003.

164527 MO0307SEPFEPS4.000. LA FEP List. Submittal date: 07/31/2003. (Used as reference only.)

164821 MO0308SPATRCRC.000. Concentration Data for "2,3,4,5-Tetrafluorobenzoic Acid" Used for Tracer Testing at the C-Well Complex. Submittal date: 08/19/2003.

162614 UN0102SPA008KS.003. Concentration Dataset for Tracers (2,6-Difluorobenzoic Acid and Iodide) Used for 48-Hour Shut-in Tracer Test at the Alluvial Tracer Complex in Nye County. Submittal date: 06/11/2001.

162442 UN0109SPA008IF.006. Concentration Dataset for Tracers (2,4-Difluorobenzoic Acid and Chloride) Used for the 30-Day Shut-in Tracer Test at the Alluvial Tracer Complex in Nye County, Nevada. Submittal date: 09/28/2001.

162681 UN0109SPA008KS.005. Concentration Data Set for Tracers (2,6-Difluorobenzoic Acid And Iodide) Used For The 48 Hour Shut-In Test at the Alluvial Tracer Complex in Nye County, Nevada, in Samples Collected During the Period 02/27/01 through 04/25/01. Submittal date: 09/21/2001.

162615 UN0109SPA008KS.007. Concentration Dataset for Tracer (Pentafluorobenzoic Acid) Used for the 30-Day Shut-in Tracer Test at the Alluvial Tracer Complex in Nye County, Nevada. Submittal date: 09/21/2001.

162616 UN0109SPA008KS.008. Concentration Dataset for Tracer (Bromide) Used for the 30-Day Shut in Tracer Test at the Alluvial Tracer Complex in Nye County, Nevada. Submittal date: 09/21/2001.

8.5 OUTPUT DATA, LISTED BY DATA TRACKING NUMBER

GS030208312314.001. Filtered Water Level Data for UE-25 ONC-1. Submittal date: 02/28/2003.

GS030208312314.002. Filtered Water Level Data For USW-H4, UE-25 WT#3 and UE-25 WT#14. Submittal date: 02/28/2003.

GS031008312314.004. Hydraulic Parameters from Analysis of Hydraulic Tests Conducted in the Fractured Tuff at the C-hole Complex from 1995 to 1999. Submittal date: 10/09/2003.

GS031008312315.002. Transport Parameters from Analysis of Conservative (Non-Sorbing) Tracer Tests Conducted in the Fractured Tuff at the C-hole Complex from 1996 to 1999. Submittal date: 10/09/2003.

GS031008312316.002. Hydraulic Parameters from Analysis of Hydraulic Tests Conducted in the Alluvium at the Alluvial Testing Complex (ATC), and Total Porosity from Grain-size Distribution and from Background Monitoring. Submittal Date: 10/09/2003.

GS031008312316.003. Transport Parameters and Specific Discharge from Analysis of Single-Hole Tracer Tests Conducted in the Alluvium at the Alluvial Testing Complex (ATC), and Total Porosity from the Borehole-Gravimetry Survey at NC-EWDP-19D1. Submittal Date: 10/09/2003.

LA0303PR831231.001. Simulations Conducted to Predict Tracer Responses from Single-Well and Cross-Hole Tracer Tests at the Alluvial Testing Complex. Submittal date: 03/20/2003.

LA0303PR831231.002. Estimation of Groundwater Drift Velocity from Tracer Responses in Single-Well Tracer Tests at the Alluvial Testing Complex. Submittal date: 03/18/2003.

LA0303PR831231.003. Solute Data From ER-20-6#3 in the BULLION Forced-Gradient Field Tracer Test At The ER-20-6 Wells at NTS. Submittal date: 02/03/2003.

LA0303PR831231.004. Simulations Conducted to Generate a Spreadsheet that can be Used for Predictions of Mean, Peak, and First Tracer Arrival Times in Field Tracer Tests. Submittal date: 04/08/2003.

LA0303PR831231.005. Simple Calculations for SZ In-Situ Testing AMR. Submittal date: 03/19/2003.

LA0303PR831352.001. Calculations to Determine Detachment Rate Constant of Microspheres in a Single-Well Tracer Test in Saturated Alluvium. Submittal date: 03/31/2003.

LA0303PR831341.001. Calculations and Plots Associated with C-wells Cation Exchange Capacity Measurements. Submittal date: 04/08/2003.

LA0303PR831341.002. Model Interpretations of Alluvium Testing Complex Lithium Sorption Experiments. Submittal date: 04/16/2003.

LA0303PR831341.003. Model Interpretations of C-wells Lithium Sorption Experiments. Submittal date: 04/16/2003.

LA0303PR831361.002. Model Interpretations of ATC Alluvium-Packed Column Transport Experiments. Submittal date: 04/16/2003.

LA0303PR831361.003. Model Interpretations of C-wells Crushed Rock Column Experiments. Submittal date: 04/16/2003.

LA0303PR831361.004. Model Interpretations of C-wells Fractured Core Transport Experiments. Submittal date: 04/02/2003.

LA0303PR831362.001. Model Interpretations of C-wells Diffusion Cell Experiments. Submittal date: 04/02/2003.

LA0304PR831231.001. C-wells Tracer Test Sensitivity Calculations. Submittal date: 04/17/2003.

SN0302T0502203.001. Saturated Zone Anisotropy Distribution Near the C-wells. Submittal date: 02/26/2003.